ISSN 2367-7570

Workshop
"Solar Influences on the Magnetosphere, Ionosphere and Atmosphere"

Book
of
Proceedings

Eighteenth Workshop
June, 2026

Organized by:
Space Research and Technology Institute
Bulgarian Academy of Sciences

Editorial Board

Katya Georgieva (Space Research and Technology Institute, Sofia, Bulgaria) - Editor-in-Chief
Atila Özgüç (Boğaziçi University, Kandilli Observatory, Istanbul, Türkiye)
Crisan Demetrescu (Institute of Geodynamics, Romanian Academy)
Dragan Roša (Zagreb Astronomical Observatory, Croatia)
Jean-Pierre Rozelot (Université Côte d'Azur, France)
Nat Gopalswamy (NASA Goddard Space Flight Center, USA)
Olga Malandraki (IAASARS, National Observatory of Athens, Greece)
Petra Koucká-Knižová (Institute of Atmospheric Physics, Czech Academy of Sciences, Czech Republic)
Vladimir Obridko (IZMIRAN, Moscow, Russian Federation)

Editors: Katya Georgieva, Boian Kirov, Simeon Asenovski

Scientific Organizing Committee

Katya Georgieva (Space Research and Technology Institute, Sofia, Bulgaria) – *Chair*
Atila Özgüç (Boğaziçi University, Kandilli Observatory, Istanbul, Türkiye)
Crisan Demetrescu (Institute of Geodynamics, Romanian Academy, Romania)
Dragan Roša (Zagreb Astronomical Observatory, Croatia)
Jean-Pierre Rozelot (Université Côte d'Azur, France)
Ke Wang (Technology and Engineering Center for Space Utilization, Chinese Academy of Sciences, China)
Nat Gopalswamy (NASA Goddard Space Flight Center, USA)
Olga Malandraki (IAASARS, National Observatory of Athens, Greece)
Petra Koucká-Knižová (Institute of Atmospheric Physics, Czech Academy of Sciences, Czech Republic)
Vladimir Obridko (IZMIRAN, Moscow, Russian Federation)

Preface

The Eighteenth International Workshop "Solar Influences on the Magnetosphere, Ionosphere and Atmosphere" was held on June 8–12, 2026, in Primorsko, Bulgaria.

The scientific program featured 40 oral presentations and 29 posters covering a broad range of topics in solar physics, solar–terrestrial relations, space weather, the magnetosphere, ionosphere, atmosphere, and related observational and modelling studies. A special session dedicated to space science and utilization aboard the China Space Station was also included in the program.

These Proceedings include peer-reviewed contributions selected from the works presented at the Workshop. The Scientific Organizing Committee and the Editors of the Proceedings thank all participants for their valuable contributions and lively discussions, and the session chairs for their dedication in shaping a stimulating scientific program.

We are grateful to our hosts in Primorsko and to all colleagues who contributed to the organization and successful realization of the Workshop.

DOI: 10.31401/WS.2026.proc

CONTENTS

Sun and Solar Activity

Asenovski S.N., Georgieva K., Kirov B., Kilcik A., Gerçeker K., Calisir M. **Solar-Cycle Evolution in a Dimensionless Sun–Heliosphere–Earth State Space** 01
Boneva D.B., Yankova Kr., Dimitrijević M.S., Rusev D. **Sources and Mechanisms of Activity of the Solar-Type Dwarf Star 61 Cyg A** 10
Dorovskyy V.V., Melnik V.N., Shevchuk M.V. **Radio Manifestations of the CME Occurred on 21 August 2015** 18
Gopalswamy N., Yashiro S., Makela P., Xie H., Akiyama S. **Solar Energetic Particle Events of Cycles 23-25** 27
Kilcik A., Calisir M., Ozguc A. **Chaotic Behavior of Selected Solar and Geomagnetic Activity Indices during the Last Three Solar Cycles** 34
Kirov B., Georgieva K., Kirov B.B, Asenovski S. **Relationship between Sunspot Number, Sunspot Magnetic Field Strength, CME Activity, and Geomagnetic Storms during Solar Cycle 24** 43
Koleva K., Duchlev P., Nacheva Y. **Kinematics of the Prominence Eruption on May 27, 2013 Observed from Three Viewpoints** 51
Melnik V.M., Dorovskyy V.V., Shergelashvili B.M. **A Model of Non-Isothermal Solar Corona** 57
Muraközy J. **Variation in the Tilt Angle of Sunspot Groups During Their Lifetimes** 64
Podgorny A.I., Podgorny I.M. **Main Magnetic Lines of the Pre-flare Arcade Surface with Increased Current Density: Analysis of the Field Configuration Obtained by MHD Simulation to Determine the Position of the Solar Flare** 74
Şahin S. **Statistical Study of Type-II Spicules Utilizing Chromospheric Imaging Data from the Goode Solar Telescope** 80
Semkova J., Bankov N., Benghin V., Dachev Ts., Drobyshev S., Georgiev G., Golovin D., Gopalswamy N., Jordanova M., Koleva R., Krastev K., Litvak M., Lukyanov N., Maltchev St., Matviichuk Yu., Mitrofanov I., Mokrousov M., Sanin A., Shurshakov V., Tomov B. **Multi-Spacecraft and Multi-Instrument Observations of the Martian Radiation Environment During Solar Cycles 24 and 25** 92
Yankova K.D., Dimitrijević M.S., Srećković V.A., Vujčić V. **Solar-Like Corona of the Thin Disk in the AGN** 103

Solar Wind-Magnetosphere-Ionosphere Interactions

Bojilova R., Mukhtarov P. **Verification of Empirical Models for Forecasting Critical Ionospheric Frequencies in the Conditions of Geomagnetic Storms on 12- 13 November 2025** 107
Gromova L.I., Kleimenova N.G., Gromov S.V., Malysheva L.M. **Extremely Space Weather Events of May and October 2024: High-Latitude Geomagnetic Disturbances** 114
Guineva V., Raykova L., Werner R. **Geomagnetic effects of the substorms during the superstorm on 10-13 May 2024 on the midlatitudes magnetic field, observed at the Bulgarian station Panagyurishte** 122
Komendant V.H. **Statistical Analysis of the B-star Drag Term and Solar, and Geomagnetic Activity Indices** 133
Raykova L., Guineva V. **Geomagnetic Substorm Signatures at Mid-Latitudes: The March 23, 2023 Case Study from Geomagnetic Station Panagyurishte** 145

Tsvetkov Ts., Petrov N., Minev M. **Case Study of the First Forbush Decrease Detected by MNM ROZH Station** 157
Werner R. **Development of the Total Ozone Column over Sofia Between 1979 and 2022** 167

Instrumentation for Space Weather Monitoring

Dachev T.P., Tomov B.T., Matviichuk Yu.N., Dimitrov P.G., Mitev M.M., Jordanova M.M., Semkova J.V., Koleva R.T., Malchev St., Bankov N.G., Mitrofanov I., Golovin D., Litvak M., Sanin A., Shurshakov V., Benghin V., Ivanova O., Ploc O., Kubancak J., Häder D.-P., Lebert M., Schuster M., Reitz G., Horneck G., Uchihori Y., Kitamura H., Tobiska W., Hogan B., Gersey B., Okuyama K-I., Tapia I., Fajardo I., Saganti P. **Bulgarian Instruments for Aircraft, Space and Ground Based Radiation Dosimetry and Their Main Scientific Results** 179
Georgiev G., Simeonov R. **Prototype Evaluation of an Open SDR-Based Framework for Long-Term VOR Signal Observations** 192
Minev M., Petrov N., Tsvetkov Ts. **Ground-Based Monitoring of Global Solar Radiation and Ultraviolet Irradiance at NAO Rozhen** 200
Nikolov I.D. **Exploring the Impact of Solar Activity and Other Physical Events in the Troposphere and Stratosphere by Using Research Balloon with Autonomously Returning Unmanned Aerial Vehicle** 211
Nikolov N.D. **Atmospheric Dosimetry** 216
Ognianov O.D. **Complex Observation of the Ionosphere for Enhanced Satellite Trajectory Planning** 227

Solar Influences on the Lower Atmosphere and Climate

Ivanova E., Koleva K. **From Space to Land: Impact of Two Large Solar Events on Key Climate Indicators from Land Surface Stations Globally** 236
Potužníková K., Koucká Knížová P. **Sporadic E and Ionospheric Variability During Different Tropospheric Gravity-Wave Source Events** 245
Tonev P. **Examination of Extremely Big Mesospheric Electric Fields from Rocket-Borne Measurements on October 21 1989** 252
Veretenenko S.V., Koval A.V. **Influence of strong Solar Proton Events of the 23rd Solar Cycle on the High-Latitudinal Atmosphere of the Northern Hemisphere** 259

Data Processing and Modelling

Bachev R., Strigachev A., Dechev M. **Photometric Reverberation Mapping Through Theory-Agnostic Fitting of the Light Curves** 266
Krastev K. **Numerical Analysis of Genuine and Secondary-Induced Events in the Liulin-MO Telescope aboard ExoMars Trace Gas Orbiter** 271
Simić Z., Samurović S., Pavlović R., Cvetković Z., Damljanović G. **Light Pollution - New Measurements: The UrbObsBel Project** 282
Zolnikova N.N., Shkevov R., Mikhailovskaya L.A. **Some Examples of Reflectionless Propagation of Electromagnetic Waves in Nonuniform Space Plasma** 287

Solar Effects in the Biosphere and Lithosphere

Jelev G., Ivanova I., Tsvetkova M., Zhelezov G., Benderev A., Gerginov P., Chanev M. **Determining the Influence of Solar Radiation on the Dynamics of Lake Srebarna's Water Surface Area through Remote Sensing** 293

Tsvetkova M., Filchev L., Chanev M. **Deep Learning Architectures for Monitoring Spruce Forest Health via Sentinel-2 Multi-Spectral Data: A Review of Current Trends** 303

DOI: 10.31401/WS.2026.proc.01

Solar-Cycle Evolution in a Dimensionless Sun–Heliosphere–Earth State Space

Asenovski S.N.[1], *Georgieva K., Kirov B., Kilcik A.*[2], *Gerçeker K.*[2], *Calisir M.*[2]

[1]Space Research and Technology Institute – Bulgarian Academy of Sciences, Sofia, Bulgaria
asenovski@space.bas.bg
[2]Department of Space Science and Technologies, Akdeniz University Faculty of Science, 07058 Antalya, Turkey
alikilcik@akdeniz.edu.tr

Abstract

The solar cycle is usually described by individual activity indices, although the physical state of the Sun–heliosphere–Earth system is determined simultaneously by photospheric activity, the large-scale solar magnetic configuration, interplanetary conditions, and the geomagnetic response. We introduce a dimensionless five-component state vector constructed from the sunspot number (SSN), heliospheric current-sheet (HCS) tilt, interplanetary magnetic-field magnitude B, solar-wind speed VSW, and the geomagnetic ap index. After common standardization and 13-month smoothing, solar cycles 21–24 are represented as trajectories in a multidomain state space. Principal-component analysis shows that the first two components account for about 91% of the total variance, indicating a strongly organized low-dimensional structure. A crossing-based metric is then introduced to compare rising and declining states at equivalent normalized SSN levels. The resulting rising–declining separation is largest for solar cycle 23 and demonstrates that equal photospheric activity does not imply an equal heliospheric and geomagnetic state. Component decomposition shows that the physical origin of this separation is cycle dependent; during cycle 23 it is dominated by solar-wind speed over a broad range of activity levels. The principal results remain stable for smoothing windows between 9 and 25 months and under leave-one-out tests of the state-vector components. The approach provides a compact geometric description of solar-cycle evolution and a quantitative framework for studying phase-dependent solar-terrestrial coupling.

Keywords: solar cycle; solar wind; heliospheric current sheet; geomagnetic activity; state space; principal-component analysis; solar-terrestrial relations

1. Introduction

Solar activity is commonly represented by the sunspot number or related photospheric proxies, but the state of near-Earth space is not a one-parameter response to photospheric activity. The heliospheric magnetic field, solar-wind plasma, and geomagnetic activity evolve with their own characteristic amplitudes and phase relationships. Long-term studies have shown that solar-wind and geomagnetic parameters are not all in phase with the sunspot cycle, and that weak and strong solar cycles can produce substantially different solar-wind–magnetosphere coupling [Hajra, 2021]. In particular, high-speed solar-wind streams associated with coronal holes become important during declining phases and can maintain recurrent geomagnetic forcing even when sunspot activity is already decreasing [Tsurutani et al., 2011; Verbanac et al., 2011; Grandin et al., 2019].

Solar cycle 23 provides an especially clear example of this non-equivalence between photospheric and heliospheric states. Its late declining phase contained persistent high-speed streams associated with long-lived coronal holes, while the subsequent minimum was characterized by unusually weak polar fields and low heliospheric magnetic and plasma pressure [Luhmann et al., 2009; Tulasi Ram et al., 2010]. Comparisons of cycles 23 and 24

likewise show that weaker interplanetary magnetic fields and reduced solar-wind driving during cycle 24 were accompanied by substantially weaker geomagnetic activity [Rawat et al., 2018; Manu et al., 2023]. These results motivate a description in which photospheric, heliospheric, interplanetary, and geomagnetic quantities are treated jointly rather than as separate time series.

Multivariate methods provide a natural way to search for such organization. Principal-component analysis (PCA) has been used in solar and geomagnetic studies to identify dominant modes and to separate physically distinct contributions [Mursula and Holappa, 2018]. However, the purpose here is not only dimensionality reduction. We construct a common dimensionless state vector and interpret solar-cycle evolution geometrically as a trajectory through a multidomain state space. This allows us to ask whether two epochs with the same normalized SSN can nevertheless correspond to different states of the coupled Sun–heliosphere–Earth system.

The objectives of this work are therefore: (i) to define a compact dimensionless multidomain state vector; (ii) to determine its effective dimensionality; (iii) to compare the state-space trajectories of solar cycles 21–24; and (iv) to quantify the separation between rising and declining states at equivalent levels of photospheric activity. Robustness is examined by varying the smoothing timescale and by removing individual state-vector components.

2. Data and Method

2.1. Multidomain data set

Five monthly parameters are used to represent successive physical domains of the solarterrestrial system: the international sunspot number (SSN), HCS tilt angle, interplanetary magnetic-field magnitude B, solar-wind speed VSW, and the planetary geomagnetic ap index. The SSN data were obtained from SILSO, the HCS tilt angle from the Wilcox Solar Observatory, and B, VSW, and ap from the OMNI2 database. SSN represents photospheric activity; HCS tilt describes the large-scale heliospheric magnetic configuration; B and VSW characterize near-Earth interplanetary conditions; and ap represents the global geomagnetic response. The common analysis interval covers complete solar cycles 21–24, bounded by the successive sunspot minima in March 1976, September 1986, August 1996, December 2008, and December 2019. The monthly series were placed on a common time grid and smoothed using a centered 13-month running window for the reference analysis.

2.2. Dimensionless state vector

Because the five variables have different physical units and numerical ranges, direct Euclidean distances would be dominated by variables with the largest dimensional variance. Each smoothed series is therefore standardized using its mean μ_i and standard deviation $\sigma_{i:}$ over the common interval:

$$z_i(t) = \frac{[x_i(t) - \mu_i(t)]}{\sigma_i}, \quad i = 1,...,5. \tag{1}$$

The multidomain state is then defined as:

$$z(t) = [\, z_{SSN}(t),\, z_{HCS}(t),\, z_B(t),\, z_V(t),\, z_{ap}(t) \,]. \tag{2}$$

All coordinates are dimensionless and have comparable statistical scale. The trajectory Z(t) therefore describes the simultaneous evolution of the selected domains rather than the amplitude of any one dimensional quantity.

2.3. Principal-component representation

PCA is applied to the standardized five-dimensional matrix. The principal-component scores provide an orthogonal reduced representation of the state trajectory, while the loadings quantify the contribution of the original coordinates. The first two components are used for state-space visualization because together they explain about 91% of the total variance in the reference 13-month analysis.

2.4. Rising–declining state separation

To compare the two phases without imposing equal calendar times, the smoothed SSN of each cycle is converted to a normalized activity coordinate S between the cycle minimum and maximum. For each selected S level, the first upward crossing on the rising branch and the last downward crossing on the declining branch are identified. Linear interpolation gives the corresponding multidomain states $Z_{rise}(S)$ and $Z_{decline}(S)$. Their separation is:

$$D_{RD}(S) = \| \mathrm{z}_{\mathrm{rise}}(\mathrm{S}) - \mathrm{z}_{\mathrm{decline}}(\mathrm{S}) \| . \quad (3)$$

Because the two states are matched at the same SSN level, the SSN coordinate contributes approximately zero to this distance. The metric therefore measures the degree to which the remaining heliospheric, interplanetary, and geomagnetic state differs between the rising and declining phases.

The squared distance can be decomposed into coordinate contributions:

$$D_{RD}{}^{2}(S) = \sum_i [\mathrm{z}_{\mathrm{i,\,rise}}(\mathrm{S}) - \mathrm{z}_{\mathrm{i,\,decline}}(\mathrm{S})]^2 . \quad (4)$$

Relative contributions are obtained by dividing each squared coordinate difference by $D_{RD}{}^{2}$. This decomposition is used to identify which physical domain carries the phase asymmetry in each cycle.

2.5. Trajectory length and state-space evolution rate

The length of each solar-cycle trajectory is calculated as the cumulative Euclidean displacement between consecutive monthly states:

$$L = \sum_{k=1}^{N-1} \left\| Z(t_{k+1}) - Z(t_k) \right\| . \quad (5)$$

The instantaneous state-space evolution rate is defined as:

$$v(t_k) = \frac{Z(t_{k+1}) - Z(t_k)}{t_{k+1} - t_k} \quad (6)$$

and the mean evolution rate for a given solar cycle is obtained by averaging $v(tk)$ over all monthly intervals within that cycle. These quantities describe how far and how rapidly the multidomain state evolves through the standardized state space.

2.6. Robustness tests

Two robustness tests are performed. First, the complete analysis is repeated with smoothing windows of 9, 13, 17, and 25 months. Second, leave-one-out configurations are constructed by removing SSN, HCS tilt, IMF B, VSW, or ap from the distance calculation and PCA. These tests determine whether the reduced dimensionality and rising–declining separation depend critically on the reference smoothing timescale or on a single state coordinate.

3. Results

3.1. Evolution of the dimensionless state components

The standardized components (Figure 1) exhibit the common solar-cycle modulation but also substantial differences in timing and shape. SSN and HCS tilt show the clearest broad solar-cycle organization, whereas VSW and ap contain stronger intermediate-timescale structure. In particular, elevated solar-wind speed can persist into declining phases after photospheric activity has already decreased. This behavior is consistent with the known importance of recurrent coronal-hole high-speed streams during declining phases [Tsurutani et al., 2011; Verbanac et al., 2011; Grandin et al., 2019].

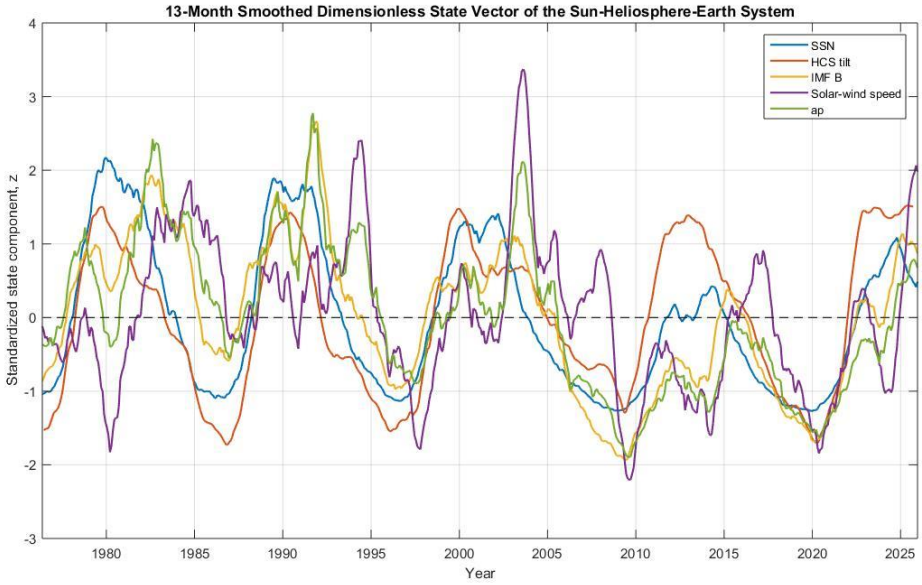
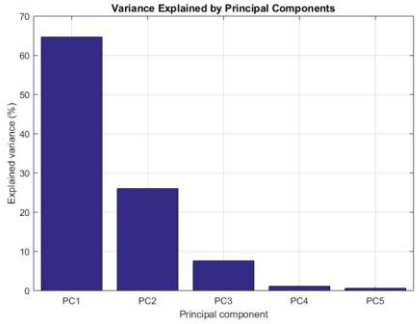


Figure 1. *Thirteen-month smoothed components of the dimensionless multidomain state vector. Each parameter is standardized over the common analysis interval.*

3.2. Effective dimensionality

The first principal component explains approximately 65% of the total variance and the second approximately 26%, so that PC1 + PC2 account for about 91% of the five-dimensional variability (Figure 2). The third component raises the cumulative explained variance to about 98%. Thus, despite combining parameters from distinct physical domains, the long-term evolution is strongly organized in a low-dimensional subspace.



Parameter	PC1	PC2	PC3
SSN	0.476	−0.417	−0.171
HCS tilt	0.387	−0.519	0.644
IMF B	0.532	0.044	−0.385
Solar-wind speed	0.308	0.658	0.574
ap	0.496	0.350	−0.281

Figure 2. *Fraction of the total standardized variance explained by the principal components of the five-dimensional state vector.*

For the reference analysis, the loadings of PC1 are 0.476 (SSN), 0.387 (HCS tilt), 0.532 (IMF B), 0.308 (VSW), and 0.496 (ap). All have the same sign, suggesting that PC1 primarily represents a broad common activity/coupling mode. PC2 has loadings −0.417 (SSN), −0.519 (HCS tilt), 0.044 (IMF B), 0.658 (VSW), and 0.350 (ap), and therefore separates solar-wind/geomagnetic behavior from the photospheric and large-scale magnetic configuration. A comparable role of high-speed solar wind in secondary PCA modes of geomagnetic variability has been reported by Mursula and Holappa (2018).

3.3. Solar-cycle trajectories in reduced state space

Projection onto PC1–PC2 transforms each solar cycle into a trajectory rather than a single amplitude curve (Figure 3). To make the cycle-to-cycle differences more visible, SC21–SC24 are shown in separate panels using identical PC1 and PC2 scales. The trajectories occupy overlapping but non-identical regions of the reduced state space and differ substantially in their geometry and spatial extent. In particular, SC23 describes a broad trajectory extending toward high positive PC1 and PC2 values, whereas SC24 remains confined to a considerably more compact region.

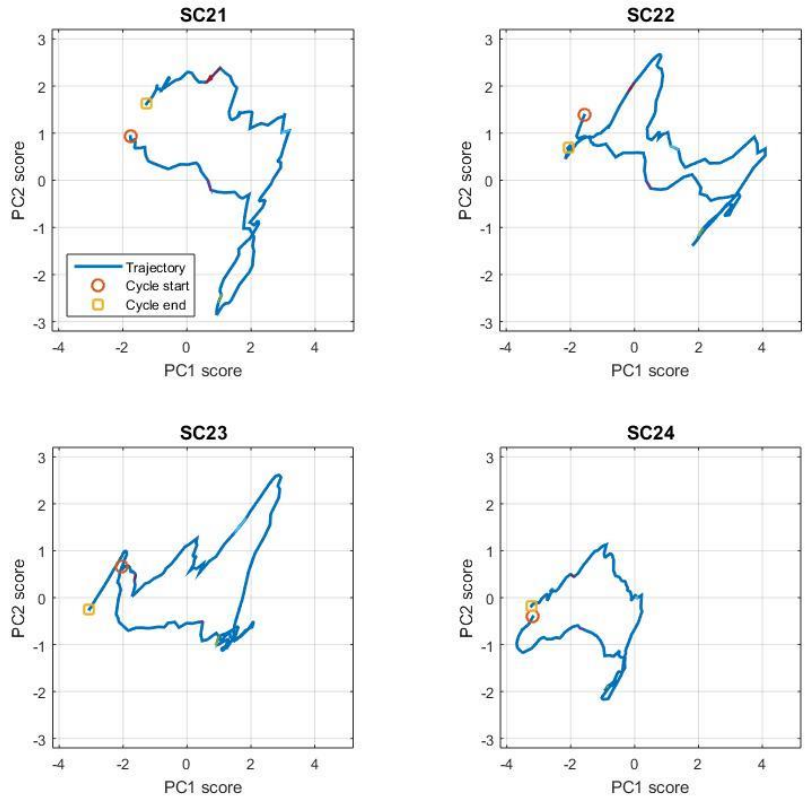


Figure 3. *Solar-cycle trajectories for SC21–SC24 projected onto the PC1–PC2 reduced state space. Each solar cycle is shown separately using identical axis limits to facilitate direct comparison. Circles and squares indicate the beginning and end of each cycle, respectively.*

The trajectories also indicate that the system does not generally retrace the same path during the rising and declining portions of a cycle. This provides a geometric indication of a phase-dependent multidomain state: similar levels of photospheric activity may correspond to different heliospheric, interplanetary, and geomagnetic conditions depending on the phase of the solar cycle. This behavior is not equivalent to the familiar double-peaked structure of SSN, because the reduced coordinates simultaneously incorporate the large-scale heliospheric

magnetic configuration, interplanetary magnetic-field strength, solar-wind speed, and geomagnetic response.

3.4. Rising–declining asymmetry at equivalent SSN

The crossing-based metric makes the phase asymmetry quantitative (Figure 4). At the same normalized SSN level, the multidomain state on the rising branch generally differs from that on the declining branch. The mean separation is largest for SC23, about 2.7 standardized state-space units for the 13-month reference smoothing. SC21 shows an intermediate mean separation near 2.0, while SC22 and SC24 are lower, near 1.6–1.8. Thus, equivalent photospheric activity does not imply equivalent heliospheric or geomagnetic conditions.

This result is physically plausible in view of the strong phase dependence of solar-wind sources. Recurrent high-speed streams and associated interaction regions are particularly important in declining phases, and cycle 23 exhibited persistent and geoeffective high-speed-stream structures during its decline (Tsurutani et al., 2011; Verbanac et al., 2011; Tulasi Ram et al., 2010). The state-space result generalizes this behavior by measuring the simultaneous difference across several domains rather than comparing a single solar-wind or geomagnetic parameter.

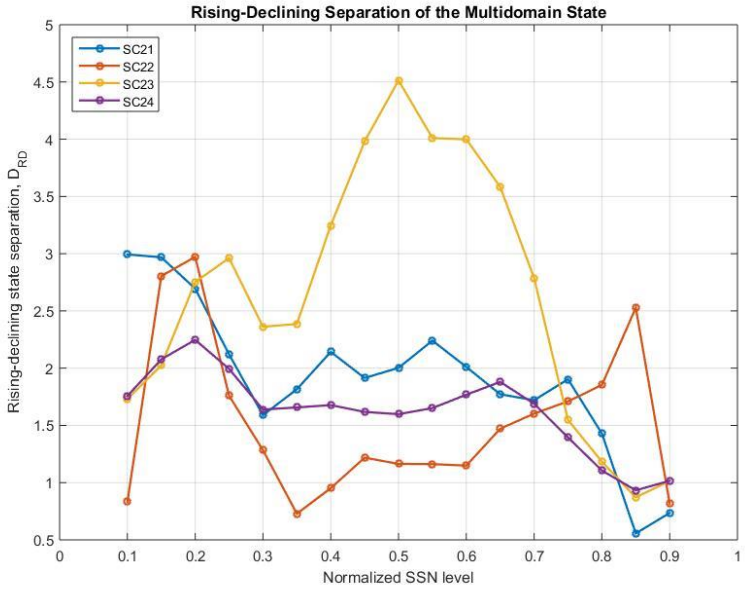


Figure 4. *Rising–declining state separation D_{RD} as a function of normalized SSN level for solar cycles 21–24.*

3.5. Physical composition of the phase separation

The component decomposition shows that the source of the rising–declining separation is not universal. Averaged over the central activity range $0.30 \leq S \leq 0.70$, SC21 has a mixed contribution with a substantial solar-wind-speed term; SC22 has a stronger geomagnetic ap contribution; SC23 is overwhelmingly dominated by VSW; and SC24 shows a comparatively large IMF B contribution (Figure 5). For SC23, VSW accounts for roughly three quarters of D_RD^2 over much of the central activity range, while the IMF B contribution is small there.

The dominance of VSW in SC23 is consistent with independent studies of its declining phase. Luhmann et al. (2009) related the high-speed wind structure to persistent coronal holes and the unusual large-scale solar magnetic field. Grandin et al. (2019) found that SIR/HSS occurrence and velocity peaked in the late declining phase of SC23. These results provide a

physical basis for the large state-space displacement carried by the solar-wind-speed coordinate.

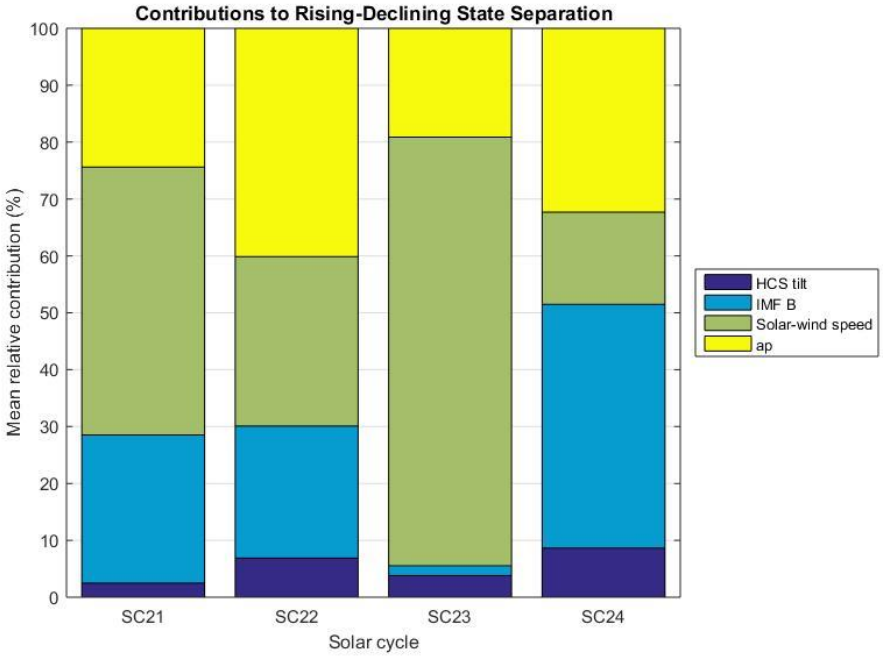


Figure 5. *Mean relative contributions of HCS tilt, IMF B, solar-wind speed, and ap to D_{RD}^{2} over 0.30 ≤ normalized SSN ≤ 0.70.*

The leave-one-out analysis confirms that solar-wind speed is the main contributor to the rising–declining state separation, particularly in SC23: removing V_{SW} reduces its mean separation to approximately 52% of the full-state value (Figure 6). Removing SSN has almost no effect, as expected from matching the two phases at equivalent SSN levels.

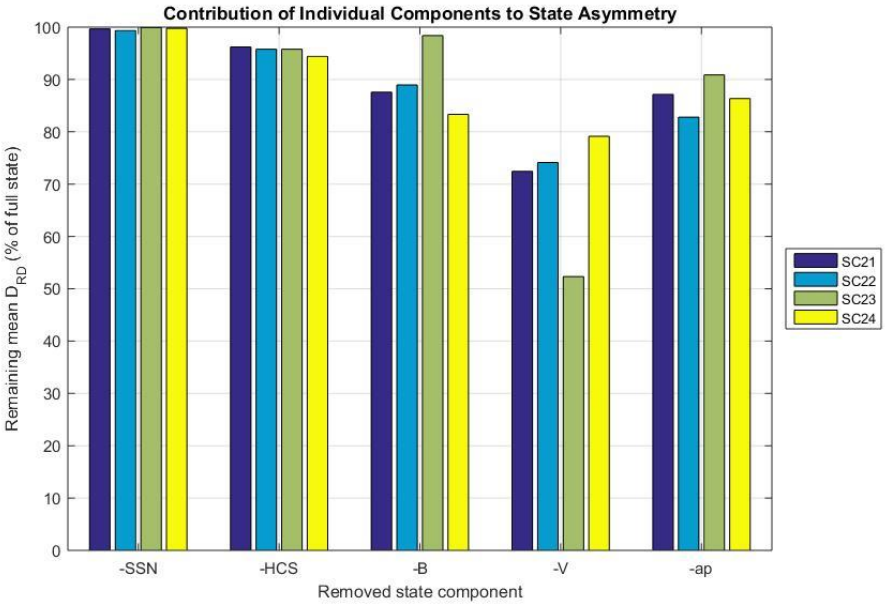


Figure 6. *Leave-one-out sensitivity of the mean rising–declining separation. Values are expressed as a percentage of the full-state D_{RD} for each solar cycle.*

4. Discussion

The main result of the present analysis is that solar-cycle evolution can be represented compactly as motion through a common dimensionless state space. The strong concentration of variance in two principal components indicates that the selected photospheric, heliospheric, interplanetary, and geomagnetic parameters do not evolve independently on solar-cycle timescales. Instead, they form an organized low-dimensional pattern. This should not be interpreted as evidence that the physical system itself has only two degrees of freedom; rather, it shows that the long-term covariance of these five observables is strongly constrained.

A second result is the systematic difference between rising and declining states at the same SSN level. In this sense, the trajectory displays a hysteresis-like geometry: the system state depends not only on the instantaneous level of photospheric activity but also on the phase through which that level is reached. We use the term 'hysteresis-like' descriptively rather than implying a specific thermodynamic or dynamical hysteresis mechanism. The physical origin is consistent with known phase-dependent changes in coronal-hole occurrence, high-speed streams, heliospheric magnetic structure, and solar-wind–magnetosphere coupling [Tsurutani et al., 2011; Verbanac et al., 2011; Grandin et al., 2019].

Cycle 23 is the clearest example. Its state-space separation is both larger than in the other cycles and strongly carried by the solar-wind-speed coordinate. The result is consistent with the unusual persistence of high-speed streams during the declining phase and the subsequent extended minimum. Importantly, the large separation is not produced by SSN itself: removing SSN from the state-distance calculation leaves the result essentially unchanged. This confirms that SSN acts here as the phase-matching coordinate, whereas the asymmetry resides in the other domains.

Cycle 24 illustrates a different aspect of the framework. Previous studies have documented its weaker heliospheric conditions and reduced geomagnetic activity relative to cycle 23 [Rawat et al., 2018; Hajra et al., 2021; Manu et al., 2023]. In the present representation, SC24 also has the smallest trajectory length and the lowest mean state-space evolution rate in the reference analysis. Although those dynamical metrics are not required to define D_{RD}, they support the view that SC24 occupied a comparatively weak and slowly evolving multidomain regime.

The present state vector is intentionally compact. Other coordinates, such as solar-wind dynamic pressure, IMF Bz, AE, Dst, polar magnetic field strength, or coronal-hole measures, could be added in future work. Increasing the number of coordinates, however, would change both the statistical geometry and the physical interpretation of Euclidean distance. The five-variable construction used here should therefore be regarded as a minimal multidomain representation rather than a unique or complete state description.

5. Conclusions

- A five-component dimensionless vector combining SSN, HCS tilt, IMF B, solar-wind speed, and ap provides a common geometric representation of solar-cycle evolution across the Sun–heliosphere–Earth system.
- The first two principal components explain about 91% of the total variance in the reference analysis, and this low-dimensional organization remains stable for smoothing windows from 9 to 25 months and in leave-one-out tests.
- Solar cycles 21–24 follow distinct trajectories in the reduced state space and do not generally retrace the same path during their rising and declining phases.
- At equivalent normalized SSN levels, rising and declining phases occupy different multidomain states. The mean separation is strongest for SC23.

- The physical composition of the separation is cycle dependent. In SC23, solar-wind speed is the dominant contributor over a broad range of activity levels, consistent with the importance of recurrent high-speed streams during its declining phase.
- The state-space approach provides a compact framework for comparing solar cycles and for quantifying phase-dependent solar-terrestrial coupling beyond a single solar-activity index.

Acknowledgements

This work was supported by the bilateral research project "Nonlinear Prediction of Space Weather and Solar Activity Parameters", Project No. IC-TR/12/2024-26, within the scientific cooperation between the Bulgarian Academy of Sciences (BAS) and the Scientific and Technological Research Council of Türkiye (TÜBİTAK), with the corresponding TÜBİTAK project No. 124N011.

References

Grandin, M., Aikio, A. T., and Kozlovsky, A. (2019). Properties and geoeffectiveness of solar wind high-speed streams and stream interaction regions during solar cycles 23 and 24. *Journal of Geophysical Research: Space Physics*, 124(6), 3871–3892. https://doi.org/10.1029/2018JA026396

Hajra, R., Marques de Souza Franco, A., Echer, E., and Bolzan, M. J. A. (2021). Long-term variations of the geomagnetic activity: A comparison between the strong and weak solar activity cycles and implications for the space climate. *Journal of Geophysical Research: Space Physics*, 126, e2020JA028695. https://doi.org/10.1029/2020JA028695 Wiley Online Library

Luhmann, J. G., Lee, C. O., Li, Y., Arge, C. N., Galvin, A. B., Simunac, K., Russell, C. T., Howard, R. A., and Petrie, G. (2009). Solar wind sources in the late declining phase of Cycle 23: Effects of the weak solar polar field on high speed streams. *Solar Physics*, 256, 285–305. https://doi.org/10.1007/s11207-009-9354-5

Manu, V., Balan, N., Zhang, Q.-H., and Xing, Z.-Y. (2023). Double superposed epoch analysis of geomagnetic storms and corresponding solar wind and IMF in solar cycles 23 and 24. *Space Weather*, 21, e2022SW003314. https://doi.org/10.1029/2022SW003314

Mursula, K., and Holappa, L. (2018). Principal component analysis of geomagnetic activity: New information on solar wind. *Proceedings of the International Astronomical Union*, 13(S335), 197–200. https://doi.org/10.1017/S1743921317010146 Cambridge Core

Rawat, R., Echer, E., and Gonzalez, W. D. (2018). How different are the solar wind-interplanetary conditions and the consequent geomagnetic activity during the ascending and early descending phases of the solar cycles 23 and 24? *Journal of Geophysical Research: Space Physics*, 123. https://doi.org/10.1029/2018JA025683

Tsurutani, B. T., Echer, E., Guarnieri, F. L., and Gonzalez, W. D. (2011). The properties of two solar wind high speed streams and related geomagnetic activity during the declining phase of solar cycle 23. *Journal of Atmospheric and Solar-Terrestrial Physics*, 73(1), 164–177. https://doi.org/10.1016/j.jastp.2010.04.003

Tulasi Ram, S., Liu, C. H., and Su, S.-Y. (2010). Periodic solar wind forcing due to recurrent coronal holes during 1996–2009 and its impact on Earth's geomagnetic and ionospheric properties during the extreme solar minimum. *Journal of Geophysical Research: Space Physics*, 115. https://doi.org/10.1029/2010JA015800

Verbanac, G., Vršnak, B., Živković, S., Hojsak, T., Veronig, A. M., and Temmer, M. (2011). Solar wind high-speed streams and related geomagnetic activity in the declining phase of solar cycle 23. *Astronomy & Astrophysics*, 533, A49. https://doi.org/10.1051/0004-6361/201116615

DOI: 10.31401/WS.2026.proc.02

Sources and Mechanisms of Activity of the Solar-Type Dwarf Star 61 Cyg A

Boneva D.B.[1], Yankova Kr.[1], Dimitrijević M.S.[2], Rusev D.[1]
[1]Space Research and Technology Institute, Bulgarian Academy of Sciences, Sofia, Bulgaria
danvasan@space.bas.bg
[2]Astronomical Observatory, Belgrade, Serbia

Abstract

In this survey, we present activity states and explore their sources in different time intervals of the visual binary star 61 Cyg. The object contains a solar-type dwarf of spectral type K5 - 61 Cyg A and a K7 dwarf - 61 Cyg B. We apply observational data, obtained from both the Transiting Exoplanet Survey Satellite (TESS) and XMM-Newton X-ray mission. The resulting light curves demonstrate variations in the light flux with periodic and non-periodic increases in values. Depending on the observational facility, these are represented as either the flux or count rate vs. time, respectively. The K5 component 61 Cyg A is known as a strong X-ray source, which is related to its chromospheric activity. We examine the types of fluctuations in its chromosphere, whose properties are similar to those of the solar corona. A possibility of arising the Rossby instabilities in the object's chromosphere is discussed. We estimate an existence of horizontal types of Rossby vortices and their relationship with magnetic loops in the stellar corona, which is in analogy to the solar one. In accordance with the obtained accretion efficiency of 61 Cyg A, which has a relatively low value, we could also suppose about its influence on the star's A component activity.

Keywords: Stars: solar-type dwarfs; Individual: 61 Cyg; TESS and XMM-Newton data; Sun: chromosphere; Rossby vortices

1. Introduction

In some types of binary star systems, processes and activity similar to those in the Sun's chromosphere are observed. One approach for identifying this is to analyze their optical or X-ray light curves.

The considered here object 61 Cyg is a visual binary that contains a solar-type dwarf of spectral type K5 - 61 Cyg A (its individual names: HD 201091, V1803 Cyg) and a K7 dwarf 61 Cyg B [Saikia et al., 2016]. The distance to the star is measured as ≈ 3.5 pc (Gaia DR3 [Collaboration et al., 2021]). The pair has a very long orbital period (≈ 650 yrs). The radii of both components are obtained by interferometric data and their photospheric linear values are $R_A = 0.665 \pm 0.005 R_\odot$ and $R_B = 0.595 \pm 0.008 R_\odot$ [Kervella et al., 2008]. The obtained values of the masses vary throughout the years in the results of different authors and applying methods. We will use here their average values. Using a stellar evolutionary code, Takeda et al. (2007) and also previously Walker et al. (1995), determined the mass of the star 61 Cyg A as $M_A \approx 0.660 M_\odot$ and the mass of 61 Cyg B is $M_B \approx 0.59 M_\odot$. The effective temperature for 61 Cyg A is measured as $T_{\text{eff}} = 4545 \pm 40$ K [Boro Saikia et al., 2016] and 4354 K (Gaia DR3 [Collaboration et al., 2021]). The rotation periods are estimated: 35 ± 1.7 days for the companion A [Boro Saikia et al., 2016] and 38 ± 1.5 days for the B companion [Donahue et al., 1996]. The object is defined with its solar-type variability, but the activity cycle of 61 Cyg A is $\approx 7.3 \pm 0.1$ years [Baliunas et al., 1995; Robrade et al., 2012], while the observed cycle of the K7 component, its B companion, is closer to the Sun's value $\approx 11.7 \pm 0.4$ yr, with a registered chromospheric activity only [Hempelmann et al., 2006].

The star is also known as a strong X-ray source. Its X-ray luminosity varies in a range $L_X = (7.4 - 19.5) \times 10^{26} ergs^{-1}$ (with a descending trend for the years 2002 – 2005) (according to XMM-Newton data, [Hempelmann et al., 2006]), with released energy about $1 \times 10^{31} erg$ in soft X-rays.

61 Cyg A is a relatively photometrically bright object. Its mean apparent magnitudes, according to Gaia DR3 [Collaboration et al., 2021] bands are: 4.7667 ± 0.0006 mag in G; Mean BP: 5.4398 ± 0.0007 mag; Mean RP: 3.9772 ± 0.0029 mag. In the standard photometric system the star's mean magnitudes are: B = 6.39 mag, V = 5.21 mag ([Nicolet, 1978] by Simbad). The optical luminosity of the A component reaches $\approx 0.15 L_{\odot}$, while for the fainter companion B it is $\approx 0.08 L_{\odot}$ [Kervella et al., 2008].

Cyclic X-ray activity was also detected for our target star 61 Cyg A [Robrade et al., 2012].

In the solar type stars the corona fluctuations are most similar to those of the Sun. These variations are observed to be in the chromosphere, which produce the optical and X-ray activity seen in their light curves. Similar properties of the corona have been found for 61 Cyg A [Robrade et al., 2012]. The fluctuations in the chromosphere could be related to: Rossby vortices and their movement between the layers.

In this paper, we focus our research on the 61 Cyg A component of the binary star 61 Cyg. In Section 2, we present observational results to demonstrate the activity of 61 Cyg A in the optical (data from TESS - Transiting Exoplanet Survey Satellite) and X-ray (data from XMM-Newton) bands. The estimated accretion efficiency values are given in Section 3. We consider the Rossby number range values and the possible formation of the Rossby vortices (Section 3.2).

2. Observational results

In this section, we present data and results, obtained with two different and independent observational facilities. By using data from both, we are able to monitor the variations of 61 Cyg A in the optical and X-ray bands over several time intervals.

2.1. TESS light curves

In this section, we apply data for 61 Cyg A from TESS. The TESS main goal is to search for the transiting Earth-sized exo-planets [Günther et al., 2020]. Its large field of view, separated within 26 sectors, gives the opportunity to observe more than 200 000 selected astrophysical objects. Each of the obtained light curves of the pointed objects are analyzing with a 120 s cadence [Ricker et al., 2015]. The observational data in this paper are taken from sector 56, for the time-interval September 02 – September 30, 2022. The data were downloaded and reducing from the Mikulski Archive for Space Telescopes (MAST, https://archive.stsci.edu). The light curves are constructed as flux rate [electrons/s](e-/s) vs. time [days] (Fig. 1a). The exposure time for the object during this time-interval was 20 s. For a better fit, we binned the curve with the number of bins 250. The higher flux-rate value is $\sim 7.795 \times 10^{10}$ e-/s, marked with a red vertical line.

To find any periodicity of variations in the light curve we create the Power-period diagram with the same TESS data. The Lomb-Scargle algorithm [Lomb, 1976; Scargle, 1982] is applied, the wrapping phase is 0.5, with a period derivative of 0.15. The higher signal in this periodogram could be seen in Fig. 1b and it has periodicity of $\sim 10 \pm 0.05$ days, which could be correlated to some flares production. Simple Aperture Photometry (SAP) Flux data were used for both the resulting light curves and power-period diagrams analysis.

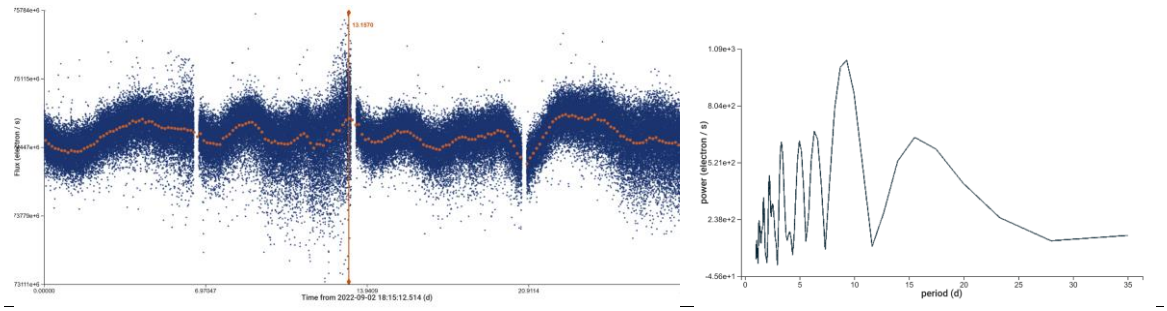


Figure 1. *Light curve of 61Cyg A (left) and the power-period diagram (right), created with data obtained from TESS for the observational time–interval: September 02 – September 30, 2022.*

2.2. XMM-Newton X-ray observations

In this section, we use the reduced and processed public data taken from the XMM-Science Archive (https://nxsa.esac.esa.int/nxsa-web). The XMM-Newton spacecraft is a large scientific satellite, 4 tonne and 10 m long, launched by the European Space Agency (ESA) almost 27 years ago [Barré et al., 1999]. XMM-Newton is designed for studying X-ray sources across the Universe as the ESA's X-ray observatory, which is an X-ray Multi-Mirror Mission. The spacecraft consists of six science instruments that operate simultaneously and they also could work independently, according to the targets' brightness limits (or thresholds). The X-ray telescopes on board have the effective area of a focusing telescope at 1.5 keV energy of ≈ 1550 cm^2 for each telescope, i.e., 4650 cm^2 in total. Data for this research are obtained by using the European Photon Imaging Camera (EPIC), included in a toolkit of three X-ray CCD cameras. All EPIC CCDs operate in photon counting mode at the bandpass range 0.15 - 12 keV [Strüder et al., 2001; Turner et al., 2001]. More technical details of the instruments could be found in the XMM-Newton Users Handbook (https://xmm-ttools.cosmos.esa.int/external/xmm_user_support/documentation/uhb/).

Although the available data obtained with XMM-Newton are very useful for monitoring the X-ray variations of 61 Cyg A, they are for a very short time-interval and are inadequate to present the full range of the object activity.

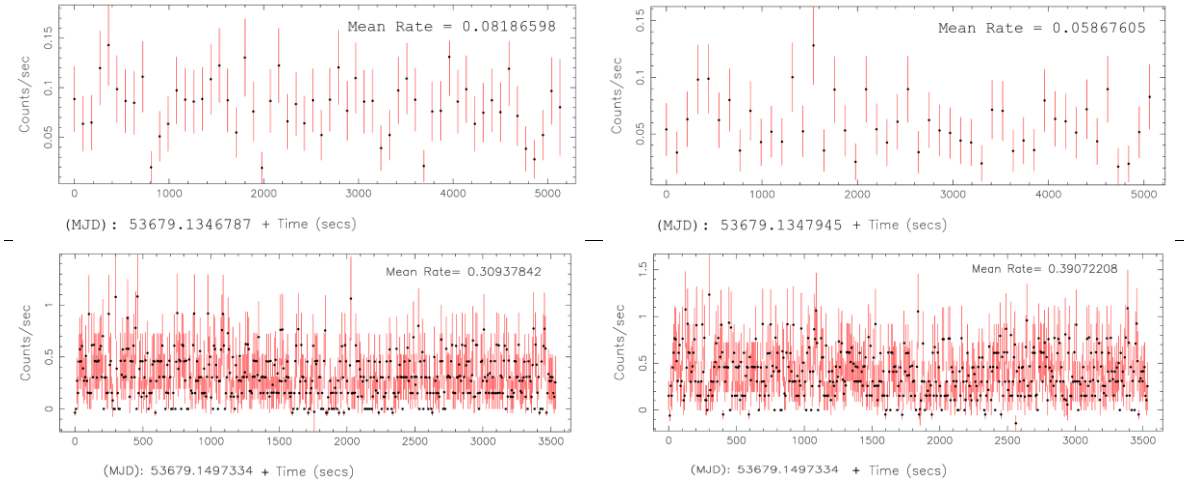


Figure 2. *Time-series X-ray data and light curves for two different Julian dates, obtained from source 1 (2b, 2c, upper right and down left panels) and source 2 (2a, 2d, upper left and down right panels), Obs. Id: 0202610401. Subtracted time-series/*10^{-3}.

The data of 61 Cyg A are obtained for the date 53679 MJD (Modified Julian Date) from two independent sources, separated in time-intervals of seconds. The produced light curves

are presented in four panels (Figs. 2a - 2d), as the times and mean-rate values in [c/s] (counts per second) are given in the Table 1 below.

Table 1. *Mean-rate values in [c/s] during the short time-intervals.*

MJD	UTC date	Source	mean rate [c/s]	Figure
53679.1346787	2005-11-04 15:13:56	S2	0.08186598	2a
53679.1346787	2005-11-04 15:14:06	S1	0.05867605	2b
53679.1497334	2005-11-04 15:35:36	S1	0.30937842	2c
53679.1497334	2005-11-04 15:35:36	S2	0.39072208	2d

An increase in the mean rate is observed with factors of 5-10, in a time-frame of just ≈ 20s. Non-periodic fluctuations within the pointed time-frames are detected. The higher mean-rates [counts/sec.] are seen for the second observational date.

3. A theoretical approach and vortex formation

In this section, we make a relation between the observational activity of the object 61 Cyg A and the sources coming from the star's matter, realized here by the theoretical approach.

3.1. An accretion efficiency estimation

It is important to measure the accretion efficiency, since it estimates the level of accretion as an energy generator. In definition, the efficiency expresses the amount of energy gained from the matter with mass M, in units of its mass energy [Kolb, 2010]. It measures how much of the rest mass energy per unit mass of the accreted material is converted into radiation. In order to know the efficiency values for the star 61 Cyg A, we calculate an average accretion efficiency ξ for the object, by using the expression of Kolb (2010): $\xi_{acc} = GM_1/R_1c^2$, obtained by the luminosity for both: spherical $L_{sph} = \xi_{acc}\dot{M}_{sph}c^2$ and disc accretion $L_d = \eta_{acc}\dot{M}_d c^2$. M_1 and R_1 are the mass and radius of the central object, in this case of the A component and referred to as M_A and R_A. Here, $\dot{M}_d$ denotes the disc accretion rate; $\dot{M}_{sph}$ is for the spherical accretion rate; G is the gravitational constant; c is the speed of light. We use the maximum values of luminosity, based on the observational data. Since ξ depicts the spherical accretion, we evaluate the disc accretion efficiency η in order to estimate the dominant accretion mode (see Table 2) by the relation $\eta \approx \xi \left(\frac{4H_d}{R_d}\right)^{-1}$ (R_d is the disc radius; also see Boneva & Yankova (2021) for detailed explanation).

Table 2. *The mean values of accretion efficiency for the two modes: disc η and spherical ξ.*

Object | Parameter	η	ξ
61 Cyg A	$(2.05 \pm 0.10) \times 10^{-6}$	$(0.34 \pm 0.02) \times 10^{-6}$

The values in the table show that the accretion efficiency is relatively low in both calculated modes, with the mean accretion efficiency of $(1.20 \pm 0.05) \times 10^{-6}$. According to this, we could suggest that no signs of an accretion disc or spherical accretion are found in 61 Cyg A. While this is not referred to in the current case, if an extraction of a larger accretion efficiency could be detected by other methods, which is not evident in our results, the disc that might form would be a short-lived one.

3.2. Rossby vortices and atmospheric activity

In general case, formation of vortices in astrophysical fluid matter plays a vital role in gas dynamics. They are considered as a transport mechanism of angular momentum [Barranco and Marcus, 2005] in a direction of the flow rotation. As a special type in this study, Rossby vortices might appear in inner or outer parts of the accretion disc as a result of the baroclinic instability [Klahr and Bodenheimer, 2003]. In our case, the disc is not evidently to be formed, and the vortices could be developed during the chromospheric layers movements, with different velocities and probably density. The flow is considered to be differentially rotating. In our work, an additional term, the Rossby number, that has influence on the instability processes is implied. It is named for Carl-Gustav Rossby and he explained for the first time the large-scale motion in the atmosphere by using the fluid mechanics' terms. Then, we use the next definition of the Rossby number [Blandford and Thorne, 2008]: The dimensionless ratio of an inertia force to the Coriolis force, giving an indication of the importance of rotation on the flow. It is described by:

$$R_{on} = \frac{|v.\nabla v|}{2|\Omega \times v|} = \frac{v}{2\Omega L \sin\Theta} \quad (1)$$

where v is the speed of fluid flow, Ω is the angular velocity or rotation, Θ is the angle between the axis of rotation and the direction of fluid motion and L is the horizontal length-scale.

The transition of the flow from its laminar state to a state of developed non-linear shear turbulence can occur when the critical Rossby number reaches its critical value [Richard, 2003]. It is found in the paper [Morize et al., 2005] that during the decay of initially three-dimensional homogeneous turbulence in a rotating frame, strong cyclonic coherent vortices emerge, while the Rossby number value decreases below the value of 2 ± 0.5. This number has an important role to determine the behavior of large-scale astrophysical fluid dynamics. In many simulations the balance in rotating stratified turbulence at different Rossby numbers [McKiver and Dritschel, 2006] is examined. A significant difference is found in the behavior of potential vorticity at low and high Rossby number. An increasing Rossby number causes a decrease in balance of vorticity, then the structures that appear in such unbalanced flow are mainly in small-scale. Now, we can rewrite the Rossby number for the mean flow in terms of a quantity which is usually referred to in astrophysics – the epicyclic frequency ω:

$$\frac{\omega^2}{4\Omega^2} = (1 + R_{on}). \quad (2)$$

Although, by this equation, we can say that the vorticity here simply depends on the square of this frequency. The form of expression, in which ω is involved is very complicated and many other important parameters are part of the relations (see Lovelace et al., (1999); Meheut et al., 2010).

In our case, to give an estimation of the critical Rossby number that operate in the chromosphere of the studied here object 61 Cyg A, we use the relation by the model of Richard (2003):

$$R_{on} = \frac{r(\partial/\partial r)\Omega_0}{2\Omega_0}, \quad (3)$$

where r is the local radius (the height in the chromosphere from the surface H), Ω_0 is the mean rotation. We assume for the radius of the stellar chromosphere $r = H \approx 10^3$ km, and that the solar chromosphere radius $R_{sc} = 3000 - 5000$ km is applicable to use [Zhang et al.,

1998]. As already mentioned in the Introduction, the radius of the star is $R_A = 0.66 \pm 0.005 R_\odot$. Then, we can extrapolate that $H \approx 0.66 R_{sc}$.

We obtain the value of the mean rotation using one time interval range between the min and max values of the counts/s rate in the X-ray light curves from XMM-Newton (section 2.2, Figs. 2). Then, we roughly estimate $\partial \Omega_H / \partial r$ as a simple difference of the angular velocity change between these values. It is yielded that $\Omega_0 = 30$ km/s. This could be expressed as $\partial \Omega_H / \partial r \Rightarrow \Delta(\Omega_H)|_{min}^{max}$. Our calculations for the Rossby number give $R_{on} = 0.13 \pm 0.03$. This value is consistent with the condition of the vortex development given in the preceding text.

Large-scale flows are defined as it is influenced by the star's rotation, L is sufficiently large and the Rossby number R_{on} should be of the order of < 1. (e.g., flows with sufficiently small Rossby number are in geostrophic balance). We have simulated vortices formation in such large-scale flows in Boneva and Filipov (2012) and the flow structure looks like in Fig. 3 there.

3.3. A retention mechanism

Due to the observed X-ray variations in the object light curves, we should expect the presence of accretion in the system. However, as we showed in Table 2, the low efficiency values indicate that either very low or no accretion occurs in 61 Cygni A. Therefore, we could correlate the appearance of X-rays with the chromospheric activity. The activity of chromospheres is similar to the solar activity. This is due to magnetic reconnection that occurs between loops of different sizes. In the presence of Rossby vortices, we can assume that two types of instabilities (as Rossby and Parker instabilities) could interact. Basically, the power of flares activity is not dependent on the sizes of magnetic arcs or Rossby vortex, but rather on the lifetimes of their interaction configurations. This lifetime influences the dynamics of the processes in the chromosphere. It also correlates with the degree of flares amplification.

4. Discussion and conclusions

As it is already found [Robrade et al., 2012], the source of the observed activity in 61 Cyg A is coming from the variations in its chromosphere (or coronal properties), which is similar to the properties of the solar corona fluctuations.

The observational results in section 2 show optical and X-ray variations, similar to the solar flares and in the flux values to the solar X-ray flares. Since, a very low or no accretion of 61 Cygni A is observed, then we could not relate it to the chromospheric activity.

The Rossby vortices could be formed under the conditions of instability. Their possible localization is the upper parts of the object's chromosphere. If it is a single formation, it could be associated with the activity cycle of ≈ 7.3 years of the A component of 61 Cyg. This is in analogy with the sunspots and their distribution close to the Sun chromosperic surface. On the other hand, the possible interaction of horizontal Rossby vortices in the chromosphere with the magnetic arcs formed there will lead to much rarer, but significantly more powerful flares.

Acknowledgements

This paper includes data collected with the TESS mission, obtained from the MAST data archive at the Space Telescope Science Institute (STScI). Funding for US Institutions for the TESS mission is provided by the NASA Explorer Program. STScI is operated by the Association of Universities for Research in Astronomy, Inc., under NASA contract NAS 5–26555. This work used public data available in the XMM-Newton Science Archive (XSA), an ESA science mission with instruments and contributions directly funded by ESA Member States and NASA. We acknowledge the project "Accretion flows in binary stars" KP-06-H98/8 (Bulgarian National Science Fund). The authors acknowledge the research project

"Observational effects and accretion processes in selected binary stars" IC-RS/12/2026-2028 (Bilateral agreement between BAS and SANU, financially supported from the Bulgarian Academy of Sciences).

References

Baliunas, S., Donahue, R., Soon, W., Horne, J., Frazer, J., et al. (1995). Chromospheric variations in main-sequence stars, *Astrophysical Journal*, Vol. 438, pp. 269–287.

Barranco, J.A., Marcus, P.S. (2005). Three-dimensional vortices in stratified protoplanetary disks, *Astrophysical Journal*, Vol. 623, No. 2, pp. 1157–1170, DOI: 10.1086/428639.

Barré, H., Nye, H., Janin, G. (1999). An overview of the XMM observatory system, *ESA Bulletin*, Vol. 100, pp. 15–20.

Blandford, R.D., Thorne, K.S. (2008). *Applications of Classical Physics*, California Institute of Technology Lecture Notes, pp 12.

Boneva, D., Filipov, L. (2012). Density distribution configuration and development of vortical patterns in accreting close binary star system, *arXiv e-prints*, arXiv:1210.2767, DOI: 10.48550/arXiv.1210.2767.

Boneva, D., Yankova, K. (2021). Accretion efficiency and mass transfer in two binary star systems, *Proceedings of the 20.5th Cambridge Workshop on Cool Stars, Stellar Systems, and the Sun (CS20.5)*, p. 328, DOI: 10.5281/zenodo.4748796.

Boro Saikia, S., Jeffers, S.V., Morin, J., Petit, P., Folsom, C.P., et al. (2016). A solar-like magnetic cycle on the mature K-dwarf 61 Cygni A (HD 201091), *Astronomy & Astrophysics*, Vol. 594, A29, DOI: 10.1051/0004-6361/201628262.

Gaia Collaboration, Brown, A.G.A., Vallenari, A., Prusti, T., de Bruijne, J.H.J., Babusiaux, C., et al. (2021). Gaia Early Data Release 3, *Astronomy & Astrophysics*, Vol. 649, A1, DOI: 10.1051/0004-6361/202039657.

Donahue, R.A., Saar, S.H., Baliunas, S.L. (1996). A relationship between mean rotation period in lower main-sequence stars and its observed range, *Astrophysical Journal*, Vol. 466, pp. 384–391.

Günther, M.N., Zhan, Z., Seager, S., et al. (2020). Stellar flares from the first TESS data release: Exploring a new sample of M dwarfs, *Astronomical Journal*, Vol. 159, No. 2, Art. 60, DOI: 10.3847/1538-3881/ab5d3a.

Hempelmann, A., Robrade, J., Schmitt, J.H.M.M., Favata, F., Baliunas, S.L., Hall, J.C. (2006). Coronal activity cycles in 61 Cygni, *Astronomy & Astrophysics*, Vol. 460, No. 1, pp. 261–267, DOI: 10.1051/0004-6361:20065459.

Kervella, P., Mérand, A., Pichon, B., Thévenin, F., et al. (2008). The radii of the nearby K5V and K7V stars 61 Cygni A and B: CHARA/FLUOR interferometry and CESAM2k modeling, *Astronomy & Astrophysics*, Vol. 488, No. 2, pp. 667–674, DOI: 10.1051/0004-6361:200810080.

Klahr, H.H., Bodenheimer, P. (2003). Turbulence in accretion disks: Vorticity generation and angular momentum transport via the global baroclinic instability, *Astrophysical Journal*, Vol. 582, No. 2, pp. 869–892, DOI: 10.1086/344743.

Kolb, U. (2010). *Extreme Environment Astrophysics*, Cambridge University Press.

Lomb, N.R. (1976). Least-squares frequency analysis of unequally spaced data, *Astrophysics and Space Science*, Vol. 39, pp. 447–462, DOI: 10.1007/BF00648343.

Lovelace, R.V.E., Li, H., Colgate, S.A., Nelson, A.F. (1999). Rossby wave instability of Keplerian accretion disks, *Astrophysical Journal*, Vol. 513, No. 2, pp. 805–810, DOI: 10.1086/306900.

McKiver, W.J., Dritschel, D.G. (2006). The stability of a quasi-geostrophic ellipsoidal vortex in a background shear flow, *Journal of Fluid Mechanics*, Vol. 560, pp. 1–17, DOI: 10.1017/S0022112006000462.

Méheut, H., Casse, F., Varnière, P., Tagger, M. (2010). Rossby wave instability and three-dimensional vortices in accretion disks, *Astronomy & Astrophysics*, Vol. 516, A31, DOI: 10.1051/0004-6361/201014000.

Morize, C., Moisy, F., Rabaud, M. (2005). Decaying grid-generated turbulence in a rotating tank, *Physics of Fluids*, Vol. 17, No. 9, Art. 095105, DOI: 10.1063/1.2046710.

Nicolet, B. (1978). Catalogue of homogeneous data in the UBV photoelectric photometric system, *Astronomy and Astrophysics Supplement Series*, Vol. 34, pp. 1–49.

Richard, D. (2003). On non-linear hydrodynamic instability and enhanced transport in differentially rotating flows, *Astronomy & Astrophysics*, Vol. 408, pp. 409–414, DOI: 10.1051/0004-6361:20031010.

Ricker, G.R., Winn, J.N., Vanderspek, R., et al. (2015). Transiting Exoplanet Survey Satellite (TESS), *Journal of Astronomical Telescopes, Instruments, and Systems*, Vol. 1, No. 1, Art. 014003, DOI: 10.1117/1.JATIS.1.1.014003.

Robrade, J., Schmitt, J.H.M.M., Favata, F. (2012). Coronal activity cycles in nearby G and K stars: XMM-Newton monitoring of 61 Cygni and α Centauri, *Astronomy & Astrophysics*, Vol. 543, A84, DOI: 10.1051/0004-6361/201219046.

Scargle, J.D. (1982). Studies in astronomical time series analysis. II. Statistical aspects of spectral analysis of unevenly spaced data, *Astrophysical Journal*, Vol. 263, pp. 835–853, DOI: 10.1086/160554.

Strüder, L., Briel, U., Dennerl, K., Hartmann, R., Kendziorra, E., Meidinger, N., et al. (2001). The European Photon Imaging Camera on XMM-Newton: The pn-CCD camera, *Astronomy & Astrophysics*, Vol. 365, pp. L18–L26, DOI: 10.1051/0004-6361:20000066.

Takeda, G., Ford, E.B., Sills, A., Rasio, F.A., Fischer, D.A., Valenti, J.A. (2007). Structure and evolution of nearby stars with planets. II. Physical properties of approximately 1000 cool stars from the SPOCS catalog, *Astrophysical Journal Supplement Series*, Vol. 168, No. 2, pp. 297–318, DOI: 10.1086/509763.

Turner, M.J.L., Abbey, A., Arnaud, M., Balasini, M., Barbera, M., Belsole, E., et al. (2001). The European Photon Imaging Camera on XMM-Newton: The MOS cameras, *Astronomy & Astrophysics*, Vol. 365, pp. L27–L35, DOI: 10.1051/0004-6361:20000087.

Walker, G.A.H., Walker, A.R., Irwin, A.W., Larson, A.M., Yang, S.L.S., Richardson, D.C. (1995). A search for Jupiter-mass companions to nearby stars, *Icarus*, Vol. 116, No. 2, pp. 359–375, DOI: 10.1006/icar.1995.1130.

Zhang, J., White, S.M., Kundu, M.R. (1998). The height structure of the solar atmosphere from the extreme-ultraviolet perspective, *Astrophysical Journal Letters*, Vol. 504, No. 2, pp. L127–L130, DOI: 10.1086/311587.

DOI: 10.31401/WS.2026.proc.03

Radio Manifestations of the CME Occurred on 21 August 2015

Dorovskyy V.V., Melnik V.N., Shevchuk M.V.

Institute of Radio Astronomy, Kharkiv, Ukraine
dorovsky@rian.kharkov.ua

Abstract

We discuss spectral and spatial properties of the solar radio bursts associated with the CME that occurred on 21 August 2015. The CME was triggered by the M1.4 flare that started in AR NOAA 12403 (S17E26) at 09:32 UT. In turn, this CME initiated a sequence of radio bursts consisting of a Type II burst with harmonic structure and multiple band splitting and two successive Type IV bursts of different morphology. The Type II burst and the first Type IV burst were observed while the associated CME was completely shielded by the LASCO C2 coronagraph occulter. Hence, this CME could not be studied in visible light, at least during the initial phase of its lifetime. Using spectral and interferometric data, the speed and direction of the Type II burst source were determined. The Type II burst source appeared to be Earth-directed. Since Type II burst sources are believed to lie at a shock front, the shock associated with the observed Type II burst was found to move with acceleration. Its velocity increased from 400 km/s at a distance of 1.5 Rs to 720 km/s at 2.4 Rs. The two Type IV bursts differ in duration, frequency range, morphology, and source dynamics. Interferometric observations showed that the first Type IV burst was moving, whereas the second was most likely stationary. In addition, the spatial dynamics of the source of an individual fiber burst, which formed part of the fine structure of the second Type IV burst, were determined for the first time. We therefore conclude that the source of the first Type IV burst was most probably inside the CME core, unlike the source of the second burst, which was likely located in a coronal structure such as a coronal loop. The CME velocity at a distance of approximately 4 Rs, derived from interferometric observations of the first Type IV burst, was approximately 600 km/s. This agrees well with the value of 630 km/s measured by an optical coronagraph. These results show that the properties and dynamics of Earth-directed CMEs during the initial phase of their life cycle are difficult to determine using optical coronagraphs, but can be investigated using radio telescopes capable of spatial measurements.

Keywords: Coronal Mass Ejection; Type II bursts; Type IV bursts; Radio Emission Source; Radio Interferometry

1. Introduction

A Coronal Mass Ejection (CME) is one of the most powerful manifestations of the solar activity. These are large amounts of solar matter thrown away from the Sun into the heliosphere. Having masses up to 10^{17} g and velocities up to 3000 km/s particular CME can reach kinetic energy of about 10^{19}erg [Gopalswamy, 2022]. Such huge energy makes the CMEs the most significant drivers of the space weather. From this point of view finding the size and direction of the CMEs is very important for the geomagnetic disturbances forecast. It is obvious that the most geoeffective CMEs are the Earth-directed ones. On the other hand, such CMEs can be poorly studied in visible light by the coronagraphs especially during their initial phases due to shielding by the occulter. Fortunately, there is a possibility to study the properties of the Earth-directed CMEs with radio astronomical methods. It is well known that CMEs often trigger enhanced sporadic radio emissions in the form of Type II [Nelson, 1985] and Type IV [Stewart, 1985] bursts. The former is believed to origin from the shock front ahead of moving CME [Shen, 2013] while the source of the latter is assumed to be inside the CME core [Melnik, 2018].

Due to this close connection determining the velocity and the direction of the sources of mentioned bursts sources can provide the information about physical properties of the CME, which determine its geo-efficiency, such as its speed, direction, size and mass.

In this paper we demonstrate the perspectives of determining the physical properties of the Earth-directed CME using spectral and interferometric analysis of the radio astronomical data obtained during the observations performed with the UTR-2 radio telescope.

2. Observations and spectral analysis

On 21 August 2015, an M1.4-class flare was recorded above the active region NOAA12403. The flare began at 09:34 UT, and peaked at 09:48 UT. At that moment the AR was near the central meridian at coordinates S17, E26. This flare initiated a Halo-CME, which appeared in the SOHO-LASCO-C2 FOV around 10:12 UT, half an hour after the flare begun. In turn this CME triggered a sequence of solar bursts, consisting of Type II burst with harmonic structure and two Type IV bursts.

These bursts were observed by the radio telescope UTR-2 in frequency range 8-32 MHz with time and frequency resolutions of 100 ms and 4 kHz respectively. Simultaneously these bursts were recorded by the Nancay Decameter Array (NDA) in frequency band 20-80 MHz. The resolutions were 1 s and 175 kHz in time and frequency accordingly. The whole sequence of the bursts is shown in Figure 1.

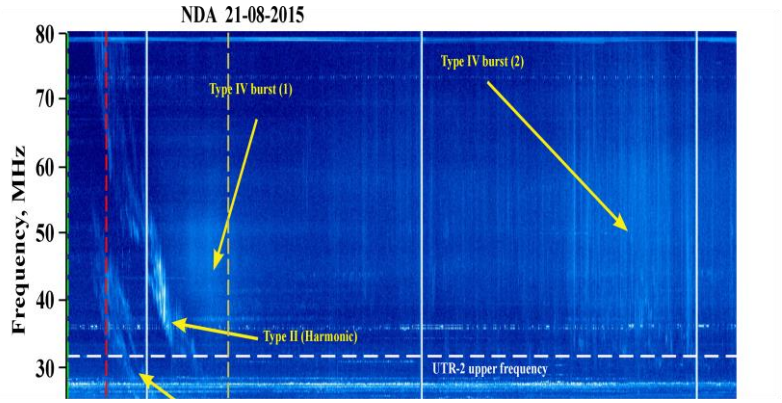


Figure 1. *The sequence of the bursts observed by NDA on 21 August 2015.*

The fundamental lane of the Type II burst began at frequency of 55 MHz at 9:42 UT. The harmonic lane apparently started beyond the upper frequency of the NDA. On the dynamic spectrum (Figure 1) t1 denotes the flare onset time (9:34 UT), t2 denotes the flare peak time (9:48 UT) and t3 is the time when the CME appeared in the LASCO-C2 FOV (10:12 UT). It shows that the CME started during the rising phase of the flare. At the same time the whole Type II burst and almost entire first Type IV burst were observed when the associated CME was shielded by the coronagraph occulting disk and was not visible in white light. Thus in this particular case the properties of the CME at its initial phase (during 30 min) could be studied only by radio astronomical methods. The analysis of the dynamic spectrum of the Type II burst can provide the radial speed and heliocentric height of the shock, driven by the CME assuming one of the existing coronal models. For this Type II burst measured drift rates and retrieved radial velocity assuming the Newkirk corona model [Newkirk, 1961] are shown in Table 1. Here we should note that in case of non-radial movement the velocity obtained from the frequency drift rate (the third column of Table 1) is only a component of the full linear velocity

vector parallel to the density gradient. To retrieve full velocity, the angle between the velocity vector and the density gradient is required. These projection corrections are discussed below.

As it is seen from Table 1 the shock at its initial phase moves with acceleration. This CME velocity was also estimated by LASCO-C2 coronagraph at heliocentric heights >2.2Rs, where Rs is the solar radius.

According to the SOHO/LASCO CME Catalog https://cdaw.gsfc.nasa.gov/CME_list/ the velocity of the discussed CME was about 630 km/s at 12 Rs and 765 km/s being extrapolated to 20 Rs. We must note that for Earth-directed CMEs optical coronagraphs measure the expansion speed rather than the radial one. Using the relation between the CMEs radial and expansion speeds [Gopalswamy, 2022] the above velocities appear to be 720 and 870 km/s respectively. Both the coronagraphs and radio observations confirm that the CME moved with acceleration.

The first Type IV burst followed immediately after the Type II burst. The upper frequency of this burst according to NDA data (Figure 1) was 60 MHz while the lowest one was about 23 MHz judging from the UTR-2 data (Figure 2). This burst lasted for 15 min and was extremely weak. Its flux didn't exceed 3 s.f.u. (1 s.f.u. = WHzm). The front edge of this burst almost coincided with the harmonic lane of the preceding Type II burst. Thus its drift rate is apparently close to that of the Type II burst, that characterizes it as moving Type IV or Type IVm burst [Ramesh et al. 2013]. Nevertheless, it is difficult to estimate the linear velocity of the CME from the Type IVm dynamic spectrum, since its source is believed to be inside the CME core [Melnik et al. 2018] and there is no clear relationship between the plasma density in the core and the height of that core in the solar corona.

The second Type IV burst started at around 10:35 UT and lasted for about 1 hr 50 min (Figure 3a). The morphologies of two observed Type IV bursts were considerably different. While the first burst was unstructured with continuum-like emission the second one consisted of fine structure in the form of numerous fiber-bursts (Figure 3b). This Type IV burst was much longer and wider in frequency with upper frequency being far beyond the upper frequency of the NDA radio telescope (Figure1). Maximal fluxes of this burst reached 40 s.f.u., that is an order of magnitude larger than in the first Type IV burst. The fiber bursts constituting the whole Type IV burst had Type III-like appearance with average duration of 4 s and negative frequency drift rates in the range from -1 to -5 MHz/s.

Table 1. *Drift rates of the Type II burst at different frequencies and retrieved radial velocities of its source at corresponding heights*

Frequency (MHz)	**Mean drift rate (kHz/s)**	**Radial speed (km/s)**	**Linear speed (km/s)**	**Heliocentric height (Rs)**
44-55 [1]	-61	350	400	1.5
28-34 [1]	-38	500	580	1.7
20-25 [2]	-26	580	670	2
13-17 [2]	-12	620	720	2.4

[1] measured from NDA data.

[2] measured from UTR-2 data.

3. Spatial properties of the observed bursts

The remarkable feature of the observations conducted with UTR-2 on that day was antenna configuration. Three separate sections of the radio telescope (South, North and West) formed a local short-base interferometer with two orthogonal baselines, each 992 m long. This configuration made it possible to estimate the size of the bursts sources along two perpendicular

axes and also to detect the source spatial dynamics in the sky plane. The antenna configuration and the analysis method were similar to those described in [Dorovskyy et al. 2018].

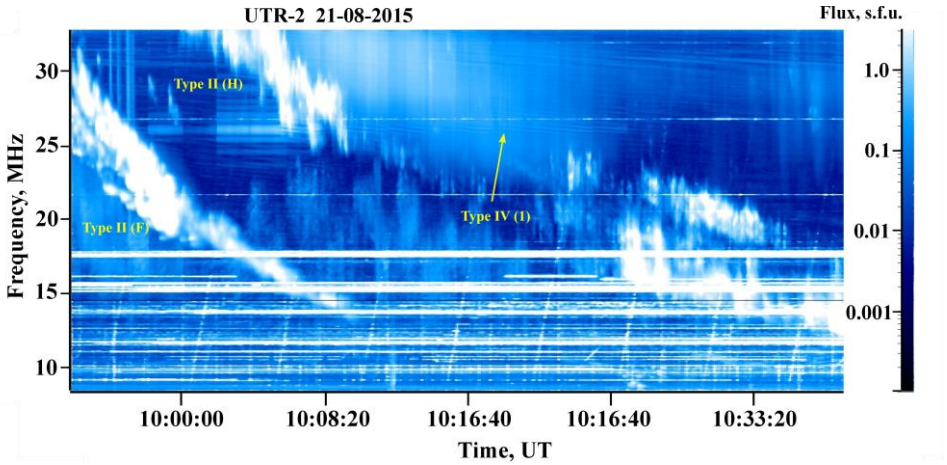


Figure 2. *The low-frequency part of the first Type IV burst observed by UTR-2 instrument.*

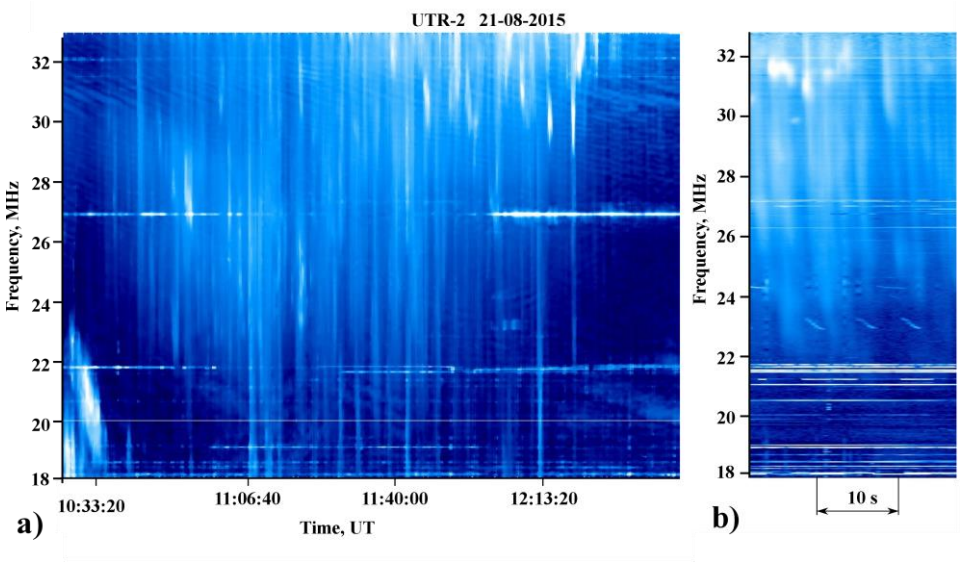


Figure 3. *The dynamic spectrum of the second Type IV burst observed on 21 08 2015 (a) and zoomed spectrum of the fiber bursts (b).*

Spatial dynamics of the source of the fundamental lane of the Type II bursts during its drift from ~32 MHz down to ~17 MHz is shown in Figure 4.

Since we can measure only two sizes of the source along two perpendicular axes the most representative shape of the source is an ellipse. Figure 4 shows that the shape of the source is close to a circle with the diameter of 27′ at frequency of 30 MHz. This yields the emission brightness temperature of $1.5 \cdot 10^8$K. The source of a Type II burst is believed to be located at the front of the shock moving ahead of a CME. Thus negative frequency drift is attributed to the movement of this source away from the Sun and hence is closely connected to the shock movement. At the same time Figure 4 doesn't show any systematic movement of the source in time. One of the possible scenario is that the source was moving directly toward the observer. Combining spatial data obtained from interferometric observations and the radial velocity calculated from the frequency drift rate the 3D trajectory of the Type II burst source can be retrieved. We suppose that the Type II bursts source moved directly toward the observer non-

radially at the angle θ of about 30° to the density gradient, as shown in Figure 5. Thus the velocities obtained from the drift rates (the third column in Table 1) should be corrected taking into account the projection effects. The corrected velocities are given in the fourth column of the Table.

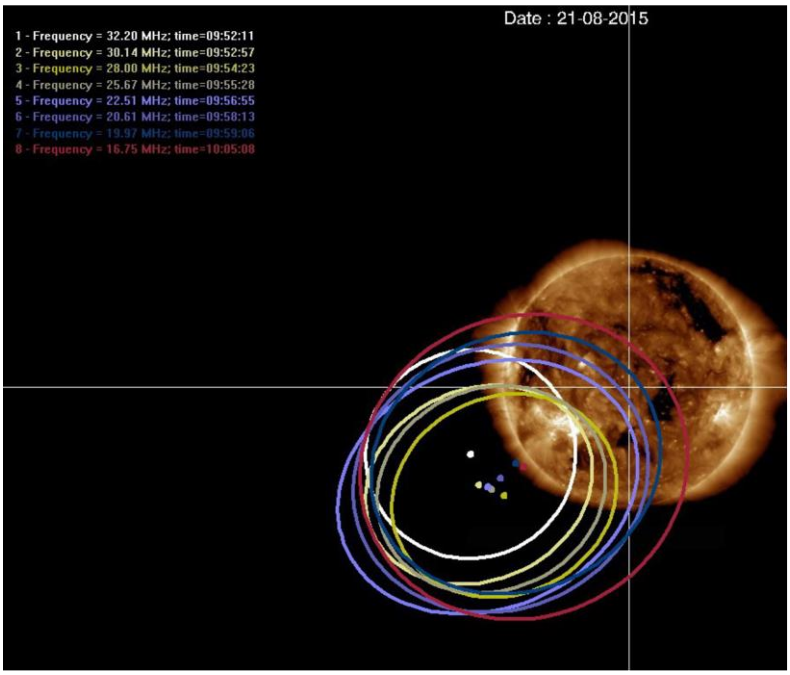


Figure 4. *Schematic view of the source of the Type II burst fundamental lane during its drift from 32 down to 17MHz.*

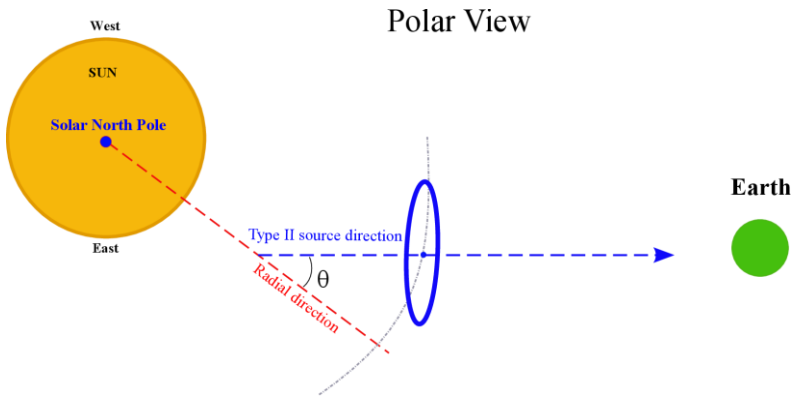


Figure 5. *The trajectory of the Type II burst source retrieved from joint analysis of spectral and interferometric data.*

We should note that the size of the whole shock is apparently much larger than the measured size of the Type II burst source. So we may conclude that radio emission of the Type II burst emanates from comparatively small area of the shock. And this small area moved directly toward the observer. It doesn't mean that the CME itself moved along the same trajectory.

Since interferometric observations of all bursts on that day were performed by the UTR-2 radio telescope, only the low-frequency part of both Type IV bursts could be spatially analyzed. As was mentioned above Type IV burst emission is believed to originate from the CME core, which is a plasmoid containing dense plasma moving away from the Sun. The velocity of this

movement can't be found from spectral parameters of the bursts, like it is done for Type III bursts. But this movement can be traced in the plane of sky using the interferometric data analysis. The results of interferometric analysis of the spatial properties of the first Type IV burst are shown in Figure 6. It can be seen that the source at fixed frequency of 32 MHz moved away from the Sun almost radially by the distance of ~0.3 Rs for 12 minutes. We attribute this displacement to the movement of the CME core. Thus the above values give the projection of the CME core velocity vector on the plane of sky (transversal velocity component) equal to ~300 km/s. Taking into account the location of the source in the sky plane as well as solar longitude and latitude of the associated active region the CME linear velocity can be estimated as ~600 km/s at heliocentric distance of around 4 Rs. These values agree rather well with those obtained by LASCO-C2 coronagraph in the white light and from frequency drift rate of the Type II burst. One can note that assuming the Newkirk corona the heliocentric height of the source of 32 MHz radio emission should be 1.7 Rs while the source of the Type IV burst of the same frequency was found to be much higher in the corona. This fact supports the hypothesis that the source of the first Type IV burst is the CME core whose density is several times greater than that of the surrounding corona [Melnik et al. 2018].

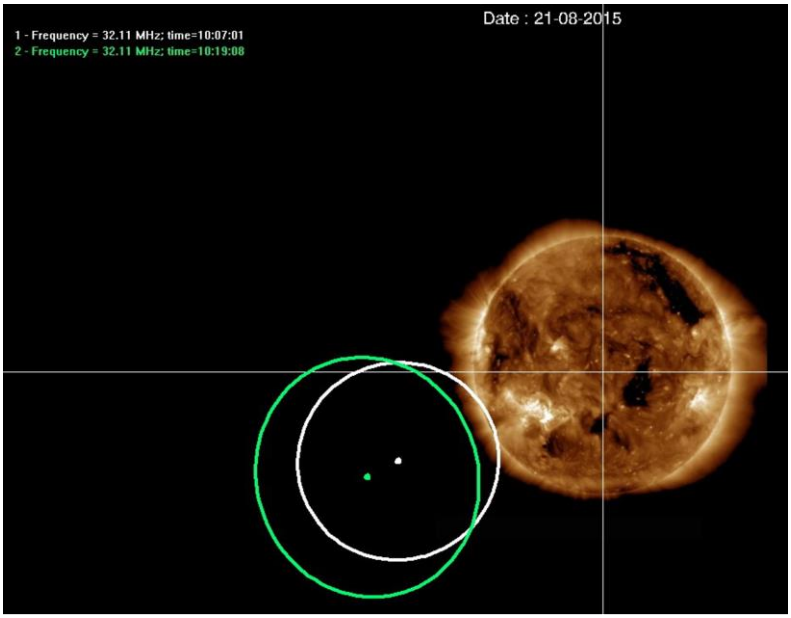


Figure 6. *The locations of the first Type IV burst source measured at fixed frequency of 32 MHz at 10:07 UT (white) and 10:19 UT (green).*

The size of the first Type IV burst source was 26′ along both axes. Thus the maximum brightness temperature of the source was $2 \cdot 10^7$ K, which is just one order of magnitude greater than the temperature of the standard corona at these heights.

As was mentioned earlier the second Type IV burst had noticeably different morphology. The analysis of the interferometric data showed that spatial dynamics of this burst source was also different. At first, the sizes and locations of the source at several fixed frequencies during the whole lifetime of the burst were obtained. Measurements were taken at 2-minute intervals, resulting in approximately 70 time-sequenced source locations on the sky plane, which are shown in Figure 7a. The source contours are not displayed in the Figure so as not to clutter the view. Only the points of maximum brightness at each time are shown. One can see that the location of the source of the second Type IV burst remains almost the same during about 1 hour 40 minutes. This fact provides firm grounds for classifying this Type IV burst as stationary one.

LASCO-C2 coronagraph shows that the associated CME moved in South-East direction. This direction meets the hypothesis that the CME moved radially from the AR location. At the same time unlike the first Type IV burst the source of the second Type IV burst preserved its location near the solar limb for almost 2 hours. Moreover, the source was located closer to the solar limb and was noticeably elongated along the vertical axis. The sizes of the source at frequency of 32 MHz were 10′ and 20′ in equatorial and polar directions respectively (Figure 7b). This fact suggests that the source of the second Type IV burst was most likely not associated with the CME core but rather was connected with high coronal loops excited the by flare and CME [Salas-Matamoros and Klein 2020].

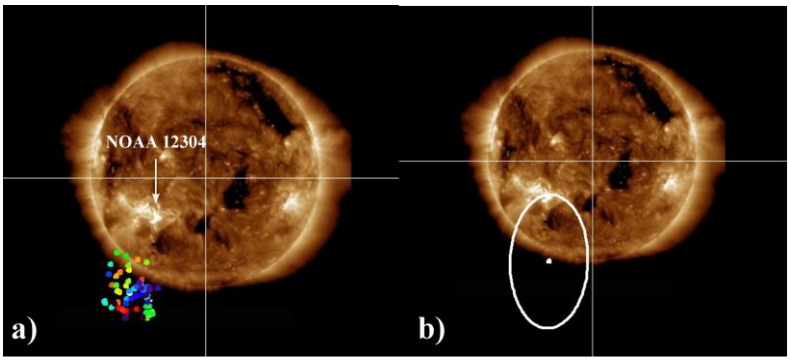


Figure 7. *Points of maximum brightness of the second Type IV burst source measured at a frequency of 32 MHz from 10:44 to 11:24 UT with time interval of 2 min (a) and the sizes of the burst measured at 12:00 UT and the same frequency (b).*

Due to excellent time, frequency and spatial resolutions of the observations it was possible to track the spatial dynamics of individual fiber bursts, which were fine structure of the Type IV burst. Spatial properties of individual fiber bursts and their variation in time have not yet been analyzed. Individual fibers could not be reliably distinguished in the NDA data due to poor sensitivity and insufficient time resolution (1s) of the instrument. In contrast, spectra obtained by the UTR-2 radio telescope allowed tracking of individual fiber bursts in frequency domain from 32 MHz down to 20 MHz (see Figure 3b).

Average frequency drift rate of the selected individual fiber burst in frequency range of 20-32 MHz was -1.8 MHz/s. In the Newkirk corona such frequency drift rate corresponds to the average velocity of the source equal to $3\cdot 10^9$ cm/s or 0.1c, where c is the speed of light. At the same time the velocity calculated from the spatial displacement of the source appeared to be $7.7\cdot 10^9$ cm/s or 0.26c. Moreover, the source moved not in radial direction, as it is supposed in the Newkirk model to form a frequency drift. Figure 8 shows that the source of the fiber burst moved quasi-parallel to the solar surface while drifting in frequency, at the same time remaining approximately at the constant height. This may indicate that the electrons responsible for the fiber bursts generation move not through the Newkirk corona, but across some coronal structure, such as a coronal loop with specific density distribution. This is further evidence that the source of the second Type IV burst apparently had no relation to the CME core. Considerable difference in the velocities, shapes and locations of the sources of the first and the second Type IV bursts also supports this hypothesis.

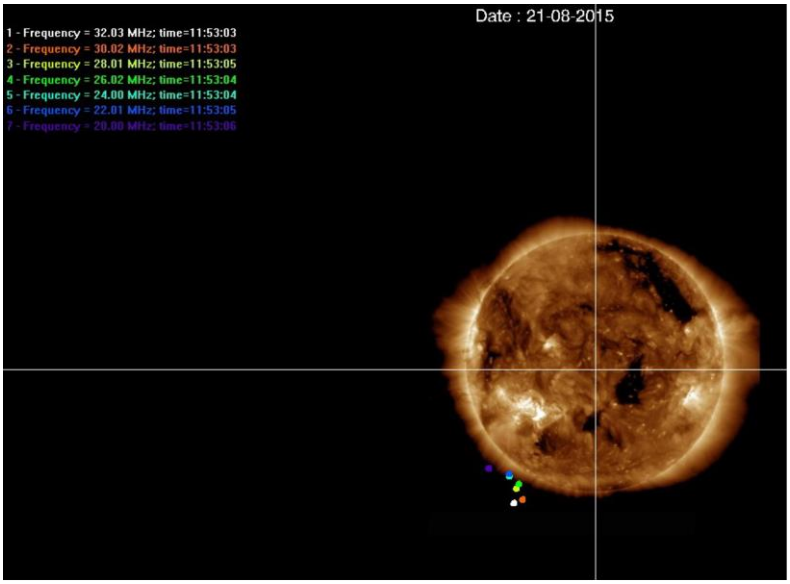


Figure 8. *Locations of the point of maximal brightness points of the source of an individual fiber burst during its drift in frequency from 32 MHz (white dot) down to 20 MHz (violet dot).*

4. Conclusions

In the present paper a series of the events associated with almost Earth-directed CME has been studied. This series consisted of the Type II burst and two successive Type IV bursts with different morphology. It was shown that combination of spectral and interferometric analyses of data obtained with UTR-2 radio telescope can provide all three coordinates of the sources of solar bursts and thus of the associated coronal structures. The source of the observed Type II burst was most likely located at the part of a shock front, which moved directly to the observer. The direction and the speed of the shock were obtained by joint use of two independent methods - interferometric and spectral. The important thing is that these values were measured while the CME itself was not visible by the optic LASCO-C2 coronagraph. The results of our analysis show that the main acceleration of the CME happened during its initial phase low in the corona. The source of the first Type IV burst was apparently located in the CME core. Movement of the source at fixed frequency with time indicates that first Type IV burst can be classified as moving Type IV burst. The source of the second Type IV burst didn’t change its location substantially during almost 2 hours. This characterizes it as stationary Type IV burst. In our opinion this burst was not directly related to the CME core. Besides the similar spectral morphology of the fiber-bursts and Type III bursts their spatial dynamics appeared to be different. The sources of fiber bursts apparently move not through the standard corona, as it takes place in the case of Type III bursts, but rather propagate across some coronal structures (e.g. coronal loops). Unlike the Type II bursts generation scenario, the direction of fibers sources movement is not radial but rather quasi-parallel to the solar surface.

Acknowledgements

The work was funded within the framework of the state budget grant "Complex researches of sporadic radio emission of the Sun during 25 cycle of solar activity" (Radius) (0122U000616). The authors would like to note that the CME catalog used in the research is generated and maintained at the CDAW Data Center by NASA and The Catholic University of America in cooperation with the Naval Research Laboratory. SOHO is a project of international cooperation between ESA and NASA. The authors would also like to thank the staff at the

Nancay Radio Observatory for providing free access to the raw observational data obtained using the NDA radio telescope.

References

Dorovskyy V., Melnik V., Konovalenko A., Brazhenko A., Rucker H. (2018). Spatial properties of the complex decameter type II burst observed on 31 May 2013. *Sun and Geosphere*, 13, 25–30.

Gopalswamy N. (2022). The Sun and Space Weather. *Atmosphere*, 13(11), 1781. https://doi.org/10.3390/atmos13111781.

Melnik V.N., Brazhenko A.I., Konovalenko A.A., Dorovskyy V.V., Rucker H.O., Panchenko M., Frantsuzenko A.V., Shevchuk M.V. (2018). Decameter Type IV burst associated with a behind-the-limb CME observed on 7 November 2013. *Solar Physics*, 293(3), 53. https://doi.org/10.1007/s11207-018-1271-z.

Nelson G.J., Melrose D.B. (1985). Type II bursts. In D.J. McLean and N.R. Labrum (Eds.), *Solar Radiophysics Studies of Emission from the Sun at Metre Wavelengths*. Cambridge University Press, 333–359.

Newkirk G. Jr. (1961). The Solar Corona in Active Regions and the Thermal Origin of the Slowly Varying Component of Solar Radio Radiation. *Astrophysical Journal*, 133, 983. https://doi.org/10.1086/147104.

Ramesh R., Kishore P., Mulay S.M., Barve I.V., Kathiravan C., Wang T.J. (2013). Low-frequency observations of drifting, non-thermal continuum radio emission associated with solar coronal mass ejections. *Astrophysical Journal*, 778(1), 30. https://doi.org/10.1088/0004-637X/778/1/30.

Salas-Matamoros C., Klein K.-L. (2020). Polarisation and source structure of solar stationary Type IV radio bursts. *Astronomy and Astrophysics*, 639, A102. https://doi.org/10.1051/0004-6361/202037989.

Shen C., Liao C., Wang Y., Ye P., Wang S. (2013). Source region of the decameter-hectometric Type II radio burst: Shock-streamer interaction region. *Solar Physics*, 282(2), 543–552. https://doi.org/10.1007/s11207-012-0161-z.

Stewart R.T. (1985). Moving Type IV bursts. In D.J. McLean and N.R. Labrum (Eds.), *Solar Radiophysics Studies of Emission from the Sun at Metre Wavelengths*. Cambridge University Press, 361–383.

DOI: 10.31401/WS.2026.proc.04

Solar Energetic Particle Events of Cycles 23-25

Gopalswamy N.[1], Yashiro S.[2], Makela P.[2], Xie H.[2], Akiyama S.[2]

[1]NASA Goddard Space Flight Center, Greenbelt, MD, USA
nat.gopalswamy@nasa.gov
[2]The Catholic University of America, Washington DC, USA

Abstract

We report on the solar cycle variability of large solar energetic particle (SEP) events that occurred during solar cycles (SCs) 23-25. The weak SC 24 witnessed mild space weather with only a couple of high-energy SEP events. Therefore, it is of interest to know the SEP situation in the moderate SC 25. We investigate the behavior of SEP events across the three cycles along with the properties of associated phenomena such as coronal mass ejections, major solar fares, and interplanetary type II radio bursts. We find that the number of ground level enhancement (GLE) events in SC 25 is larger than that in SC 24 but smaller than in SC 23. This ordering is similar to that of the cycle strength taken as the peak sunspot number (SSN). The number of halo CMEs normalized to SSN is the largest in SC 24, moderate in SC 25 and the smallest in SC 23. This ordering reflects the heliospheric pressure, which results in more halos in weaker cycles. Another finding is that the fraction of fast and wide CMEs and IP type II bursts resulting in an SEP event is the smallest in SC 25 indicating that the particle energization is least efficient in SC 25.

Keywords: solar energetic particles; coronal mass ejections; type II radio bursts.

1. Introduction

Solar energetic particles (SEPs) represent an important source of space weather hazards. SEPs can modify the ionospheric conductivity, cause ozone depletion in Earth's atmosphere, enhance energetic particle density in the inner radiation belt, reduce the lifetime of spacecraft solar panels, and present radiation hazard to interplanetary spacecraft. SEP events occur frequently during intervals of high solar activity in the solar maximum phase. Variation in the strength of solar cycles, therefore, affects the number, maximum energy, and intensity of SEP events. SEPs are accelerated by fast mode MHD shocks driven by energetic coronal mass ejections (CMEs) [e.g., Reames 1999]. These CMEs are accompanied by intense soft X-ray flares and interplanetary (IP) type II radio bursts. All these energetic phenomena are closely related to solar activity represented by the sunspot number (SSN). Thus, understanding the solar cycle variation of SEP events and the associated phenomena is important in developing long-term prediction of these events.

In this paper, we analyze the solar-cycle variation of SEP events that occurred during SCs 23-25. During this period CMEs and type II radio bursts have been continuously for the first time, so we are able to compare activities across the three cycles.

2. Data

We consider large SEP events that have an intensity ≥ 10 pfu at energies >10 MeV observed by NOAA's GOES satellites. The unit pfu (particle flux unit) is defined as 1 pfu = 1 particle cm^{-2} s^{-1} sr^{-1}. These events are listed at NOAA's SWPC (https://www.ngdc.noaa.gov/stp/space-weather/interplanetary-data/solar-proton-events/SEP%20page%20code.html). A similar list with added plots and links to various combination movies are available at the CDAW Data Center (https://cdaw.gsfc.nasa.gov/CME_list/sepe). We use the CME catalog (https://cdaw.gsfc.nasa.gov/CME_list) that lists all CMEs manually identified from the

coronagraph images obtained by the Solar and Heliospheric Observatory (SOHO), For interplanetary type II radio bursts we use the online list compiled from the radio and plasma waves (WAVES) experiment on board Wind and Solar Terrestrial Relations Observatory (STEREO). SSN is from Sunspot Index and Long-term Solar Observations (SILSO), World Data Center for the production, preservation and dissemination of the international SSN (https://www.sidc.be/SILSO/home). We also use the list of soft X-ray flares observed by the GOES satellites; for this study, we selected events with flare size ≥ M1.0. The list of intense geomagnetic storms defined as the ones with the disturbance storm time (Dst) index ≤ -100 nT and made available https://cdaw.gsfc.nasa.gov/CME_list/dst100 are also used as a complementary energetic phenomenon.

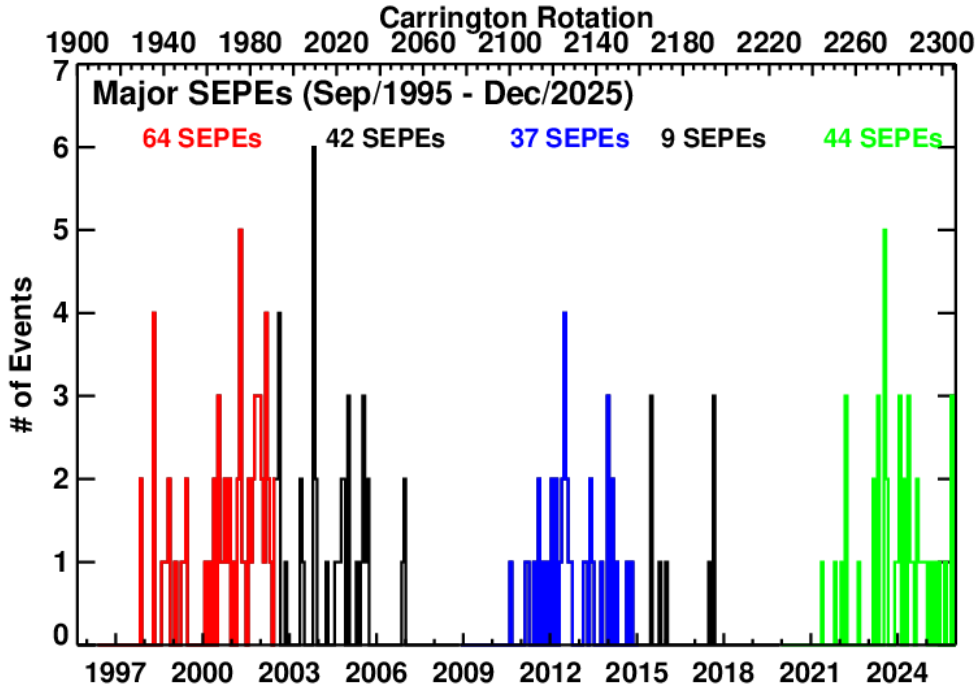


Figure 1*. The number of SEP events occurring in each Carrington rotation (CR) period during SCs 23-25. The X-axis at the top is the CR numbers. The red and blue numbers correspond to the first 73 months of SCs 23 and 24 to match the incomplete SC 25 (green). The black numbers indicate the additional events in SCs 23 and 24 that occurred during the rest of the cycles. Note that there are no large SEP events during October 1995 - November 1997, December 2006 - August 2010, and September 2017 - May 2021.*

3. Observational Results

In this section we compare the occurrence rates of SEP events, their intensity distributions, CME sky-plane speed distributions, and the source locations of SEP-associated CMEs (SEP CMEs, for short). Most of the events are regular SEP events, but in a few cases, the SEP intensity does not reach the 10 pfu level except when the shock arrives the GOES satellite. These events are known as energetic storm particle (ESP) events.

3.1. Occurrence rate of large SEP events

Figure 1 shows the solar cycle variation of the number of SEP events summed over Carrington rotation (CR) periods. We see that SEP events occur mostly during solar maxima. There are 2-3-year intervals during solar minima with no large SEP events. Among the three cycles, SC 23 has the greatest number of SEP events, SC 24 has the least number of events, and

SC 25 has intermediate numbers. The number of SEP events points to the strength of the solar cycle: SC 23 is the strongest, SC 24 is the weakest, and SC 25 is of intermediate strength.

3.2. SEP intensities in Solar Cycles 23-25

Figure 2 compares the SEP intensity distributions during SCs 23-25. It is clear that SEPs in SC 23 are frequent and often reach high intensities. The average intensities are 1520, 485, and 204 pfu, respectively. Even though solar activity in SC 25 is higher than that in SC 24, the SEP intensities did not reach high values. The median values are much smaller because of the many low-intensity events during the three cycles but the intensity ordering is similar to mean values. When we restrict the number of events to the first 73 months in each cycle (to match the epoch of SC 25 still in progress), the distributions did not change significantly. GOES-14 and 15 data products discontinued Mar 4, 2020 (https://www.ncei.noaa.gov/products/goes-1-15/space-weather-instruments). GOES-16 onwards there are no integral proton channels; values calculated from differential energy channels. More investigation is needed to confirm the lower intensities of SC 25 events.

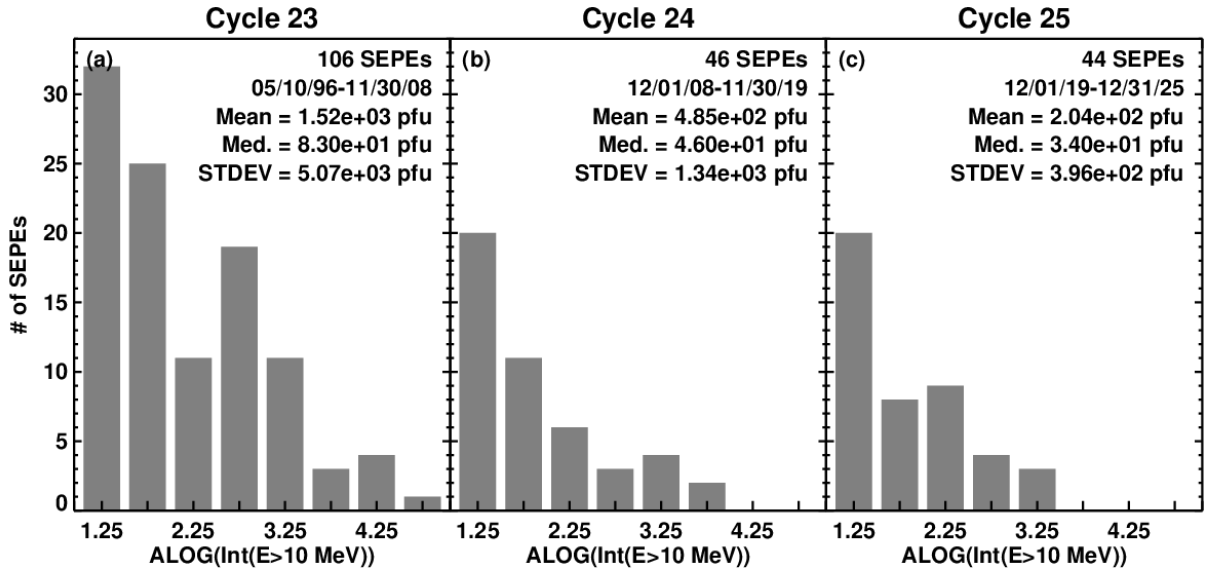


Figure 2. *Distributions of SEP intensities during SCs 23-25 in the >10 MeV integral channel. The mean, median, and standard deviations of the distributions are shown on the plots along with the number of events in each cycle. SCs 23 and 24 are full cycles, while SC 25 is in its early declining phase.*

3.3. Kinematic of SEP CMEs intensities in Solar Cycles 23-25

Figure 3 summarizes the major properties of SEP CMEs. The sky-plane speeds range from ~400 km/s to >3000 km/s with a most probable speed of ~1400 km/s and an average speed of ~1545 km/s (Fig. 3a). SOHO observations over the past three decades have shown that the average sky-plane speed of all CMEs is ~400 km/s. Thus, the SEP CMEs are ~4 times faster than the CMEs in the general population. The width distribution in Fig. 3b shows that more than 82% of SEP CMEs are halos. Halo CMEs for a given coronagraph are more energetic on average, consistent with the high speeds in Fig. 3a [Gopalswamy et al. 2010; 2026]. Halo CMEs also have important implications for the strength of solar cycles, as will be discussed below. The widths are ≥ 90º and the average width of non-halos is ~185º. Since wider CMEs are generally faster, the speed and width distributions imply that the SEP CMEs are very energetic [Gopalswamy et al. 2005]. Figure 3c shows the distribution of source locations of SEP CMEs on the Sun. The source locations are obtained as the heliographic coordinates of the associated

soft X-ray flare from NOAA Space Weather Prediction Center (SWPC) or SolarSoft (https://www.lmsal.com/solarsoft/last_events/). When source locations are not available, we obtain them from EUV, H-alpha, or other observations. The distribution also distinguishes four intensity levels. We see that most of the sources are located in the western hemisphere with some low-intensity events originating from the eastern hemisphere. This is a well-known effect of the Parker spiral magnetic field lines along with the SEPs propagate to Earth. For this reason, an eastern eruption can result in a large SEP event at locations well-connected to these eruptions. Note that there are many events that have source locations behind the west limb, which are not plotted.

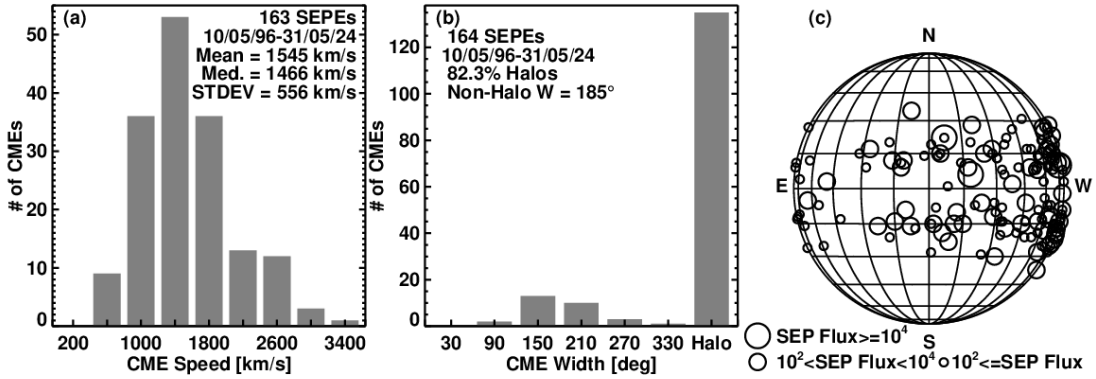


Figure 3. *Distributions of SEP intensities during SCs 23-25. The mean median, and standard deviations of the distributions are shown on the plots. SCs 23 and 24 are full cycles, while SC 25 is in its early declining phase.*

The SEP CME speed distributions are shown during individual cycles in Fig. 4. The median speeds are about the same in each cycle. The average speed is the highest in SC 24 and lowest in SC 23. However, the difference is small.

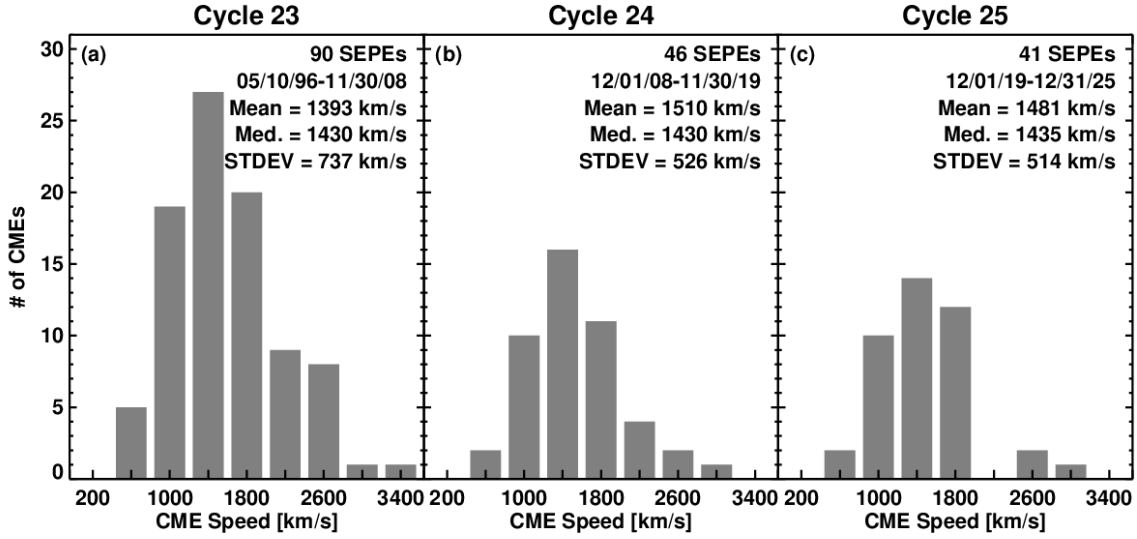


Figure 4. *Distributions SEP CME speeds during SCs 23-25. SC 25 is incomplete and is currently in its declining phase.*

3.4. Solar source locations as a function of time

Figure 5 shows the source locations of large SEP events plotted as a function of time. All events with known latitudes are plotted including events occurring behind the limb. We see that

the events are clustered around the solar maxima, as is also seen from Fig. 1. The plot is reminiscent of sunspot butterfly diagram because most of the SEP events originate from sunspot regions. The plot distinguishes SEP events with ground level enhancement (GLE). GLE events are considered to be extreme SEP events in that particles are accelerated to GeV energies. The plot shows that GLE events mostly occur during solar maxima. They also occur in the declining phase originating from occasional large active regions. Since active regions emerge closer to the equator in the declining phase, CMEs from these regions are better connected to Earth and hence increase the chance of observing a GLE. GLEs pose significant hazard to airplane passengers and crew in polar routes because the primary protons and the secondaries produced during their interaction with aircraft material contribute to the lifetime radiation dosage.

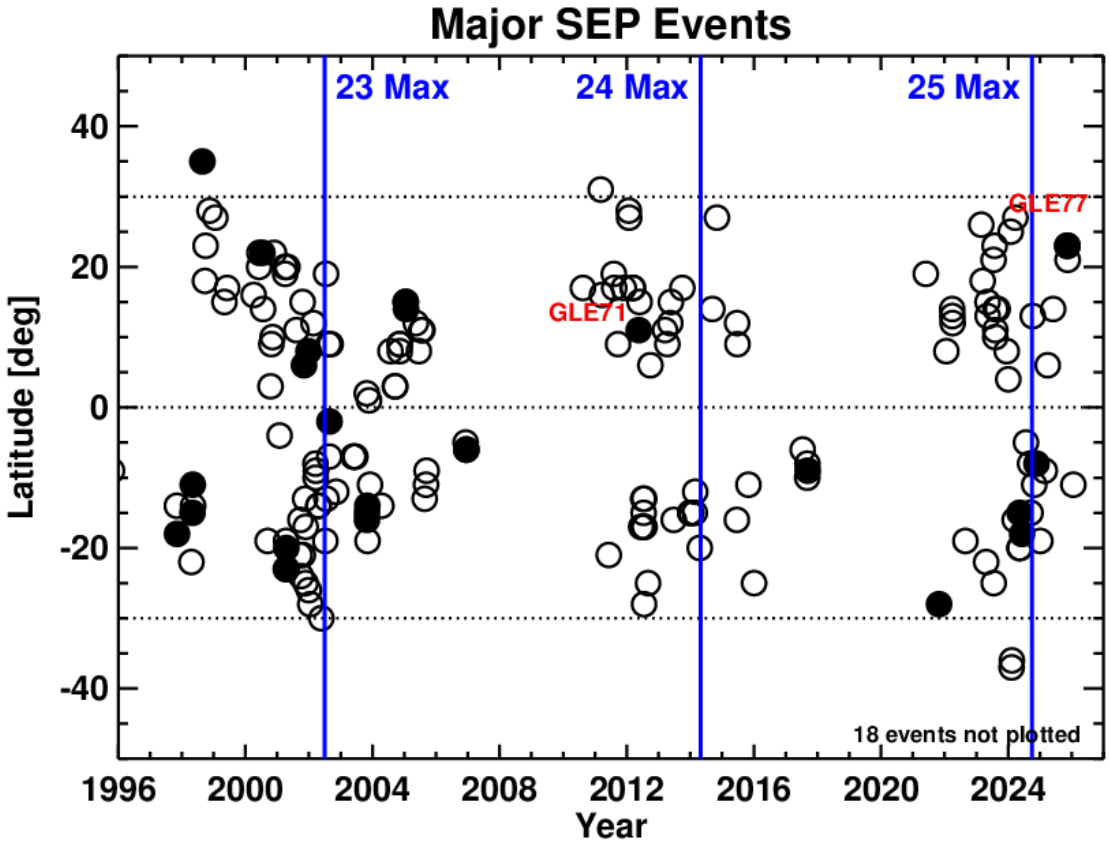


***Figure 5**. Source locations of CMEs that resulted in a large SEP event at Earth, as observed by GOES satellites. The filled circles mark those SEP events that have a ground level enhancement (GLE). Times of maximum sunspot number in each cycles are marked by the vertical blue lines. The first GLE of SC 24 (GLE 71) and the most recent one in SC 25 (GLE 77) are marked.*

This figure also shows that strong solar cycles result in more SEP events, especially the GLE events. Comparing SCs 23, 24, and 25, we see that the strongest among the three (SC 23) had the largest number of GLEs (16). The weakest of the three (SC 24) had only two GLEs. The current cycle 25 produced 5 GLEs until the end of 2025. SC 25 is already in the declining phase and there may not be too any GLEs. The solar-cycle dependent occurrence frequency of large SEP events and GLE events points to the importance of predicting the strength of solar cycles.

3.5. Comparison of SEP occurrence rates with those of other energetic events

Table 1 compares the number of SEP events during the first 73 months of SCs 23-25 and its comparison with other energetic events such as halo CMEs, fast and wide (FW) CMEs, type II

radio bursts at decameter-hectometric (DH) wavelengths, intense geomagnetic storms, and major soft X-ray flares (≥M1.0 GOES class). FW CMEs are those with a sky-plane speed of ≥900 km/s and angular width ≥60º.

The top row of Table 1 compares the monthly SSN averaged over the first 73 months in each cycle. We see that SC 23 is the strongest; SC 24 is the weakest; SC 25 is of intermediate strength. Compared to SC 23, the SSN dropped by 41% (SC 24) and 23% (SC 25). While the absolute number of SEP events follows the same trend as SSN, the numbers normalized to SSN are very different: while the SC 24 SEP activity is similar to that in SC 23, the SC 25 SEP activity dropped by ~12%. In the case of GLE events, which are highest-energy SEP events, the solar-cycle variations are quite pronounced. The number of GLEs is the largest in SC 23 with 9 events, the smallest in SC 24 with 1 event, and moderate in SC 25 with 5 events. It must be noted that in full cycles 23 and 24, the number of GLEs stands at 16 and 2, respectively. SC 25 is in its declining phase, it remains in the intermediate level. While the absolute GLE event numbers dropped by 89% (SC 24) and 44% (SC 25) relative to SC 23, the normalized numbers dropped by 75% and 25%, respectively. Thus, the reduction in the number of GLE events is more drastic than the reduction in solar activity (SSN). The number of intense geomagnetic storms show a trend similar to the GLEs. Relative to SC 23, the number of storms dripped by 58% in SC 24 and 27% in SC 25.

Table 1. *SEP events compared with associated energetic events.*

Property	SC23	SC 24[b]	SC 25[b]	SC24/SC23	SC25/SC23
Averaged SSN	111.5	66.1	86.3	0.59	0.77
#SEP events	64 (0.57)	37 (0.56)	44 (0.51)	0.58(0.98)	0.69 (0.89)
# GLE events	9 (0.08)	1 (0.02)	5 (0.06)	0.11(0.25)	0.56 (0.75)
#Magnetic storms	53 (0.48)	13 (0.20)	26 (0.30)	0.26(0.42)	0.49 (0.63)
#Halo CMEs	221 (1.98)	261 (3.95)	288 (3.34)	1.18 (2.0)	1.30 (1.67)
#SEP events/Halo CME	0.29	0.14	0.15	0.48	0.52
#FW CMEs	256 (2.30)	205 (3.10)	335 (3.39)	0.80(1.35)	1.31 (1.47)
#SEP events/FW CME	0.25	0.18	0.13	0.72	0.52
#DH Type II bursts	205 (1.84)	144 (2.18)	219 (2.54)	0.70(1.19)	1.07 (1.38)
#SEP events/Type II	0.31	0.26	0.20	0.84	0.65
# ≥M1.0 flares	1564(14.03)	941(14.23)	1881(21.80)	0.60(1.01)	1.20 (1.55)
#SEP events/M1 flare	0.033	0.039	0.023	1.18	0.70

Halo CMEs are more abundant in the weaker cycle 24 [Gopalswamy et al. 2015; 2026]. This trend is confirmed in SC 25 as well. Relative to SC 23, the number of halos normalized to SSN increased by 100% in SC 24 compared to 67% in SC 25. This result is consistent with the fact that SC 25 is stronger than SC 24 but weaker than SC 23. Normalizing the number of SEP events to that of halo CMEs, we see that SCs 24 and 25 have decreased SEP activity relative to halo CMEs.

The number of FW CMEs normalized to SSN increased by 35% in SC 24 and 47% in SC 25 relative to SC 23. The number of SEP events normalized to FW CMEs shows a progressive decline from SCs 23 to 25. In other words, the SEP activity normalized to SSN shows a 28% drop in SC 24 and a 48% drop in SC 25. This indicates that FW CMEs in SC 25 are less efficient in accelerating SEPs. The smaller average SEP intensity shown in Fig. 2 is consistent with this result. The reduction in acceleration efficiency is likely affected by the Alfven speed and magnetic field profiles in the corona and interplanetary medium [Gopalswamy et al. 2014]. The solar-cycle variation of the number of DH type II bursts has the same trend as FW CMEs because these two phenomena are closely related. The number of SEP events relative to the DH type II bursts dropped by 16% and 35% in SCs 24 and 25, respectively when compared to SC23.

The occurrence of major X-ray flares is more pronounced in SC 25, with 21.8 flares per SSN compared to 14.03 in SC 23. The flare activity in SC 24 is similar to that in SC 23 normalized to SSN.

The number of SEPs normalized to major flares does not show the same trend as FW CMEs and DH type II bursts. Relative to SC 23, the SEP rate slightly increased (18%) in SC 24 and decreased by 30% in SC 25. In other words, SC 25 witnessed many flares without an SEP association.

The results presented in Table 1 point to a complex relationship that SEP events have with the associated phenomena. The complexity arises from source and environmental factors. While these results describe the "average behavior" over a period of ~5 years in each cycle, more insight can be obtained by considering smaller time steps.

4. Summary and Conclusions

We investigated the solar-cycle variation of intensity and occurrence rate of SEP events during cycle 23-25, with the sunspot number defining solar activity. Since the current solar cycle 25 is still in progress, we focus on the first 73 months of each cycle to compare activity over corresponding epochs. We also compared the variation of energetic phenomena such as CMEs, type II radio bursts, and major solar flares with that of SEP events. We also compared the variation of GLE events and intense geomagnetic storms during the three solar cycles. The main conclusions of this study are as follows:

1. The sunspot number averaged over 73 months is 111.5, 66.1, and 86.3 for solar cycles 23, 24, and 25, respectively indicating that the cycle strength dropped by 41% and 23% in cycle 24 and 25 relative to cycle 23.
2. The absolute number of SEP events had similar trend as the sunspot number. The number of SEP events normalized to the sunspot number are similar in the three cycles with a slight reduction in cycle 25 relative to cycle 23.
3. The SEP activity is heavily concentrated during solar maxima with no SEP events for 2-3 years during solar minima.
4. The number of GLE events normalized numbers dropped by 75% and 25%, respectively relative to cycle 23.
5. The number intense geomagnetic storms normalized to the sunspot number dropped by 57% and 27% respectively, relative to cycle 23.
6. The sky-plane speed of the associated CMEs did not show significant variation during the three solar cycles
7. The number of halos normalized to the sunspot number confirms the impact of the heliospheric pressure: largest number of halos in the weakest cycle (24) and the smallest number during the strongest cycle (23).
8. The number of SEP events normalized to the number of fast and wide CMEs and DH type II bursts shows a significant reduction in cycles 24 and 25. Fast and Wide CMEs in SC 25 seem to be least effective in accelerating particles.
9. The number of SEP events normalized to major flares showed a reduction by 30% in SC 25 relative to SC 23, while SC 24 did not show any reduction (there was an 18% increase).

References

Gopalswamy, N., Yashiro, S., Michalek, G., Xie, H., Mäkelä, P., Vourlidas, A., Howard, R.A. (2010). A catalog of halo coronal mass ejections from SOHO, *Sun and Geosphere*, Vol. 5, No. 1, pp. 7–16.

Gopalswamy, N., Akiyama, S., Yashiro, S., Xie, H., Mäkelä, P., Michalek, G. (2014). Anomalous expansion of coronal mass ejections during solar cycle 24 and its space weather implications, *Geophysical Research Letters*, Vol. 41, pp. 2673–2680, DOI: 10.1002/2014GL059858.

Gopalswamy, N., Xie, H., Akiyama, S., Mäkelä, P., Yashiro, S., Michalek, G. (2015). The peculiar behavior of halo coronal mass ejections in solar cycle 24, *Astrophysical Journal Letters*, Vol. 804, No. 1, Art. L23, DOI: 10.1088/2041-8205/804/1/L23.

Gopalswamy, N., Michalek, G., Yashiro, S., Mäkelä, P., Akiyama, S., Xie, H. (2026). Implications of the abundance of halo coronal mass ejections for the strength of solar cycle 25, *Proceedings of the International Astronomical Union*, Vol. 20, Symposium S388, pp. 261–266, DOI: 10.1017/S1743921325000547.

Reames, D.V. (1999). Particle acceleration at the Sun and in the heliosphere, *Space Science Reviews*, Vol. 90, Nos. 3–4, pp. 413–491, DOI: 10.1023/A:1005105831781.

DOI: 10.31401/WS.2026.proc.05

Chaotic Behavior of Selected Solar and Geomagnetic Activity Indices during the Last Three Solar Cycles

Kilcik A.[1], *Calisir M.*[1], *Ozguc A.*[2]

[1]Department of Space Science and Technologies, Akdeniz University Faculty of Science, 07058, Antalya, Turkey
alikilcik@akdeniz.edu.tr; muhammed.calisirr@gmail.com
[2]Kandilli Observatory and Earthquake Research Institute, 34684, Bogazici University, Istanbul, Turkey

Abstract

In this study, we investigated the cycle-to-cycle chaotic variations in SSN, Ap, ScalarB, and solar wind speed data by applying the Surrogate Test, Hurst exponent, Lyapunov exponent, and correlation dimension analyses. In results of our analysis we found followings; i) the Hurst Exponent analysis show that the ScalarB has the lowest memory and the SSN has the highest one, ii) the surrogate test analysis show that all data sets have some level of noise, iii) based on the Lyapunov Exponent analysis we found that solar cycle 24 is more chaotic than the cycle 23 and solar cycle 25 is more chaotic than cycle 24, iv) Crassberger-Proaccia analysis results gave correlation dimensions between 1.48 and 3.47 for all the investigated data sets and cycles.

Keywords: Hurst exponent; Lyapunov exponent; correlation dimension; chaos analysis

1. Introduction

The Sun's complex and not yet fully understood magnetic field forms the foundation of solar activity [Svalgaard, 2013]. This activity is of great importance due to its role in shaping space weather conditions and its direct impacts on technological systems on Earth and in orbit. Understanding these complex solar and geomagnetic dynamics not only helps resolve fundamental physical mechanisms, but is also crucial for protecting modern technology and developing accurate forecasting models.

Long-term modeling of the solar magnetic field plays an important role in forecasting solar activity [Jiang et al., 2011; Henney et al., 2012; Bhowmik and Nandy, 2018]. Although solar and geomagnetic activity cycles have specific periods, it is emphasized in the literature that individual cycles are not entirely independent of one another. These processes do not progress in a linear structure; on the contrary, the system's sensitive dependence on initial conditions indicates the presence of chaotic dynamics. This demonstrates that solar activity indices are neither purely random (stochastic) nor completely periodic, and should be evaluated through a deterministic chaos approach.

Long-term relationships between the solar and geomagnetic activity indices exhibit different variations, particularly across the maximum and minimum phases of the cycle. Cliver et al. (1996) demonstrated a strong link between SSN and geomagnetic activity, showing that this relationship becomes more pronounced during solar maximum periods. An increase in sunspot numbers indicates an intensification of geomagnetic activity, resulting in more frequent and severe geomagnetic storms [Richardson and Cane, 2012]. Stamper et al. (1999) examined long-term correlations between SSN and the aa index, revealing that this relationship varies across different phases of the solar cycle. During the cycle maximum, an increase in SSN leads to a noticeable rise in the aa index, whereas this correlation weakens during the cycle minimum.

The chaotic properties of solar activity indices have been extensively investigated in the literature using time series analysis and chaos theory. Letellier et al. (2006) demonstrated that SSN exhibits chaotic dynamics associated with the solar magnetic cycle, employing the

Lyapunov exponent to reveal its sensitive dependence on initial conditions. Similarly, Spiegel (2009) analyzed the chaotic nature of the solar cycle and proposed that these cycles result from a nonlinear system. Zhou et al. (2014) used the Lyapunov exponent to evaluate the chaotic features of SSN, confirming that the time series display low-dimensional chaos and fractal properties. Sello (2001) calculated the Hurst exponent for SSN, reporting that the series carry long-term memory behavior and a chaotic structure.

Similarly, the chaotic properties of geomagnetic activity indices have been investigated in the literature using similar methods. Yu et al. (2007) analyzed the time series of the Dst index and reported that the data exhibit chaotic behavior associated with ring current dynamics in the magnetosphere. Ogunjo et al. (2021) examined the dynamic complexity of the Dst index and identified chaotic structures linked to magnetospheric processes during geomagnetic activity. Such chaos analyses demonstrate that solar and geomagnetic activities exhibit deterministic chaos and can be modeled more accurately using nonlinear methods. Therefore, analyzing the nonlinear properties of these indices with techniques such as Lyapunov exponents, time-delay reconstruction, and the Hurst exponent provides an essential foundation for understanding both solar magnetic cycles and geomagnetic processes, thereby advancing space weather forecasting.

In this study, we investigated the cycle-to-cycle chaotic variations in SSN, Ap index, ScalarB, and solar wind speed data across the last three solar cycles (SC23, SC24, and SC25) by applying the Surrogate Test, Hurst exponent, Lyapunov exponent, and correlation dimension analyses.

2. Data and Method

2.1. *Data*

We used following daily solar and geomagnetic activity data for the last three solar cycles (from Cycle 23 to 25, from August 1996 to December 2025).

Sunspot Number (SSN): SSNs are direct indicators of solar magnetic activity and exhibit a cycle of approximately 11 years (Schwabe Cycle). They have been widely used in the literature for tracking, modeling, and forecasting solar activity [Pesnell, 2008; Hathaway, 2015]. SSN data were obtained from the World Data Center SILSO, Royal Observatory of Belgium (https://www.sidc.be/SILSO/datafiles).

ScalarB (Interplanetary Magnetic Field – IMF): The Interplanetary Magnetic Field (IMF) represents the magnetic field component, carried by plasma originating from the Sun, as measured in interplanetary space. It serves as a fundamental driver of space weather. The IMF, which constantly reaches Earth along with the solar wind, directly influences the dynamics of the magnetosphere [Parker 1958; Owens and Forsyth, 2013]. The average magnitude of the IMF represents the overall strength of the interplanetary magnetic field.

Solar Wind Speed: Solar wind speed refers to the velocity at which charged particles, continuously ejected from the Sun's corona into space, reach the Earth. While this speed is around 300–400 km/s during solar minimum, it can rise to over 800 km/s during the solar cycle maximum due to solar eruptions or coronal holes. High-speed solar winds are the primary source of geomagnetic storms. Due to plasma dynamics and magnetohydrodynamic turbulence structures, these processes are inherently non-linear. ScalarB and Solar Wind Speed data were obtained from the NASA/OMNIWeb database (https://omniweb.gsfc.nasa.gov).

Ap index: The Ap index is the arithmetic mean of eight 3-hour ap values calculated throughout a day and is expressed in 'ap units' [Menvielle et al., 2010]. The Ap index is used to examine daily variations in geomagnetic activity and long-term trends in space weather conditions [Mayaud, 1980]. Geomagnetic Ap index data were obtained from the World Data Center for Geomagnetism, Kyoto (https://wdc.kugi.kyoto-u.ac.jp/).

*2.2.**Methodology***

In this study, we applied non-linear time series analyses methods to investigate the chaotic dynamics of the four selected parameters across different solar cycles. First, the Surrogate Data Test was applied to understand the noise levels in the data. Then Hurst exponent, Lyapunov exponent, and Correlation Dimension analyses were performed to examine the memory and chaotic behavior of the used datasets.

2.2.1. Surrogate Test

The surrogate data test is applied as a preliminary step before chaos analysis to determine whether the complexity observed in a time series represents true deterministic chaos or stochastic (random) noise. Surrogate datasets are synthetic time series generated by randomizing the phase or order of the original data while preserving its primary linear statistical properties (such as mean, variance, and power spectrum). The logic of the test is based on hypothesis testing: if the non-linear complexity metric of the original data differs significantly from that of the surrogate data, the null hypothesis of a linear random process is rejected. This confirms that the time series contains an underlying deterministic chaotic structure rather than simple random noise. To reconstruct the phase space required for non-linear analysis, two fundamental parameters are determined:

Time Delay (tau): Calculated using the Mutual Information method, time delay represents the optimal time interval where the correlation between past and future states first reaches a minimum. It provides the necessary time lag to construct independent coordinates for phase space reconstruction.

Embedding Dimension (m): Represents the minimum number of dimensions required to fully unfold the system's dynamics in phase space without trajectory overlap. The upper limit for the embedding dimension is constrained by the Eckmann-Ruelle criterion to ensure reliable dynamic estimation given the finite data length.

2.2.2. Correlation Dimension

The correlation dimension (D_2) measures the fractal dimensionality of an attractor and reflects the effective degrees of freedom of the system. It was first developed by Grassberger and Procaccia (1983a, 1983b) to estimate the fractal dimension of strange attractors in deterministic chaotic systems. This method analyzes the distances between reconstructed vectors in phase space to understand the geometric complexity of the dynamic system represented by a time series. Especially for time series with a limited number of observations, it is often preferred as an alternative to more complex criteria like the Lyapunov exponent to characterize chaotic dynamics and reveal the presence of deterministic structures. The correlation dimension aims to determine the fractal dimension of the system by examining the relationship between the correlation sum C(r) —which is the probability of vector pairs within a certain radius r—and the radius itself on a log-log plane. D_2 is calculated as the slope of the linear relationship between C(r) and r, and numerically expresses the effective degrees of freedom sustaining the system's dynamics. It is one of the fundamental quantities of chaotic systems and allows for the statistical estimation of the dimension of the geometric structure filled by the time series embedded in the phase space. This method not only measures the dynamic complexity of the system but also reveals whether it possesses a fractal structure. Based on the magnitude of the obtained value, information about the system's chaotic structure and predictability can be acquired as follows:

- $D_2 < 2$: The system has a low-dimensional deterministic chaos. The behavior of the system is predictable, and its dynamics can be explained by a small number of degrees of freedom. In other words, since the system's behavior can be described by

a few fundamental variables, its structure exhibits characteristics that are both modelable and predictable in the short term.

- $2 < D_2 < 5$: The system contains a moderate level of complexity and a deterministic chaotic structure. This range represents structures that are chaotic but predictable to a certain extent.
- $D_2 > 5$: The system exhibits high-dimensional, complex, and likely stochastic behavior. In this case, the predictability of the system is low, and even non-linear deterministic models provide only a limited degree of success.

2.2.3. Hurst Exponent

The Hurst exponent (H) was first defined in 1951 by the English hydrological engineer Harold Edwin Hurst. Hurst introduced this concept during his studies to optimize the capacity of water reservoirs while examining long-term observations of Nile River floods. He observed long-term memory or persistence behavior in time series that ordinary random trend models could not explain, and he developed the criterion known as the Hurst exponent to express this observation quantitatively. This method reveals the long-term memory of a time series, thereby indicating whether the time series follows a trend, reverts to the mean, or behaves randomly. Based on the values of H, the dataset is interpreted as follows:

- $H < 0.5$: The time series has negative autocorrelation. Increases are generally followed by decreases, and decreases by increases. This indicates that the series has a mean-reverting structure; that is, future values tend to move in the opposite direction of the past.
- $H = 0.5$: The time series has a memoryless structure and exhibits white noise behavior. In this case, past values have no effect on future values.
- $H > 0.5$: Positive autocorrelation is observed in the series. A series with an increasing trend is likely to continue increasing, while a decreasing series is likely to continue decreasing. This structure indicates that the series shows persistent behavior and that future behavior will tend to follow the same trend as the past.

2.2.4. The largest Lyapunov exponent (LLE)

The largest Lyapunov exponent measures the sensitive dependence on initial conditions in a system, which is the defining characteristic of deterministic chaos. It was first developed by the Russian mathematician Aleksandr Mikhailovich Lyapunov in 1892 to study the stability of systems defined by differential equations. The Lyapunov exponent (λ) provides important information about the behavior of the system over time, particularly when it is negative, close to zero, or positive. This exponent represents the average logarithmic rate of separation between two close trajectories per unit time and can be interpreted as follows:

- $\lambda < 0$: The system's trajectories are converging and settling into a stable state, such as a single equilibrium point or a fixed state. However, since dynamic diversity is limited in such systems, predictive models are generally simple.
- $\lambda = 0$: The system is in a state of neutral equilibrium or exhibits periodic/quasi-periodic behavior. In this case, trajectories may remain constant or enter a periodically repeating cycle. There is no chaotic structure; the system is predictable, and the level of complexity is low.
- $\lambda > 0$: The system exhibits chaotic behavior. Due to high sensitivity to initial conditions, trajectories starting from very close initial points diverge exponentially over time. This makes long-term predictions impossible.

3. Analysis and Results

The chaotic dynamics of Sunspot Number (SSN), ScalarB, Solar Wind Speed, and Ap index were analyzed using daily data across the last three solar cycles (Cycles 23, 24, and 25). The Surrogate Test, Hurst Exponent, and Lyapunov Exponent analysis were applied to evaluate the non-linear characteristics of each time series. The graphical results for SSN are shown in Figure 1, ScalarB in Figure 2, Solar Wind Speed in Figure 3, and Ap index in Figure 4. Also, the calculated numerical values for all parameters across the three solar cycles are presented in Table 1.

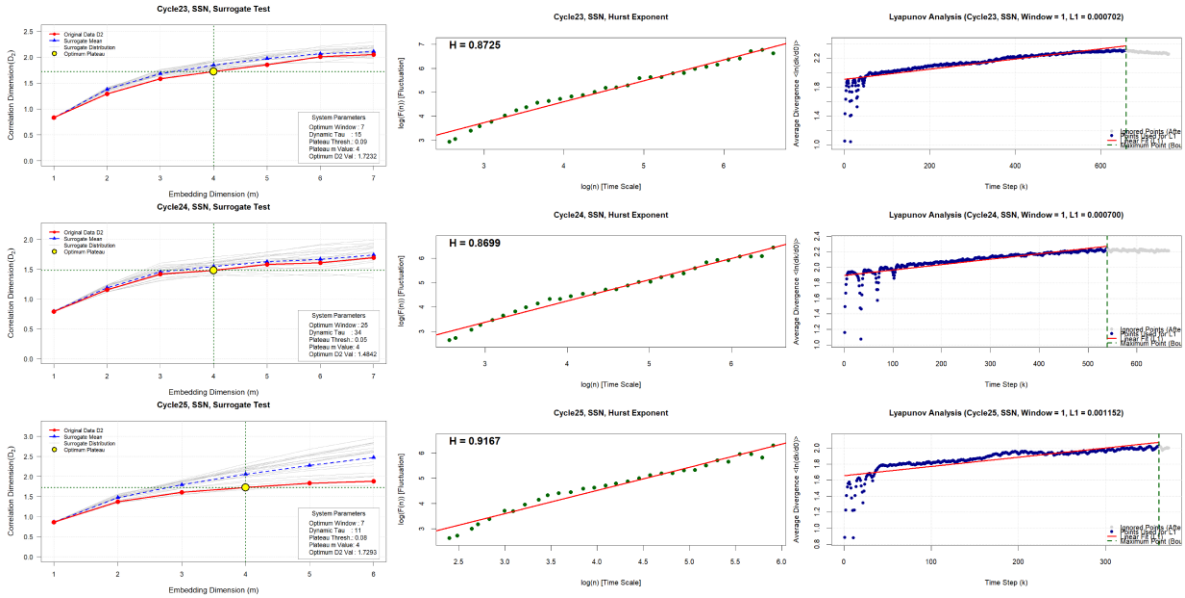


Figure 1. *SSN analysis results. Columns from left to right show the surrogate test, Hurst exponent, and Lyapunov exponent analysis results. Rows from top to bottom correspond to Solar Cycles 23, 24, and 25.*

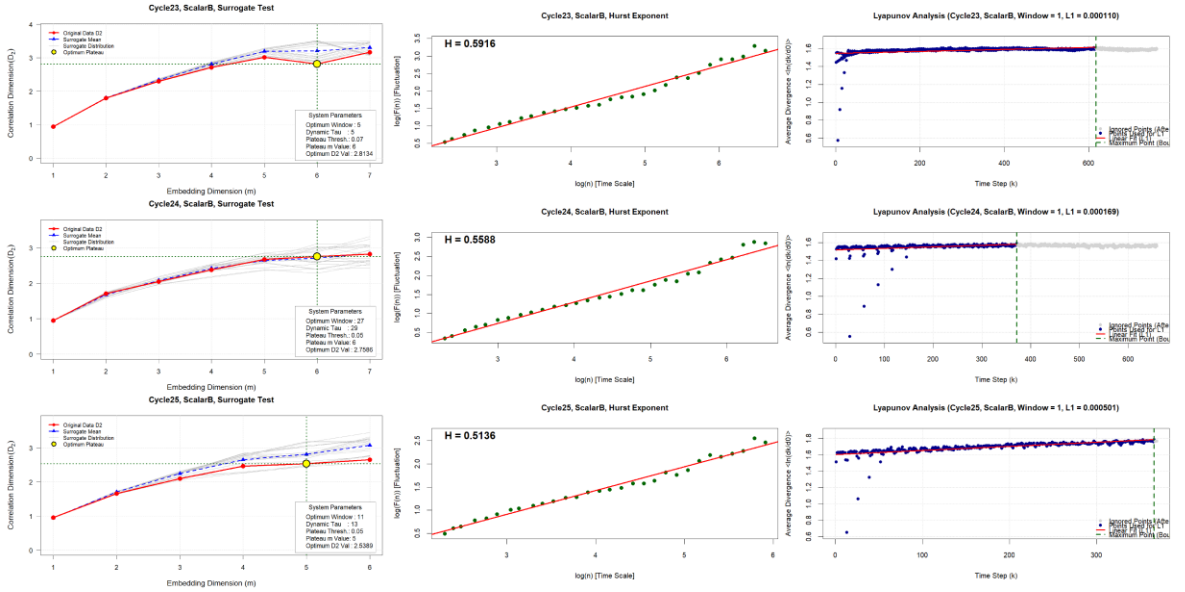


Figure 2. *Same as Figure 1, but showing the analysis results for ScalarB.*

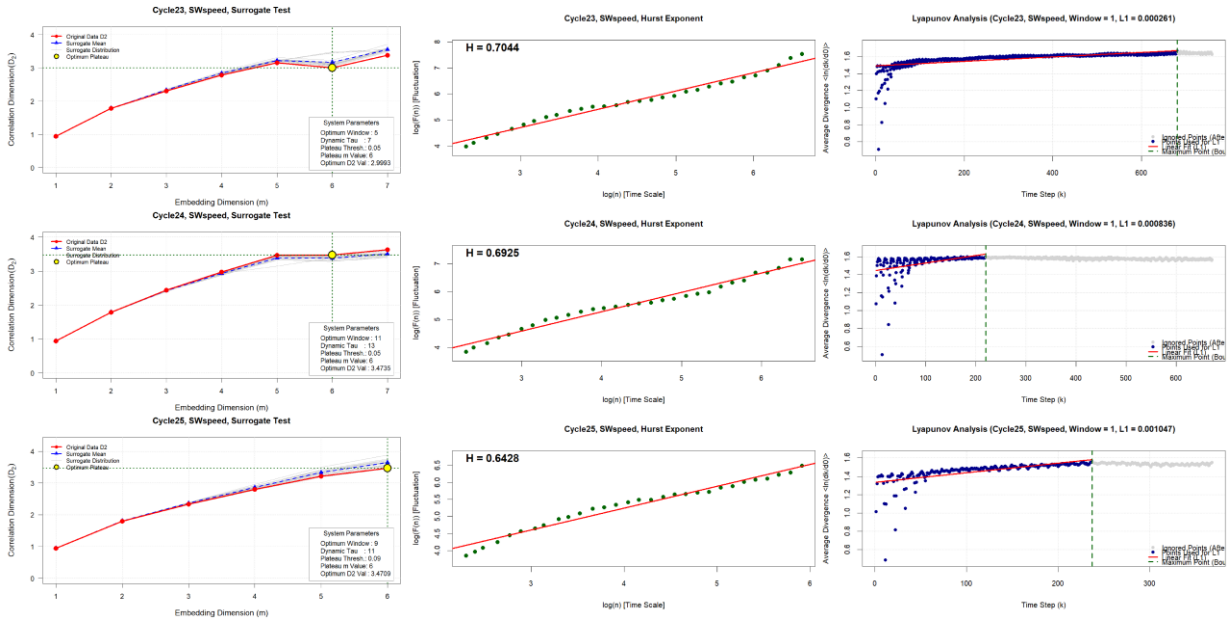


Figure 3. *Same as Figure 1, but showing the analysis results for SW speed.*

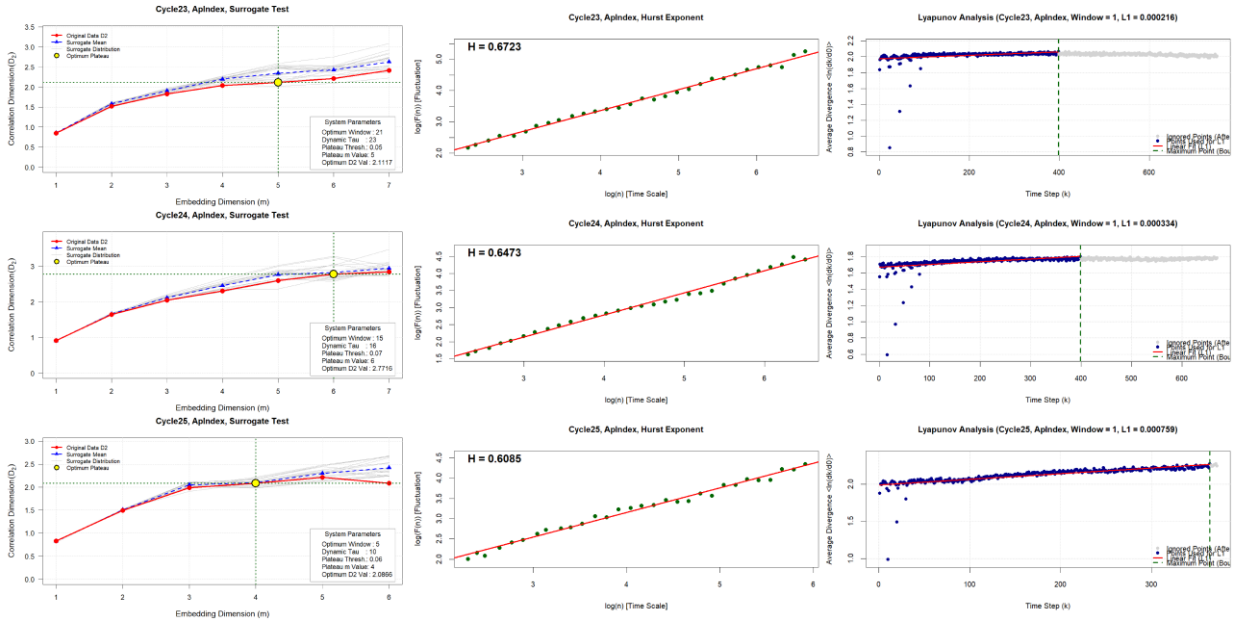


Figure 4. *Same as Figure 1, but showing the analysis results for Ap Index.*

Complete list of the results for analyzed parameters for each solar cycle are presented in Table 1.

Table 1. *List of the results for analyzed parameters for each solar cycle*

	Cycle 23					
	Hurst Exponent	**Optimum Window**	**Lyapunov Exponent**	**Tau**	**Correlation Dimension**	**M**
SSN	0.8725	7	0.000702	15	1.7232	4
ScalarB	0.5916	5	0.00011	5	2.8134	6
Solar Wind Speed	0.7044	5	0.000261	7	2.9993	6
Ap Index	0.6723	21	0.000216	23	2.1117	5

	Cycle 24					
	Hurst Exponent	**Optimum Window**	**Lyapunov Exponent**	**Tau**	**Correlation Dimension**	**M**
SSN	0.8699	25	0.0007	34	1.4842	4
ScalarB	0.5588	27	0.000169	29	2.7586	6
Solar Wind Speed	0.6925	11	0.000836	13	3.4735	6
Ap Index	0.6473	15	0.000334	16	2.7716	6
	Cycle 25					
	Hurst Exponent	**Optimum Window**	**Lyapunov Exponent**	**Tau**	**Correlation Dimension**	**M**
SSN	0.9167	7	0.001152	11	1.7293	4
ScalarB	0.5136	11	0.000501	13	2.5389	5
Solar Wind Speed	0.6428	9	0.001047	11	3.4709	6
Ap Index	0.6085	5	0.000759	10	2.0866	4

4. Conclusions and Discussions

The application of chaos theory and nonlinear dynamics has provided valuable information to understand the complexity of solar cycles and improve long term prediction models [Jevtic et al. 2001; Letellier et al. 2006; Spiegel 2009; Kilcik et al. 2009; Crosson and Binder 2009; McIntosh et al. 2017, 2020; Petrovay 2020]. In this study we analyzed the daily data of four solar and geomagnetic activity parameters (SSN, ScalarB, Solar Wind Speed, and Ap index) for the last three solar cycles (Cycles 23, 24, and 25) and try to determine their chaotic behaviors. Our main results are as follows:

- *Presence of Deterministic Chaos in All Parameters:* In all analyzed cycles and for all parameters, the Lyapunov exponent is positive ($\lambda > 0$) and the Hurst exponent is greater than 0.5 ($H > 0.5$). This confirms that none of the parameters represent pure random noise; rather, they are all persistent, deterministic chaotic systems sensitive to initial conditions and possessing long-term memory.
- *Most Predictable and Stable Parameter (SSN):* The Sunspot Number (SSN) exhibits the highest Hurst exponent (0.87 - 0.91) and the lowest Correlation Dimension (1.48 - 1.72) across all cycles. This indicates that SSN possesses very strong long-term memory and its dynamics can be explained with a small number of degrees of freedom (low-dimensional chaos, m=4). It is the most straightforward parameter to model and predict.
- *Most Complex Parameter (Solar Wind Speed):* Solar Wind Speed is the parameter with the highest Correlation Dimension (~3.47 in Cycles 24 and 25). This indicates that the system has a high-dimensional and complex structure, requiring more variables (embedding dimension m=6) to explain its underlying dynamics.
- *Parameter Closest to Randomness (ScalarB):* The Hurst exponent of ScalarB is the closest among all parameters to 0.5 (white noise), particularly in Cycle 25 at 0.5136. It is the dataset with the weakest autocorrelation and the highest tendency toward random behavior.
- *Increasing Chaoticity in Cycle 25 (Lyapunov Trend):* One of the most remarkable findings in the table is the steady increase in the Lyapunov exponent across all parameters from Cycle 23 to Cycle 25 (e.g., from 0.0007 to 0.0011 for SSN, and from 0.0002 to 0.0010 for Solar Wind Speed). This result indicates that Cycle 25 is significantly more sensitive to initial conditions compared to previous cycles, and consequently, its long-term predictability is lower (more chaotic).

- *Loss of Memory in Interplanetary/Geomagnetic Parameters (Hurst Trend):* The Hurst exponents of ScalarB, Solar Wind Speed, and the Ap Index show a consistent downward trend from Cycle 23 to Cycle 25 (approaching 0.5). Space weather and geomagnetic systems are gradually losing their long-term memory in the most recent cycle, taking on a noisier structure.

Solar activity and geomagnetic indices show complex interactions and sudden changes beyond simple periodic behaviors [Mundt et al. 1991; Consolini et al. 1996; Donner et al. 2019; Alberti et al. 2020; Alberti et al. 2021]. Although these cycles appear to follow a regular order, they are actually nonlinear dynamic systems highly sensitive to initial conditions. This means the activity is neither completely random nor perfectly predictable, but it is governed by deterministic chaos. Because of this hidden chaotic structure, predicting solar and geomagnetic indices using only linear models is insufficient. For this reason, the nonlinear chaotic approach provides a much better framework for understanding such complex systems [Sugihara 1994; Tsonis et al. 2015].

The findings of our study are important for space weather research. Analyzing the last three solar cycles provides a long time series, and using daily data over this extensive period helps to clearly observe the dynamic changes in the system. By calculating the chaotic properties of SSN, ScalarB, Solar Wind Speed, and the Ap index, we reveal the complex behavior of solar and geomagnetic activity. Consequently, understanding this chaotic behavior will improve the reliability of future prediction models.

Acknowledgments

This study was supported by Project 124N011 awarded by the Scientific and Technological Research Council of Türkiye.

References

Alberti, T., Consolini, G., De Michelis, P. (2021). Complexity measures of geomagnetic indices in the last two solar cycles, Journal of Atmospheric and Solar-Terrestrial Physics, Vol 217, pp. 105583, DOI: 10.1016/j.jastp.2021.105583.

Alberti, T., Lekscha, J., Consolini, G., De Michelis, P., Donner, R.V. (2020). Disentangling nonlinear geomagnetic variability during magnetic storms and quiescence by timescale dependent recurrence properties, Journal of Space Weather and Space Climate, Vol 10, pp. 25, DOI: 10.1051/swsc/2020026.

Bhowmik, P., Nandy, D. (2018). Prediction of the strength and timing of sunspot cycle 25 reveal decadal-scale space environmental conditions, Nat Commun, Vol 9, pp. 5209, DOI: 10.1038/s41467-018-07690-0.

Cliver, E.W., Boriakoff, V., Bounar, K.H. (1996). The 22-year cycle of geomagnetic and solar wind activity, Journal of Geophysical Research: Space Physics, Vol 101, No A12, pp. 27091-27109, DOI: 10.1029/96JA02037.

Consolini, G., Marcucci, M.F., Candidi, M. (1996). Multifractal structure of auroral electrojet index data, Physical Review Letters, Vol 76, No 21, pp. 4082, DOI: 10.1103/PhysRevLett.76.4082.

Crosson, I.J., Binder, P.M. (2009). Chaos-based forecast of sunspot cycle 24, Journal of Geophysical Research: Space Physics, Vol 114, No A1, DOI: 10.1029/2008JA013859.

Donner, R.V., Balasis, G., Stolbova, V., Georgiou, M., Wiedermann, M., Kurths, J. (2019). Recurrence-based quantification of dynamical complexity in the Earth's magnetosphere at geospace storm timescales, Journal of Geophysical Research: Space Physics, Vol 124, No 1, pp. 90-108, DOI: 10.1029/2018JA025318.

Grassberger, P., Procaccia, I. (1983a). Characterization of strange attractors, Physical Review Letters, Vol 50, No 5, pp. 346-349, DOI: 10.1103/PhysRevLett.50.346.

Grassberger, P., Procaccia, I. (1983b). Measuring the strangeness of strange attractors, Physica D: Nonlinear Phenomena, Vol 9, No 1-2, pp. 189-208, DOI: 10.1016/0167-2789(83)90298-1.

Hathaway, D.H. (2015). The Solar Cycle, Living Rev. Sol. Phys., Vol 12, No 4, pp. 4, DOI: 10.1007/lrsp-2015-4.

Henney, C.J., Toussaint, W.A., White, S.M., Arge, C.N. (2012). Forecasting F10.7 with solar magnetic flux transport modeling, Space Weather, Vol 10, No 2, pp. S02011, DOI: 10.1029/2011SW000748.

Hurst, H.E. (1951). Long-term storage capacity of reservoirs, Transactions of the American Society of Civil Engineers, Vol 116, pp. 770-799, DOI: 10.1061/TACEAT.0006518.

Jevtic, N., Schweitzer, J.S., Cellucci, C.J. (2001). Research Note: Nonlinear time series analysis of northern and southern solar hemisphere daily sunspot numbers in search of short-term chaotic behavior, Astronomy & Astrophysics, Vol 379, No 2, pp. 611-615, DOI: 10.1051/0004-6361:20011277.

Jiang, J., Cameron, R.H., Schmitt, D., Schuessler, M. (2011). The solar magnetic field since 1700 - I. Characteristics of sunspot group emergence and reconstruction of the butterfly diagram, Astronomy & Astrophysics, Vol 528, pp. A82, DOI: 10.1051/0004-6361/201016167.

Kilcik, A., Anderson, C.N.K., Rozelot, J.P., Ye, H., Sugihara, G., Ozguc, A. (2009). Nonlinear prediction of solar cycle 24, The Astrophysical Journal, Vol 693, No 2, pp. 1173-1177, DOI: 10.1088/0004-637X/693/2/1173.

Letellier, C., Aguirre, L.A., Maquet, J., Gilmore, R. (2006). Evidence for low dimensional chaos in sunspot cycles, Astronomy & Astrophysics, Vol 449, No 1, pp. 379-387, DOI: 10.1051/0004-6361:20053947.

Lyapunov, A.M. (1892). The General Problem of the Stability of Motion, Kharkov Mathematical Society.

Mayaud, P.N. (1980). Derivation, meaning, and use of geomagnetic indices, American Geophysical Union, Vol 22, pp. 154, DOI: 10.1029/GM022.

McIntosh, S.W., Chapman, S., Leamon, R.J., et al. (2020). Overlapping Magnetic Activity Cycles and the Sunspot Number: Forecasting Sunspot Cycle 25 Amplitude, Sol Phys, Vol 295, pp. 163, DOI: 10.1007/s11207-020-01723-y.

McIntosh, S.W., Leamon, R.J. (2017). Deciphering solar magnetic activity: Spotting solar cycle 25, Frontiers in Astronomy and Space Sciences, Vol 4, pp. 4, DOI: 10.48550/arXiv.1702.04414.

Menvielle, M., Iyemori, T., Marchaudon, A., Nosé, M. (2010). Geomagnetic Indices. In: Geomagnetic Observations and Models, IAGA Special Sopron Book Series, Vol 5, DOI: 10.1007/978-90-481-9858-0_8.

Mundt, M.D., Maguire, W.B., Chase, R.R. (1991). Chaos in the sunspot cycle: Analysis and prediction, Journal of Geophysical Research: Space Physics, Vol 96, No A2, pp. 1705-1716, DOI: 10.1029/90JA02150.

Ogunjo, S.T., Rabiu, A.B., Fuwape, I.A., Obafaye, A.A. (2021). Evolution of dynamical complexities in geospace as captured by Dst over four solar cycles 1964-2008, Journal of Geophysical Research: Space Physics, Vol 126, No 4, pp. e2020JA027873, DOI: 10.1029/2020JA027873.

Owens, M.J., Forsyth, R.J. (2013). The Heliospheric Magnetic Field, Living Rev. Sol. Phys., Vol 10, No 5, pp. 5, DOI: 10.12942/lrsp-2013-5.

Parker, E.N. (1958). Dynamics of the interplanetary gas and magnetic fields, Astrophysical Journal, Vol 128, pp. 664, DOI: 10.1086/146579.

Pesnell, W.D. (2008). Predictions of Solar Cycle 24, Sol Phys, Vol 252, pp. 209-220, DOI: 10.1007/s11207-008-9252-2.

Petrovay, K. (2020). Solar cycle prediction, Living Rev Sol Phys, Vol 17, pp. 2, DOI: 10.1007/s41116-020-0022-z.

Richardson, I.G., Cane, H.V. (2012). Near-earth solar wind flows and related geomagnetic activity during more than four solar cycles (1963-2011), J. Space Weather Space Clim., Vol 2, pp. A02, DOI: 10.1051/swsc/2012003.

Sello, S. (2001). Solar cycle forecasting: a nonlinear dynamics approach, Astronomy & Astrophysics, Vol 377, No 1, pp. 312-320, DOI: 10.1051/0004-6361:20011068.

Spiegel, E.A. (2009). Chaos and intermittency in the solar cycle, Space Science Reviews, Vol 144, pp. 25-51, DOI: 10.1007/s11214-008-9470-9.

Stamper, R., Lockwood, M., Wild, M.N., Clark, T.D.G. (1999). Solar causes of the long-term increase in geomagnetic activity, Journal of Geophysical Research: Space Physics, Vol 104, No A12, pp. 28325-28342, DOI: 10.1029/1999JA900311.

Sugihara, G. (1994). Nonlinear forecasting for the classification of natural time series, Philosophical Transactions of the Royal Society of London. Series A: Physical and Engineering Sciences, Vol 348, No 1688, pp. 477-495, DOI: 10.1098/rsta.1994.0106.

Svalgaard, L. (2013). Solar activity-past, present, future, J. Space Weather Space Clim., Vol 3, pp. A24, DOI: 10.1051/swsc/2013046.

Tsonis, A.A., et al. (2015). Dynamical evidence for causality between galactic cosmic rays and interannual variation in global temperature, Proceedings of the National Academy of Sciences, Vol 112, No 11, pp. 3253-3256, DOI: 10.1073/pnas.1420291112.

Yu, Z.G., Anh, V.V., Wanliss, J.A., Watson, S.M. (2007). Chaos game representation of the Dst index and prediction of geomagnetic storm events, Chaos, Solitons & Fractals, Vol 31, No 3, pp. 736-746, DOI: 10.1016/j.chaos.2005.12.046.

Zhou, S., Feng, Y., Wu, W.Y., Li, Y., Liu, J. (2014). Low-dimensional chaos and fractal properties of long-term sunspot activity, Research in Astronomy and Astrophysics, Vol 14, No 1, pp. 104, DOI: 10.1088/1674-4527/14/1/009.

DOI: 10.31401/WS.2026.proc.06

Relationship between Sunspot Number, Sunspot Magnetic Field Strength, CME Activity, and Geomagnetic Storms during Solar Cycle 24

Kirov B.[1], *Georgieva K.*[1], *Kirov B.B*[2,3,4], *Asenovski S.*[1]

[1]Space Research and Technology Institute, Bulgarian Academy of Sciences, Sofia, Bulgaria
corresponding author e-mail: bkirov@space.bas.bg
[2]Faculty of German Engineering Education and Industrial Management (FDIBA), Technical University of Sofia
[3]BioInfoTech Laboratory, Sofia Tech Park, 111 Tsarigradsko Shose Blvd., 1784 Sofia, Bulgaria
[4]Department Industrial Automation, Technical University of Sofia, 1756 Sofia, Bulgaria

Abstract

Coronal mass ejections (CMEs) generally follow sunspot activity, but their occurrence and terrestrial effects vary substantially within a solar cycle. We examine monthly sunspot number (SSN), CME occurrence, the monthly mean of daily maximum sunspot magnetic-field strengths, and geomagnetic storms with sudden commencement (SSC) during Solar Cycle 24. CME occurrence is strongly correlated with SSN for the complete cycle (r = 0.90) and also with the magnetic-field parameter (r = 0.69), but the maxima do not coincide: the strongest monthly mean sunspot fields occurred in 2011, whereas the largest SSN and CME occurrence were mainly observed in 2013-2014. The CME-SSC correlation is weak (r = 0.20). Dividing the cycle into four phases reveals pronounced changes in these relationships. The declining phase has the lowest mean maximum sunspot magnetic field (1719 G) but the highest relative occurrence of SSC storms per CME (0.423 SSC per 100 CMEs), while the inter-maximum interval has a stronger mean field but the lowest ratio (0.196). The results show that sunspot magnetic-field strength contains information complementary to SSN, but its independent relation to CME productivity is phase dependent. They also show that the relative occurrence of SSC storms per CME cannot be described by a simple one-parameter dependence on CME occurrence or sunspot magnetic-field strength.

Keywords: sunspot magnetic fields; coronal mass ejections; sudden commencement

1. Introduction

Sunspot number (SSN) is the traditional index of the approximately 11-year solar cycle, but it does not fully describe the magnetic properties of active regions. CMEs are major drivers of heliospheric and geomagnetic disturbances, and their occurrence generally follows SSN. Nevertheless, the CME-SSN relation varies within and between cycles [Kirov et al., 2023; Lamy et al., 2019; Mishra et al., 2019]. Cycle 24 was relatively weak in SSN, yet its CME occurrence did not decrease proportionally [Lamy et al., 2019; Mishra et al., 2019].

This non-proportional behavior is important for long-term solar-terrestrial studies. Sunspot number measures the abundance of visible spots, whereas eruptive activity is controlled by magnetic energy stored in active regions. Consequently, intervals with similar SSN may differ in CME productivity if their magnetic properties differ. This motivates the search for a complementary index capable of describing the magnetic state of the strongest sunspots present during a given interval.

Because the energy of solar eruptions is magnetic, sunspot magnetic fields may provide information that is not contained in SSN alone. Long-term measurements show that magnetic-field strength and sunspot number do not evolve identically; this is also seen in Crimean observations during Cycle 24 [Tsap et al., 2021]. At Earth, only part of the observed CME population produces shock-associated disturbances. SSC occurrence depends on CME

direction and kinematics, shock formation, propagation, and the ambient solar wind [Zhang et al., 2021].

The use of a magnetic-field parameter is therefore intended here as a complement to, rather than a replacement for, SSN. We focus on the strongest field measured on the disk each day because it provides a simple long-term measure of the upper end of the observed sunspot-field distribution. At the geomagnetic end, SSC storms are used as a statistical indicator of shock-associated terrestrial impacts; the SSC/CME ratio is interpreted only as the relative occurrence of SSC storms per CME and not as a measure of storm intensity.

Cycle 24 also exhibited a pronounced double maximum separated by a Gnevyshev-gap-like interval [Takalo, 2021]. We therefore investigate the four monthly parameters both for the complete cycle and for four characteristic phases. Our working questions are whether sunspot magnetic-field strength helps characterize CME productivity beyond SSN and whether the relative occurrence of SSC storms per CME changes systematically with cycle phase.

2. Data and Methods

2.1. Sunspot Number and CME Data

Monthly SSN data are from WDC-SILSO [WDC-SILSO, n.d.]. For consistency with our earlier studies, Version 1 values are used to 1 July 2015 and V1-equivalent values reconstructed from Version 2 thereafter, following [Kirov et al., 2023]. CME data are monthly totals from the manually compiled SOHO/LASCO CDAW catalog [SOHO/LASCO CME Catalog, n.d.], chosen for its long and internally consistent series [Boursier et al., 2009; Byrne et al., 2012; Richardson et al., 2015; Lamy et al., 2019].

The CDAW catalog contains CMEs identified in SOHO/LASCO coronagraph images since 1996. Different automated procedures can detect different numbers of faint or narrow events and can return different speeds or angular widths; these catalog-dependent effects are important when long-term occurrence rates are compared [Boursier et al., 2009; Byrne et al., 2012; Richardson et al., 2015]. We therefore retain one catalog throughout the analysis.

2.2. Sunspot Magnetic Field Strength

Sunspot magnetic-field measurements are taken from the Crimean Astrophysical Observatory archive [Crimean Astrophysical Observatory, n.d.]. For each observing day we select the largest absolute magnetic-field value measured in any sunspot on the visible disk. The original labels give polarity and field strength in units of 100 G; all values used here are converted to gauss. The monthly parameter is the arithmetic mean of the daily maxima:

$$B_{MMF} = \frac{1}{N}\sum_{i=1}^{N} B_{max,i}, \quad (1)$$

where N is the number of usable daily observations in that month. Thus, the parameter BMMF characterizes the strongest fields present during a month rather than the mean field of all sunspots.

This definition is important for interpreting the results. BMMF is not the average magnetic field of all sunspots and is not assigned to a particular CME source region. It is a monthly index of the strongest fields present on the visible Sun. For example, a label S33 corresponds to 3300 G; the polarity sign is retained in the archive, but the present analysis uses the absolute field strength. A working monthly value such as 25.87 in units of 100 G is therefore reported here as 2587 G.

Days explicitly marked “no sunspots” are included as 0 G; observations with sunspots but unreadable field values are excluded, duplicate images of the same date are counted once, and months without usable observations are treated as missing. Figure 1 illustrates the procedure.

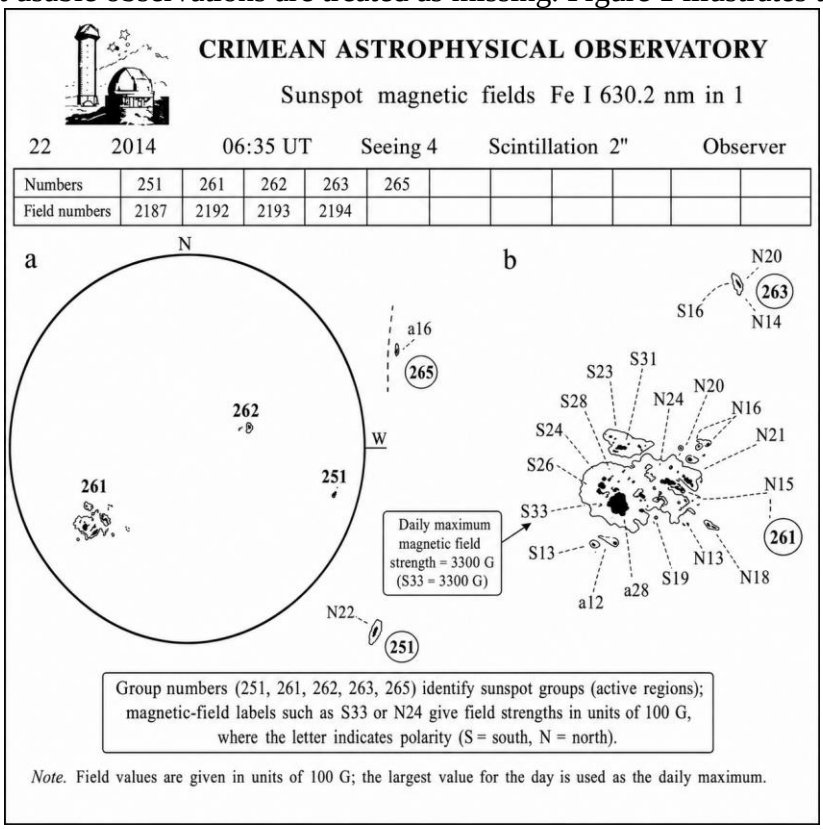


Figure 1. *Example of a CrAO sunspot magnetic-field observation for 28 May 2014 [Crimean Astrophysical Observatory, n.d.]. Group numbers are distinct from field labels. The largest absolute field shown, S33, corresponds to 3300 G and is selected as the daily maximum; the annotation was added by the authors.*

2.3. Geomagnetic Storms and Statistical Analysis

SSC storms are taken from the IZMIRAN catalog [Pushkov Institute/IZMIRAN, n.d.], which lists event onset and end times, duration, intensity class, and magnetic disturbance parameters. Events are assigned to months by starting date, and the monthly number of storms is used. Because the analysis is monthly and the CDAW denominator contains all catalogued CMEs, SSC/CME is treated only as a comparative phase indicator.

We compare SSN, CME number, monthly mean maximum field, and SSC number using Pearson and Spearman correlations. Partial correlations are used to test B-CME after controlling for SSN and B-SSC after controlling for CME count. Solar Cycle 24 is also divided using turning points of the 13-month smoothed SSN: Phase I, Dec 2008-Mar 2012; Phase II, Apr 2012-Apr 2013; Phase III, May 2013-Apr 2014; and Phase IV, May 2014-Nov 2019. The ratio SSC/CME is used only as a statistical measure of the relative occurrence of SSC storms per CME, not as a measure of storm intensity.

3. Results

3.1. Temporal Evolution and Whole-Cycle Relationships

The four monthly series are shown in Figure 2. Their general cycle variation is related, but their maxima differ. The highest SSN (103.16) occurred in February 2014. The largest CME monthly total was 261 in May 2013 (SSN = 84.87), and 259 CMEs occurred in June 2014 at

SSN = 72.66. In contrast, the strongest monthly mean maximum fields occurred earlier: 3525 G in October 2011 and 3509 G in November 2011. A total of 57 SSC storms occurred during the 132-month interval, with a maximum of four in February 2014.

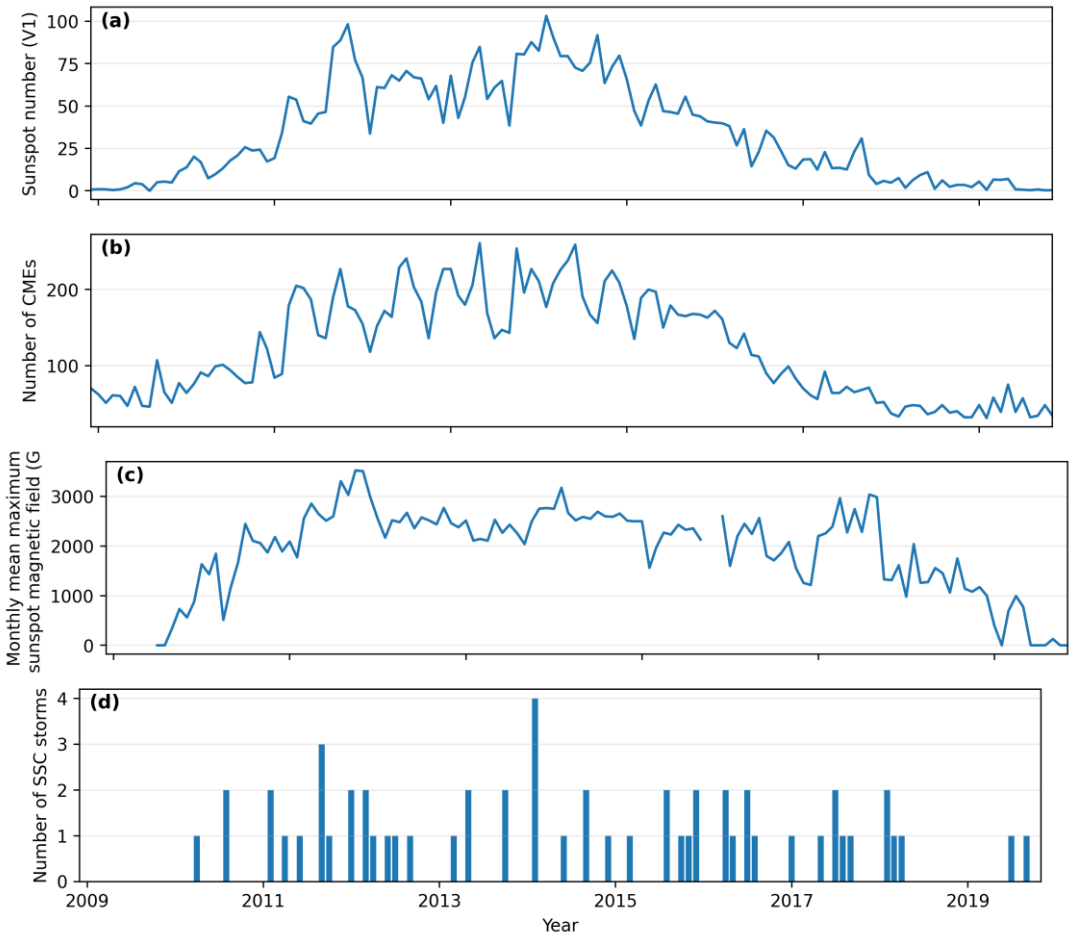


Figure 2. *Monthly variations of (a) sunspot number, (b) CME number, (c) monthly mean maximum sunspot magnetic-field strength, and (d) SSC storm number during Solar Cycle 24.*

For the complete cycle, CME occurrence is strongly related to SSN (Pearson $r = 0.90$, $p < 0.001$; Spearman $\rho = 0.91$, $p < 0.001$). The magnetic-field parameter correlates with SSN ($r = 0.77$, $p < 0.001$) and with CME occurrence ($r = 0.69$, $p < 0.001$). The CME-SSC correlation is much weaker ($r = 0.20$, $p = 0.020$); SSC correlates only weakly with SSN ($r = 0.28$) and with the magnetic-field parameter ($r = 0.26$). Figure 3 illustrates the strong overall SSN-CME relation and its substantial month-to-month scatter.

The timing of the peaks highlights the same point. During 2011-2012 the mean SSN was about 58.3, the mean CME number 173.6 month-1, and the mean maximum field about 2637 G. During 2013-2014 the corresponding values were about 73.2, 200.7 month-1, and 2509 G. Thus the second broad maximum was stronger in SSN and CME occurrence, while the first had stronger characteristic sunspot fields.

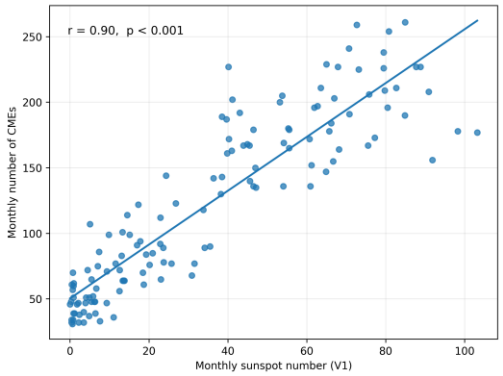


Figure 3. *Monthly SSN versus CME occurrence; r = 0.90, p < 0.001.*

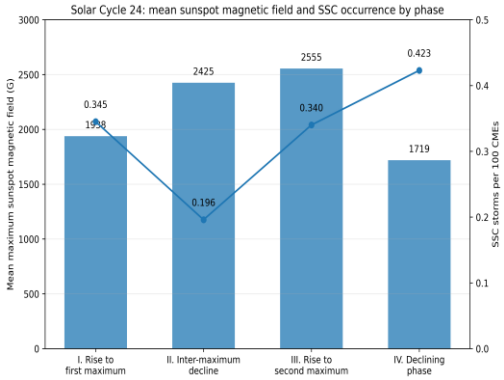


Figure 4. *Mean magnetic field and SSC storms per 100 CMEs for the four cycle phases.*

3.2. Phase Dependence

The phase averages (Table 1) reveal a marked contrast. Phases II and III have nearly identical CME rates (~196 CMEs month-1), despite different SSN and magnetic-field levels. Most importantly, the declining phase has the weakest mean maximum field (1719 G) but the highest relative SSC occurrence (0.423 SSC per 100 CMEs); the inter-maximum interval has a stronger field but the lowest value (0.196). Figure 4 visualizes this contrast.

Table 1. *Mean parameters and SSC occurrence by phase. Magnetic-field means use only months with usable CrAO observations.*

Phase	Interval	Mean SSN	Mean CME/mo	Mean B (G)	SSC	SSC/100 CME
I	Dec 2008-Mar 2012	27.44	108.70	1938	15	0.345
II	Apr 2012-Apr 2013	61.18	196.69	2425	5	0.196
III	May 2013-Apr 2014	75.68	196.25	2555	8	0.340
IV	May 2014-Nov 2019	26.99	102.43	1719	29	0.423

Correlations also change strongly with phase (Table 2). SN-CME is strong in Phase I (r = 0.870) and strongest in Phase IV (r = 0.924), but weak in Phase II (r = 0.163). B-CME is strong in Phase I (r = 0.805) and significant in Phase IV (r = 0.627), whereas CME-SSC remains weak in most phases. B-SSC is weakly positive in the declining phase (r = 0.262, p = 0.035). After controlling for SSN, the B-CME partial correlations are 0.309 (p = 0.080), -0.324 (p = 0.280), -0.615 (p = 0.033), and -0.049 (p = 0.697) for Phases I-IV, respectively. The Phase III result should be treated cautiously because it is based on only 12 months. In Phase IV, B-SSC remains weakly positive after controlling for CME occurrence (partial r ≈ 0.256, p = 0.039).

The phase averages and the within-phase correlations therefore convey different information. Across the four phase means, the lowest field coincides with the largest SSC/CME ratio, but within the declining phase stronger-field months show a weak positive relation with SSC occurrence. The data do not support a simple inverse causal relation between sunspot magnetic field and SSC occurrence.

Table 2. *Pearson correlation coefficients for the four phases of Solar Cycle 24.*

Phase	SN-CME	B-CME	CME-SSC	B-SSC
I	0.870	0.805	0.388	0.282
II	0.163	-0.279	0.124	-0.101
III	0.615	0.361	0.277	0.544
IV	0.924	0.627	0.124	0.262

4. Discussion

4.1. Magnetic Field and CME Productivity

The strong whole-cycle SSN-CME correlation agrees with earlier work [Kirov et al., 2023; Lamy et al., 2019; Mishra et al., 2019], but the phase analysis shows that the relationship is not invariant. The magnetic-field parameter also tracks CME activity, yet its maximum occurs near the first activity peak rather than with the largest SSN and CME counts in 2013-2014. This supports its use as complementary information on the magnetic state of active regions [Tsap et al., 2021].

However, the partial correlations do not show a universal independent linear contribution of B to monthly CME number once SSN is accounted for. This is physically reasonable: our B parameter is the strongest field observed anywhere on the disk, not necessarily the field of the CME source region, and CME production also depends on magnetic complexity, shear, free energy, topology, and active-region evolution. An event-by-event source-region analysis would be required to test the magnetic hypothesis more directly.

This distinction is central to the original working hypothesis. A significant B-CME correlation by itself does not establish an independent magnetic-field control because both B and CME occurrence vary with the solar cycle and with SSN. The phase-dependent partial correlations show that the residual relationship can even change sign. The present parameter should therefore be regarded as a diagnostic of the large-scale magnetic state of sunspot activity rather than a deterministic predictor of CME production.

4.2. SSC Occurrence and the Declining Phase

The weak CME-SSC correlation shows that total coronagraphic CME number is not a direct measure of shock-associated disturbances at Earth. Only a fraction of CMEs are Earth-directed, and SSC occurrence depends on propagation direction, speed, shock formation, interaction with the ambient solar wind, and the magnetic and plasma properties of the arriving structure [Zhang et al., 2021]. CME-driven storms show SSCs much more frequently than CIR-driven storms [Borovsky and Denton, 2006], while shock/sheath structures can themselves be geoeffective [Lugaz et al., 2016].

This wording also avoids equating SSC occurrence with general geomagnetic effectiveness. An SSC reflects a rapid magnetospheric compression, whereas the intensity of the subsequent storm main phase depends strongly on the southward interplanetary magnetic-field component and solar-wind coupling. A fast shock may therefore produce a clear SSC without a correspondingly intense storm, while a magnetic cloud with strong southward Bz may be highly geoeffective [Gopalswamy et al., 2015].

The most striking phase result is that Phase IV combines the weakest mean field with the largest SSC/CME ratio. This does not imply that weaker sunspot fields directly make CMEs more SSC-producing. The comparison contains only four phase averages, and within Phase IV the monthly B-SSC relation is weakly positive. More plausibly, the CME population and heliospheric propagation environment change with cycle phase. CME speed and width distributions, the fraction of Earth-directed events, CME-CME interaction, and preconditioning of the solar wind may all contribute. CIR/high-speed-stream activity also becomes more prominent in declining phases, although CIR-driven storms are less commonly associated with SSCs [Borovsky and Denton, 2006].

The declining-phase result is therefore best viewed as evidence that the efficiency with which the observed CME population is associated with shock-related terrestrial impacts changes with cycle phase. The total CME rate drops strongly after the maximum, while SSC occurrence decreases much less. This raises the SSC/CME ratio even though the sunspot magnetic-field index is lower. Determining the physical cause requires separating Earth-

directed from non-Earth-directed CMEs and examining event properties at the Sun and at 1 AU.

4.3. Double Maximum and Limitations

The inter-maximum interval is characterized by a breakdown of the simple relationships: SN-CME falls to r = 0.163 and the other correlations are also weak. This transitional behavior is consistent with the complexity of double-peaked cycles and the Gnevyshev gap [Takalo, 2021], but the present data cannot establish whether it results from hemispheric asymmetry or changing active-region populations.

The main limitations are methodological. Monthly averaging removes event-by-event information and introduces possible month-boundary offsets between a CME and its SSC. The CDAW denominator includes many non-Earth-directed CMEs. The magnetic-field index is global rather than source-region specific, and SSC count does not measure storm intensity. In addition, some CrAO months are missing. Future work should associate individual SSC storms with their source CMEs and include CME speed, width and source longitude, source-region magnetic parameters, and solar-wind/IMF conditions at 1 AU.

These limitations are especially relevant when interpreting the SSC/CME ratio quantitatively. Because the denominator contains all CDAW CMEs, the ratio is not the probability that an Earth-directed CME produces an SSC. It is a cycle-phase indicator based on a common catalog definition. Its value is therefore in comparative changes between phases rather than in its absolute magnitude.

5. Conclusions

Solar Cycle 24 shows a strong overall relation between SSN and CME occurrence (r = 0.90), but this relation changes substantially with cycle phase. The monthly mean maximum sunspot magnetic field is correlated with both SSN and CME occurrence and evolves differently from them, providing complementary information, although its independent linear contribution to CME productivity is not uniform across the cycle. The CME-SSC relation is weak (r = 0.20), confirming that total CME number alone does not describe the occurrence of shock-associated geomagnetic disturbances. The strongest phase result is the declining phase, where the mean maximum field is lowest (1719 G) but the relative occurrence of SSC storms per CME is highest (0.423 per 100 CMEs). This contrast should be interpreted as evidence for phase-dependent solar-terrestrial coupling rather than as a direct inverse effect of sunspot magnetic-field strength. Event-by-event source associations are required to determine which CME and interplanetary properties control this phase dependence.

References

Borovsky, J.E., Denton, M.H. (2006). Differences between CME-driven storms and CIR-driven storms, *Journal of Geophysical Research: Space Physics*, Vol. 111, A07S08, DOI: 10.1029/2005JA011447.

Boursier, Y., Lamy, P., Llebaria, A., Goudail, F., Robelus, S. (2009). The ARTEMIS catalog of LASCO coronal mass ejections, *Solar Physics*, Vol. 257, pp. 125–147, DOI: 10.1007/s11207-009-9370-5.

Byrne, J.P., Morgan, H., Habbal, S.R., Gallagher, P.T. (2012). Automatic detection and tracking of coronal mass ejections. II. Multiscale filtering of coronagraph images, *Astrophysical Journal*, Vol. 752, Art. 145, DOI: 10.1088/0004-637X/752/2/145.

Crimean Astrophysical Observatory (CrAO) (n.d.). Sunspot magnetic fields, observational archive, available at: https://sun.crao.ru/observations/sunspots-magnetic-field (accessed 20 August 2026).

Gopalswamy, N., Yashiro, S., Xie, H., Akiyama, S., Mäkelä, P. (2015). Properties and geoeffectiveness of magnetic clouds during solar cycles 23 and 24, *Journal of Geophysical Research: Space Physics*, Vol. 120, pp. 9221–9245, DOI: 10.1002/2015JA021446.

Kirov, B., Georgieva, K., Asenovski, S. (2023). The relationship between sunspot numbers and coronal mass ejections within an 11-year solar cycle, *Solar and Solar-Terrestrial Physics – 2023*, Saint Petersburg, Pulkovo, 9–13 October 2023, pp. 157–160, DOI: 10.31725/0552-5829-2023-157-160.

Lamy, P., Floyd, O., Boclet, B., Wojak, J., Gilardy, H., Barlyaeva, T. (2019). Coronal mass ejections over solar cycles 23 and 24, *Space Science Reviews*, Vol. 215, Art. 39, DOI: 10.1007/s11214-019-0605-y.

Lugaz, N., Farrugia, C.J., Winslow, R.M., Al-Haddad, N., Kilpua, E.K.J., Riley, P. (2016). Factors affecting the geoeffectiveness of shocks and sheaths at 1 AU, *Journal of Geophysical Research: Space Physics*, Vol. 121, pp. 10861–10879, DOI: 10.1002/2016JA023100.

Mishra, W., Srivastava, N., Wang, Y., Mirtoshev, Z., Zhang, J., Liu, R. (2019). Mass loss via solar wind and coronal mass ejections during solar cycles 23 and 24, *Monthly Notices of the Royal Astronomical Society*, Vol. 486, pp. 4671–4685, DOI: 10.1093/mnras/stz1001.

Pushkov Institute of Terrestrial Magnetism, Ionosphere and Radio Wave Propagation, Russian Academy of Sciences (IZMIRAN) (n.d.). Catalog of geomagnetic storms with sudden commencement, available at: https://www.izmiran.ru/magnetism/magobs/catalog_sudden.txt (accessed 20 August 2026).

Richardson, I.G., von Rosenvinge, T.T., Cane, H.V. (2015). The properties of solar energetic particle event-associated coronal mass ejections reported in different CME catalogs, *Solar Physics*, Vol. 290, pp. 1741–1759, DOI: 10.1007/s11207-015-0701-4.

SOHO/LASCO CME Catalog, CDAW Data Center (n.d.). SOHO/LASCO CME catalog, available at: https://cdaw.gsfc.nasa.gov/CME_list/ (accessed 20 August 2026).

Takalo, J. (2021). Comparison of geomagnetic indices during even and odd solar cycles SC17–SC24: Signatures of Gnevyshev gap in geomagnetic activity, *Solar Physics*, Vol. 296, Art. 19, DOI: 10.1007/s11207-021-01765-w.

Tsap, Yu.T., Kleeorin, N.I., Akhtemov, Z.S., Malashchuk, V.M. (2021). Evolution of sunspot magnetic fields from the measurements at the BST-2 telescope of the Crimean Astrophysical Observatory in solar cycle 24, *Geomagnetism and Aeronomy*, Vol. 61, pp. S62–S66, DOI: 10.1134/S0016793221330021.

WDC-SILSO, Royal Observatory of Belgium, Brussels (n.d.). Sunspot number data, available at: https://www.sidc.be/silso/datafiles (accessed 20 August 2026).

Zhang, J., Temmer, M., Gopalswamy, N., et al. (2021). Earth-affecting solar transients: A review of progresses in solar cycle 24, *Progress in Earth and Planetary Science*, Vol. 8, Art. 56, DOI: 10.1186/s40645-021-00426-7.

DOI: 10.31401/WS.2026.proc.07

Kinematics of the Prominence Eruption on May 27, 2013 Observed from Three Viewpoints

Koleva K., Duchlev P., Nacheva Y.

Space Research and Technology Institute, Bulgarian Academy of Sciences, Sofia, Bulgaria;
kkoleva@space.bas.bg

Abstract

We present our analysis of the dynamic activity of the prominence eruption occurring on May 27, 2013, using multi-spacecraft observations. Three perspectives are used to investigate the morphological evolution and kinematics of the eruption. We used high-resolution data from the two Solar Terrestrial Relations Observatory (STEREO) spacecraft and the Atmospheric Imaging Assembly (AIA) on board the Solar Dynamics Observatory (SDO). The eruption was associated with a partial-halo coronal mass ejection (CME), registered by the Large Angle and Spectrometric Coronagraph (LASCO) on board SOHO and the COR1 and COR2 coronagraphs on board the STEREO spacecraft.

Keywords: solar prominences; prominence eruption; coronal mass ejection

1. Introduction

Solar prominence eruptions (or filament eruptions when observed on the solar disk) are among the most extensively studied phenomena in solar physics, since they are most frequently associated with coronal mass ejections (CMEs), e.g., [Munro et al., 1979; Schmieder et al., 2013]. These events contribute significantly to the transfer of magnetic energy and plasma from the lower solar atmosphere into interplanetary space and therefore play an essential role in the heliospheric environment and space weather.

In addition, it is believed that prominence eruptions (PEs) play a key role in the onset of CMEs, e.g., [Schmieder et al., 2013; Filippov, 2018; Sinha et al., 2019]. Moreover, the kinematic evolution of a CME low in the solar corona can be obtained by following the prominence eruption features of the preeruptive configuration. Prominences, as cool and dense plasma embedded in the hot and tenuous corona, are among the most common precursors (or progenitors) of pre-eruptive CME configurations [Gibson and Fan, 2006; Mackay et al., 2010; Liu et al., 2012; Sinha et al., 2019]. Statistically, over 70% of CMEs are associated with erupting filaments/prominences [Sinha et al., 2019] and references therein.

According to [Sterling and Moore, 2004a, 2004b], a common pattern can be identified in the kinematics of prominence eruptions: an initial slow-rise phase characterized by negligible acceleration, during which the filament ascends gradually, followed by a rapid transition to a phase of fast acceleration.

In this work we study the evolution of an eruptive loop-shaped prominence using observations in the 304 Å EUV passband from three distinct observatories—the two STEREO spacecraft A and B and the Atmospheric Imaging Assembly (AIA) onboard the Solar Dynamics Observatory (SDO). Thus, by combining limb and on-disk data, we may examine the eruption from three distinct perspectives. Our goal is to study prominence's kinematic characteristics during the eruption. The set of observations used in this investigation is described in Sect. 2. The primary findings are presented in Sect. 3, and the conclusions are derived and discussed in Sect. 4.

2. Data and observations

The prominence eruption investigated in the present study occurred on May 27, 2013 between 18:06 UT and 19:29 UT. For the present analysis, extreme-ultraviolet images taken at a 1 min cadence in the He II 304 Å wavelength by the Atmospheric Imaging Assembly

(AIA) [Lemen et al., 2012] on board the Solar Dynamics Observatory (SDO) [Pesnell et al., 2012] were used. This spectral channel is particularly suitable for investigating prominence material because it records emission originating from relatively cool plasma.

In addition, observations from the Extreme Ultraviolet Imager (EUVI) on board STEREO-A and STEREO-B [Wuelser et al., 2004] were analyzed. We used images in the He II 304 Å channel with an average cadence of 3 min for EUVI A and 10 min for EUVI B.

Images obtained by the Large Angle and Spectrometric Coronagraph (LASCO)/C2 [Brueckner et al., 1995] aboard SOHO and the COR-A and COR-B coronagraphs on board the STEREO spacecraft were also used in the study.

3. Results

The prominence eruption (PE) occurred on May 27, 2013 and was detected by SDO and two STEREO spacecraft, A and B. The STEREO spacecraft were separated by 81.4° during this event, so that the prominence was observed at the limb from STEREO-A and partially on-disk from STEREO-B.

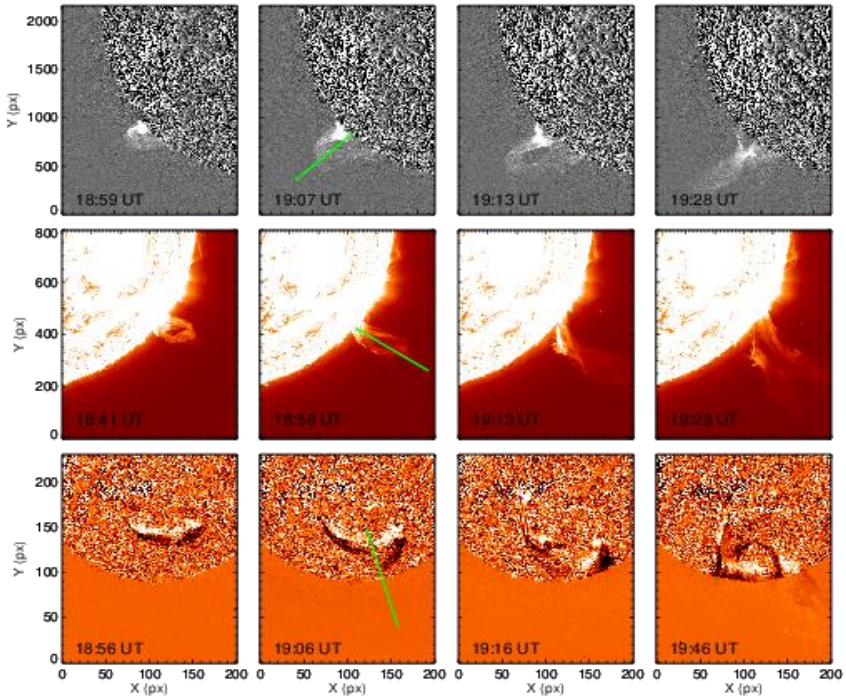


Figure 1. *Prominence eruption in AIA/SDO He II 304 Å running difference images (upper panel); EUVI A images in 304 Å channel (middle panel) and EUVI B He II 304 Å (bottom panel) running difference images. The green lines indicate slice position used for kinematic analysis.*

Figure 1 shows the eruption evolution in the three observing instruments' field-of-view (FOV). The eruption in AIA/SDO FOV in running difference images in the He II 304 Å passband is displayed in the upper panel. Eruption's evolution is shown in the FOV of EUVI A and B, respectively, in the center and bottom panels. For EUVI A and B we used again images in He II 304 Å line. The brightness of the EUVI A images is enhanced in order to improve the visibility of objects above the limb, while the observations in EUVI B are presented in running difference images.

To investigate the temporal and spatial evolution of the erupted prominence, we used the time-distance analysis. This technique is based on the exploration of the motion of plasma material along an artificial slit. For this reason, we have chosen three slits in the respective instruments' fields of view, which are indicated by green lines in Figure 1.

The eruption was also associated with a partial halo CME with linear velocity of 528 km/s, observed by LASCO together with the COR-A and COR-B coronagraphs on board the

STEREO spacecraft. Figure 2 shows the associated CME as observed by the three coronagraphs.

The white-light coronagraph observations extend the analysis beyond the low corona and establish the relationship between the erupting prominence and the corresponding CME propagating through the outer corona. Although the present work concentrates primarily on the low-coronal evolution of the prominence, the coronagraph observations provide additional evidence that the eruption developed into a large-scale coronal ejection.

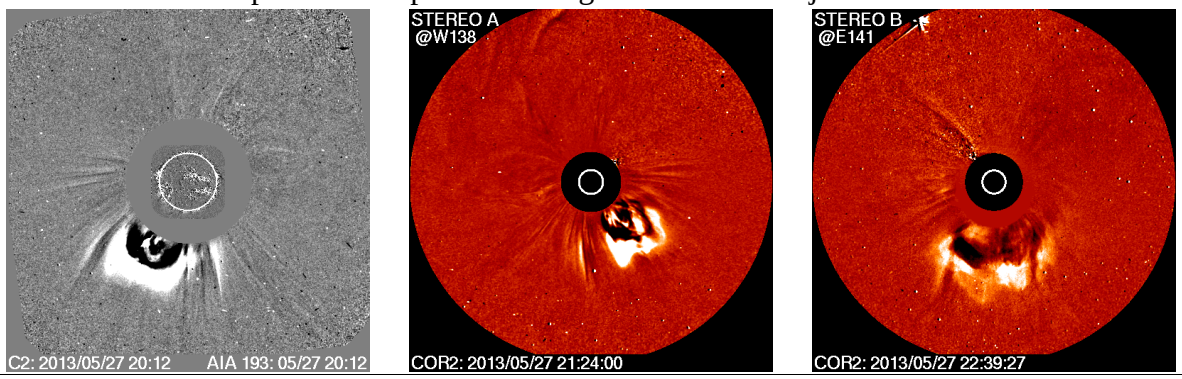


Figure 2. *Associated partial halo CME. From left to right: SOHO/LASCO/C2 white-light and AIA/SDO 193 Å running differential composite image at 20:12 UT; STEREO A/COR2 running difference image at 21:24 UT; and STEREO B/COR2 running difference image at 22:39 UT*

3.1. Kinematics

3.1.1. AIA/SDO FOV

In the AIA/SDO field of view, the eruption was observed on the southeast limb. The time–distance plot along the slit shown by the green line in Figure 1 (upper panel) and the corresponding height-time profile are presented in Figure 3. The distance-time data were obtained by tracing the leading edge of the erupting prominence. The red curve in Figure 3 (left) is the result of fitting a second-order polynomial to the data. According to [Cheng et al., 2020], the uncertainty of the measured heights is supposed to be two or three pixels for the hot channels.

The prominence eruption began behind the limb. In the AIA/SDO FOV the prominence started to rise at around 18:46 UT and reached a projected height of about 328 Mm along the selected slit. From the first and second derivatives of the polynomial fit of the height-time curve, we defined the speed and acceleration of the prominence eruption. In the AIA/SDO FOV the prominence was rising with increasing projected velocity between 24 km/s and 230 km/s and acceleration of about 93 m/s^2.

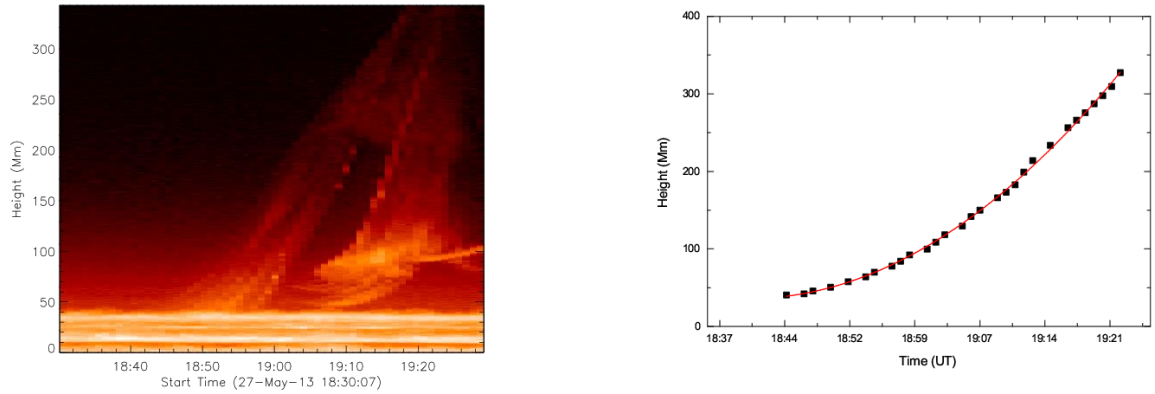


Figure 3. *Time-distance plot along the slit, shown with green line in Figure 1 (upper panel) and the corresponding height-time profile.*

3.1.2. EUVI-A FOV

In the EUVI A FOV the eruption was observed at southwest limb. The prominence started to erupt at about 18:09 UT. Figure 4 displays the time-distance plot along the slit, shown with the green line in Figure 1 (middle panel) and the corresponding height-time profile. To examine the eruption's kinematic evolution, we tracked the leading edge of the erupting prominence. A second-order polynomial fit was used to fit the data.

The eruption within the EUVI A FOV showed two separate eruptive phases. The slow rise phase was observed between 18:09 UT and 18:43 UT. The average estimated velocity for this phase was about 25 km/s. During the second phase, the prominence material continued to rise rapidly with an average speed of about 152 km/s and acceleration of 51 m/s^2. The prominence material reaches a height of approximately 352 Mm in the STEREO A FOV, which is similar to the results obtained in the AIA/SDO field of view.

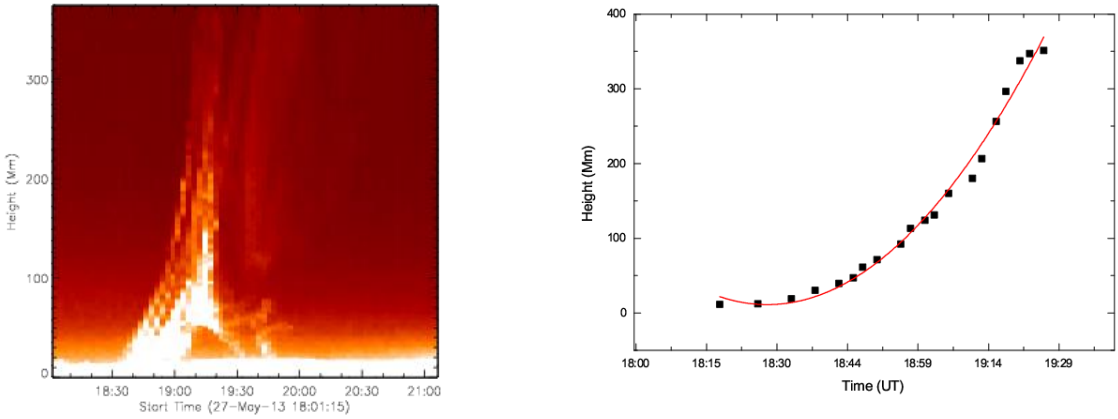


Figure 4. *Time-distance plot along the slit, shown with green line in Figure 1 (middle panel) and the corresponding height-time profile of the prominence eruption in EUVI A FOV.*

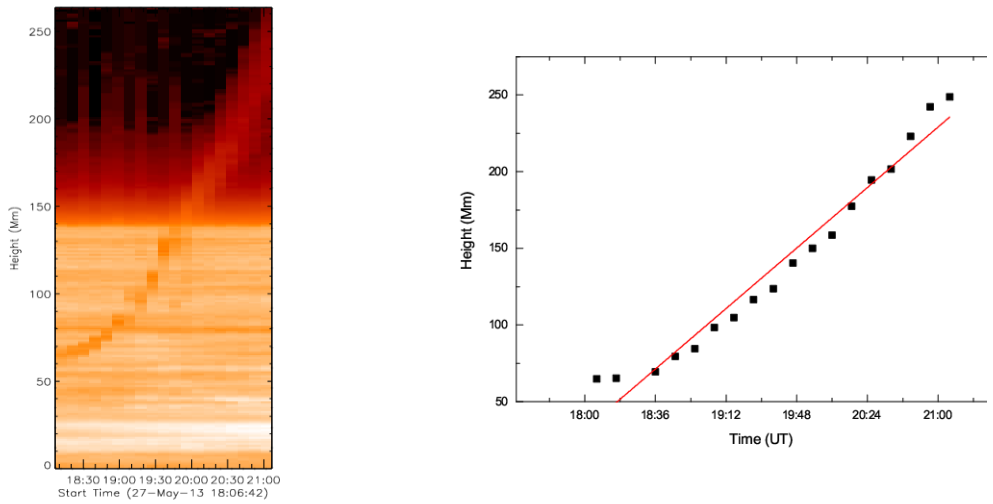


Figure 5. *Time-distance plot along the slit, shown with green line in Figure 1 (bottom panel) and the corresponding height-time profile of the filament eruption in EUVI B FOV.*

4.1.3. EUVI-B FOV

In STEREO B the prominence was observed as a filament in the southern hemisphere.

In Figure 5 (left panel) is displayed the time-distance plot, obtained from data in the 304 Å channel of EUVI/STEREO B. The slit position is presented with the green line in Figure 1,

bottom panel. Figure 5 (right panel) shows the height-time profile of the eruption as seen by the EUVI instrument. The fitting curve for the data points along the slice is represented by the red solid line. The fitting function used to obtain the projected height and velocity is $H = 44.57 + 1.14 \times T$.

Around 18:06 UT, the filament began to rise, reaching heights of around 249 Mm in the STEREO B FOV with average projected speed of about 20 km/s.

4. Discussion and conclusions

Three phases typically characterize the kinematic evolution of PEs: a slow-rise phase with nearly constant velocity, a fast main-acceleration period, and a propagation phase with slowly varying velocity [Zhang et al., 2001; Zhang et al., 2004]. Notably, some PEs only show two phases of evolution: a slow-rise phase and fast-acceleration phase see [Joshi and Srivastava, 2011] and references therein. It should be noted that numerous investigations have demonstrated that prominences are erupting in a variety of ways. For example, observations of a near-limb PE [Schrijver et al., 2008] show a slow-rise phase prior to the actual eruption, either with constant velocity [Sterling et al., 2011] or with a constant acceleration [Joshi and Srivastava, 2007]. The gradual initial rising of PEs often shows velocities between 1 km/s and 15 km/s. Velocities rise to a range of 100 to more than 1000 km/s during the primary acceleration phase.

The following results were obtained for the PE on May 27, 2013:

In the AIA/SDO FOV the eruption was observed in the southeast, behind the limb. Prominence started to rise at around 18:46 UT and reached a projected height of about 328 Mm along the selected slice. The prominence was rising with increasing projected velocity between 24 km/s and 230 km/s and acceleration of about 93 m/s^2.

The eruption within the EUVI A FOV showed two separate eruptive phases. The slow rise phase was observed between 18:09 UT and 18:43 UT. The average estimated velocity for this phase is about 25 km/s. During the second phase, the prominence material continued to rise rapidly with an average speed of about 152 km/s and acceleration of 51 m/s^2. The prominence material reaches heights of about 352 Mm in the STEREO A FOV.

The prominence was seen in the southern hemisphere of STEREO B FOV as an erupting filament. Around 18:06 UT, the filament began to rise, reaching heights of around 249 Mm in the STEREO B FOV with average projected speed of about 20 km/s.

References

Brueckner, G.E., Howard, R.A., Koomen, M.J., Korendyke, C.M., Michels, D.J., Moses, J.D., Socker, D.G., Dere, K.P., Lamy, P.L., Llebaria, A., Bout, M.V., Schwenn, R., Simnett, G.M., Bedford, D.K., Eyles, C.J. (1995). The Large Angle Spectroscopic Coronagraph (LASCO), *Solar Physics*, Vol. 162, Nos. 1–2, pp. 357–402, DOI: 10.1007/BF00733434.

Cheng, X., Zhang, J., Kliem, B., Török, T., Xing, C., Zhou, Z.J., Inhester, B., Ding, M.D. (2020). Initiation and early kinematic evolution of solar eruptions, *Astrophysical Journal*, Vol. 894, No. 2, Art. 85, DOI: 10.3847/1538-4357/ab886a.

Filippov, B. (2018). Two-step solar filament eruptions, *Monthly Notices of the Royal Astronomical Society*, Vol. 475, No. 2, pp. 1646–1652, DOI: 10.1093/mnras/stx3277.

Gibson, S.E., Fan, Y. (2006). Coronal prominence structure and dynamics: A magnetic flux rope interpretation, *Journal of Geophysical Research: Space Physics*, Vol. 111, No. A12, Art. A12103, DOI: 10.1029/2006JA011871.

Joshi, V., Srivastava, N. (2007). On the study of kinematics of eruptive quiescent prominences observed in He II 304 Å, *Bulletin of the Astronomical Society of India*, Vol. 35, pp. 447–455.

Joshi, A.D., Srivastava, N. (2011). Acceleration of coronal mass ejections from three-dimensional reconstruction of STEREO images, *Astrophysical Journal*, Vol. 739, No. 1, Art. 8, DOI: 10.1088/0004-637X/739/1/8.

Lemen, J.R., Title, A.M., Akin, D.J., Boerner, P.F., Chou, C., Drake, J.F., Duncan, D.W., Edwards, C.G., Friedlaender, F.M., Heyman, G.F., Hurlburt, N.E., Katz, N.L., Kushner, G.D., Levay, M., Lindgren, R.W., Mathur, D.P., McFeaters, E.L., Mitchell, S., Rehse, R.A., Schrijver, C.J., Springer, L.A., Stern, R.A., Tarbell,

T.D., Wuelser, J.P., Wolfson, C.J., Yanari, C., Bookbinder, J.A., Cheimets, P.N., Caldwell, D., DeLuca, E.E., Gates, R., Golub, L., Park, S., Podgorski, W.A., Bush, R.I., Scherrer, P.H., Gummin, M.A., Smith, P., Auker, G., Jerram, P., Pool, P., Soufli, R., Windt, D.L., Beardsley, S., Clapp, M., Lang, J., Waltham, N. (2012). The Atmospheric Imaging Assembly (AIA) on the Solar Dynamics Observatory (SDO), *Solar Physics*, Vol. 275, Nos. 1–2, pp. 17–40, DOI: 10.1007/s11207-011-9776-8.

Liu, R., Kliem, B., Török, T., Liu, C., Titov, V.S., Lionello, R., Linker, J.A., Wang, H. (2012). Slow rise and partial eruption of a double-decker filament. I. Observations and interpretation, *Astrophysical Journal*, Vol. 756, No. 1, Art. 59, DOI: 10.1088/0004-637X/756/1/59.

Mackay, D.H., Karpen, J.T., Ballester, J.L., Schmieder, B., Aulanier, G. (2010). Physics of solar prominences. II. Magnetic structure and dynamics, *Space Science Reviews*, Vol. 151, No. 4, pp. 333–399, DOI: 10.1007/s11214-010-9628-0.

Munro, R.H., Gosling, J.T., Hildner, E., MacQueen, R.M., Poland, A.I., Ross, C.L. (1979). The association of coronal mass ejection transients with other forms of solar activity, *Solar Physics*, Vol. 61, No. 1, pp. 201–215, DOI: 10.1007/BF00155456.

Pesnell, W.D., Thompson, B.J., Chamberlin, P.C. (2012). The Solar Dynamics Observatory (SDO), *Solar Physics*, Vol. 275, Nos. 1–2, pp. 3–15, DOI: 10.1007/s11207-011-9841-3.

Schmieder, B., Démoulin, P., Aulanier, G. (2013). Solar filament eruptions and their physical role in triggering coronal mass ejections, *Advances in Space Research*, Vol. 51, No. 11, pp. 1967–1980, DOI: 10.1016/j.asr.2012.12.026.

Schrijver, C.J., Elmore, C., Kliem, B., Török, T., Title, A.M. (2008). Observations and modeling of the early acceleration phase of erupting filaments involved in coronal mass ejections, *Astrophysical Journal*, Vol. 674, No. 1, pp. 586–595, DOI: 10.1086/524294.

Sinha, S., Srivastava, N., Nandy, D. (2019). Solar filament eruptions as precursors to flare–CME events: Establishing the temporal connection, *Astrophysical Journal*, Vol. 880, No. 2, Art. 84, DOI: 10.3847/1538-4357/ab2239.

Sterling, A.C., Moore, R.L. (2004a). Evidence for gradual external reconnection before explosive eruption of a solar filament, *Astrophysical Journal*, Vol. 602, No. 2, pp. 1024–1036, DOI: 10.1086/379763.

Sterling, A.C., Moore, R.L. (2004b). External and internal reconnection in two filament-carrying magnetic cavity solar eruptions, *Astrophysical Journal*, Vol. 613, No. 2, pp. 1221–1232, DOI: 10.1086/423297.

Sterling, A.C., Moore, R.L., Freeland, S.L. (2011). Insights into filament eruption onset from Solar Dynamics Observatory observations, *Astrophysical Journal Letters*, Vol. 731, No. 1, Art. L3, DOI: 10.1088/2041-8205/731/1/L3.

Wuelser, J.P., Lemen, J.R., Tarbell, T.D., Wolfson, C.J., Cannon, J.C., Carpenter, B.A., Duncan, D.W., Gradwohl, G.S., Meyer, S.B., Moore, A.S., Navarro, R.L., Pearson, J.D., Rossi, G.R., Springer, L.A., Howard, R.A., Moses, J.D., Newmark, J.S., Delaboudinière, J.P., Artzner, G.E., Auchère, F., Bougnet, M., Bouyries, P., Bridou, F., Clotaire, J.Y., Colas, G., Delmotte, F., Jérôme, A., Lamare, M., Mercier, R., Mullot, M., Ravet, M.F., Song, X., Bothmer, V., Deutsch, W. (2004). EUVI: The STEREO-SECCHI extreme ultraviolet imager, *Telescopes and Instrumentation for Solar Astrophysics*, Vol. 5171, pp. 111–122, DOI: 10.1117/12.506877.

Zhang, J., Dere, K.P., Howard, R.A., Kundu, M.R., White, S.M. (2001). On the temporal relationship between coronal mass ejections and flares, *Astrophysical Journal*, Vol. 559, No. 1, pp. 452–462, DOI: 10.1086/322405.

Zhang, J., Dere, K.P., Howard, R.A., Vourlidas, A. (2004). A study of the kinematic evolution of coronal mass ejections, *Astrophysical Journal*, Vol. 604, No. 1, pp. 420–432, DOI: 10.1086/381725.

DOI: 10.31401/WS.2026.proc.08

A Model of Non-Isothermal Solar Corona

Melnik V. M.[1], *Dorovskyy V.V.*[1], *Shergelashvili B.M.*[2,3,4]

[1]Institute of Radio Astronomy, Kharkov, Ukraine; melnik@rian.kharkov.ua
[2]A Theoretical Physics IV, Ruhr-Universität Bochum, Universitätsstrasse 150, 44780 Bochum, Germany
[3]Centre for Computational Helio Studies, Faculty of Natural Sciences and Medicine, Ilia State University, Cholokashvili Ave. 3/5, 0162 Tbilisi, Georgia
[4]Evgeni Kharadze Georgian National Astrophysical Observatory, M. Kostava street 47/57, 0179 Tbilisi, Georgia

Abstract

A model of the non-isothermal solar corona is proposed. This model was obtained as a solution of hydrodynamic equations, in which the density of the solar corona varies with distance following a power-law dependence. The power law index is determined by the polytropic index. The dependences of the polytropic indexes on the distance from the Sun are shown for the Baumbach-Allen model. It is shown that the temperature of the coronal plasma in the proposed model is inversely proportional to the distance from the Sun. The possibilities for probing the solar corona on an example of a single Type III burst, observed by PSP on March 13, 2023 in a wide frequency range are discussed.

Keywords: corona; model; non-isothermal; Type III burst.

1. Introduction

For a long time, the electron density models for solar corona are discussed by different authors. It is well-known such laws as the Baumbach-Allen dependence [Allen, 1947] $n(r) = 10^8[2.99\left(\frac{R_S}{r}\right)^{16} + 1.55\left(\frac{R_S}{r}\right)^{6}]cm^{-3}$, the Newkirk one [Newkirk, 1961] $n(r) = 4.2 \cdot 10^4 \cdot 10^{4.32\frac{R_S}{r}} cm^{-3}$ or the Saito et al. one [Saito et al., 1977] $n(r) = [1.36 \cdot 10^6\left(\frac{R_S}{r}\right)^{2.14} + 1.68 \cdot 10^8\left(\frac{R_S}{r}\right)^{6.13}]cm^{-3}$, where Rs is the solar radius. All these laws were obtained from optical and radio observations using rather fine statistics. Later other authors using the same methods and sometimes others methods [Leblanc et al., 1998, Vrsnak et al., 2004] got in the most cases different exponential dependences. The presence of different models reflects the fact that these models were obtained in different conditions, which were defined by conditions on the solar surface – the density of coronal plasma bottom, their temperature there and presence of energy sources. In 1999 Mann et al. [Mann et al., 1999] attempted to find a density model for coronal plasma from main hydrodynamic equations in the isothermal case. Close to the Sun they had got:

$$N(r) = N_S \exp\left[\frac{A}{R_S}\left(\frac{R_S}{r} - 1\right)\right], \quad (1)$$

with $A = \tilde{\mu} G M_S / k_B T$ and $N(r = R_S) = N_S$. This law is the Newkirk model [Newkirk, 1961] at the temperature $T = 1.5 \cdot 10^6 K$. They also concluded that the numerical solution of the corresponding hydrodynamic equations agreed better with Type III bursts observations at the temperature $= 1 \cdot 10^6 K$. But everyone knows (see, for example, Suzuki and Dulk, 1985) that temperature of coronal plasma slowly but steadily decreases with distance from the Sun, so it is desirable to consider more realistic case of non-isothermal coronal plasma. In this case it is necessary to add the equation for energy of coronal plasma to main hydrodynamic

equations. In this case, as shown by Shergelashvili et al., [Shergelashvili et al., 2020]. there can be discontinuous solutions, which can be defined by polytropic exponent in essential way [Westrich et al., 2026].

In this paper we analyze the case when the density is continuous dependence on the distance. In particular, we consider a quasi-isothermal solution and compare it with that derived by Mann et al. [Mann et al. 1999] for isothermal plasma. We show that the last one is correct in a narrow region near the solar surface. Especial attention we devote to the case when the solar corona model is presented in the form of sum of exponents. We show that in this case exponent index is defined by polytropic one. Also, we discuss the solar model, which was obtained from the results of Type III observations by PSP in the wide frequency band from 0.3 to 19 MHz.

2. Main hydrodynamic equations and their solutions in non-isothermal case.

Plasma of solar corona in one-dimensional approximation is described by the following main hydrodynamic equations:

$$\frac{\partial \rho}{\partial t} + \frac{1}{r^2}\frac{\partial}{\partial r}\rho v r^2 = 0 \tag{2}$$

$$\rho\left[\frac{\partial v}{\partial t} + v\frac{\partial}{\partial r}v\right] = -\frac{\partial}{\partial r}p - \rho\frac{G\,M_S}{r^2} \tag{3}$$

$$\frac{\partial}{\partial t}\left(1 + v\frac{\partial}{\partial r}\right)\left(\frac{T}{\rho^{\alpha-1}}\right) = 0 \tag{4}$$

where $\rho = m_p n$, v, $p = nkT$, T, α– are the plasma mass density, the velocity, the (thermal) pressure, the temperature, the polytropic index, respectively. G, M_S are the gravitational constant and the mass of the Sun.

In the stationary case from the first equation we have the law of mass conservation:

$$R^2 N(R) V(R) = 1, \tag{5}$$

where $N(R) = N(r)/N(R_S)$, $V(R) = v(r)/v(R_S)$, $R = r/R_S$.

The solution of the second equation for isothermal plasma ($T(r) = \text{const}, \alpha = 1$) is the solution by Mann et al. [Mann et al. , 1999] near the Sun (equation (1), where the velocity of solar wind is small.

In the non-isothermal case ($\alpha \neq 1$) we have from the equation (4)

$$T(R) = N(R)^{\alpha-1}, \tag{6}$$

where $T(R) = T(r)/T(R_S)$.

Then the equation (3) can be rewritten as:

$$v(R)\frac{d}{dR}v(R) = -\frac{v_s^2}{N(R)}\frac{d}{dR}N(R)^{\alpha} - \frac{v_G^2}{R^2} \tag{7}$$

where $v_g(R_S) = (\frac{GM_S}{R_S})^{1/2} = 4.37 \cdot 10^7 cm/s$, and $v_s(R_S) = (\frac{k_B T_s}{\mu m_p})^{1/2}$ is the sound speed at $r = R_S$ (for the temperature $T = 2 \cdot 10^6 K$, $v_s(R_S) = 1.6 \cdot 10^7 cm/s$).

The equation (7) can be transformed to the form:

$$v(R)\frac{d}{dR}v(R) = -v_s^2\frac{\alpha}{\alpha-1}\frac{d}{dR}N(R)^{\alpha-1} - \frac{v_G^2}{R^2} \tag{8}$$

This equation can be integrated:

$$\frac{1}{2}[(V^2(R)-1] = -\frac{\alpha}{(\alpha-1)}V_s^2(R_S)[N^{\alpha-1}(R)-1] + V_g^2(R_S)(\frac{1}{R}-1) \quad (9)$$

Near the Sun, where the speed of the solar wind is small, we have for the plasma density:

$$N^{\alpha-1}(R) = 1 + \frac{(\alpha-1)\cdot V_g^2(R_S)}{\alpha\cdot V_s^2(R_S)}\cdot(\frac{1}{R}-1) \quad (10)$$

Let us consider three different cases:

$$\frac{(\alpha-1)V_g^2(R_S)}{\alpha\cdot V_s^2(R_S)} \ll 1 \quad (11)$$

$$\frac{(\alpha-1)V_g^2(R_S)}{\alpha\cdot V_s^2(R_S)} \geq 1 \quad (12)$$

$$\frac{(\alpha-1)V_g^2(R_S)}{\alpha\cdot V_s^2(R_S)} = 1 \quad (13)$$

1. When polytropic index $\alpha \approx 1$ this is quasi-isothermal case because when $\alpha = 1$, we have isothermal plasma of Mann et al. [Mann et al., 1999].

Compare the results for the isothermal and the quasi-isothermal plasmas.

If $\frac{(\alpha-1)\cdot V_g^2(R_S)}{\alpha\cdot V_s^2(R_S)} \ll 1$ then from (10) we have:

$$N(R) \approx 1 + \frac{v_g^2(R_S)}{\alpha}\left(\frac{1}{R}-1\right) \quad (14)$$

At the plasma temperature $T(R_S) = 1 \div 2\cdot 10^6 K$, $v_s^2(R_S) \ll v_g^2(R_S)$ and the plasma density decreases with distance very quickly. Figure 1 shows changing of the plasma density dependences on distance according to equations (11) and (1) in the case of temperatures $T = 1\cdot 10^6 K$, $T = 1.5\cdot 10^6 K$ and $T = 2\cdot 10^6 K$. We see that these dependences are close only at small distances and with increasing temperature this distance is also increasing.

Beginning from $R \approx 1 + \frac{\alpha v_s^2}{v_g^2}$ the plasma density decreases very quickly. At the same time according to (5) the velocity of solar wind increases very quickly also and we need to account the term with this velocity in equation (6) when $V(R) \approx V_s(R_S)$ and then for the density we have such expression:

$$N = 1 + \frac{V_g^2(R_S)}{\alpha V_s^2(R_S)}\left(\frac{1}{R}-1\right) - \frac{1}{2\alpha V_s^2(R_S)}(V^2(R)-1) \quad (15)$$

We see that in this case the density decreases more quickly and the density turns to zero closer to the Sun correspondingly. So, we can consider that the density becomes zero approximately at

$$R \approx 1 + \frac{\alpha v_s^2}{v_g^2} \quad (16)$$

Physically it means that the coronal plasma with temperatures $T = 1 \div 2\cdot 10^6 K$ cannot overcome gravitational attraction.

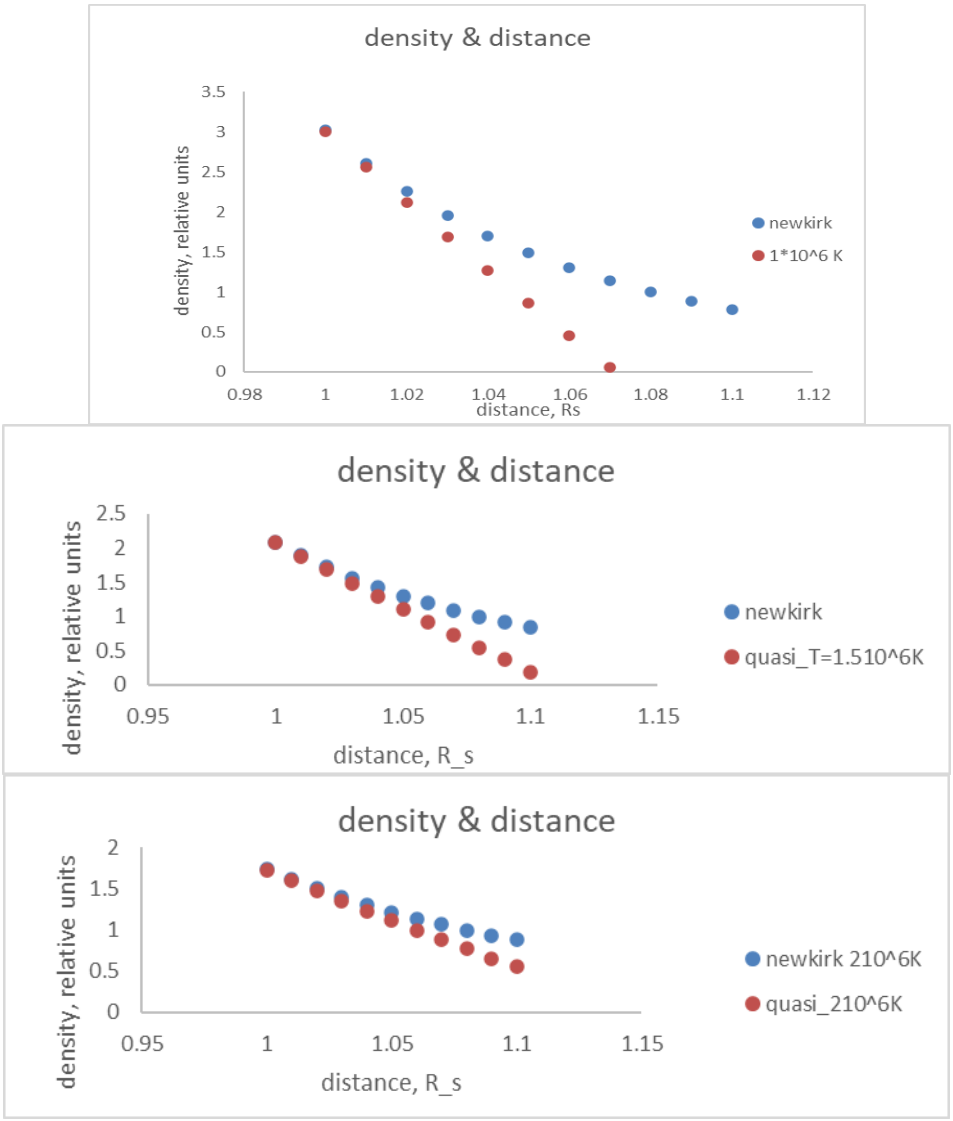


Figure 1. *Dependences of coronal plasma density on distance for quasi-isothermal (11) and isothermal (1) cases.*

2. When $\frac{(\alpha-1)V_g^2(R_S)}{\alpha \cdot V_s^2(R_S)} \geq 1$ for the density we have the following expression:

$$N^{\alpha-1}(R) = 1 + \frac{(\alpha-1)\cdot V_g^2(R_S)}{\alpha \cdot V_s^2(R_S)} \cdot \left(\frac{1}{R} - 1\right) \tag{17}$$

and in velocity terms:

$$N^{(\alpha-1)} = 1 + \frac{(\alpha-1)V_g^2(R_S)}{\alpha V_s^2(R_S)}\left(\frac{1}{R} - 1\right) - \frac{(\alpha-1)}{2\alpha V_s^2(R_S)}(V^2(R) - 1) \tag{18}$$

Again, the coefficient $\frac{V_g^2(R_S)}{V_s^2(R_S)}$ is a high value for temperatures $T = 1 \div 2 \cdot 10^6 K$ and as a consequence the density decreased very quickly at distances $R \approx 1 + \frac{\alpha v_s^2}{(\alpha-1)v_g^2}$. According to (6) the temperature of the solar wind decreased also very quickly.

So, we see that in both cases, 1 and 2, the plasma density of solar wind becomes small close to the Sun. This is natural result because the average energy of plasma particles is not enough to get away from the Sun ($V_s^2(R_S) \ll V_g^2(R_S)$).

3. The case $\frac{(\alpha-1)V_g^2(R_S)}{\alpha \cdot V_s^2(R_S)} = 1$ is the special one. In this occasion we have from (10) and (6) condition for exponential solution for the density dependence:

$$N^{\alpha-1}(R) = 1/R \tag{19}$$

and

$$N^{\alpha-1}(R) = 1/R \tag{20}$$

correspondingly and as a result

$$N(R) = R^{-\gamma} = R^{-1/(\alpha-1)} \tag{21}$$

For the polytropic index we have $\alpha = 1 + 1/\gamma$.

Different authors obtained different density dependences from the observational data in the form of sum of various power-law relations. So, the well-known Baumbach-Allen model [Allen, 1947] $n(r) = 10^8[2.99\left(\frac{R_S}{r}\right)^{16} + 1.55\left(\frac{R_S}{r}\right)^{6}]cm^{-3}$ consists from two power-law terms with exponents $\gamma_1 = 16$ та $\gamma_2 = 6$. Transit from one dependence to the another one occurs at the distance $R_2 = 1.07$ $(R_1 = R_S)$. The polytropic indexes are $\alpha_1 = 1.06$ and $\alpha_2 = 1.17$ in the regions $R_1 < R < R_2 = 1.07$ and $R > R_2 = 1.07$ correspondingly. For the first region $R_1 < R < R_2$ the condition $\frac{(\alpha_1-1)V_g^2(R_S)}{\alpha_1 \cdot V_s^2(R_S)} = 1$ is fulfilled if the sound velocity $v_s(R_S) = \sqrt{(\alpha_1 - 1)/\alpha_1} \cdot v_g(R_S) = \frac{v_g(R_S)}{4} = 1.09 \cdot 10^7 cm/s$, and the temperature $T(R_S) = 0.93 \cdot 10^6 K$. In the second region $R > R_2$ the equality $\frac{(\alpha_2-1)V_g^2(R_2)}{\alpha_2 V_s^2(R_2)} = 1$ holds true at $v_s(R_2) = \sqrt{(\alpha_2 - 1)/\alpha_2} v_g(R_2) = 1.6 \cdot 10^7 cm/s$ and the temperature $T(R_2) = 2 \cdot 10^6 K$ correspondingly. But according to (20) the temperature decreases as $T(R) = 1/R$ in the first region and at the distance R_2 it should be $T(R_2)' = 0.87 \cdot 10^6 K$. The difference between values $T(R_2) = 2 \cdot 10^6 K$ and $T(R_2)' = 0.87 \cdot 10^6 K$ means that some heating occurs in the first region. In respect to the second region the temperature decreases there as:

$$T(R) = T(r)/T(R_2) = 1/R \tag{22}$$

Variations of polytropic indexes and temperatures in the case of larger number of power-law relations we analyze on the example of the coronal model, which was obtained from the analysis of spectral characteristics of powerful Type III burst observed in the wide frequency range from 0.3 to 19 MHz by PSP on 13 March 2023 [Melnik and Dorovskyy, 2026]. Analysis of frequency drift rates of different levels of this Type III burst showed that the source of this burst moved through the plasma, in which its density changed in such way (Figure 2):

$$n(R) = \begin{cases} 1.55 \cdot 10^8 \cdot R^{-5.5} cm^{-3}, & 1.9 < R < 3.1 \\ 5.9 \cdot 10^6 \cdot R^{-2.6} cm^{-3}, & 3.1 < R < 9.3 \\ 3 \cdot 10^6 \cdot R^{-2.3} cm^{-3}, & 9.3 < R < 31 \end{cases} \tag{23}$$

The generation of radio emission at the first harmonic at frequency 19 MHz (the plasma density in this place $n(R_1 = 1.9) = 4.43 \cdot 10^6 cm^{-3}$) occurs at the distance $R_1 = 1.9$.

Correspondingly the generation at distances $R_2 = 3.1$, $R_3 = 9.3$ and $R_4 = 31$ happens at frequencies 5 MHz ($n(R_2 = 3.1) = 3.1 \cdot 10^5 cm^{-3}$), 1.2 MHz ($n(R_3 = 9.3) = 1.77 \cdot 10^4 cm^{-3}$) and 0.3 MHz ($n(R_4 = 31) = 1.1 \cdot 10^3 cm^{-3}$).

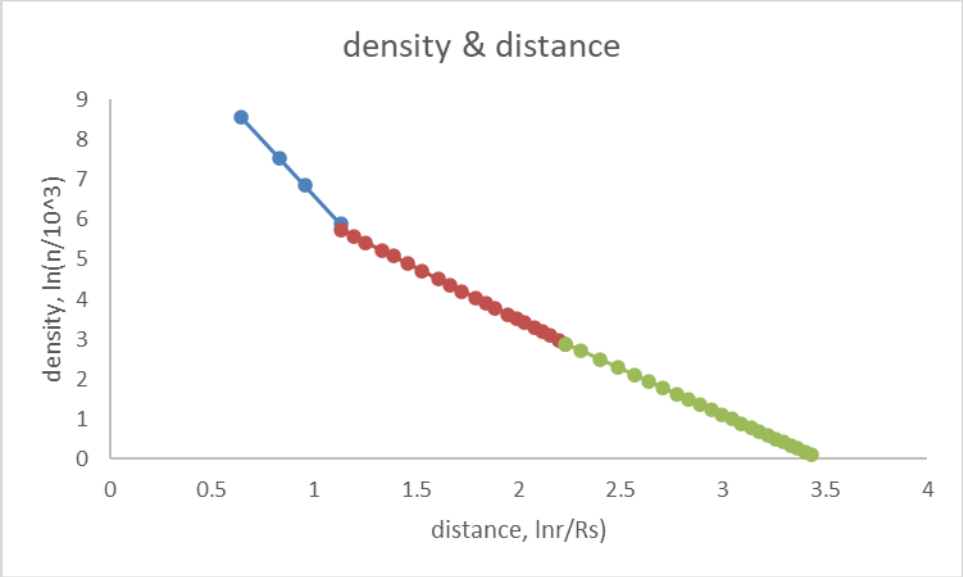


Figure 2. *The density of coronal plasma through which the source of Type III burst observed in the frequency range 0.3-19 MHz by PSP on 13 March 2023 moved.*

Polytropic indexes in these regions were the next:

$$\alpha = \begin{cases} 1.18, & 1.9 < R < 3.1 \\ 1.38, & 3.1 < R < 9.3 \\ 1.43, & 9.3 < R < 31 \end{cases} \quad (24)$$

Plasma temperatures at the distances $R_1 = 1.9$, $R_2 = 3.1$ and $R_3 = 9.3$ according to conditions $\frac{(\alpha_i - 1)V_g^2(R_i)}{\alpha_i V_s^2(R_i)} = 1$ are the following $T(R_1) = 1.2 \cdot 10^6 K$ ($v_s(R_1) = 1.25 \cdot \frac{10^7 cm}{s}, v_g(R_1) = 3.17 \cdot 10^7 cm/s$), $T(R_2) = 1.32 \cdot 10^6 K$ ($v_s(R_2) = 1.3 \cdot 10^7 cm/s$, $v_g(R_2) = 2.48 \cdot 10^7 cm/s$) and $T(R_3) = 0.49 \cdot 10^6 K$ ($v_s(R_3) = 0.79 \cdot 10^7 cm/s$, $v_g(R_3) = 1.44 \cdot 10^7 cm/s$). At the same time temperature dependences following (20) are (Figure 3):

$$T(R) = \frac{10^6 K}{R} \begin{cases} 1.2, & 1.9 < R < 3.1 \\ 1.32, & 3.1 < R < 9.3 \\ 0.49, & 9.3 < R < 31 \end{cases} \quad (25)$$

We see that in the region $1.9 < R < 3$ a heating of solar corona should increases the temperature from $T'(R_2) = 0.74 \cdot 10^6 K$ to $T(R_2) = 1.32 \cdot 10^6 K$ and in the region $3.1 < R < 9.3$ - from $T'(R_3) = 0.44 \cdot 10^6 K$ to $T(R_3) = 0.49 \cdot 10^6 K$. If the third region extends to the Earth's orbit ($R_E = 215$) then the density of solar wind was $n(215) = 13 cm^{-3}$ and its temperature was $T(215) = 2.1 \cdot 10^4 K$. Herein the velocity of solar wind increased by a factor of $\frac{v(215)}{v(1.9)} = \frac{1.9}{215} \frac{n(1.9)}{n(215)} = 3 \cdot 10^3$.

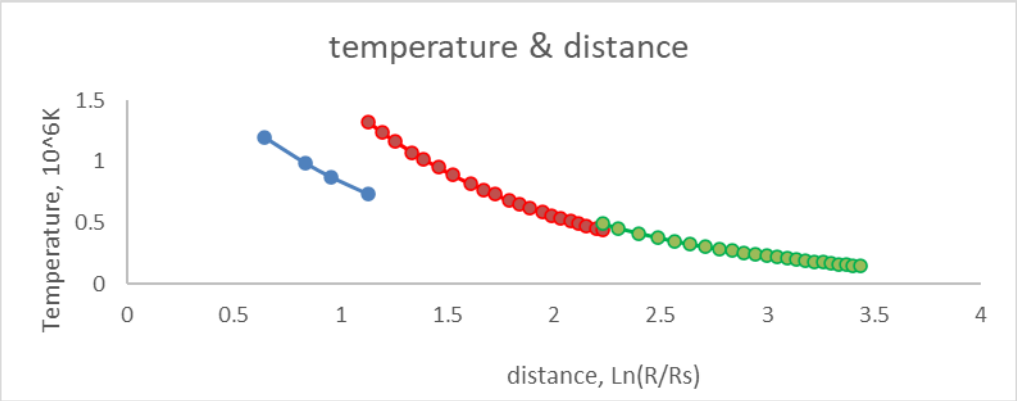


Figure 3. *The temperature dependences in the regions from* $R_1 = 1.9$ *to* $R_3 = 9.3$.

3. Conclusions

We found the solutions of the hydrodynamic equations for solar wind in non-isothermal case. We show that density dependencies consisting of exponential terms can exist if there is some connection between polytropic indexes and temperatures of coronal plasma. At the examples of Baumbach-Allen model and model, which was obtained from observation of powerful Type III burst in the wide frequency band of 0.3-19 MHz, we study the changing of polytropic indexes and temperatures at different distances from the Sun. The spectral analysis of a single powerful Type III burst in the wide frequency band of 0.3-19 MHz showed that the density of solar coronal plasma changed as a sum of three power-law relations with exponents $\gamma = 5.5, 2.6, 2.3$. This model can be understood as a solution of hydrodynamic equations in the case of non-isothermal plasma with corresponding polytropic indexes $\alpha = 1.18, 1.38, 1.43$ in the regions $1.9 < R < 3.1$, $3.1 < R < 9.3$ and $9.3 < R < 31$. At that in the places of transition there should be jumps of temperatures that says about necessity of heating in corresponding regions.

References

Allen, C.W. (1947). Interpretation of electron densities from corona brightness. *Monthly Notices of the Royal Astronomical Society*, 107, 426–432.

Leblanc, Y., Dulk, G.A., Bougeret, J.-L. (1998). Tracing the electron density from the corona to 1 AU. *Solar Physics*, 183, 165–180.

Mann, G., Jansen, F., MacDowall, R.J., Kaiser, M.L., Stone, R.G. (1999). A heliospheric density model and Type III radio bursts. *Astronomy and Astrophysics*, 348, 614–620.

Melnik, V.N., Dorovskyy, V.V. (2026). Spectral analysis of a single Type III burst in the wide frequency range of 0.3–19 MHz according to PSP observations. *Solar Physics*, submitted.

Newkirk, G. Jr. (1961). The solar corona in active regions and the thermal origin of the slowly varying component of solar radio radiation. *Astrophysical Journal*, 133, 983–1012. https://doi.org/10.1086/147104

Saito, K., Poland, A.I., Munro, R.H. (1977). A study of the background corona near solar minimum. *Solar Physics*, 55, 121–134.

Shergelashvili, B.M., Melnik, V.N., Dididze, G., Fichtner, H., Brenn, G., Poedts, S., Foysi, H., Khodachenko, M.L., Zaqarashvili, T.V. (2020). A new class of discontinuous solar wind solutions. *Monthly Notices of the Royal Astronomical Society*, 496, 1023–1034.

Suzuki, S., Dulk, G.A. (1985). Bursts of Type III and Type V. In D.J. McLean and N.R. Labrum (Eds.), *Solar Radiophysics: Studies of Emission from the Sun at Metre Wavelengths*. Cambridge University Press, 289–332.

Vršnak, B., Magdalenić, J., Zlobec, P. (2004). Band-splitting of coronal and interplanetary Type II bursts. III. Physical conditions in the upper corona and interplanetary space. *Astronomy and Astrophysics*, 413, 753–763.

Westrich, L., Shergelashvili, B., Fichtner, H., Melnik, V.N. (2026). Polytropic stellar wind models with strongly localized heating. *Monthly Notices of the Royal Astronomical Society*, 548, 755, 12 pp.

DOI: 10.31401/WS.2026.proc.09

Variation in the Tilt Angle of Sunspot Groups During Their Lifetimes

Muraközy J.

HUN-REN Institute of Earth Physics and Space Science, Sopron, Hungary
murakozy.judit@epss.hu

Abstract

During the evolution of sunspot groups, not only do the magnetic flux and the leading-following separation distance change, but the tilt angle of the line connecting the leading and following polarity centers, measured with respect to the solar equator, also varies. The aim of this study is to investigate the evolution of the tilt angle throughout the lifetime of sunspot groups using the largest carefully verified statistical sample currently available. A total of 277 distinct sunspot groups were selected from the SOHO/MDI-Debrecen Sunspot Data catalog, which covers Solar Cycle 23. Because this catalog provides the area, position, and magnetic data for each individual sunspot, the leading and following polarities can be identified with high precision. The evolution of the tilt angle follows a three-stage pattern. Sunspot groups emerge at the solar surface with relatively large tilt angles, reflecting the subsurface pitch angle of the magnetic flux tube together with the effect of the Coriolis force. Around the time of maximum development, the tilt angles relax, followed by a slight increase during the late decay phase. The tilt angle is found to be inversely correlated with both the peak area and the leading-following separation of the sunspot groups. These results suggest that active regions emerge with an intrinsic tilt, which is subsequently modified during their growth and decay by subsurface flows, turbulent diffusion, and meridional motions.

Keywords: solar photosphere; solar active regions; tilt angles

1. Introduction

The angle between the main axis of a sunspot group, defined by the line connecting the centers of the opposite magnetic polarity regions, and the solar equator is known as the tilt angle. According to the currently accepted theory, the tilt angle of an active region (AR) is generated by the Coriolis force acting on the magnetic flux tube as it rises from the bottom of the solar convection zone. Hale et al. (1919) reported that sunspot group tilt angles increase with increasing latitude. This relationship is known as Joy's law, which has been widely investigated. Among these studies, Tian et al. (2003) examined more than 500 bipolar solar active regions located on the central meridian and referred to the tilts as a function of the latitudes. Ivanov (2012) studied Joy's law by using three sunspot catalogs and found that active-region tilt angles are not linearly dependent on latitude and decrease slightly above 25-30°. Senthamizh Pavai et al. (2015), studying solar cycles 7-10, showed that the average tilt angle is 5.85°, with the leading polarity located closer to the equator, and found good agreement with tilt angles obtained from 20th-century data sets. Li (2018) studied tilts of Hale and anti-Hale sunspot groups and pointed out that Hale groups, i.e. when the leading part is closer to the equator, obey Joy's law, while the anti-Hale ones do not.

Howard (1996) showed that groups with tilt angles near the average value have a faster rotation rate than those with extreme tilts. Sivaraman et al. (1999) pointed out a relationship between tilt angles and latitude drifts by investigating the Kodaikanal and Mount Wilson sunspot data sets.

Some studies have investigated the tilt of ARs as a function of their evolutionary phase. Based on the daily variation of tilt angles derived from Mount Wilson magnetograms, Howard (1991) identified relationships between magnetic flux, tilt angles, and latitude, and showed that even decaying regions can occasionally undergo rapid rotation. Stenflo and Kosovichev (2012) analyzed more than 160,000 bipolar ARs during their emergence phases using magnetograms, and together with Kosovichev and Stenflo (2008), concluded that the tilt is already established in

the source regions beneath the solar surface. This interpretation challenges the widely accepted theory that the tilt angles appear to be independent of the emerged magnetic flux. Kosovichev and Stenflo (2008) and Pevtsov et al. (2014) noted that the tilts of decaying groups relax toward a mean tilt angle characteristic of a given latitude. McClintock and Norton (2016) reported increasing tilt angles in larger regions during their decay, whereas the tilts of small and medium-sized regions remained relatively steady. Will et al. (2024) investigated tilt angles during different phases of sunspot groups flux emergence using automatically identified active regions from solar cycle (SC) 23 to the beginning of SC 25. Other studies have analyzed the relationship between tilt angle and polarity separation and found a connection between these quantities. A positive linear relationship between tilt angle and the separation distance of ARs has been reported by several authors [Howard, 1993, 1996; Sivaraman et al., 1999]. D'Silva and Howard (1993) argued that the relationship between tilt angle and polarity separation is a genuine phenomenon rather than merely a consequence of Joy's law. Using magnetogram data for 517 bipolar ARs, Tian et al. (2003) reported that the tilt angle increases with increasing separation for separation distances below 8x10 cm. Investigating sunspot groups during SC 23, Zharkova and Zharkov (2008) pointed out that the latitude-dependent variations in polarity separation are in anti-phase with those of the tilt angles, with the latter reaching a maximum at a latitude of 35°.

This article aims to study variations in tilt angles during the evolution of sunspot groups using a large, reliable, and visually inspected statistical sample.

2. Materials and Methods

Although the tilt angle of a sunspot group was defined and used before the advent of magnetographic observations, its value can be determined more accurately by taking the magnetic polarity of the sunspots into account. Since this research aims to investigate the variation in the tilt angle of sunspot groups throughout their entire lifetimes, the SOHO/MDI-Debrecen Sunspot Data (hereafter SDD) catalog [Baranyi et al., 2016] is used. This database contains area and position data as well as magnetic data for each observed sunspot covering the period from 1996 to 2010, i.e., the entire SC 23. To ensure the reliability of the tilt-angle calculations, all sunspot groups located within $\pm$ 60 deg of the central meridian (CM) and having a peak area larger than 10 millionths of the solar hemisphere (MSH) are considered. Hereafter, the area of a sunspot group refers to its umbral area corrected for foreshortening. The following criteria are applied to select groups that are observed both near and at the times of their peak area, i.e., groups that exhibit both growth and decay phases. A group is selected if its area increases by at least 20 % of its maximum area during the day preceding the time of the maximum area and subsequently decreases by at least 60 % of its maximum area over the following three days. In addition, the sunspot group is required to be bipolar at the time of its peak area. The first and last observation times of a sunspot group are defined as the first and last times when the center of the sunspot group is located within $\pm$ 60 deg of the CM and its leading and following portions can be observed simultaneously. To correctly identify the sunspot groups included in the study, we exclude all groups for which the absolute difference between the maximum and minimum tilt angles is smaller than 5 degrees. These criteria help eliminate measurement-related errors and, in this way, allow us to safely exclude unipolar groups from our study. Using these criteria, a total of 277 distinct sunspot groups are selected. Considering that smaller and larger sunspot groups develop in different ways, the areal evolution phase (hereafter AEP) is introduced instead of the time elapsed from the time of peak area [Muraközy, 2022, 2024]. The AEP is defined as

$$AEP = \left(1 - \frac{a}{A}\right) 100, \tag{1}$$

where a denotes the observed umbral area of a sunspot group and A denotes its maximum area. To distinguish between the growth and decay phases of sunspot groups, the AEP is multiplied by -1 for observations obtained before the time of peak area.

Although the SDD contains tilt-angle data for each sunspot group, the database does not take the leading magnetic polarity into account; instead, the westward portion of each sunspot group is always considered to be the leading part [Baranyi, 2015]. To eliminate this ambiguity, I visually determined the leading magnetic polarity of each group using the HTML version of the catalog [Baranyi et al., 2016] which also contains white-light images and magnetograms for each observation time. Thus, the leading magnetic polarity can be determined reliably, even for sunspot groups observed near solar cycle minima. After this verification, the sunspot group tilt angle (γ) is calculated for each observation time, including the conversion from degrees to radians, as

$$\gamma = \arctan\left(\left|B_f - B_l\right| / \left|L_f - L_l\right| / cos(B/360 * 2 * \pi)\right) /2/\pi * 360 * sign\left(\left|B_f\right| - |B_l|\right), \quad (1)$$

where B and L denote the area-weighted heliographic latitude and longitude of the sunspot group, respectively, while the subscripts l and f refer to its leading and following parts, respectively. Delta groups, i.e., groups in which umbrae of opposite magnetic polarities are present within the same penumbra, are excluded from this study. The values of γ range from -90 deg to +90 deg. $\gamma = 0$ means that the latitudes of leading and following polarities are identical, i.e., the line connecting the centers of the leading and following parts is parallel to the solar equator. Regardless of the solar hemispheres, a positive/negative tilt angle indicates that the leading/following part of the group is closer to the equator, respectively.

3. Results

The selected 277 distinct sunspot groups span the entirety of SC 23 and the beginning of SC 24. The left panel of Figure 1 shows their temporal and latitudinal distribution, i.e., the butterfly diagram. No significant gaps are present in either the temporal or the latitudinal coverage, except near the very end of SC 23, during the period of April 03, 2008 to January 09, 2009. The variation in tilt angles is studied as a function of the sunspot evolutionary phases of sunspot groups. In this study, the absolute values of the tilt angles are used because we aim to investigate the actual tilts of sunspot groups with respect to the east-west direction. Averaging tilt angles with different signs can mask their actual variation, as positive and negative tilts can cancel each other out. The variation in tilt angles for all sunspot groups at each observation time is shown in Figure 2. Instead of time, the areal evolution phase is used as the independent variable.

The top panel of Figure 1 shows the mean area of sunspot groups as a function of their tilt angles for the entire data set, while the bottom panel depicts the number of sunspot groups in each bin. Each group is counted as many times as it was observed within $\pm$ 60 deg of the CM. The distribution of the number of samples (bottom panel of Figure 1) approximately follows a normal distribution, with its maximum value of 4183 occurring between 0 deg and +10 deg. This panel shows that most groups are only slightly tilted relative to the horizontal direction, whereas tilt angles above 30 deg are relatively uncommon. Meanwhile, the largest groups cluster around the zero tilt, however several larger ARs (191 in total), albeit with larger errors, can also be observed at the upper edge of the distribution. Higher tilt angles mainly characterize the smallest sunspot groups.

The top panel of Figure 2 shows the variation in absolute tilt angles throughout the lifetime of sunspot groups. The evolution of ARs appears to consist of two or three phases. After emergence, sunspot groups are most strongly inclined with respect to the solar equator, and their tilt angles then decrease during the first phase of their evolution, up to AEP $\approx$ -20 %. During the second phase, sunspot groups maintain approximately the tilt angle reached at the end of the first phase. This phase appears to extend over an AEP range of approximately 60 %. During the final, third phase, a slight increase in the tilt angle can be observed. These observations are in good agreement with the results shown in the upper right panel of Figure 1: the larger the area of an AR, the smaller its tilt angle. The bottom panel of this figure shows the relative number and area of sunspots within an AR. These quantities are normalized to 1 for each sunspot group, i.e., the total area and number

of sunspots within a group are normalized to their respective maximum values. Red dots indicate the mean leading - following separation distance, calculated as described in [Muraközy, 2024]. Although the relative area and number of sunspots peak around the time of the maximum area of the ARs, breaks can be observed on their curves around this time. During the emergence phase, the number of sunspots increases slowly, whereas their total area increases more rapidly. Throughout the tilt-relaxation phase, the trends of both curves are reversed. The rates of these decreases change during the final phase of the tilt-angle variation: the number of sunspots continues to decrease at a slower rate, while their total area decreases more rapidly. After the emergence of the AR, both the area and the separation distance begin to increase. This expansion, together with the Coriolis force, could cause the observed variation in tilt angles during the evolution of the AR (Figure 2).

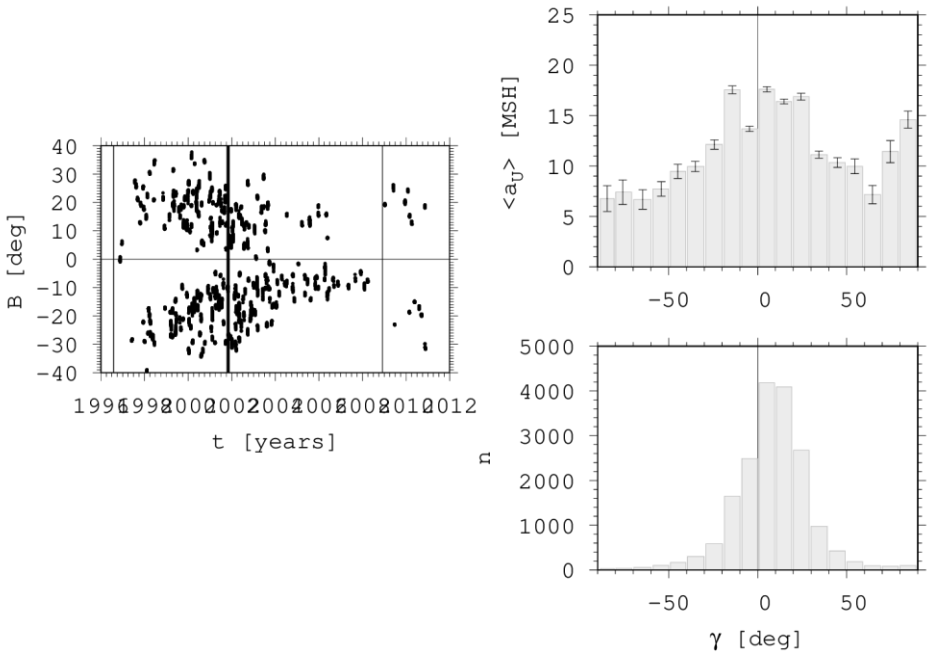


Figure 1. *Left figure: Butterfly diagram of the selected sunspot groups. Each point represents an AR at one observation time. The thin black vertical lines denote the minima of the SCs 23 and 24, while the thick black vertical line marks the time of the peak activity of SC 23 (taken from the SILSO Sunspot Number database that can be found at https://www.sidc.be/SILSO/cyclesminmax. Right figure: Mean umbral area of sunspot groups with their errors (top panel) and number of sunspot groups (bottom panel) averaged over 10 deg bins of tilt angle. Error bars represent the standard error of the mean.*

These findings are similar to those of [Schunker et al., 2020], who also found that during the emergence phase, the tilt angle initially increases, followed by a relaxation phase.

To facilitate comparison between the tilt angles and the separation distance, they are plotted together in the same figure (right panel of Figure 2). The relationship between the two quantities is approximately linear; however, a break in the trend of the absolute tilt angles occurs between separation distance of 12.5 and 15 degrees. Below a separation of 12.5 degrees, the absolute tilt angle decreases with increasing separation distance. This can also be observed in Figures 2 and 3, where, regardless of the peak area of the ARs, the highest tilt angles are observed shortly after emergence, when the separation has just begun to increase. This suggests that, after emergence, initially tilted sunspot groups begin to expand while their tilt angles decrease until a certain point.

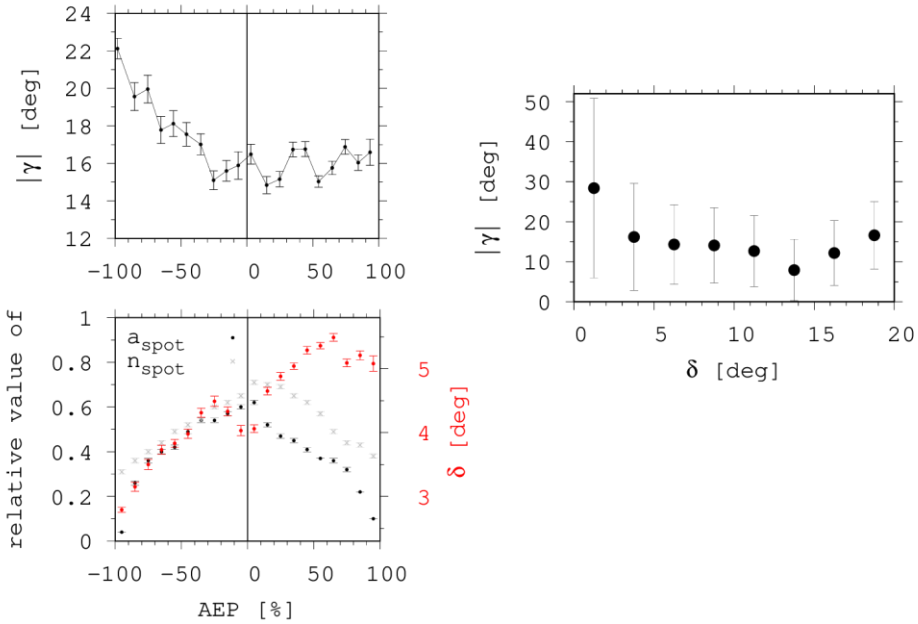


Figure 2. *Left top panel: Mean absolute tilt angle (depicted by black dots) as a function of AEP. Left bottom panel: Relative sunspot area (black, measured on the left axis) and the number of sunspots (gray, measured on the left axis) within ARs in each bin, as well as the mean leading - following separation distance (red, measured on the right axis). The values are averaged over 10 AEP bins. The solid black vertical line marks the time of peak umbral area. Right panel: absolute tilts of sunspot groups as a function of the leading-following separation distances. The tilts are averaged over 2.5 degree bins of separation distances. Error bars indicate the standard errors.*

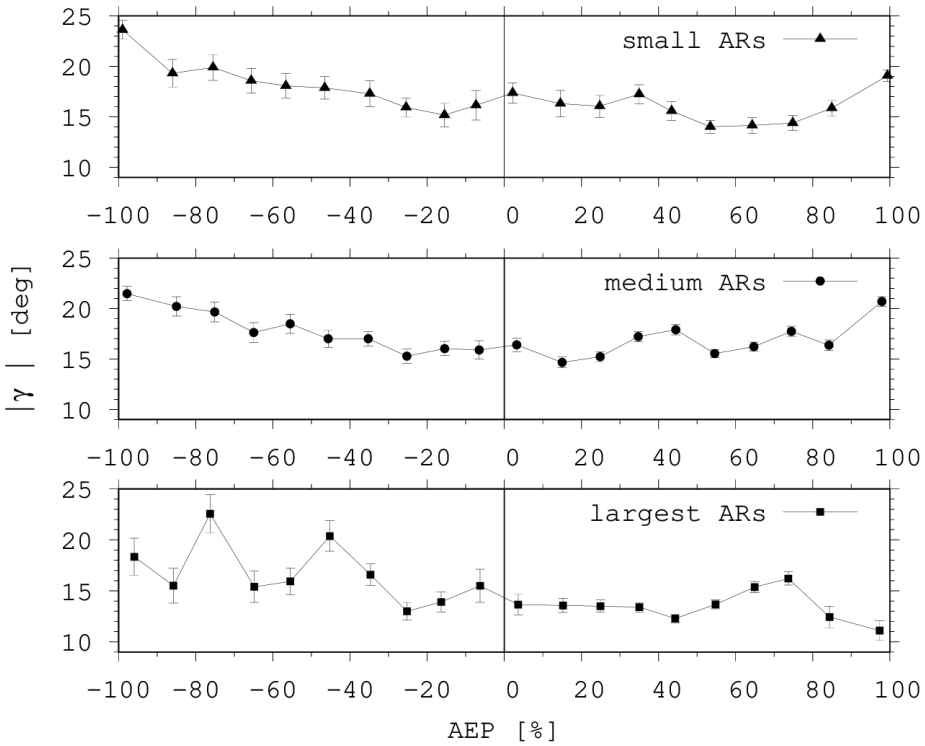


Figure 3. *Variation of the mean absolute tilt angle as a function of AEP for three ARs size categories. Top panel: the smallest ARs (A<20 MSH), middle panel: medium-sized ARs (20 MSH A < 60 MSH), bottom panel: the largest ARs (A 60 MSH). The absolute tilt angles are averaged over 10 AEP bins, and the error bars indicate the standard errors. The black vertical lines mark the times of peak area.*

Since the upper-right panel of Figure 1 reveals a relationship between the area and tilt angle of sunspot groups, the studied ARs are divided into three groups according to their peak areas. As the smallest groups, we considered those with a peak area below 20 MSH. The medium-sized and largest groups are defined as those with peak area between 20 and 60 MSH and above 60 MSH, respectively. Figure 3 is analogous to the top panel of Figure 2, but shows the results for different AR size categories. The curves for the smallest and medium-sized ARs most closely resemble the curve obtained from the aggregated data. At the beginning of the sunspot groups' lifetimes, the relatively high absolute tilt angles decrease until approximately -20 % AEP, after which they undergo a relaxation phase. Toward the end of their lifetimes, the mean absolute tilt angles increase again. The curve for the largest sunspot groups is the most irregular during the initial phase, up to the beginning of the tilt relaxation. Moreover, toward the end of their lifetimes, the mean tilt angles appear to decrease rather than increase.

Above a 12.5-degree separation the tilt-separation relationship is linear (right panel of Figure 2). This upper branch is produced mainly by small groups toward the end of their lifetimes, consistent with Figure 4 in [Muraközy, 2024].

The selected data allow us to study the so-called anomalous sunspot groups. Here, the sunspot groups are divided into three sets based on their latitudinal configurations. The first set consists of Joy's law region (JRs), in which the leading part is always closer to the solar equator than the following part. The second set contains anti-Joy regions (AJRs), in which the following part is always closer to the equator. Those ARs in which the Joy and anti-Joy configurations continuously alternate belong to the third group, referred to as mixed. The left panel of Figure 4 shows the variation in the tilt angle during the evolution of these groups. The magnetically anomalous ARs are shown in the right panel as red dots. Altogether, 10 groups in the sample are identified as anti-Hale regions (AHRs), in which the leading polarity is opposite to the usual leading polarity for the given solar cycle. In this case, mixed group is not distinguished.

The previously discussed three-step variation can also be observed in all curves, regardless of their type. However, the average absolute tilt angle of the JRs is significantly higher, by a 33 % and 45 %, than those of the AJRs and the most common type, the mixed groups, respectively. For the HRs and AHRs, the results are similar to those for the JRs and AJRs, respectively; however, the tilt angles of the AHRs are 22 % higher than those of the HRs. A very interesting and unexpected finding is the very high tilt angles observed during the emergence phases of the AJRs and AHRs.

It appears that the increase observed during the dispersal phase in Figure 2 is mainly caused by the anti-Joy groups.

4. Conclusion and Discussion

In contrast to previous studies, this paper investigates the variation in absolute tilt angles during the evolution of sunspot groups by analyzing data from both white-light observations and magnetograms. The selected sample was visually inspected. The main results are as follows.

- The tilt angles of sunspot groups are negatively correlated with their umbral areas: the larger the umbral area, the lower the tilt angle. The distribution of tilt angles follows a normal distribution. Most ARs have tilt angles between 0 and 10 degrees (Figure 1).
- The variation in the absolute tilt angles during the lifetime of solar active regions exhibits a three-step process, which largely follows the variation in the leading-following separation distance (Figure 2). The absolute tilt angles are inversely proportional to the separation distance when the latter is below 15 degrees (right panel of Figure 2). The existence of these three phases is independent of the peak area of the sunspot groups, although the pattern is more pronounced for small- and medium-sized groups. The tilt angles of larger groups show a more chaotic variation during their evolution (Figure 3).

For rule-breaking sunspot groups, the first and second phases are more pronounced than for the mixed and normal groups (Figure 4), and their average tilt angles also differ.

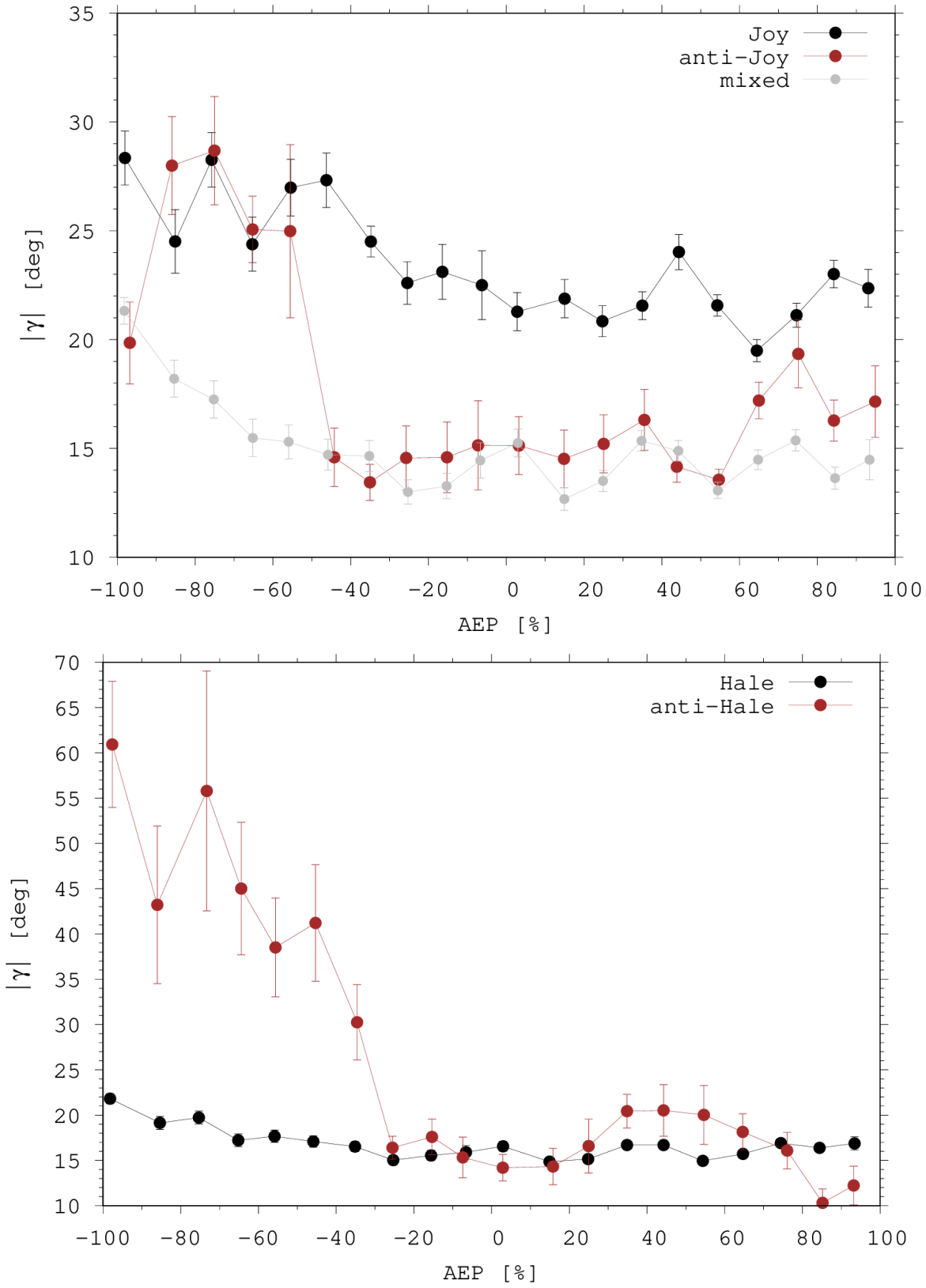


Figure 4. *Variations in the tilt angles of rule-breaking sunspot groups during their evolution. Left panel: for the JR (black dots), AJR (red dots), and mixed regions (gray dots). Right panel: HR (black dots) and AHR (red dots). Absolute tilt angles are averaged over 10 % bins of AEP; error bars indicate the standard errors of the mean.*

Several previous studies have investigated various aspects of tilt-angle variations. However, some of them used only magnetograms, while others analyzed tilt angles solely from white-light images. Other studies employed larger datasets but did not include visual inspection. The majority of previous studies used signed average rather than absolute values, thereby potentially obscuring the true inclination of ARs, since positive and negative tilt angles can cancel each other out. Moreover, most of these studies focused only on the emergence phase of ARs [Schunker et al., 2020; Wang et al., 2021; Will et al., 2024]. Although the size of our sample is relatively small due to the strict selection criteria, the studied ARs were visually inspected and cover the entire solar cycle (Figure 1). The sample also includes anomalous ARs that violate Hale's or Joy's law. The distribution of the studied sample shows that most ARs have tilt angles between 0 and 10 degrees, which is consistent with the results of [Howard, 1996; Arlt et al., 2016].

The mean absolute tilt angles differ slightly among ARs of different areas. The relationship is an inverse proportionality, the largest tilts observed in the smaller regions, although the difference is not statistically significant. Nevertheless, this result suggests that smaller ARs may also contribute to the reversal of the solar dipole field. This finding is consistent with [Sivaraman et al., 1999; McClintock and Norton, 2016], but is inconsistent with [Stenflo and Kosovichev, 2012], who found no dependence of tilt angles on region size, suggesting that the tilts were not produced by the Coriolis force acting on rising flux tubes. The aim of the present study is to track the variation in tilt angles throughout the entire evolution of ARs. During the emergence phase, relatively high tilt angles are observed, followed by a decrease. This behavior is also consistent with the findings of [Wang et al., 2021], who studied the emergence phase of an AHR. According to the most widely accepted explanation for the variation in tilt angles, flux ropes emerging from the bottom of the convection zone are affected by buoyancy and the Coriolis force, which deflects their leading part toward the solar equator. The tilt angle of the emerged AR reflects the spiral orientation of the subsurface toroidal magnetic field, which is influenced by large-scale motions such as differential rotation and meridional circulation. As a result, the tilt angle evolves toward the orientation expected from Joy's law after emergence, until the upward motion of the flux rope ceases and the influence of the Coriolis force diminishes ([Kosovichev and Stenflo, 2008] and references therein). Howard (1991) suggested that, if tilt angles vary with time, the tilts of young and old sunspot groups should differ, with those of decaying groups being closer to the average tilt than those of emerging groups. This is consistent with our findings. The results of [Will et al., 2024], however, are not consistent with ours, as they found that AR emerge with nearly east-west orientations and that their tilt angles subsequently increase. One possible explanation for this discrepancy is that they analyzed signed tilt angles, whereas our results are based on absolute tilt angles (Figure 2). Near the time of peak area (AEP -20%), the tilt angle appears to begin relaxing toward the value reached at the end of the emergence phase. This phase lasts until approximately 60 % of AEP. The relaxation of tilt angles is a commonly reported behavior (e.g., [Kosovichev and Stenflo, 2008; Schunker et al., 2020; Wang et al., 2021]). During this phase, the flux tube appears to be sufficiently strong to withstand the dispersive effects, while the mean orientation of ARs becomes more east-west directed. During part of this phase, around the time of peak area, sunspot groups are in a state of magnetic stability, during which the leading-following separation is temporarily halted [Muraközy, 2024]. On average, the decay of solar ARs has been less studied than their emergence. This is also true for the evolution of AR tilt angles. Toward the end of the AR evolution, from approximately AEP 60 % onward, the absolute tilt angle begins to increase (Figures 2 and 3). This is the phase during which the leading-following separation starts to decrease, caused by the backward motion of the leading part of sunspot groups [Muraközy, 2024]. During this phase, the area of individual sunspots decreases more rapidly than their number, resulting in a more rapid decrease in the relative area covered by sunspots (bottom panel of Figure 2), suggesting a role for turbulent erosion [Petrovay and Moreno-Insertis, 1997]. Studying a complex anti-Hale AR during its decay, Elmhamdi et al. (2014) reported a three-phase decrease in the tilt angle, correlated with the three-phase variation in the accumulation of magnetic

helicity flux, with M- and X-class solar flares occurring near the phase transitions. Tian et al. (2005) noted that ARs violating Hale's law exhibit high flaring activity. Our results are in agreement with those of [McClintock and Norton, 2016], who found similar variations in their small and medium-sized ARs, but differ from those of [Schunker et al., 2020]. During this phase, sunspots become fewer and smaller, while the tilt angles become more variable, possibly due to underlying large-scale motions, such as meridional flow.

Several studies [Howard, 1993, 1996; Tian et al., 2003] have reported that the tilt angles of sunspot groups increase with increasing leading-following polarity separation. In our study, the trend is opposite below separation distance of 12.5 deg (right panel of Figure 2). One possible explanation for this difference is the use of absolute tilt angles. A break in the curve is observed at approximately 12.5 deg. Tian et al. (2005) found a linear relationship between the separation distance and tilt angle for separation distances below 8x10 cm. If we consider a separation of 12.5 deg, this corresponds to 1.52x10 cm. Similar cut-off can be observed at a separation distance of approximately 110 Mm (1.1x10 cm) in [Fisher et al., 1995].

Khlystova and Sokoloff (2009) and Muñoz-Jaramillo et al. (2021) did not identify any spatial or temporal preferences of AHRs and AJRs; however, their tilt-angle variations differ from the average behavior (Figure 4). Anomalous sunspot groups exhibit relatively high tilt angles and standard errors during their emergence phases. More detailed investigations are needed to better understand the tilt-angle evolution of these types of ARs. These investigations, together with the effects of energy dissipation on the evolution of solar active regions, will be the subject of future work based on a larger database.

Acknowledgements

The solar cycle minimum–maximum data source is the WDC-SILSO, Royal Observatory of Belgium, Brussels. This research has received funding from National Research, Development and Innovation Office – NKFIH, 141895.

References

Arlt, R., Senthamizh Pavai, V., Schmiel, C., and Spada, F. (2016). Sunspot positions, areas, and group tilt angles for 1611-1631 from observations by Christoph Scheiner. *Astronomy and Astrophysics*, 595, A104. https://doi.org/10.1051/0004-6361/201629000.

Baranyi, T. (2015). Comparison of Debrecen and Mount Wilson/Kodaikanal sunspot group tilt angles and the Joy's law. *Monthly Notices of the Royal Astronomical Society*, 447, (2), 1857–1865. https://doi.org/10.1093/mnras/stu2572.

Baranyi, T., Győri, L., and Ludmány, A. (2016). On-line Tools for Solar Data Compiled at the Debrecen Observatory and Their Extensions with the Greenwich Sunspot Data. *Solar Physics*, 291, (9-10), 3081–3102. https://doi.org/10.1007/s11207-016-0930-1.

D'Silva, S., and Howard, R.F. (1993). Limits on the Magnetic Field Strength at the Base of the Solar Convection Zone. *Solar Physics*, 148, (1), 1–9. https://doi.org/10.1007/BF00675531.

Elmhamdi, A., Romano, P., Kordi, A.S., and Al-trabulsy, H.A. (2014). Twist and Writhe of the Magnetic Flux in the Super Active Region NOAA 11429. *Solar Physics*, 289, (8), 2957–2970. https://doi.org/10.1007/s11207-014-0507-9.

Fisher, G.H., Fan, Y., and Howard, R.F. (1995). Comparisons between Theory and Observation of Active Region Tilts. *The Astrophysical Journal*, 438, 463. https://doi.org/10.1086/175090.

Hale, G.E., Ellerman, F., Nicholson, S.B., and Joy, A.H. (1919). The Magnetic Polarity of Sun-Spots. *The Astrophysical Journal*, 49, 153. https://doi.org/10.1086/142452.

Howard, R.F. (1991). Axial Tilt Angles of Sunspot Groups. *Solar Physics*, 136, (2), 251–262. https://doi.org/10.1007/BF00146534.

Howard, R.F. (1991). The Magnetic Fields of Active Regions - Part Six. *Solar Physics*, 132, (2), 257–270. https://doi.org/10.1007/BF00152287.

Howard, R.F. (1993). Axial Tilt Angles of Active Regions and Their Polarity Separations. *Solar Physics*, 145, (1), 105–109. https://doi.org/10.1007/BF00627986.

Howard, R.F. (1996). Axial Tilt Angles of Active Regions. *Solar Physics*, 169, (2), 293–301. https://doi.org/10.1007/BF00190606.

Ivanov, V.G. (2012). Joy's law and its features according to the data of three sunspot catalogs. *Geomagnetism and Aeronomy*, 52, (8), 999–1004. https://doi.org/10.1134/S0016793212080130.

Khlystova, A.I., and Sokoloff, D.D. (2009). Toroidal magnetic field of the Sun from data on Hale-rule-violating sunspot groups. *Astronomy Reports*, 53, (3), 281–285. https://doi.org/10.1134/S106377290903010X.

Kosovichev, A.G., and Stenflo, J.O. (2008). Tilt of Emerging Bipolar Magnetic Regions on the Sun. *The Astrophysical Journal*, 688, (2), L115. https://doi.org/10.1086/595619.

Li, J. (2018). A Systematic Study of Hale and Anti-Hale Sunspot Physical Parameters. *The Astrophysical Journal*, 867, (2), 89. https://doi.org/10.3847/1538-4357/aae31a.

McClintock, B.H., and Norton, A.A. (2016). Tilt Angle and Footpoint Separation of Small and Large Bipolar Sunspot Regions Observed with HMI. *The Astrophysical Journal*, 818, (1), 7. https://doi.org/10.3847/0004-637X/818/1/7.

Muñoz-Jaramillo, A., Navarrete, B., and Campusano, L.E. (2021). Solar Anti-Hale Bipolar Magnetic Regions: A Distinct Population with Systematic Properties. *The Astrophysical Journal*, 920, (1), 31. https://doi.org/10.3847/1538-4357/ac133b.

Muraközy, J. (2022). Variations of the Internal Asymmetries of Sunspot Groups during Their Decay. *The Astrophysical Journal*, 925, (1), 87. https://doi.org/10.3847/1538-4357/ac3de6.

Muraközy, J. (2024). Variation in the polarity separation of sunspot groups throughout their evolution. *Astronomy and Astrophysics*, 690, A257. https://doi.org/10.1051/0004-6361/202450194.

Petrovay, K., and Moreno-Insertis, F. (1997). Turbulent Erosion of Magnetic Flux Tubes. *The Astrophysical Journal*, 485, (1), 398–408. https://doi.org/10.1086/304404.

Pevtsov, A.A., Berger, M.A., Nindos, A., Norton, A.A., and van Driel-Gesztelyi, L. (2014). Magnetic Helicity, Tilt, and Twist. *Space Science Reviews*, 186, (1-4), 285–324. https://doi.org/10.1007/s11214-014-0082-2.

Schunker, H., Baumgartner, C., Birch, A.C., Cameron, R.H., Braun, D.C., and Gizon, L. (2020). Average motion of emerging solar active region polarities. II. Joy's law. *Astronomy and Astrophysics*, 640, A116. https://doi.org/10.1051/0004-6361/201937322.

Senthamizh Pavai, V., Arlt, R., Dasi-Espuig, M., Krivova, N.A., and Solanki, S.K. (2015). Sunspot areas and tilt angles for solar cycles 7-10. *Astronomy and Astrophysics*, 584, A73. https://doi.org/10.1051/0004-6361/201527080.

Sivaraman, K.R., Gupta, S.S., and Howard, R.F. (1999). Measurement of Kodaikanal white-light images - IV. Axial Tilt Angles of Sunspot Groups. *Solar Physics*, 189, (1), 69–83. https://doi.org/10.1023/A:1005277515551.

Stenflo, J.O., and Kosovichev, A.G. (2012). Bipolar Magnetic Regions on the Sun: Global Analysis of the SOHO/MDI Data Set. *The Astrophysical Journal*, 745, (2), 129. https://doi.org/10.1088/0004-637X/745/2/129.

Tian, L., Liu, Y., and Wang, H. (2003). Latitude and Magnetic Flux Dependence of the Tilt Angle of Bipolar Regions. *Solar Physics*, 215, (2), 281–293. https://doi.org/10.1023/A:1025686305225.

Tian, L., Liu, Y., Yang, J., and Alexander, D. (2005). The Role of the Kink Instability of a Long-Lived Active Region AR 9604. *Solar Physics*, 229, (2), 237–253. https://doi.org/10.1007/s11207-005-6884-3.

Wang, J., Yan, X., Kong, D., Xue, Z., Yang, L., Li, Q., Zhang, Y., and Li, H. (2021). Naked emergence of an anti-Hale active region. I. Overall evolution and magnetic properties. *Astronomy and Astrophysics*, 652, A55. https://doi.org/10.1051/0004-6361/202140685.

Will, L.W., Norton, A.A., and Hoeksema, J.T. (2024). The Dependence of Joy's Law and Mean Tilt as a Function of Flux Emergence Phase. *The Astrophysical Journal*, 976, (1), 20. https://doi.org/10.3847/1538-4357/ad82e3.

Zharkova, V.V., and Zharkov, S.I. (2008). Tilts and polarity separation in the sunspot groups and active regions at the ascending and descending phases of the cycle 23. *Advances in Space Research*, 41, (6), 881–892. https://doi.org/10.1016/j.asr.2007.02.082.

DOI: 10.31401/WS.2026.proc.10

Main Magnetic Lines of the Pre-flare Arcade Surface with Increased Current Density: Analysis of the Field Configuration Obtained by MHD Simulation to Determine the Position of the Solar Flare

Podgorny A.I.[1], *Podgorny I.M.*[2]

[1]Lebedev Physical Institute RAS, Moscow, Russia; podgorny@lebedev.ru
[2]Institute of Astronomy RAS, Moscow, Russia

Abstract

The complex, tangled configuration of the field in the solar corona makes it difficult to find the positions of singular X-type magnetic field lines near which conditions exist for the occurrence of solar flares. A divergent magnetic field can be superimposed on the X-type field. The study of the properties of the magnetic field configuration at the site of the solar flare is continued in order to determine the position of the solar flare. At the site of flare, the maximum current density does not necessarily have to be reached, but the magnetic field configuration must promote to the occurrence of a flare (predominance of the X-type field over the divergent field and other properties that promote to instability causing the flare).

Keywords: Solar flare; current sheet; MHD simulation; X-type singular line; divergent field.

1. Introduction: General imagination of the solar flare mechanism

Work continued on studying the magnetic field configuration at the location where a solar flare occurs in the corona, and developing a method for determining the flare's position based on the results of MHD simulation. As is well known, according to numerous observations, the primordial release of solar flare energy occurs in the solar corona at an altitude of 15,000 km - 70,000 km ([Lin et al., 2003] and other observations).

At present, a mechanism is known in principle that can explain the gradual accumulation of energy in the magnetic field of the emerging current in a stable configuration, and then the transition of the configuration to an unstable state, which is necessary for the appearance of a flare in an unlimited space with plasma in a magnetic field that occur high in the corona. Such a mechanism is the release of energy stored in the magnetic field of a current in the form of a thin sheet that is formed in the vicinity of a singular X-type magnetic field line [Syrovatskii, 1966, Bratenahl and Hirsch, 1966]. The current sheet is formed as a result of the disturbances accumulation, which can take place due to the appearance of magnetic forces of the corresponding directions in such a configuration. As a result of quasi-stationary evolution, the current sheet transit into an unstable state. The instability causes to an explosive release of the magnetic energy of the sheet with the observed manifestations of the flare, which are explained by the electrodynamic model of the solar flare proposed by I. M. Podgorny [Podgorny et al. 2010]. According to the electrodynamic model, hard beam X-ray emission with energies of 100 keV and higher, arising on the solar surface, is explained by the deceleration of electrons accelerated in field-aligned currents caused by the Hall electric field in the current sheet. The electrodynamic model also explains other observed manifestations of the flare. The electrodynamic model of a solar flare uses analogies with the electrodynamic model of a substorm, previously proposed by its author based on measurements on the Intercosmos-Bulgaria-1300 spacecraft [Podgorny et al., 1988].

Since it is impossible to obtain the magnetic field configuration in the corona from observations, MHD simulation in the solar corona is necessary to study the flare situation. The method for numerically solving the MHD equations uses an upwind absolutely implicit

finite-difference scheme, specifically developed to improve the stability of the numerical solution [Podgorny and Podgorny, 2004; 2019].

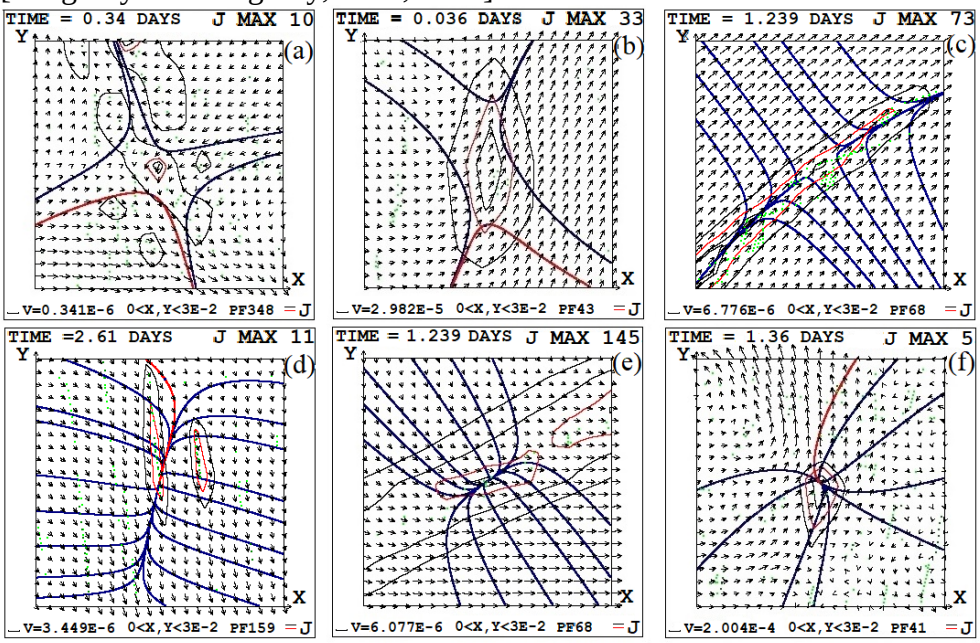


Figure 1. *"Flat" configurations of superpositions of X-type magnetic field and divergent magnetic field in the vicinity of a singular line of magnetic field*

2. Properties of "flat" magnetic field configurations. The problem of finding flare positions using the developed system

The given general idea of the solar flare mechanism creates the impression that the problem of determining the location of the flare from the magnetic field can be solved by searching for an X-type configuration with singular lines. In reality, such a search is difficult due to the complexity of the magnetic field configuration in the corona, which can be very confusing. The X-type magnetic field configuration may be superimposed by a divergent magnetic field, which further complicates the situation (see Figure 3 in [Podgorny and Podgorny, 2025]). Therefore, in many cases it is impossible to determine such a configuration, even with the direct use of the currently developed graphical system for searching for flare positions [Podgorny and Podgorny, 2013], although such a system helps in analyzing the magnetic field configuration, during which it is subsequently possible to find the flare position. The system of search of flare position is based on the assumption that the absolute value of the current density maximum is reached in the center of the current sheet. All local current density maxima are searched for, and the magnetic field configuration in the vicinity of each is examined.

Examples of superpositions of a divergent magnetic field on an X-type field in a configuration above the active region obtained by MHD simulation are shown in Figures 1a-f. In these Figures, in planes perpendicular to the magnetic field vector at the point of current density maximum, it is not the actual magnetic field lines that are depicted, but the so-called "plane magnetic field lines", i.e. lines tangent to the projections of the magnetic field vector onto the plane. It is the projections of the magnetic field onto the plane that determine the magnetic forces responsible for the creation of the plasma flow causing to the formation of the current sheet, therefore these "flat" magnetic field configurations best illustrate the possibility of the formation of the current sheet. The increase of these same magnetic forces occurs during the flare instability of the current sheet, therefore such "plane" configurations also illustrate the possibility of the emergence of instability. In Figures 1a, b, the magnetic

field superposition may be dominated by the X-type field, creating promotable conditions for the occurrence of a flare. Also, the superposition can be dominated by a divergent magnetic field (Figure 1e, f), which creates a rotational motion around a singular line (Figure 3 in [Podgorny and Podgorny, 2025]), inhibiting the formation of a current sheet and flare instability in the current sheet. The influence of the X-type field and the divergent magnetic field can be almost equal with a slight dominance of one of them (Figures 1c, d).

In a real situation, the current density does not necessarily reach its maximum in the middle of the current sheet. However, the flare position can be found by analysis using a graphical search system, since the flare position is related to the position of the maximum current density, and the system has the ability to determine the magnetic field configuration that promote to the flare occurrence.

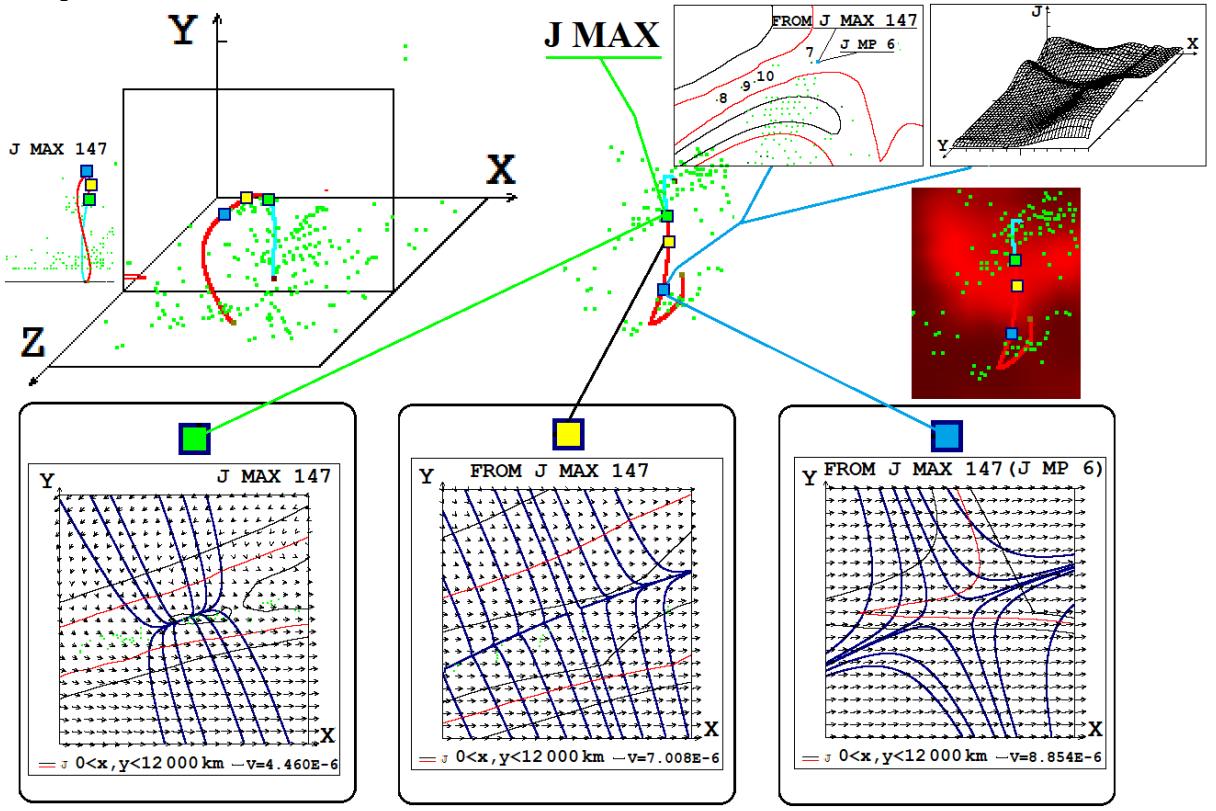


Figure 2. *Configurations of the magnetic field in the vicinity of points of a magnetic line passing through the maximum current density*

3. Basic concepts of properties of magnetic field configuration at the site of the flare

The basic idea of explaining where a solar flare occurs is illustrated in Figure 2. The current density reaches its maximum value at the point marked by the green square. This maximum has the number 147 in the chosen numbering: the graphical search system numbers all maximums in descending order. The magnetic line passing through this current density maximum have the shape of loop. It is represented as a line in three-dimensional space in the computational domain of the corona above the active region and as projections onto planes. The projection of the magnetic line onto the solar surface is shown, also together with the intensity distribution of microwave radio emission at a frequency of 17 GHz, obtained with the Nobeyama Radioheliograph (NoRH) (https://solar.nro.nao.ac.jp/norh/index.html). From the Figure it is clear that the selected maximum current density is located far from the center of the bright region of flare emission. This position of the selected maximum is explained by the fact that the plane configuration of the field in the vicinity of the selected maximum is

poorly promote to the appearance of a flare due to the predominance of the diverging magnetic field over the X-type field. The X-type field will dominate the divergent field most strongly in the vicinity of the point at the top of the loop, indicated by the blue square, so that at this point the field configuration is promote to the appearance of a flare. Also, the X-type field is dominant in the vicinity of the loop point in the middle of the bright region of flare emission, indicated in yellow. At the blue and yellow points, the current density, although not reaching its maximum value, is not significantly different from the current density at its maximum. Thus, a significant portion of the loop at points of which the field configuration promotes flare appearance is located in the bright region of flare emission. This arrangement of a significant part of the loop makes it possible to find the position of the flash in places where the maximum current density may not be achieved.

4. Arcades of magnetic lines. Main magnetic lines

Another property that can be used to search for flare positions is the appearance of a surface of magnetic lines in the form of an arcade with increased current density, i.e. an extended current sheet with a size of ~50 Mm. The selected magnetic loop passing through the 147th maximum of current density belongs to such surface of arcade as shown in the upper part of Figure 2 and in detail in Figure 3. In our case, the arcade lines were found because they pass through the chain maxima with numbers 145, 149, 148, 150, 147, marked in green. To them, lines are also added that pass through the "plane" maxima of the current density, located in the constructed planes perpendicular to the magnetic field vector.

The lines of arcade in the computational domain in the corona are shown in Fig. 3a, their projections onto the plane of the photosphere are shown in Fig. 3b. In Fig. 3c, these projections are superimposed on the intensity distribution of microwave radio emission at a frequency of 17 GHz, obtained with the Nobeyama Radioheliograph (https://solar.nro.nao.ac.jp/norh/index.html). Fig. 3d shows the current density distribution in the current sheet at the top of the arcade. In Figures 3e-s, the 3D and 2D configurations are depicted inside cubes and squares of large size 80 Mm. The centers of these cubes, which are also the centers of these squares, are located on the central loop of the arcade. This center of the cube and square for Figures 3c, h, k, n, q is at the point of the central maximum of the chain with number 148, for Figures 3f, i, l, o, r it is in the middle of the bright region of the flare emission, and for Figures 3g, j, m, p, s it is at the top of the loop. The location of the current sheet is shown by the lines of equal current density in Figures 3h-j and 3k-m.

The "plain" magnetic field configuration at the location of the chain of current density maxima (Figure 3n) is poorly promote to the occurrence of a flare, since the diverging magnetic field dominates the X-type field. In the middle of the bright region of the flare emission and at the top of the arcade, the plane magnetic field configuration promotes the appearance of the flare, since the X-type field dominates here (Figures 3o and 3p). The X-type field is most significantly dominant over the divergent field at the top of the arcade. The same conclusion can be made taking into account the longitudinal component of the magnetic field by the divergence of the field along the singular line in 3D configurations (Figures 3q-s). A significant part of the discovered arcade, at the points of which the field configuration promotes to the appearance of a flare, is located in the bright region of flare emission. This result is expected to be used in the future to search for the positions of the flares.

Figures 3e, f, g, h, i, j show all the found main lines of arcade passing through the three-dimensional maxima of the chain and the “plane” maxima.

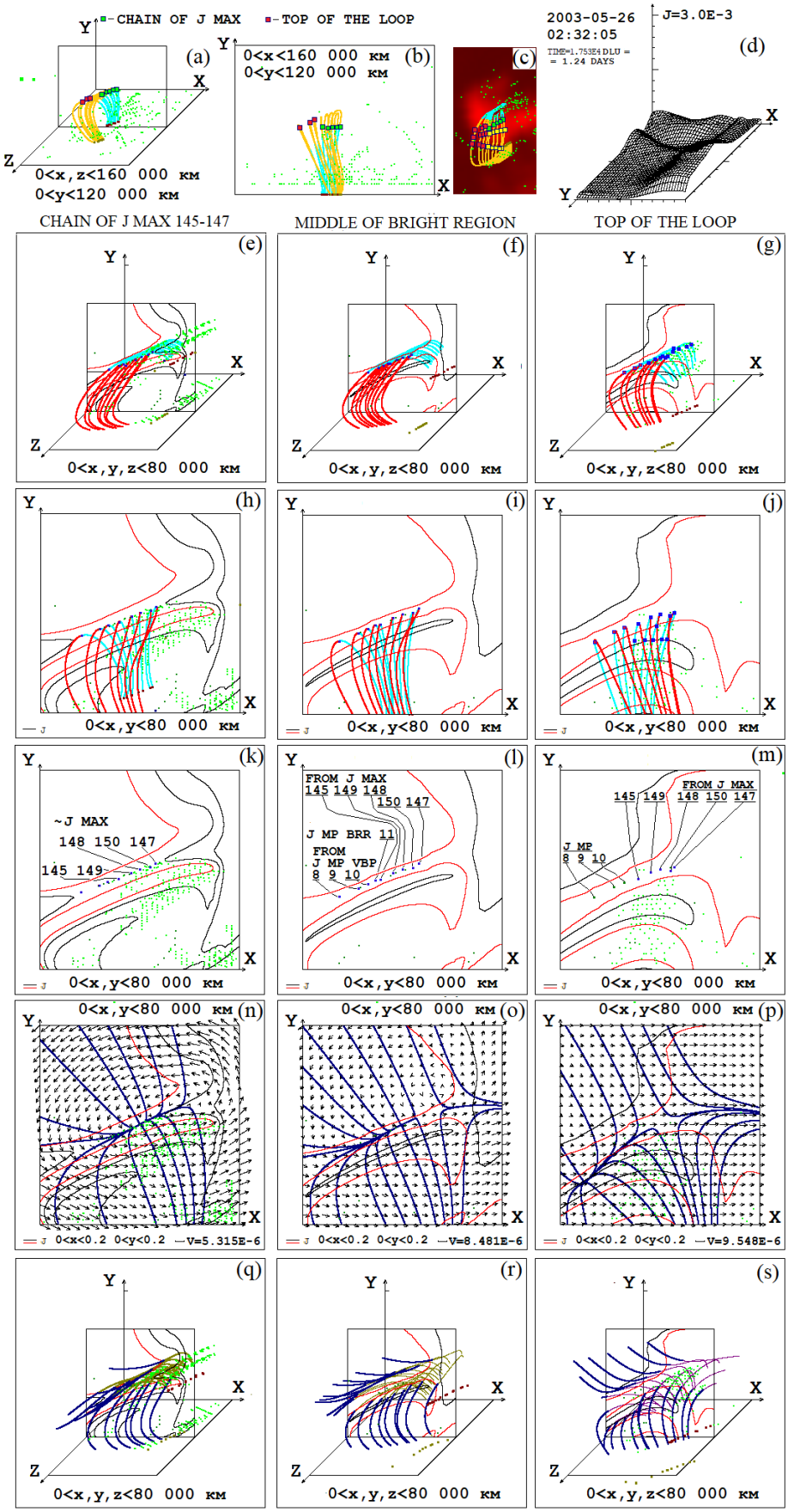


Figure 3. *The surface of magnetic lines of arcade of a large size ~50 Mm with increased current density, which is the extended current sheet.*

5. Conclusions

1. Difficulties arise when establishing the flare position based on the results of MHD modeling, due to the fact that in the rather highly entangled field of the corona it is difficult to determine the configuration of the X-type magnetic field. The flare release of energy may not occur at the location of maximum current density. At the same time, the configuration of the magnetic field at the site of the flare should promote to the occurrence of the flare: the X-type field should dominate over the diverging magnetic field. Also, at the location of the flare, a "one-dimensional" current density maximum must appear on a straight line intersecting the current sheet, and the current density must not be much less than at the maximum current density. The accumulation of magnetic energy for a flare can occur in a complex magnetic field configuration such as an arcade of magnetic lines, which is a large surface of ~50 Mm with an increased current density (an extended current sheet in the field of which energy for a flare accumulates).

2. The results of the analysis of magnetic field configurations above the active region provide guidance on how to upgrade the existing graphical system for searching for solar flare positions. It is necessary to search for "one-dimensional" current density maxima at the tops of loops to determine the locations of large arcades (~50,000 km) with increased current density.

Acknowledgements

The authors are grateful to the SOHO/MDI (Michelson Doppler Imager on the spacecraft Solar and Heliospheric Observatory) team and the Nobeyama radioheliograph team (The Nobeyama Radio Observatory, the division of the National Astronomical Observatory of Japan, located near Minamimaki, Nagano at an elevation of 1350 m.) for the scientific data provided as well as to the many professional cloud service specialists who made it relatively easy for us to configure rented remote computers for GPU computing.

References

Bratenahl, A., Hirsch, W. (1966). An experimental study of a neutral point in a plasma. In: *Proceedings of the AIAA Plasmadynamics Conference*, Monterey, CA, USA, 2–4 March 1966, Paper No. 66–152. https://doi.org/10.2514/6.1966-152

Lin, R.P., Krucker, S., Hurford, G.J., et al. (2003). RHESSI observations of particle acceleration and energy release in an intense gamma-ray line flare. *Astrophysical Journal*, **595**, L69–L76. https://doi.org/10.1086/378932

Podgorny, I.M., Dubinin, E.M., Israilevich, P.L., Nicolaeva, N.S. (1988). Large-scale structure of the electric field and field-aligned currents in the auroral oval from the Intercosmos-Bulgaria satellite data. *Geophysical Research Letters*, **15**, 1538–1540. https://doi.org/10.1029/GL015i013p01538

Podgorny, A.I., Podgorny, I.M. (2004). MHD simulation of phenomena in the solar corona by using an absolutely implicit scheme. *Computational Mathematics and Mathematical Physics*, **44**, 1784–1806.

Podgorny, I.M., Balabin, Y.V., Vashenyuk, E.V., Podgorny, A.I. (2010). The generation of hard X-rays and relativistic protons observed during solar flares. *Astronomy Reports*, **54**, 645–656. https://doi.org/10.1134/S1063772910070085

Podgorny, A.I., Podgorny, I.M. (2013). MHD simulation of solar flare current sheet position and comparison with X-ray observations in active region NOAA 10365. *Sun and Geosphere*, **8**, 71–76.

Podgorny, I.M., Podgorny, A.I. (2019). Physical mechanism of a solar flare based on the accumulation of the energy in the magnetic field of the current sheet in the solar corona. *Cosmic Research*, **57**(6), 389–406. https://doi.org/10.1134/S0010952519060054

Podgorny, A.I., Podgorny, I.M. (2025). Solar flare location on the extended arc of magnetic lines with increased current density, obtained by analyzing the results of MHD simulation. In: *Proceedings of the Seventeenth Workshop "Solar Influences on the Magnetosphere, Ionosphere and Atmosphere"*, Primorsko, Bulgaria, June 2025, 68–73. https://doi.org/10.31401/WS.2025.proc.10

Syrovatskii, S.I. (1966). Dynamic dissipation of energy in the vicinity of the magnetic field neutral line. *Soviet Physics JETP*, **23**, 754–762. http://jetp.ras.ru/cgi-bin/e/index/e/23/4/p754?a=list

DOI: 10.31401/WS.2026.proc.11

Statistical Study of Type-II Spicules Utilizing Chromospheric Imaging Data from the Goode Solar Telescope

Şahin S.[1,2]

[1]Department of Space Sciences and Technologies, Akdeniz University Faculty of Science, 07058, Antalya, Türkiye
[2]Big Bear Solar Observatory, New Jersey Institute of Technology, 40386 North Shore Lane, Big Bear City, CA 92314, USA
seraysahin@akdeniz.edu.tr, seray.sahinsolakci@njit.edu

Abstract

Type II spicules are highly dynamic chromospheric jet-like structures that are considered to be potential contributors to coronal heating and the solar wind mass supply. In this study, we investigate on-disk Type II spicules using high-spatial and high-temporal resolution Hα data acquired at ± 0.8 from the line centre, acquired with the Goode Solar Telescope. To enhance and systematically identify fine-scale elongated type II spicules, we applied the Rolling Hough Transform (RHT), making it the first implementation of this method to high-resolution on-disk data. Our analysis revealed a significant asymmetry between the two Hα wings, with approximately eight times more spicules detected in -0.8 images compared to $+0.8$ images. Radial velocity measurements exhibited a broad distribution ranging from approximately -85 to $+85$ km s^{-1}, indicating highly dynamic plasma motions. However, the mean radial velocities remained close to zero, while the mean projected speeds were approximately 33–34 km s^{-1}. The radial velocity distributions were nearly symmetric, with typical absolute values of about 22 km s^{-1}, indicating substantial apparent motions but little net preference for inward or outward propagation. The results also demonstrate the effectiveness of combining chromospheric imaging with RHT-based detection techniques for investigating the dynamics and morphology of on-disk Type II spicules and other small-scale features, thus opening new opportunities for statistical analyses of chromospheric fine structures at unprecedented resolution.

Keywords: solar chromosphere; spicules; chromospheric heating; coronal heating

1. Introduction

The solar chromosphere is a highly dynamic and structured layer of the solar atmosphere where energy and mass are continuously exchanged between the underlying photosphere and the overlying corona. Among the most prominent fine-scale structures observed in this region are spicules, thin jet-like features that dominate the chromospheric limb. They are believed to play a significant role in mass and energy transport into the upper solar atmosphere [e.g., Beckers, 1968; de Pontieu et al., 2007]. They are categorized into two groups, Type-I and Type-II spicules, based on their distinct kinematic and thermodynamic properties. While Type-I spicules follow traditional ballistic trajectories with lifetimes of minutes, Type-II spicules are characterized by shorter lifetimes (10-100 s), higher apparent velocities (30-100 km s^{-1}), and rapid fading in chromospheric lines, making them prime candidates for localized coronal heating and solar wind acceleration [De Pontieu et al., 2011; Martínez-Sykora et al., 2017]. When observed on the solar disk, Type-II spicules manifest as Rapid Blue and Red shifted Excursions (RBEs and RREs) in the wings of chromospheric spectral lines, such as Hα and Ca II 8542 Å [Langangen et al., 2008; Rouppe van der Voort et al., 2009; Sekse et al., 2012]. Modern analyses suggest that type II spicules may not be purely ballistic jets, but instead may arise from a combination of wave-driven processes, magnetic reconnection, and intermittent heating events in the lower solar atmosphere [Tsiropoula et al., 2012; Pereira et al., 2014; Samanta et al., 2019]. High-resolution numerical simulations also support this interpretation, showing that spicule-like features can naturally emerge from magneto-hydrodynamic processes involving shock formation and magnetic field

reconfiguration [Martínez-Sykora et al., 2017; Martínez-Sykora et al., 2020]. With the advent of high-resolution observations significant effort has been made to unravel the physical origin and nature of these events. For instance [Bose et al., 2021] analyzed spectral signatures of RBEs and RREs using chromospheric inversions, demonstrating that these excursions are accompanied by localized heating in the lower solar atmosphere, often showing a clear correlation with photospheric magnetic flux emergence (see also [Yurchyshyn et al., 2013], [Samanta et al., 2019]). More recent works showed that spicule populations may not be homogeneous, but instead consist of multiple coexisting components with distinct temporal and spatial behavior, including faint, rapidly evolving structures and longer-lived jet-like events [Yurchyshyn et al., 2026; Lee et al., 2026]. These findings further support the idea that chromospheric fine structures are not purely single-mechanism phenomena but rather the observational manifestation of multiple interacting physical processes. Despite these insights into their spectral properties, identifying and tracking these structures on-disk poses a challenge. Unlike limb observations where spicules stand out against the dark background, on-disk spicules are embedded within a highly complex, dynamic, and optically thick chromosphere dominated by fibrils, mottles, shocks, jets, canopy structures, etc. To mitigate the difficulty, we present a novel, fully automated spicule-tracking routine optimized for the complex on-disk environment, leveraging the Rolling Hough Transform (RHT) tool. Originally designed to isolate linear and filamentary structures in interstellar media and the corona [Clark et al., 2014], RHT was later adapted to track highly dynamic, time-dependent evolution of off-limb coronal rain [Schad, 2017]. Our primary objective is to demonstrate the scalability and reliability of this routine, enabling a transition from isolated case studies to robust statistical studies. Here, we applied this pipeline to high-resolution Hα $\pm$0.8Å images acquired at the Goode Solar Telescope (GST).

This paper is organized as follows. Section 2 describes the observations and methods used in this study. In Section 3, we present the results of the analysis. In Section 4 and 5, we discuss and summarize our findings, respectively.

2. Materials and Methods

The observation was done with the Visible Imaging Spectrometer (VIS) of the 1.6 m GST operating at the Big Bear Solar Observatory (BBSO) under excellent seeing conditions. The VIS uses a combination of a broad-band interference filter and a single Fabry-Pérot etalon to perform high-cadence, narrow-band imaging spectroscopy using the Hα 6563 spectral line. The incoming wavefront is corrected by the GST's advanced high-order adaptive optics system [Shumko et al., 2014], and the instrument features a $70''\times70''$ field of view (FOV) recorded by a high-speed CCD camera with a spatial sampling of $0''.029$.

The data analyzed in this study were taken on 2024 August 4 by scanning the Hα line between -1.2 and +1.2 with a 0.2 stepping. To automatically identify and track RBEs and RREs in the $H\alpha \pm 0.8$ images, we employed the RHT tool, which processes a $[x, y, t]$ data cube in a two-step coupled execution to deliver spatial (θ_{xy}) and the temporal (θ_t) mean angles [Schad, 2017]. First, the spatial RHT is applied to each off-band image taken at a given time step to determine the instantaneous orientation of RBEs/RREs. The spatial angle is measured from the studied image x-axis. Next, to extract temporal evolution without losing the field-aligned connectivity, the routine uses a pre-determined spatial mean angle to construct an inclined space-time ($x - t$) plane for each detected feature. Here, x represents the coordinate along the spine of the spicule, and t denotes the temporal axis. The RHT accumulator is then computed within this field-aligned space-time domain. The resulting temporal mean angle defines the orientation of the trajectory within this $x - t$ plane, serving as a direct diagnostic of the field-aligned apparent velocity. Further technical details regarding the algorithm's implementation can be found in [Schad, 2017] and [Şahin et al., 2023].

3. Results

The RHT routine was applied to the VIS/Hα data to determine spatial and temporal distributions of RBEs/RREs in an area containing a small cluster of photospheric bright points. It is worth noting that this is the first of its kind tracing of RBE/RREs over extended spatial and temporal domains.

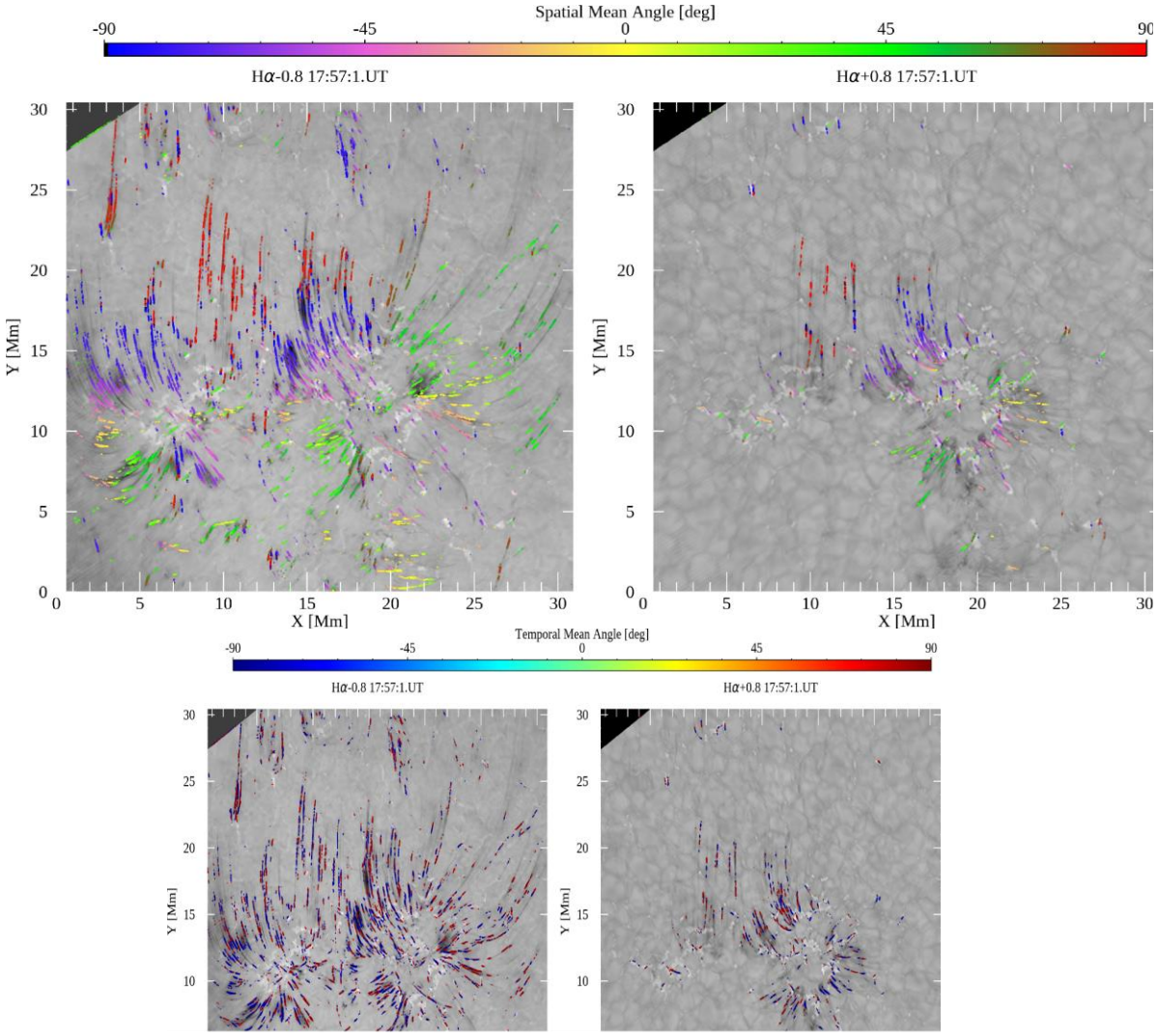


Figure 1. *Spatial (top) and temporal (bottom) mean angles of RBEs/RREs measured by applying the RHT routine to 17:57 UT H0.8 (left) and H0.8 (right) images. The map of the spatial mean angle shows the inclination of RBEs/RREs with respect to the horizontal direction of the images.*

The spatial (top panels) and temporal (bottom panels) mean angle maps derived from the RHT routine are presented in Figure 1. All colored contours in these panels indicate RBE/RRE structures successfully detected and tracked by this routine. Positive/negative spatial mean angles are counted counter-clockwise/clockwise from the horizontal axis. The temporal mean angles indicate the field-aligned displacement of the detected entity and the sign of θ_t is a direct proxy for the direction of the apparent plasma motion along the RBE/RRE axis. Specifically, positive temporal angles ($\theta_t > 0$) define trajectories where the feature moves upward, representing the initial injection phase away from the magnetic bright points. Conversely, negative temporal angles ($\theta_t < 0$) correspond to trajectories where the feature moves downward, capturing the retraction phase or counter-streaming flows back toward the solar surface. As shown in Figure 1, the spicules

occupy a much larger area in the Hα -0.8 images as compared to the Hα $+0.8$ images. To provide a quantitative comparison of RBE and RRE population, we calculated the spatio-temporal occupancy factor (η) throughout the observation period. This factor represents the fraction of the total observed volume in $[x, y, t]$ that is occupied by identified RBE or RRE structures. The total volume of our data cube is defined by $[N_x \times N_y \times N_t]$, where $N_x = 31.5$ Mm, $N_y = 30.5$ Mm, and $N_t = 182$ snapshots (roughly 35 minutes). Our analysis revealed a significant asymmetry in the detection counts. For the blue wing (-0.8) data, we identified 6.11×10^6 RBE pixels, yielding an occupancy factor of $\eta_{RBE} \approx 1.54 \times 10^{-2}$ (1.54%). For the red wing ($+0.8$), the total pixel count was 7.12×10^5, resulting in $\eta_{RRE} \approx 1.8 \times 10^{-3}$ (0.18%). This order-of-magnitude difference ($\eta_{RBE}/\eta_{RRE} \approx 8.5$) indicates a strong dominance of blueshifted features during the observing sequence. Such a discrepancy suggests that the upward mass flux or the initial heating phase of RBEs is much more readily captured at ± 0.8 than the subsequent cooling phases. This distinct variation and its temporal evolution are further illustrated in Figure 2.

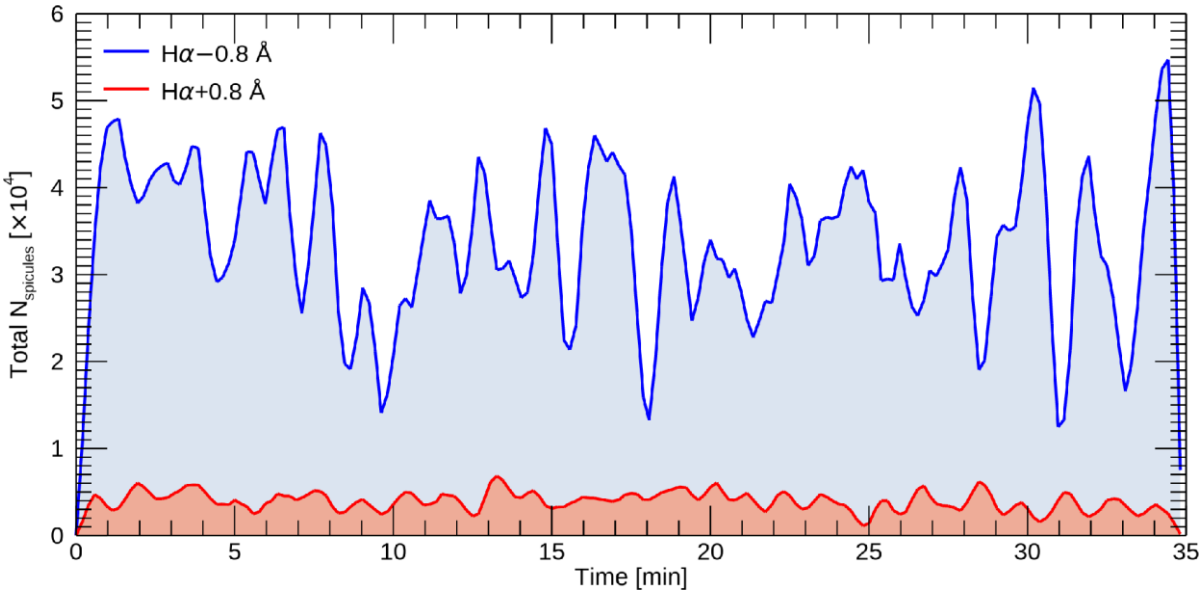


Figure 2. *Temporal evolution of the total detected spicules observed in the 0.8 (blue) and 0.8 (red) line profiles during the 35 minutes observational time.*

To study the overall velocity budget and mass balance within the spicule region, we performed a kinematic reconstruction for each detected spicule pixel. First, the apparent velocity along the inclination of the spicule, $v_{||}$, was derived from the temporal mean angle. Since θ_t represents the inclination in the field-aligned space-time domain, the field-aligned velocity is calculated as:

$$v_{||} = \left(\frac{\Delta x}{\Delta t}\right) tan(\theta_t), \tag{1}$$

where Δx is the spatial pixel size scaled to kilometers (Δx =21 km) and Δt is the cadence of the observations (Δt =12 s). By using the spatial mean angle, the field-aligned velocity vector can be decomposed using the spatial Cartesian components, v_x and v_y, in the image plane:

$$\begin{aligned} v_x &= v_{||} cos(\theta_{xy}) \\ v_y &= v_{||} sin(\theta_{xy}). \end{aligned} \tag{2}$$

During the observation sequence, the GST FOV was located approximately 80″ East and 150″ South of disk center. This information was used to define the local radial direction and the corresponding position angle, ϕ, at each pixel within the FOV, The radial velocity component was then calculated as:

$$v_{rad} = v_x cos(\phi) + v_y sin(\phi). \tag{3}$$

Through this transformation, a positive v_{rad} explicitly quantifies the radial expansion (upward motion away from the solar surface), while a negative v_{rad} signifies a radial contraction (downward motion toward the solar surface).

Figure 3 shows the frequency distributions of the calculated radial velocities for the tracked on-disk RBEs/RREs over the entire 35-minute observational sequence. Each distribution is fitted with a single Gaussian profile (solid black curve) to characterize the central tendencies and structural variances. The primary result emerging from this statistical analysis is the stark order-of-magnitude asymmetry in total feature detections. The RBE's exhibit a higher detection rate, with peak frequencies reaching approximately 1.5×10^5. In contrast, the RREs distribution peaks at roughly 1.7×10^4, establishing an nearly 8-fold dominance of the blueshifted structures across the observed FOV. Despite this profound contrast in overall counts, the profiles of the radial velocity distributions exhibit striking structural similarities. Both distributions are tightly centered near zero, with mean radial velocities (blue and red vertical dashed lines) of roughly $+0.18$ km s^{-1} and -1.40 km s^{-1} for the blue and red wing respectively. These small signed mean values might result from either the nearly balanced contributions of positive and negative radial motions or intrinsically low spicule expansion rate. The mean absolute radial velocities are 22.55 km s^{-1} and 22.28 km s^{-1} for the blue- and red-wing detections, respectively. The Gaussian fitting of the histograms revealed that 69% of the total velocity events detected in H$\alpha-0.8$ and 71% for the H$\alpha+0.8$ wings are within their respective $\pm1\sigma$ domains (indicated by the black vertical dashed lines), that corresponds to the roughly -30 to $+30$ km s^{-1} velocity range. These fractions are close to the theoretical value of 68.3% expected for a Gaussian distribution, indicating that the central parts of both velocity distributions are well described by a Gaussian profile. Nevertheless, both distributions also exhibit extended tails reaching approximately ±85 km, s^{-1}, associated with a smaller population of high velocity events.

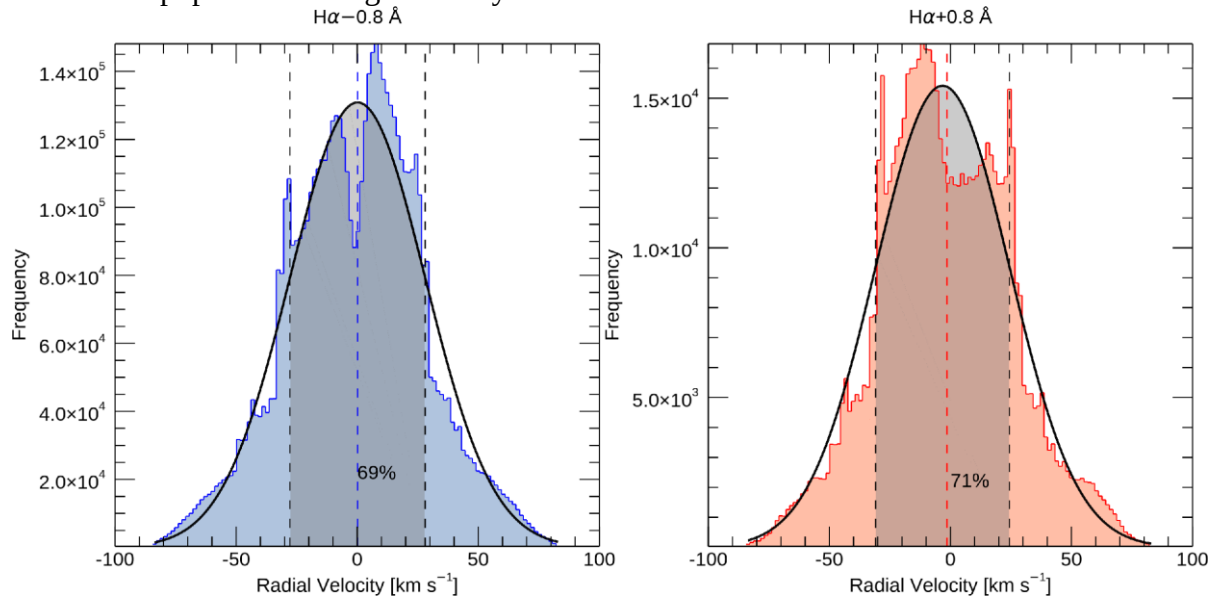


Figure 3. *Radial velocity histograms computed for the blue (H, left) and red (H, right) line wings over the entire 35-minute observational sequence. The vertical blue and red dashed lines indicate the average radial velocities. TThe solid black curves show the best-fit Gaussian profiles applied to the core of the histograms. The black dashed lines and shaded regions indicate the standard deviation thresholds.*

To study whether these statistical mean velocities are driven by short-lived temporal excursions or reflect a persistent kinematic state, we plot the time evolution of the average radial velocity for both channels in Figure 4. The time-series reveal a highly consistent and well-separated velocity stratification throughout the entire observational time sequence. The blue wing average radial velocity (blue curve) operates exclusively within the positive domain between $+1$ and $+3$ km s^{-1}. This sustained positive offset confirms that the blue wing channel continuously isolates the

upwardly propagating, blue-shifted spicular phase across the FOV. Conversely, the red wing average radial velocity (red curve) remains predominantly confined to the negative velocity regime, fluctuating between 0 and -9 km s^{-1}. Interestingly, the two channels exhibit distinct dynamic profiles. The blue wing radial velocities exhibit small fluctuations around their mean zero value, generally within a narrow range of approximately -2 to $+2$ km s^{-1} throughout most of the sequence. In contrast, the red wing velocities show substantially larger temporal variations and are predominantly shifted toward negative values, with several short lived excursions reaching approximately -6 to -7 km s^{-1}. Despite these differences in amplitude, both channels show frequent changes in the magnitude and sign of the radial velocity, indicating that the detected spicule expand in both radial directions throughout the observation time although the rate of expansion is dependable on the observation wavelength. The stronger and more intermittent negative velocities in the red wing suggest greater contribution from inward directed motions (downflows) compared with the more balanced behavior observed in the blue wing.

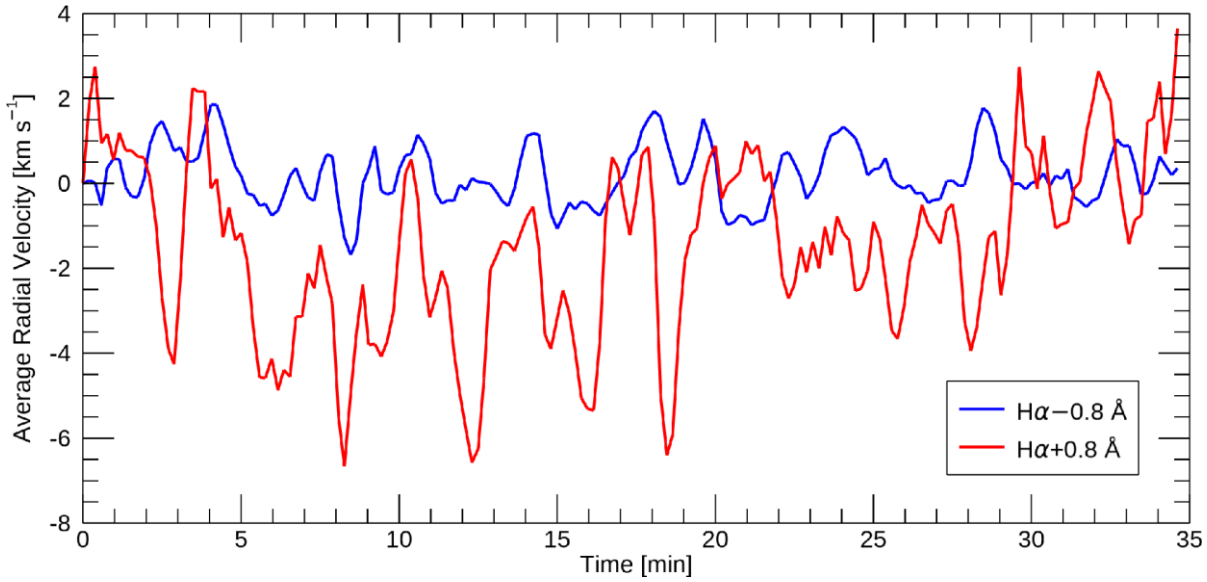


Figure 4. *Temporal evolution of the average radial velocity for the H (blue) and H (red) throughout the time sequence.*

To characterize the overall apparent motion of the detected pixels of RBEs and RREs, we also calculated their total projected velocity in the image plane. Using the same local position angle, ϕ, the tangential velocity component was obtained as:

$$v_{tan} = -v_x sin(\phi) + v_y cos(\phi). \quad (4)$$

The total projected velocity was then calculated by combining the radial and tangential components:

$$v_{proj} = \sqrt{v_{rad}^2 + v_{tan}^2}. \quad (5)$$

Here, v_{proj} represents the magnitude of the apparent motion in the image plane. The mean projected velocities are 32.6 km s^{-1} for the H$\alpha - 0.8$ and 34.2 km s^{-1} for the H$\alpha + 0.8$. The similar values obtained for the two wings indicate that, despite their different radial velocity behavior, the detected RBE and RRE populations have comparable overall apparent velocities.

To quantitatively correlate this statistical dynamic with the thermodynamic evolution of RBEs/RREs, we analysed integrated light curves of the detected features. For each frame, we computed the average intensity, I, of RBE/RRE occupied pixels as identified by the RHT algorithm. This provided a time-dependent measure of chromospheric brightness associated with detected spicule structures. The average intensity was then normalized using a reference quiet-Sun granulation region (I_0):

$$I_{norm}(t) = \frac{I(t)}{I_0}, \tag{6}$$

where I_0 is the average intensity of a selected background region. To quantify the spatial coverage of RBEs and RREs , we defined the area filling factor as:

$$f(t) = \frac{N_{spicule}(t)}{N_{total}}, \tag{7}$$

where $N_{spicule}$ is the number of detected pixels and N_{total} is the total number of pixels in the FOV.

Figure 5 shows the temporal variations of the normalized intensity (I/I_0) for both the blue and red wings over the 35-minute observation window. The total average intensity values indicate that the red wing exhibits a higher overall intensity (175.61 I/I_0) compared to the blue wing (172.98 I/I_0). As seen in the time-series plot, the red wing curve consistently tracks at a slightly higher intensity level than the blue wing for the majority of the time sequence. Since Hα on-disk structures are observed in absorption, this behaviour reflects a systematic blue-red asymmetry in the spicular plasma, where the deeper absorption in the blue wing indicates a higher opacity or greater mass allocation in the advancing (upward-moving) components compared to the receding (downward-moving) ones.

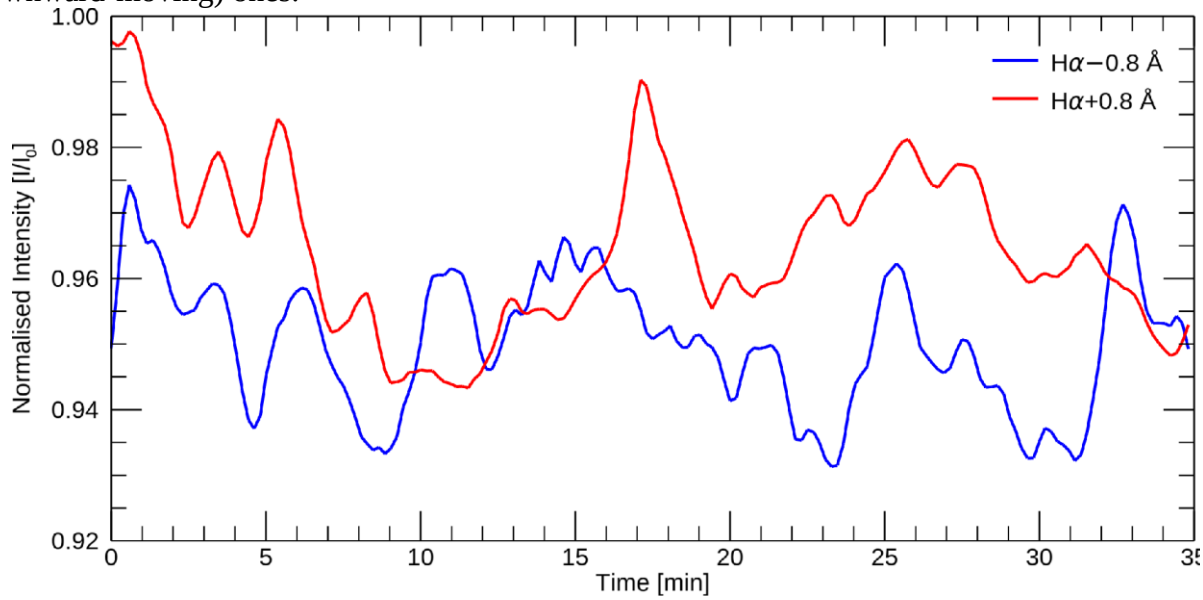


Figure 5. *Temporal evolution of the normalised intensity () in H (blue) and H (red) over the observational time sequence.*

Both wings exhibit highly dynamic, quasi-periodic oscillations characterized by prominent, recurring intensity peaks throughout the entire observational sequence. These multi-peaked fluctuations indicate that the spicular field might be driven by intermittent, episodic energy release mechanisms or magnetic wave modulations originating from the lower solar atmosphere rather than a steady-state mass injection. Importantly, a noticeable phase relationship and temporal offset exist between the two wings at specific intervals. For instance, between $t = 10$ and $t = 12$ min, the blue wing intensity experiences a distinct rise and peak, which is closely followed by a major, pronounced intensity surge in the red wing between $t = 14$ and $t = 17$ min. A similar alternating behavior is visible around $t = 23 - 26$ min. However, a cross-correlation analysis of the blue and red wing intensity time series did not reveal the presence of a time delay between the two signals. We therefore we may interpret these features as localized episodes of alternating blue and red wing intensity enhancement rather than as evidence for a characteristic evolutionary timescale.

The initial intensity enhancement in the blue wing might reflect the sudden upflows and injection phase of cool (even cold) chromospheric plasma moving along the magnetic conduit. As this material reaches its maximum height, it might be subjected to thermal relaxation, and might drain back toward the surface under gravity (red wing absorption). However, since no well-defined global time delay was found, the present data do not allow us to establish a one-to-oneconnection between the two signatures.

Figure 6 shows time variations of the normalized intensity and the average radial velocity for each respective channel. Although the two quantities occasionally show similar or opposite variations over short intervals, no persistent relationship is evident throughout the observing sequence. In the blue wing (H$\alpha - 0.8$, top panel), the zero-lag correlation coefficient is $r = -0.01$, indicating essentially no correlation between the intensity and radial velocity variations. The red wing shows a weak positive tendency, with a zero-lag correlation coefficient of $r = 0.18$. A cross-correlation analysis over a range of temporal lags similarly reveals no strong systematic relationship between the two quantities.These results suggest that the temporal variations in Hα wing intensity are not directly determined by the average radial motion of the detected spicule population. This is not unexpected, since the observed Hα wing intensity can be influenced by several factors, including the amount of absorbing material, line-of-sight velocity, opacity, and changes in the number of structures contributing within the FOV.

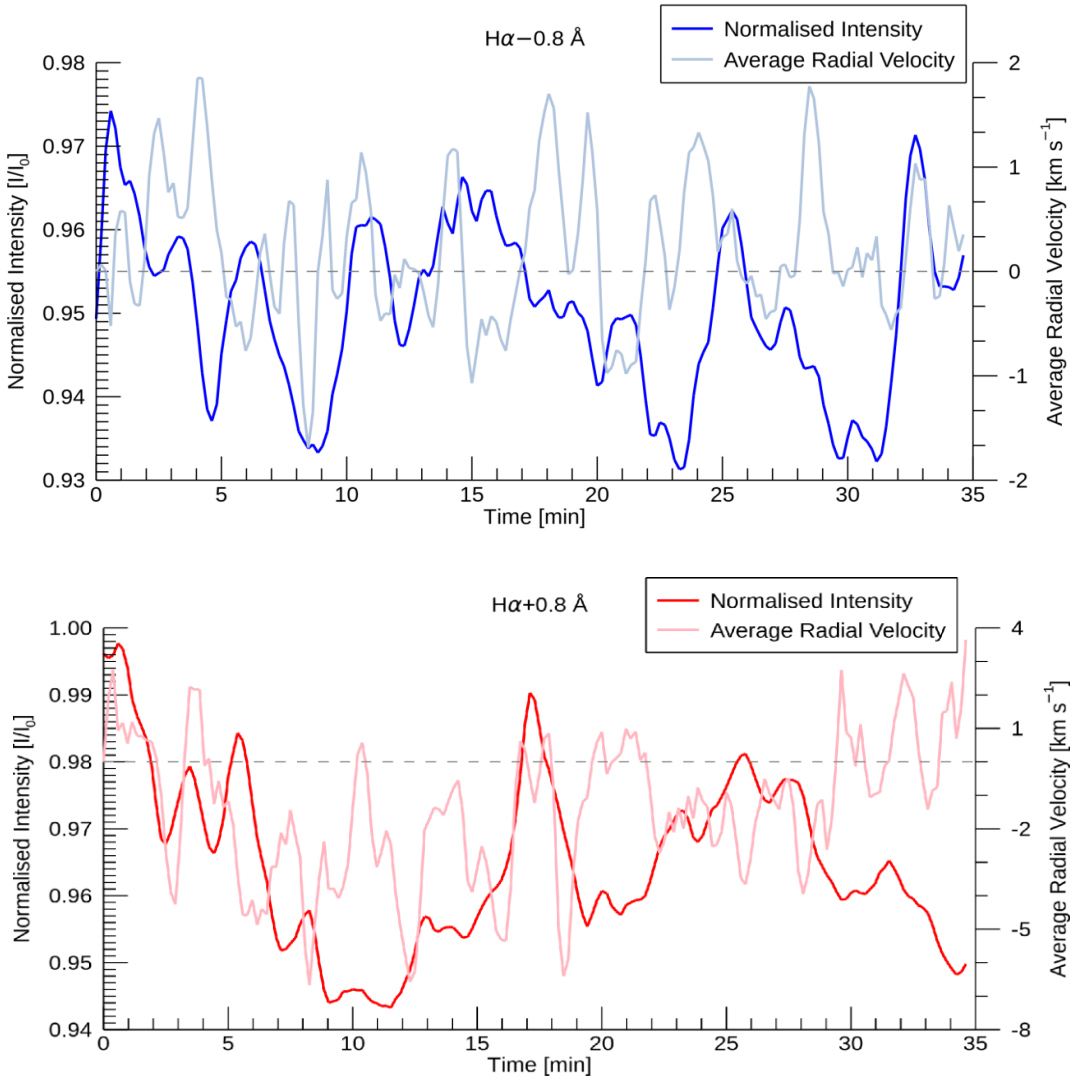


Figure 6. *Co-temporal coupling between the normalised intensity (I/I_0) and average radial velocity for the H (top panel) and H (bottom panel). The horizontal gray dotted line indicates, with positive and negative values corresponding to outward and inward radial motions, respectively.*

4. Discussion

The RHT has been widely used as a numerical tool to trace linear features like chromospheric fibrils, coronal rain, and coronal loops [Clark et al., 2014; Schad, 2017; Şahin et al., 2023]. The extension of the RHT framework into the temporal domain [Schad, 2017] has enabled the characterization of the evolution of linear structures in the time-distance space. To our knowledge, however, this approach has not been previously applied to on-disk absorption features , providing the motivation for the present study. Previous studies of on-disk type II spicules, RBEs, and RREs predominantly relied on Doppler-based identification schemes. For example, [Rouppe van der Voort et al., 2009] detected RBEs by isolating elongated absorption features appearing as large blueshifts and imposing geometrical constraints to exclude intergranular lanes and unrelated structures. This approach has proven to be highly effective for constructing large statistical samples and deriving the occurrence rates and basic properties of RBEs [Deng et al., 2015; Bose et al., 2020]. However, such methods primarily identify structures based on their manifestation at selected Doppler offsets and predefined morphological thresholds. In this context, the RHT offers a complementary framework by characterizing locally coherent linear structures directly from their spatial and temporal morphology. Rather than serving solely as a detection algorithm, the RHT also provides a statistical description of the orientation and kinematic evolution of fine-scale structures, allowing the characterization of features that may be fragmented, partially resolved, or embedded within complex superpositions. In this sense, the RHT should be regarded as complementary to traditional Doppler-based detection techniques.

One of the principal findings of this study is the pronounced asymmetry between blue- and red-wing detections, with the number of spicule signatures identified in the Hα -0.8 (blue wing) exceeding those found in the Hα $+0.8$ (red wing) by approximately a factor of 8.5. The predominance of the blusehifted chromospheric excursions was first reported by [Rouppe van der Voort et al., 2009]. Subsequent investigations further demonstrated that while RREs are also present, blueshifted events occur more frequently and generally dominate the observed population [Sekse et al., 2012]. More recently, high-resolution GST observations by [Yurchyshyn et al., 2026] similarly showed a clear predominance of blueshifted plasma across the FOV, while redshifted signatures were less widespread and more localized around network magnetic fields. Our results therefore reinforce the previously reported RBE-RRE asymmetry, but reveal a substantially stronger imbalance, with approximately 8.5 times more blue-wing than red-wing detections. The strong blue-red asymmetry found here is therefore consistent with the view that upward-directed motions constitute the primary observational signature of on-disk type-II spicules [Pereira et al., 2012]. The considerably smaller number of red-wing detections does not necessarily imply the existence of a physically distinct population. Numerical and observational studies have suggested that transverse motions, torsional motions, and LOS projection effects can periodically shift the absorption signature from the blue-wing into the red wing and vice versa [Sekse et al., 2013; De Pontieu et al., 2012].

The radial velocity distributions derived in the present study are centered close to zero, with mean values of approximately 2 km s^{-1} and nearly 69-71% of all measurements confined within $\pm$30 km s^{-1}. These values are substantially smaller than the characteristic Doppler velocities commonly reported for type-II spicules and RBEs, which typically range from several tens to more than 100 km s^{-1} [de Pontieu et al., 2007; Rouppe van der Voort et al., 2009; Sekse et al., 2012]. However, these values should be compared with some caution, as the velocity estimates are obtained using different measurement approaches. Previous studies have commonly derived spicule velocities either from Doppler shifts or by tracking the apparent motion of individual features in consecutive images. The temporal RHT used here similarly measures apparent motions in the image plane, but derives them systematically from the orientation of coherent linear structures in space–time rather than from manual or feature-by-feature tracking.

The derived velocities should therefore be interpreted as pattern speeds that characterize the apparent displacement of morphological structures rather than direct measurements of plasma

flow velocities. The predominance of relatively low pattern speeds may indicate that a significant fraction of on-disk spicules undergo gradual morphological evolution or consist of intermittent fine-scale threads that repeatedly appear, disappear, split and merge. Such rapid changes in morphology have been reported in high-cadence Hα observations of RBEs and suggest that the observed evolution of these structures cannot always be represented by a single coherent plasma flow [Yurchyshyn et al., 2020]. To characterize the overall apparent motion independently of its radial direction, we combined the radial and tangential components to obtain the projected velocity. The mean projected velocities are 32.6 km s^{-1} and 34.2 km s^{-1} for the blue- and red-wing detections, respectively. These values are considerably larger than the signed mean radial velocities because oppositely directed radial motions largely cancel when averaged. The projected speeds therefore provide a more representative measure of the magnitude of the apparent motions detected by the RHT. Recent numerical studies indicate that type-II spicules possess highly complex three-dimensional morphologies [Yurchyshyn et al., 2026] and that their apparent motions depend strongly on viewing angle and Doppler sampling [Chandra et al., 2026]. These effects should be taken into account when comparing RHT-derived apparent motions with Doppler velocities or velocities obtained by tracking individual spicules in other observations.

An interesting result of this study is that the pronounced asymmetry in occurrence rates is not reflected in the intensity distributions. While blue wing features are detected 8.5 times more frequently than their red wing counterparts, the normalized intensity distributions of the two populations are remarkably similar. Previous spectroscopic and imaging studies of RBEs and RREs have reported broadly comparable absorption properties between the two populations, including similar Doppler widths and line depths, suggesting a common physical origin [Sekse et al., 2012, 2013; Rouppe van der Voort et al., 2009]. The present results extend this picture by demonstrating that even in the presence of a strong imbalance in detection frequency, the radiative signatures of the identified structures remain nearly symmetric. This apparent decoupling between occurrence and intensity suggests that the visibility of these features is primarily governed by geometric and detection effects rather than by intrinsic differences in thermodynamic conditions. In particular, the similarity in normalised intensities implies that once detected, blue and red wing structures are formed under comparable plasma conditions, and that the observed asymmetry in occurrence likely reflects a combination of LOS projection effects, Doppler sensitivity, and the persistence criteria imposed by the detection method.

Taken together, these results suggest that the temporal implementation of the RHT provides access to a complementary observational regime, one that quantifies the statistical evolution of coherent morphological patterns rather than directly measuring Doppler excursions or plasma flow speeds. This approach therefore provides a complementary diagnostic to conventional RBE detection methods and offers new constraints on the fine-scale structuring and evolution of chromospheric spicule-like features.

5. Conclusions

In this study, we have used the RHT in both spatial and temporal domains to investigate the statistical and dynamical properties of RBEs and RREs inferred from H$\alpha \pm 0.8$ GST observations. With this automated approach, thousands of individual features across the FOV were tracked and analyzed statistically. Operating on this large dataset provided a comprehensive overview of type II spicules dynamics, moving beyond isolated case studies. The main conclusions of this work are summarized as follows:

- The temporal implementation of the RHT provides a complementary approach to RBE and RRE detection by quantifying coherent morphological evolution in time-distance space.
- We identified a strong asymmetry in the occurrence rates between blue and red wing detections, with blue wing features being approximately 8.5 times more frequent.

- Despite this asymmetry, the normalized intensity distributions of blue and red wing populations are remarkably similar, indicating broadly comparable thermodynamic conditions.
- The time-averaged signed radial velocities of both the blue- and red-wing features remain close to zero, despite mean projected speeds of approximately 33–34 km s^{-1}. The nearly symmetric radial-velocity distributions indicate substantial apparent motions of individual structures but no strong net preference for inward or outward propagation across the observed population.
- Although the radial velocity distributions show high-velocity tails extending toward ± 84 km s^{-1}, a Gaussian fit analysis demonstrates that more than 69% of the detected type-II spicule population is concentrated within the low-velocity core (≈ 10 km s^{-1}). This behavior marks a clear physical distinction between macroscopic bulk motion and localized internal dynamics. Similarly to a stationary cloud that remains in place while hosting internal structural turbulence.
- The combination of these results suggest that the temporal RHT primarily traces the evolution of cohorent morphological patterns rather than direct plasma flow velocities. This highlights the importance of distinguishing between morphological pattern speeds and physical plasma velocities when interpreting high resolution chromospheric observations.

Overall, our results show that the temporal extension of the RHT offers a powerful complementary diagnostic for studying the fine-scale structuring and evolution of chromospheric spicule-like phenomena.

Acknowledgements

The author acknowledge the use of data from the Goode Solar Telescope (GST) of the Big Bear Solar Observatory (BBSO). BBSO operation is supported by the US NSF AGS 2309939 grant and the New Jersey Institute of Technology. The GST operation is partly supported by the Korea Astronomy and Space Science Institute and the Seoul National University. The author also thanks Dr. Vasyl Yurchyshyn for helpful discussions and constructive suggestions on the analysis.

References

Beckers, J.M. (1968). Solar Spicules (Invited Review Paper). *Solar Physics*, 3, (3), 367–433. https://doi.org/10.1007/BF00171614.

Bose, S., Henriques, V.M.J., Joshi, J., and Rouppe van der Voort, L. (2020). Characterization and formation of on-disk spicules in the Ca II K and Mg II k spectral lines (Corrigendum). *Astronomy and Astrophysics*, 637, C1. https://doi.org/10.1051/0004-6361/201936617e.

Bose, S., Joshi, J., Henriques, V.M.J., and Rouppe van der Voort, L. (2021). Spicules and downflows in the solar chromosphere. *Astronomy and Astrophysics*, 647, A147. https://doi.org/10.1051/0004-6361/202040014.

Chandra, S., Cameron, R., Przybylski, D., and Solanki, S.K. (2026). Diversity of morphology of type II spicules in MURaM-ChE simulations. *arXiv e-prints*, arXiv:2605.25886. https://doi.org/10.48550/arXiv.2605.25886.

Clark, S.E., Peek, J.E.G., and Putman, M.E. (2014). Magnetically Aligned H I Fibers and the Rolling Hough Transform. *Astrophysical Journal*, 789, (1), 82. https://doi.org/10.1088/0004-637X/789/1/82.

De Pontieu, B., Carlsson, M., Rouppe van der Voort, L.H.M., Rutten, R.J., Hansteen, V.H., and Watanabe, H. (2012). Ubiquitous Torsional Motions in Type II Spicules. *Astrophysical Journal Letters*, 752, (1), L12. https://doi.org/10.1088/2041-8205/752/1/L12.

de Pontieu, B., McIntosh, S., Hansteen, V.H., Carlsson, M., Schrijver, C.J., Tarbell, T.D., Title, A.M., Shine, R.A., Suematsu, Y., Tsuneta, S., Katsukawa, Y., Ichimoto, K., Shimizu, T., and Nagata, S. (2007). A Tale of Two Spicules: The Impact of Spicules on the Magnetic Chromosphere. *Publications of the Astronomical Society of Japan*, 59, S655. https://doi.org/10.1093/pasj/59.sp3.S655.

De Pontieu, B., McIntosh, S.W., Carlsson, M., Hansteen, V.H., Tarbell, T.D., Boerner, P., Martinez-Sykora, J., Schrijver, C.J., and Title, A.M. (2011). The Origins of Hot Plasma in the Solar Corona. *Science*, 331, (6013), 55. https://doi.org/10.1126/science.1197738.

Deng, N., Chen, X., Liu, C., Jing, J., Tritschler, A., Reardon, K.P., Lamb, D.A., Deforest, C.E., Denker, C., Wang, S., Liu, R., and Wang, H. (2015). Chromospheric Rapid Blueshifted Excursions Observed with IBIS and their

Association with Photospheric Magnetic Field Evolution. *Astrophysical Journal*, 799, (2), 219. https://doi.org/10.1088/0004-637X/799/2/219.

Langangen, Ø., De Pontieu, B., Carlsson, M., Hansteen, V.H., Cauzzi, G., and Reardon, K. (2008). Search for High Velocities in the Disk Counterpart of Type II Spicules. *Astrophysical Journal Letters*, 679, (2), L167. https://doi.org/10.1086/589442.

Lee, J., Lim, E.-K., and Hansteen, V. (2026). Spatial and Dynamical Relations between Spicules and Network Bright Points. *Astrophysical Journal*, 997, (2), 170. https://doi.org/10.3847/1538-4357/ae2747.

Martínez-Sykora, J., De Pontieu, B., Hansteen, V.H., Rouppe van der Voort, L., Carlsson, M., and Pereira, T.M.D. (2017). On the generation of solar spicules and Alfvénic waves. *Science*, 356, (6344), 1269–1272. https://doi.org/10.1126/science.aah5412.

Martínez-Sykora, J., Leenaarts, J., De Pontieu, B., Nóbrega-Siverio, D., Hansteen, V.H., Carlsson, M., and Szydlarski, M. (2020). Ion-neutral Interactions and Nonequilibrium Ionization in the Solar Chromosphere. *Astrophysical Journal*, 889, (2), 95. https://doi.org/10.3847/1538-4357/ab643f.

Pereira, T.M.D., De Pontieu, B., and Carlsson, M. (2012). Quantifying Spicules. *Astrophysical Journal*, 759, (1), 18. https://doi.org/10.1088/0004-637X/759/1/18.

Pereira, T.M.D., De Pontieu, B., Carlsson, M., Hansteen, V., Tarbell, T.D., Lemen, J., Title, A., Boerner, P., Hurlburt, N., Wülser, J.P., Martínez-Sykora, J., Kleint, L., Golub, L., McKillop, S., Reeves, K.K., Saar, S., Testa, P., Tian, H., Jaeggli, S., and Kankelborg, C. (2014). An Interface Region Imaging Spectrograph First View on Solar Spicules. *Astrophysical Journal Letters*, 792, (1), L15. https://doi.org/10.1088/2041-8205/792/1/L15.

Rouppe van der Voort, L., Leenaarts, J., de Pontieu, B., Carlsson, M., and Vissers, G. (2009). On-disk Counterparts of Type II Spicules in the Ca II 854.2 nm and Hα Lines. *Astrophysical Journal*, 705, (1), 272–284. https://doi.org/10.1088/0004-637X/705/1/272.

Şahin, S., Antolin, P., Froment, C., and Schad, T.A. (2023). Spatial and Temporal Analysis of Quiescent Coronal Rain over an Active Region. *Astrophysical Journal*, 950, (2), 171. https://doi.org/10.3847/1538-4357/acd44b.

Samanta, T., Tian, H., Yurchyshyn, V., Peter, H., Cao, W., Sterling, A., Erdélyi, R., Ahn, K., Feng, S., Utz, D., Banerjee, D., and Chen, Y. (2019). Generation of solar spicules and subsequent atmospheric heating. *Science*, 366, (6467), 890–894. https://doi.org/10.1126/science.aaw2796.

Schad, T. (2017). Automated Spatiotemporal Analysis of Fibrils and Coronal Rain Using the Rolling Hough Transform. *Solar Physics*, 292, (9), 132. https://doi.org/10.1007/s11207-017-1153-9.

Sekse, D.H., Rouppe van der Voort, L., and De Pontieu, B. (2012). Statistical Properties of the Disk Counterparts of Type II Spicules from Simultaneous Observations of Rapid Blueshifted Excursions in Ca II 8542 and Hα. *Astrophysical Journal*, 752, (2), 108. https://doi.org/10.1088/0004-637X/752/2/108.

Sekse, D.H., Rouppe van der Voort, L., De Pontieu, B., and Scullion, E. (2013). Interplay of Three Kinds of Motion in the Disk Counterpart of Type II Spicules: Upflow, Transversal, and Torsional Motions. *Astrophysical Journal*, 769, (1), 44. https://doi.org/10.1088/0004-637X/769/1/44.

Shumko, S., Gorceix, N., Choi, S., Kellerer, A., Cao, W., Goode, P.R., Abramenko, V., Richards, K., Rimmele, T.R., and Marino, J. (2014). AO-308: the high-order adaptive optics system at Big Bear Solar Observatory. *Adaptive optics systems IV*, 9148, 914835. https://doi.org/10.1117/12.2056731.

Tsiropoula, G., Tziotziou, K., Kontogiannis, I., Madjarska, M.S., Doyle, J.G., and Suematsu, Y. (2012). Solar Fine-Scale Structures. I. Spicules and Other Small-Scale, Jet-Like Events at the Chromospheric Level: Observations and Physical Parameters. *Space Science Reviews*, 169, (1-4), 181–244. https://doi.org/10.1007/s11214-012-9920-2.

Yurchyshyn, V., Abramenko, V., and Goode, P. (2013). Dynamics of Chromospheric Upflows and Underlying Magnetic Fields. *Astrophysical Journal*, 767, (1), 17. https://doi.org/10.1088/0004-637X/767/1/17.

Yurchyshyn, V., Cao, W., Abramenko, V., Yang, X., and Cho, K.-S. (2020). Rapid Evolution of Type II Spicules Observed in Goode Solar Telescope On-disk H α Images. *Astrophysical Journal Letters*, 891, (1), L21. https://doi.org/10.3847/2041-8213/ab7931.

Yurchyshyn, V., Şahin, S., Schmidt, A., Lim, E.-K., Gorceix, N., Yang, X., and Cao, W. (2026). Chromospheric Spectra of Small-scale Dynamic Features Observed on and off Solar Disk with Goode Solar Telescope. *Astrophysical Journal*, 999, (2), 266. https://doi.org/10.3847/1538-4357/ae472c.

DOI: 10.31401/WS.2026.proc.12

Multi-Spacecraft and Multi-Instrument Observations of the Martian Radiation Environment During Solar Cycles 24 and 25

Semkova J. [1], *Bankov N.* [1], *Benghin V.* [2], *Dachev Ts.* [1], *Drobyshev S.* [2], *Georgiev G.* [1], *Golovin D.* [3], *Gopalswamy N.*[4], *Jordanova M.* [1], *Koleva R.* [1], *Krastev K.* [1], *Litvak M.*[3], *Lukyanov N.* [3], *Maltchev St.* [1], *Matviichuk Yu.* [1], *Mitrofanov I.* [3], *Mokrousov M.* [3], *Sanin A.* [3], *Shurshakov V.* [2], *Tomov B.* [1]

[1]Space Research and Technology Institute, Bulgarian Academy of Sciences, Sofia, Bulgaria; jsemkova@stil.bas.bg
[2]State Scientific Center of Russian Federation, Institute of Biomedical Problems, Russian Academy of Sciences, Moscow, Russia
[3]Space Research Institute, Russian Academy of Sciences, Moscow, Russia
[4]NASA Goddard Space Flight Center, Greenbelt Maryland, USA

Abstract

Presented are multi-spacecraft – Trace Gas Orbiter (TGO), Mars Odyssey, Mars Science Laboratory, etc. and multi-instrument observations of the particle radiation environment in Mars vicinity during solar cycles 24 and 25. According the observations conducted by the dosimeter Liulin-MO onboard TGO at Martian orbit from May 2018 to May 2026, lowest dose equivalent rates for a 6-months period – the approximate time for a transit to Mars or vice versa, are registered during the decreasing phase, near to the maximum of solar cycle 25 – they are about 1.5-2 times less that the dose rates during the other phases of solar cycles 24 and 25. Highest dose rates are registered around the minimum of solar cycle 24 as a result of the galactic cosmic rays contribution. Particular attention is drawn to the results for the radiation parameters obtained by multiple detectors located at the orbit and on the surface of Mars during the most intensive solar energetic particle (SEP) events registered up to the moment during solar cycle 25 – those in October 2021, February 2022, May 2024, and August 2025. Responsible for most of these SEPs are halo coronal mass ejections (CMEs) associated with major X and M class flares. The results show the importance of long-term multipoint measurements of the radiation conditions in Mars vicinity. Such measurements will provide the data necessary for the planning of future manned missions to the planet. The data on the observed SEPs add details regarding the solar activity during solar cycle 25.

Keywords: multispacecraft particle radiation measurements; galactic and solar cosmic rays; Mars

1. Introduction

Sources of considerable health hazards for manned space missions to Mars are the omnipresent galactic cosmic rays (GCR), sudden solar energetic particle (SEP) events and secondary radiation from the interaction of the primary cosmic rays with the spacecraft structures, Mars atmosphere and surface. In the Solar system GCR flux is isotropic and their flux and spectra show a long term modulation that anti-correlates with the solar activity. The GCR spectrum is wide in both composition (from protons to the heaviest nuclei) and energies (from a few keV to 10^{21} eV) [Potgieter, 2013]. Radiations induced by GCR nuclei, especially those with high energy (e.g., protons above 100 MeV) and high charge ions, remain one of the major concerns in the planning of long-term deep-space human and robotic missions [Townsend et al., 1994; Cucinotta et al, 2013; Dachev et al, 2020; Guo et al, 2021]. SEP events are transient injections into the heliosphere of protons, electrons, and higher mass

charged particles with a wide range of energies (tens of keVs to GeVs), spectra, compositions, and intensities. They follow energetic solar eruptions that are generally associated with flares and coronal mass ejections (CMEs) [Reames, 2013; Velinov et al, 2013]. SEP events take place much more frequently during the increasing phase of the solar cycle. Typical SEPs are known to pose a small health risk to astronauts and can be effectively attenuated by using relatively thin shielding materials, even though they can influence mission planning or interfere with mission activities such as extravehicular activities. Previous investigations based on calculations show that the expected doses to a future manned trip to Mars with start at the solar maximum are significantly lower than the doses to be obtained during other phases of the solar cycle [Shafirkin and Grigoryev, 2009; Cucinotta, 2015]. Nevertheless, although rare, large SEP events can be lethal [Committee for Evaluation of Space Radiation Cancer Risk Mode, 2012].

Other permanent sources of radiation are the secondary charged particles and neutrons from interaction of primary radiation with the spacecraft structures and albedo radiation from Mars atmosphere and surface.

The current astronaut career exposure limits are between 0.6 Sv (NASA) and 1 Sv (other space agencies and countries) for astronauts in low earth orbits. The limits are age and gender specific [Shavers et al, 2023].

In this paper we present multispacecraft - Trace Gas Orbiter (TGO), Mars Odyssey, Mars Science Laboratory (MSL), etc. and multiinstrument observations of the particle radiation environment at Mars orbit and surface during the last 2 solar cycles. Shown are some examples and practical results of application of the Mars radiation environment observational data.

2. Particle radiation environment investigations on different space missions in Mars vicinity

The sunspot numbers and the period of available radiation data at Mars orbit and surface from multispacecraft observations are presented in Figure 1.

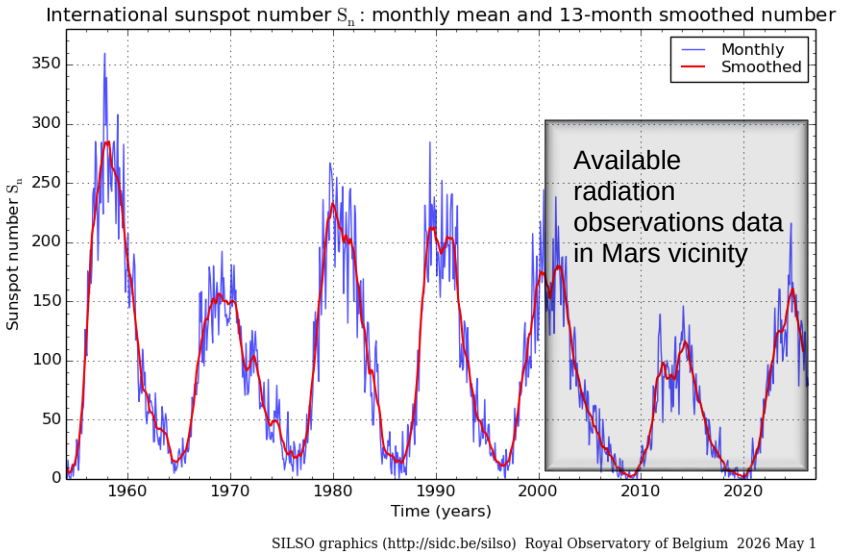


Figure 1. *Sunspot numbers and the period of available radiation data at Mars orbit and surface from multispacecraft observations*

Particle radiation environment investigations have been conducted during the transit to Mars, in Mars orbit and on the surface aboard several space missions in last three solar cycles.

Table 1 presents the radiation environment investigations on different space missions in Mars vicinity conducted since 2001. The columns from left to right contain: the mission, responsible space agency or country, type of the mission (orbiter or rover); start year of the operation at Mars; instrument(s) for particle radiation measurements aboard the mission; measured particles (charged, neutrons or both).

Table1. *Particle radiation environment investigations on different space missions in Mars vicinity*

Mission/Type	Mission operation at Mars since	Instrument/s	Measured particles
Mars Odyssey/ NASA/Orbiter	2001	HEND (High-Energy Neutron Detector)	neutrons protons
Mars Express (MEX)/ ESA/Orbiter	2003	ASPERA-3 IMA (Analyzer of Space Plasma and Energetic Atoms-Ion Mass Analyzer)	charged
Mars Science Laboratory (MSL)/NASA/Rover	2012	RAD (Radiation Assessment Detector), DAN (Dynamic Albedo of Neutrons)	charged, neutrons neutrons
Mars Atmosphere and Volatile Evolution (MAVEN)/NASA/Orbiter	2014	SEP (Solar Energetic Particle)	charged
Trace Gas Orbiter (TGO)/ESA, Russia/Orbiter	2018	Liulin-MO, (Dosimeter Liulin-MO), FREND (Fine Resolution Epithermal Neutron Detector)	charged neutrons
Tianwen-1(TW-1)/ China/Orbiter	2021	MEPA (Mars Energetic Particle Analyzer)	charged

3. Results and discussion

3.1. Long term measurements

The dose rate and particle flux of cosmic rays measured by Liulin-MO dosimeter on TGO in the period May 2016 - May 2026 are presented in Figure 2 (top and middle panels). The values from May to September 2016 were measured during the transit to Mars. The values in the period May 2018 - May 2026 were measured at Mars Science Orbit of TGO (circular orbit with 400 km altitude, 74° inclination, ~ 2 hours orbit period). TGO/Liulin-MO absorbed dose rate and particle flux of GCR during the maximum of solar cycle 25 (October 2024) are about 38-39% of the corresponding values during the minimum of solar cycle 24 (March 2020). During the 25th solar cycle till May 2026 a number of SEP events were observed on TGO (the spikes - not scaled) superposed on the GCR time profiles in the top panel of Figure 2.

The bottom panel of Figure 2 represents the dose rate measured by MSL/RAD during the transit to Mars in 2012 (left) and on Mars surface at Gale crater from 6 August 2012 to 9

September 2024 –right part of the panel [Löwe et al , 2025]. Red arrows indicate SEP events. Vertical dashed lines in the plot indicate the transition from the 24th to the 25th solar cycle.

The gradual increase of the dose rates and fluxes registered at Martian orbit and surface up to February 2020 corresponds to the increase of GCR intensity during the declining phase of solar cycle 24. During March–August 2020, the radiation values of GCR are maximal, corresponding to the minimum of cycle 24 and the transition to cycle 25. Since September 2020, a decrease of the GCR dose rates and fluxes is seen, corresponding to the increasing phase of solar cycle 25.

Table 2 presents the absorbed dose rates (in water) and dose equivalent rates at Mars orbit from TGO/Liulin-MO measurements during different phases of solar cycles 24 and 25. Data are averaged over 6-months periods. The 1st column contains the period of measurement, the radiation contributors – GCR or GCR plus SEPs and the solar cycle phase; the 2nd column shows the absorbed dose rates in water and the 3rd column - the dose equivalent rates.

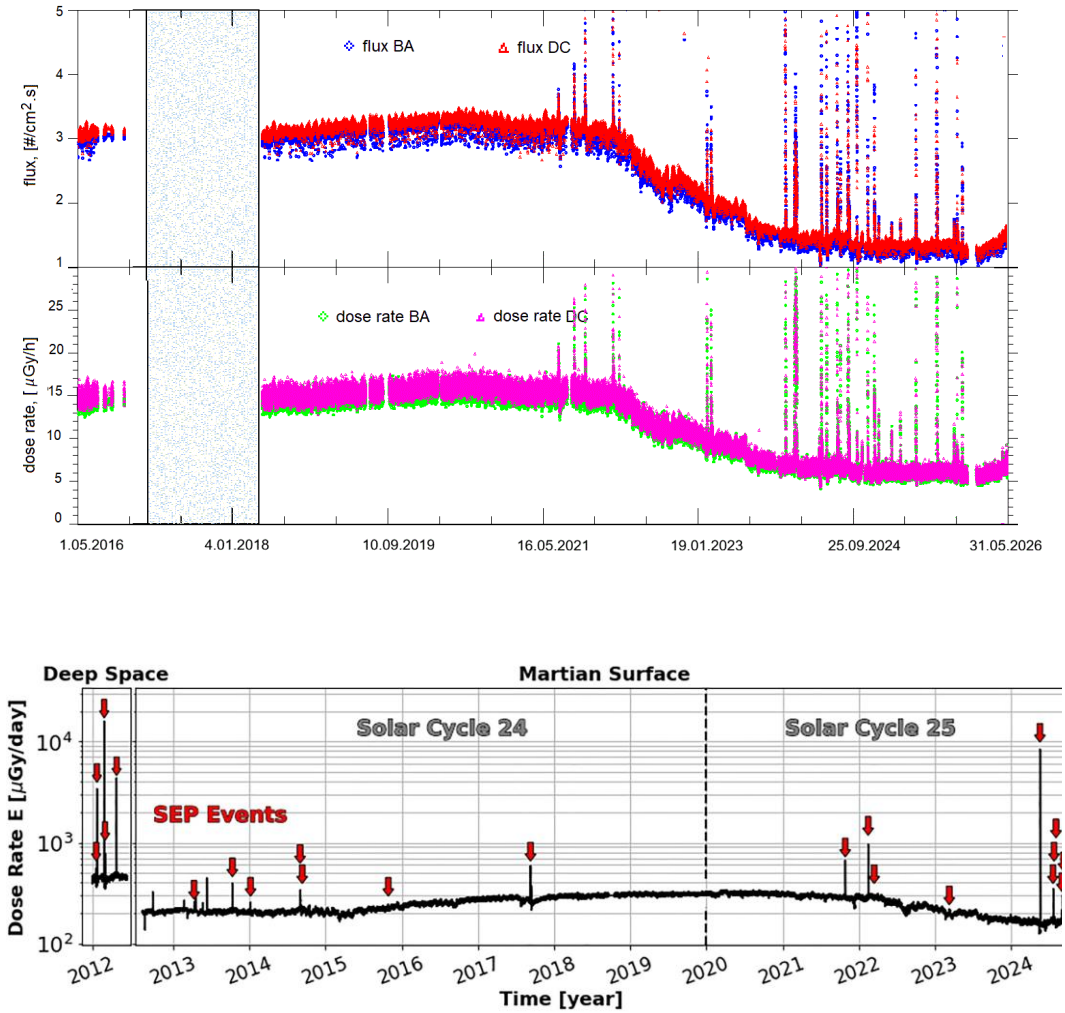


Figure 2. *Fluxes (top) and dose rates (middle) in free space (left) and in Mars orbit (May 2018 -May 2026) obtained from the measurements by TGO/Liulin-MO. The plots marked as BA and DC represent measurements from the Liulin-MO detectors in 2 perpendicular directions BA and DC. The shaded area indicates a period of missing data. Bottom - dose rate in free space (left) and on Mars surface (6 August 2012 to 9 September 2024) obtained from the measurements by MSL/RAD. Red arrows indicate SEP events. Bottom picture is taken from Löwe et al, 2025.*

The absorbed dose rate both from GCR and SEPs near to and at the maximum of solar cycle 25 in May-October 2024 is below, but comparable to the absorbed dose rate received from GCR near to and at the minimum of solar cycle 24 in February-July 2020. This is an important result as in the period May-October 2024 six strong SEP events were registered, including the most powerful SEP observed up to now by Liulin-MO – the event of 20 May 2024 (see Semkova et al, 2025) but nevertheless the biologically significant dose equivalent rate during the maximum of cycle 25 is significantly lower than the dose equivalent rate during the minimum of cycle 24. This is because the radiation quality factor $<Q>$ of the combined field of GCR and SEPs is lower than $<Q>$ of the GCRs itself [Semkova et al, 2023; 2025].

Table 2. *Absorbed dose rate D and dose equivalent rate H from TGO/Liulin-MO measurements at Mars orbit during different phases of the solar cycle.*

Months, Year, (Radiation contributors) - Solar cycle phase	**D in water [mGy d^{-1}]**	**H [mSv d^{-1}]**
May-October, 2018, (GCR, no SEPs)-second half of decreasing phase of cycle 24	0.455	1.6
February-July, 2020, (GCR, no SEPs)-around the minimum of cycle 24	0.494	1.7
February-July, 2022, (GCR and SEPs)-first half of increasing phase of cycle 25	0.507	1.76
May-October, 2024, (GCR and powerful SEPs)-near to and at the maximum of cycle 25	0.429	1.2
December 2024-May 2025, (GCR and weak SEPs) maximum and start of the decreasing phase of cycle 25	0.182	0.73
July-December 2025 (GCR and a strong SEP) –first half of the decreasing phase of Cycle 25	0.247	0.81
February-May 2026 (GCR) –first half of the decreasing phase of Cycle 25	0.182	0.72

The lowest dose rates for 6-months time intervals are registered in December 2024 - May 2026 - the period covering the maximum and first half of the declining phase of cycle 25 – they are about 1.5-2 times less that the dose rates during the other phases of cycles 24 and 25.

These results are in agreement with calculations, showing that the expected doses to a future manned trip to Mars, that will start at solar maximum are lowest [Shafirkin and Grigoryev, 2009; Cucinotta, 2015].

The absorbed dose rates and dose equivalent rates obtained from measurements at Martian orbit and surface during the solar minimum of cycle 24/5 are summarized in Table 3.

The absorbed dose rates and dose equivalent rates obtained from measurements at Martian orbit and surface in the period 28 November 2019 -3 October 2020 are due to contribution of GCRs and secondary radiation. No SEP events were registered in this period. One can see that the dose rates on Mars surface at Gale crater are significantly lower than the corresponding values at TGO Martian orbit – this is because the planet itself and its atmosphere shield a significant part of GCRs. Guo et al, 2019 show that only the most energetic particles are able to reach the surface through Martian atmosphere and the atmospheric cutoff energy under different surface pressures is 140–190 MeV/nuc.

Table 3. *Dose rates at Mars surface from MSL/RAD and at Mars orbit from TGO/Liulin-MO during solar minimum of Cycle 24/5 measured from 28 November 2019 to 3 October 2020*

Quantity	MSL/RAD data [Ehresmann et al, 2023]	TGO/Liulin-MO data	Ratio of TGO/Liulin-MO to MSL/RAD value
Absorbed dose rate in water [mGy d^{-1}]	0.314	0.48	1.53
Dose equivalent rate [mSv d^{-1}]	0.72	1.68	2.33

3.2. Measurements during SEP events

On TGO a total of 30 SEP events were observed till May 2026. More detailed information about SEP events registered at Martian orbit by TGO /Liulin-MO may be found in Koleva et al, 2025.

17 SEP events were measured on the Martian surface by MSL/RAD from 6 August 2012 to 9 September 2024 [Löwe et al, 2025].

The most powerful SEP events of Cycle 25 observed at Mars orbit and surface up to now are presented in Table 4. The columns from left to right show the start date of the event, the duration of the event at TGO orbit, the TGO/Liulin-MO absorbed dose from SEPs, the MSL/RAD absorbed dose from SEPs, and the ratio of SEP dose surface to SEP dose orbit in [%]. The ratio of SEP dose surface to SEP dose orbit in the table is only few percent. This show that the Mars surface at Gale crater was relatively well protected against SEPs during the giant SEP events in the current solar cycle. The reason for that is the fact that the Mars atmosphere stops the charged particles with energies below 140-190 MeV/nuc, while TGO/Liulin-MO measure particles of energies > 30 MeV/nuc at Mars orbit.

Multiple detectors located at the orbit and on the surface of Mars have registered SEP events shown in Table 4. Some more details on the multispacecraft and multiinstrument observations during these SEP events are given below.

Table 4*. Most powerful SEP events of Cycle 25 observed at Mars orbit and surface up to now*

Start date of SEP event	Duration [hours] (TGO/Liulin-MO) [Semkova et al, 2023; 2025]	Dose from SEPs (in water) [mGy] (TGO/Liulin-MO-orbit) [Semkova et al, 2023; 2025]	Dose from SEPs [mGy] (MSL/RAD-surface) [Löwe et al, 2025]	SEP dose surface/SEP dose orbit [%]
28 October 2021	~79	8.45	0.161	1.9
15 February 2022	~76	17.94	0.323	1.8
20 May 2024	~64	32.06	1.73	5.4
21 August 2025	~100	8.76	Presently no literature data	

4.2.1. Measurements during the SEP event on 28 October 2021

Dose rate and accumulated doses were measured by different detectors on Mars orbit and surface (Liulin-MO and RAD), Moon orbit and surface (CRaTER and LND), and Earth polar orbit (RAMIS) during the 28 October 2021 SEP event [Guo et al, 2023]. The doses during this event at Mars orbit and Earth polar orbit are very close. Highest doses were registered at Moon orbit, lowest –at Mars surface. The SEP event caused the first GLE of solar cycle 25 at Earth [Papaioannou, et al, 2022]. During this event Mars and Earth were on opposite sides of the Sun. These SEP are related to a X1.0 flare located at S26W05 and a halo CME on 28 October 2021 [Koleva et al, 2025].

4.2.2. Measurements during the SEP event on 15 February 2022

The SEP event on 15 February 2022 was investigated by almost all radiation environment measurement instruments operating at Mars orbit and surface. The proton flux was measured by MAVEN/SEP and TW-1/MEPA and dose rates were measured by TGO/Liulin-MO and MSL/RAD. Reconstructed were the spectra of the SEP event from MAVEN/SEP, MEPA/TW-1 and MSL/RAD datasets integrated for the initial 12 hs after the event onset [Zhang J. et al, 2024]. Penetrating particle count rates from MAVEN/SEP and MEX/ASPERA-3 IMA were registered [Khoo et al, 2024]. The time profiles of count rates of TGO/FREND, TGO/Liulin-MO, and Mars Odyssey/HEND were compared [Semkova et al, 2023]. The solar source of SEPs is behind the east limb halo CME which occurred on 15 February 2022 [Koleva et al, 2025].

4.2.3. Measurements during the SEP event on 20 May 2024

The biggest SEP event registered up to now in Mars vicinity started on 20 May 2024. The total absorbed dose from SEPs equals the dose from the GCR received for about 200 days at TGO orbit. The SEPs dose equivalent for the entire event according TGO/Liulin-MO data is 43.7 mSv - approximately the dose equivalent received for 57 days from GCR. The maximum count rates exceed by more than 300 times the count rate of GCR. Compared were the normalized SEP count rates measured by TGO/FREND, TGO/Liulin-MO, Mars Odyssey/HEND [Semkova et al, 2025]. On MSL the absorbed dose equals the GCR dose received for about 7 days according to MSL/RAD data [Löwe et al, 2025]. The neutron dose on the Martian surface during the SEP event provided by MSL/DAN is 0.6 mSv- equals the dose during approximately 11 days in quiet Sun environment; the maximum neutron count rate exceeds 3 times the background count rate [Mitrofanov et al, 2025]. Responsible for this SEP event was an eruption located at S18W171 involving an X12 flare and a backside halo CME on 20 May 2024 [Semkova et al, 2025; Koleva et al, 2025].

4.2.4. Measurements during the SEP event on 21 August 2025

The SEP event on 21 August 2025 was registered by TGO/FREND and TGO/Liulin-MO instruments. At present there is no literature data about other radiation measurements during this event in Mars vicinity. The total dose during this event according to TGO/Liulin-MO data is comparable to the dose received during the 28 October 2021 SEP event (see Table 4).

Figure 3 shows the time profiles of TGO/Liulin-MO dose rate (top plot) and the normalized count rates measured by the ^{3}He and scintillator detectors of TGO/FREND and by TGO/Liulin-MO (bottom plot). The unusual profile of the dose rate and particle flux during this event is a subject of an upcoming publication. The observed SEPs are probably related to >X3 class flare and a behind the limb halo CME that occurred on 21 August 2025.

4.2.5. Examples of Mars radiation environment observational data application and some practical results

- Estimated is the dose equivalent from GCR for a round-trip to Mars with current propulsion systems for different phases of Cycle 24 from MSL/RAD and TGO/Liulin-MO data [Zeitlin, et al, 2013; Semkova et al, 2018; Posner & Strauss, 2020; Guo et al, 2021]. The results show that the accumulated GCR dose equivalent, via a Hohmann transfer, is larger than the astronauts career limit of 1 Sv.
- Estimated is the albedo radiation at Mars orbit (4% -5% of the total flux) and on the surface (18% -24% of the total dose) [Semkova et al, 2022; Guo et al, 2026].
- Methods are developed to calculate the absorbed dose rate and particle flux of cosmic

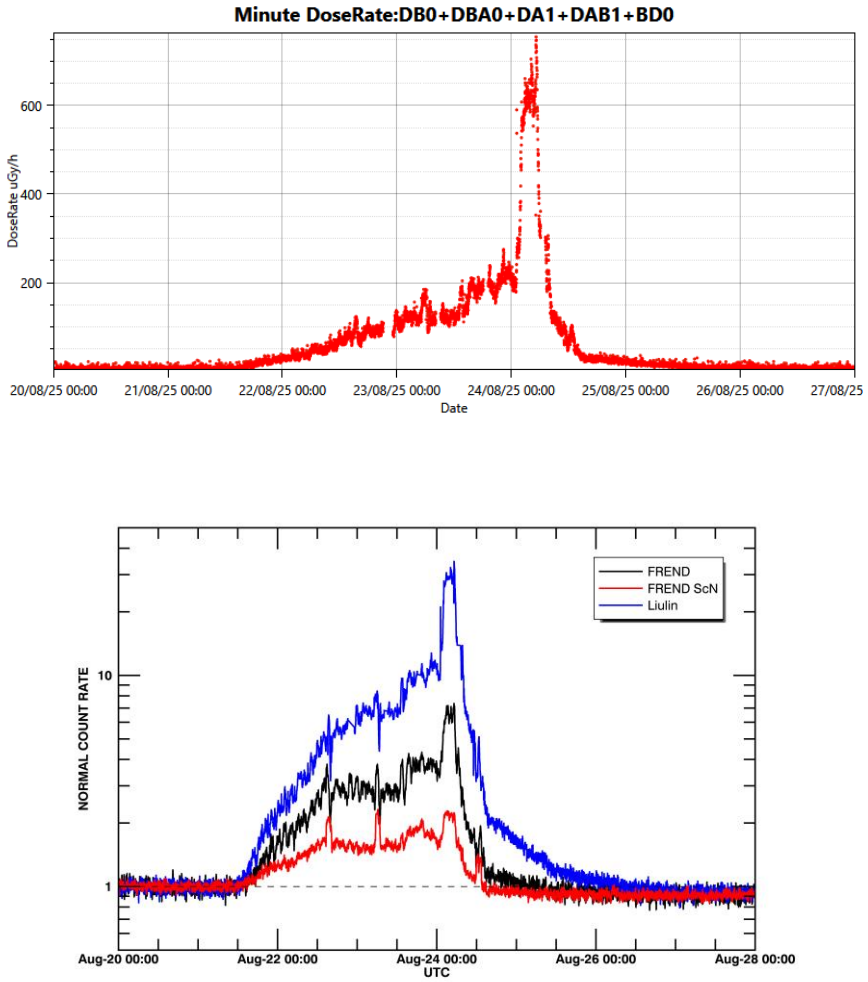


***Figure 3**. Time profiles of TGO/Liulin-MO minute dose rate in the direction BA (top) and normalized count rates measured by TGO/FREND detectors and TGO/Liulin-MO (bottom) during the SEP event on 21 August 2025*

rays in free space from the TGO/Liulin-MO measurements in Mars orbit [Krastev et al, 2019; Semkova et al, 2025b; Zhang C. et al, 2026].

- Based on MSL/RAD data a nowcasting system for SEP events has been developed that is applicable in deep space and on the surface of Mars. The avoidable SEP dose is at least 90% of the total SEP dose that can be mitigated using this system [Löwe et al, 2025].
- A map of the neutron dose on the surface of Mars has been created from TGO/FREND data [Litvak et al, 2025]. The neutron effective dose equivalent rate in the energy range up to 1000 MeV varies within 85 – 145 μSv/day depending on the content of subsurface water and the thickness of the atmosphere - consistent with Mars Odyssey/HEND and MSL/RAD observations.
- Simulated energy deposition spectra are compared with measured spectra from TGO/Liulin-MO during SEP events of October 2021, February 2022, May 2024. The results demonstrate that numerical simulations can offer an initial approximation of the composition of solar proton events detected by instruments of the Liulin-MO type [Krastev, 2025].
- A statistical analysis of SEPs rise times has been conducted using Earth and Mars observations [Cao et al, 2026]. Data were derived from SOHO/ERNE, TW-1/MEPA and TGO/Liulin-MO.
- The daily solar modulation potential Φ for Mars has been obtained based on TGO/Liulin-MO observations. The influence of Mars topography on radiation dose detected by MSL/RAD for the same values of Φ is investigated [Guo et al, 2026].
- The cumulative effective dose from GCRs has been obtained for 3 different Mars exploration missions (1964-2025) predicted by empirical models derived from measurements by TGO/Liulin-MO and LRO/CRATER [Zhang C. et al, 2026]. The result shows that even for the shortest mission (total 440 days, of which 410 days transit) around the solar min in the 23rd and 24th Cycles, NASA career exposure limit of 0.6 Sv is exceeded.

These results show the importance of careful planning for future manned Mars missions, regarding optimisation of the transfer trajectories, launch windows, Mars landing site selection, etc. in order to remain within the radiation limits. A real time nowcasting, warning of SEP events and a radiation shelter onboard the spacecraft may reduce the radiation risk to the crew.

Conclusion

The main results and conclusions from the multispacecraft and multiinstrument investigation of the Martian radiation environment can be summarized as follow:

- Confirmed and specified are the calculations that the expected crew dose for a Mars mission launched during the solar maximum is significantly less than the dose for a mission taken around the solar minimum.
- Shown is that in order to remain within the astronauts radiation limits during a manned flight to Mars it is necessary for mission planning to optimise transfer trajectories, launch windows, Mars landing site selection, etc. A real time nowcasting and warning of SEP events and a radiation shelter onboard the spacecraft may reduce the radiation risk to the crew. The most effective countermeasure for the radiation risk would be reducing the transit time using new technological developments.
- The data obtained may be used to verify and benchmark the cosmic ray models in the free space and in Mars vicinity.
- The data obtained contribute to space weather research and prediction.

References

Cao, Y., Guo, J., Wang, Y., Zou, Z., Zhang, Y., and Li, C. (2026). Statistical analysis of solar energetic particle rise times using Earth and Mars observations and constraints on particle transport parameters. *arXiv preprint*, arXiv:2605.01437. https://doi.org/10.48550/arXiv.2605.01437

Committee for Evaluation of Space Radiation Cancer Risk Model, Space Studies Board, National Research Council (2012). *Technical Evaluation of the NASA Model for Cancer Risk to Astronauts Due to Space Radiation*. Washington, DC: National Academies Press. https://www.ncbi.nlm.nih.gov/books/NBK189542/

Cucinotta, F. A., Kim, M. H. Y., Chappell, L. J., and Hu, J. L. (2013). How safe is safe enough? Radiation risk for a human mission to Mars. *PLoS ONE*, 8, e74988. https://doi.org/10.1371/journal.pone.0074988

Cucinotta, F. A. (2015). Review of NASA approach to space radiation risk assessments for Mars exploration. *Health Physics*, 108(2), 131–142. https://doi.org/10.1097/HP.0000000000000255

Dachev, T. P., Tomov, B. T., Matviichuk, Y. N., Dimitrov, P. G., Semkova, J. V., et al. (2020). Solar modulation of the GCR flux and dose rate observed in space between 1991 and 2019. *Life Sciences in Space Research*, 26, 114–124. https://doi.org/10.1016/j.lssr.2020.06.002

Ehresmann, B., Zeitlin, C., Hassler, D. M., Guo, J., Wimmer-Schweingruber, R. F., et al. (2023). The Martian surface radiation environment at solar minimum measured with MSL/RAD. *Icarus*, 393, 115035. https://doi.org/10.1016/j.icarus.2022.115035

Guo, J., Wimmer-Schweingruber, R. F., Grande, M., Lee-Payne, Z. H., and Matthia, D. (2019). Space weather in the inner Solar System: Effects of the September 2014 CME chain. *Journal of Space Weather and Space Climate*, 9, A7. https://doi.org/10.1051/swsc/2019004

Guo, J., Zeitlin, C., Wimmer-Schweingruber, R. F., Hassler, D. M., Ehresmann, B., et al. (2021). Radiation environment for future human exploration on the surface of Mars: The current understanding based on MSL/RAD dose measurements. *The Astronomy and Astrophysics Review*, 29, 8. https://doi.org/10.1007/s00159-021-00136-5

Guo, J., Li, X., Zhang, J., Dobynde, M. I., Wang, Y., Xu, Z., et al. (2023). The first ground-level enhancement seen on three planetary surfaces: Earth, Moon, and Mars. *Geophysical Research Letters*, 50, e2023GL103069. https://doi.org/10.1029/2023GL103069

Guo, J., Tian, C., Charpentier, G., Wimmer-Schweingruber, R. F., Khaksarighiri, S., et al. (2026). Influence of Mars topography on radiation dose detected by the Mars Science Laboratory and assessment of Mars surface albedo radiation. *Journal of Geophysical Research: Planets*, 131(4), e2026JE009704. https://doi.org/10.1029/2026JE009704

Khoo, L. Y., Sánchez-Cano, B., Lee, C. O., Rodríguez-García, L., Kouloumvakos, A., et al. (2024). Multispacecraft observations of a widespread solar energetic particle event on 2022 February 15–16. *The Astrophysical Journal*, 963, 107. https://doi.org/10.3847/1538-4357/ad167f

Koleva, R., Semkova, J., Benghin, V., Gopalswamy, N., Matviichuk, Y., et al. (2025). Catalog of solar energetic particle events registered by Liulin-MO dosimeter in Martian orbit during the current solar cycle. In *Proceedings of the Seventeenth Workshop "Solar Influences on the Magnetosphere, Ionosphere and Atmosphere"*, 144–153. https://doi.org/10.31401/WS.2025.proc

Krastev, K., Semkova, J., Koleva, R., Bankov, N., Benghin, V., and Drobishev, S. (2019). The shading effect for doses and galactic cosmic ray fluxes measured by Liulin. In *Proceedings of the Eleventh Workshop "Solar Influences on the Magnetosphere, Ionosphere and Atmosphere"*, 31–34. https://doi.org/10.31401/WS.2019.proc

Krastev, K. (2025). Solar proton events recorded by the Liulin instrument—composition analysis using numerical modeling. In *Proceedings of the Seventeenth Workshop "Solar Influences on the Magnetosphere, Ionosphere and Atmosphere"*. https://doi.org/10.31401/WS.2025.proc.20

Litvak, M., Mitrofanov, I., Sanin, A., Golovin, D., Nikiforov, S., et al. (2025). Neutron radiation dosimetry on Mars. *Acta Astronautica*, 234. https://doi.org/10.1016/j.actaastro.2025.04.048

Löwe, J. L., Khaksarighiri, S., Wimmer-Schweingruber, R. F., Hassler, D. M., Ehresmann, B., et al. (2025). Nowcasting solar energetic particle events for Mars missions. *Space Weather*. https://doi.org/10.1029/2025SW004372

Mitrofanov, I., Litvak, M., Sanin, A., Golovin, D., Nikiforov, S., et al. (2025). The solar particle event at Mars on 2024 May 20: Neutron component of the radiation environment. *Acta Astronautica*, 234, 734–741. https://doi.org/10.1016/j.actaastro.2025.05.043

Papaioannou, A., Kouloumvakos, A., Mishev, A., Vainio, R., Usoskin, I., et al. (2022). The first ground-level enhancement of solar cycle 25 on 28 October 2021. *Astronomy & Astrophysics*, 660, L5. https://doi.org/10.1051/0004-6361/202142855

Posner, A., and Strauss, R. (2020). Warning time analysis from SEP simulations of a two-tier release system applied to Mars exploration. *Space Weather*, 18(4), e2019SW002354. https://doi.org/10.1029/2019SW002354

Potgieter, M. S. (2013). Solar modulation of cosmic rays. *Living Reviews in Solar Physics*, 10, 3. https://doi.org/10.12942/lrsp-2013-3

Reames, D. V. (2013). The two sources of solar energetic particles. *Space Science Reviews*, 175, 53–92. https://doi.org/10.1007/s11214-013-9958-9

Semkova, J., Koleva, R., Benghin, V., Dachev, T., Matviichuk, Y., et al. (2018). Charged-particle radiation measurements with the Liulin-MO dosimeter of the FREND instrument aboard ExoMars Trace Gas Orbiter during the transit and in high elliptic Mars orbit. *Icarus*, 303, 53–66. https://doi.org/10.1016/j.icarus.2017.12.034

Semkova, J., Benghin, V., Guo, J., Zhang, J., Da Pieve, F., et al. (2022). Comparison of the flux measured by Liulin-MO dosimeter in ExoMars TGO science orbit with the calculations. *Life Sciences in Space Research*, 35, 119–130. https://doi.org/10.1016/j.lssr.2022.08.007

Semkova, J., Koleva, R., Benghin, V., Krastev, K., Matviichuk, Y., et al. (2023). Observation of the radiation environment and solar energetic particle events in Mars orbit in May 2018–June 2022. *Life Sciences in Space Research*, 39, 106–118. https://doi.org/10.1016/j.lssr.2023.03.006

Semkova, J., Koleva, R., Benghin, V., Gopalswamy, N., Matviichuk, Y., et al. (2025a). Radiation environment on TGO Mars orbit during solar particle events in January–October 2024: Corresponding solar eruptions and GOES proton flux data. *Life Sciences in Space Research*, 45, 117–134. https://doi.org/10.1016/j.lssr.2025.02.010

Semkova, J., Koleva, R., Benghin, V., Krastev, K., Matviichuk, Y., et al. (2025b). Radiation conditions in Mars vicinity during different phases of the solar cycle according to measurements by the Liulin-MO dosimeter aboard the Trace Gas Orbiter. In *Proceedings of the Seventeenth Workshop "Solar Influences on the Magnetosphere, Ionosphere and Atmosphere"*, 164–171. https://doi.org/10.31401/WS.2025.proc.22

Shafirkin, A. V., and Grigoryev, Y. G. (2009). *Interplanetary and Orbital Space Flights: The Radiation Risk to Astronauts (Radiobiological Basis)*. Moscow: Economica. 412 pp. (in Russian).

Shavers, M., Semones, E., Tomi, L., Jing, J., Straube, U., et al. (2023). Space agency-specific standards for crew dose and risk assessment of ionising radiation exposures for the International Space Station. *Zeitschrift für Medizinische Physik*. https://doi.org/10.1016/j.zemedi.2023.06.005

Townsend, L. W., Cucinotta, F. A., Wilson, J. W., et al. (1994). Solar modulation and nuclear fragmentation effects in galactic cosmic ray transport through shielding. *Advances in Space Research*, 14, 853–861. https://doi.org/10.1016/0273-1177(94)90550-9

Velinov, P. I. Y., Asenovski, S., Kudela, K., Laštovička, J., Mateev, L., et al. (2013). Impact of cosmic rays and solar energetic particles on the Earth's ionosphere and atmosphere. *Journal of Space Weather and Space Climate*, 3, A14. https://doi.org/10.1051/swsc/2013036

Zeitlin, C., Hassler, D. M., Cucinotta, F. A., Ehresmann, B., Wimmer-Schweingruber, R. F., et al. (2013). Measurements of energetic particle radiation in transit to Mars on the Mars Science Laboratory. *Science*, 340(6136), 1080–1084. https://doi.org/10.1126/science.1235989

Zhang, C., Liu, W., Guo, J., Dobynde, M., and Wimmer-Schweingruber, R. F. (2026). The constraint of crewed Mars missions based on current radiation dose measurements. *Space Weather*, 24(3), e2025SW004724. https://doi.org/10.1029/2025SW004724

Zhang, J., Guo, J., Zhang, Y., Cao, Y., Dobynde, M., et al. (2024). The 2022 February 15 solar energetic particle event at Mars: A synergistic study combining multiple radiation detectors on the surface and in orbit of Mars with models. *Geophysical Research Letters*, 51, e2024GL111775. https://doi.org/10.1029/2024GL111775

DOI: 10.31401/WS.2026.proc.13

Solar-Like Corona of the Thin Disk in the AGN

Yankova K.D.[1], Dimitrijević M.S.[2], Srećković V.A.[3], Vujčić V.[2]

[1]Space Research and Technology Institute – Bulgarian Academy of Sciences
[2]Astronomical Observatory, Volgina 7, 11060 Belgrade 38, Serbia
[3]Institute of Physics Belgrade, UB, P.O. Box 57, Belgrade, 11001, Serbia
f7@space.bas.bg

Abstract

We have built a model of a hot advective disk in aim to unify the physical behavior of the central object in dormant and active galactic nuclei. Here we will use our work to show the possibility of the thin disk component to develop and maintain a solar-like corona. We will investigate the behavior of two real sources, representatives of the respective studied groups Syg A* (dormant) and NGC 3516 (AGN).

Keywords: AGN; Solar-like corona

1. Introduction

- The active core - the quasar comprises five main elements: a supermassive black hole, an outer torus, a Keplerian accretion disk from which the solar-like corona can arises, and jets.
- Profile variability in lines active galactic nucleus may indicate a change geometry in the region from which it comes:

Popovic´ et al., (2023) modelled the broad-line profiles (Hβ line) in NGC 3516 spectrum, they showed that there is superposition the emission from the accretion disc with emission from a surrounding region that is outside the disc. Coronal spectrum is overlays on the basic disk spectrum.

2. The develop a solar-type disk corona

Each accretion disk, in the system with presence a magnetic field, can develop a solar-type disk corona. In this number: Symbiotic Nova; Micro-quasar; AGN and others: The formation of the corona is directly related to the inner active zone developed in the disk.

In hot accretion magnetic disks, diffusion is slower than dissipation. Along with the viscous and a magnetic dissipations and the nonlinear interactions in the spectrum transitions the MR-modes, emit additional photons [Hirose et al., 2009], which works to the flux saturation. The important contribution of the field is by partially freezing, the current leads the plasma, she follows it and is compacting. This means that together with the natural processes of absorption and scattering in the disk, works refraction of formed radiation in layers of the rings. Optically dense fluidal lightguides, holds radiation in the flow [Yankova, 2014]. Thus energy is saved to disk in the form of heat and radiation, and

Manages the radial gradient of entropy. Negative entropy creates conditions for energy absorption of the instabilities and leads them to new state by irreversible transition - turning them into (vortex-) structures; Stimulates feedback and naturally intensifies the effects of heating from nonlinear interactions. This inverse cascade provides necessary thermal excitation to maintain advection in self-induction mode [Yankova, 2017].

In the inner the disk it is the trigger, which increases the accretion rate by of up to about 15 percent due to the advection action, the real active zone is formed. In such case in disk the advection manages to force more photons to move in orbits for massive particles because they cannot leave the mainstream due to high flow density. The self-induced Advection moves the rings, they are mobile and provides active advective heating in the pad which will maintains a long-lived corona [Yankova, 2014].

The active zone can be determined by indicators such as: The outer radius of the corona, obtained by condition $v_a^2 \leq v_s^2$ [Iankova, 2007]; Inner disk radius, $\langle v_a \rangle^2 \approx (9/4)\langle v_\varphi \rangle^2$ [Iankova, 2009]; Temperature distribution in the disk; and The critical value of the heating K > 1. K is dimensionless magnitude obtained in the modelling process, which is a measure of the disc ability to qualitative cooling [Iankova, 2009].

However, it the best can register in radial Luminosity distribution the disk.

2.1. Formation mechanism

Most of the energy is in the long-wave mode of magneto-rotational instabilities MRI s; it is from them that the main momentum transport in the disk comes. Nonlinear saturation is the growth of the amplitudes (kinetic E_k and magnetic E_m energy growing exponentially). Their growth strongly depends on the configuration of the main field: from a toroidal field, where they are absent, to a vertically uniform one, where they are best expressed. The approximation for the main field in our case tends to the second limit. For a vertical field (possibly non-uniform), the asymmetric MR-modes grow the fastest. The saturation of the field creates a powerful magnetic pressure, which, with the help of the Parker and RT-instabilities, is transported and will form a strongly magnetized corona. This will preserve the balance of energies $E_m \sim E_k$ in the disk and the magnetic field will not be able to suppress the rotational effects and quench the magneto-rotational instabilities.

Similar to the solar corona, loops rise from the disk and the differential rotation twists them. The crossing and reconnection of the loops causes a flares from the field annihilation.

2.2. Solar-like corona - similarities and differences

Similarities:

- Formation mechanism and
- Stricture;
- Significant similarity is the difference in the effective temperatures of the pad (sun; disk) and its corona: Sun - corona 3-order difference in effective temperature; disk corona 3-5 orders of magnitude difference in temperature.

Differences:

- The significant difference with the Sun, in this case, is that self-gravity pulls the plasma raised in the loops back into the disk. This way the crown becomes more transparent.
- But main difference is that disk corona is closed from above by a magnetic field - the central jet-funnel expands and the flow returns to the torus. So creates conditions for multiple internal reflection.

2.3. Observational effects

The disk gives a blackbody spectrum; and the corona has a non-thermal step-step spectrum; which clearly distinguishes the two elements of the DCAJ-system (disk-corona-accretor-jets).

Annihilation lines in the spectrum show flares like in the solar corona.

Multiple internal reflection makes coronal caps above the disk's rotation lines (see fig.1).

3. Observation objects – luminosities curves

Active zone is separated on two parts:

- Plateau in the Luminosities (see Figs.2, 3) indicates the outer active zone in where the advection conceals the activity and forms a bed for the corona.
- In the inner active zone the activity becomes observable [Yankova, 2019].

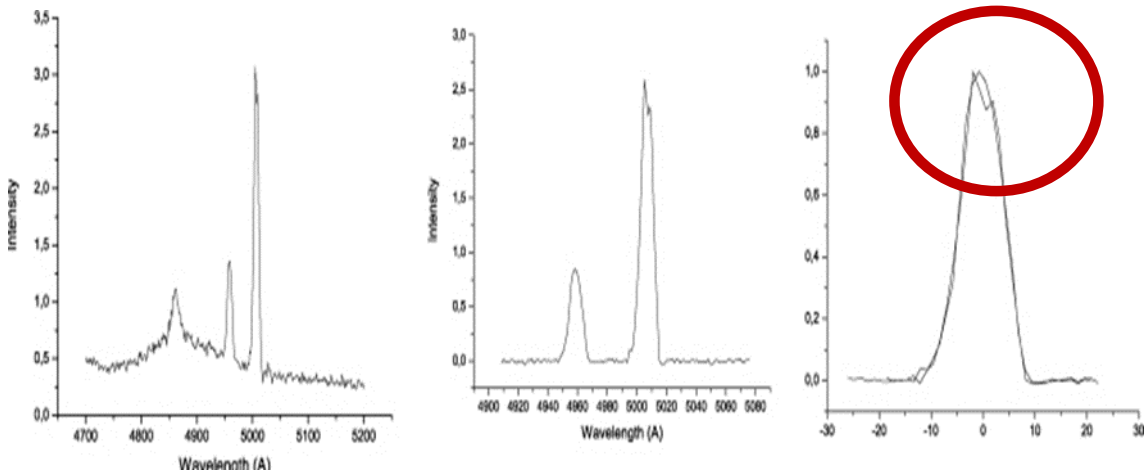


Figure 1. *Example of a spectrum, where the line shapes show the superposition show the superposition of the superimposed emissions [Dimitrijević et al., 2007].*

3.1. Solar-like corona in Syg A (dormant AGN)*

We obtained real active zones for Syg A* in ~ (0,05; 0,6)R_o (fig.2) and the corona is located in the region ~ (0,2; 0,6)R_o;

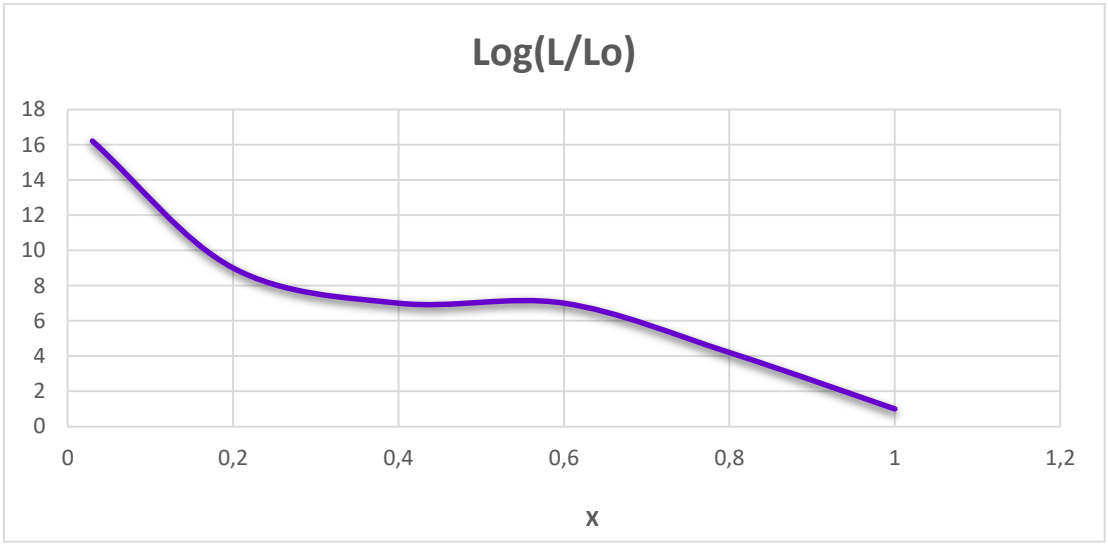


Figure 2. *Luminosity radial distribution in the Sgr A* thin disk.*

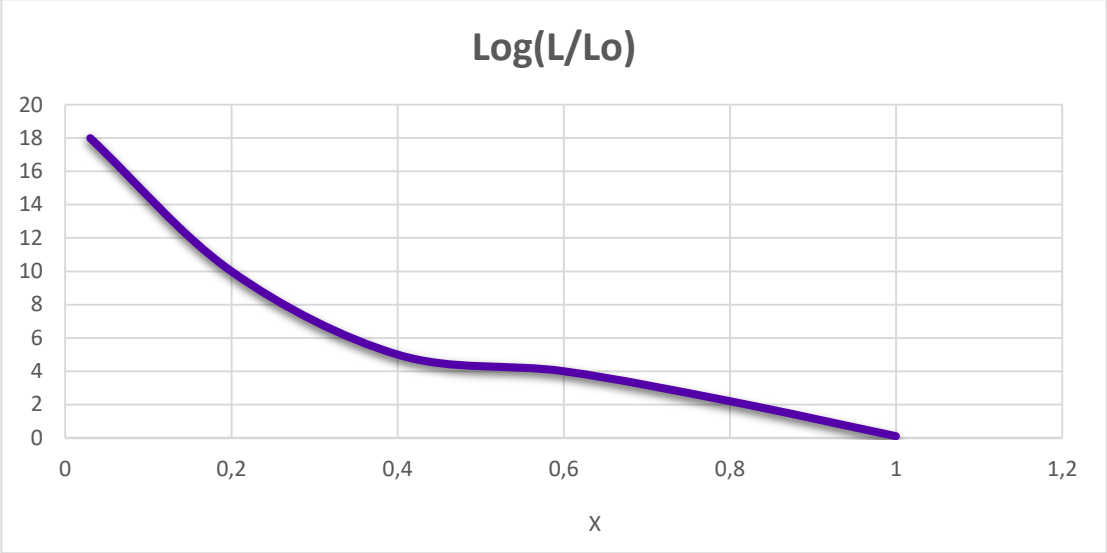


Figure 3. *Luminosity radial distribution in the NGC 3516 thin disk.*

5. Conclusions

- Similar to the solar corona, loops rise from the disk and the differential rotation twists them. The crossing and reconnection of the loops causes flares from the field annihilation.
- The phenomenon can be observed as annihilation lines in the spectrum of the corona. Such lines are observed in the spectrum of the coronal element in the system DCAJ of Sgr A* [Cesare G. De: 2011], and the Sp-lines in NGC 3516 spectrum show internal reflection [Popovic´ et al. (2023) and Dimitrijevi´c et al. (2007)].
- The Active core shows more powerful jets, and the central funnel pushes the disk corona back, where it again inflow into a tor.

References

De Cesare, G. (2011). Searching for the 511 keV annihilation line from Galactic compact objects with the IBIS gamma-ray telescope. *Astronomy & Astrophysics,* 531, A56. https://doi.org/10.1051/0004-6361/201116516

Dimitrijević, M. S., Popović, L. Č., Kovačević, J., Dačić, M., and Ilić, D. (2007). The flux ratio of the [O III] λλ5007, 4959 lines in AGN: Comparison with theoretical calculations. *Monthly Notices of the Royal Astronomical Society*, 374, 1181–1184. https://doi.org/10.1111/j.1365-2966.2006.11238.x

Hirose, S., Krolik, J. H., and Blaes, O. (2009). Radiation-dominated disks are thermally stable. *The Astrophysical Journal*, 691(1), 16–31. https://doi.org/10.1088/0004-637X/691/1/16

Iankova, K. D. (2007). Evinces of interaction of flow in disk with magnetic field. *Bulgarian Journal of Physics*, 34(S2), 326–329.

Iankova, K. D. (2009). Stability and evolution of magnetic accretion disk. Publications of the Astronomical Society "Rudjer Bošković", 9, 327–333.

Popović, L. Č., Ilić, D., Burenkov, A., Patiño Alvarez, V. M., Marčeta-Mandić, S., Kovačević-Dojčinović, J., et al. (2023). Long-term optical spectral monitoring of a changing-look active galactic nucleus NGC 3516. II. *Astronomy & Astrophysics*, 675, A178. https://doi.org/10.1051/0004-6361/202345949

Yankova, K. (2014). Theoretical analysis on the development in relationships of the system disk–corona. *In Proceedings of the Tenth Anniversary Scientific Conference "Space, Ecology, Safety" (SES 2014)*, 35–40. ISSN 1313-3888. Published in 2015.

Yankova, K. (2017). Unified model of the AGN. *In Proceedings of the Ninth Workshop "Solar Influences on the Magnetosphere, Ionosphere and Atmosphere"*, 77–82. https://doi.org/10.31401/WS.2017.proc

Yankova, K. (2019). RS Ophiuchi and advection. *In Proceedings of the Eleventh Workshop "Solar Influences on the Magnetosphere, Ionosphere and Atmosphere"*, 60–64. https://doi.org/10.31401/WS.2019.proc

DOI: 10.31401/WS.2026.proc.14

Verification of Empirical Models for Forecasting Critical Ionospheric Frequencies in the Conditions of Geomagnetic Storms on 12- 13 November 2025

Bojilova R., Mukhtarov P.

National Institute of Geophysics, Geodesy and Geography - Bulgarian Academy of Sciences
rbojilova@geophys.bas.bg

Abstract

The present study provides an opportunity to verify the quality of the created empirical models for forecasting the critical frequencies of the ionospheric E and F regions for the territory of Sofia-Bulgaria. The work examines the anomalies in the behavior of the ionospheric F2 region critical frequency (foF2) and the ionospheric E region critical frequency (foE) under the conditions of the geomagnetic storms on 12-13 November 2025. Data from selected European ionospheric stations were used to compare the model values of the critical frequencies for Sofia. The choice of these stations is related to the fact that this ionosondes are located at the geographic latitude close to the latitude of Sofia, which suggests similar behavior of the ionosphere. In addition, the determination of the relative deviation of foF2 has been introduced. The results of the comparison of the model and measured values for both ionospheric characteristics show a good coincidence during the considered time interval. In the data for foE no anomalous behavior is observed during the storms, but for foF2 a decrease is observed during the first geomagnetic storm, while an increase is observed during the second. The relative deviation of foF2 illustrates the inertia in the response of the quantity and its anomalous behavior of a negative response, followed by a positive anomaly, which is observed in both cases. The results of this study can be used to improve the created empirical models for forecasting the critical frequencies of the ionosphere for the territory of Bulgaria.

Keywords: geomagnetic storm; critical frequencies; empirical modeling

1. Introduction

The influence of geomagnetic storms on the ionosphere is a geophysical problem that is of interest to both scientists and radio amateurs and weather-sensitive people. One of the phenomena leading to geomagnetic storms are coronal mass ejections (CMEs), which represent large expulsions of plasma and magnetic field from the Sun's corona or a corotating interaction in a region dominated by solar wind, originating from a region of weak magnetic field on the Sun's surface [Gonzalez et al., 1994]. The streams of charged particles that the Sun erupts in these cases are part of the solar wind and, under certain conditions, interact sequentially with the Earth's magnetosphere-thermosphere-ionosphere. In this particular case, the most significant are the so-called ionospheric storms, which are characterized by variations of the electron density, as the ionospheric response for different ionospheric regions is different. The explanation for the different response of the ionospheric F layer, as well as the E and D regions, is related to differences in physical mechanisms leading to these changes in electron density. In regions E and D, the cause of the changes is in the ionization rate due to corpuscular penetration, while in region F the changes in electron density are due to neutral composition and dynamic processes. An interesting effect in the response of the ionospheric F2 region to geomagnetic disturbances

is that both an increase and a decrease in electron density are observed relative to quiet conditions and can be divided into a "positive" and a "negative" phase of the storm [Danilov A.D. and Lastovicka J., 2001]. Studies reveal that the negative ionospheric response is related to Joule heating, in contrast to the positive one, which is attributed to two mechanisms of action: the increase of in the circulation - moving from the dayside cusp through polar oval to the nightside thermosphere, and the lifting up of the peak of F region due to disturbed meridional winds into the region with weaker recombination [Danilov A.D., and Belik L.D., 1992].

Everything described above provides motivation to study the ionospheric response in the separate ionospheric regions - F2 and E for selected European points where there is data from the vertical sounding. It is interesting to compare the results with the data obtained for the same quantities using the empirical models created for predicting the ionosphere for the territory of Bulgaria.

2. Data and Methods

The Kp index is obtained byground-based magnetometers around the world. This calculated 3-hour planetary Kp index ranges from 0 to 9. In this study the geomagnetic activity is described by the planetary Kp index, received from Goddard Space Flight Center - https://omniweb.gsfc.nasa.gov/.

The data for the two critical frequencies foE and foF2 for station Sofia (42.4°N, 23.2°E) were obtained through empirical modeling of the measured values from station SQ143 for the period 1995-2014. The development of similar models for short-term prediction of the ionosphere is necessary in cases of the absence of fresh data from the vertical sounding.

Two solutions have been proposed for the determination of foF2: a) in one case, the dependence of the critical frequency on the variations in solar and geomagnetic activity is considered [Bojilova R. and Mukhtarov P., 2021a)]; b) in its second variant foF2 is determined by its dependence on the Total Electron Content (TEC) [Bojilova R. and Mukhtarov P., 2021b)], and the model error for the entire period of almost two solar cycles was obtained, which can be used to assess its accuracy [Mukhtarov P. and Bojilova R., 2021c)].

The hourly values of the foE over Bulgaria were obtained using an empirical model for forecasting which includes the dependence of the ionospheric characteristic on the index of the solar activity described by F10.7 and the cosine of solar zenith angle [Bojilova R. and Mukhtarov P., 2021d)].

Data on the critical frequencies of the ionosphere, namely foE and foF2 are based on vertical sounding of the ionosphere by Digisondes providing their data to the Global Ionosphere Radio Observatory (GIRO) - https://giro.uml.edu/index.html. Table 1 illustrates a detailed list of the European stations as part of the GIRO used with their codes and location (by latitude and longitude).

Table 1. *List of used data from selected ionospheric stations over Europe.*

Station code	Station name	Lat [deg]	Lon [deg]
RM041	ROME	41.80	12.50
VT139	SAN VITO	40.60	17.80
AT138	ATHENS	38.00	23.50
NI135	NICOSIA	35.03	33.16

$$r(t)foF2 = \sqrt[3]{\frac{foF2(t)}{foF2_{med}(UT)}} - 1 \quad (1)$$

Formula 1 illustrates the methodology for obtaining the relative deviation (rfoF2) of its values from the hourly medians (foF2med), which allows for analyzing variations in foF2 from quiet conditions.

3. Results

To analyze the impact of the selected CMEs on the geomagnetic conditions of the Earth, the Kp index, presented in Figure 1, were considered [Huttunen et al., 2002].

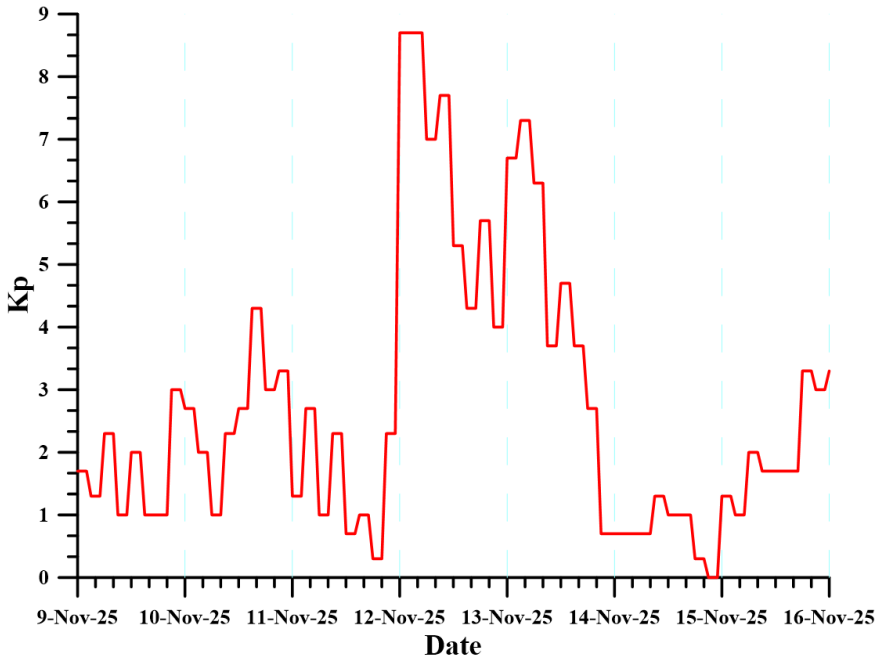


Figure 1. *Geomagnetic conditions presented by Kp-index.*

Figure 1, which illustrates the behavior of the Kp index, shows that around 20UT on 11 November 2025 the index suddenly increases and in the hours between 00-06UT on 12 November 2025 it reaches values of 8.67. According to the accepted classifications for the Kp index, this geomagnetic storm is of class G4 (Severe) [https://www.swpc.noaa.gov/noaa-scales-explanation]. This increase is followed by a decrease in the Kp index, which has another maximum in the Kp index value of around 7.33 in the hours shortly after midnight on 13 November 2025. This second increase in the index is followed by a gradual normalization of the Kp index values to quiet conditions.

Figure 2 presents the course of the ionospheric E region critical frequency for the period 11-15 November 2025 based on data from the ionospheric stations described in Table 1, and in addition, the model values for the Sofia station are also included. The figure shows the well-defined and well-known diurnal variation of the quantity, and the comparison between the measured and model values turns out to be satisfactorily good. In the considered time interval and in the selected European region, no anomalous behavior was observed in foE due to the fact that this quantity may react to a geomagnetic storm at high latitudes [Buonsanto M.J., 1999].

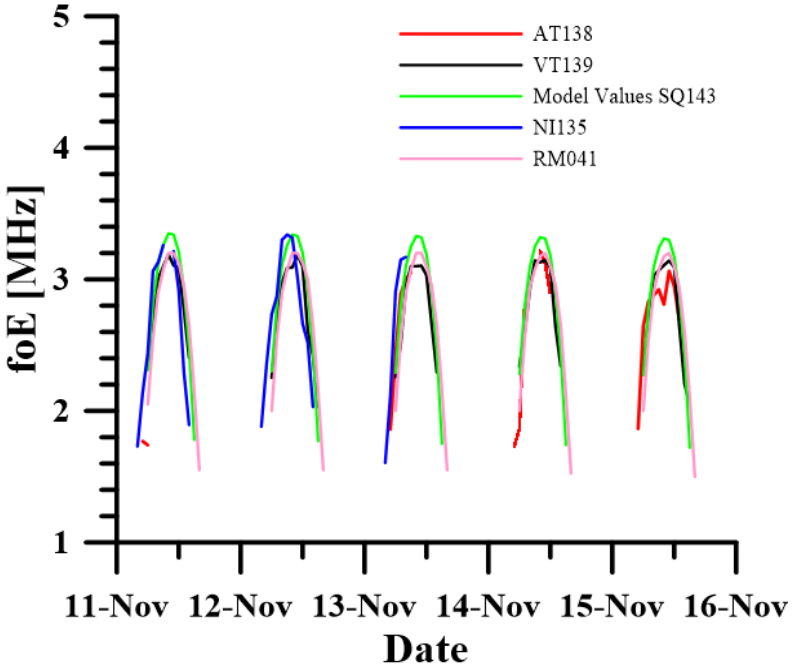


Figure 2. *Comparison between measured and model values of foE.*

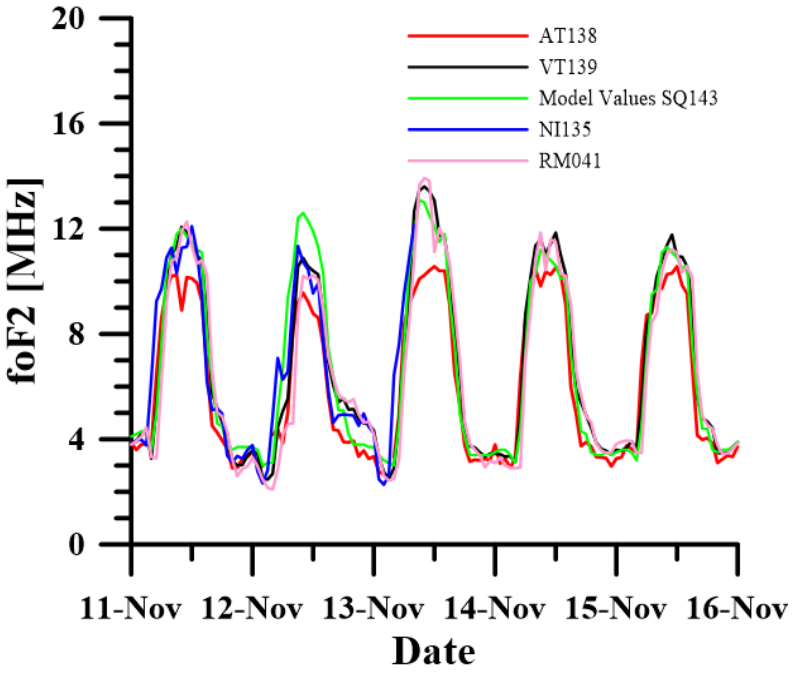


Figure 3. *Comparison between measured and model values of foF2.*

Figure 3 shows the behavior of the ionospheric F region critical frequency for the same period as Figure 2. Similarly, data for the European region and those obtained through the empirical model for forecasting the ionosphere over Bulgaria were used. The figure illustrates a decrease in foF2 on November 12 (around noon) compared to days without a geomagnetic storm in all data except the modeled ones. Another interesting effect in the hours around sunset on the same day is an increase turning into a decrease, which is not typical for quiet conditions. A similar effect was obtained by scientists for the ionospheric response to the geomagnetic storm in March 2023. The analysis is based on ionospheric vertical sounding

data covering the middle-latitudinal European region. The results of this study show that a pre-storm enhancement was observed, characterized by an increase in electron density at northern stations [Mošna Z. et. al, 2024]. The next day- 13 November, an increase is observed at stations RM041, VT139, NI135 as well as the model data. Only station AT138 did not show a similar response, and there is no data for station NI135 for the whole observed period, but according to the coordinates of these stations they are located to the east, which may explain the different response at station AT138. Confirmation of this hypothesis was proposed by [Prölss, 1995], in which strong longitudinal and latitudinal asymmetries or the completely different storm-induced disturbance behavior of foF2 for two points with close coordinates were obtained.

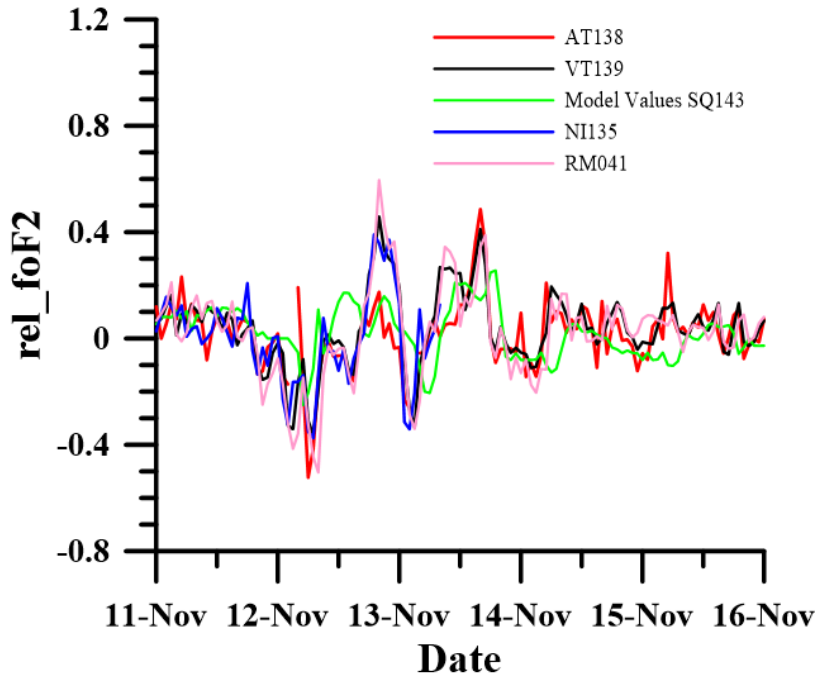


Figure 3. *Comparison between measured and model values of relative deviation in foF2.*

In order to determine the ionospheric response to the quantity foF2 in more detail and accurately, Formula 1 was applied to determine its relative deviation. The advantage of the introduced mathematical operation is related to the representation of the relative deviation of the quantity compared to quiet conditions. From the comparison shown in Figure 4, including all the points considered, the negative response of quantity is visible already in the late hours on 11 November, when is the onset of the storm (See Figure 1). The most pronounced negative reaction is observed in the hours around 02-03UT, namely a few hours after the maximum of the Kp index. In this time interval the values of the relative foF2 are around -0.4 to -0.6 except for the model data, which show a weaker response. The strongest negative anomaly is observed at station AT138 and station RM041, while weaker and almost identical variations are observed at station VT139 and station NI135. The model presents a good coincidence with the vertical sounding data, but with an underestimated negative response. After this point, a slow recovery begins, which after noon on 12 November turns into a positive response. Maximum positive values (up to 0.6) were recorded around 18-19UT on 12 November. All stations show this positive anomaly, with the weakest one being at station AT138 and the model data, and the most significant one at RM041. An explanation for this difference could be the fact that station RM041 is located in the north, while AT138 is one of the southern ones. In the hours after midnight on 13 November, a second negative

response was observed, which was weaker than the first (the relative deviation had values up to about -0.4), but in this case all stations responded synchronously and in the same way. Shortly after noon on 13 November, a positive response of relative foF2 was obtained again, reaching about 0.4. This positive anomaly is visible at three of the stations except NI135 due to a lack of data, while the model data underestimate the resulting effect.

4. Discussion

The present investigation analyzes the ionospheric response over Europe as a result of geomagnetic storms during the period 12-13 November 2025. The analysis also compared the variations in foF2 and FoE obtained from ground-based stations for vertical sounding of the ionosphere and the data for the same ionospheric characteristics obtained through empirical modeling for the territory of Bulgaria. The behavior of the ionospheric E region critical frequency does not illustrate significant anomalies in the period under consideration, unlike the ionospheric F2 region critical frequency. Due to the practical application of this quantity for radio communications and the availability of data for the whole day, it was studied by presenting its relative deviation from quiet (median) conditions. Corresponding positive and negative anomalies in the relative foF2 are obtained. The explanation for the negative effects obtained at mid-latitudes is that the anomalies are a result of changes in the neutral gas composition. The positive short duration ionospheric effects are due to Travelling atmospheric disturbances (TADs) and thermospheric wind circulation [Prölss, 1995]. The storm under consideration is characterized by a winter type circulation, which indicates that during the daytime the circulation is poleward and it hinders the storm-induced circulation from expanding toward middle latitudes. The equatorward wind at middle latitudes is weakened and an additional component of the upward vertical wind appears, all of which explains the positive daytime anomalies in foF2 [Borries et al., 2017].

The proposed approach for comparison and verification of the created forecasting methodologies for the territory of Bulgaria shows good results, and the study provides additional guidance on which type of ionospheric response the models fail to "recreate" satisfactorily.

References

Gonzalez, W.D., Joselyn, J.A., Kamide, Y., Kroehl, H.W., Rostoker, G., Tsurutani, B.T., and Vasyliunas, V.M.: 1994, What is a geomagnetic storm?, *J. Geophys. Res. Space Phys.* 99, 5771–5792, doi:10.1029/93JA02867.

Danilov, A.D. and Laštovička, J.: 2001, Effects of geomagnetic storms on the ionosphere and atmosphere, *Int. J. Geomagn. Aeron.* 2, 209–224.

Danilov, A.D. and Belik, L.D.: 1992, Thermospheric composition and the positive phase of an ionospheric storm, *Adv. Space Res.* 12, 257–260, doi:10.1016/0273-1177(92)90475-D.

Bojilova, R. and Mukhtarov, P.: 2021a, A new approach for forecasting the main ionospheric parameters over Bulgaria, in *Proceedings of the Thirteenth Workshop "Solar Influences on the Magnetosphere, Ionosphere and Atmosphere"*, 165–170, doi:10.31401/WS.2021.proc.30.

Bojilova, R. and Mukhtarov, P.: 2021b, Reconstruction of ionospheric critical frequencies based on the total electron content over Bulgaria, *C. R. Acad. Bulg. Sci.* 74, 110–119.

Bojilova, R. and Mukhtarov, P.: 2021c, An empirical model for forecasting the critical frequency of the ionospheric E-region over Bulgaria, in *International Multidisciplinary Scientific GeoConference SGEM*, 21, 403–410, doi:10.5593/sgem2021/1.1/s05.075.

Mukhtarov, P. and Bojilova, R.: 2021, Accuracy assessment of the ionospheric critical frequencies reconstructed by TEC over Bulgaria, *C. R. Acad. Bulg. Sci.* 74, 250–259, doi:10.7546/CRABS.2021.02.12.

Huttunen, K.E.J., Koskinen, H.E.J., and Schwenn, R.: 2002, Variability of magnetospheric storms driven by different solar wind perturbations, *J. Geophys. Res. Space Phys.* 107, SMP 20-1–SMP 20-8, doi:10.1029/2001JA900171.

National Oceanic and Atmospheric Administration: n.d., NOAA Space Weather Scales, available at: https://www.swpc.noaa.gov/noaa-scales-explanation.

Buonsanto, M.J.: 1999, Ionospheric storms—A review, *Space Sci. Rev.* 88, 563–601, doi:10.1023/A:1005107532631.

Prölss, G.W.: 1995, Ionospheric F-region storms, in Volland, H. (ed.), *Handbook of Atmospheric Electrodynamics*, Vol. 2, CRC Press, Boca Raton, 195–248.

Burešová, D., Laštovička, J., and De Franceschi, G.: 2007, Manifestation of strong geomagnetic storms in the ionosphere above Europe, in Lilensten, J. (ed.), *Space Weather: Research Towards Applications in Europe*, Astrophysics and Space Science Library, Vol. 344, Springer, Dordrecht, 185–202, doi:10.1007/1-4020-5446-7_17.

Mošna, Z., Barta, V., Berényi, K.A., Mielich, J., Verhulst, T., Kouba, D., et al.: 2024, The March and April 2023 ionospheric storms over Europe, *Front. Astron. Space Sci.* 11, 1462160, doi:10.3389/fspas.2024.1462160.

Borries, C., Jakowski, N., Kauristie, K., Amm, O., Mielich, J., and Kouba, D.: 2017, On the dynamics of large-scale traveling ionospheric disturbances over Europe on 20 November 2003, *J. Geophys. Res. Space Phys.* 122, 1199–1211, doi:10.1002/2016JA023050.

DOI: 10.31401/WS.2026.proc.15

Extremely Space Weather Events of May and October 2024: High-Latitude Geomagnetic Disturbances

Gromova L.I.[1], *Kleimenova N.G.*[2], *Gromov S.V.*[1], *Malysheva L.M.*[2]

[1]IZMIRAN, Moscow, Troitsk, Russia; gromova@izmiran.ru
[2]Schmidt Institute of Physics of the Earth RAS, Moscow, Russia

Abstract

The geomagnetic storms of 10-11 May and 10-11 October 2024 were the strongest geomagnetic events in over two decades. The May 10–11 storm was the strongest while the 10 October event was the second strongest one. Both were caused by the arrival of powerful magnetic clouds, and the Interplanetary Magnetic Field (IMF) and the solar wind conditions and the development of the storms would seem similar. So, it was observed the similar intense high-latitude geomagnetic disturbances (|SML| up to ~4000 nT) in the beginning and in the early recover phases of both these storms. In the beginning of the storms they could be caused by Sheath effect while in the early recover phase they could be developed under conditions of the magnetic clouds. It was shown that the occurrence of these intense high-latitude geomagnetic disturbances is possible during different phases of the storms under any ring current conditions, and among them there are both "classic" substorms and convective bays. The global distributions of the high-latitude geomagnetic disturbances were studied by applying the planetary maps of the ionospheric currents derived from the magnetic measurements on 66 LEO satellites of the AMPERE project. Here it was also discussed how the appearance of supersubstorms and convective bays can depend on conditions of the interplanetary environment.

Keywords: space weather; magnetic storm; substorm

1. Introduction

The geomagnetic storms of 10-11 May and 10-11 October 2024 were the strongest geomagnetic events in over two decades caused by the arrival of powerful magnetic clouds. In several papers (see also references therein) it have been discussed the drivers and different geophysical effects in the space and on the ground of the May 2024 storm, e.g. [Hajra et al., 2024; Haykawa et al., 2025; Kleimenova et al., 2025a; Zou et al., 2025], and the October 2024 storm, e.g. [Kleimenova et al., 2025b; Pierrard et al., 2025; De Michelis et al., 2026]. It was found some unusual and interesting features in different geophysical phenomena. However, the problems of storm-substorm relations and specific substorm properties during extremal strong geomagnetic storms remain open.

As one can see in Figure 1 that shown the solar wind and IMF conditions, the development of the storms would seem similar. During the May 2024 storm, at least 12 intense substorms can be identified, 5 of them were observed in the main storm phase and 7 ones were observed in the storm recovery phase. There were at least 5 very intense substorms during the October 2024 storm.

Our study was addressed to the global behavior and properties of intense (higher 1500 nT) magnetic substorms exited during these storms.

2. Data. AMPERE maps

We studied the global distribution of the high-latitude geomagnetic disturbances by applying the planetary maps of the ionospheric and field-aligned currents derived from the magnetic

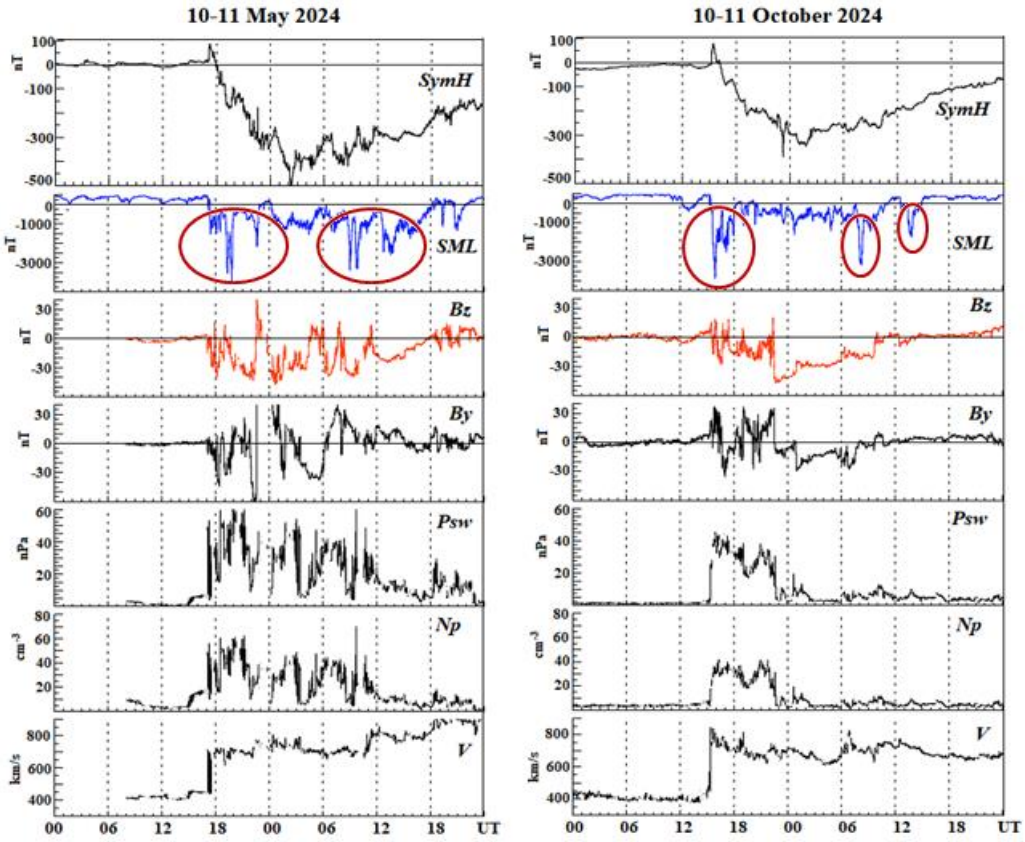


Figure 1. *Variations of the IMF and the solar wind parameters during the extremely strong magnetic storms on 10-11 May 2024 and 10-11 October 2024 (https://omniweb.gsfc.nasa.gov/, https://supermag.jhuapl.edu/).*

measurements on 66 satellites of the AMPERE project. They equipped with identical magnetometers, their polar orbits are at an altitude of 780 km in six equally spaced plan es [Gjerloev and Hoffman, 2014]. Figure 2 shows the example of such planetary maps.

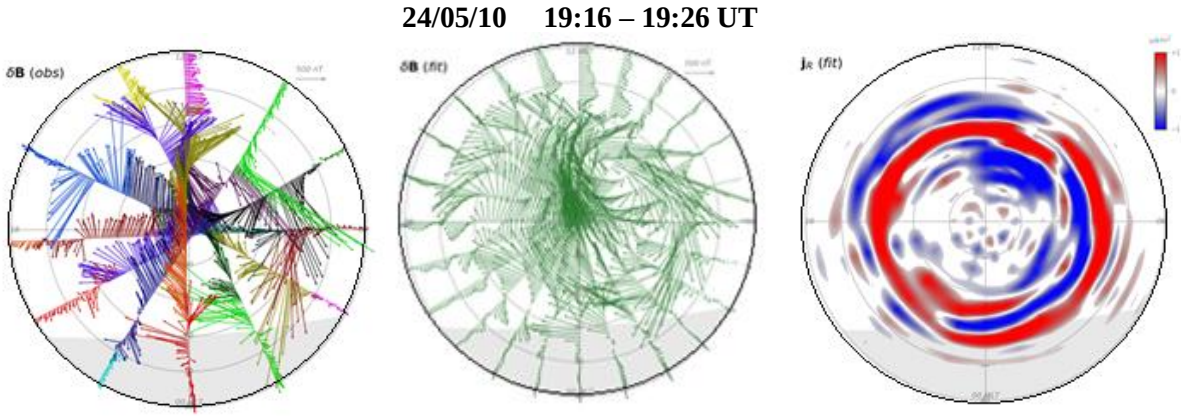


Figure 2. *Example of AMPERE maps. Left panel - satellite data; central map - global distribution of the ionospheric currents as results of spherical harmonic analysis of magnetic registrations: right map - global distribution of the field aligned currents (FACs) derived from the ionosheric currents. Upward currents are marked by red, downward – by blue color (https://ampere.jhuapl.edu).*

In the left one can see a map with satellite orbits and measurements of the magnetic field. They provide to construct the generalized 10-min global maps of the ionospheric currents distribution basing on the results of spherical harmonic analysis of magnetic registrations (central map). There are techniques [e. g., Anderson et al., 2014] to process these magnetic field data and obtain global maps of the field aligned currents (right map).

The global maps are in geomagnetic coordinates for latitudes above 40° MLAT at 2 min cadence over a 10 min window with a spatial resolution of 1° MLAT and 1 h MLT in longitude.

3. Morning vortex in the westward electrojet

In our investigation we compared the maps of global distributions of the electrojets in the intensity maximum of the selected intense substorms and found a similar characteristic feature of all of them - the development of the large morning vortex with the clockwise rotation indicating an enhancement of the downward Field Aligned Currents (FACs). Two such substorms durng the storm of 10-11 May 2024 are shown in Figure 3.

On the bottom panel of Figure 3 one can see not only the AMPERE maps of the ionospheric electrojets but also SuperMAG maps derived from ground-based magnetic measurements in the maximum of the same intense substorms. It should be noted that ground stations are distributed extremely unevenly across the continents and vast areas of the Earth are covered by oceans and seas where there are no observation stations at all. That’s why the uniformity of satellite data coverage of the Earth's surface makes the analysis of AMPERE maps preferable to the analysis of the ground-based data.

4. Convective magnetic bay and "classical" substorm

Due to the interaction of the solar wind with the Earth's magnetosphere, the plasma convection is constantly observed in the auroral and high-latitude ionosphere. Some of their intensifications were called the "convective bay" [Pytte et al., 1978]. It represents the development of a two-sells current system *DP2*. In contrast to a convective bay, a "classical" substorm is accompanied by the formation of a single-sell current system *DP1*. Schematic diagram of Figure 4a shows the location and flow direction of the convection electrojets and substorm current wedge according to [Baumjohann, 1983].

4.1 Event of 11 May 2024

In Figure 4 one can see AMPERE planetary distribution of the ionospheric (upper plots of Figure 4b) and field-aligned currents (bottom plots of Figure 4b) in magnetic bays observed sequentially with the substorm interval less than one hour. It is seen that the first bay is characterized by the *DP1+DP2* current system and the second one illustrated the pure *DP2* current system which is typical for convection bays. We assumed that the second bay was not a substorm, but the enhancement of general magnetospheric convection drove by the solar wind dynamic pressure increase.

4.2 Event of 10 October 2024

The supersubstorm that recorded during October 2024 geomagnetic storm can be attributed to some convection bay (not substorm) as well. It was observed in the storm beginning about 10 min after *SC* when the sign of the IMF *Bz* changed from positive to negative and caused a sharp development of a huge negative morning magnetic bay with an amplitude up to ~ 4000 nT. As one can see in Figure 5 a two-vortex current system *DP2* was formed.

The AMPERE maps show the development of two large-scale ionospheric vortices, representing a typical *DP2* system of convective currents and did not show the typical *DP1* single-vortex current system for a classical substorm.

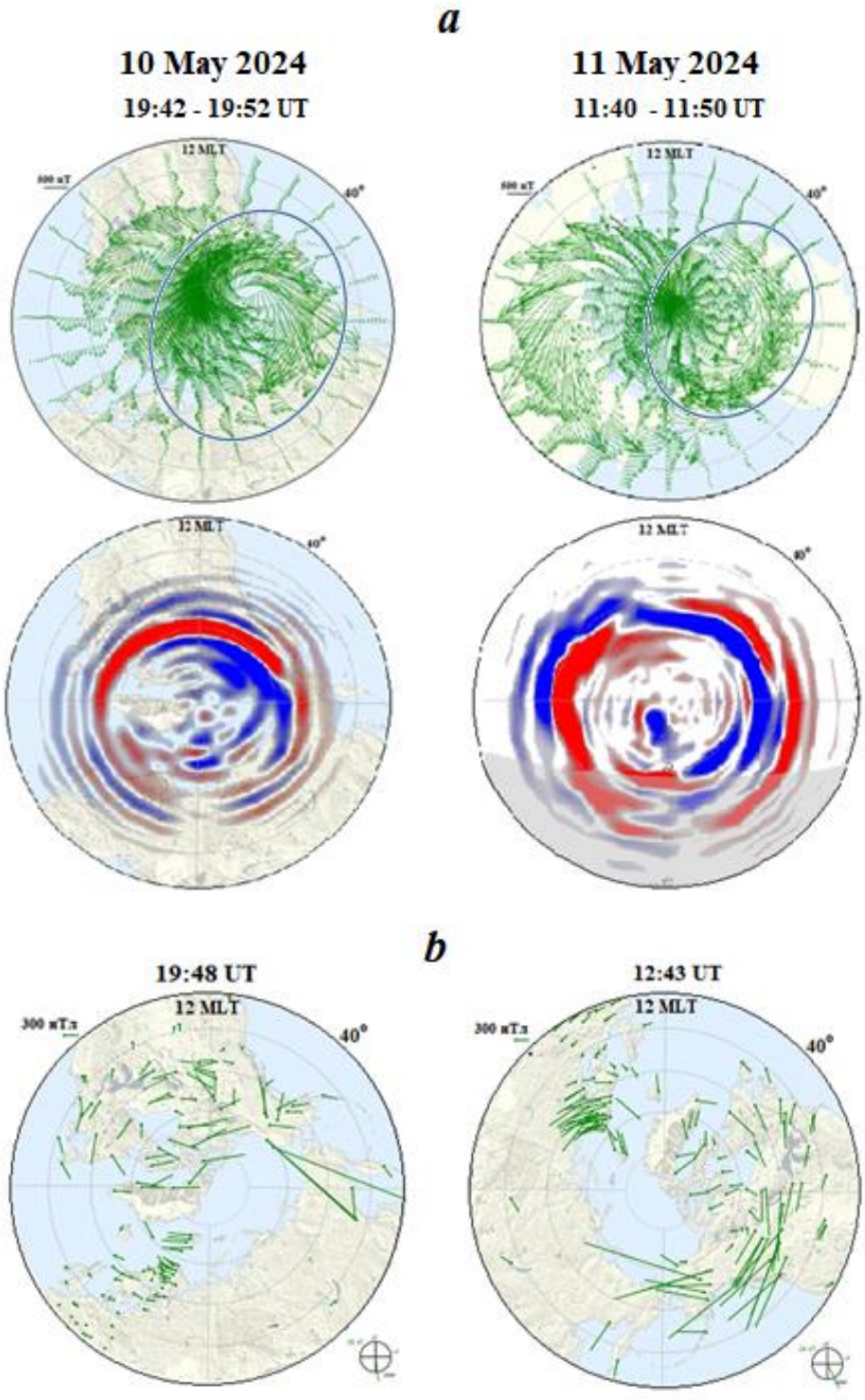


Figure 3. *(a) The AMPERE maps of the ionospheric electrojets (upper plots) and FACs (bottom plots) during 10-minute interval near intense substorm maximums. Morning vortices in the westward electrojet are marked by circles. (b) The SuperMAG maps of the ionospheric electrojets derived from ground-based magnetic measurements in the maximum of the same intense substorms.*

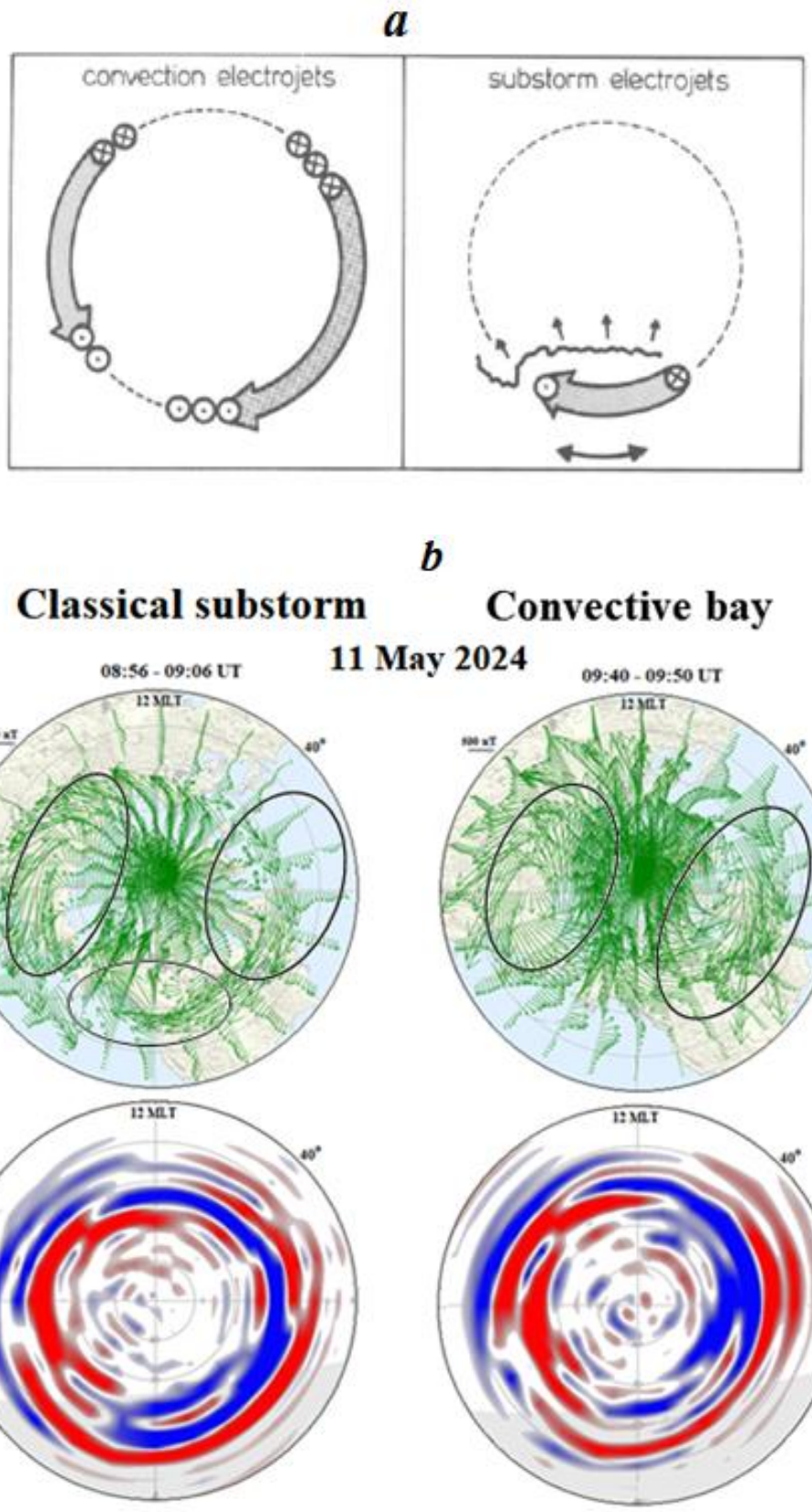


Figure 4. *(a) Schematic diagram of the location and flow direction of the convection electrojets and substorm current wedge, adopted from [Baumjohann, 1983]. (b) The AMPERE maps of the ionospheric electrojets (upper plots) and field aligned currents (bottom plots).*

In this case, we also assumed that this unusual huge magnetic bay is not a substorm as well, but rather a giant convective magnetic bay, the source of which could be associated with a very high dynamic pressure of the solar wind under the negative IMF *Bz*.

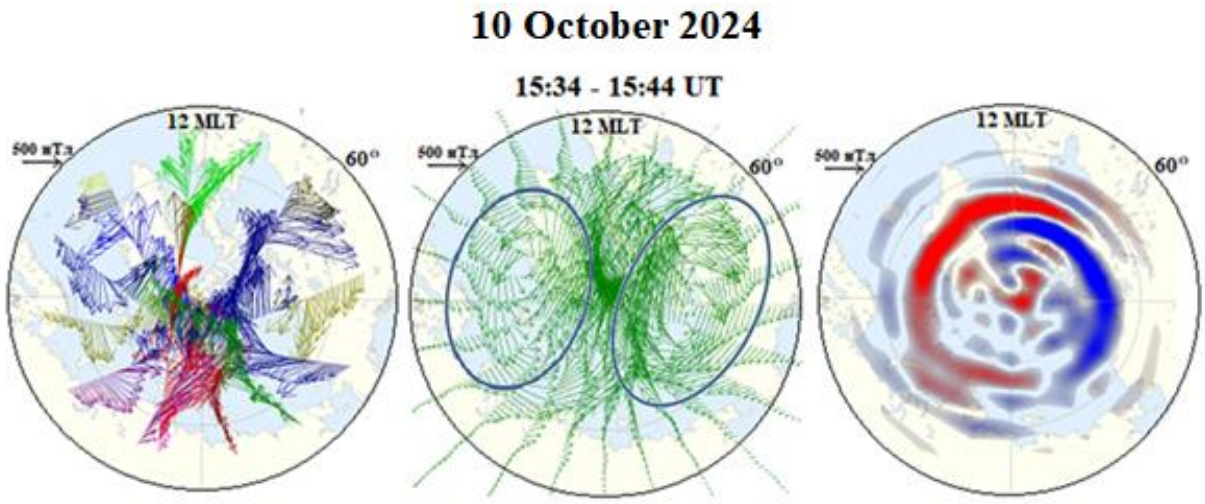


Figure 5*. The AMPERE maps of the ionospheric electrojets and FAC. The DP2 system in the maximum intensity of the convection magnetic bay is marked by circles.*

5. Polar electrojet direction near the noon direction near the noon

The electrojet located at the dayside ionosphere at the geomagnetic latitudes above 70-75° MLAT is often called *DPY*-currents [Friis-Christensen and Wilhjelm, 1975] or "polar electrojet"– *PE* [Feldstein et al., 2006]. In the early time, it was concluded that the sign of such magnetic bays and the correspondent ionospheric currents is controlled by the sign of the IMF *Bz* [Friis-Christensen and Wilhjelm, 1975; Feldstein et al., 2006].

Strong polar electrojet was observed during both considered extreme magnetic storms. We confirmed that the direction of the high-latitude ionospheric currents near noon are controlled by the sign of the IMF *By* but *regardless* of the sign of the IMF *Bz*.

5.1 Event of 11 May 2024

The left map in Figure 6 shows the strong eastward currents under the IMF *By* ~+20 nT and IMF *Bz* ~ -20 nT, and the right map shows the strong westward currents under the IMF *By* ~-40 nT and IMF *Bz* ~ +5 nT

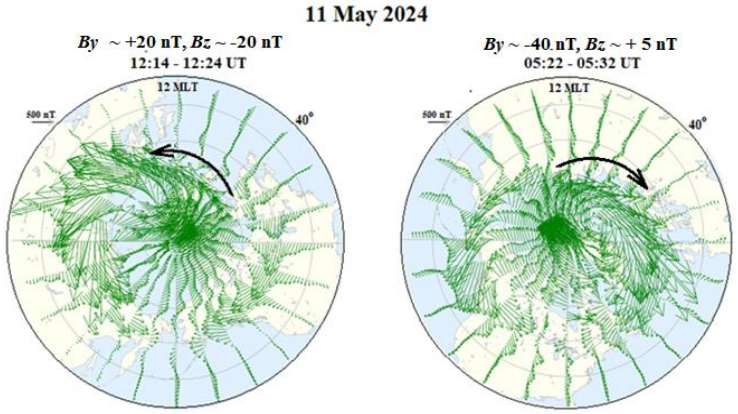


Figure 6. *The AMPERE maps of the ionospheric electrojets in two different time intervals under the IMF By > 0 and IMF By.*

5.2 Event of 11 October 2024

We found that the abrupt change of the sign of the IMF *By* leads to a corresponding abrupt change of the dayside polar electrojet direction. Figure 7 demonstrates an examples of such quick change observed by the AMPERE maps obtained sequentially within short intervals on 10 October 2024 when the IMF *By* changed from +30 nT to -25 nT in the interval-1 (Figure 7b, upper plots) and from -20 nT to +25 nT under very high solar wind dynamic pressure (~40 nPa) in the interval-2 (Figure 7b, bottom plots) under very high solar wind dynamic pressure (~40 nPa). Variations of By and Bz components of the IMF and the solar wind dynamic pressure (Psw) are shown in Figure 7a.

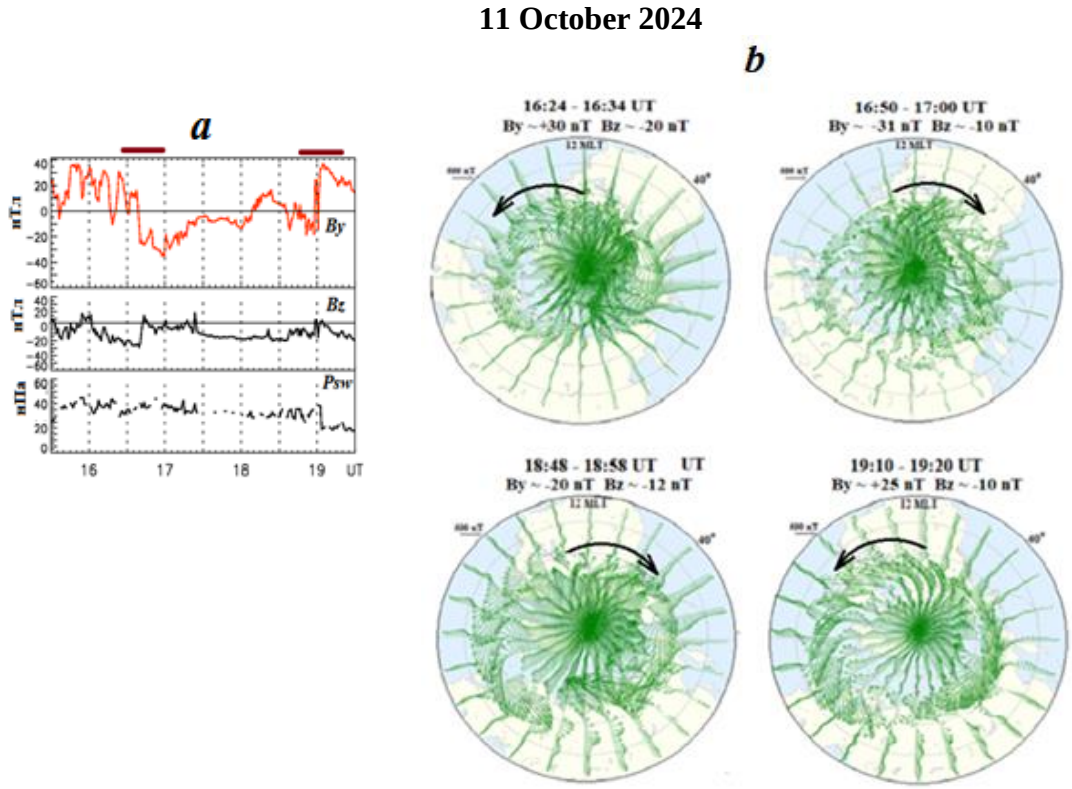


Figure 7. *(a) Variations of the IMF By and Bz and the solar wind dynamic pressure (Psw). Dark bars are marked the intervals under consideration. (b) The AMPERE maps of the ionospheric electrojets of two consecutive intervals with sharp change of the IMF By sign.*

6. Summary

Our study of the global features of the intense (higher 1500 nT) magnetospheric substorm, exited during the May and October 2024 extreme geomagnetic storms, we discovered its specific behavior.

- The development of a strong large-scale clockwise morning vortex in the westward electrojet is a typical feature of an intense magnetic substorm as a proxy of strong local downward field aligned current enhancement.

- The huge magnetic bays (up to 4000 nT) can be not the typical classical ("Akasofu-type") substorm, but being some convection bays. They could be generated by different drivers, for instance, by enhancement of general plasma convection associated with southward IMF direction (negative IMF Bz) under strong solar wind dynamic pressure.

- The abrupt change of the sign of the IMF By leads to a corresponding abrupt change of the dayside polar electrojet direction.

References

Anderson, B.J., Korth, H., Waters, C.L., Green, D.L., Merkin, V.G., Barnes, R.J., and Dyrud, L.P.: 2014, Development of large-scale Birkeland currents determined from the Active Magnetosphere and Planetary Electrodynamics Response Experiment, *Geophys. Res. Lett.* 41, 3017–3025, doi:10.1002/2014GL059941.

Baumjohann, W.: 1983, Ionospheric and field-aligned current systems in the auroral zone: A concise review, *Adv. Space Res.* 2, 55–62, doi:10.1016/0273-1177(82)90363-5.

De Michelis, P., Consolini, E., Giannattasio, F., and Consolini, G.: 2026, Intense ground magnetic perturbations during the 2024 May and October geomagnetic storms, *J. Geophys. Res. Space Phys.* 131, e2025JA034945, doi:10.1029/2025JA034945.

Feldstein, Y.I., Popov, V.A., Cumnock, J.A., Prigancova, A., Blomberg, L.G., Kozyra, J.U., Tsurutani, B.T., Gromova, L.I., and Levitin, A.E.: 2006, Auroral electrojets and boundaries of plasma domains in the magnetosphere during magnetically disturbed intervals, *Ann. Geophys.* 24, 2243–2276, doi:10.5194/angeo-24-2243-2006.

Friis-Christensen, E. and Wilhjelm, J.: 1975, Polar cap currents for different directions of the interplanetary magnetic field in the Y–Z plane, *J. Geophys. Res.* 80, 1248–1260, doi:10.1029/JA080i010p01248.

Gjerloev, J.W. and Hoffman, R.A.: 2014, The large-scale current system during auroral substorms, *J. Geophys. Res. Space Phys.* 119, 4591–4606, doi:10.1002/2013JA019176.

Hajra, R., Tsurutani, B.T., Lakhina, G.S., Lu, Q., and Du, A.: 2024, Interplanetary causes and impacts of the 2024 May superstorm on the geosphere: An overview, *Astrophys. J.* 974, 264, doi:10.3847/1538-4357/ad7462.

Hayakawa, H., Ebihara, Y., Mishev, A., Koldobskiy, S., Kusano, K., Bechet, S., et al.: 2025, The solar and geomagnetic storms in May 2024: A flash data report, *Astrophys. J.* 979, 49, doi:10.3847/1538-4357/ad9335.

Kleimenova, N.G., Gromova, L.I., Gromov, S.V., and Malysheva, L.M.: 2025a, Ground-based geomagnetic disturbances and Pi2 pulsations in the main phase of the superstorm on May 10, 2024, *Adv. Space Res.* 76, 7533–7545, doi:10.1016/j.asr.2025.04.025.

Kleimenova, N.G., Gromova, L.I., Gromov, S.V., and Malysheva, L.M.: 2025b, Planetary feature of the ionospheric current activity during the 10–11 October 2024 extremely strong magnetic storm, *J. Atmos. Solar-Terr. Phys.* 277, 106631, doi:10.1016/j.jastp.2025.106631.

Pierrard, V., Verhulst, T.G.W., Chevalier, J.-M., Bergeot, N., and Winant, A.: 2025, Effects of the geomagnetic superstorms of 10–11 May 2024 and 7–11 October 2024 on the ionosphere and plasmasphere, *Atmosphere* 16, 299, doi:10.3390/atmos16030299.

Pytte, T., McPherron, R.L., Hones, E.W., and West, H.I.: 1978, Multiple-satellite studies of magnetospheric substorms. III. Distinction between polar magnetic substorms and convection-driven negative bays, *J. Geophys. Res.* 83, 663–679, doi:10.1029/JA083iA02p00663.

Zou, Y., Shin, O., Gjerloev, J.W., Anderson, B.J., Waters, C.L., Wang, C.-P., Liang, J., Lyons, L.L., and Bhatt, A.: 2025, Are supersubstorms substorms? Extreme nightside auroral electrojet activities during the May 2024 geomagnetic storm, *J. Geophys. Res. Space Phys.* 130, e2024JA033303, doi:10.1029/2024JA033303.

.

DOI: 10.31401/WS.2026.proc.16

Geomagnetic effects of the substorms during the superstorm on 10-13 May 2024 on the midlatitudes magnetic field, observed at the Bulgarian station Panagyurishte

Guineva V., Raykova L., Werner R.

Space Research and Technology Institute (SRTI) – Bulgarian Academy of Sciences, Stara Zagora Department, Bulgaria; venetaguineva@gmail.com

Abstract

Space weather hazards pose a significant threat to both space-borne and ground-based technological systems. As society becomes increasingly dependent on the technologies, understanding the geophysical response to extreme solar activity has become essential for improving space weather forecasting and mitigating its impacts. This study investigates the occurrence of midlatitude positive bays (MPBs) during the geomagnetic superstorm of 10–13 May 2024, the strongest event of Solar Cycle 25. The analysis is based on geomagnetic observations from the midlatitude Bulgarian station Panagyurishte (PAG). MPBs, which represent the midlatitude magnetic signatures of magnetospheric substorms, are identified and characterized according to their occurrence, amplitude, and temporal evolution. A total of 15 MPBs were detected during 10–12 May 2024, with the largest event reaching maximal value of 88 nT. Their occurrence is examined in relation to the regional IL index derived from the IMAGE magnetometer PPN-NAL chain and the global SML index, both of which monitor auroral electrojet activity. The results reveal a close temporal correspondence between the identified MPBs and the negative excursions of the IL and SML indices, confirming that the observed bays are associated with individual substorm expansion phases. The unusually large number and amplitude of the MPBs indicate sustained and intense substorm activity throughout the May 2024 superstorm, demonstrating that the effects of extreme magnetosphere–ionosphere coupling extended well into middle latitudes. These findings contribute to a better understanding of substorm signatures during severe geomagnetic storms and emphasize the importance of continuous geomagnetic observations at midlatitude stations.

Keywords: superstorm, geomagnetic substorms, midlatitude positive bays

1. Introduction

Space weather, driven by solar flares and coronal mass ejections (CMEs), can produce severe disturbances in the Earth's magnetosphere and ionosphere, affecting modern technological systems. Severe geomagnetic storms may disrupt satellite operations, global navigation satellite systems (GNSS), radio communications, electric power transmission networks, and other critical technological infrastructures. Consequently, understanding the magnetospheric and ionospheric response to extreme solar events has become a key objective of modern space weather research [Pulkkinen, 2007; Schrijver et al., 2015].

The geomagnetic superstorm of 10–13 May 2024 (also referred to as the Mother's Day or Gannon superstorm) was the most intense event of Solar Cycle 25 and the first G5 (Extreme) geomagnetic storm since the Halloween storms of 2003. According to Lockwood et al. (2024), geomagnetic storms of such intensity belong to the class of great geomagnetic storms, which occur only rarely and represent some of the most severe manifestations of solar activity affecting the near-Earth environment. With a minimum Dst of −412 nT and a minimum SYM-H of −518 nT, the May 2024 event ranks among the strongest geomagnetic storms of the satellite era and represents the most intense storm since the Halloween storms of 2003,

providing an exceptional opportunity to investigate geospace dynamics under extreme solar wind forcing [Lockwood et al., 2024; Kleimenova et al., 2025; Hajra et al., 2024]. Recent studies have investigated its solar origin and interplanetary evolution [Lockwood et al., 2024; Wang et al., 2024], magnetosphere–ionosphere coupling and substorm development [Ohtani et al., 2025; Kleimenova et al., 2025], ionospheric and thermospheric disturbances [Astafyeva et al., 2024; Huang et al., 2024; Lazzus and Salfate, 2024], and regional geomagnetic effects over Europe [Guineva et al., 2025].

In addition to the exceptional ring current development reflected by the SYM-H minimum, the storm was characterized by repeated and intense magnetospheric substorms, including four supersubstorms (SSSs) [Hajra et al., 2025]. Two of these SSSs occurred during the daytime sector and were not associated with MPBs at PAG, whereas the other two occurred during the evening-to-midnight sector considered in the present study and were accompanied by MPB activity.

Among the characteristic ground magnetic manifestations of magnetospheric substorms are midlatitude positive bays (MPBs), which are interpreted as magnetic signatures of the substorm current wedge observed at middle latitudes. Although MPBs have been documented during geomagnetic storms of varying intensity, observations during an extreme G5 superstorm remain scarce. Because the May 2024 event combined an exceptionally intense magnetic storm with repeated substorm activity, it offers a unique opportunity to investigate the occurrence and properties of MPBs under extreme space weather conditions. Such observations contribute to a better understanding of the midlatitude response to substorms and of magnetosphere–ionosphere coupling during great geomagnetic storms. The analysis focuses on the evening-to-midnight sector (20:00–02:00 MLT), when substorm signatures are expected to be most pronounced. The present study investigates the occurrence, temporal evolution and characteristics of MPBs recorded at the Bulgarian station Panagyurishte PAG, on 10-12 May 2024, encompassing the main phase and the most of the recovery phase of the superstorm. A total of 15 MPBs were identified during the analyzed interval, providing a valuable data set for investigating substorm activity at middle latitudes during an extreme geomagnetic storm.

2. Data used

The interplanetary and geomagnetic conditions during the superstorm were examined by data of OMNI database (https://cdaweb.gsfc.nasa.gov/).

To characterize the global magnetic disturbances we used the SML index from the SuperMAG database (https://supermag.jhuapl.edu/).

To follow the magnetic field disturbances over Europe we used data from the IMAGE database (https://space.fmi.fi/image/www/il_index_panel.php), specifically the X-component variations recorded at the stations of the PPN–NAL chain, together with the IL index derived from measurements at the same stations. The PPN – NAL chain covers a longitudinal band from 12° to 27°E (96° – 113° GMLon.). Because Panagyurishte (24°E, 96.9° GMLon) is located within the longitudinal sector covered by the PPN–NAL chain, the IL index provides a useful regional measure of substorm-related magnetic activity for comparison with the MPBs observed at PAG.

To study the midlatitude disturbances at Panagyurishte (PAG), we used data from INTERMAGNET (https://imag-data.bgs.ac.uk/GIN_V1/GINForms2). The X-component variations were obtained from the Catalog of Magnetic Variations at the Panagyurishte Station (PAG), developed at the Space Research and Technology Institute of the Bulgarian Academy of Sciences (http://space.bas.bg/Catalog_MPB/). For the data covering the superstorm a special additional processing was performed. Composite plots of the midlatitude

positive bays identified using the methodology developed in Werner et al. (2021) and Guineva et al. (2024a) were prepared for the evening-to-midnight period on 10–12 May 2024.

To compare the substorm activity manifested by the midlatitude positive bays (MPBs) observed at PAG with the overall substorm development during the same periods, we used the global SML index from SuperMAG (https://supermag.jhuapl.edu/indices/) and the regional IL index from the IMAGE database (https://space.fmi.fi/image/www/il_index_panel.php).

3. Interplanetary and geomagnetic conditions

The interplanetary and geomagnetic conditions during the 10–13 May 2024 superstorm and its main characteristics have been discussed in a number of studies [e.g., Hajra et al., 2024; Lockwood et al., 2024; Kleimenova et al., 2025; Guineva et al., 2025, and references therein]. Since our primary aim is to present the timing of MPB occurrence in the context of the superstorm development, only its basic characteristics are briefly described below.

The May 2024 superstorm was a rare event, classified as G5 (Kp = 9), with a minimum hourly Dst index of −412 nT and a minimum 1-min SYM/H index of −518 nT, reached at 02:00 UT and 02:14 UT on 11 May 2024, respectively. In terms of intensity, it is comparable to the strongest geomagnetic storms observed since the beginning of the space age. Based on the geomagnetic latitude reached by the auroral oval during each night, the second night of the superstorm (11 May) ranked as the third most extensive auroral event, and the first night (10 May) ranked sixth [Lockwood et al., 2024]. The superstorm resulted from a complex sequence of solar eruptions in May 2024. A series of eruptive events originated from the active region AR13664/8. This active region was characterized by strong and persistent magnetic flux over approximately three days and produced multiple M-class flares and four X-class flares, each accompanied by a halo CME. Based on combined satellite observations, five CMEs were identified near Earth within a 28-h interval. Their interaction resulted in a complex interplanetary magnetic field structure [Weiler et al., 2025]. These knotty near-Earth solar wind and IMF conditions contributed to the development of a superstorm with a complex structure, as well.

The superstorm had a three-step storm main phase, from ~17:15 UT on May 10, lasted ~9 hours, with SYM/H intensity of -518 nT. The recovery phase was highly structured due to the passage of three magnetic clouds (MCs) by the Earth and lasted approximately 2.8 days. The SYM/H index returned to approximately its initial zero level only about six days after the beginning of the recovery phase. During the superstorm, numerous intense substorms, including four supersubstorms (SSSs). The storm-scale evolution provides the background for the analysis of the substorm-related magnetic disturbances at midlatitudes presented below. Figure 1 shows the interplanetary and geomagnetic conditions from 10 to 14 May 2024. From top to bottom, the panels show the IMF magnitude (B), the north–south IMF component (Bz), the solar wind velocity (V), proton density (Np), temperature (T), dynamic pressure (P), and the AL and SYM/H indices. The occurrence times of the MPBs detected at PAG on 10–12 May 2024 are indicated by red vertical lines.

4. Results and discussion

On 10, 11, and 12 May 2024, a total of 15 MPBs associated with substorm activity were detected during the evening-to-midnight sector (18:00–24:00 UT, corresponding approximately to 20:00–02:00 MLT). Their occurrence times are indicated in Figure 1. In a previous study, we investigated the effects of supersubstorms at the midlatitude station PAG

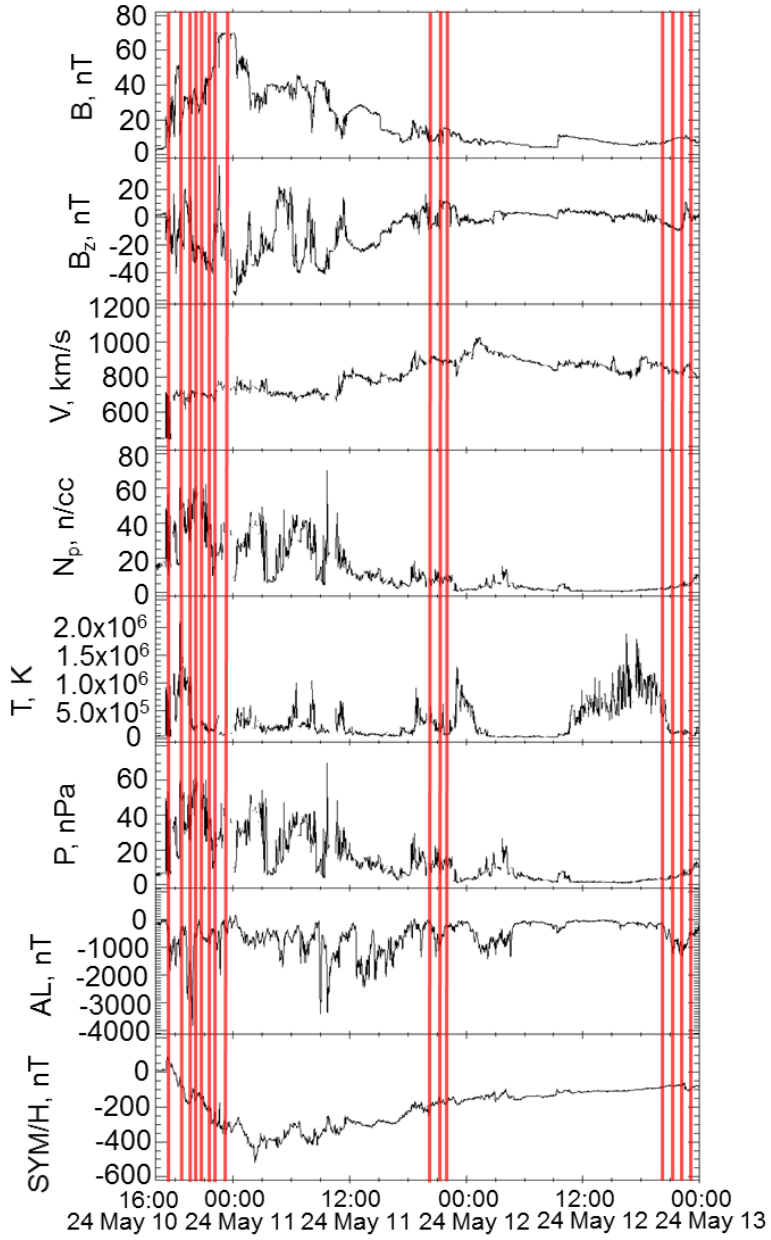


Figure 1. *Interplanetary and geomagnetic conditions during the superstorm on 10-13 May 2024. The red vertical lines indicate the time of the registered MPB's on 10, 11 and 12 May 2024.*

Table 1. *Some parameters of the MPB's detected at PAG on 10-12 May 2024: the beginning time, the time of maximum and the maximal value of the MPB's. The serial number of the MPB and the occurrence date are given in the two upper rows.*

No	1	2	3	4	5	6	7	8	9	10	11	12	13	14	15
	10.05.2024								11.05.2024			12.05.2024			
Beginning time, UT	17:02	18:18	19:24	20:09	20:38	21:13	21:58	22:54	20:37	21:05	21:30	20:18	21:05	22:03	23:03
Time of max., UT	17:39	18:55	19:56	20:25	20:49	21:29	22:34	23:27	20:49	21:12	21:35	20:38	21:31	22:23	23:20
Max., nT	88	63	75	42	37	28	64	67	55	14	5	6	12	16	9

[Guineva et al., 2025]. In the present study, we focus on MPBs associated with substorms occurring in the evening-to-midnight sector. Table 1 summarizes the main characteristics of the identified MPBs. The first two rows give the sequential numbers of the MPBs and their dates of occurrence. The rows below give, for each MPB, the beginning time, time of maximum, and maximum amplitude.

Eight MPBs were identified on 10 May, three on 11 May, and four on 12 May 2024.

4.1. Midlatitude positive bays, registered on 10 May 2024

On 10 May 2024, immediately after the onset of the superstorm, eight consecutive MPBs were observed, associated with substorm activity at higher latitudes. Figure 2 shows, from top to bottom, the SML and SMU indices, the IL index, and the X-component variations at PAG from 17:00 to 24:00 UT.

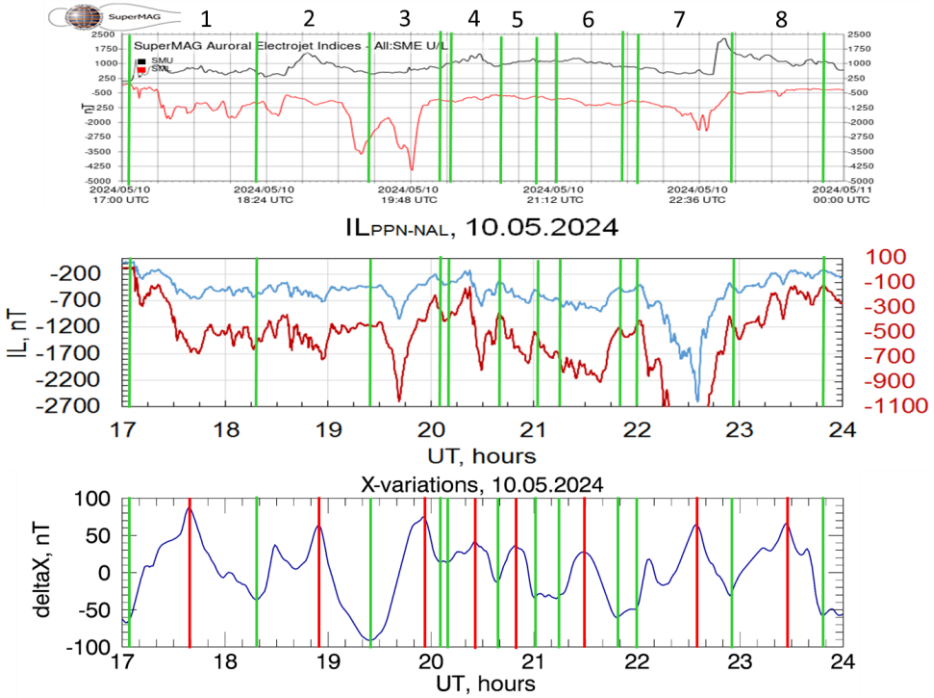


Figure 2. *Global and regional magnetic indices and the 8 registered MPB's from 17 to 24 UT on 10 May 2024: SML and SMU indices (up), IL index by the PPN-NAL chain (middle), and X variations at PAG station (bottom). The green vertical lines indicate the beginning and end times of the detected MPB's at PAG, and the red lines – the times of MPB maxima.*

The green vertical lines indicate the beginning and end times of the MPBs, while the red lines indicate their times of maximum amplitude. Above Figure 2, the serial numbers of the MPBs are written. The regional IL index is presented on two scales to better resolve the details of moderate-to-strong disturbances.

Figure 3 shows the X-component variations recorded at the IMAGE stations of the PPN–NAL chain from 17:00 to 21:00 UT (left panel) and from 21:00 to 24:00 UT (right panel). The green vertical lines indicate the beginning times of the midlatitude positive bays.

Figure 4 presents SuperMAG magnetic field maps from the poleward region to 30° geomagnetic latitude at the times of the MPB maxima. The dark red ellipses mark the area of the IMAGE stations.

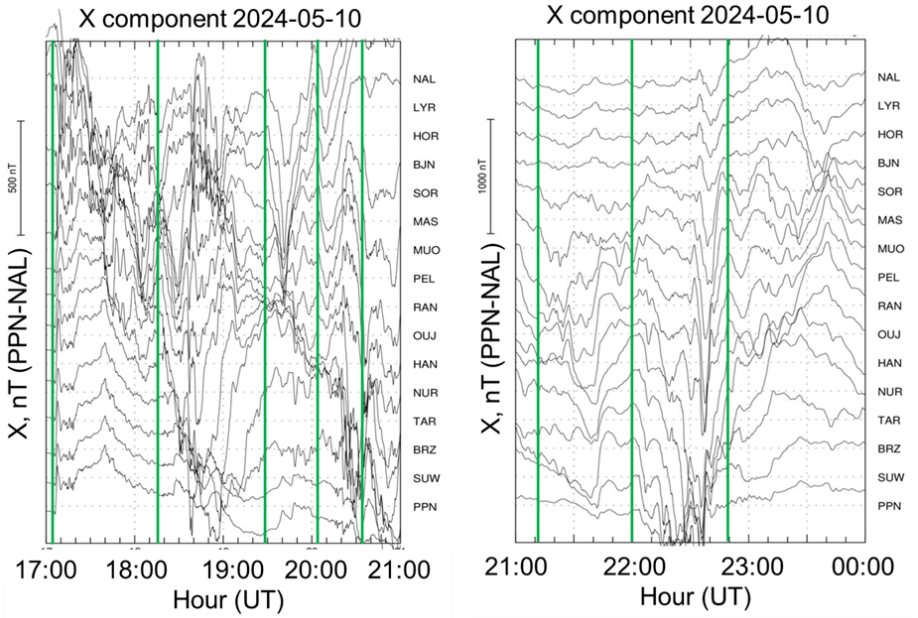


Figure 3. *IMAGE magnetic field data, 10.05.2024, from 17 to 21 UT (left panel) and from 21 to 24 UT (right panel).*

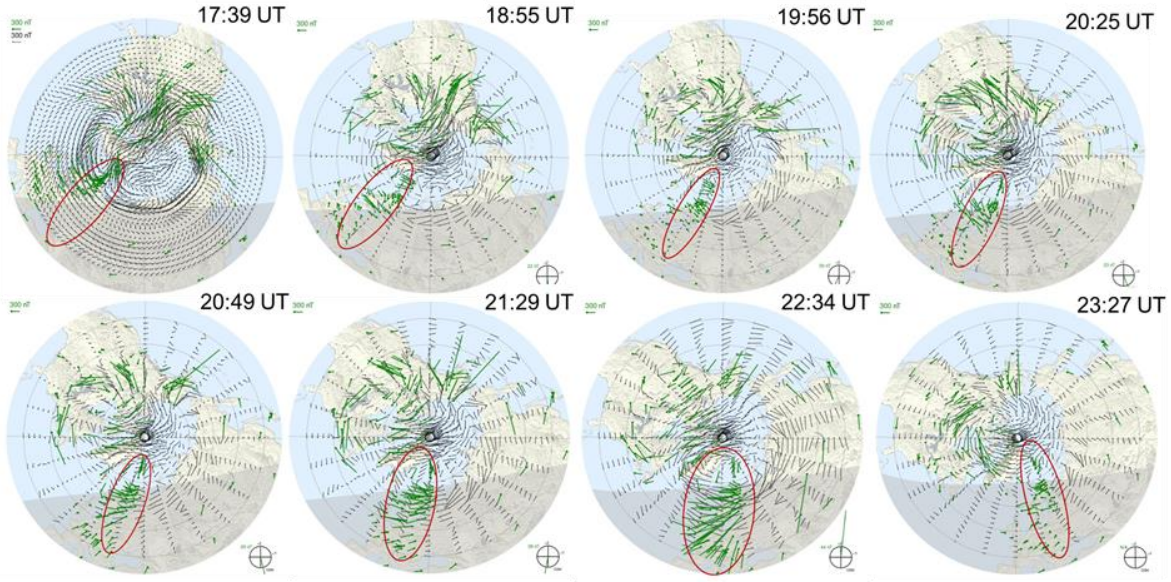


Figure 4. *SuperMAG magnetic field data at the maxima times of the MPB’s on 10.05.2024. The dark red ellipses indicate the area of the IMAGE magnetometers.*

All MPBs observed on 10 May 2024 occurred during the main phase of the superstorm.

MPB 1. The first MPB occurred shortly after the onset of the superstorm. At the same time, negative excursions of both the IL and SML indices reached approximately −1700 nT, indicating strong substorm activity over the European sector (Figure 2). The X-component variations at the PPN–NAL stations simultaneously show pronounced disturbances at high geomagnetic latitudes (Figure 3). The magnetic field map (the first one of the upper row in Figure 4) confirms the presence of magnetic variations at high latitudes over Europe. This MPB had the largest amplitude, reaching 88 nT.

MPB 2. During the second MPB, stronger substorm disturbances were observed over Europe, as indicated by the IL index (Figure 2). The PPN–NAL data show pronounced substorm disturbances at auroral latitudes (Figure 3), which are also clearly visible in the magnetic field map (Figure 4). The MPB reached a maximum amplitude of 63 nT.

MPB 3. The third MPB was associated with the second intensification of the first supersubstorm (SSS) during the superstorm. It is discussed in detail in Guineva et al., 2025, where the effects of the supersubstorms (SSS) at midlatitude, namely at PAG, are studied. This SSS developed in two intensifications, as indicated by the SML index (Figure 2). During the first intensification, the westward electrojet was not located over Europe, and consequently no pronounced substorm disturbance was observed in the European sector, as indicated by the IL index. During the second intensification, the European sector turned out under the westward electrojet, resulting in a strong substorm disturbance with an IL minimum of approximately −1100 nT. This disturbance represented a substantial component of the global substorm activity and extended over auroral and high latitudes (Figures 3 and 4). The resulting MPB at PAG reached a maximum amplitude of 75 nT.

MPB 4 – 6. MPBs 4–6 were associated with successive, gradually intensifying substorm disturbances, clearly seen in Figures 2–4. Their maximum values were 42, 37, and 28 nT, respectively.

MPB 7. The seventh MPB was associated with the second supersubstorm (SSS) during the May superstorm. This SSS was examined in detail by Guineva et al. (2025). The substorm disturbance observed at the PPN–NAL chain was the strongest during the superstorm, with the IL index reaching approximately −2700 nT (Figure 2). During this SSS, magnetic disturbances extended over the largest latitudinal range (Figures 3 and 4). The X-component variations at PAG closely followed the variations in the IL index, and the MPB reached a maximum of 64 nT, coinciding with the maximum development of the SSS.

MPB 8. The eighth MPB was associated with a comparatively weak substorm disturbance at auroral latitudes and reached a maximum amplitude of 67 nT.

5.2. Midlatitude positive bays, occurred on 11 May 2024

On 11 May 2024, during the recovery phase of the superstorm, three MPBs were detected between 20:00 and 22:00 UT. Figure 5 shows the SML and IL indices and the X-component variations at PAG (left panel), together with the X-component variations at the PPN–NAL chain (right panel).

The maps of the horizontal magnetic variations at the maxima of the detected midlatitude bays are presented in Figure 6.

Three consecutive, gradually decreasing substorm intensifications are evident in the SML and IL indices (Figure 5). Initially, the processing procedure identified a single MPB encompassing all three intensifications. This resulted from the characteristics of the detection procedure and the initial constraints imposed on the analysis. Inspection of the temporal evolution of the X-component variations showed that the three intensifications could be distinguished as separate substorm-related disturbances. Therefore, the initially identified MPB was divided into three individual MPBs corresponding to the three successive intensifications. The PPN–NAL X-component data and magnetic field maps (Figures 5 and 6) show that the three substorms occurred at auroral latitudes and became progressively weaker. The MPB maxima were 55, 14, and 5 nT, respectively.

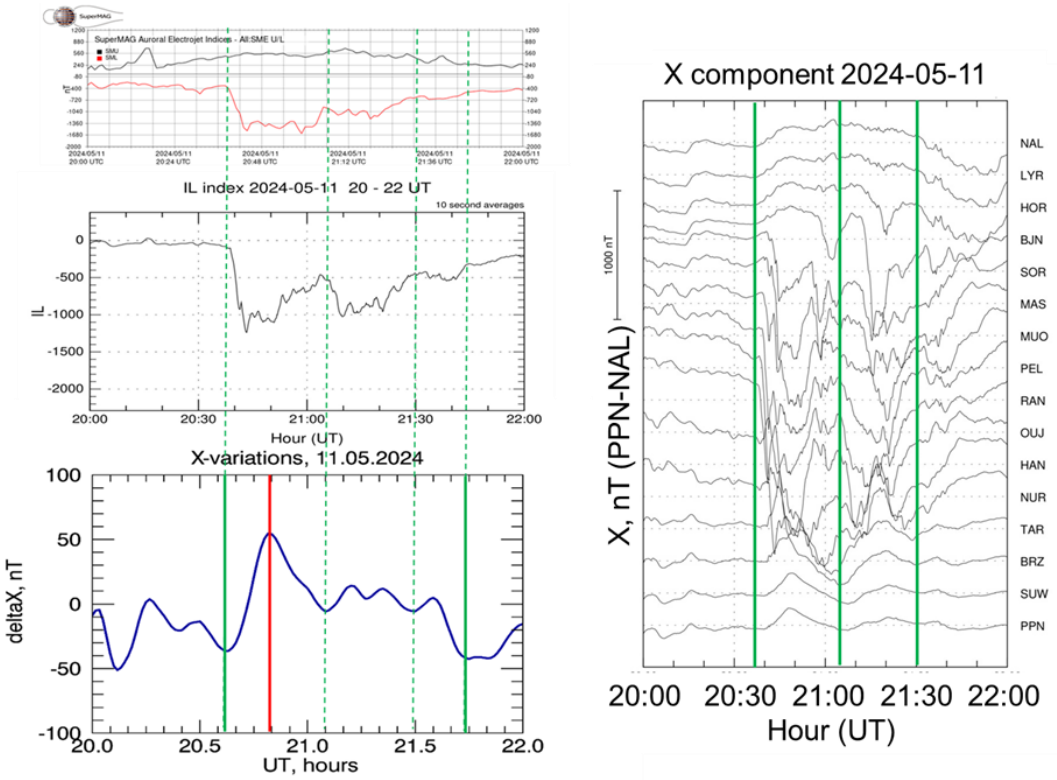


Figure 5. *Global and regional magnetic indices and the registered MPB from 20 to 22 UT on 11 May 2024 (left panel): SML and SMU indices (up), IL index by the PPN-NAL chain (middle), and X variations at PAG station (bottom). The green vertical lines indicate the beginning and end times of the detected MPB at PAG, and the red line – the time of MPB maximum. The green vertical dotted lines mark the boundaries of the three consecutive substorm intensifications, observed by the SML and IL data. The right panel presents the magnetic field data from the PPN-NAL chain from the same time interval (20-22 UT on 11.05.2024). The green vertical lines show the beginning times of the registered substorm intensifications.*

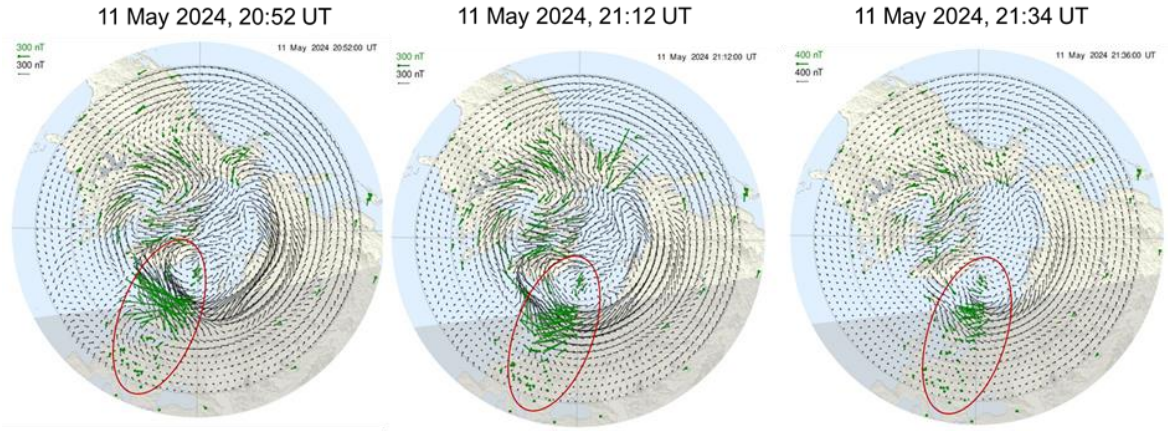


Figure 6. *SuperMAG magnetic field data at the maxima times of the MPB's on 11.05.2024. The dark red ellipses indicate the area of the IMAGE magnetometers.*

5.3. Midlatitude positive bays on 12 May 2024

On 12 May 2024, during the late recovery phase, four consecutive MPBs were detected between 20:00 and 24:00 UT. Figure 7 shows, from top to bottom in the left panel, the SML and IL indices and the X-component variations at PAG from 20:00 to 24:00 UT. The right panel shows the X-component variations at the PPN–NAL IMAGE stations. The green vertical lines in the PAG panel indicate the beginning and end times of the identified MPBs, while the red lines indicate their maxima times. The dotted green lines in the SML and IL panels mark the MPB beginning times. The green vertical lines in the PPN–NAL X-component variations panel indicate the corresponding MPB beginning times.

Figure 8 presents the magnetic field maps at the times of the MPB maxima. The dark red ellipses indicate the area of the IMAGE magnetometers.

It is seen that the examined midlatitude bays correspond temporally to substorm intensifications at auroral latitudes. Their maximal values were 6, 12, 16, and 9 nT, respectively.

All 15 midlatitude positive bays observed on 10–12 May 2024 were temporally associated with substorm activity at auroral or high latitudes. A good correspondence between the different data sets was observed. In particular, the X-component variations at PAG generally followed the mirrored temporal evolution of the IL index, while the negative excursions of both IL and SML indicated enhanced substorm activity. The most intense MPBs occurred during the main phase of the superstorm, whereas substantially weaker bays were observed during the late recovery phase as geomagnetic activity gradually decreased. For comparison, the most intense MPBs previously observed at Panagyurishte during geomagnetic storms generally have maxima of 20–30 nT, with only a few events exceeding 30 nT [Guineva et al., 2024b]. During the May 2024 superstorm, considerably larger MPB maxima were observed, representing the highest values in the PAG record since the beginning of regular 1-min measurements in 2007. Five MPBs had maxima between 60 and 90 nT, three had maxima between 30 and 60 nT, six had maxima between 5 and 20 nT, and one had a maximum of 28 nT.

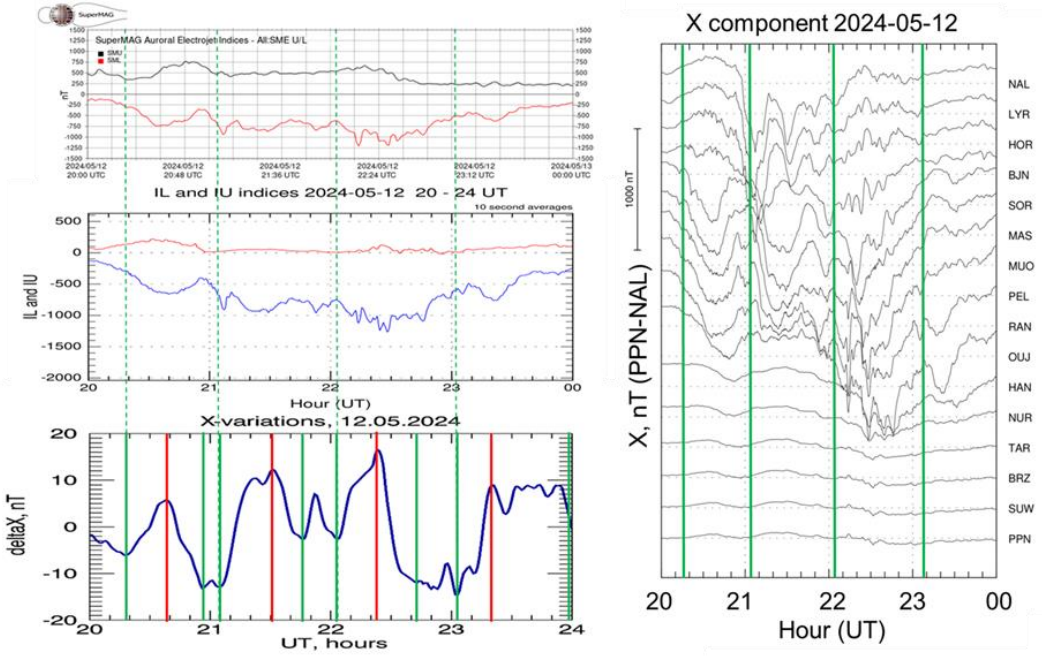


Figure 7. *The same as in Fig.5, for the 4 MPB's registered on 12.05.2024. The vertical green dotted lines SML and IL panels (the two upper figures in the left panel) indicate the beginning times of the detected MPB's at PAG.*

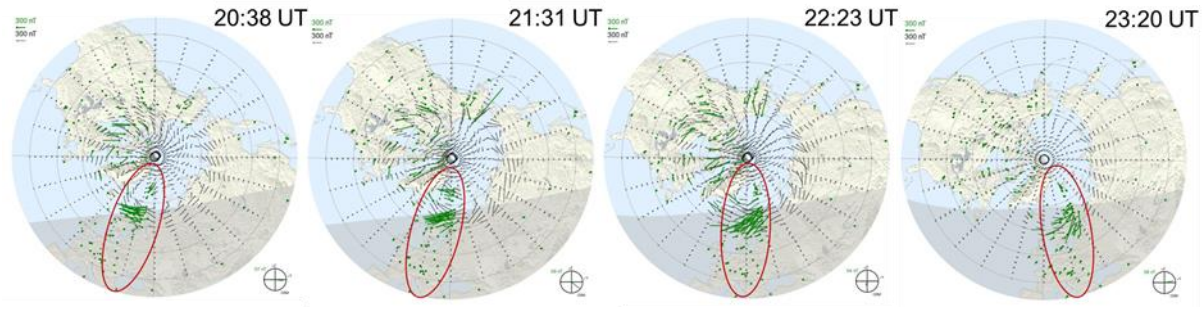


Figure 8. *The same as in Fig.6 for the maxima times of the MPB’s observed on 12.05.2024.*

5. Summary

The May 2024 superstorm was characterized by both an exceptionally strong storm-time ring current and recurrent substorm activity. At the Panagyurishte (PAG) station, 15 midlatitude positive bays (MPBs) were identified during the evening-to-midnight sector. The MPBs were temporally associated with enhanced substorm activity and were particularly pronounced during the two supersubstorms (SSSs) that developed in this sector.

On 10 May, eight consecutive MPBs were observed shortly after the onset of the superstorm, during its main phase. They were associated with substorm activity extending over auroral and high latitudes in the European sector. Two of these MPBs were associated with the two SSSs that occurred during the evening-to-midnight interval.

On 11 May, during the recovery phase, three consecutive MPBs were identified between 20:00 and 22:00 UT. They corresponded to three successive substorm intensifications at auroral latitudes, which were observed in the IL index and in the X-component variations at the PPN–NAL chain stations. The initial processing procedure identified these three intensifications as a single MPB; subsequent inspection and additional processing allowed them to be distinguished as three separate MPBs.

On 12 May, during the late recovery phase, four consecutive MPBs were detected between 20:00 and 24:00 UT, associated with substorm activity in the auroral European sector.

The MPBs were temporally associated with negative excursions of both the IL and SML indices, consistent with their relation to enhanced substorm activity. The X-component variations at PAG generally followed the mirrored temporal evolution of the IL index, demonstrating a close temporal relationship between the regional substorm activity and the midlatitude magnetic response.

The most intense MPBs occurred during the main phase of the superstorm, whereas substantially weaker bays were observed during the late recovery phase. The MPB amplitudes during this event were unusually high, representing the largest values in the PAG record since the beginning of regular 1-min measurements in 2007. Five MPBs had maxima between 60 and 90 nT, three had maxima between 30 and 60 nT, six had maxima between 5 and 20 nT, and one MPB had a maximum of 28 nT. The largest MPB reached 88 nT.

The analysis also demonstrates that the identification of MPBs under extremely disturbed geomagnetic conditions can be challenging. Strong and rapid magnetic variations may produce complex MPB profiles, including multiple maxima and, in some cases, pronounced minima between successive peaks. Such features may affect the results of automated or semi-automated detection procedures. Therefore, under extreme geomagnetic conditions, the assumptions and limitations of the detection methodology should be carefully considered, and individual events may require additional processing and verification.

These results demonstrate that pronounced midlatitude positive bays can occur repeatedly during an extreme geomagnetic superstorm and provide clear ground-based signatures of substorm activity well equatorward of the auroral zone.

Acknowledgements: We acknowledge the SuperMAG collaboration (Gjerloev et al. 2012). The authors are grateful to the creators of the databases SuperMAG (https://supermag.jhuapl.edu/), IMAGE (http://space.fmi.fi/image/), OMNI (https://cdaweb.gsfc.nasa.gov/), and INTERMAGNET (http://intermagnet.org/) for the opportunity to use them in this work.

References

Akasofu, S.-I.: 1964, The development of the auroral substorm, *Planet. Space Sci.* 12, 273–282, doi:10.1016/0032-0633(64)90151-5.

Astafyeva, E., Maletckii, B., Förster, M., Ouar, I.D., Huba, J.D., Hairston, M.R., and Coley, W.R.: 2025, Electrodynamic and ionospheric puzzles of the 10–11 May 2024 geomagnetic superstorm, *J. Geophys. Res. Space Phys.* 130, e2024JA033284, doi:10.1029/2024JA033284.

Guineva, V., Werner, R., Bojilova, R., Raykova, L., Atanassov, A., and Valev, D.: 2024a, A methodology to estimate the MPB parameters, in *Proceedings of the 47th Annual Seminar "Physics of Auroral Phenomena"*, 16–19, doi:10.51981/2588-0039.2024.47.003.

Guineva, V., Werner, R., Bojilova, R., Raykova, L., Atanassov, A., and Valev, D.: 2024b, Analysis of substorms related to strong MPB at Panagyurishte station in 2022, in *Proceedings of the Sixteenth Workshop "Solar Influences on the Magnetosphere, Ionosphere and Atmosphere"*, 56–63, doi:10.31401/WS.2024.proc.

Guineva, V.H., Despirak, I.V., Werner, R., Lubchich, A.A., Raykova, L., and Bojilova, R.: 2025, The geomagnetic midlatitude effects of the supersubstorms during the May 10–12, 2024 superstorm, in *Proceedings of the Seventeenth Workshop "Solar Influences on the Magnetosphere, Ionosphere and Atmosphere"*, 92–109, doi:10.31401/WS.2025.proc.

Hajra, R., Tsurutani, B.T., Lakhina, G.S., Lu, Q., and Du, A.: 2024, Interplanetary causes and impacts of the 2024 May superstorm on the geosphere: An overview, *Astrophys. J.* 974, 264, doi:10.3847/1538-4357/ad7462.

Hajra, R., Tsurutani, B.T., Lu, Q., Du, A., and Lakhina, G.S.: 2025, Supersubstorms during the May 2024 superstorm, *J. Space Weather Space Clim.* 15, 51, doi:10.1051/swsc/2025047.

Kleimenova, N.G., Gromova, L.I., Gromov, S.V., and Malysheva, L.M.: 2025, Ground-based geomagnetic disturbances and Pi2 pulsations in the main phase of the superstorm on May 10, 2024, *Adv. Space Res.* 76, 7533–7545, doi:10.1016/j.asr.2025.04.025.

Lazzús, J.A. and Salfate, I.: 2024, Report on the effects of the May 2024 Mother's Day geomagnetic storm observed from Chile, *J. Atmos. Solar-Terr. Phys.* 261, 106304, doi:10.1016/j.jastp.2024.106304.

Lockwood, M., Owens, M.J., Brown, W., and Vázquez, M.: 2025, The 2024 May event in the context of auroral activity over the past 375 yr, *Mon. Not. R. Astron. Soc.* 540, 3596–3624, doi:10.1093/mnras/staf827.

Milan, S.E., Clausen, L.B.N., Coxon, J.C., Carter, J.A., Walach, M.-T., Laundal, K.M., et al.: 2017, Overview of solar wind–magnetosphere–ionosphere–atmosphere coupling and the magnetospheric substorm, *Space Sci. Rev.* 206, 547–573, doi:10.1007/s11214-017-0333-0.

Pulkkinen, A.: 2007, Space weather: Terrestrial perspective, *Living Rev. Solar Phys.* 4, 1, doi:10.12942/lrsp-2007-1.

Schrijver, C.J., Kauristie, K., Aylward, A.D., Denardini, C.M., Gibson, S.E., Glover, A., et al.: 2015, Understanding space weather to shield society: A global road map for 2015–2025, *Adv. Space Res.* 55, 2745–2807, doi:10.1016/j.asr.2015.03.023.

Wang, R., Liu, Y.D., Zhao, X., and Hu, H.: 2024, Unveiling key factors in solar eruptions leading to the solar superstorm in 2024 May, *Astron. Astrophys.* 692, A112, doi:10.1051/0004-6361/202452008.

Weiler, E., Möstl, C., Davies, E.E., Veronig, A.M., Amerstorfer, U.V., Amerstorfer, T., Le Louëdec, J., Bauer, M., Lugaz, N., Haberle, V., Rüdisser, H.T., Majumdar, S., and Reiss, M.: 2025, First observations of a geomagnetic superstorm with a sub-L1 monitor, *Space Weather* 23, e2024SW004260, doi:10.1029/2024SW004260.

Werner, R., Guineva, V., Atanassov, A., Bojilova, R., Raykova, L., Valev, D., Lubchich, A., and Despirak, I.: 2021, Calculation of the horizontal power perturbations of the Earth surface magnetic field, in *Proceedings of the Thirteenth Workshop "Solar Influences on the Magnetosphere, Ionosphere and Atmosphere"*, 159–164, doi:10.31401/WS.2021.proc.

DOI: 10.31401/WS.2026.proc.17

Statistical Analysis of the B-star Drag Term and Solar, and Geomagnetic Activity Indices

Komendant V.H.

Space Research and Technology Institute, Bulgarian Academy of Sciences
vova_komendant@space.bas.bg, votan1360@gmail.com

Abstract

Vast increase in population of the artificial Earth satellites (AES) in near-Earth space, and prediction of their lifetime and location, maintain modeling and prediction of the state of the upper Earth atmosphere relevant for decades. The availability of modern processing tools and the increase of computational possibilities don't provide accurate prediction results. The data of the atmospheric models are used in the models of prediction of movement of the AES for the fast and approximate calculation of the ephemerides of the satellites. One of the popular prediction models are SGP models. They use the two line elements (TLE) format for their calculations. There is the B-star drag term (B*) among them. It is the modified ballistic coefficient which is used to account for atmospheric drag. The B-star for satellites that move in an uncontrolled mode were taken for analysis. The study period for the drag term and indices of solar and geomagnetic activity is: end of the 23rd solar cycle, the 24th solar cycle, and minimum between them. This work is the compilation of three statistical methods for processing the B-Star, and the solar and geomagnetic indices. They are: windowed Fourier transform, multiple regression models, and cross-spectral analysis of two time series. The first method gives periodic components in the studied data and time of their existence. With the second method, I select the indices of solar and geomagnetic activity that had the greatest impact on the B-star. The third method allows to track relationships between the found periods in the frequency domain.

Keywords: *B-star drag term, solar activity, space weather*

Introduction

The existence of a gas layer of our planet has been known for a long time. Practical experiments for establishing its physical properties were held at least from the 17th century (experiments of Torricelli, Pascal's researches, Boyle-Mariott's law [Webster, 1965]). The studies of the Earth's atmosphere, Sun and geomagnetic field were separate science directions at those times and for a long time developed separately. The studies of the atmosphere were held on with the meteor observations, the self-airglow, the weather balloons, the rocket measurements and the radars from the end of the 19th to the middle of the 20th centuries. The basic knowledge of temperature stratification of the atmosphere of the Earth and corresponding terminology were formed before the launch of the first artificial satellite of the Earth. However, only satellite measurements gave the possibility to receive long and global data about structure, composition and variability of the Earth's upper atmosphere. First attempts to link the atmosphere, Sun and geomagnetic field studies in one science direction began after cyclic behaviour of the solar activity discovery in approximately 1844 year [Schwabe, 1844; Wolf, 1852] and Sir Edward Sabine's publication in 1852 year [Sabine, 1852]. The Carrington geomagnetic storm of 1859 year [Cliver and Svalgaard, 2004; Georgieva and Veretenenko, 2023], the first documented case of the influence of the solar activity on the ground technical systems, only fueled those attempts. After that, a lot of studies

appeared which consistently pointed to solar-terrestrial relationships. It was possible to demonstrate those relationships statistically, but the full physical mechanisms weren't known [Georgieva and Veretenenko, 2023].

Satellite measurements showed that the space between the Sun and the Earth is filled with plasma and magnetic fields [Parker, 1958; Neugebauer and Snyder, 1962]. They made it possible to measure its parameters and determine its configuration [Coleman, 1966; Dessler, 1967]. Technical equipment improvement made it possible to receive and process the bigger volume of data about the physical state of the near Earth space [Asenovski et al., 2022]. All that data helps in development of main physical mechanisms of the solar-terrestrial relationships. The complex of processes which determines the state of the near-Earth space under the influence of the solar activity was established. The chain of the solar-terrestrial interactions is as follows. Solar ultraviolet and x-ray radiation interact directly with the Earth's upper atmosphere, without interacting with the magnetosphere, causing atmospheric heating and expansion, which leads to an increase in atmospheric density at fixed orbital altitudes. After solar radiation the solar plasma, with a frozen-in magnetic field, reaches the Earth (within tens hours or several days, depending on its speed). Depending on its physical parameters (speed, pressure, density, magnetic field orientation) magnetic reconnection occurs on the day side of the magnetosphere, after which part of energy transfers through the magnetosphere tail and plasma sheet (within geomagnetic storms) into regions closer to Earth's upper atmosphere. Despite significant progress, many processes of energy transfer from solar plasma streams to Earth's magnetosphere and upper atmosphere still remain the subject of active research. In general, energy transfers through mechanisms of geomagnetic storms, particle precipitation and Joule heating, which lead to an increase in temperature of Earth's upper atmosphere [Georgieva and Veretenenko, 2023]. The combined influence of solar ultraviolet, x-ray and corpuscular radiations of the solar activity is dangerous not only for ground-base systems but for artificial satellites too [Kirov et al., 2022a]. High-energy electrons can shut down their systems or even damage them. That is typical for geostationary satellites, navigation satellites in the medium Earth orbits and satellites with high elliptical orbits (for example how it was with Anik E1 and Anik E2 satellites in 1994) [Lam et al., 2012]. Increase in the Earth's atmosphere density in low orbital altitudes leads to accelerated and premature orbital decay of low-Earth-orbit satellites, for example the loss of 38 SpaceX satellites in February 2022 [Hapgood et al. 2022].

Periodic processes present in the solar activity are transmitted through various solar-terrestrial interaction mechanisms and manifest themselves in variations of geomagnetic activity [Kirov et al., 2015] and in the parameters and density of the upper atmosphere [Thayer et al., 2008]. Therefore, spectral analysis is one of the methods to confirm the relations between them [Koucká Knížová et al., 2018]. Spectral analysis of solar and geomagnetic indices have already been performed. The periodicities in solar activity have been reliably identified: 11 years (Schwabe cycle) [Kirov et al., 2022b], 40-60 days, 27 days and its harmonics 13.5 and 9 days [Qian et al., 2010]. Many of these periodicities were identified in changes of the upper atmosphere density [Xu et al., 2015] and geomagnetic activity. Moreover reliably known about semiannual and annual variations [Qian et al., 2009], but their interpretation is complicated [Jones et al., 2018] because of mixing several factors: seasonal changes of atmosphere consistency [Qian et al., 2009]; the Russell-McPherron effect [Russell and McPherron, 1973]; changes in interaction geometry of solar wind with magnetosphere; changes of thermospheric circulation. Hale magnetic cycle - 22 years cycle, is also well established [Hathaway, 2015]. It is worth mentioning that the established periodicities aren't fixed. Their duration can vary due to the non-stationarity of solar activity

[Georgieva, 2025]. For example, the duration of the solar rotation period (~27 days) observed in solar activity indices can vary approximately from 25 to 30 days, depending on the latitude of active regions and their evolution.

It is important to take into account the aerodynamic drag in the Earth's upper atmosphere for the movement and lifetime propagation of the low orbit artificial satellites [Gondelach and Linares, 2020]. Empirical and semi empirical models of the Earth's upper atmosphere were developed for that purpose. Those models are usually used in the high accuracy numerical propagators of the Earth's artificial satellites. Data of the specific satellites equipped with accelerometers or other instrumentations are used to build those models [Emmert, 2015]. That data is limited by number of missions, altitude range and time of their functioning. Despite their widespread use, they need regular calibration [Doornbos et al., 2008; He et al., 2018]. That's why the alternative sources of information are interesting. One of them is the catalog of orbital data in two line element format (TLE) provided by NORAD and publicly available. TLE is the standard data format containing mean orbital elements and auxiliary parameters for Earth-orbiting objects used with the SGP orbit propagator. The B-star drag term (B*) is used in that propagator to account for atmospheric drag on artificial satellites. In most of studies TLE orbital parameters are used to retrieve the atmospheric density without using of B* [Ashruf et al., 2026; Yamamoto and Sori, 2026]. B* considers like a technical parameter for orbit propagation in the SGP model. In present study B* is used as an effective parameter that reflects the atmospheric density variations. It should be mentioned that B* is a semi empirical parameter and its variations are determined not only by the atmospheric density variations but also by the characteristics of the SGP model, orbit determination errors, and variations in the satellite's ballistic parameters. The TLE catalog has been published for more than ten thousand objects with different orbital parameters since 1980. Modern data on atmospheric density variations are retrieved from the measurements of accelerometers and they are not direct measurements of the atmospheric density. Therefore, using B* variations to describe variations in atmospheric density is an interesting alternative.

2. Data used

In present study the B-star drag term (B*) from the TLE format was used as an effective parameter that reflects the atmospheric density variations.

$$B = \frac{C_D * A}{m} \quad (1)$$

where B – the ballistic coefficient, C_D – the aerodynamic drag coefficient. If the mean free path of air molecules is much larger than the geometric size of the satellite, then C_D is close to 2, A – the midsection area (cross–sectional area of the satellite), m – the satellite mass.

The B–star drag term coefficient is related to the ballistic coefficient with next equation:

$$B^* = B * \frac{\rho_0}{2} \quad (2)$$

where B* – the modified ballistic coefficient or B–star drag term, B – the ballistic coefficient, ρ_0 – some standard density value for a given altitude. The B–star drag term coefficient has the dimension of $1/R_E$, where R_E=6 371 km is the radius of the Earth.

The B* for the three satellites was taken for the calculation:

NORAD ID 04922 - COSMOS 394 i = 65.8 °; e = 0.0027; rmin = 490 km; rmax = 517 km (Figure 1).

NORAD ID 00063 - TIROS 2 i = 48.5 °; e = 0.0027; rmin = 465 km; rmax = 481 km; in 2014 burned up (Figure 2).

NORAD ID 00746 - ELEKTRON 1 i = 60.8 °; e = 0.31; rmin = 399 km; rmax = 6409 km (Figure 3).

Where i – the inclination of the orbit, e – the value of the eccentricity of the orbit, rmin and rmax – the average value of the minimum and maximum distances from the Earth's surface.

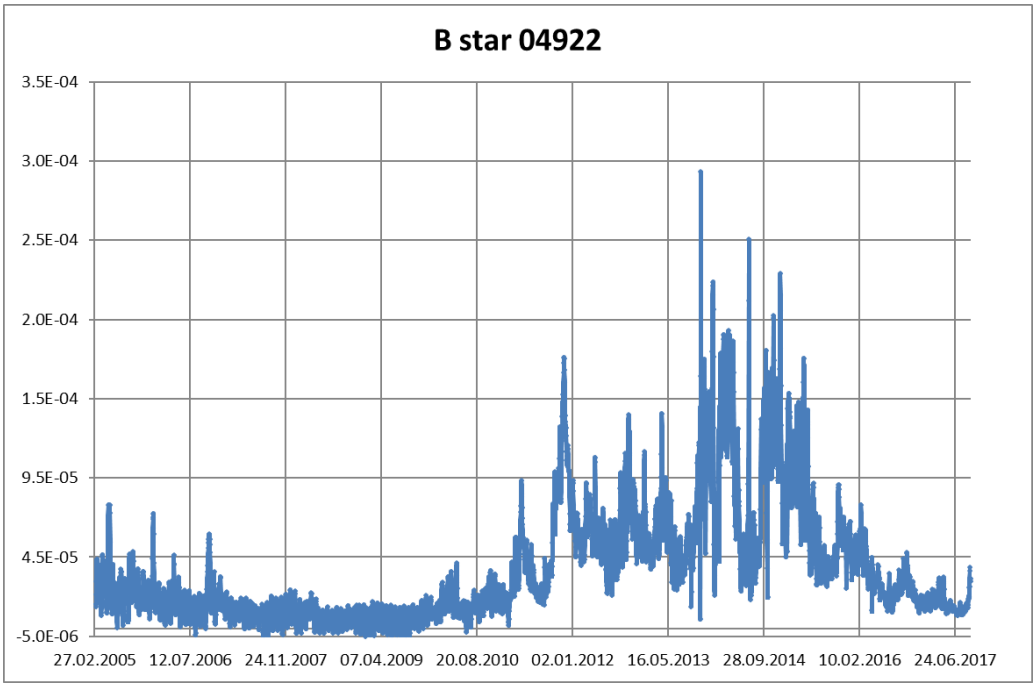


Figure 1. *An example of the B–star drag term for the 04922 satellite after the cubic B-spline interpolation (the x-axis represents date, the y-axis represents the B* values).*

Many factors of gravitational and non–gravitational nature affect the flight of artificial objects in near–earth orbit. Solar and geomagnetic activity have a significant impact on the change in the satellite's orbit among the disturbing factors of a non–gravitational nature. The wide range of indices reflecting the state of space weather are used in this work: The Wolf number (W) and the total area of the sunspots (Sp-T) characterize the general course of the 11–year cycle of solar activity. The F10.7 (the solar radio flux at 10.7 cm), TSI (Total Solar Irradiance) and Lα (the Lyman-alpha) indices characterize the ultraviolet and x-ray component of the solar radiation. The electron fluxes with energies greater than 0.6 MeV and 2 MeV (E>0,6 and 2 MeV) and the solar wind parameters (speed, density, pressure) reflect the corpuscular radiation of the Sun. They reflect the effect on ionospheric currents, which forms the magnetosphere. The indices IMF (the Interplanetary Magnetic Field), Ap (Planetary geomagnetic activity), and Dst (Disturbance Storm Time) show the disturbance of the interplanetary environment, the magnetosphere reaction to changes in the conditions in the interplanetary environment, and the intensity of disturbances in the magnetosphere, respectively. TCI (the "Thermosphere Climate Index"), the temperature at the top of Earth's atmosphere. TCI–a number expressed in Watts that tells how much heat nitrogen oxide (NO) molecules in the thermosphere are dumping into space [King and Papitashvili, 2005].

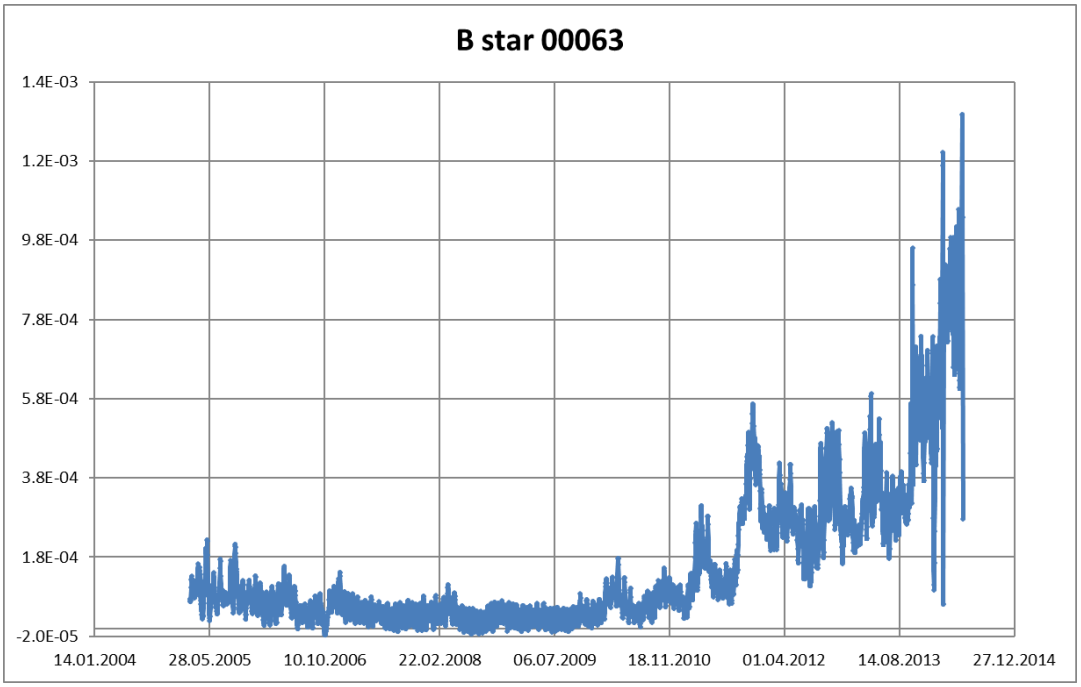


Figure 2. *An example of the B–star drag term for the 00063 satellite after the cubic B-spline interpolation (the x-axis represents date, the y-axis represents the B* values).*

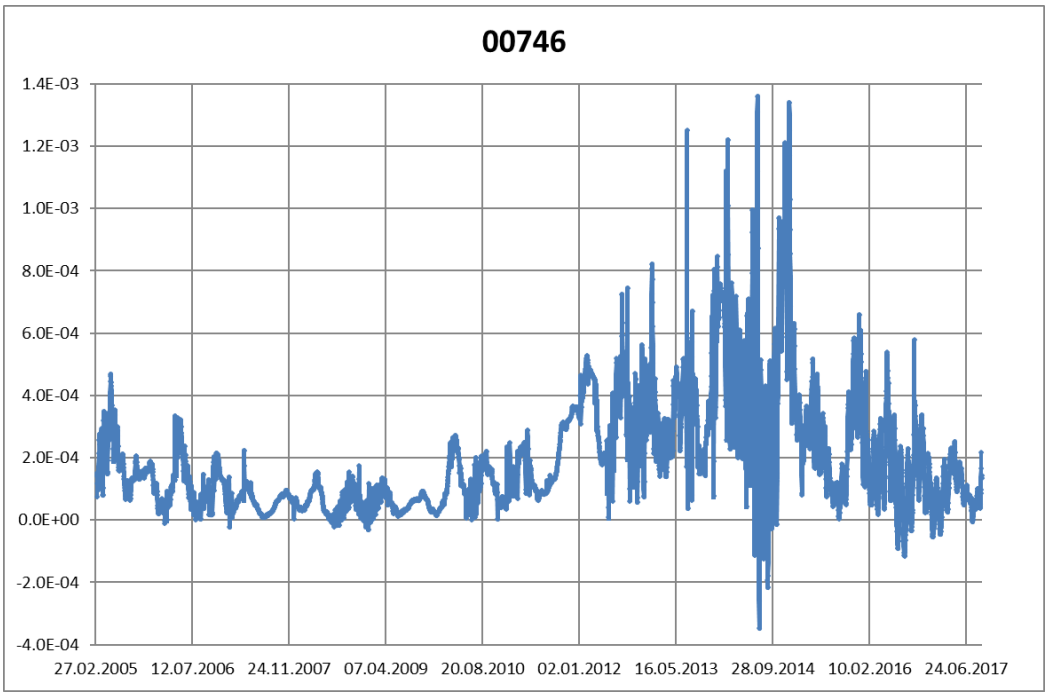


Figure 3. *An example of the B–star drag term for the 00746 satellite after the cubic B-spline interpolation (the x-axis represents date, the y-axis represents the B* values).*

The studied time period covers the declining phase of the 23rd solar cycle (s.c.), the period of a prolonged minimum at the end of the 23rd solar cycle, the ascending, maximum and declining

phases of cycle 24 (03.04.2005–12.09.2017). Figure 4 shows the daily values of the total Wolf number index and s.c. phases for the period under study.

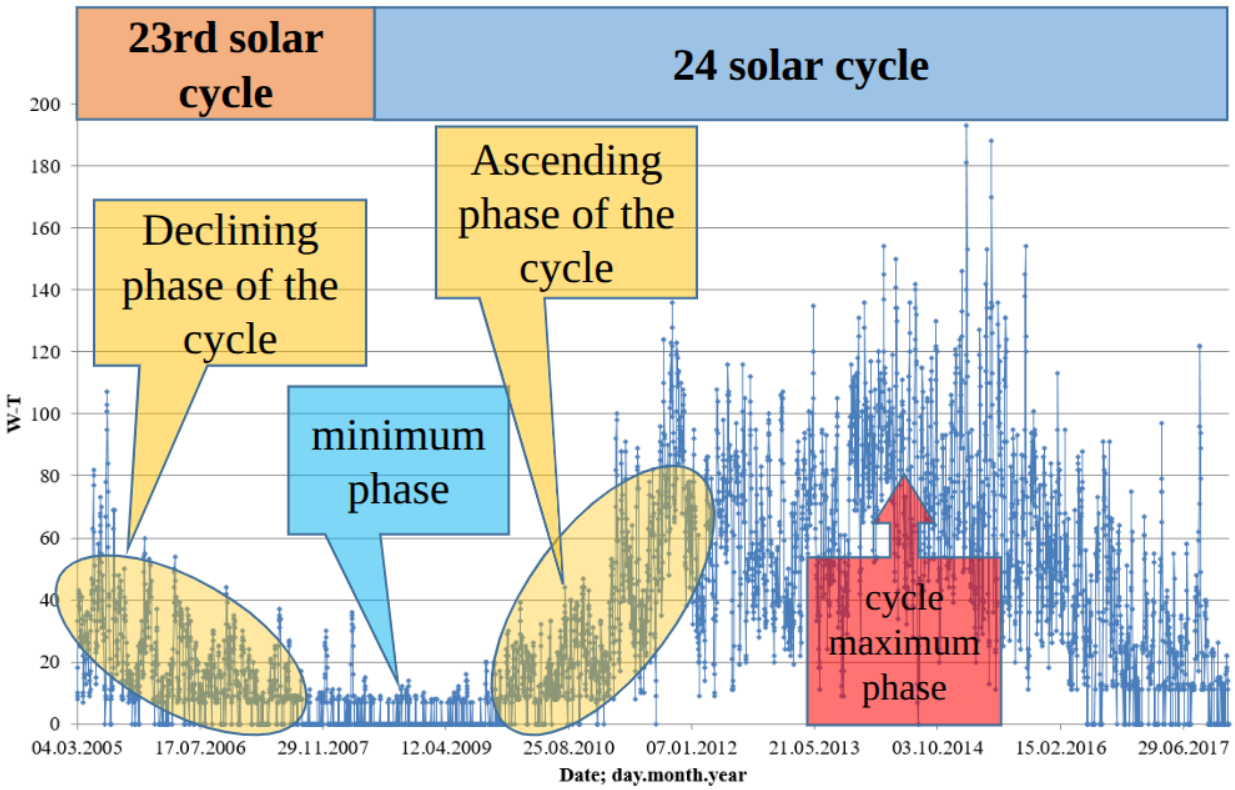


Figure 4. *Daily values of the total Wolf number and solar cycle phases.*

3. Statistical analysis

The characteristic feature of TLE data is that the B* values are provided at irregular intervals, with a frequency no higher than once every 8 hours [Kelso, 1998]. Therefore, cubic B-spline interpolation was applied to the satellite drag coefficient (Figure 1, 2, 3) as well as the solar and geomagnetic activity indices at one-day intervals. After interpolation, the trend component and the mean were subtracted using the AutoSignal program. A 30-day free trial was used. This program uses vector-based trend subtraction procedures. After this, data were then normalized to the range 0 to 1.

Next, the data with an equal step were used to construct periodograms for B-star and indices of solar and geomagnetic activity. It is the method for estimating power spectral density based on calculating the squared modulus of the Fourier transform. Power spectral density describes the power per unit frequency interval. This way, we obtain a visual and quantitative assessment of the periods present in the studied data. We can also estimate the contribution of each of the resulting frequency components. In the AutoSignal program, I used the Bartlett window transform, displaying the data in PSD SumSq with confidence levels. An example of periodograms is shown in Figure 5 and Figure 6. They contain additional labels indicating the periods in days, months, and years.

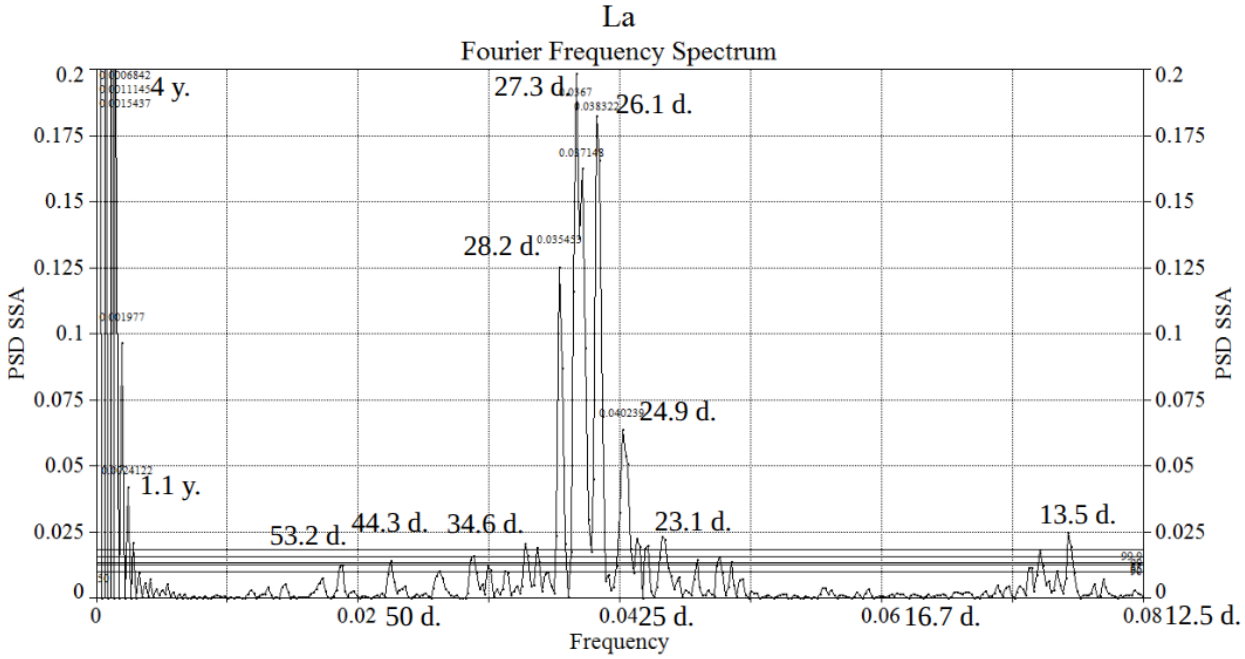


Figure 5. *An example of the periodogram for the La index.*

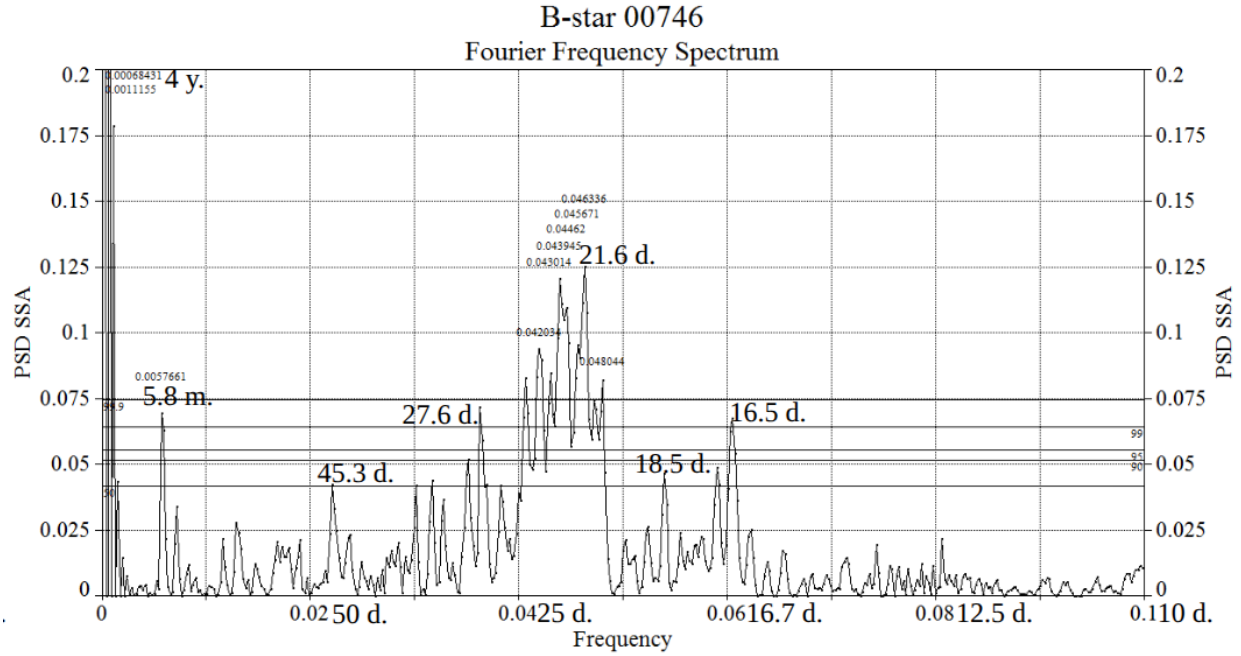


Figure 6. *An example of the periodogram for the B* for the 00746 satellite.*

Periodogram graphs for indices reflecting the ultraviolet and x-ray radiation of solar activity showed that significant periodicities (with a confidence level of 90% or higher) are concentrated in the ranges from 4 years to 1 year, and from 3 months to 20 days, with periods of 7-9 days and 12-15 days. The six-month period for these indices is significantly below the 50% confidence level. The largest contribution to the formation of the initial value graphs comes from frequencies corresponding to periods of 4 years, 27 days, and 25 days.

Periodograms for indices reflecting the corpuscular radiation of solar activity (electron fluxes and solar wind parameters) show that the greatest contribution comes from frequencies corresponding to 27-25 days, 14-13.5 days, and 9 days. The 9-day period does not differ even in fractions of a day for these indices, while other periods differ among themselves in fractions of a day. Among them, the flow pressure index stands out for its behavior. For it, the greatest contribution comes from frequencies corresponding to a 9-day period. Periods of 27-25 days are well below the 50% confidence level, while periods of 7-6.7 days reach the 90% confidence level (for other "corpuscular" indices, these periods are well below the 50% confidence level). Moreover, if we examine the graphs in the following order: E>0.6 MeV, E>2 MeV, flow speed, proton density, flow pressure. A shift in significant periodicities (amplitude values of periods on the PSD SumSq graphs) toward increasing frequency (decreasing period values) can be observed.

The periodogram graph for the TCI index shows that significant periodicities correspond to: 4 years, 1 year, 6 months, 4 and 3 months, 44.4 days, and 25.9 days. Periodicities shorter than 20 days do not reach the 50% confidence level.

The IMF and Ap periodograms are similar to those for "corpuscular" indices, but with some differences. The main frequency components of the IMF are periods of 9 days (10, 9, and 8 days), 7.1, and 6.7 days. Ap is similar, but the periods of 13.5 and 7-6 days are above the 50% confidence level and do not reach 90%, while periods from 15 days to 8 months are below the 50% confidence level. Significant frequencies for the Dst index are within periods from 54 days to 25 days (44.4, 34.2, 28.6, 25.7 days), also from 4 years to 1 year.

Periodograms help identify the presence of specific frequency components in the data. The periodogram method cannot show us if a particular harmonic changed over a given period of time; in other words, it will never tell us at what exact moment in time this occurred.

Spectrograms, a method that shows how the PSD changes over time, are helpful. Spectrograms were calculated in the PSELab program using the fast Fourier transform (Winograd's algorithm) in a sliding window. For spectrograms, the more saturated and bright the color, the greater the period amplitude. Significant frequencies can be found directly in these spectrograms, but the question of the reliability of periods determined by eye arises. Therefore, they were calculated in conjunction with periodograms. Figure 7 and Figure 8 show an example of spectrograms paired with periodograms (for which confidence levels were determined in AutoSignal) for 04922 and 00063 satellites. The images show periods as slanted lines. One frequency component gradually transition into another. No such periods are observed on the spectrogram for satellite 00746 and indices of solar and geomagnetic activity. This may be due to the selected size of the moving window.

Spectrogram images for the indices: the Wolf number, the Sp-T, the F10.7, TSI, and Lα - show that of all the detected periodicities, the 25-27 day period is the most stable. It is present at all phases of the solar cycle (p.s.c.). Moreover, in all spectrograms, during the time interval corresponding to the minimum phase between 23 and 24 s.c., it appears to split into several periodicities of very similar magnitude. For the TSI index, this is barely noticeable. For the Sp-T, a division into two periods of 20 days and 2 months occurs at the beginning of the ascending phase of s.c. 24 before the beginning of the maximum phase. On the spectrogram, this looks like a "mirror image" (not identical). At the maximum, they "weaken" (become less saturated on the spectrogram), and a clear period of 26 days appears. During the declining p.s.c. 24, these periods become clearly distinguishable. A similar pattern can be seen in the spectrogram for the F10.7 index, only over shorter time intervals.

Spectrograms for the indices: E>0.6 MeV, E>2 MeV, flow speed, proton density, and flow pressure - show the presence of a "stable" (distinguishable over the entire interval) period of 25-27 days over the entire time interval, except for flow pressure (for proton density, it is weak but distinguishable). A "weakening" is visible during the solar minimum and the beginning of the ascending p.s.c. 24.

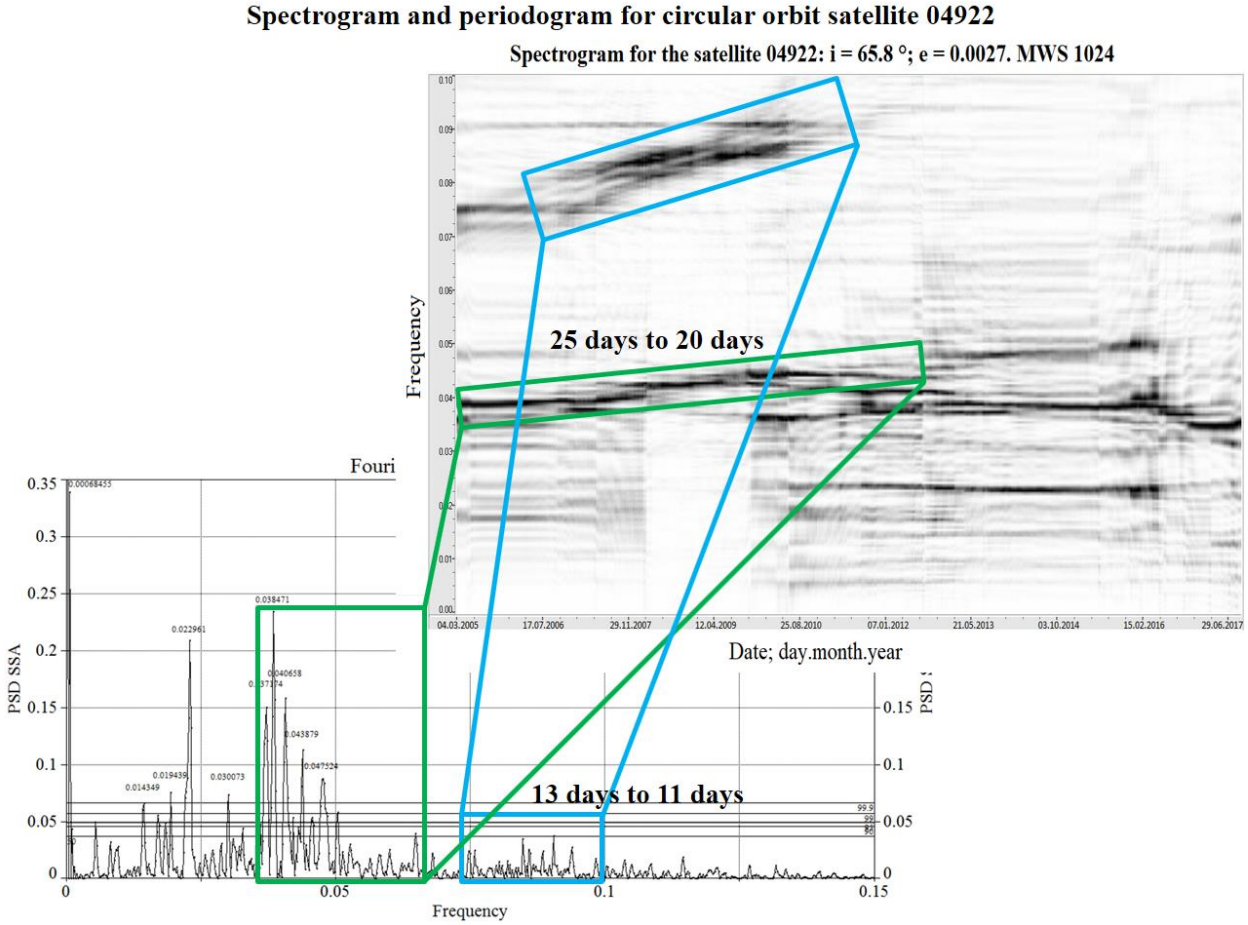


Figure 7. *An example of spectrograms paired with periodograms for 04922 satellite.*

Spectrogram for the flow pressure index shows that a 9-day period is present throughout the entire time interval, while a 7-6 day period is less clear during the declining p.s.c. 23 and minimum. The 7-6 day period becomes clearly visible at the beginning of the ascending phase of solar cycle 24 and until the declining phase of this cycle. A clearly visible 25-27 day period appears only during the maximum phase of s.c. 24.

The spectrogram for the TCI index shows: The presence of a semi-annual period in the time intervals corresponding to the declining p.s.c. 23, the middle and end of the minimum between s.c., and the declining phase of the 24th s.c. The period of 44 days (~1.5 months) is visible in all phases of the 24th s.c. (weakly visible in the declining phase of the 23rd s.c. and the minimum). The period of 26 days is clearly visible in the minimum, the maximum, and the declining phase of the 24th s.c.

On the spectrogram of the Dst index, the following periods are clearly distinguished: the 1.7 year period throughout the entire time interval; the 6 month period (on the periodogram its

significance level is well below 50%) during the declining phase of 23rd s.c. and the ascending phase of 24th s.c.; periods of 44.4 and 34.2 days during the ascending phase of 24th s.c.; and the 25.7 day period during the solar minimum, together with the 28.5 day period during the maximum and declining phases of 24th s.c. (these periods are only weakly distinguishable during the remaining time intervals).

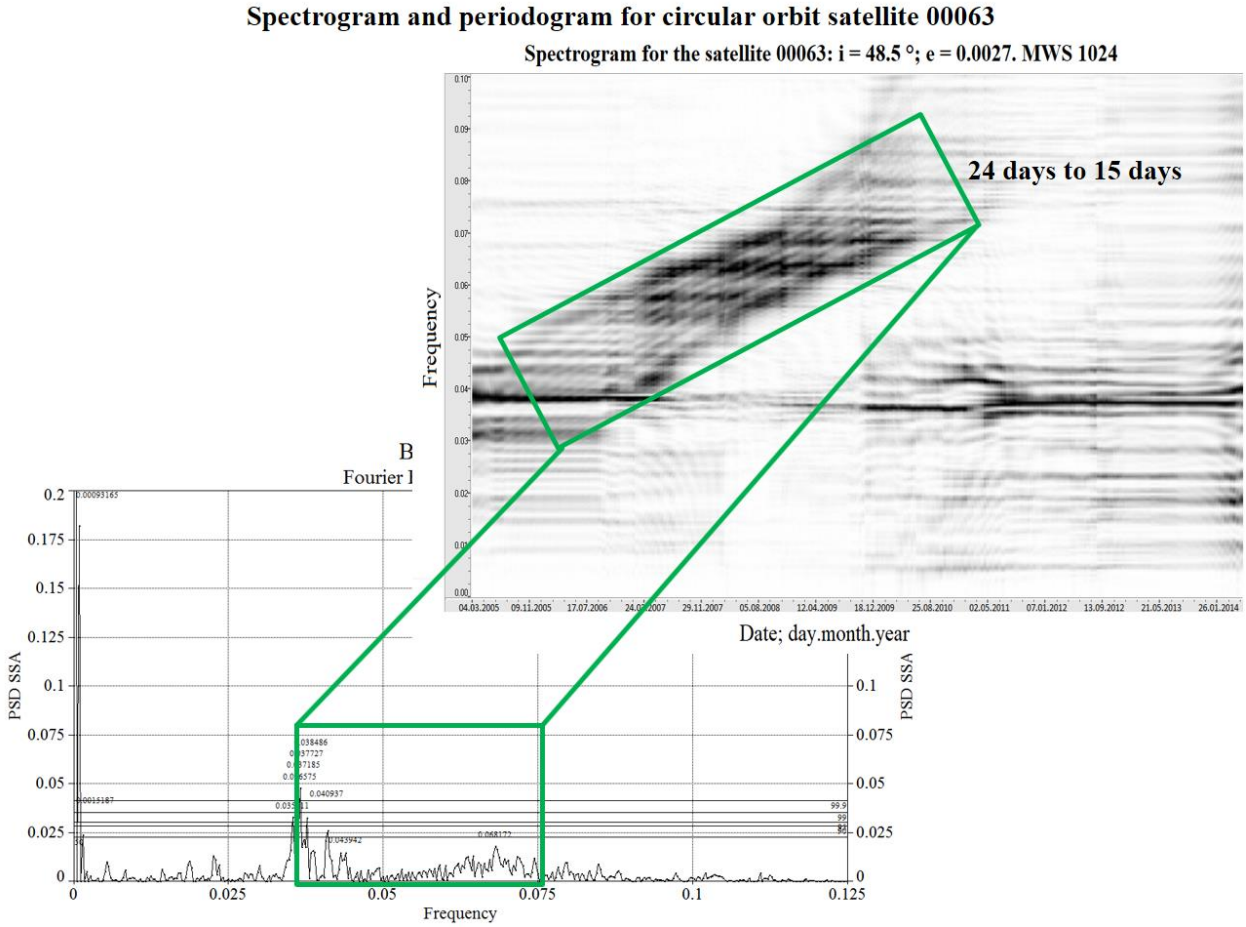


Figure 8. *An example of spectrograms paired with periodograms for 00063 satellite.*

Cross-spectral analysis was used to analyze the dependence of artificial satellites drag on the influence of solar and geomagnetic activity indices. This part of study will be published in the Bulgarian Astronomical Journal (BAJ), Volume 46 (2027): "Cross-spectral analysis of the B-star drag term and solar and geomagnetic activity indices". Was accepted on 18.06.2026. Available at the following link: [https://astro.bas.bg/AIJ/issues/n46/index.php].

4. Conclusions

The presence of peaks at certain frequencies in periodograms does not necessarily indicate physically meaningful periodicities in the analyzed time series. In the case of B* such peaks may be associated with features of the SGP model, orbit determination errors, and variations in the satellite's ballistic characteristics. For this reason, significance levels were calculated. They

indicate statistically significant spectral peaks but do not provide evidence of their physical origin. The interpretation of the detected peaks therefore requires comparison with physical models, as well as consideration of methodological and systematic effects.

Periodicities identified in the B* time series correspond to those found in the time series of solar and geomagnetic activity indices.

The resulting spectrograms depend on the chosen trade-off between frequency and temporal resolution. Changes in the intensity of the periodic components and their splitting into closely spaced periods coincide with changes in the phase of the solar activity cycle.

References

Asenovski, S., Georgieva, K. and Kirov, B. (2022) 'Open access database for different types of solar wind', in *Proceedings of the Fourteenth Workshop "Solar Influences on the Magnetosphere, Ionosphere and Atmosphere"*, pp. 83–86. doi: 10.31401/WS.2022.proc.14.

Ashruf, A.M., Bhaskar, A., Vineeth, C. and Pant, T.K. (2026) 'Characterizing solar cycle influence on long-term orbital deterioration of low-Earth-orbiting space debris', *Frontiers in Astronomy and Space Sciences*, 13, article 1797886. doi: 10.3389/fspas.2026.1797886.

Cliver, E.W. and Svalgaard, L. (2004) 'The 1859 solar–terrestrial disturbance and the current limits of extreme space weather activity', *Solar Physics*, 224, pp. 407–422. doi: 10.1007/s11207-005-4980-z.

Coleman, P.J. Jr. (1966) 'Variations in the interplanetary magnetic field: Mariner 2: 1. Observed properties', *Journal of Geophysical Research*, 71(23), pp. 5509–5531. doi: 10.1029/JZ071i023p05509.

Dessler, A.J. (1967) 'Solar wind and interplanetary magnetic field', *Reviews of Geophysics*, 5(1), pp. 1–41. doi: 10.1029/RG005i001p00001.

Doornbos, E., Klinkrad, H. and Visser, P. (2008) 'Use of two-line element data for thermosphere neutral density model calibration', *Advances in Space Research*, 41(7), pp. 1115–1122. doi: 10.1016/j.asr.2006.12.025.

Emmert, J.T. (2015) 'Thermospheric mass density: A review', *Advances in Space Research*, 56(5), pp. 773–824. doi: 10.1016/j.asr.2015.05.038.

Georgieva, K. and Veretenenko, S. (2023) 'Solar influences on the Earth's atmosphere: Solved and unsolved questions', *Frontiers in Astronomy and Space Sciences*, 10, article 1244402. doi: 10.3389/fspas.2023.1244402.

Georgieva, K., Kirov, B. and Asenovski, S. (2025) 'Hemispheric asymmetry of the solar dynamo', in *Proceedings of the Seventeenth Workshop "Solar Influences on the Magnetosphere, Ionosphere and Atmosphere"*, pp. 10–16. doi: 10.31401/WS.2025.proc.02.

Gondelach, D.J. and Linares, R. (2020) 'Real-time thermospheric density estimation via two-line element data assimilation', *Space Weather*, 18(2), article e2019SW002356. doi: 10.1029/2019SW002356.

Hapgood, M., Liu, H. and Lugaz, N. (2022) 'SpaceX—Sailing close to the space weather?', *Space Weather*, 20, article e2022SW003074. doi: 10.1029/2022SW003074.

Hathaway, D.H. (2015) 'The solar cycle', *Living Reviews in Solar Physics*, 12, article 4. doi: 10.1007/lrsp-2015-4.

He, C., Yang, Y. and Carter, B.A. (2018) 'Review and comparison of empirical thermospheric mass density models', *Progress in Aerospace Sciences*, 103, pp. 31–51. doi: 10.1016/j.paerosci.2018.10.003.

Jones, M. Jr., Emmert, J.T., Drob, D.P., Picone, J.M. and Meier, R.R. (2018) 'Origins of the thermosphere–ionosphere semiannual oscillation: Reformulating the "thermospheric spoon" mechanism', *Journal of Geophysical Research: Space Physics*, 123, pp. 931–954. doi: 10.1002/2017JA024861.

King, J.H. and Papitashvili, N.E. (2005) 'Solar wind spatial scales in and comparisons of hourly Wind and ACE plasma and magnetic field data', *Journal of Geophysical Research: Space Physics*, 110, article A02104. doi: 10.1029/2004JA010649.

Kirov, B., Asenovski, S., Georgieva, K. and Obridko, V.N. (2015) 'What causes geomagnetic activity during sunspot minimum?', *Geomagnetism and Aeronomy*, 55(8), pp. 1033–1038. doi: 10.1134/S0016793215080149.

Kirov, B., Georgieva, K. and Asenovski, S. (2022a) 'Space weather and its effects on spacecraft charging', in *Proceedings of the Fourteenth Workshop "Solar Influences on the Magnetosphere, Ionosphere and Atmosphere"*, pp. 68–76. doi: 10.31401/WS.2022.proc.11.

Kirov, B., Georgieva, K., Asenovski, S., Madjarska, M.S. and Dineva, E. (2022b) 'A comparison between the solar activity in the 11-year sunspot cycles during the last two centennial solar activity minima. A comparison of the

geomagnetic activity during the same periods', in *Proceedings of the Fourteenth Workshop "Solar Influences on the Magnetosphere, Ionosphere and Atmosphere"*, pp. 87–91. doi: 10.31401/WS.2022.proc.15.

Koucká Knížová, P., Georgieva, K., Mošna, Z., Kozubek, M., Kouba, D., Kirov, B., Potužníková, K. and Boška, J. (2018) 'Solar signals detected within neutral atmospheric and ionospheric parameters', *Journal of Atmospheric and Solar-Terrestrial Physics*, 171, pp. 147–156. doi: 10.1016/j.jastp.2017.12.003.

Lam, H.-L., Boteler, D.H., Burlton, B. and Evans, J. (2012) 'Anik-E1 and E2 satellite failures of January 1994 revisited', *Space Weather*, 10, article S10003. doi: 10.1029/2012SW000811.

Neugebauer, M. and Snyder, C.W. (1962) 'Solar plasma experiment', *Science*, 138(3545), pp. 1095–1097. doi: 10.1126/science.138.3545.1095-a.

Parker, E.N. (1958) 'Dynamics of the interplanetary gas and magnetic fields', *The Astrophysical Journal*, 128, pp. 664–676. doi: 10.1086/146579.

Qian, L., Solomon, S.C. and Kane, T.J. (2009) 'Seasonal variation of thermospheric density and composition', *Journal of Geophysical Research: Space Physics*, 114, article A01312. doi: 10.1029/2008JA013643.

Qian, L., Solomon, S.C. and Mlynczak, M.G. (2010) 'Model simulation of thermospheric response to recurrent geomagnetic forcing', *Journal of Geophysical Research: Space Physics*, 115, article A10301. doi: 10.1029/2010JA015309.

Russell, C.T. and McPherron, R.L. (1973) 'Semiannual variation of geomagnetic activity', *Journal of Geophysical Research*, 78(1), pp. 92–108. doi: 10.1029/JA078i001p00092.

Sabine, E. (1852) 'On periodical laws discoverable in the mean effects of the larger magnetic disturbances. No. II', *Philosophical Transactions of the Royal Society of London*, 142, pp. 103–124. doi: 10.1098/rstl.1852.0009.

Schwabe, H. (1844) 'Sonnen-Beobachtungen im Jahre 1843', *Astronomische Nachrichten*, 21, pp. 233–236. doi: 10.1002/asna.18440211505.

Thayer, J.P., Lei, J., Forbes, J.M., Sutton, E.K. and Nerem, R.S. (2008) 'Thermospheric density oscillations due to periodic solar wind high-speed streams', *Journal of Geophysical Research: Space Physics*, 113, article A06307. doi: 10.1029/2008JA013190.

Webster, C. (1965) 'The discovery of Boyle's law, and the concept of the elasticity of air in the seventeenth century', *Archive for History of Exact Sciences*, 2, pp. 441–502.

Wolf, R. (1852) 'Neue Untersuchungen über die Periode der Sonnenflecken und ihre Bedeutung', *Mittheilungen der Naturforschenden Gesellschaft in Bern*, 255, pp. 249–270.

Xu, J., Wang, W., Zhang, S.-R., Liu, X. and Yuan, W. (2015) 'Multiday thermospheric density oscillations associated with variations in solar radiation and geomagnetic activity', *Journal of Geophysical Research: Space Physics*, 120, pp. 3829–3846. doi: 10.1002/2014JA020830.

Yamamoto, M. and Sori, T. (2026) 'Thermospheric density from Starlink TLE: Data analysis and preliminary results', *Earth, Planets and Space*, 78, article 60. doi: 10.1186/s40623-026-02402-1.

DOI: 10.31401/WS.2026.proc.18

Geomagnetic Substorm Signatures at Mid-Latitudes: The March 23, 2023 Case Study from Geomagnetic Station Panagyurishte

Raykova L., Guineva V.

Space Research and Technology Institute (SRTI), Bulgarian Academy of Sciences, Stara Zagora Department, Bulgaria; L.Raykova@stzagora.com

Abstract

This study analyzes the genesis and terrestrial consequences of the strong G4-class geomagnetic storm that began on March 23, 2023. At the core of the disturbance lays a relatively rare solar event characterized as a filament-driven CME and two CME interaction observed by SOHO/LASCO coronagraphs. Analysis of H-alpha solar imagery from El Teide and SDO/AIA 304 Å data confirms that the event was driven by filament eruptions rather than strong X-ray flare.

The energy transfer from these solar sources resulted in a powerful geomagnetic storm, with the DST and SYM-H indices reaching minimum values of -163 nT and -170 nT, respectively. The ground-based response to the event was investigated in detail using high-resolution data from the IMAGE, SuperMAG, and INTERMAGNET networks, with a specific focus on the Panagyurishte Magnetic Station (PAG). Additionally, field-aligned currents were analyzed using data from the AMPERE system, which provides space-based magnetic measurements from the Iridium satellite constellation.

Four Midlatitude Positive Bay (MPB) events were recorded at the Panagyurishte station, occurring as a result of substorm development at auroral and high latitudes. The substorm presence was verified by the SuperMAG substorm lists, as well. The results of the study show that local magnetic disturbances follow closely the global and regional disturbances represented by the SML and IL auroral indices. These observations illustrate the process of energy transfer from high to mid-latitudes during geomagnetic disturbances.

Keywords: solar flare, geomagnetic storm, midlatitude positive bay

1. Introduction

Geomagnetic storms are large-scale disturbances of Earth's magnetosphere driven by enhanced coupling between the solar wind and the terrestrial magnetic field. The primary sources of geoeffective solar wind structures are transient eruptions from the Sun. With their variety of signatures including prominences, solar flares, coronal mass ejections (CMEs), radio emissions, etc., they play a significant role in generating space weather. All of them most often formed in active regions, the common ground for their occurrence is magnetic reconnection and magnetohydrodynamic instability [Temmer, 2026]. Solar active regions characterized by intense magnetic fields and complex sunspot structures are commonly linked to enhanced eruptive potential [Sammis et al., 2000]. A significant fraction of these CMEs has been associated with the eruption of solar prominences [Gopalswamy et al., 2003].

Such large-scale eruptions can develop into CMEs, which propagate through the solar wind and may eventually interact with Earth's magnetosphere initiating a chain of processes [Munro et al., 1979; Gosling, 1993]. These include magnetic field reconfiguration, compression, and the development of substorms in the magnetotail [Russell and McPherron, 1973; Gosling et al., 1991]. The highly variable energy input from both the solar wind and magnetospheric processes leads to pronounced disturbances in the ionosphere [Buonsanto, 1999; Tsurutani et al., 2004]. At the same time, the thermosphere is heated and expands due

to the absorption of extreme ultraviolet (EUV) and X-ray radiation, as well as through the injection of energetic particles during magnetic reconnection. As a result, the neutral density at higher altitudes increases, causing enhanced atmospheric drag on low Earth orbit satellites [Knipp et al., 2004].

The geoeffectiveness of such disturbances depends not only on their speed and dynamic pressure, but also on their internal magnetic structure and orientation upon arrival at Earth. When conditions are highly geoeffective, they trigger geomagnetic storms—global disturbances in which solar energy drives complex processes within the Earth's magnetosphere, ionosphere, and atmosphere, including particle acceleration, atmospheric heating, and geomagnetically induced currents on the ground [Gonzalez et al., 1994]. During severe storms, enhanced convection injects energetic protons and ionospheric oxygen ions, leading to a rapid intensification of the ring current and decrease in the horizontal component of the geomagnetic field [Daglis et al., 1999]. In this context, the storm-substorm relationship becomes vital: although large-scale solar wind conditions govern the overall storm development, the frequent occurrence of substorms plays a critical role in energizing the ring current by supplying and accelerating ionospheric plasma during the main phase [Kamide et al., 1998].

On a structural level, magnetospheric substorms represent one of the main components of space weather, driving the primary transient disturbances observed within Earth's magnetosphere. According to the current theory, during magnetospheric substorms, a current system known as the Substorm Current Wedge (SCW) forms through the diversion of the tail current along magnetic field lines into the ionosphere, forming auroral electrojets [McPherron, 1972; McPherron et al., 1973a]. This phenomenon has been investigated since the 1970s [McPherron et al., 1973b; Kisabeth and Rostoker, 1974]. During the substorm expansion phase, the SCW produces characteristic geomagnetic signatures on the ground, including sharp negative bays in the X-component at auroral latitudes and mid-latitude positive bays (MPBs), which represent positive deviations of the horizontal magnetic field recorded at mid-latitude stations [McPherron, 1972; Kepko et al., 2014; Guineva et al., 2021a; Guineva et al., 2024a,b; Guineva et al., 2025]. Consequently, ground-based magnetic observations remain a core dataset for studying substorm dynamics.

Variations in the mid-latitude geomagnetic field serve as a powerful diagnostic tool for investigating magnetospheric substorms. MPBs can serve as useful indicators of substorm onset and, in some cases, may provide a more reliable indication of substorm onset than the global SML index [McPherron and Chu, 2017]. The sign of the Y-component can also be used to estimate the direction of field-aligned currents at a given longitude [Meng and Akasofu, 1969].

In this context, the purpose of this work is to examine the manifestation of magnetospheric substorms during the geomagnetic storm of 23 March 2023 and to analyze the MPB events recorded at the Panagyurishte (PAG) station in relation to the development of substorms. Four MPBs identified during the storm are examined and compared with the corresponding substorm activity. The MPBs were selected from the *Catalog of magnetic variations at the Panagyurishte station* [Guineva et al., 2021b] (http://space.bas.bg/Catalog_MPB/).

2. Data Analysis and Instruments

The identification of the solar source of the geomagnetic storm on 23 March 2023 was based on a multi-instrument, multi-wavelength dataset combining coronagraph observations, in situ solar wind considerations, and ground-based solar imaging.

Coronal mass ejection data were obtained from the CDAW CME Catalog (https://cdaw.gsfc.nasa.gov/CME_list/), based on observations from the SOHO/LASCO

coronagraphs (C2 and C3). A total of 22 CMEs were identified in the period 19-22 March 2023, covering the expected transit window for solar wind disturbances reaching Earth on 23 March. For each CME, parameters such as central position angle (CPA), angular width (AW), and linear speed were used.

An initial filtering of candidate events was performed by estimating the CME arrival time at 1 AU using a ballistic approximation. This approach allowed the identification of a subset of CMEs whose expected arrival coincides with the onset of the geomagnetic storm.

For refined propagation analysis, the Drag-Based Model (DBM) was applied. In this framework, the CME acceleration is governed by:

$$a = -\gamma\left(v_{\{CME\}} - v_{\{SW\}}\right)\left|v_{\{CME\}} - v_{\{SW\}}\right| \quad (1)$$

where is the ambient solar wind speed and γ is the drag parameter. A representative value of was adopted, consistent with typical values reported in the literature [Vršnak et al., 2013; 2017].

To investigate possible low-coronal signatures of the eruption, solar disk observations were analyzed using:

- H-alpha data from the Teide Observatory,
- EUV imagery (304 Å channel) from SDO/AIA,
- X-ray flux measurements from GOES for flare identification.

Active region associations were examined using NOAA active region catalogs to assess possible magnetic sources of the eruptions (https://www.swpc.noaa.gov/products/solar-region-summary).

The global intensity and energetics of the geomagnetic storm, along with the interplanetary conditions, were monitored using the SYM-H index, retrieved together with space weather parameters from the CDAWeb database (https://cdaweb.gsfc.nasa.gov/). High-latitude auroral electrojet activity and global substorm signatures were evaluated using the SML and SMU indices from the SuperMAG network. The regional IL index was obtained from the PPN-NAL magnetometer chain, which is part of the IMAGE (International Monitor for Auroral Geomagnetic Effects) network (http://space.fmi.fi/image/). Global-scale field-aligned current (FAC) systems, characterizing the upward and downward current structures, were analyzed using space-based magnetic measurements from the next-generation AMPERE system, utilizing the Iridium satellite constellation (https://ampere.jhuapl.edu/).

Local mid-latitude geomagnetic variations were obtained from the Panagyurishte (PAG) station, Bulgaria, a full member of the global INTERMAGNET program (https://imag-data.bgs.ac.uk/GIN_V1/GINForms2). To identify the MPBs associated with the geomagnetic storm of 23 March 2023, the Catalog of magnetic variations at the Panagyurishte station, developed at the Space Research and Technology Institute of the Bulgarian Academy of Sciences, was used [Guineva et al., 2021b] (http://space.bas.bg/Catalog_MPB/). The four MPBs occurring during the storm were selected from this catalog for further analysis of their relationship to the associated substorm activity.

3. Results

3.1.Solar sources

The initial ballistic filtering identified six CMEs with potential arrival times consistent with the geomagnetic storm onset on 23 March 2023. However, three of these events were classified as "poor events" in the LASCO catalog and exhibited either low speeds or narrow angular widths, making them unlikely drivers of a strong geomagnetic storm. Applying the Drag-Based Model further refined the candidate list. One CME originating on 21 March yielded an estimated arrival time of 24 March (03:35 UT), significantly later than

the observed storm onset (~14:49 UT on 23 March), and was therefore excluded. This process left two CMEs, both observed on 20 March 2023 at 14:00 UT and 14:42 UT, as the only viable candidates (Table 1).

To further validate the selection, the candidate events were compared with independent near-Earth ICME association catalogs. The Richardson and Cane ICME List (https://izw1.caltech.edu/ACE/ASC/DATA/level3/icmetable2.htm) associates the ICME observed on 23 March 2023 with two CMEs from 20 March 2023, occurring at 02:41 UT and 14:42 UT, where the latter is classified as a halo CME [Richardson and Cane, 2024] and is additionally supported by the CCMC DONKI database. This independent association confirms that at least one of the selected halo CMEs (14:42 UT) is considered a probable source of the geomagnetic storm by operational heliospheric propagation models and ICME catalogs.

The CME at 02:41 UT, although included in the Richardson and Cane association, was classified in the LASCO catalog as a poor event with a substantially lower geoeffectiveness potential. Consequently, it was not retained as a primary candidate in the present analysis. In contrast, the two halo CMEs observed at 14:00 UT and 14:42 UT exhibit Earth-directed halo morphology, appropriate transit times, and a strong likelihood of mutual interaction, making them the most plausible contributors to the geomagnetic storm.

Table 1. *Summarized data for the two CMEs that caused the solar storm from 23 March 2023 including the date and time of their first appearance in LASCO C2 field of view, central position angle (CPA), angular width (AW), and linear speed (V). The arrival time at Earth is estimated using the drag-based model and data for the solar wind speed during the days of propagation.*

Date [yyyy-mm-dd]	Time [hh:mm]	CPA	AW [°]	V [km s^{-1}]	Estimated Arrival Time
2023-03-20	14:00	Halo	360	851	2023-03-23 13:08
2023-03-20	14:42	Halo	360	727	2023-03-23 14:42

The two remaining events share several key characteristics:

- Both are halo CMEs, indicating a significant Earth-directed component and high geoeffectiveness potential.
- They occur within less than one hour, suggesting a possible interaction.
- Their speeds and estimate arrival times match the observed storm onset.

The close temporal proximity strongly suggests that the two eruptions are not independent, but rather represent a multi-stage or interacting CME event. Such CME-CME interactions are known to enhance geoeffectiveness by increasing compression in the sheath region, amplifying magnetic field and modifying propagation dynamics [Koehn et al., 2022; Temmer et al., 2023]. These factors are consistent with the unexpectedly strong geomagnetic response.

The possibility of CME-CME interaction is further supported by the fact that the two halo events were launched only 42 minutes apart and have comparable propagation times toward Earth. Under such conditions, the trailing CME may partially overtake or compress the preceding ejecta, producing a more geoeffective interplanetary structure than either CME alone. Halo morphology alone does not uniquely prove an Earth-directed trajectory. However, the combination of halo appearance, drag-based arrival-time estimates, and independent DONKI/Richardson-Cane associations provides substantially stronger evidence for an Earth-directed component than visual LASCO morphology alone.

An analysis of soft X-ray data from GOES shows no significant M- or X-class flares during the relevant time window. Only weak C-class flares were observed, and no clear temporal or spatial association with the identified CMEs could be established. This indicates

that the eruptions were not flare-driven in the classical sense, and that flare activity did not play a dominant role in this event.

Active region analysis suggests a possible association of the second CME (14:42 UT) with NOAA AR 13260 near the eastern limb. However, the first CME does not show a clear connection to a well-developed active region, instead being linked to a region of weak and fragmented magnetic activity.

Hα observations from El Teide Observatory reveal the eruption and subsequent disappearance of a filament after approximately 09:00 UT on 20 March, followed by a weak brightening around 14:00 UT (Figure 1). These signatures suggest a filament destabilization preceding the CME onset.

The presence of well-defined filament on the solar disk, combined with weak flare signatures, suggests that the event most probably belongs to a class of filament-driven CMEs, where the low-coronal signatures are subtle or partially occulted. Other authors also link the intense geomagnetic storm to a "slow halo CME that erupted from a solar filament on 20 March 2023" [Amaechi et al., 2025] or with the CME of 19 March 2023 at 22:52 UT [Gopalswamy et al., 2025], which was also considered as a possible candidate in the present study but was not retained in the final selection due to its low speed of 135 km s^{-1}.

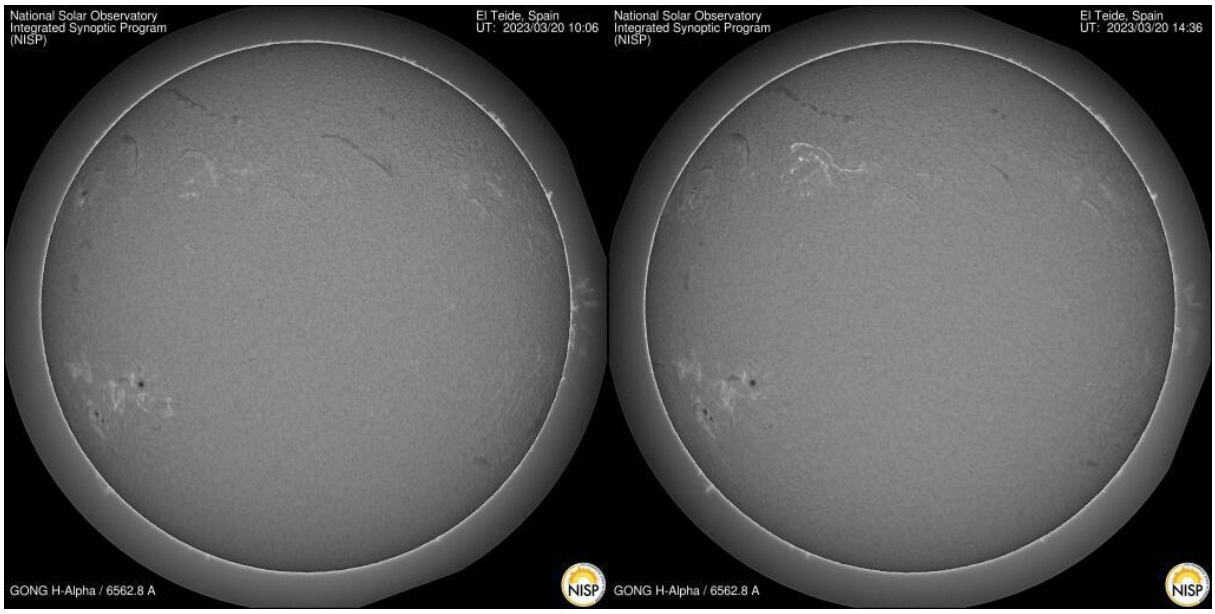


Figure 1. *Hα observations of the solar disk from El Teide Observatory, Spain on 20 March 2023 showing the erupting filament and signs of a flare in the northern hemisphere.*

EUV observations (AIA 304 Å) indicate additional activity near the western limb, although without a clearly pronounced mass ejection (Figure 2).

3.2.Interplanetary and geomagnetic conditions

The interplanetary and geomagnetic conditions during the geomagnetic storm of 23–25 March 2023 are presented in Figure 3. The figure covers the interval from 02:00 UT on 23 March to 00:00 UT on 25 March 2023 and shows, from top to bottom, the IMF magnitude B, the southward Bz component of the IMF, the solar-wind velocity Vx, proton density, temperature, pressure, and the AL and SYM/H indices. The intervals corresponding to the interplanetary shock (IS), sheath, and magnetic cloud (MC) are marked by green vertical lines, while the red vertical lines indicate the beginnings of the MPBs.

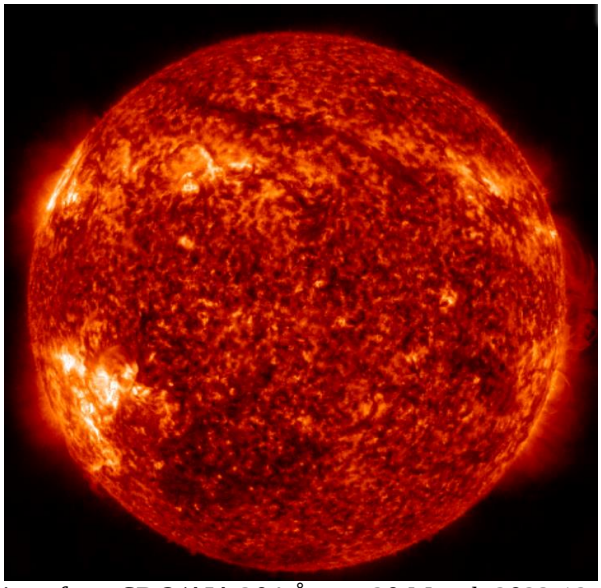


Figure 2*. EUV observations from SDO/AIA 304 Å s on 20 March 2023 12:31 UT.*

The IS (Interplanetary Shock), SHEATH and MC (Magnetic Cloud) time intervals are marked by green vertical lines. The red vertical lines indicate the MPB beginnings. The total magnetic field intensity B increases progressively, showing an initial rise at the interplanetary shock IS passage and continuing to intensify throughout the SHEATH region, with the peak magnitude of slightly above 20 nT being achieved only upon entering the Magnetic Cloud (MC). The B_z component of the magnetic field exhibits strong fluctuations within the IS and SHEATH regions but decreases sharply upon entering the Magnetic Cloud (MC), reaching a minimum of approximately -15 nT. Following the initial jump at the interplanetary shock (IS), the solar wind speed V_x exhibits a highly variable profile with continuous rises and falls throughout the entire SHEATH region and during the Magnetic Cloud (MC) period, but the trend is to diminish during the SHEAT and gradually increase during the MC. The proton density Np shows no perceptible change immediately after the shock (IS) passage, but it begins to rise sharply during the SHEATH region, reaching its highest values. Upon entering the Magnetic Cloud (MC), the density decreases abruptly and remains at its minimum values throughout the entire cloud period. The temperature T profile demonstrates a trend that closely shows a broadly similar variation to the proton density N_p. The pressure P follows an almost identical trend to that of the proton density N_p. This behavior is physically well-founded. Upon the shock (IS) passage, the AL index exhibits only minor variations.

Within the SHEATH region, there is initially no significant response, followed by a sharp drop and subsequent recovery. However, the main geomagnetic disturbances unfolds upon entering the Magnetic Cloud (MC) and shortly after it, showing a repeated substorm activity From the SYM/H index it is seen, that the geomagnetic storm was initiated by the IS, the main phase continues during the SHEAT and MC. The SYM/H index reached -170 nT, which determines this geomagnetic storm as strong. All four MPBs identified at PAG occurred on 23 March, during the main phase of the storm. Their temporal relationship to the interplanetary structures and the associated substorm activity is examined in the following subsections.

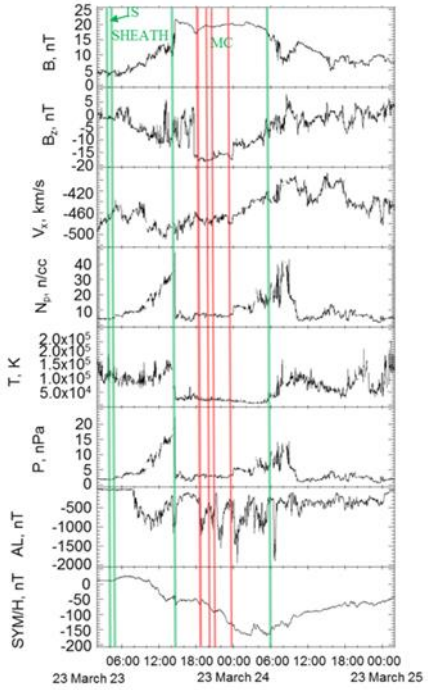


Figure 3*. Interplanetary and geomagnetic conditions from 23 to 25 March 2023. From top to bottom: IMF Magnitude B, southward Bz component of IMF, Vx component of the solar wind velocity, proton density, temperature, pressure, AL index, and SYM/H index are presented.*

3.3. Parameters of the Registered MPB Events at the Panagyurishte Station

The influence of substorms at mid-latitudes manifests itself as specific, relatively smooth variations in the geomagnetic field. These disturbances are observed as mid-latitude positive bays (MPBs), characterized by positive deviations of the northward X component near the midnight sector [Akasofu and Meng, 1968; Meng and Akasofu, 1969; McPherron, 1972].

To describe the temporal and amplitude characteristics of the four distinct MPB events observed at PAG during the geomagnetic storm of 23–25 March 2023, Table 2 presents their main parameters. From left to right, the table gives the MPB beginning times, the times of the maximum values, the maximum X-component values, the MPB end times, and the MPB amplitudes.

As shown in Table 2, four successive MPBs were observed during the evening-to-night period of 23 March 2023, all during the main phase of the geomagnetic storm. The maximum X-component values of two MPBs exceeded 30 nT, one was slightly above 20 nT, and one was in the 5–10 nT range. Their amplitudes were also substantially different: the largest exceeded 60 nT, two were between 50 and 60 nT, and the smallest was slightly above 10 nT. The occurrence of such high maximum X-component values is consistent with the results of previous studies, which showed that the most intense MPBs, in terms of their maximum X-component values, are preferentially associated with intense geomagnetic storms [Guineva et al., 2024a,b].

Table 2. *Parameters of the four registered MPB (Midlatitude Positive Bay) events at the Panagyurishte (PAG) geomagnetic observatory during the geomagnetic storm of March 23–24, 2023.*

Beginning Time on 23.03.2023 (UT)	Time of Max (UT)	Xmax (nT)	End Time (UT)	Amplitude (nT)
18:42	19:02	32.7	19:56	64.6
19:56	20:15	9.9	20:48	10.8
20:48	21:56	20.7	22:59	50.7
23:28	00:36, 24.03	30.1	01:51, 24.03	53.4

3.4. Field-Aligned Current (FAC) Observations from AMPERE

To investigate the relationship between the registered Midlatitude Positive Bays (MPBs) and substorm activity, field-aligned current (FAC) distributions derived from the AMPERE system were analyzed at the times corresponding to the maxima of the four MPB events. Figure 4 presents the FAC distributions at the times corresponding to the maxima of the four MPB events. The dark red ellipses indicate the longitudinal sector covered by the PPN–NAL magnetometer chain.

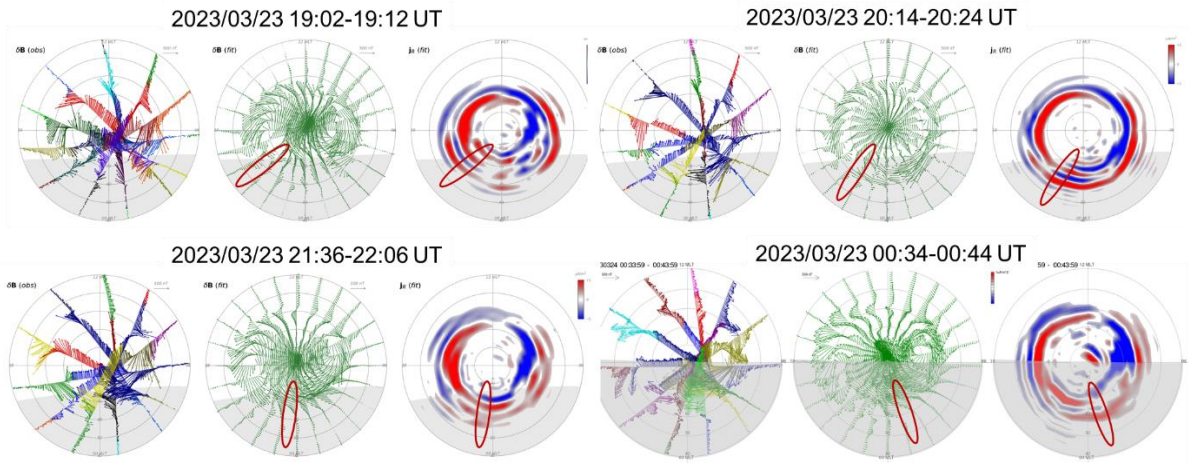


Figure 4. *AMPERE field-aligned current (FAC) distributions at the times corresponding to the maxima of the four MPB events observed at PAG on 23 March 2023. The dark red ellipses indicate the longitudinal sector of the PPN–NAL magnetometer chain and the Panagyurishte (PAG) station.*

The AMPERE observations reveal well-developed systems of upward and downward field-aligned currents during all four events (the right images in the four AMPERE panels). The images show that the current systems expand equatorward during the storm development, reaching 50° geomagnetic latitude in the third panel and extending beyond 50° in the fourth panel in the night sector. Such an equatorward expansion is characteristic of intense substorm activity and indicates that, during the registered MPB events, the auroral current systems extended to lower geomagnetic latitudes, reaching regions that are not typically affected during weaker substorms. Despite the complex structure of the current systems, it can be seen that near the MPB maxima the European sector was located under the western electrojet (the dark red ellipses in Figure 4).

3.5. Relationship between MPBs and SML/IL variations

To further examine the relationship between the observed MPB events and substorm activity, the temporal variations of the global SML and SMU indices, the regional IL index derived from the PPN–NAL magnetometer chain, and the X component recorded at the PAG geomagnetic station were compared. The results for the time interval 18:00 UT on 23 March 2023 – 02:00 UT on 24 March 2023 are presented in figure 5. The SML and IL indices exhibit similar temporal variations throughout the analyzed interval, indicating a strong contribution of substorm activity in the European sector. The maxima of the four MPBs coincide with pronounced minima in both the SML and IL indices, occurring at 19:02, 20:15, and 21:56 UT on 23 March, and at 00:36 UT on 24 March 2023. This close temporal correspondence provides strong evidence for the association of the observed MPBs with substorm activity.

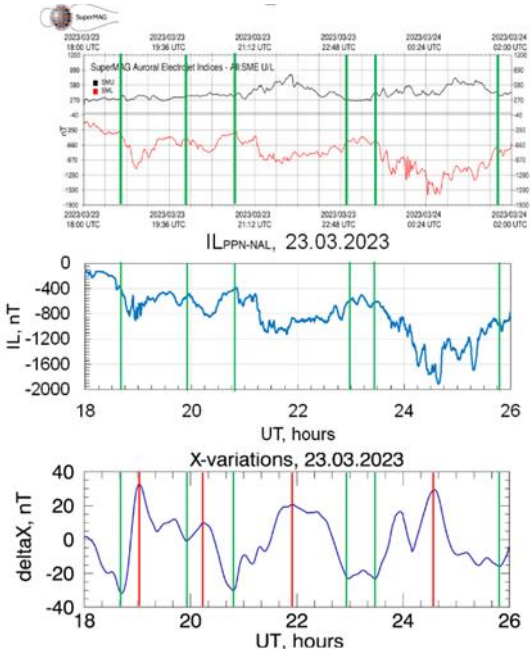


Figure 5. *Temporal variations of the SML and SMU indices (upper panel), the IL index derived from the PPN–NAL chain (middle panel), and the X component recorded at the Panagyurishte (PAG) geomagnetic station (bottom panel) during the geomagnetic storm of 23–24 March 2023. The green vertical lines indicate the beginning and end of the registered Midlatitude Positive Bay (MPB) events, while the red vertical lines in the bottom panel mark the MPB maxima.*

3.6. Comparison of the MPB occurrence times with the substorm onset lists

The beginning times of the four MPBs were compared with the substorm onset times given in the available substorm lists. Three of the four MPB beginnings closely coincide with substorm onsets identified over Europe. The second MPB, which was the weakest of the four events, has no corresponding substorm onset in the lists. Nevertheless, its association with substorm activity is supported by the simultaneous variations of the SML and IL indices. The absence of a listed substorm onset may reflect differences in the detection criteria and processing procedures used to construct the substorm lists, particularly for weaker or localized substorm activity.

The first MPB at Panagyurishte (PAG, 42.5° geographic latitude, 24.2° geographic longitude), beginning at 18:42 UT on 23 March 2023, closely coincides with the substorm onset at White Sea (WSE; 66.55° geographic latitude, 33.1° geographic longitude) at 18:40 UT, identified by the Newell and Gjerloev (2011) technique. The close temporal

correspondence supports the association of the MPB with substorm activity occurring near the longitude of PAG.

The third MPB, beginning at 20:48 UT, is also in close temporal agreement with substorm onsets identified at Sodankylä (SOD; 67.37° geographic latitude, 26.23° geographic longitude) at 20:45 UT by Newell and Gjerloev (2011), and near Mekrijärvi (MEK; 62.77° geographic latitude, 30.97° geographic longitude) at 20:51 UT, reported by Forsyth et al. (2015).

The fourth MPB, beginning at 23:28 UT, corresponds closely to three entries in the substorm lists. These include the onset at Solund (SOL; 61.08° geographic latitude, 4.84° geographic longitude) at 23:29 UT from Newell and Gjerloev (2011), the onset at 23:14 UT near Hankasalmi (HAN; 62.25° geographic latitude, 26.60° geographic longitude) from Forsyth et al. (2015), and an onset at 00:00 UT on 24 March at 66.84° geographic latitude and 31.25° geographic longitude, also from Forsyth et al. (2015). Inspection of the SML and IL variations suggests that the onsets at 23:14 and 23:29 UT may represent the same substorm, with the exact onset time depending on the method used for its identification. The event listed at 00:00 UT appears to represent an intensification of the same substorm rather than a separate substorm.

4. Conclusions

The observational data from both ground- and space-based solar telescopes supports the conclusion that the geomagnetic storm of 23 March 2023 was driven by two closely timed, likely interacting halo CMEs originating on 20 March 2023, associated with a weak filament eruption rather than a strong flare or well-defined active region. This provides an example of a potentially complex scenario involving a filament-driven CME followed by CME-CME interaction.

Such events highlight the importance of coronagraph observations and propagation modeling, as traditional indicators (strong flares or prominent active regions) may be absent.

On 23 March 2023, four distinct, consecutive MPB events were identified at Panagyurishte (PAG) during the main phase of the geomagnetic storm. All four events exhibited the characteristic temporal evolution of the X component associated with mid-latitude positive bays. Their maximum X-component values ranged from the 5–10 nT interval to values exceeding 30 nT. The occurrence of such high maximum X-component values is consistent with previous results showing that the most intense MPBs are preferentially associated with intense geomagnetic storms.

The association of the four MPBs with substorm activity is supported by several independent observations. The SML and regional IL indices exhibit pronounced negative variations coinciding with the MPB maxima, while AMPERE observations reveal well-developed systems of upward and downward field-aligned currents during all four events. The FAC systems show an equatorward expansion during the sequence of events, reaching and subsequently extending beyond 50° geomagnetic latitude in the night sector. Near the MPB maxima, the European sector was located under the western electrojet.

The comparison with available substorm onset lists shows that three of the four MPB beginnings closely coincide with independently identified substorm onsets. The first, third, and fourth MPBs are associated with substorm onsets over Europe, in regions near the longitude of PAG. The second, weakest MPB has no corresponding onset in the available lists, but its association with substorm activity is supported by the simultaneous SML and IL variations. The results demonstrate that MPBs can provide a useful ground-based indication of substorm activity at mid-latitudes, including during intense geomagnetic storms.

Acknowledgments: This work is supported by the National Science Fund of Bulgaria with contract No. KP-06-N64/3.

We acknowledge the use of the data from SOHO/LASCO and the CDAW CME catalog (generated and maintained at the CDAW Data Center by NASA and The Catholic University of America in cooperation with the Naval Research Laboratory), GOES X-ray flare listing (by NOAA/NCEI), and NOAA Space Weather Prediction Center's active region list.

We acknowledge the substorm timing list identified by the Newell and Gjerloev technique, the SMU and SML indices (Newell and Gjerloev, 2011); and the SuperMAG collaboration. The authors are grateful to the creators of the databases AMPERE (https://ampere.jhuapl.edu/), IMAGE (http://space.fmi.fi/image/), OMNI (https://cdaweb.gsfc.nasa.gov/), INTERMAGNET (http://intermagnet.org/) and the solar wind large-scale phenomena catalog (http://www.iki.rssi.ru/omni/) for the opportunity to use them in this work.

References

Akasofu, S.-I. and Meng, C.-I. (1968) 'Low latitude negative bays', *Journal of Atmospheric and Terrestrial Physics*, 30, pp. 227–241. doi: 10.1016/0021-9169(68)90078-0.

Amaechi, P.O., Messanga, H., Grodji, F.O. et al. (2025) 'Risk assessment of the ground magnetic response to the March and April 2023 geomagnetic storms using geomagnetically induced currents indices', *Space Weather*, 23, article e2024SW004324. doi: 10.1029/2024SW004324.

Buonsanto, M.J. (1999) 'Ionospheric storms – A review', *Space Science Reviews*, 88, pp. 563–601. doi: 10.1023/A:1005107532631.

Daglis, I.A., Thorne, R.M., Baumjohann, W. and Orsini, S. (1999) 'The ring current', *Reviews of Geophysics*, 37(4), pp. 407–438. doi: 10.1029/1999RG900009.

Forsyth, C., Rae, I.J., Coxon, J.C., Freeman, M.P., Jackman, C.M., Gjerloev, J. and Fazakerley, A.N. (2015) 'A new technique for determining substorm onsets and phases from indices of the electrojet (SOPHIE)', *Journal of Geophysical Research: Space Physics*, 120, pp. 10592–10606. doi: 10.1002/2015JA021343.

Gonzalez, W.D., Joselyn, J.A., Kamide, Y., Kroehl, H.W., Rostoker, G., Tsurutani, B.T. and Vasyliunas, V.M. (1994) 'What is a geomagnetic storm?', *Journal of Geophysical Research: Space Physics*, 99(A4), pp. 5771–5792. doi: 10.1029/93JA02867.

Gopalswamy, N., Shimojo, M., Lu, W., Yashiro, S., Shibasaki, K. and Howard, R.A. (2003) 'Prominence eruptions and coronal mass ejection: A statistical study using microwave observations', *The Astrophysical Journal*, 586(1), pp. 562–578. doi: 10.1086/367614.

Gosling, J.T., McComas, D.J., Phillips, J.L. and Bame, S.J. (1991) 'Geomagnetic activity associated with Earth passage of interplanetary shock disturbances and coronal mass ejections', *Journal of Geophysical Research*, 96(A5), pp. 7831–7839. doi: 10.1029/91JA00316.

Gosling, J.T. (1993) 'The solar flare myth', *Journal of Geophysical Research*, 98(A11), pp. 18937–18949.

Guineva, V., Werner, R., Despirak, I., Bojilova, R. and Raykova, L. (2021a) 'Mid-latitude positive bays during substorms under quiet and disturbed conditions', *Comptes rendus de l'Académie bulgare des Sciences*, 74(8), pp. 1192–1200. doi: 10.7546/CRABS.2021.08.11.

Guineva, V., Werner, R., Lubchich, A., Atanassov, A., Bojilova, R., Raykova, L., Valev, D. and Despirak, I. (2021b) 'Development of a substorms catalog including the MPB observed at Panagjurishte Station, Bulgaria', *EPJ Web of Conferences*, 254, article 01002. doi: 10.1051/epjconf/202125401002.

Guineva, V., Werner, R., Bojilova, R., Raykova, L., Atanassov, A. and Valev, D. (2024a) 'Analysis of substorms related to strong MPB at Panagjurishte Station in 2022', in *Proceedings of the Sixteenth Workshop "Solar Influences on the Magnetosphere, Ionosphere and Atmosphere"*, pp. 56–63.

Guineva, V., Werner, R., Bojilova, R., Raykova, L., Atanassov, A. and Valev, D. (2024b) 'Study of the midlatitude positive bays at the magnetic station Panagyurishte during the descending phase of Solar Cycle 24', in *Proceedings of the Twentieth Anniversary International Scientific Conference "Space, Ecology, Safety" (SES 2024)*, Sofia, Bulgaria.

Guineva, V.H., Despirak, I.V., Werner, R., Ljubich, A.A., Raykova, L. and Bojilova, R. (2025) 'The geomagnetic midlatitude effects of the supersubstorms during the May 10–12, 2024 superstorm', in *Proceedings of the Seventeenth Workshop "Solar Influences on the Magnetosphere, Ionosphere and Atmosphere"*, pp. 92–109. doi: 10.31401/WS.2025.proc.14.

Kamide, Y., Baumjohann, W., Daglis, I.A. et al. (1998) 'Current understanding of magnetic storms: Storm-substorm relationship', *Journal of Geophysical Research: Space Physics*, 103(A7), pp. 14135–14161. doi: 10.1029/97JA02338.

Kepko, L., McPherron, R.L., Amm, O., Apatenkov, S., Baumjohann, W., Birn, J. et al. (2014) 'Substorm current wedge revisited', *Space Science Reviews*, 190(1–4), pp. 1–46. doi: 10.1007/s11214-014-0124-9.

Kisabeth, J.L. and Rostoker, G. (1974) 'The expansive phase of magnetospheric substorms: 1. Development of the auroral electrojets and auroral arcs configuration during substorm', *Journal of Geophysical Research*, 79(7), pp. 972–984. doi: 10.1029/JA079i007p00972.

Knipp, D.J., Tobiska, W.K. and Emery, B.A. (2004) 'Direct and indirect thermospheric heating sources for Solar Cycles 21–23', *Solar Physics*, 224(1–2), pp. 495–505. doi: 10.1007/s11207-005-6393-4.

Koehn, G.J., Desai, R.T., Davies, E.E., Forsyth, R.J., Eastwood, J.P. and Poedts, S. (2022) 'Successive interacting coronal mass ejections: How to create a perfect storm', *The Astrophysical Journal*, 941(2), article 139. doi: 10.3847/1538-4357/aca28c.

McPherron, R.L. (1972) 'Substorm-related changes in the geomagnetic tail: The growth phase', *Planetary and Space Science*, 20(9), pp. 1521–1539. doi: 10.1016/0032-0633(72)90054-2.

McPherron, R.L., Russell, C.T. and Aubry, M. (1973a) 'Satellite studies of magnetospheric substorms on August 15, 1968: 9. Phenomenological model for substorms', *Journal of Geophysical Research*, 78(16), pp. 3131–3149. doi: 10.1029/JA078i016p03131.

McPherron, R.L., Russell, C.T., Kivelson, M.G. and Coleman, P.J. Jr. (1973b) 'Substorms in space: The correlation between ground and satellite observations of the magnetic field', *Radio Science*, 8(11), pp. 1059–1076. doi: 10.1029/RS008i011p01059.

McPherron, R.L. and Chu, X. (2017) 'The midlatitude positive bay and the MPB index of substorm activity', *Space Science Reviews*, 206(1–4), pp. 91–122. doi: 10.1007/s11214-016-0316-6.

Meng, C.-I. and Akasofu, S.-I. (1969) 'A study of polar magnetic substorms: 2. Three-dimensional current system', *Journal of Geophysical Research*, 74(16), pp. 4035–4053. doi: 10.1029/JA074i016p04035.

Munro, R.H., Gosling, J.T., Hildner, E., MacQueen, R.M., Poland, A.I. and Ross, C.L. (1979) 'The association of coronal mass ejection transients with other forms of solar activity', *Solar Physics*, 61, pp. 201–215.

Newell, P.T. and Gjerloev, J.W. (2011) 'Evaluation of SuperMAG auroral electrojet indices as indicators of substorms and auroral power', *Journal of Geophysical Research: Space Physics*, 116, article A12211. doi: 10.1029/2011JA016779.

Russell, C.T. and McPherron, R.L. (1973) 'The magnetotail and substorms', *Space Science Reviews*, 15(2–3), pp. 205–266. doi: 10.1007/BF00169321.

Sammis, I., Tang, F. and Zirin, H. (2000) 'The dependence of large flare occurrence on the magnetic structure of sunspots', *The Astrophysical Journal*, 540(1), pp. 583–587. doi: 10.1086/309303.

Temmer, M., Scolini, C., Richardson, I.G. et al. (2023) 'CME propagation through the heliosphere: Status and future of observations and model development', *Advances in Space Research*. doi: 10.1016/j.asr.2023.07.003.

Temmer, M. (2026) 'CME observations from Sun to impact on geospace', in Gopalswamy, N., Banyś, D. and Gadimova, S. (eds), *Proceedings of the United Nations/Germany Workshop on the International Space Weather Initiative: ISWI 2024*, Springer Proceedings in Physics, 431.

Tsurutani, B., Mannucci, A., Iijima, B. et al. (2004) 'Global dayside ionospheric uplift and enhancement associated with interplanetary electric fields', *Journal of Geophysical Research: Space Physics*, 109, article A08302. doi: 10.1029/2003JA010342.

Vršnak, B., Žic, T., Vrbanec, D. et al. (2013) 'Propagation of interplanetary coronal mass ejections: The drag-based model', *Solar Physics*, 285(1–2), pp. 295–315. doi: 10.1007/s11207-012-0035-4.

Vršnak, B., Dumbović, M., Čalogović, J., Verbanac, G. and Poljančić Beljan, I. (2017) 'Geomagnetic effects of corotating interaction regions', *Solar Physics*, 292(9), article 140. doi: 10.1007/s11207-017-1165-5.

DOI: 10.31401/WS.2026.proc.19

Case Study of the First Forbush Decrease Detected by MNM ROZH Station

Tsvetkov Ts., Petrov N., Minev M.

Institute of Astronomy and National Astronomical Observatory, Bulgarian Academy of Sciences
tstsvetkov@nao-rozhen.org

Abstract

A mini neutron monitor station (MNM-ROZH) was recently deployed at the National Astronomical Observatory of the Bulgarian Academy of Sciences at 1730 m and has been operational since June 2025. The instrument includes three compact neutron monitor units equipped with BF_3 proportional counters (type LND2043). The main scientific goal of the instrument is to measure variations, including transients, of the incoming cosmic rays—high-energy particles produced in a variety of astrophysical environments, including explosive stellar phenomena and processes related to solar activity. They are composed mainly of protons, along with heavier nuclei and electrons, and their flux near Earth is strongly influenced by solar-driven disturbances in the heliosphere. We summarize the initial results from the first year of operation of the station. The reliability of the measurements is illustrated by the clear detection of a significant Forbush decrease in June 2025. These results demonstrate the station's capability to contribute to continuous cosmic ray monitoring and to studies of solar-terrestrial interactions.

Keywords: Mini Neutron Monitor; Ground-based Measurements; Cosmic Rays; Forbush Decrease

1. Introduction

Galactic cosmic rays (GCRs) constitute a persistent flux of high-energy charged particles reaching the heliosphere from sources outside the Solar System. Their propagation through interplanetary space is strongly influenced by the heliospheric magnetic field and by transient structures associated with solar activity. Consequently, the intensity of GCRs observed near Earth exhibits variations over a wide range of time scales, from the approximately 11-year solar cycle to short-term transient disturbances lasting from several hours to several days. Among the most prominent short-term variations are Forbush decreases (FDs), which provide an important means of investigating the interaction between solar disturbances and the GCR population.

A FD is generally defined as a transient reduction in the intensity of GCRs observed near Earth. The phenomenon was first reported by Forbush in the 1930s using ionization chambers [Forbush, 1937]. A typical FD is characterized by a relatively rapid decrease in cosmic ray (CR) intensity, followed by a more gradual recovery toward the pre-event level. The magnitude and temporal profile of an individual event can vary considerably, with some events showing a single-step decrease and others exhibiting a two-step structure. In the latter case, the first decrease is commonly associated with the turbulent sheath region preceding an interplanetary coronal mass ejection (ICME), while the second decrease can be related to the magnetic structure of the ejecta itself [Cane, 2000]. Although the detailed physical mechanisms responsible for individual FDs remain an active subject of research, the phenomenon is generally understood in terms of the modulation and transport of GCRs by disturbed heliospheric magnetic fields.

The connection between FDs and solar transients makes these events particularly useful for studying solar-terrestrial relations. Coronal mass ejections (CMEs) can substantially modify

the magnetic field configuration and particle transport conditions in the inner heliosphere. When an ICME and its associated shock propagate past the Earth, the enhanced magnetic turbulence and magnetic field strength can reduce the access of GCRs to the observer, producing a measurable decrease in the CR intensity [Cane, 2000]. The amplitude, duration, onset profile, and recovery phase of an FD therefore contain information about the interplanetary disturbance and about the rigidity-dependent propagation of CRs. In addition, comparisons of the same event at different observing locations can provide information about the spatial and rigidity dependence of the CR modulation [Lockwood, 1971].

Ground-based neutron monitors (NMs) have played a central role in the continuous observation of CR variability for more than half a century. Unlike direct measurements of primary CRs, NMs detect secondary particles generated when primary CR interact with nuclei in the Earth's atmosphere. High-energy primary particles initiate atmospheric nuclear cascades, producing secondary neutrons and other particles that can subsequently be detected at ground level. In a conventional NM, the neutrons are moderated and detected using gas-filled proportional counters, with the surrounding producer, moderator, and reflector providing the necessary neutron multiplication and detection efficiency [Simpson, 1957; Clem and Dorman, 2000].

The indirect nature of NM measurements is nevertheless one of their major strengths. Because the atmospheric cascade converts primary CR interactions into a large number of secondary particles, NMs provide high counting rates and consequently good statistical precision. Their continuous operation, relatively stable long-term response, and high temporal resolution make them particularly well suited to detecting small and rapid variations in CR intensity. The worldwide network of NMs also provides measurements at different geomagnetic latitudes, altitudes, and cutoff rigidities. This geographical distribution makes it possible to study the rigidity dependence of CR variations and to distinguish local or instrumental effects from large-scale changes in the GCR flux [Clem and Dorman, 2000; Okike et al., 2021].

Despite their scientific value, conventional NMs are relatively large, heavy, and resource-intensive instruments. A standard NM64-type monitor contains multiple proportional counters and a substantial amount of moderator, reflector, and neutron-producing material. These characteristics provide a high counting rate and stable response but make conventional NMs difficult to deploy at many locations. The resulting limitations in geographical coverage have motivated the development of more compact NM designs.

Mini-neutron monitors (MNMs) represent an important development in this direction. The MNM is essentially a portable implementation of the NM concept, designed to retain the essential detection principle while reducing the material requirements, physical dimensions, and operational complexity of a conventional instrument [Caballero-Lopez, 2016; Strauss et al., 2020]. An important advantage of MNMs is their potential for increasing the spatial density of CR monitoring stations. Strauss et al., (2020) emphasized that their relatively small size, reduced cost, and possibility of semi-autonomous operation make MNMs suitable for deployment in remote locations and for expanding the existing NM network. A denser network can improve the characterization of transient CR variations and contribute to near-real-time space weather monitoring. In particular, the detection of FDs by compact NMs demonstrates that such instruments can provide scientifically useful measurements of short-term GCR variability while complementing the observations obtained by established NM stations. This was our motivation to establish a MNM station at the National Astronomical Observatory Rozhen (Bulgaria). See more about the instrument in Section 2.

The detection of a FD by a ground-based NM therefore represents more than a simple decrease in the count rate. It provides a ground-based signature of a transient disturbance in the heliospheric environment and can be used, together with observations from other NMs

and space-based instruments, to investigate the propagation and impact of solar-driven interplanetary structures. The present work focuses on a case study of the first FD detected by the MNM ROZH station – the one from June 2025.

2. Mini-Neutron Monitor Station

The mini-neutron monitor station (MNM-ROZH) is installed at the National Astronomical Observatory Rozhen (41°41′ N, 24°44′ E, altitude: 1730 m) and provides continuous ground-based measurements of the secondary neutron component of CRs. The station consists of three independent MNM units based on BF_3 proportional counters (LND2043), operating according to the modern mini NM concept for long-term CR observations (see more about the technical parameters of the instrument in [Petrov et al., 2025; Tsvetkov et al., 2026]).

The detector is complemented by an integrated meteorological station that continuously records atmospheric pressure, temperature, relative humidity, precipitation, etc. These environmental measurements provide the basis for evaluating and, where appropriate, correcting local atmospheric effects on the neutron count rate.

Since becoming operational, MNM-ROZH has demonstrated stable long-term performance and the capability to register both gradual CR variations and transient events associated with space weather. The station is dedicated to the detection and analysis of Forbush effects and Ground Level Enhancement related studies and its real-time observations are integrated into the observatory data services and contribute to the international NM community.

3. Solar Origin and Interplanetary Conditions

The FD observed by MNM-ROZH between 31 May and 10 June 2025 occurred during a period of enhanced solar and interplanetary activity. In order to identify the solar drivers of the event, we considered the sequence of solar flares (SFs) and coronal mass ejections (CMEs) observed between 29 and 31 May, together with the subsequent solar wind (SW) and interplanetary magnetic field (IMF) conditions at Earth. CME times and kinematic parameters quoted below are taken primarily from SOHO/LASCO CME Catalog [Yashiro et al., 2004; Gopalswamy et al., 2024]. SF information is based on GOES/SIDC observations, while near-Earth SW and IMF parameters are taken from the ACE and DSCOVR observations and the NASA/GSFC OMNI data set [King and Papitashvili, 2005].

3.1. Preconditioning

The solar-terrestrial environment was already disturbed before the CME sequence associated with the June 2025 FD. On 29 May, a G3-level geomagnetic storm was observed in response to the arrival of a high-speed SW stream originating from an extended negative-polarity equatorial coronal hole [National Oceanic and Atmospheric Administration (NOAA) and National Weather Service (NWS) 2025a]. The coronal hole, identified as a combination of SIDC Coronal Holes 116 and 112, began crossing the solar central meridian on 26 May. The stream had begun to affect the near-Earth environment several days earlier and produced SW speeds of approximately 650–830 km s^{-1} on 30 May. The associated enhancement of the IMF reached about 24 nT, with B_z decreasing to approximately -24 nT during the initial high-speed-stream interaction [National Oceanic and Atmospheric Administration (NOAA) and National Weather Service (NWS) 2025b; Solar-Terrestrial Centre of Excellence (STCE) 2025]. This preceding high-speed stream is important for interpreting the subsequent CME-driven disturbance. It provided an already elevated SW background into which the CMEs of 30–31 May propagated. The 29 May disturbance should nevertheless be distinguished from the main FD studied here. In particular, the geomagnetic activity associated with the coronal hole high-speed stream preceded the abrupt CR decrease beginning on 1 June and did not exhibit the characteristic shock-associated CR depression observed during the later CME

passage. We therefore regard the coronal hole high-speed stream as a preconditioning agent rather than as the primary cause of the June 2025 FD.

3.2. Solar Activity of 30–31 May

Solar activity increased substantially on 30–31 May, primarily due to NOAA Active Region (AR) 4100. On 30 May, it produced three C-class SFs and an M3.4-class flare peaking at 06:13 UT. It was accompanied by an on-disk dimming and an Earth-directed CME first observed by SOHO/LASCO C2 at 07:12 UT [Solar Influences Data Analysis Center (SIDC) 2025a] with an angular width of 163° and a linear speed of 353 km s^{-1} and is classified as a partial halo CME [Gopalswamy et al., 2024]. Its wide angular extent and Earth-directed component make it a plausible precursor to the subsequent interplanetary disturbance, although its relatively low catalogued speed suggests that it could not by itself account for the unusually rapid shock observed at Earth on 1 June. Several other CMEs were also registered on 30 May. Their morphology, kinematics and propagation directions do not provide equally strong evidence for a direct Earth impact. Consequently, they are not considered primary candidates for the disturbance responsible for the observed FD.

The most significant solar eruption occurred shortly afterwards. AR 4100 produced a long-duration M8.1 flare peaking at 00:05 UT on 31 May. It occurred close to the solar central meridian and was accompanied by a Type II radio burst, coronal dimming, and a fast Earth-directed halo CME at 00:12:05 UT on 31 May [Solar Influences Data Analysis Center (SIDC) 2025b] (an angular width of 360° and a linear speed of 1752 km s^{-1} [Gopalswamy et al., 2024]). The combination of its full-halo morphology, high speed, source location close to the solar central meridian, and its direct association with the M8.1 flare makes this CME the strongest individual candidate for the major interplanetary disturbance observed at Earth on 1 June.

The temporal proximity of the 30 May and 31 May eruptions is also important. The much faster halo CME of 31 May was launched into a heliosphere already containing slower CME material from the preceding day. Independent space weather analyses therefore suggested that the fast CME could overtake the slower CME first observed on 30 May, resulting in an interacting or compound interplanetary structure [Solar Influences Data Analysis Center (SIDC) 2025b]. Such CME–CME interaction provides a plausible explanation for the unusually strong and extended SW disturbance observed at Earth.

3.3. First Interplanetary Disturbance

A clear interplanetary shock was detected near the Earth on 1 June at approximately 05:22 UT by both the ACE and DSCOVR spacecraft. The shock was characterized by an abrupt increase in the total IMF strength from approximately 7 nT to about 25 nT, accompanied by an increase in SW speed from approximately 700 km s^{-1} to more than 1100 km s^{-1}. The SW ion temperature also increased significantly, while the subsequent magnetic field evolution included a smooth rotation of the field components, consistent with the passage of structured ICME material [NASA Community Coordinated Modeling Center (CCMC) 2025b; King and Papitashvili, 2005].

The timing and magnitude of this disturbance provide strong evidence for its association with the CME sequence of 30–31 May. In particular, the CCMC/NASA analysis explicitly associates the 1 June 05:22 UT shock with the combined arrival of the CMEs observed on 30 May and the fast halo CME of 31 May [NASA Community Coordinated Modeling Center (CCMC) 2025b]. This interpretation is also consistent with independent space weather analyses, which associate the fast halo CME with the severe geomagnetic storm observed on 1 June. The geomagnetic response reached K_p=8 during the main phase of the storm, while

the minimum Dst value was approximately -120 nT [CDAW Data Center 2025; Solar-Terrestrial Centre of Excellence (STCE) 2025].

The arrival of this interplanetary structure is temporally consistent with the onset of the pronounced CR decrease observed by MNM-ROZH as well as other NMs. Thus, the first phase of the FD can be physically associated with the arrival of the shock and the following CME-driven sheath and magnetic structure. The enhanced magnetic field strength and turbulent conditions in these regions provide efficient scattering and exclusion of GCRs, producing the rapid decrease in NM count rates.

3.4. Subsequent Interplanetary Disturbance

The CR depression remained pronounced for several days after the first shock, indicating that the 1 June disturbance was followed by additional interplanetary structure rather than by an immediate return to undisturbed conditions. SW observations show a further interplanetary disturbance on 2 June at approximately 20:02 UT. At this time, the total magnetic field strength increased from an already elevated level of about 10 nT to 12.4 nT and subsequently to approximately 14.5 nT, while the SW speed increased from about 580 to 660 km s^{-1}. The event was detected by ACE and DSCOVR, although the corresponding ICME signature was classified as weaker than that of the 1 June event [NASA Community Coordinated Modeling Center (CCMC) 2025c].

The interplanetary medium remained disturbed after the arrival of the first CME complex. On 31 May, AR 4100 produced several additional M-class flares, including M2.4 and M4.5 and M2.9 SFs peaking at 05:18, 08:18 and 15:49 UT, respectively [Solar-Terrestrial Centre of Excellence (STCE) 2025]. No distinct fast Earth-directed CME associated with these two flares is identified in the SOHO/LASCO CME Catalog. A further CME was nevertheless catalogued by the NASA CCMC DONKI database with an event start time of 14:23 UT on 31 May. This event was observed by STEREO-A/COR2 and GOES/CCOR-1 and was reported only very faintly in SOHO/LASCO-C3; DONKI gives an estimated speed of approximately 680 km s^{-1} and an opening half-angle of about 35°. Its solar source is uncertain, although a small brightening and field-line motion near AR 4100 were identified as a possible source [NASA Community Coordinated Modeling Center (CCMC) 2025a]. A recent analysis of the same event using the SEVAN network identified a two-step FD and associated the two phases with sudden storm commencements at 05:22 UT on 1 June and 10:19 UT on 2 June [Karapetyan et al., 2026].

4. June 2025 Forbush Decrease

In this paper the CR response to the solar and interplanetary activity described in the previous section was investigated using the MNM-ROZH measurements and simultaneous observations from the Oulu and Rome NMs (Figure 1). To allow a direct comparison, the data from the three stations were averaged to a common temporal resolution of 60 min and expressed as relative variations with respect to their individual pre-event reference levels. The mean count rate on 30 May 2025 was adopted as the reference level, and the relative variation was calculated as

$$\Delta I(t) = \frac{I(t) - I_0}{I_0} \times 100\%, \quad (1)$$

where $I(t)$ is the hourly count rate and I_0 is the corresponding mean count rate during the reference interval.

4.1. Forbush decrease observed by MNM-ROZH

The MNM-ROZH measurements reveal a pronounced and prolonged decrease in the GCR intensity beginning on 1 June 2025 (Figure 1). Prior to the event, the count rate remained close to the reference level. During the morning of 1 June, however, a rapid decrease developed and the relative intensity fell below -10% during the afternoon. The onset of this decrease occurred within several hours of the strong interplanetary shock detected near Earth at approximately 05:22 UT, discussed in Section 3.

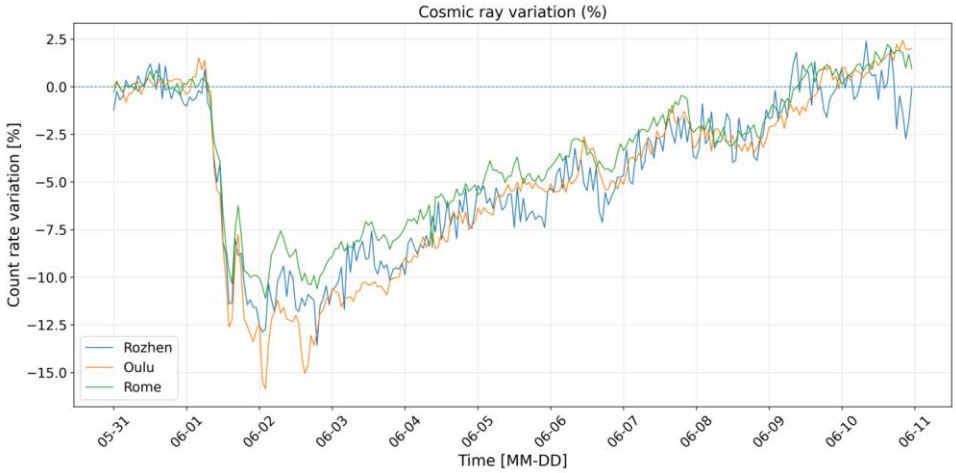


Figure 1. *Relative CR intensity variations recorded by the Rozhen, Oulu, and Rome NM stations from 31 May to 10 June 2025. The data are normalized to the mean count rate measured during the reference period on 30 May 2025, which is defined as 0% for each station. All data are corrected for the respective station response, and the measurements are presented at 1-hour temporal resolution.*

The subsequent evolution recorded at Rozhen shows a clear two-step structure – the first phase reached a minimum of approximately -12.85% at 01:00 UT on 2 June. During the following hours, the CR intensity partially recovered, reaching approximately -9.36% at 08:00 UT. This recovery was then interrupted by a renewed decrease during the second half of 2 June. The second depression reached a minimum of -13.53% at approximately 19:00 UT on 2 June. This represents the absolute minimum recorded by MNM-ROZH during the event. Relative to the preceding local recovery level, the second phase therefore corresponds to an additional CR suppression of approximately 4.17 percentage points. Interestingly, the second phase was slightly deeper than the first one in the MNM-ROZH measurements, with the two minima differing by approximately 0.68 percentage points. Following the second minimum, the CR intensity entered a prolonged recovery phase lasting several days – the overall trend was a gradual return toward the pre-event level, which was approached toward the end of the analysed interval.

4.2. Comparison with Oulu and Rome NMs

The identification of the event by MNM-ROZH is independently supported by the observations from the Oulu and Rome NMs. As shown in Figure 1, all three stations recorded a remarkably similar temporal evolution despite their different geographic locations, geomagnetic cut-off rigidities, and detector characteristics.

The first minimum is closely synchronized among the three stations (Table 1). MNM-ROZH reached a relative variation of -12.85% at approximately 01:00 UT on 2 June, while Oulu and Rome reached their first minima approximately one hour later, at 02:00 UT. The corresponding variations at Oulu and Rome were -15.87% and -11.11%, respectively. Given the common 60-min temporal resolution, the difference of one hour does not indicate a significant difference in the timing of the first minimum.

A particularly important feature is the partial recovery observed after the first minimum. The MNM-ROZH intensity increased to -9.36% by 08:00 UT. Similar local recoveries are independently observed at Oulu, where the intensity reached -11.19% at 06:00 UT, and at Rome, where it reached -7.56% at 07:00 UT. The simultaneous presence of this feature in all three records provides a natural separation between the two main phases of the event.

Following this partial recovery, the second decrease was not only detected by MNM-ROZH data. At Oulu, the second minimum of -15.05% occurred at approximately 15:00 UT. At both MNM-ROZH and Rome, the second minimum occurred at approximately 19:00 UT, reaching -13.53% and -10.60%, respectively. Relative to the local recovery preceding the second depression, the additional decreases were approximately 3.86, and 3.04 percentage points at Oulu, and Rome, respectively (4.17 for Rozhen; see 4.1).

The relative importance of the two phases is not identical at the three stations. At MNM-ROZH, the second minimum (-13.53%) was deeper than the first (-12.85%) and therefore represents the absolute minimum of the event. In contrast, the first minimum remained slightly deeper at Oulu (-15.87% compared with -15.05%) and Rome (-11.11% compared with -10.60%). Nevertheless, the overall morphology of the two-step decrease is highly consistent among the three stations.

The amplitude of the event also shows a systematic difference between the stations, with Oulu exhibiting the largest relative decrease, Rome the smallest, and MNM-ROZH an intermediate response. MNM-ROZH reproduces all of the major temporal features observed by the established Oulu and Rome stations. These include the rapid initial decrease, the first minimum, the intermediate recovery, the second depression, and the subsequent long-term recovery. The close agreement provides independent validation of the ability of MNM-ROZH to detect and characterize transient heliospheric modulations of GCRs.

Table 1. Characteristic parameters of the two-step Forbush decrease observed by MNM-ROZH, Oulu, and Rome. The partial-recovery value corresponds to the local maximum separating the two depressions. Times are given in UT.

Parameter	Rozhen	Oulu	Rome
First minimum time	2 Jun 01:00	2 Jun 02:00	2 Jun 02:00
First minimum	-12.85%	-15.87%	-11.11%
Partial-recovery time	2 Jun 08:00	2 Jun 06:00	2 Jun 07:00
Partial-recovery level	-9.36%	-11.19%	-7.56%
Second minimum time	2 Jun 19:00	2 Jun 15:00	2 Jun 19:00
Second minimum	-13.53%	-15.05%	-10.60%
Second-step decrease	4.17 p.p.	3.86 p.p.	3.04 p.p.

4.3. Relation to the interplanetary disturbances

The temporal evolution of the CR intensity can be compared with the sequence of interplanetary disturbances described in Section 3. The main decrease began shortly after the strong interplanetary shock detected near Earth at approximately 05:22 UT on 1 June. The rapid and nearly simultaneous response at MNM-ROZH, Oulu, and Rome strongly supports the association of the first phase of the FD with the arrival of the CME-driven disturbance and the subsequent passage of the disturbed interplanetary structure.

Following the first minimum, all three stations show a significant but temporary recovery during the early hours of 2 June. This recovery is followed by a coherent renewed decrease, producing a second minimum later the same day. The presence of the same sequence at three geographically separated NM stations demonstrates that the second depression represents a large-scale modulation of the GCR flux rather than a local or instrumental variation. The

temporal correspondence supports the interpretation of the event as a two-step, or more generally multi-phase, FD. As previously discussed in Section 3, the NM observations provide strong evidence for a two-step CR response, while the identification of a unique solar driver for the second step remains uncertain. A similar two-step structure of the 1–2 June 2025 FD has also been reported independently from observations of the SEVAN particle detector network [Karapetyan et al., 2026].

5. Conclusions

The available observations support a scenario in which the June 2025 FD was produced by a sequence of interacting solar eruptions rather than by a single isolated CME. The 29 May coronal hole high-speed stream established an already disturbed solar wind background. The M3.4-associated CME observed by LASCO on 30 May provided a slower, wide Earth-directed structure, followed by the much faster full-halo CME associated with the M8.1 flare on 31 May. The latter likely interacted with and overtook preceding CME material during interplanetary propagation, resulting in a complex CME-driven structure whose arrival at Earth was observed as a strong interplanetary shock on 1 June.

The temporal correspondence between this shock, the abrupt increase in the IMF strength and SW speed, and the onset of the CR depression provides a strong physical basis for identifying the 1 June interplanetary disturbance as the principal driver of the observed FD. The subsequent interplanetary disturbance on 2 June coincided with a renewed suppression of the CR intensity following a short partial recovery. However, its association with a specific solar eruption is considerably less certain, since no unambiguous corresponding Earth-directed CME can be identified in the SOHO/LASCO CME Catalog. The second phase may therefore reflect an additional perturbation propagating through the already disturbed interplanetary medium and/or the internal evolution and interaction of structures within the complex ICME environment.

The MNM-ROZH observations reveal a pronounced two-step structure of the FD. The first minimum of -12.85% was reached at approximately 01:00 UT on 2 June, followed by a partial recovery to -9.36% at 08:00 UT. The CR intensity subsequently decreased again by approximately 4.17 percentage points, reaching the absolute event minimum of -13.53% at approximately 19:00 UT. The event was followed by a prolonged and non-monotonic recovery extending over several days.

Comparison with the Oulu and Rome NMs confirms that the principal temporal features observed at Rozhen were not local or instrumental in origin. All three stations recorded the rapid initial decrease, a closely synchronized first minimum, the intermediate partial recovery, and a second depression on 2 June. The observed amplitude differences are qualitatively consistent with the different geomagnetic cut-off rigidities and detector response functions of the three stations. Despite these differences, the close agreement in the temporal evolution demonstrates that MNM-ROZH reliably traces the large-scale modulation of GCRs during the event.

The June 2025 event represents the first FD detected by MNM-ROZH. Although it is a recently established MNM with lower counting statistics than conventional stations, its response to the disturbance is consistent with independent observations from other stations. In particular, the instrument successfully resolved not only the main CR depression but also the more complex two-step structure and subsequent recovery. These results demonstrate the capability of MNM-ROZH to provide reliable observations of transient CR variations and support its use for future studies of FDs and other space weather related phenomena.

Acknowledgements

The research that led to these results was partially carried out with the help of infrastructure purchased under the National Roadmap for Research Infrastructure, financially coordinated by the Ministry of Education and Science of Republic of Bulgaria.

We acknowledge the NMDB database (www.nmdb.eu) founded under the European Union's FP7 programme (contract no. 213 007), and the PIs of individual neutron monitors at: Rome (SVIRCO Observatory, INAF IFSI-UNIRomaTre, Italy), Oulu (Sodankyla Geophysical Observatory of the University of Oulu, Finland).

The SOHO/LASCO CME catalog is generated and maintained at the CDAW Data Center by NASA and The Catholic University of America in cooperation with the Naval Research Laboratory. SOHO is a project of international cooperation between ESA and NASA.

References

Caballero-Lopez, R.A. (2016). An estimation of the yield and response functions for the mini neutron monitor, *Journal of Geophysical Research: Space Physics*, Vol. 121, No. 8, pp. 7461–7469, DOI: 10.1002/2016JA022690.

Cane, H.V. (2000). Coronal mass ejections and Forbush decreases, *Space Science Reviews*, Vol. 93, Nos. 1–2, pp. 55–77, DOI: 10.1023/A:1026532125747.

CDAW Data Center (2025). List of intense geomagnetic storm events, NASA Goddard Space Flight Center, Coordinated Data Analysis Workshops Data Center. Available at: https://cdaw.gsfc.nasa.gov/CME_list/dst100/.

Clem, J.M., Dorman, L.I. (2000). Neutron monitor response functions, *Space Science Reviews*, Vol. 93, Nos. 1–2, pp. 335–359, DOI: 10.1023/A:1026508915269.

Forbush, S.E. (1937). On the effects in cosmic-ray intensity observed during the recent magnetic storm, *Physical Review*, Vol. 51, No. 12, pp. 1108–1109, DOI: 10.1103/PhysRev.51.1108.3.

Gopalswamy, N., Michałek, G., Yashiro, S., Mäkelä, P., Akiyama, S., Xie, H., Vourlidas, A. (2026). The SOHO LASCO CME Catalog – Version 2, *Proceedings of the International Astronomical Union*, Vol. 20, Symposium S388, pp. 133–139, DOI: 10.1017/S1743921325000559.

Karapetyan, T., Chilingarian, A., Sargsyan, B. (2026). SEVAN network observations of the complex Forbush decrease on 1–2 June 2025, *New Astronomy*, Art. 102622, DOI: 10.1016/j.newast.2026.102622.

King, J.H., Papitashvili, N.E. (2005). Solar wind spatial scales in and comparisons of hourly Wind and ACE plasma and magnetic field data, *Journal of Geophysical Research: Space Physics*, Vol. 110, No. A2, Art. A02104, DOI: 10.1029/2004JA010649.

Lockwood, J.A. (1971). Forbush decreases in the cosmic radiation, *Space Science Reviews*, Vol. 12, No. 5, pp. 658–715, DOI: 10.1007/BF00173346.

NASA Community Coordinated Modeling Center (CCMC) (2025a). DONKI: Coronal mass ejection, 31 May 2025, 14:23 UT, *Space Weather Database of Notifications, Knowledge, Information*. Available at: https://kauai.ccmc.gsfc.nasa.gov/DONKI/view/CME/39225/1.

NASA Community Coordinated Modeling Center (CCMC) (2025b). DONKI: Interplanetary shock/CME arrival, 1 June 2025, 05:22 UT, *Space Weather Database of Notifications, Knowledge, Information*. Available at: https://kauai.ccmc.gsfc.nasa.gov/DONKI/view/IPS/39238/2.

NASA Community Coordinated Modeling Center (CCMC) (2025c). DONKI: Interplanetary shock/CME arrival, 2 June 2025, 20:02 UT, *Space Weather Database of Notifications, Knowledge, Information*. Available at: https://kauai.ccmc.gsfc.nasa.gov/DONKI/view/IPS/39265/4.

National Oceanic and Atmospheric Administration (NOAA), National Weather Service (NWS) (2025). G3 level geomagnetic event observed, *NOAA Space Weather Prediction Center*. Available at: https://www.spaceweather.gov/news/g3-level-geomagnetic-event-observed-0.

Okike, O., Alhassan, J.A., Iyida, E.U., Chukwude, A.E. (2021). A comparison of catalogues of Forbush decreases identified from individual and a network of neutron monitors: A critical perspective, *Monthly Notices of the Royal Astronomical Society*, Vol. 503, No. 4, pp. 5675–5691, DOI: 10.1093/mnras/stab680.

Petrov, N., Tsvetkov, T., Mishev, A., Yotov, V., Shirov, G. (2025). First observational data from the mini-neutron monitoring station at the Rozhen National Astronomical Observatory (MNMS-ROZH), *Publications of the Astronomical Observatory of Belgrade*, Vol. 107, pp. 37–42, DOI: 10.69646/14sbac05p.

Simpson, J.A. (1957). Cosmic-radiation neutron intensity monitor, *Annals of the International Geophysical Year*, Vol. 4, pp. 351–373, DOI: 10.1016/B978-1-4832-1304-0.50020-8.

Solar Influences Data Analysis Center (SIDC) (2025a). Bulletin on solar and geomagnetic activity – 30 May 2025, Royal Observatory of Belgium/SIDC. Available at:

https://www.spaceweatherlive.com/en/archive/2025/05/30/sidc-ursigram.html.

Solar Influences Data Analysis Center (SIDC) (2025b). Bulletin on solar and geomagnetic activity – 31 May 2025, Royal Observatory of Belgium/SIDC. Available at: https://www.spaceweatherlive.com/en/archive/2025/05/31/sidc-ursigram.html.

Solar-Terrestrial Centre of Excellence (STCE) (2025). Fast CME, severe geomagnetic storm, *STCE Newsletter*. Available at: https://www.stce.be/newsletter/html/2025/STCEnews20250605.html.

Strauss, D.T., Poluianov, S., van der Merwe, C., Krüger, H., Diedericks, C., Krüger, H., Usoskin, I., Heber, B., Nndanganeni, R., Blanco-Ávalos, J.J., García-Tejedor, I., Herbst, K., Caballero-Lopez, R.A., Moloto, K., Lara, A., Walter, M., Giday, N.M., Traversi, R. (2020). The mini-neutron monitor: A new approach in neutron monitor design, *Journal of Space Weather and Space Climate*, Vol. 10, Art. 39, DOI: 10.1051/swsc/2020038.

Tsvetkov, Ts., Petrov, N., Mishev, A., Poluianov, S., Minev, M. (2026). New mini neutron monitor at National Astronomical Observatory Rozhen: First measurements, *Advances in Space Research*, Vol. 78, No. 6, pp. 6634–6643, DOI: 10.1016/j.asr.2026.07.017.

Yashiro, S., Gopalswamy, N., Michalek, G., St. Cyr, O.C., Plunkett, S.P., Rich, N.B., Howard, R.A. (2004). A catalog of white light coronal mass ejections observed by the SOHO spacecraft, *Journal of Geophysical Research: Space Physics*, Vol. 109, No. A7, Art. A07105, DOI: 10.1029/2003JA010282.

DOI: 10.31401/WS.2026.proc.20

Development of the Total Ozone Column over Sofia Between 1979 and 2022

Werner R.

Space Research and Technology Institute, Bulgarian Academy of Sciences, Stara Zagora Department, Bulgaria; rolwer52@yahoo.co.uk

Abstract

Since the restriction of ozone depleting substances by the Montreal Protocol of 1987 the global ozone depletion was stopped and after an onset phase that has now lasted more than 30 years, an increase of ozone is already expected. The trends of total ozone column (TOC) depend on the latitudes and vary from region to region. This study examines the development of TOC over Sofia from 1979 up to 2022. Using the monthly ozone overpass data based on Multi Sensor Reanalyse (MSR2), we have performed trend analysis by help of a linear multiple regression model. We have analysed the distribution and the scedasticity of the residuals. The residuals of the series, which covers all months, are neither normally distributed nor homoscedastic. The reason of the heteroscedasticity lies in the high variability of the ozone levels during the winter periods, when subtropical air masses are frequently replaced by air masses from polar origin. We have divided the TOC series into the ozone winter (Dec.-March) and the ozone summer (May-Oct) ones. The residuals of these series are close to or are normally distributed and the series are homoscedastic. The stratospheric temperature at 100 hPa has a significant influence on TOC over Sofia. A lag of only one month was observed for the solar flux during ozone summer. In contrast the lag during the ozone winter is between two and three years. The cause could be related to the age of the ozone within the vortex. With regard to the zonal stratospheric winds, the best results were obtained with a lag of almost one year. After the turnaround point, no statistically significant increase in TOC was observed over Sofia.

Keywords: Total ozone column, linear multiple regression, ozone trend

1. Introduction

The amount of ozone in the Earth's atmosphere is determined mainly by the balance between ozone formation through photo dissociative processes in the ultraviolet range, on the one hand, and the catalytic breakdown of ozone molecules, on the other. Transport processes also play an important role. The discovery of the so-called ozone hole over Antarctica in 1985 [Farman et al., 1985] and subsequent publications on ozone depletion outside Antarctica, together with the fact that more harmful UV radiation not absorbed by the ozone layer reaches the Earth's surface, led to an intensification of ozone monitoring on a global scale. After the entry into force of the Montreal protocol of 1987 on substances that are responsible for ozone depletion the production and consumption of ozone depletion substances were phase out. Within about a decade, beginning with a slowdown of ozone decline, the decline was stopped. The approximate date when the ozone ceased decreasing in ozone researches, often called turnaround point [Herman et al., 2023], is in range from the mid 1990 up to 2000 depending on the geographical latitude [Weber et al., 2022; Herman et al., 2023]. To detect a turnaround point statistical methods as piece wise regression were applied [Reinsel et al., 2002]. Weber et al., 2018, used a trend model with two trends independent of each other (with slopes and shifts). Another way of describing ozone regeneration is to include Equivalent Effective Stratospheric Chlorine (EESC) as a predictor in the regression, on a more physically sound basis. However, the Stratosphere is cooling due to climate change by rising of greenhouse gases concentration followed by a

reduction of the gas-phase ozone depletion and to an acceleration of the Brewer-Dobson circulation (for more details see Langematz, 2019). The decrease of EESC is not the only physical-chemical process that determines ozone concentrations. Therefor today in regression ozone trend models statistical trend models are widely used. To analyze trends, time series of total global ozone, the average total ozone at various latitudes, regional averages or total ozone at local monitoring stations are used, drawing on monthly or annual ozone data. In this paper we study the monthly total ozone column over Sofia. In doing so, we take into account statistical properties of the time series, such as the stationarity.

2. Regression model for the ozone time development

To study the total ozone long-time trend it is necessary to remove influences of various dynamical and chemical processes that act on short and long-time scales [Dhomse et al., 2006]. By multiple regression the trend slopes and structures don't change in general [Ball et al., 2018], but they can reduce the residuals. Smaller errors are important, because the trends itself after 1996 are small. Like other time series, the local total ozone column can be represented by its mean, the trend component, the annual cycle, the natural variability and the residuals. The mean is often included in the trend. At a first look, we applied Lowess regression to smooth the Sofia TOC time series. The Lowess plot, presented in Figure 1, (see Figure 1) shows very clearly that TOC values fell by around 25 DU from 1979 until they reached a minimum in the late 1990s, followed by an increase of around 7 DU in the mid-2000s, reaching approximately the minimum value at the end of the period under investigation. The minimum is in coincidence with the maximum of EESC and a turnaround point in the late 1990 is to be expected.

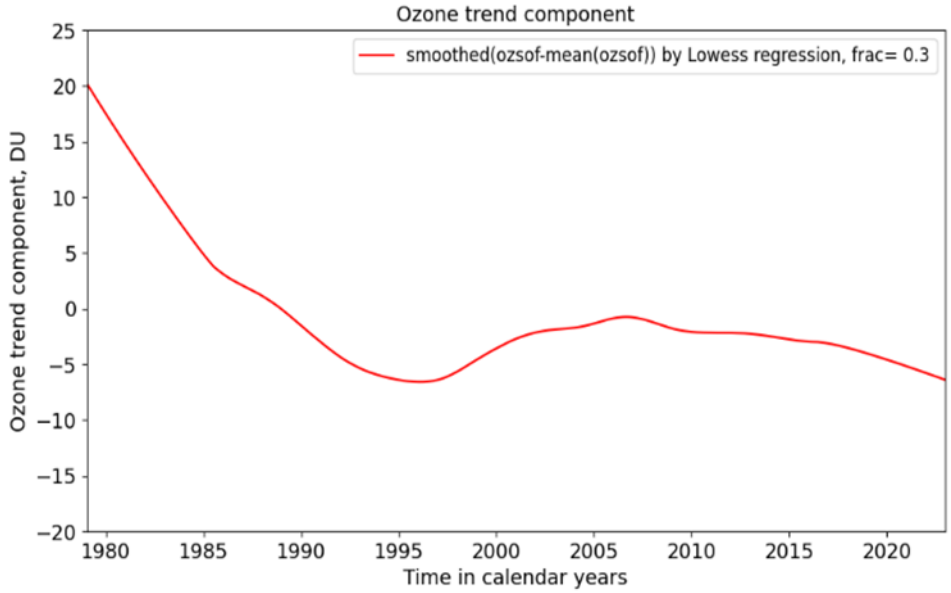


Figure 1. *Smoothing of the Sofia TOC by Lowess regression*

2.1.Trend component

It remains to be seen whether there was a further structural break in the mid-2000s. To determine possible k structural break points the trend component was described by piece wise regression:

$$\boldsymbol{trend} = \boldsymbol{\alpha} + \boldsymbol{\beta_0 t} + \sum_{\boldsymbol{i=1}}^{\boldsymbol{k}} \boldsymbol{\delta_i d_i\,(t - t_i)}$$

with $\boldsymbol{d_i = 1 \quad for \quad t \geq t_i}$ elsewhere 0 (1)

$$\boldsymbol{t_i \; are \; the \; k \; break \; points}$$

and the slopes $\boldsymbol{\beta_i \; are \; given \; by \quad \beta_i = \beta_0 + \sum_{i=1}^{k} \delta_i}$.

This trend model is like a uniform trend model, where it is assumed that the trend doesn't show seasonal variations. However, it was shown that trend depends on the season (see Bojkov et al., 1990 and the citations herein). So in seasonal trend models the linear trend term $\beta_0 t$ could be replaced by:

$$\boldsymbol{trend(n) = \sum_{m=1}^{12} \beta_m \, t_m \delta_{mn}\,, \;\; where \; \delta_{mn} = 1 \quad for \; m = n \; else \; where \; 0}. \qquad (2)$$

2.2. Seasonal cycle

In the simplest way the seasonal cycle can be determined by the Epoch method [e.g. Ambroz, 1979], where a year is regarded as an epoch and the seasonal cycle is calculated by the averages of the respective months (e.g. for January, all monthly values for January are averaged). The method to calculate the seasonal cycle recommended by the World Meteorological Organization is identical to Epoch method [WMO, 1988]. A second way of identifying an annual cycle is to decompose the data into Fourier harmonics. This can be done by applying a Fourier regression. Using the full set of six harmonics for the twelve months the result is almost identical to the one obtained by the Epoch method. In total ozone trend studies different number of harmonics is used, from a full set of all Fourier components [e.g. Svendby and Dahlback, 2004], to the fundamental components and three harmonics [Stolarski et al., 1991], or the first two harmonics [Brönnimann, 2022]. We have used the four significant harmonics: $X_1 = sin\frac{2\pi t}{12}$, $X_2 = cos\frac{2\pi t}{12}$, $X_3 = sin\frac{4\pi t}{12}$, $X_6 = cos\frac{6\pi t}{12}$, to describe the annual Sofia TOC cycle (see Table 1). The variance between the cycles obtained by the Epoch method and the ones obtained by significant Fourier harmonics is about 2.0 DU^2. In Figure 2, the annual cycle of the Sofia TOC, calculated by different methods, is presented. The computations by the Epoch method are indicated by yellow line, the results of the regression using Fourier harmonics with six harmonics (full set) – by green line and the results of the regression using Fourier harmonicsonly the four significant harmonics – by magenta line.

2.3. Explanatory variables

2.3.1. Quasi-Biennial Oscillation

The natural variability of ozone is determined by the influence of Quasi-Biennial Oscillation (QBO), the Solar activity, the activity of volcanos, the stratospheric temperature and Teleconnections as the El-Niño climate phenomena and the Atlantic Oscillation, and especially for Europe - the North Atlantic Oscillation. To characterise the strength and the phase of the QBO related to total ozone we have done test regressions including the mean zonal wind at 50 hPa (u50) and at 30 hPa (u30) at the same time.

The explanatory variables, used in the regression analyses are presented in Figure 3. In the panels from top to bottom, the ozone variations, the temperature, the aerosol optical depth index, the zonal wind, the NAO index and the F10.7 index for the examined period are shown.

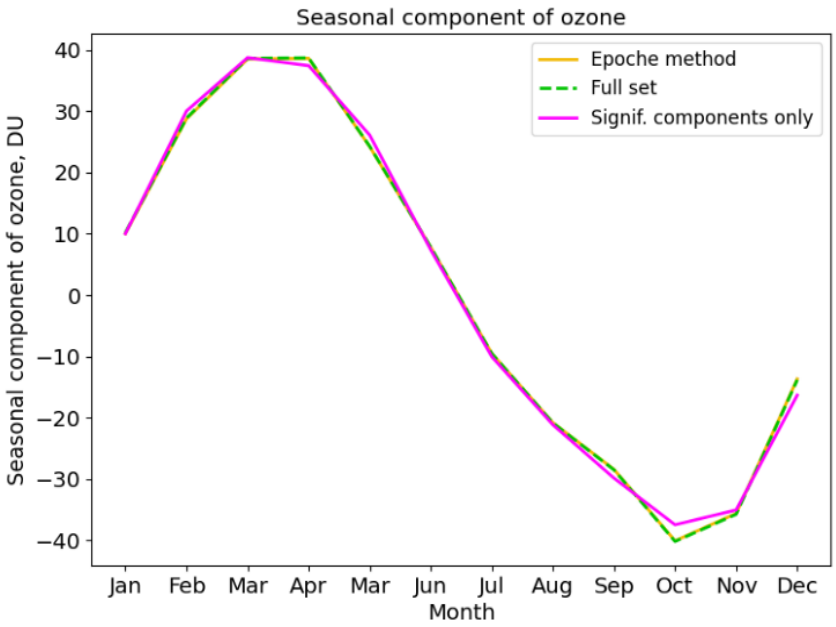


Figure 2. *Annual cycle of the Sofia TOC calculated by the Epoch method (yellow line) and by regression using Fourier harmonics with six harmonics (full set green line) and significant harmonics (magenta line).*

2.3.1. Quasi-Biennial Oscillation

The natural variability of ozone is determined by the influence of Quasi-Biennial Oscillation (QBO), the Solar activity, the activity of volcanos, the stratospheric temperature and Teleconnections as the El-Niño climate phenomena and the Atlantic Oscillation, and especially for Europe - the North Atlantic Oscillation. To characterise the strength and the phase of the QBO related to total ozone we have done test regressions including the mean zonal wind at 50 hPa (u50) and at 30 hPa (u30) at the same time. The monthly average zonal wind components were downloaded from https://cds.climate.copernicus.eu/datasets/reanalysis-era5-pressure-levels-monthly-means?tab=download at geography coordinates for Sofia between 42.25°N – 42.75°N and 23.25°E – 23.75°E. We obtained better regression results by using only the mean wind speed u30 with a delay of 11 months in relation to ozone, regardless of the season. Using seasonal models for the QBO (see e.g. Dhomse et al., 2006) different seasonal regression coefficients for QBO were found. To reduce the number of coefficients for the seasonal cycles, Fourier coefficients can be used [Coldewey-Egbers et al., 2014]. For the first harmonic we have

$$(c0+c1*X1+c2*X2)*u30, \quad (3)$$

where c0 is the constant for the uniform term, c1 for the sine term X1 and c2 for the cosine term of first harmonics.

2.3.2. Stratospheric temperature

Svendby et al. (2004) have observed the strongest influence on ozone variability for the stratospheric temperature at 100 hPa (T100) and including this explanatory variable the best improvement of the correlation coefficient (R^2) is established. To remove possible effects of climatic changes and anthropogenic influence from the temperature data, we have detrended the T100 series before its inclusion in the regression equation [Svendby and Dahlback, 2004]. The temperature series were detrended and deseasonalized in the same way as the ozone series. We have found the highest correlation (0.23 for year around) between detrended and

deseasonalised ozone and T100. The T100 temperatures for Sofia were downloaded as the QBO series from the ERA-5 reanalysed data.

2.3.3. Solar activity

The ozone production rate is determined primarily by solar ultraviolet radiation. Consequently, all ozone trend analyses make use of solar indices that describe solar activity, with particular attention paid to fluctuations in the ultraviolet spectral range. These solar indices include the MgII core-to-wing index and the solar radio flux at 10.7 cm (F10.7). The 11-year solar activity cycle influences ozone not only through its cycle on a decadal timescale, but also through its long-term trend. It is therefore essential to take solar activity into account when determining the ozone trend. In an earlier work Willett (1962) has found a peak correlation of 1.5 to 2 years of the sunspot cycle related to ozone. Staehelin et al. (1998) has found a delay of ozone maximum to solar flux maximum by 32 months. Svendby and Dahlback (2004) have found the highest significances in their regression study of total ozone over Oslo in respect to F10.7 with a time lag of 12, 22 and 32, were lowest p-values was registered for the lag of 22 months. In our regression models we also use the solar radio flux F10.7 to describe solar activity with the option of including a time lag of up to three years. The monthly F10.7 radio flux values from 1976 up to 2022 was downloaded from https://psl.noaa.gov/data/correlation/solar.data.

2.3.4. Stratospheric aerosols

Stratospheric aerosol concentrations increase significantly as a result of volcanic eruptions, whereby directly injected large quantities of SO_2, which forms liquid sulfate aerosols. These aerosols cause a change in the stratospheric temperature, in the circulation and enhance ozone depletion by catalytic reactions [Weber et al., 2022]. Aerosol plays a role by heterogeneous chemical processes, as well [Scientific Assesment of Ozone Depletion: 2002]. As explanatory variable for the aerosol concentration usually the aerosol optical depth at 550nm is used. With the time interval of interest here two major volcano eruptions contributed essentially to the aerosols loading: the El Chichón eruption in 1982 and the Mt. Pinatubo eruption in 1991. Although the AODs are similar as a result of both volcanic eruptions, the eruptive characteristics are nevertheless very different. Thus, by the Pinatubo eruption, 17 million metric tonnes SO_2 were injected in the atmosphere. This is about two and a half times more than by the El Chichón eruption, where 7 million metric tonnes SO_2 were emitted. Thus the influences of the volcanic eruptions on ozone are not linear to the observed AODs. This is why we have separated the two AOD events in AOD1 from El Chichón and AOD2 from Pinatubo, using a ramp function (see Figure 3, third panel from up to down). We have used the Sato's AOD data extended by Lacis from http://data.giss.nasa.gov/modelforce/strataer/ from 1979 up to 2016, where the missing data up 2022 where filled by background data of 0.0034.

2.3.5. North Atlantic Oscillation

The North Atlantic Oscillation (NAO) is a large scale variations of atmospheric pressure anomalies over Island and the Azores. It is very pronounced especially during winter. In its positive phase strong subtropical high pressure system is located over the Azores and strong low pressure system is located over Iceland. In its negative phase the pressure systems are much weaker. Changes in the NAO are associated with weather phenomena, as wind speed and direction, temperature and moister. It is related to storm tracks also. The NAO is linked to

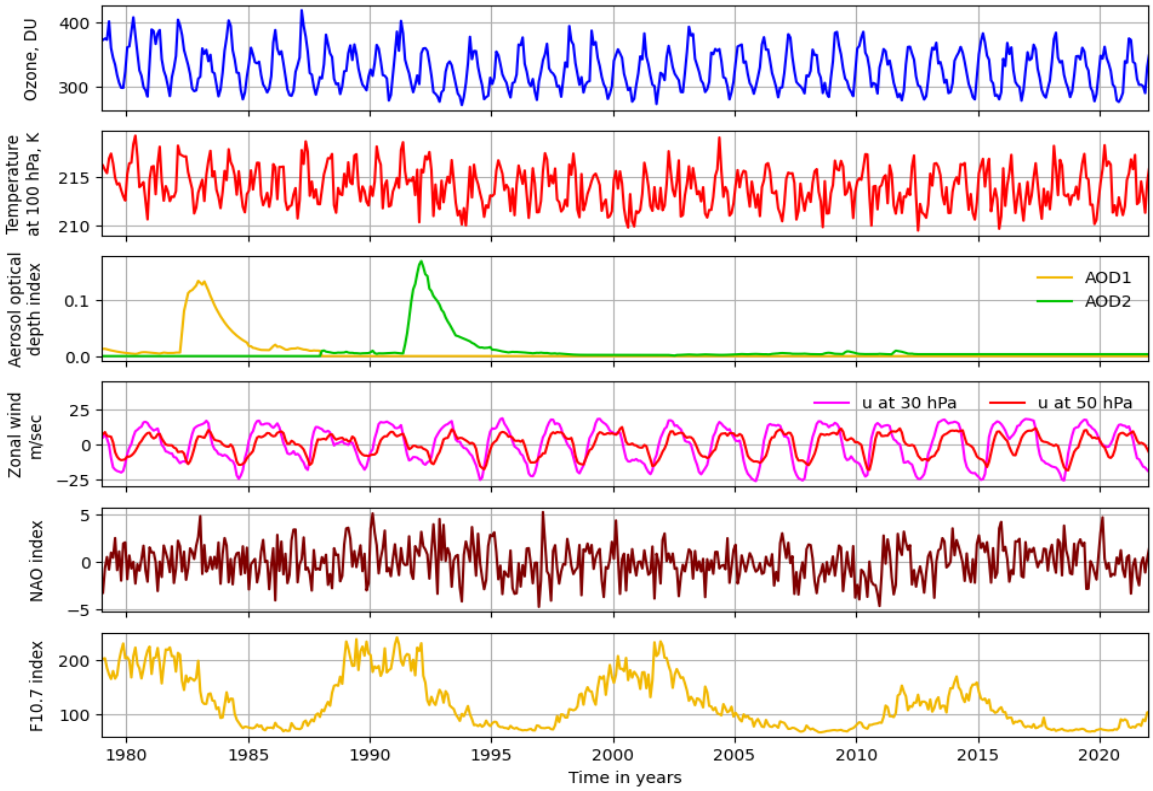


Figure 3. *Graphical presentation of the development of the explanatory variables used in the regression analysis.*

changes of ozone over the European continent [Appenzeller et al., 2000]. The NAO index used here is defined as difference of the normalized atmospheric pressure at sea level between Iceland and Gibraltar (crudata.uea.ac.uk/cru/data/nao/nao.dat). To describe the seasonal component, we limit ourselves to the first harmonics of the Fourier coefficients like for QBO, however without lags.

2.4. Residuals

The residuals ε of time series very often can be described in good approximation as autoregressive process of first order:

$$\varepsilon_t = \rho(1)\varepsilon_{t-1} + u_t \text{ , where } \rho(1) \text{ is the autocorrelation at lag 1 and } u_t \text{ is the white noise.} \quad (4)$$

3. Determining separate time intervals in the TOC series

As it is well known the ozone variability in summer is much smaller than in winter. In an earlier work we have observed that the variance of the TOC ozone over Stara Zagora (about 190 km easterly of Sofia) during February 2015- March 2025 is approximately 4 times greater in the winter months than during the summer time [Werner et al., 2025]. To perform regression based on least squares method the variances has to be nearly constant over the time groups, in other words they have to be homoscedastic. If this condition is not valid the time series are heteroscedastic, the variance is biased and significance tests are invalid! The least squares estimators are still unbiased but inefficient, meaning the estimators have not the minimal variances. In one of our earlier papers, based on the daily TOC Sofia overpass MRS-2 data,

after removing the linear trend und the seasonal component we had found two significant breakpoints every year. One about mid-November and the next - about mid-April. For detecting multiple breaks of variances, the iterated method of cumulative squares sums is applied [Inclán and Tiao,1994]. For the in interval November-April, when the polar vortex is developed, higher variances are clearly evident. These arise as a result of frequently replacing of subtropical air masses by air masses from polar origin. Usually to overcame the problem of heteroscedasticity weighted regression or generalized regression is applied. Here we separated the TOC time series into two groups, the one when the vortex is not developed, namely the time interval May-October (hereinafter referred to as 'Ozone Summer') and the other December-March (hereinafter referred to as 'Ozone Winter') when the vortex is developed. For comparison we have analysed the regression results on year around base including all months. The months April and November are regarded as transitional months.

4. Regression and significance tests

The regressions were performed with the help of the Statsmodels library in Python. The regression coefficients were calculated stepwise on base of Ordinary Least Squares (OLS) beginning with the full model, including the trend and seasonal components and the explanatory variables. We consider the regression coefficients of the explanation variables as significant if $P < 0.05$, corresponding to a t-value of 1.96 at a significance level of $\alpha = 0.05$ (confidence level 0.95), meaning the maximum probability accepted to reject the true Hypothesis (for large observation numbers). Non-significant variables were excluded step by step. The outputs of Pythons standard procedure sm.summary(), among other things, the test statistic D for the Durbin-Watson test, for which the following relationship $D \sim 2(1-\rho_1)$ holds approximately, where ρ_1 is the autocorrelation at lag 1. It is in order between 0.20 and 0.23. Using the effective standard deviation for large sample numbers $\sigma_{eff} = \sigma\sqrt{[1+\rho(1)]/[1-\rho(1)]}$ for the correction of the standard deviation for the trend slopes caused by autocorrelation [Krzyścin, 1995], the critical value t_{cr} is given by $t_{cr}(\rho_1) = t_{cr}(0)\sqrt{[1+\rho(1)]/[1-\rho(1)]}$. For example if $\rho_1 \sim 0.23$ and $t_{cr}(0)$, for which is to take the tabulated quantils $t_{n,\gamma}$ of the t-distribution e.g. for the significance level $\alpha = 0.05$ for two side test $\gamma = 1-\alpha/2 = 0.975$ and of about n=200 observations we would obtain $t_{cr}(0.23) \sim 1.97*1.26 \sim 2.49$. If the obtained t-value is greater than 2.49 we consider the regression coefficient of the trend as significant at the level of 0.05. This critical t-value corresponds to a P-value of 0.0136. (The concrete values are given in table 1).

5. Results

Program runs were started to test the influence of the Atlantic Multidecadal Oscillation (AMO) and the influence of El Niño Southern Oscillation (ENSO) on Sofia TOC. Not significant ozone responses were found. Therefor these variables were not taken into account in the regression model. The monthly mean zonal wind velocities u30 and u50 were included together in the regression. The significance of u50 was low and we obtained better regression results using only the mean wind speed u30 with a delay of 11 months in relation to ozone, regardless of the season. To estimate the moment of break point in the trend systematic tests was done with break points between 1994 and 1998. The best regression correlation was established for the break point about 1996. (The exact moment is not crucial, because the correlation coefficient changes only slightly.) Searches for additional breakpoints - for example, around 2006 - were unsuccessful.

The ozone trends were calculated by piece wise regressions as described in section 2.1. The regression model includes seasonal component and different explanatory variables, which were average-adjusted. The regression results are shown in Table 1. All the regression coefficients and their standard errors are displayed. Their relations – the t-values – and the corresponding

p-values are given. In the bottom part of the table the residual autocorrelations to the lag 1, the critical effective t-value t_{cr}, determined for the significance level of 0.05, and the corresponding critical p-value p_{cr} are shown. Coefficients are considered as significant if the observed t-value is greater than the critical effective t-value or the observed p-value is smaller than the critical p-value. A not significant explanatory variable is removed from the regression. The goodness of fits is expressed by the corresponding correlation coefficients R^2 and the standard deviations of the residuals (included in the bottom part of Table 1). The correlation coefficient of the ozone summer regression is higher than during ozone winter. This is partly caused by the greater observation numbers and by the lower ozone variability during the ozone summer season. The cross correlation of the predictors was inspected by cross correlation map (not shown here). The cross correlations between the explanatory variables are smaller than 0.2. A stronger correlation up to 0.48 is observed only between the trend variables and the radio flux. This is because, over the time interval under investigation, F10.7 itself exhibits a linear trend. The calculated variance inflation factors (VIFs) are less than approximately 1.5, and multicorrelation can be characterized as moderate and is acceptable

Table 1. *Regression results for year around analysis, for ozone summer and winter seasons*

	year around				ozone summer				ozone winter			
	coef	std err	t	p	coef	std err	t	p	coef	std err	t	p
const	7.98	2.04	3.92	0.000	8.08	1.17	6.91	0.000	17.8	2.73	6.53	0.000
t1	-0.071	0.009	-8.12	0.000	-0.046	0.008	-5.78	0.000	-0.110	0.019	-5.90	0.000
t2	0.081	0.012	6.58	0.000	0.046	0.011	4.22	0.000	0.137	0.027	5.06	0.000
X1	37.69	0.60	62.4	0.000								
X2	8.55	0.62	13.9	0.000	The epoch method is used							
X3	4.85	0.59	8.21	0.000								
X6	2.34	0.59	4.00	0.000								
T100	5.68	0.34	16.9	0.000	4.98	0.31	16.0	0.000	6.70	0.67	10.0	0.000
AOD2	-125.1	20.3	-6.15	0.000	-82.4	19.4	-4.24	0.000	-147.3	39.8	-3.70	0.000
u30	0.198	0.033	5.93	0.000	n.s.	-	-	-	n.s.	-	-	-
u30*X1	0.196	0.045	4.33	0.000	0.120	0.038	3.15	0.002	0.47	0.14	3.30	0.001
u30*X2	0.210	0.048	4.43	0.000								
NAO	-0.62	0.24	-2.56	0.011								
NAO*X2	-1.27	0.32	-3.96	0.000	n.s.	-	-	-	-2.41	0.55	-4.39	0.000
F10.7 with lags	0.037	0.010	3.63	0.000	0.052	0.009	5.62	0.000	0.060	0.022	2.70	0.008
F10.7 without lags	0.025	0.010	2.55	0.011	0.045	0.009	4.89	0.000	0.003	0.021	0.139	0.890
R^2	0.907				0.936				0.813			
σ	9.5 DU				6.0 DU				12.3 DU			
ρ(1)	0.225				0.223				0.203			
t_{cr}	2.46				2.46				2.42			
p_{cr}	0.014				0.015				0.017			

[1] t_{cr} and p_{cr} are valid for significance tests of the regression coefficients of the trend slopes

Among the explanatory variables the stratospheric temperature T100 is most significant and have a strong influence on ozone. During the ozone summer the 2σ ozone response is about 12 DU and during the winter season, it reaches nearly 19 DU (see Table 2). We have found a significant influence for the stratospheric winds u30 and for the cosine term of the seasonal component of u30 on ozone, only for the year around analysis. The sinus term of the seasonal component of u30 is significant during all seasons but highly significant in the winter season. During this period the influence on ozone is about three times stronger than during summer. (Compare regression coefficients for u30*X1 and the 2σ ozone response for the u30*X1 changes in Table1 and Table 2, respectively.)

In our analysis we have found an ozone response to the cosine term of the seasonal component of the North Atlantic Oscillation only of about 2 DU and of the cosine term of about 3 DU during the whole year. During the ozone winter a stronger impact on ozone is obtained

Table 2. 2σ of the ozone response to explanatory variables changes in DU

	year around	ozone summer	ozone winter
u30	5.14	n.s.	n.s.
u30*X1	3.68	2.33	6.13
u30*X2	3.93	n.s.	n.s.
T100	14.25	11.98	18.96
NAO	2.26	n.s.	n.s.
NAO*X2	3.37	n.s.	6.38.
F10.7 (with lags)	3.59	4.69	5.69
min(AOD2)	-21.16	-11.73	-24.92

for the cosine term of the NAO seasonal component. The corresponding ozone response is more than 6 DU. Heterogenic reactions on aerosol surfaces especially by low temperatures in the polar vortex forced the ozone depletion additionally [Carslaw et al. 1994] and it is to expect that the AOD impact on ozone is about twice during the ozone winter compared to the ozone reaction during the ozone summer season. As it was mentioned above, one of the aims is to investigate the lagged correlation between f10.7 and ozone. The P-values for the lagged solar radio fluxes F10.7 for different time intervals are shown in Figure 4. During the summer months, ozone's response to changes in the solar radio flux is immediate, and the observed lag averages just one month. The Brewer Dobson circulation is a global circulation pattern, where tropical air rises up in the stratosphere and then moves to the high latitudes and the poles in connection with cooling of air mases. The cooled air masses descend downwards in regions stretching from the high latitudes to the poles. The average circulation life is 1-5 years, depending on the latitude [Butchart, 2014]. The longest circulation life is observed near the pools.

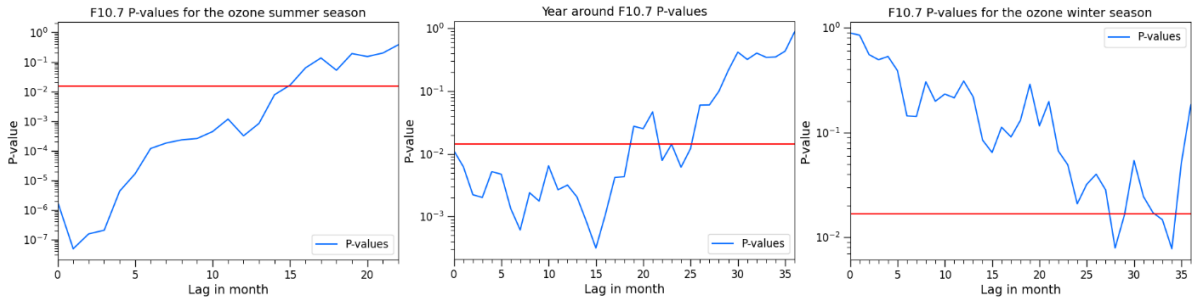


Figure 4*. P-values for the lagged solar radio fluxes F10.7 for different seasons. The critical p=values were determined to the corresponding effective t-values. They are displayed by horizontal red lines related to the significance level 0.05.*

At midlatitudes during ozone winter subtropical air masses are frequently replaced by air masses from polar origin. This ozone is therefore several years older than it was at the time of its formation. So it is not a surprise that we established a minimum of P-values at lags of 28 and 34 months during the ozone-winter season. In the analysis performed for all months the lags are 7 and 15 months. This is in good agreement with the investigation from Svendby et al. (2004), who reported lags of 12, 22 and 33 months (where the lag of 22 months is the most significant) for a regression of TCO over Oslo including all months. For comparison the

regression results regarding F10.7 is given in Table 1 without lags. In this case the regression coefficients as noted by Svendby et al. (2004) are smaller. Here for the analysis for the ozone winter season the impact of F10.7 on ozone is very small (nearly zero) and not significant. This underlines the importance of taking into account the time lags of F10.7 in relation to ozone.

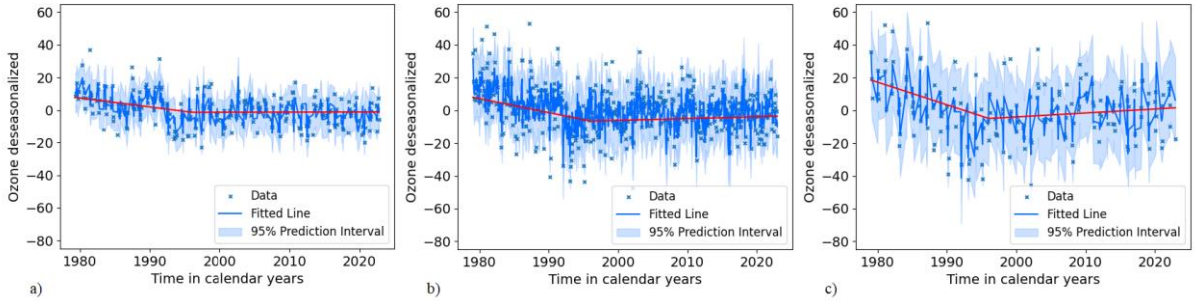


Figure 5*. Deseasonalized ozone over Sofia together with the predictions (shown as fitted line), their 95% prediction intervals and the trend calculate by piece wise regression a) for the ozone summer season b) the for all months and c) for the ozone winter season.*

Taking into account the lags of F10.7 relative to TOC there is only a minor impact (maximum around 10 per cent) on the trends, which is not statistically significant. The trends are shown in Figure 5 for the analysed here time interval. As is to expect the TOC levels fall most sharply during ozone winter by 23.8 DU (or 13.2 DU/per decade), when the influence of ozone of polar origin at mid latitudes is strongest. During the ozone summer, the decrease is only 9.8 DU (corresponding to 5.5 DU/per decade). The increase in ozone after 1996 is determined by the sum of the slopes β_0 and the slope change δ_1 for the two sub-intervals (according to equation 1). For the ozone summer season, the slope change is near to zero and we observed no change of the ozone level since 1996. During the ozone winter we have observed a small increase of TOC and a slope change of 6.9 DU from 1996 up to 2022 was established. The standard error of this slope change is given by $\mathrm{Var}(\beta_0 + \delta_1) = \mathrm{Var}(\beta_0) + 2\mathrm{Cov}(\beta_0, \delta_1) + \mathrm{Var}(\delta_1)$. Taking into account the autocorrelation no significant slope change $\beta_0 + \delta_1$ at the level of 0.05 was found for the ozone winter season.

The TOC responses to all significant explanatory variables during the ozone winter season are stronger than in ozone summer (see Table 2). This indicate a complex interaction with Rossby waves.

In Figure 5 the increase of the variability of the TOC residuals from ozone summer ($\sigma = 6.0\ DU$) to the winter ($\sigma = 12.3\ DU$) is very clearly outlined.

Finally, we carried out a visual inspection of the normality of u by Q-Q plots. For the ozone summer and winter season the sample Q-values are close to the theoretical ones and lie within the 95% confidence intervals or close to its boundary. The Q-Q plot of the regression residuals performed for all months show two sample Q values greater than 3σ. These values can be interpreted as statistical outliers and the distribution of u can be assumed as normal. Therefor the regression results for the analysis of the TOC over Sofia for the ozone summer and the ozone winter season are valid. When the transitional months are included in the Ozone winter season, the standard deviation decreases only slightly, to 12.2 DU. The variances between the two seasons differ by a factor of four and we can conclude with high confidence, taking in to account the normality of the series that the full series including all months is heteroscedastic. Thus, the results of the analysis based on all months should be treated with caution due to the heteroscedasticity of this time series.

6. Summary

The TOC time series over Sofia from 1979 – 2022 were analysed by multiple linear regression. The trend was described by piece wise linear regression model, the season components were calculated using Fourier harmonics or Epoch means. As explanatory variables were used the zonal stratospheric wind u30 describing the Quasi-Biennial Oscillation, the solar radio flux F10.7 for the Solar activity, the aerosol density to characterize the volcano activity, the stratospheric temperature at 100 hPa and the North Atlantic Oscillation. The TOC ozone series were separated in three groups. One group, includes all months, a second group, called ozone summer season consists of the months from May to October and the ozone winter season covers the months from December to March. It was found that the residuals of the regression analysis of all three groups can be considered as normal. However, the full series including all month is heteroscedastic. It has been found that, whilst during the summer ozone season, ozone reacts immediately to changes in the solar radio flux, in winter the response occurs with a delay of around two to three years. This corresponds to the average age of ozone of polar origin. For the winter ozone season, a decrease in TOC over Sofia of 23.1 DU (or 12.8 DU per decade) was observed over the period from 1979 to 1996. In contrast, TOC in summer shows a decrease of only 9.8 DU (or 5.5 DU per decade). This result reflects the well-known more pronounced ozone depletion over the Arctic compared to mid-latitudes during the same period. Following the significant decline in TOC, no significant increase of TOC over Sofia was observed.

Acknowledgments. The authors thank the team carried out the Reanalysis of ERA-5 stratospheric winds and temperatures, and the Physical Sciences Laboratory of the NOAA provided the F10.7 data. We are also grateful to the GISS of NASA for the preparation of the stratospheric optical depth data, to the University of Anglia for the deployment of the NAO data. The authors would like to thank the Themis team of the KNMI for possibility of public use of the monthly ozone MSR2 data.

References

Ambrož, P. (1979). Statistical method of superposition of epochs. I: Methodical analysis and some criteria of application, *Bulletin of the Astronomical Institutes of Czechoslovakia*, Vol. 30, pp. 114–121.

Appenzeller, C., Weiss, A.K., Staehelin, J. (2000). North Atlantic Oscillation modulates total ozone winter trends, *Geophysical Research Letters*, Vol. 27, No. 8, pp. 1131–1134, DOI: 10.1029/1999GL010854.

Ball, W.T., Alsing, J., Mortlock, D.J., Staehelin, J., Haigh, J.D., Peter, T., et al. (2018). Evidence for a continuous decline in lower stratospheric ozone offsetting ozone layer recovery, *Atmospheric Chemistry and Physics*, Vol. 18, No. 2, pp. 1379–1394, DOI: 10.5194/acp-18-1379-2018.

Bojkov, R.D., Bishop, L., Hill, W.J., Reinsel, G.C., Tiao, G.C. (1990). A statistical trend analysis of revised Dobson total ozone data over the Northern Hemisphere, *Journal of Geophysical Research: Atmospheres*, Vol. 95, No. D7, pp. 9785–9807, DOI: 10.1029/JD095iD07p09785.

Brönnimann, S. (2022). Century-long column ozone records show that chemical and dynamical influences counteract each other, *Communications Earth & Environment*, Vol. 3, Art. 143, DOI: 10.1038/s43247-022-00472-z.

Brunner, D., Staehelin, J., Maeder, J.A., Wohltmann, I., Bodeker, G.E. (2006). Variability and trends in total and vertically resolved stratospheric ozone based on the CATO ozone data set, *Atmospheric Chemistry and Physics*, Vol. 6, pp. 4985–5008, DOI: 10.5194/acp-6-4985-2006.

Butchart, N. (2014). The Brewer–Dobson circulation, *Reviews of Geophysics*, Vol. 52, No. 2, pp. 157–184, DOI: 10.1002/2013RG000448.

Carslaw, K.S., Luo, B.P., Clegg, S.L., Peter, T., Brimblecombe, P., Crutzen, P.J. (1994). Stratospheric aerosol growth and HNO_3 gas-phase depletion from coupled HNO_3 and water uptake by liquid particles, *Geophysical Research Letters*, Vol. 21, No. 23, pp. 2479–2482, DOI: 10.1029/94GL02799.

Coldewey-Egbers, M., Loyola, D.G., Braesicke, P., Dameris, M., van Roozendael, M., Lerot, C., Zimmer, W. (2014). A new health check of the ozone layer at global and regional scales, *Geophysical Research Letters*, Vol. 41, pp. 4363–4372, DOI: 10.1002/2014GL060212.

Dhomse, S., Weber, M., Wohltmann, I., Rex, M., Burrows, J.P. (2006). On the possible causes of recent increases in Northern Hemisphere total ozone from a statistical analysis of satellite data from 1979 to 2003, *Atmospheric Chemistry and Physics*, Vol. 6, pp. 1165–1180, DOI: 10.5194/acp-6-1165-2006.

Farman, J.C., Gardiner, B.G., Shanklin, J.D. (1985). Large losses of total ozone in Antarctica reveal seasonal ClO_x/NO_x interaction, *Nature*, Vol. 315, pp. 207–210, DOI: 10.1038/315207a0.

Herman, J., Ziemke, J., McPeters, R. (2023). Total column ozone trends from the NASA Merged Ozone time series 1979 to 2021 showing latitude-dependent ozone recovery dates (1994 to 1998), *Atmospheric Measurement Techniques*, Vol. 16, pp. 4693–4707, DOI: 10.5194/amt-16-4693-2023.

Inclán, C., Tiao, G.C. (1994). Use of cumulative sums of squares for retrospective detection of changes of variance, *Journal of the American Statistical Association*, Vol. 89, No. 427, pp. 913–923, DOI: 10.2307/2290916.

Krzyścin, J.W. (1997). Detection of a trend superimposed on a serially correlated time series, *Journal of Atmospheric and Solar-Terrestrial Physics*, Vol. 59, No. 1, pp. 21–30, DOI: 10.1016/S1364-6826(96)00003-X.

Langematz, U. (2019). Stratospheric ozone: Down and up through the Anthropocene, *ChemTexts*, Vol. 5, Art. 8, DOI: 10.1007/s40828-019-0082-7.

NASA/WMO Ozone Trends Panel (1988). *Present State of Knowledge of the Upper Atmosphere 1988: An Assessment Report*, NASA Reference Publication 1208, World Meteorological Organization, Geneva.

Reinsel, G.C., Weatherhead, E.C., Tiao, G.C., Miller, A.J., Nagatani, R.M., Wuebbles, D.J., Flynn, L.E. (2002). On detection of turnaround and recovery in trend for ozone, *Journal of Geophysical Research: Atmospheres*, Vol. 107, No. D10, Art. 4078, DOI: 10.1029/2001JD000500.

World Meteorological Organization (WMO) (2003). *Scientific Assessment of Ozone Depletion: 2002*, Global Ozone Research and Monitoring Project – Report No. 47, Chapter 4: Global ozone: Past and future, Geneva.

Staehelin, J., Kegel, R., Harris, N.R.P. (1998). Trend analysis of the homogenized total ozone series of Arosa (Switzerland), 1926–1996, *Journal of Geophysical Research: Atmospheres*, Vol. 103, No. D7, pp. 8389–8399, DOI: 10.1029/97JD03650.

Stolarski, R.S., Bloomfield, P., McPeters, R.D., Herman, J.R. (1991). Total ozone trends deduced from Nimbus 7 TOMS data, *Geophysical Research Letters*, Vol. 18, No. 6, pp. 1015–1018, DOI: 10.1029/91GL01302.

Svendby, T.M., Dahlback, A. (2004). Statistical analysis of total ozone measurements in Oslo, Norway, 1978–1998, *Journal of Geophysical Research: Atmospheres*, Vol. 109, Art. D16107, DOI: 10.1029/2004JD004679.

Weber, M., Coldewey-Egbers, M., Fioletov, V. E., Frith, S. M., Wild, J. D., Burrows, J. P., Long, C. S., and Loyola, D. (2018). Total ozone trends from 1979 to 2016 derived from five merged observational datasets – the emergence into ozone recovery. *Atmospheric Chemistry and Physics*, 18, 2097–2117. https://doi.org/10.5194/acp-18-2097-2018 the emergence into ozone recovery

Weber, M., Arosio, C., Coldewey-Egbers, M., Fioletov, V. E., Frith, S. M., Wild, J. D., Tourpali, K., Burrows, J. P., and Loyola, D. (2022). Global total ozone recovery trends attributed to ozone-depleting substance (ODS) changes derived from five merged ozone datasets. *Atmospheric Chemistry and Physics*, 22, 6843–6859. https://doi.org/10.5194/acp-22-6843-2022

Werner, R., Petkov, B., Guineva, V., Bojilova, R., Raykova, L., Valev, D., and Kirillov, A. S. (2025). Basic statistical properties of the 10-years ozone daily time series from Stara Zagora. *Proceedings of the 17th Workshop "Solar Influences on the Magnetosphere, Ionosphere, and Atmosphere"*, 207–220. https://doi.org/10.31401/WS.2025.proc.28

Willett, H. C. (1962). The relationship of total atmospheric ozone to the sunspot cycle. *Journal of Geophysical Research*, 67(2), 661–670. https://doi.org/10.1029/JZ067i002p00661

DOI: 10.31401/WS.2026.proc.21

Bulgarian Instruments for Aircraft, Space and Ground Based Radiation Dosimetry and Their Main Scientific Results

Dachev T.P.[1], Tomov B.T. [1], Matviichuk Yu.N.[1], Dimitrov P.G. [1], Mitev M.M.[1], Jordanova M.M. [1], Semkova J.V.[1], Koleva R.T. [1], Malchev St[1]., Bankov N.G. [1], Mitrofanov I., Golovin D.[2], Litvak M. [2], Sanin A. [2], Shurshakov V. [3], Benghin V. [3], Ivanova O.[3], Ploc O. [4], Kubancak J.[4], Häder D.-P[5]., Lebert M. [6], Schuster M.[6], Reitz G. [7], Horneck G.[7], Uchihori Y. [8], Kitamura H.[8], Tobiska W. [9], Hogan B. [9], Gersey B. [9], Okuyama K-I. [10], Tapia I. [10], Fajardo I. [10], Saganti P.[11]

[1]Space Research and Technology Institute, Bulgarian Academy of Sciences, Sofia, Bulgaria, tdachev59@gmail.com

[2]Space Research Institute, Russian Acad. of Sciences, Moscow, Russia

[3]Institute of Biomedical Problems, Russian Acad. of Science, Moscow, Russia

[4]Nuclear Physics Institute, Czech AS, Prague, Czech Republic

[5]Neue Str. 9, 91096 Möhrendorf, Germany

[6]Friedrich-Alexander-Universität, Department for Biology, Erlangen, Germany

[7]DLR, Institute of Aerospace Medicine, Köln, Germany

[8]National Institute of Radiological Sciences-STA, Chiba, Japan

[9]Space Environment Technologies, Los Angeles, CA, USA

[10]College of Science and Technology, Nihon University, Chiba, Japan

[11]Radiation Institute for Science and Engineering, Prairie View A&M University, Prairie View, TX, USA

Abstract

The paper summarize information for Bulgarian build aircraft, space and ground based radiation dosimetry instruments and their main scientific results. The first Liulin-type spectrometer-dosimeter was developed for the scientific program of the second Bulgarian cosmonaut Alexander Alexandrov in 1986-1988. Forty-one Liulin-type spectrometers-dosimeters were developed. Twenty-three of them were tested and qualified for operation in space. Three of them did not reach the planned orbits around Earth and Mars due to technical problems with the carriers. The scientific objectives of 12 of these 23 Liulins were to measure the variations of the flux and dose rate of cosmic radiation on satellites and space stations in orbit around the Earth. Eight of the spectrometers support biological and chemical experiments in space with up-to-date information on the history of dose accumulation. Nineteen instruments worked on aircraft and on the ground. The RADOM instrument operated on the track to Moon and in circular orbit around the Moon. The Liulin-MO dosimeter is active since 2016 on the track to Mars and in a 400 km circular orbit around Mars.

Keywords: Space radiation measurements; Liulin spectrometer-dosimeter

1. Introduction

Cosmic rays as part of space radiation, at sea level consist mostly of neutrons, protons, peons, muons, electrons, and photons. The particles, which cause significant soft fails in electronics, are those particles with the strongest interaction: neutrons, protons and peons. At sea level, about 95% of these particles are neutrons.

The level of exposure to space radiation increases with the altitude since there is less air. The altitudinal profile of cosmic radiation is vital as its intensity grows with height and may create

health risks to flight crews and astronauts, apart from threatening technology, avionics for example.

The space radiation study heritage with Liulin dosimeter-spectrometers encompasses decades of experiments and data gathering, tracing the profiles of cosmic rays and solar particles at different positions and at different phases of solar cycles.

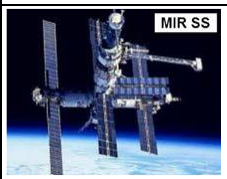
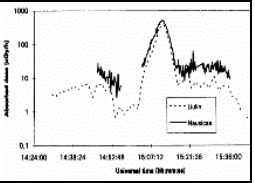
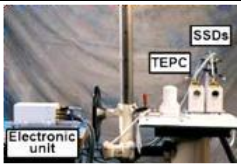
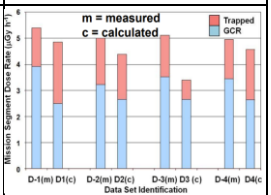
The long list of data are used in space radiation models to shapes risk limits and shielding strategies and are used by international partners all over the world as well as by ESA, NASA, ROSCOSMOS, ISRO etc..

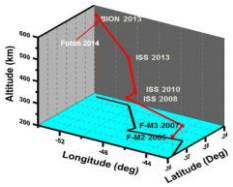
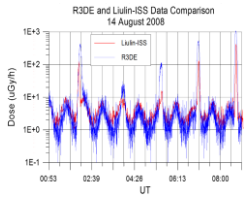
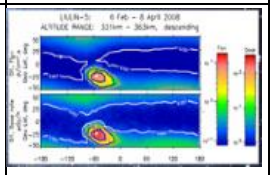
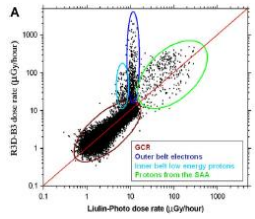
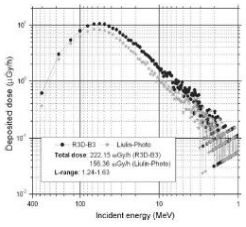
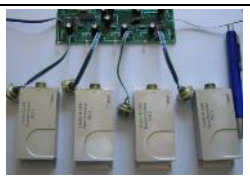
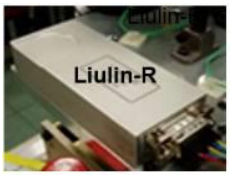
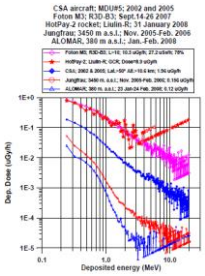
This paper is an overview of our achievements. As the list of the experiments and results is huge, they are summarized in two tables.

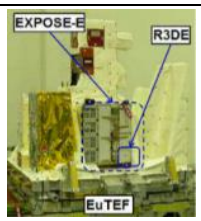
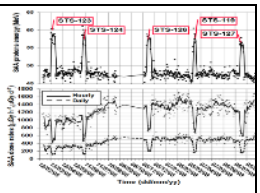
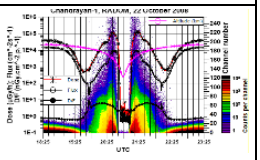
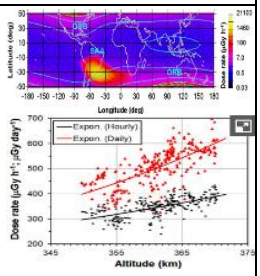
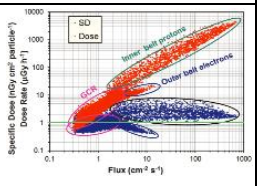
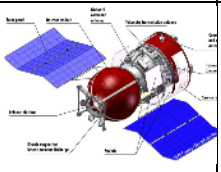
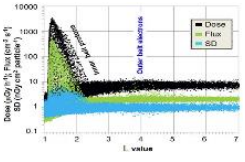
Table 1 presents in brief Liulin type instruments used in space missions. For each experiment the carrier name, the name of Liulin device, the scientific cooperation, the period of the experiments and examples of the scientific results are enumerated.

Table 2 lists most interesting Liulin type instruments used on aircraft, balloon and on the ground. Again, the name of Liulin device, the scientific cooperation, the place of the experiment and scientific result are presented. For each experiment, at least one paper published in international scientific journal, is cited.

Table 1. *Liulin Type Instruments Used in Space Missions*

No	Carrier name, Name of Liulin device, Scientific cooperation, Reference	Data time cover		External view of the carrier (satellite/station)	External view of Liulin instrument	Example of the scientific results
		Begin dd/mm/yy	End dd/mm/yy			
1	**LIULIN** Inside "MIR" Space Station, Bulgaria, Russia (Dachev et al., 1989)	16/04/1989	30/12/1994			
2	**RADIUS MD** Outside/inside Mars 96 station, Bulgaria, France, Russia (Semkova et al., 1994)	Unsuccessful launch on 16.11.1996				No data
3	**Liulin-E094 with 4 Mobile Dosimetry Units (MDUs)** Inside American laboratory module of ISS, Bulgaria, Germany (Dachev et al., 2005, 2006, 2009a)	11/05/2001 (Reitz et al. 2005) (Wilson et al., 2007, Nealy et al, 2007, Slaba et al., 2011)	25/07/2001			

4	**R3D-B2** Outside of the Foton-M2 satellite, Bulgaria, Germany (Header et al., 2009)	01/06/2005	11/06/2005			
5	**Liulin-ISS** with 4 MDU Inside of the Russian segment of the ISS, 4 MDU with displays, Bulgaria, Russia (Dachev et al., 2009a)	01/09/2005	Probably still operable at the ISS			
6	**Liulun-5-** Dosimetry Telescope, Russian segment of the ISS, Bulgaria, Russia. (Semkova et al. 2007, 2014)	17/05/2007	09/2015			
7	**R3D-B3** Outside of the Foton-M3 satellite, Bulgaria, Germany, Italy, (Header et al. 2009)	14/09/2007	26/09/2007			
8	**Liulin-Photo** Inside of the Foton-M3 satellite, Bulgaria, Italy, (Damasso et al., 2009)	14/09/2007	26/09/2007			
9	**Liulin-S** With 4 MDUs. Inside of the ROSCOSMOS, Project Space Suit (Скафандр) at the ISS. (Kartashov et al., 2010)					No information for the performance of the experiment on the ISS and bejont.
10	**Liulin-R** Outside of the HotPay2 rocket, Bulgaria, Norway (Tomov et al., 2008) (Dachev et al., 2012a)	31/01/2008 370 km Apogee at 14.04°E, 70.67°N,				

11	**R3DE** Outside of the ISS, on ESA Columbus Module and inside of ESA EXPOSE-E facility, Bulgaria, Germany (Dachev et al., 2012b)	22/02/2008	22/06/2009			
12	**RADOM** Outside of the Chandrayaan-1 satellite, Moon circular orbit at 100/200 km. Bulgaria, India (Dachev et al., 2011)	29/10/2008	07/11/2008			
13	**Liulin-Phobos** Outside of the Phobos-Grunt interplanetary station, Bulgaria, Russia, (Semkova et al., 1994)	Unsuccessful entry in interplanetary orbit on 8/11/2011				No data
14	**R3DR** Outside of the ISS "Zvezda" Module and inside the ESA EXPOSE-R facility, Bulgaria, Germany, (Dachev et al. 2015a)	20/02/2010	20/08/2010	 		
15	**RD3-B3** Inside of the BION-M No 1 satellite, Bulgaria, Germany, Russia, (Dachev et al. 2015b)	19/04/2013	13/05/2013			
16	**RD3-B3** Inside of the Foton-M No 4 satellite, Bulgaria, Germany, Russia,	18/07/2014	31/08/2014		 The R3D-B3 instrument was used for second flight on Foton-M No 4 satellite	

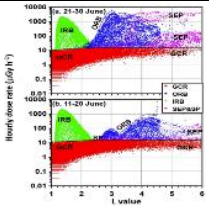
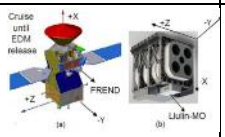
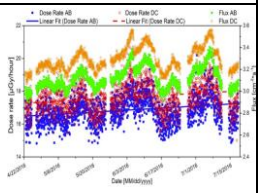
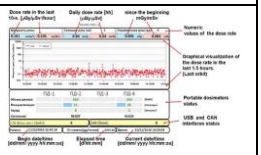
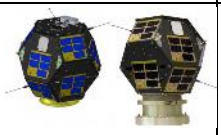
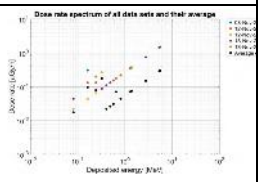
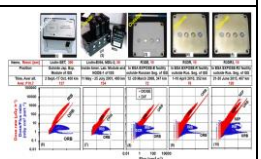
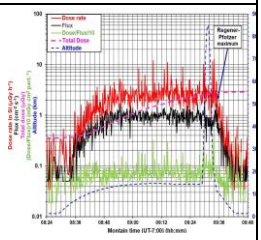
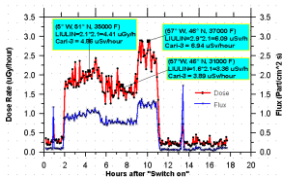
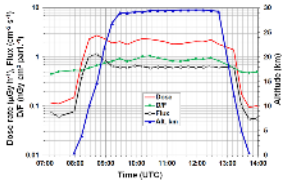
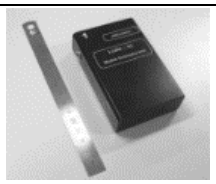
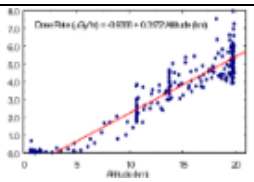
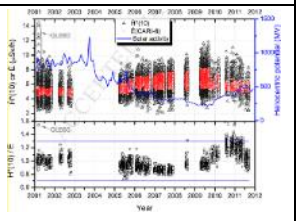
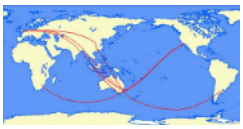
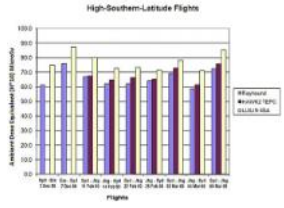
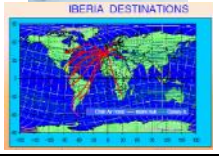
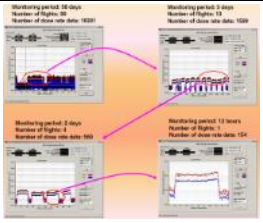
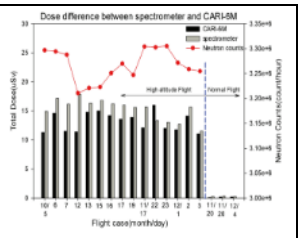
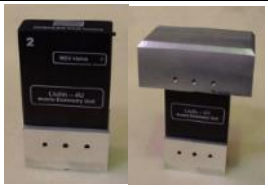
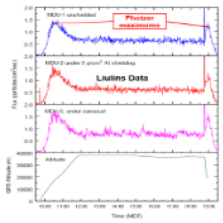
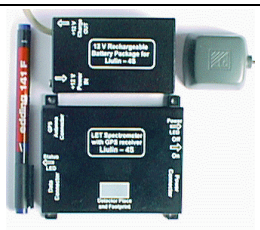
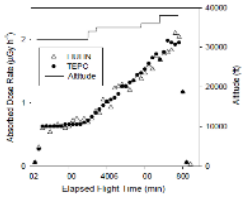
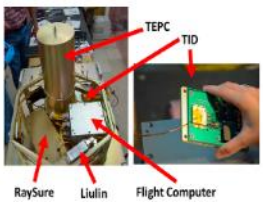
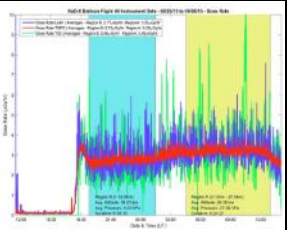
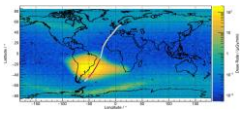
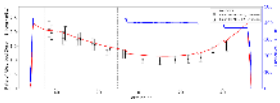
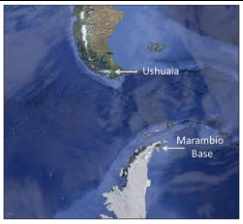
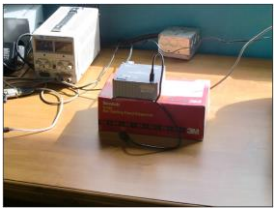
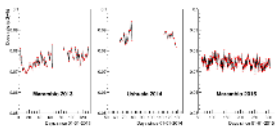
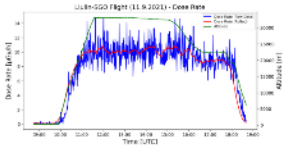
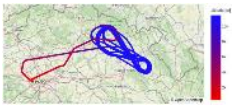
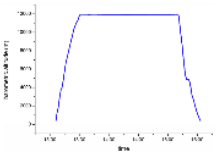
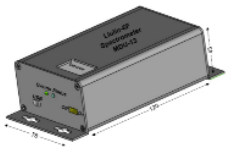
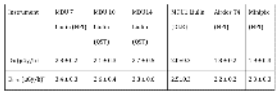
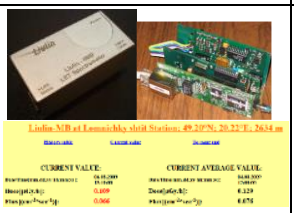
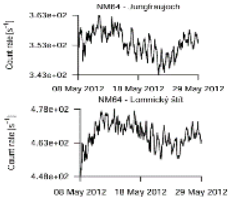
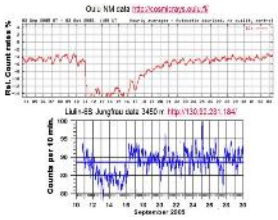
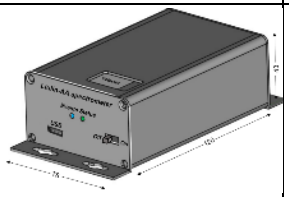
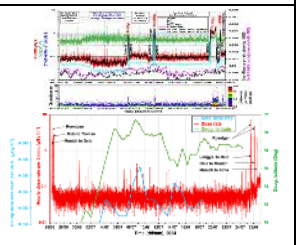
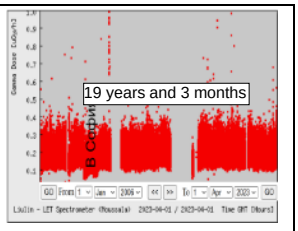
	(Damasso et al. 2016)					
17	**R3DR2** Outside of the ISS "Zvezda" Module, Bulgaria, Germany, (Dachev et al. 2017)	25/10/2014 In the Liulin database, this is the most advanced set.	10/01/2016	 ESA EXPOSE-R2 facility	 The R3DR instrument was used for second flight on ISS	
18	**Liulin-MO** Outside of the ExoMars Trace Gas Orbiter, Bulgaria, Russia, (Semkova et al., 2018, 2024)	22/04/2016, (Semkova et al., 2018)	Still operable in Mars 400 km orbit.			
19	**LIUILIN-ISS-2 SYSTEM** with 2 MDU and Getac T800 fully rugged tablet PC under Windows-8 OS	Bulgaria, Russia, (Dachev et al. 2016)	Delivered to Russian colleagues for use at Russian segment of ISS			
20	**Liulin Ten-Koh** Inside of the Ten-Koh satellite, Bulgaria, USA, Japan (Fajardo et al., 2019)	29/10/2018	16/01/2019			
21	**Liulin-SET** Outside of the Japanize experimental platform of the ISS Bulgaria, USA. (Tobiska et al. 2024)	17/03/2022	09/12/2022			
22	**Liulin-CNR-VG** Inside of VG Spaceship Two Unity, Bulgaria, Italy (Dachev et al., 2024)	Operated for about 8 hours on 29 June 2023				
23	**Liulin Ten-Koh-2** Inside of the Ten-Koh 2 satellite, Bulgaria, USA, Japan	Launched on ISS 21/10/2025 Deployed from ISS 11/03/2026	Still operable in Earth circular 500 km orbit.			Data expected

Table 2. *Liulin Type Instruments Used On Aircraft, Balloon and On the Ground*

No	Name of the Liulin device, Scientific management	Experiment (Airline picture)	External view of the Liulin instrument	Scientific result
1	**Liulin-3**, SRTI-BAS and (Space Radiation Office, NASA, Greenbelt Space center, USA, (Stasinopoulos et al. 1999)			
2	**Liulin-4C** Stratosphere balloon, Gap-Tallard aerodrome, France, F. Spurny, NPI, Czech Republic, Gap, France, 14/06/2000, (Spurny, 2000)			
3	**Liulin-J, MDU-1** High altitude flight with NASA aircraft ER-2 Oct.-Nov. 2000. (Uchihori et. al., 2002, 2003).			
4	**Liulin-C**, **MDU-5/6** CSA aircrafts, Nuclear Physics Institute (NPI), Czech Republic, Aircraft measurements from 01/04/2001 up to now, Publicly available database (Ploc et al., 2013)	 		
5	**Liulin-4SA** Quantas Airlines aircrafts Australia, 2005-2010 (Getley et al. 2010) (Getley	 		
6	**Liulin-4Sp** Implementation of cosmic radiation monitoring in airline routine at IBERIA Airline, Spain, 2004-2010 (Vergara and Román, 2009)	 		

8	**Liulin-6K** Korea Astronomy and Space Science Institute (KASI), Korea, 2010. (Lee et al., 2014) (Hwang et al., 2020,			
9	**Liulin-4U** 3 Liulin-J type spectrometers, NASA Deep Space Test Bed balloon certification flight on June 11 2005, New Mexico, USA. (Benton, 2005, Adams, 2007)			
10	**Liulin-4SN** Liulin type spectrometer with GPS receiver. Department of National Defense, Royal Military College, Ontario, Canada. (Kitching, PHD thesis, 2005) (Green et al., 2005)			 In flight comparison of Liulin and TEPC.
11	**Liulin-6SA1** NASA RaD-X balloon flight 25-26 Sept 2015, Fort Sumner, NM, USA. (Mertens, C. J., et al.,2016)			
12	**Liulin-6G** Two Liulin-6G battery operated spectrometers with LCD displays were developed for German Aerospace Center (DLR) Institute of Aerospace Medicine (Meier et al, 2016, 2023)			
13	**Liulin-I MDU-01** Radiation dosimetry at high southern latitudes (Zanini et al., 2019)			

14	**Liulin-SGO** Battery operated spectrometer developed for Sodankylä Geophysical Observatory, University of Oulu, Finland. (Mishev et al. 2022, 2023; Larsen et al. 2023),			
15	**Liulin-F** Several Liulin-F battery operated spectrometers were developed for the Institut de Radioprotection et de Sureté Nucléaire (IRSN), Paris, France and used in aircraft dosimetry. (Meier et al.2016; Desmaris, 2016; (Ambrožová et al. 2020)	 	 	CONCORD  REFLECT  Results from Liulin type spectrometers comparison in the radiation field at aviation altitudes.
16	**Liulin- Liulin-6K1** Internet based instrument, Institute of Experimental Physics, Slovak Academy of Sciences, Slovakia, operated 2009-2020 at Lomnický štít observatory (2634 meters a.s.l.). (Kubančák et al., 2014)			
17	**Liulin-6S** Internet based instrument, Physikalisches Institut, University of Bern, Swtzerland, operated 2006-2015 at Jungfrau pick, Alpen mountain, Switzerland (4158 meters a.s.l.). (Kubančák et al., 2014)			
18	**Liulin-AA** Battery operated spectrometer used for ground based and aircraft dose rate and flux measurements between Antarctica, Arctic and Sofia, Bulgaria. (Dachev et al., 2024b)			

19	**Liulin-6MB** Internet based instrument, operating since 2006 at the Institute for Nuclear Research and Nuclear Energy - Bulgarian Academy of Sciences, base station on Musala pick, Rila mountain, Bulgaria (2925 meters a.s.l.). http://beo-db.inrne.bas.bg/moussala/main.php?action=liulin_dose	 	 	

2. Conclusions

Many versions of Liulin-type spectrometers have been developed, built and flown on spacecraft, aircraft, balloons and rockets, as well as used on the ground between 1988 and 2026.

The main advantages of the Liulin type spectrometers are their low weight (100–500 g), low power consumption (100–500 mW) and low cost.

Confidence in the data obtained is increased by the extensive calibrations of Liulin devices using a number of different radioactive sources and accelerators (Uchihori et. al., 2002, 2003).

The data analysis procedure was developed using the calibrations and the great deal of experimental data. The dose to flux ratio or the specific dose has been selected and used for characterization of the absorbed and equivalent doses from different radiation sources and the incident energy of the protons event on the detectors.

Data from 10 space experiments with Liulin dosimeter-spectrometers in a unified format including data from ISS, BION, Photon, Chandrayan-1 and ExoMars TGO satellites are part of the "Unified web-based database with Liulin-type instruments" available online, free of charge at the following URL: http://esa-pro.space.bas.bg/database. The database was created under Contract No. 4000117692/16/NL/NDe funded by the Government of Bulgaria through an ESA Contract under the PECS (Plan for European Cooperating States) and by Project No. 129 for bilateral projects of the National Science Fund of Bulgaria and Russian Foundation for Basic Research.

Acknowledgements

The authors thank to all Bulgarian and foreign specialists and organizations that participated in the development and use of Liulin instruments.

References

References of Table 1

Badavi, F.F., 2014. Validation of the new trapped environment AE9/AP9/SPM at low Earth orbit. Advances in Space Research, 54(6), pp.917-928. https://doi.org/10.1016/j.asr.2014.05.010

Dachev, T.P., Matviichuk, Y.N., Semkova, J.V., Koleva, R.T., Boichev, B., Baynov, P., Kanchev, N.A., Lakov, P., Ivanov, Y.J., Tomov, P.T. and Petrov, V.M., 1989. Space radiation dosimetry with active detections for the scientific program of the second Bulgarian cosmonaut on board the Mir space station. Advances in Space Research, 9(10), pp.247-251. http://dx.doi.org/10.1016/0273-1177(89)90445-6

Dachev, T.P., Spurny, F., Reitz, G., Tomov, B.T., Dimitrov, P.G. and Matviichuk, Y.N., 2005. Simultaneous investigation of galactic cosmic rays on aircrafts and on International Space Station. Advances in Space Research, 36(9), pp.1665-1670. http://dx.doi.org/10.1016/j.asr.2005.05.073

Dachev, T., Atwell, W. Semones, E.; Tomov, B., Reddell, B. 2006. ISS Observations of SAA radiation distribution by Liulin-E094 instrument on ISS, Adv. Space Res., 37, 1672-1677, http://dx.doi.org/10.1016/j.asr.2006.01.001

Dachev, T.P., Tomov, B., Matviichuk, Y., Dimitrov, P. and Bankov, N., 2009a. Relativistic electrons high doses at International Space Station and Foton M2/M3 satellites. *Advances in space research*, *44*(12), pp.1433-1440. http://dx.doi.org/10.1016/j.asr.2009.09.023

Dachev, T.P., 2009b, Characterization of near Earth radiation environment by Liulin type instruments, Adv. Space Res., 44, 1441-1449,. http://dx.doi.org/10.1016/j.asr.2009.08.007

Dachev, T.P., J. Semkova, B. Tomov, Yu. Matviichuk, Pl. Dimitrov, R. Koleva, St. Malchev, G. Reitz, G. Horneck, G. De Angelis, D.-P. Häder, V. Petrov, V. Shurshakov, V. Benghin, I. Chernykh, S. Drobyshev, N. G. Bankov, 2011. Space Shuttle drops down the SAA doses on ISS, Adv. Space Res., 47, 2030-2038. http://dx.doi.org/10.1016/j.asr.2011.01.034

Dachev, T., Tomov, B., Matviichuk, Y., Dimitrov, P., Spurny, F., Ploc, O., Uchihori, Y., Flueckiger, E., Kudela, K. and Benton, E., 2012a. Overview of the atmospheric ionizing radiation environment monitoring by Bulgarian build instruments. Bulgarian Academy of Sciences ISSN 1313–0927, p.87. Volume 24 / 2012

Dachev, Ts., G. Horneck, D.-P. Häder, M. Lebert, P. Richter, M. Schuster, R. Demets, 2012b. Time profile of cosmic radiation exposure during the EXPOSE-E mission: the R3D instrument, Journal of Astrobiology, 12, 5, 403-411, http://dx.doi.org/10.1089/ast.2011.0759

Dachev, Ts., 2015a.G. Horneck, D.-P. Häder, M. Schuster, and M. Lebert, EXPOSE-R cosmic radiation time profile, Journal of Astrobilogy, 14, 17-25, http://dx.doi.org/10.1017/S1473550414000093

Dachev, T.P., B.T. Tomov, Yu.N. Matviichuk, Pl.G. Dimitrov, NG. Bankov, V. V. Shurshakov, O.A. Ivanova, D.-P. Häder, M.T. Schuster, G. Reitz, G. Horneck, 2015b. “BION-M” №1 spacecraft radiation environment as observed by the RD3-B3 radiometer-dosimeter in April-May 2013, Journal of Atmospheric and Solar-Terrestrial Physics. 123, 82-91. http://dx.doi.org/10.1016/j.jastp.2014.12.011

Dachev, T., B. Tomov, Y. Matviichuk, P. Dimitrov, N. Bankov, V. Petrov, V. Shurshakov, O. Ivanova, 2017. “Foton-M” № 4 Spacecraft Radiation Environment as Observed by the RD3-B3 Radiometer-Dosimeter in July-September 2014, Proceedings of Twelfth Scientific Conference with International Participation SES, Sofia, 2-4 November 2016, ISSN 1313-3888, 29-41, http://www.space.bas.bg/SES/archive/SES%202016_DOKLADI/1_Space%20Physics/1_Dachev.pdf

Dachev, T. P., Bankov, N. G., Tomov, B. T., Matviichuk, Y. N., Dimitrov, P. G., Häder, D.-P. & Horneck, G. Overview of the ISS radiation environment observed during the ESA EXPOSE-R2 mission in 2014–2016. Space Weather, 15, 1475–1489, 2017. https://doi.org/10.1002/2016SW001580

Dachev, T., J. Semkova, B. Tomov, Y. Matviichuk, P. Dimitrov, N. Bankov, R. Koleva, K. Krastev, M. Jordanova, V. Shurshakov, V. Benghin, O. Ivanova, L. Zelenyi, I. Mitrofanov, A. Malakhov, M. Mokrousov, V. Tretyakov, P. Saganti, D. Holland, K.-i. Okuyama, I. Fajardo, A. Zanini, S. Vernetto, M. Colazo, D. Caruso, M. Rabolli, V. Ciancio, Current and future spase missions with Liulin type instruments, Proceedings of the fourteenth International Scientific Conference "SPACE, ECOLOGY, SAFETY" – SES 2019, 11-19, Sofia, Bulgaria, 6-8 November, 2019. http://www.space.bas.bg/SES/archive/SES%202019_DOKLADI/PROCEEDINGS%20SES%202019.pdf

Dachev, T., Carlucci, P., Cairo, F., Tomov, B., Matviichuk, Y., Dimitrov, P., Mitev, M., Jordanova, M. and Paciucci, L., 2024. Space radiation measured during first-ever commercial suborbital mission on Virgin Galactic SpaceShipTwo Unity on 29 June 2023. Life Sciences in Space Research. https://doi.org/10.1016/j.lssr.2024.09.003

Damasso, M., Dachev, T., Falzetta, G., Giardi, M.T., Rea, G. and Zanini, A., 2009. The radiation environment observed by Liulin-Photo and R3D-B3 spectrum-dosimeters inside and outside Foton-M3 spacecraft. *Radiation Measurements*, 44(3), pp.263-272. http://dx.doi.org/10.1016/j.radmeas.2009.03.007

Fajardo, I., A.A. Lidtke, S.A. Bendoukha, J.G.-L., R. Rodríguez, R. Morales, D. Faizullin, M. Matsuoka, N. Urakami, R. Kawauchi, M. Miyazaki, N. Yamagata, K. Hatanaka, F. Abdullah, J.J. Rojas, M.E. Keshk, K. Cosmas, T. Ulambayar, P. Saganti, D. Holland, T. Dachev, S. Tuttle, R. Dudziak, and Kei-ichi Okuyama, Design, Implementation, and Operation of a Small Satellite Mission to Explore the Space Weather Effects in LEO, Aerospace, ISSN 2226-4310, 6(10), 108, 2019. https://doi.org/10.3390/aerospace6100108

Header, D.P., Richter, P., Schuster, M., Dachev, T., Tomov, B., Georgiev, P. and Matviichuk, Y., 2009. R3D-B2–Measurement of ionizing and solar radiation in open space in the BIOPAN 5 facility outside the FOTON M2 satellite. Advances in Space Research, 43(8), pp.1200-1211. http://dx.doi.org/10.1016/j.asr.2009.01.021

Карташов, Д.А., Петров, В.М., Коломенский, А.В., Акатов, Ю.А. and Шуршаков, В.А., 2010. Дозы космической радиации в антропоморфном фантоме космического эксперимента" МАТРЕШКА-Р" и в скафандре" ОРЛАН-М" при внекорабельной деятельности. Авиакосмическая и экологическая медицина,

44(2), pp.3-8. (SPACE RADIATION DOSES IN THE ANTHROPOMORPHOUS PHANTOM IN SPACE EXPERIMENT "MATRYESHKA-R" AND SPACESUIT "ORLAN-M" DURING EXTRAVEHICULAR ACTIVITY, Kartashov, D.A., Petrov, V.M., Kolomensky, A.V., Akatov, Yu.A., Shurshakov, V.A. https://www.elibrary.ru/item.asp?id=19057356

Nealy, J.E., Cucinotta, F.A., Wilson, J.W., Badavi, F.F., Dachev, T.P., Tomov, B.T., Walker, S.A., De Angelis, G., Blattnig, S.R. and Atwell, W., 2007. Pre-engineering spaceflight validation of environmental models and the 2005 HZETRN simulation code. *Advances in Space Research*, *40*(11), pp.1593-1610. http://dx.doi.org/10.1016/j.asr.2006.12.030

Reitz, G., Beaujean, R., Benton, E., Burmeister, S., Dachev, T., Deme, S., Luszik-Bhadra, M. and Olko, P., 2005. Space radiation measurements on-board ISS—the DOSMAP experiment. *Radiation Protection Dosimetry*, *116*(1-4), pp.374-379. http://rpd.oxfordjournals.org/cgi/content/abstract/116/1-4/374

Semkova, J., Ts.Dachev, Yu.Matviichuk, R.Koleva, B.Tomov, P.Bajnov, V.Petrov, V.Nguyen, M.Siegrist, J.Chene, C.d'Uston, F.Cotin, Dosimetric investigation on MARS-96 missions, 1994, Adv. Space Res., V 14, No.10, 707-710. http://dx.doi.org/10.1016/0273-1177(94)90530-4

Semkova, J., R. Koleva, St. Maltchev, G. Todorova, T. Dachev, V. Benghin, V. Shurshakov, V. Petrov, Calibration results of Liulin-5 charged particle telescope obtained in ICCHIBAN-7 experiment. New instrumentation for radiation monitoring on interplanetary missions, presented at the 11th Workshop on Radiation Monitoring for the International Space Station (WRMISS) held in Oxford, UK, September 6-8, 2006. chrome-https://wrmiss.org/workshops/eleventh/Semkova.pdf

Semkova J., Maltchev S., Tomov B., Matviichuk Yu., Dachev Ts., Koleva R., Benghin V., Chernykh I., Shurshakov V., Petrov V., Upcoming Phobos Sample Return Mission, Proceedings of Fundamental Space Research Conference, 2008._____357-360, ISSBN 978-954-322-316-9, http://www.stil.bas.bg/FSR/PDF/TOP4Semkova_Jordanka2201235.pdf

Semkova, J., T. Dachev, R. Koleva, N. Bankov, S. Maltchev, V. Benghin, V. Shurshakov, V. Petrov, 2014. Observation of radiation environment in the International Space Station in 2012–March 2013 by Liulin-5 particle telescope, J. Space Weather Space Clim., 4, A32, http://dx.doi.org/10.1051/swsc/2014029

Dachev, T., B. Tomov, Y. Matviichuk, P. Dimitrov, V. Shurshakov, V. Benghin, E. Yarmanova, O. Ivanova, I. Nikolaev, "LIUILIN-ISS-2" system for cosmonauts' dosimetry control in the ISS radiation environment, Aerospace Research in Bulgaria, 28, 38-58, 2016. http://journal.space.bas.bg/arhiv/n%2028/Articles/4.pdf

Semkova, J., Koleva, R., Benghin, V., Dachev, T., Matviichuk, Y., Tomov, B., Krastev, K., Maltchev, S., Dimitrov, P., Mitrofanov, I. and Malahov, A., *2018.* Charged particles radiation measurements with Liulin-MO dosimeter of FREND instrument aboard ExoMars Trace Gas Orbiter during the transit and in high elliptic Mars orbit. *Icarus, Volume 303, 15 March 2018, Pages 53-66,* https://doi.org/10.1016/j.icarus.2017.12.034

Semkova, J., Bengin, V., Koleva, R., Krastev, K., Matveychuk, Y., Tomov, B., Bankov, N., Malchev, S., Dachev, T., Shurshakov, V. and Drobyshev, S., 2024. New Results of Radiation Study on Board TGO ExoMars in 2018–2023. *Solar System Research*, *58*(4), pp.367-376. https://doi.org/10.1134/S0038094624700291

Slaba, T.C., S.R. Blattnig, F.F. Badavi, N.N. Stoffle, R.D. Rutledge, K.T. Lee, E.N. Zappe, T.P. Dachev and B.T. Tomov, 2011. Statistical Validation of HZETRN as a Function of Vertical Cutoff Rigidity using ISS Measurements, Adv. Space Res., 47, 600-610, http://dx.doi.org/10.1016/j.asr.2010.10.021

Tobiska, K., Gersey, B., Didkovsky, L., Judge, K., Weiman, S, Bouwer, D., Bailey, J., Dachev, T., Tomov, B., Matviichuk Y, Dimitrov, P., Jordanova, M., Mitev, M., Bankov, N, Semkova, J., International space station radiation field measurements by Liulin-SET spectrometer of ARMAS flight module 9 in 2022, 20th Proceedings of the Twentieth International Scientific Conference "SPACE, ECOLOGY, SAFETY" – SES 2024, pp 16-22, 22-15, October, Sofia, Bulgaria.
http://www.space.bas.bg/SES/archive/SES%202024_DOKLADI/Plenary%20Session/2_Dachev.pdf

Tomov B., Dimitrov Pl., Matviichuk Yu., Dachev Ts., 2008. Galactic and Solar Cosmic Rays Study by Ground and Rocketborne Space Radiation Spectrometers-Dosimeters- Liulin-6R and Liulin-R, Proceedings of Fundamental Space Research Conference, 252-257, ISSBN 978-954-322-316-9, http://www.stil.bas.bg/FSR/PDF/TOP5Tomov_Borislav2242058.pdf

Wilson, J. W., J. E. Nealy, T. Dachev, B.T. Tomov, F. A. Cucinotta, F. F. Badavi, G. de Angelis, N. Leutke, W. Atwell, 2007. Time serial analysis of the induced LEO environment within the ISS 6A, Adv. Space Res., 40, 11, 1562-1570, https://doi.org/10.1016/j.asr.2006.12.030

Zanini, A. and Torino, S., 2017. Liulin-AR spectrometer for radiation environment observation on SABIA-MAR 1 satellite. Aerospace Research in Bulgaria, *17*, p.42. liulin-ar-spectrometer-for-radiation-environment-observation-on-sabia-mar-1-satellite-satellite-2017-satellite-2017-libre.pdf

References of Table 2

Adams, J.H., Adcock, L., Apple, J., Christl, M., Cleveland, W., Cox, M., Dietz, K., Ferguson, C., Fountain, W., Ghita, B., Kuznetsov, E. (2007). Deep space test bed for radiation studies, *Nuclear Instruments and Methods in*

Physics Research Section A: Accelerators, Spectrometers, Detectors and Associated Equipment, Vol. 579, No. 1, pp. 522–525, DOI: 10.1016/j.nima.2007.04.114.

Ambrožová, I., Beck, P., Benton, E.R., Billnert, R., Bottollier-Depois, J.F., Caresana, M., Dinar, N., Domański, S., Gryziński, M.A., Kákona, M., Kolros, A. (2020). REFLECT – Research flight of EURADOS and CRREAT: Intercomparison of various radiation dosimeters onboard aircraft, *Radiation Measurements*, Vol. 137, Art. 106433, DOI: 10.1016/j.radmeas.2020.106433.

Benton, E. (2005). Deep Space ICCHIBAN: An international comparison of space radiation dosimeters aboard the NASA Deep Space Test Bed, *Proceedings of the 10th Workshop for Radiation Monitoring on the International Space Station*, Chiba, Japan, 7–9 September 2005, available at: https://wrmiss.org/workshops/tenth/pdf/08_benton.pdf.

Dachev, T., Tomov, B., Matviichuk, Y., Dimitrov, P., Spurný, F., Ploc, O., Uchihori, Y., Flückiger, E., Kudela, K., Benton, E. (2012). Overview of the atmospheric ionizing radiation environment monitoring by Bulgarian-built instruments, *Proceedings of the Scientific Conference "Space, Ecology, Safety"*, Vol. 24, pp. 87–98, available at: http://journal.space.bas.bg/arhiv/n%2024/Articles/6.pdf.

Dachev, T.P., Sapundjiev, P., Tomov, B.T., Matviichuk, Y.N., Mitev, M.M., Yordanova, M.M. (2024b). Liulin-AA spectrometer measurements of the radiation dose during the travel from the Bulgarian Antarctic Base on Livingston Island to Longyearbyen Town, Svalbard Archipelago, Norway and back to Sofia, *Proceedings of the Twentieth International Scientific Conference "Space, Ecology, Safety" – SES 2024*, Sofia, Bulgaria, 22–25 October 2024, pp. 33–42, available at: http://www.space.bas.bg/SES/archive/SES%202024_DOKLADI/1_Space%20Physics/1_Dachev.pdf.

Desmaris, G. (2016). Cosmic radiation in aviation: Radiological protection of Air France aircraft crew, *Annals of the ICRP*, Vol. 45, No. 1_suppl, pp. 64–74, DOI: 10.1177/0146645316636009.

Getley, I.L. (2007). *Cosmic and Solar Radiation Monitoring of Australian Commercial Flight Crew at High Southern Latitudes as Measured and Compared to Predictive Computer Modelling*, Doctoral dissertation, University of New South Wales, Sydney, Australia, DOI: 10.26190/unsworks/6604.

Getley, I.L., Bennett, L.G.I., Boudreau, M.L., Lewis, B.J., Green, A.R., Butler, A., Takada, M., Nakamura, T. (2007). Comparative measurements of cosmic radiation monitors for aircrew exposure assessment, *Advances in Geosciences: Solar Terrestrial*, Vol. 8, pp. 223–231.

Getley, I.L., Bennett, L.G.I., Lewis, B.J., Bennett, B., Dyer, C.S., Hands, A.D.P., Duldig, M.L. (2010). Evaluation of new cosmic radiation monitors designed for aircrew exposure assessment, *Space Weather*, Vol. 8, No. 1, Art. S01001, DOI: 10.1029/2009SW000492.

Green, A.R., Bennett, L.G.I., Lewis, B.J., Kitching, F., McCall, M.J., Desormeaux, M., Butler, A. (2005). An empirical approach to the measurement of the cosmic radiation field at jet aircraft altitudes, *Advances in Space Research*, Vol. 36, No. 9, pp. 1618–1626, DOI: 10.1016/j.asr.2005.03.061.

Hwang, J., Kwak, J., Jo, G., Nam, U.W. (2020). Validation of KREAM based on in-situ measurements of aviation radiation in commercial flights, *Journal of Astronomy and Space Sciences*, Vol. 37, No. 4, pp. 229–236, DOI: 10.5140/JASS.2020.37.4.229.

Kitching, F.W. (2005). *Use of the LIULIN Detector for the Determination of Aircrew Radiation Exposure*, PhD thesis, Royal Military College of Canada, Kingston, Canada.

Kubančák, J. (2014). *Application of Liulin Detector in the Detection and Dosimetry of Cosmic Rays*, Doctoral dissertation, Czech Technical University in Prague, Prague, Czech Republic.

Kubančák, J., Ambrožová, I., Bütikofer, R., Kudela, K., Langer, R., Davídková, M., Ploc, O., Malušek, A. (2014). Liulin silicon semiconductor spectrometers as cosmic ray monitors at the high-mountain observatories Jungfraujoch and Lomnický štít, *Journal of Instrumentation*, Vol. 9, No. 7, Art. P07018, DOI: 10.1088/1748-0221/9/07/P07018.

Larsen, N., Mishev, A., Binios, A., Leppänen, A.P., Tanskanen, E., Turunen, E., Usoskin, I., Envall, J., Lakkala, P., Iinatti, T. (2023). Altitude profile of atmospheric radiation in the Arctic region obtained during a scientific balloon flight with MDU-1 Liulin, *Proceedings of the 27th European Cosmic Ray Symposium – PoS (ECRS)*, Trieste, Italy.

Lee, J., Park, I., Kim, J., Lee, J., Hwang, J., Kim, Y.C. (2014). Measurement of the space radiation dose for flight aircrew at high altitude, *Journal of Astronomy and Space Sciences*, Vol. 31, No. 1, pp. 33–39, DOI: 10.5140/JASS.2014.31.1.33.

Lewis, B.J., Bennett, L.G.I., Green, A.R., Butler, A., Desormeaux, M., Kitching, F., McCall, M.J., Ellaschuk, B., Pierre, M. (2005). Aircrew dosimetry using the Predictive Code for Aircrew Radiation Exposure (PCAIRE), *Radiation Protection Dosimetry*, Vol. 116, Nos. 1–4, pp. 320–326, DOI: 10.1093/rpd/nci024.

Meier, M.M., Trompier, F., Ambrožová, I., Kubančák, J., Matthiä, D., Ploc, O., Santen, N., Wirtz, M. (2016). CONCORD: Comparison of cosmic radiation detectors in the radiation field at aviation altitudes, *Journal of Space Weather and Space Climate*, Vol. 6, Art. A24, DOI: 10.1051/swsc/2016017.

Meier, M.M., Berger, T., Jahn, T., Matthiä, D., Plettenberg, M.C., Scheibinger, M., Schennetten, K., Wirtz, M. (2023). Impact of the South Atlantic Anomaly on radiation exposure at flight altitudes during solar minimum, *Scientific Reports*, Vol. 13, No. 1, Art. 9348, DOI: 10.1038/s41598-023-36190-5.

Mertens, C.J., Gronoff, G.P., Norman, R.B., Hayes, B.M., Lusby, T.C., Straume, T., Tobiska, W.K., Hands, A.D.P., Ryden, K.A., Benton, E.R., Panasyuk, M.I., Petrov, V.L., Reitz, G., Meier, M.M., Matthiä, D., Berger, T., Sato, T., Kataoka, R., Yasuda, H., Lee, K., Kiefer, R., Gersey, B.B. (2016). Cosmic radiation dose measurements from the RaD-X flight campaign, *Space Weather*, Vol. 14, No. 10, pp. 874–898, DOI: 10.1002/2016SW001407.

Mishev, A., Binios, A., Turunen, E., Larsen, N., Leppänen, A.P., Tanskanen, E., Usoskin, I., Envall, J., Lakkala, P., Iinatti, T. (2022). Measurements of natural radiation with an MDU Liulin-type device at ground level and in the atmosphere under various conditions in the Arctic region, *Radiation Measurements*, Vol. 154, Art. 106757, DOI: 10.1016/j.radmeas.2022.106757.

Mishev, A.L., Kodaira, S., Kitamura, H., Ploc, O., Ambrožová, I., Tolochek, R.V., Kartsev, I.S., Shurshakov, V.A., Artamonov, A.A., Inozemtsev, K.O. (2023). Radiation environment in the high-altitude Antarctic plateau: Recent measurements and model studies, *Science of the Total Environment*, Vol. 890, Art. 164304, DOI: 10.1016/j.scitotenv.2023.164304.

Ploc, O. (2009). *Measurement of Exposure to Cosmic Radiation in the Near-Earth Environment with the Energy-Deposition Spectrometer Liulin Onboard Aircraft and Spacecraft*, Doctoral dissertation, Czech Technical University in Prague, Prague, Czech Republic.

Ploc, O., Spurný, F., Dachev, T.P. (2011). Use of an energy-depositing spectrometer for individual monitoring of aircrew, *Radiation Protection Dosimetry*, Vol. 144, Nos. 1–4, pp. 611–614, DOI: 10.1093/rpd/ncq505.

Ploc, O., Ambrožová, I., Kubančák, J., Kovář, I., Dachev, T.P. (2013). Publicly available database of measurements with the silicon spectrometer Liulin onboard aircraft, *Radiation Measurements*, Vol. 58, pp. 107–112, DOI: 10.1016/j.radmeas.2013.09.002.

Spurný, F. (2000). *Dosimetry Measurements During a Balloon Flight – June 2000*, Report DRD 485/00, Nuclear Physics Institute, Academy of Sciences of the Czech Republic.

Stassinopoulos, E.G., Stauffer, C.A., Dachev, T.P., Brucker, G.J., Tomov, B.T., Dimitrov, P.G. (1999). *The LIULIN-3M Radiometer for Measuring Particle Doses in Space and on Aircraft*, NASA Goddard Space Flight Center, Document ID 19990080920.

Tomov, B., Dimitrov, P., Matviichuk, Y., Dachev, T. (2008). Galactic and solar cosmic ray studies by ground- and rocket-borne space radiation spectrometers-dosimeters Liulin-6R and Liulin-R, *Sun and Geosphere*, Vol. 3, No. 2, pp. 87–92.

Uchihori, Y., Kitamura, H., Fujitaka, K., Dachev, T.P., Tomov, B.T., Dimitrov, P.G., Matviichuk, Y. (2002). Analysis of the calibration results obtained with the Liulin-4J spectrometer-dosimeter on protons and heavy ions, *Radiation Measurements*, Vol. 35, No. 2, pp. 127–134, DOI: 10.1016/S1350-4487(01)00286-4.

Uchihori, Y., Benton, E., Moeller, J., Bendrick, G. (2003). Radiation measurements aboard NASA ER-2 high-altitude aircraft with the Liulin-4J portable spectrometer, *Advances in Space Research*, Vol. 32, No. 1, pp. 41–46, DOI: 10.1016/S0273-1177(03)90368-1.

Vergara, J.S., Román, R.D.M. (2009). The implementation of cosmic radiation monitoring in routine flight operation of IBERIA airline of Spain: One year of experience with in-flight permanent monitoring, *Radiation Protection Dosimetry*, Vol. 136, No. 4, pp. 291–296, DOI: 10.1093/rpd/ncp131.

Wissmann, F., Burda, O., Khurana, S., Klages, T., Langner, F. (2014). Dosimetry of secondary cosmic radiation up to an altitude of 30 km, *Radiation Protection Dosimetry*, Vol. 161, Nos. 1–4, pp. 299–302, DOI: 10.1093/rpd/nct329.

Zanini, A., Vernetto, S., Ciancio, V., Di Giovan, G., Morfino, P., Liberatore, A., Giannini, G., Hubert, G. (2019). Environmental radiation dosimetry at high southern latitudes with Liulin-type instruments, *Journal of Environmental Radioactivity*, Vol. 208, Art. 105993, DOI: 10.1016/j.jenvrad.2019.105993.

Remark: in the following link: https://scholar.google.com/citations?user=uzmW_mwAAAAJ are collected all of the papers concerning Liulin instruments. This link is also the best downloading method.

DOI: 10.31401/WS.2026.proc.22

Prototype Evaluation of an Open SDR-Based Framework for Long-Term VOR Signal Observations

Georgiev G.[1,2], *Simeonov R.*[2,3]

[1]Space Research and Technology Institute, Bulgarian Academy of Sciences, Bulgaria
[2]Institute for Nuclear Research and Nuclear Energy, Bulgarian Academy of Sciences, Bulgaria
[3]Faculty of Physics, Sofia University, Bulgaria
georgiev.georgi.st@gmail.com

Abstract

A low-cost open scientific platform for long-term monitoring of radio propagation characteristics in the 3 m radio band based on the aeronautical VHF Omnidirectional Range navigation system is proposed. A prototype serving as a feasibility check for the planned technological stack is built and evaluated. Results confirm that the prototyped hardware and software algorithms are capable enough to serve as a foundation for the future measurement platform and allow for building a full-scale working prototype. The need and approaches for data reduction by online processing for the radio-propagation metrics are discussed. Several research areas where data from the platform are believed to be useful are quickly mentioned. The platform remains open to include new metrics in the stored data that can support other research.

Keywords: VHF propagation; prototype study; software-defined radio (SDR); passive radio sensing; long-term monitoring; VHF omnidirectional range (VOR); open science

1. Introduction

Understanding environmental effects on radio propagation in the Very High Frequency (VHF) band remains important from both scientific and technological point of view. Multiple sources report observations of such effects in correlation with precipitation, humidity, ambient temperature, atmospheric pressure, atmospheric turbulence and refractive index variations. Several studies also discuss physical mechanisms responsible for the observed effects [Olasunkanmi and Bello, 2017; Emeruwa 2023; Miś et al., 2025]. The VHF radio propagation can be affected by thunderstorm activity [Kákona et al., 2025], seizmotectonic activity [Moriya et al., 2010], atmospheric ionization caused by meteors [Dyrud et al., 2008], solar activity and space weather [Super Avionics, 2023] and others.

The VHF Omnidirectional Range (VOR) is an aeronautic network that serves as a ground-based navigation system for airborne vehicles, providing very good coverage over land areas and limited coverage over the open-ocean regions. VOR transmitters are stable, reliable and maintain continuous operation to serve the air traffic. The VOR signals are mainly composed of variable and reference phase subsignals and identification. The VOR network consists of widespread stations which transmit signals with unique characteristics. This makes them an attractive source for conveying systematic long-term passive measurements of the radio frequency propagation in the VHF radio band.

Open datasets for long-term VHF measurements are not widely available. This complicates the independent validation of published results and does not allow for data reusability. This issue is addressed by the Systematic Monitoring of the VHF Radiopropagation and Atmospheric Influences Analysis project (SYMORAIA-VHF) by suggesting and development of a scalable open platform. By measurements of the received signals in the VOR radio band the platform will collect data for the long-term radio propagation behaviour. Technical documentation and software codes will be made publicly available in an attempt to facilitate scalability and form a community around the platform. Collected data will be shared following the FAIR principles.

This contribution is to present a prototype study of the technological stack meant to be used for the suggested platform. Signal acquisition, parameter extraction and data storage together with a specific hardware implementation are presented and discussed.

2. Planned Measurement Platform

2.1. Vision and philosophy

An open multi-receiver scientific infrastructure for monitoring radio propagation characteristics is aimed to contribute to multiple scientific and applied studies. Utilization of existing infrastructure of radio transmitters as signal source reduces the cost, the maintenance load and the footprint of such platform. The VOR aviation system is particularly suitable as it is standardized and well maintained. Which trivially solves various problems of the presented measurement platform, including scalability, data compatibility and is worldwide deployable.

Multiple phenomena can affect radio propagation. Understanding the effects they cause and their mechanisms is fundamental from scientific point of view. Effects in the radio propagation characteristics may serve as natural sensor, providing applied information in various fields, an excellent example for such use is the principle of monitoring precipitations over wide territories using signal propagation from telecommunication networks [Overeem et al., 2013; Doumounia et al., 2014].

The platform supports multiple research directions including:

- Meteorological effects. The presence of hydro meteors, turbulent air flows, areas with different densities and refractive indices can lead to variations in received signal strength, noise floor, phase shift, etc. These effects are to be studied using meteorological data from the S-band radar system of the Bulgarian National Hail Suppression Agency and Meter.ac both of which provide very good coverage of the Bulgarian territory.
- Electric field during thunderstorms. A recent deployment of an electric field mill at BEO-Musala, Musala peak, Bulgaria [Kákona et al., 2025] may be used to find correlations between the electric field and observed radio propagation effects.
- Effects of meteor trails. A computational study suggest that radar cross section of meteor trails plasma depends on different parameters like meteor entry angle and radar frequency but the peak reflectability is usually $\lesssim 100$ MHz [Dyrud et al., 2008]. Distant VOR stations behind the line of sight may appear in the received spectrum with higher signal power due to sporadic propagation resembling passive radar for meteors.
- Extraterrestrial activity. Various data sources for solar activity and others may be correlated with measurable effects on the propagation and spectral characteristics in the VOR band.
- Seismic activity. Studies suggest effects on the radio propagation with seismic origin [Moriya et al., 2010]. Long term measurements on the radio propagation may support such studies.

2.2. Measurement concept

Rare, cyclic or low impact events could be of scientific interest. In order to maximise the observational coverage for the effects caused by these events several conceptual decisions were made. Continuous acquisition increases temporal coverage and provide information about long term tendencies and fluctuations. Multi-source layout increases the spatial coverage providing sensitivity for very severe effects based on information from closely located transmitters and long-distance effects based on information from distant ones. A multi-node system approach will also increase the spatial coverage of the system but also will provide means to factor out effects caused by the transmitters themselves. Standardized measurements will provide compatible and comparable data between the nodes and over longer acquisition times. The IQ sample stream generated by continuously operating nodes result to big amounts of data which are not practical to store in raw for the scale of the present project. This is why during regular data taking an online data processing

algorithm that reduces the amounts of data is inevitable. Multiple key parameters per VOR channel need to be evaluated among which:

- frequency of the carrier;
- phase, total signal power, net signal power, signal-to-noise ratio (SNR) and modulation depth of the 30 Hz amplitude modulated reference signal;
- phase, total signal power, net signal power, SNR, of the 30 Hz variable signal modulated on FM sub-carrier;
- total signal power, net signal power, SNR of the CW modulated identification;
- mean power, standard deviation (σ), median absolute deviation (MAD) and quartiles ($Q1$, median, $Q3$) for the noise in the signal-free spectral ranges of the VOR channel.

Presence of offline IQ samples in raw format will allow for algorithm debugging, metrics calibration and operational validation of the online processing algorithms. Thus limited amounts of raw IQ samples need to be stored along with the processed data.

The platform remains open to discuss implementations of other metrics that could reasonably appear to be meaningful for future research.

2.3. Requirements and general design

The platform will detect signals from the VOR network which are located in the range 108 MHz–118 MHz. Software Defined Radios (SDRs) are good candidates for radio receivers for the platform. By their nature they are wideband receivers and can easily cover the required bandwidth of 10 MHz. The in-phase and quadrature (IQ) components of the digitized complex signal provide high quality information which can be used to extract specific radio propagation metrics.

SDR devices are usually equipped with Automatic Gain Control (AGC) which scales the incoming signals so that they fit optimally in the dynamic range of the receiver. Such scaling optimizes the SNR and if not handled properly can completely disable the comparability between separate measurements even on the same device. The simplest solution is to ensure that the signal gain has a fixed value. A more sophisticated approach requires feedback from the AGC controller and calibration using a reference source.

VOR signals are strictly horizontally polarized. Due to various effects they may depolarize. To be able to capture change in the signal polarization, measurement nodes need to include two separate circuits for both horizontally and vertically polarized signal components. Each circuit needs to be equipped with separate antenna sensitive to the horizontal or vertical polarized signals accordingly. Both antenna types should be with omnidirectional pattern to provide uniform sensitivity in all directions. Antennas may be exposed to rough weather conditions so they need to provide enough rigidity to withstand strong winds and ice build-up.

FM-broadcast stations are notorious for their high power signals. Their section of the radio spectrum is located next to the one dedicated to the VOR system, leading to interference and suppressed performance of the receivers operating in the VOR band. A deep suppression of the FM-broadcast signals while preserving nearly flat response for the VOR signals is needed. Unfortunately such filters are not widely available and a custom solution is required.

A computer platform is needed to handle the hardware configuration, data flow and storage and perform online processing. The online processing algorithm is foreseen to be such that it scales easily for multi-channel analysis and is able to evaluate the needed signal metrics in few seconds as the aimed time resolution is also in order of seconds. Each wideband data frame corresponding to several hundreds of ms will be analysed to provide signal metrics for multiple VOR channels.

3. Technological Stack Evaluation

The technological stack for the planned measurement platform was evaluated using a prototype of the system implementing its critical components. The prototype evaluation included testing the performance of an SDR receiver, evaluate the measures needed to collect VOR signals in presence

of high power FM broadcast stations, validating the custom software for handling the SDR receiver, data storage and the algorithms for signal metrics calculation.

3.1. Hardware implementation

The prototype was built around an SDRplay RSPduo SDR receiver. It features a 14 ADC and is able to provide IQ stream with maximum sampling rate of 10 MSamples s and maximum bandwidth of 10 MHz.

Double Bazooka antennas were initially designed for radar applications. They were adapted to be built from standard coaxial cable for ham radio application in different amateur radio bands. These antennas typically present fractional bandwidth relative to the resonant frequency about 15 % at $VSWR \leq 2{:}1$ [Whysall, 1968]. Other significant benefits of these antennas are that they have predictable impedance behaviour and noticeably lower received noise [Prabakaran, 2026]. Non-foiled cables like RG213 are preferred due to technical complications with foil removal at the feed point [Prabakaran, 2026]. Other source also suggest that the reduced leakage by the foil can lead to a partial reduction of the antenna's bandwidth [K3DAV, 2010]. The antenna used for the prototype was a self-made double bazooka antenna built from 8D-FB which is a shielded and foiled coaxial cable with impedance of 50 Ω and foam insulation. This cable was selected because it provides better mechanical stability. Resonant frequency of the antenna was selected to be around 113 MHz.

An RF a choke made by toroid of 61 material and 6 winds of RG58 coaxial cable was built to suppress common mode signals and reduce the RF interference.

A shorted-stub filter made out of RG58 coaxial cable was used to partially suppress the powerful FM broadcast transmitters.

3.2. Software implementation

SDRplay proprietary software tools were used to operate the RSPduo receiver. Automatic gain control was switched off and the RF gain was fixed to the lowest possible gain (20 units) using sdrconnect application in server mode. The websocket server was provided by another instance of sdrconnect which was ran in headless client mode. This multi-layer solution was used due to the WebSocket API that currently lacks support for several essential features like obtaining calibration information about the wideband signal, nor is able to control RF gain.

The client side for SDRPlay's WebSocket API version 1.3 was implemented in a custom made software package written in Rust programming language. The software runs a separate thread dedicated to the API interactions. It is capable of sending configuration commands and requests to the SDR receiver, monitor status responses and handle IQ, audio and spectrum streams. Of high importance was to count and timestamp each IQ chunk and optionally to forward the stream of IQ chunks to the main thread where consecutive IQ chunks were merged to unified size collections, referred to as IQ frames. The software collects IQ frames on fixed intervals and stores them to local storage device for further analysis. The stored by the prototype IQ frames were in raw format without any reduction. This facilitated the development and the validation of the online processing algorithms.

Data from separate acquisitions were stored in dedicated groups in HDF5 files. Metadata relevant to the acquisition as center frequency, sample rate and active device and antenna were stored as attributes to the group. IQ frames, IQ chunk timestamps and IQ chunk sequential numbers were stored to 3 distinct datasets. Data inconsistencies due to incomplete writing can occur. In order to mitigate this potential problem, another scalar dataset was introduced and used to store the index of the last record which was successfully stored. Every consecutive write attempt in the datasets will happen at position of the last stored index incremented with 1. In case of inconsistency the last stored index will not be updated and the inconsistent record will be overwritten by the incoming data.

Algorithms for analysis of VOR signals were implemented in Python programming language. It was used to develop and verify algorithms that are meant to perform online processing in the future

platform. During the prototype study this software was used offline with stored raw data. This made the results reproducible and simplified the algorithm development.

3.3. Experimental setup and data acquisition

The measurements were performed on the pillar of a decommissioned structure for an axial windmill prototype at the Institute for Nuclear Research and Nuclear Energy, Bulgarian Academy of Sciences. The custom made double bazooka antenna placed horizontally facing North and was elevated with additional 2 m using a PVC pipe, which was used to reduce the effects of the metal structure. The RF choke was located near the antenna feed point. The shorted stub filter was attached at the receiver and effectively suppressed the FM broadcast signals and enabled the measurements. A RaspberryPi 5 with an attached SSD storage was used to run the proprietary SDRconnect software and custom made software that handled the data stream and stored the raw data into a HDF5 file with compression.

Frames of 10 sample chunks were collected. Each frame has 5×10^6 complex samples with sample rate of 10 MS s. The frame period was configured to be ≈ 3.84 s so that longer time window was covered.

4. Results and Discussion

During the data acquisition all the requirements from the hardware were met. Measurements showed that the bandwidth of the custom built antenna at $VSWR \leq 2:1$ were about 12.3 %. Such antenna confidently covers the VOR radio band. The shorted-stub filter provides maximum RF suppression of 25 dB at 92.8 MHz, and RF suppression for the VOR band of 2.1 dB and 0.7 dB respectively for 108 MHz and 118 MHz. Even though this filter is not performing ultimately well it is reducing the load on the receiver with interfering signals significantly and leads to at least 3 dB gain in SNR.

A successful data acquisition using the prototype was achieved. The acquisition of 500 frames took 32 minutes and the resulting HDF5 file was about 9 .

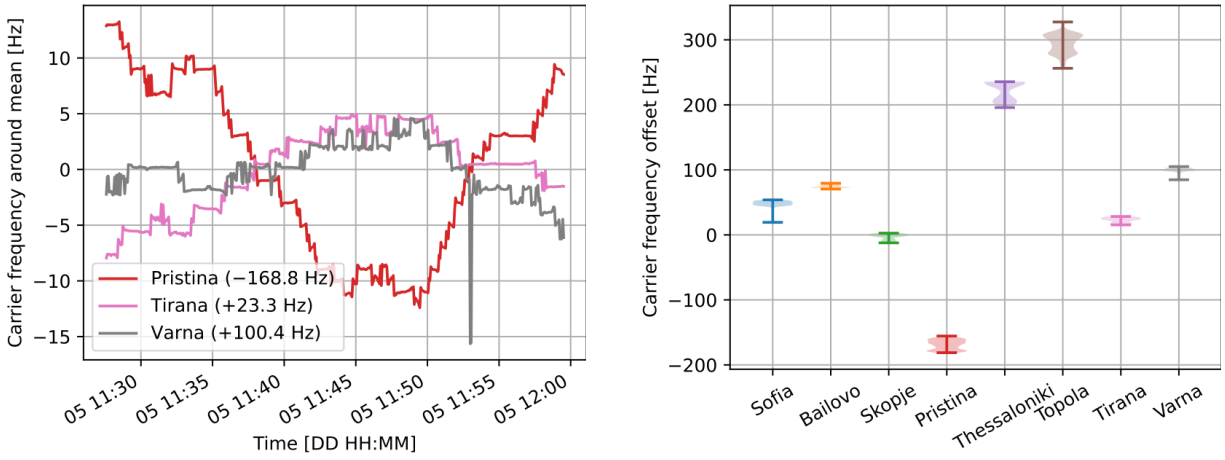
The collected raw data were analysed using the prototype implementation of the algorithms for online processing. Various parameters including carrier frequency, signal power and noise floor were calculated for 40 VOR stations within 400 km range from the measurement location. From those 8 selected stations with higher signal strength and are listed in table 1.

Table 1. *Data about the selected VOR station. Distance and bearing from the measurement point (INRNE-BAS) to each station are calculated using spherical Earth approximation.*

DVOR	Frequency [MHz]	Elevation [m]	Distance [km]	Bearing [deg]
Sofia	112.6	540	5	2
Bailovo	117.5	930	35	87
Skopje	112.8	266	165	242
Pristina	113.3	555	193	268
Thessaloniki	112.1	203	246	188
Topola	116.8	465	270	309
Tirana	117.7	38	333	247
Varna	112.4	60	366	78

Carrier frequency offsets and variations over time were observed for all analysed signals. The origin of the frequency offset from the true channel frequency is not analysed in detail but it is highly likely to originate form the transmitter RF generator. The offsets are visible on Fig. 1b and are on the order of 100 Hz which is in fact negligible for their practical applications. The frequency variations over time could be due to instabilities in the transmitters, the receiver or due to some factors in the propagation medium. From Fig. 1a it is obvious that the receiver is not the only source

of such variations as the fluctuations observed in the different channels are independent. Raw data collected with 5×10^6 samples per frame with sample rate of 10 MSamples s provide 2 Hz frequency resolution per bin. The implemented algorithm, however, allows for higher inter-bin resolution. The algorithm verifies that the SNR is high enough so that the carrier frequency estimate is reliable. In the cases of low SNR no frequency estimate is provided.

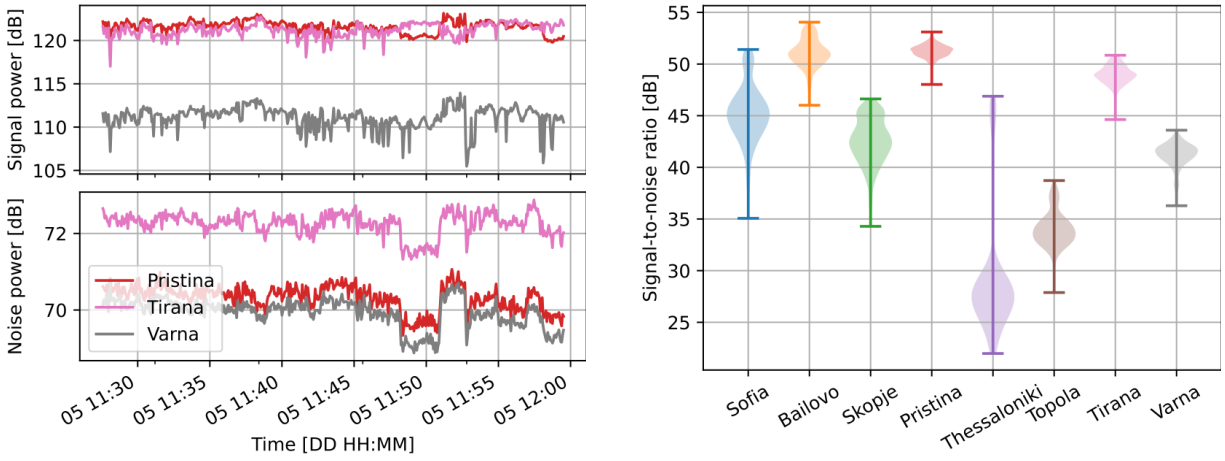


(a) Carrier frequencies over time centered around their mean values shown in parentheses.

(b) Distribution of carrier frequencies.

Figure 1. Carrier frequency drift for selected VOR stations.

Signal strength is another parameter that is highly important for the future measurement platform. Time series of total signal power in the interval ± 150 Hz around the estimated carrier frequency are shown on the top plot of fig. 2a and the noise floor power calculated in free of emission spectral ranges for the given VOR channel are shown on the bottom plot of Fig. 2a. That figure reveals time dependent fluctuations for both signal and noise providing a clue that the typical variations are detectable. Local effects are also visible: the noise drop around time 11:50 which is common for all the channels. SNR distributions for the selected VOR stations are visible on Fig. 2b. Multiple observations at this plot attract attention: the higher SNRs for Pristina and Tirana compared to much closely located Sofia and Bailovo, the asymmetric profiles for Sofia, Bailovo and Skopje and the outliers for Thessaloniki.



(a) Total signal power of the phase-reference signal (fC ± 150 Hz) and noise power.

(b) Signal-to-noise ratio distributions.

Figure 2. *Signal strength for selected VOR stations.*

The signal metrics are calculated using the prototype implementation of the algorithms meant to be part of the software for online analysis and data reduction. The prototype implementation demonstrated that the algorithms were robust enough to be migrated to the software for online analysis. The prototype built over the technological stack described in section 3 managed to collect, process and store data from VOR stations. All this renders the prototype successful and allow to step over towards building full scale working prototype able to measure horizontally and vertically polarized signals with online processing capabilities. The deployment sites are also to be decided after in-situ survey.

In this section multiple observed phenomena remain unexplained as their origins and physical mechanisms are out of the scope of this prototype research. These observations are, however, to show the operability and the performance of the studied prototype together with the potential for various future researches.

5. Conclusions

A prototype to evaluate the technological stack for the SYMORAIA-VHF open measurement platform was built and studied. The results show that the hardware is appropriate for the needs of the project and was able to acquire data stored in raw format. The prototype implementation for the online processing software that will evaluate key signal metrics for the received signals was also tested. Evaluated signal metrics provide the needed resolution to capture the natural fluctuations of the observed VOR stations. Following these results a full-scale working prototype will be built. Best locations to deploy the proposed measurement nodes will be evaluated with a scheduled in-situ survey over Bulgarian territory.

Acknowledgements

The authors thank Eng. Zlatislav Kolev and Eng. Simeon Shivachev for their valuable support, insights, and discussions throughout the project. In particular, Eng. Kolev contributed expertise in radio engineering, while Eng. Shivachev provided expertise in aviation, particularly VOR systems.

The presented activities and research are supported by Bulgarian Science Fund under grant KP-06-M94/1/10.12.2025 (SYMORAIA-VHF).

References

Doumounia, A., Gosset, M., Cazenave, F., Kacou, M., Zougmore, F. (2014). Rainfall monitoring based on microwave links from cellular telecommunication networks: First results from a West African test bed, *Geophysical Research Letters*, Vol. 41, No. 16, pp. 6016–6022, DOI: 10.1002/2014GL060724.

Dyrud, L., Wilson, D., Boerve, S., Trulsen, J., Pecseli, H., Close, S., Chen, C., Lee, Y. (2008). Plasma and electromagnetic wave simulations of meteors, *Advances in Space Research*, Vol. 42, No. 1, pp. 136–142, DOI: 10.1016/j.asr.2007.03.048.

Emeruwa, C. (2023). Analysis of some weather variables' impacts on UHF and VHF receivers in Yenagoa Southern, Nigeria, *World Journal of Advanced Research and Reviews*, Vol. 19, No. 2, pp. 675–681, DOI: 10.30574/wjarr.2023.19.2.1552.

K3DAV, D. (2010). *Build a Double Bazooka Antenna*, available at: https://www.kapstadt.de/DF1KW-ZS1AI/build-double-bazooka.pdf (accessed 1 August 2026).

Kákona, M., Kákona, J., Dvořák, R., Ambrožová, I., Velychko, O., Lužová, M., Šlegl, J., Sommer, M., Hanousek, V., Langer, R., Štefánik, S., Ploc, O. (2025). Measurements with angular sensitive electric field mill in thunderstorms, *Journal of Physics: Conference Series*, Vol. 2985, No. 1, Art. 012014, DOI: 10.1088/1742-6596/2985/1/012014.

Miś, T., Kazubski, W., Zieliński, M. (2025). Preliminary analysis of atmospheric front-related VHF propagation enhancements for navigation aids, *Sensors*, Vol. 25, No. 14, Art. 4455, DOI: 10.3390/s25144455.

Moriya, T., Mogi, T., Takada, M. (2010). Anomalous pre-seismic transmission of VHF-band radio waves resulting from large earthquakes, and its statistical relationship to magnitude of impending earthquakes, *Geophysical Journal International*, Vol. 180, No. 2, pp. 858–870, DOI: 10.1111/j.1365-246X.2009.04461.x.

Olasunkanmi, S.K., Bello, I. (2017). Effect of temperature and ground water on VHF radio wave propagation in tropical climate, *International Journal of Scientific and Engineering Research*, Vol. 8, No. 2, pp. 1391–1396.

Overeem, A., Leijnse, H., Uijlenhoet, R. (2013). Country-wide rainfall maps from cellular communication networks, *Proceedings of the National Academy of Sciences*, Vol. 110, No. 8, pp. 2741–2745, DOI: 10.1073/pnas.1217961110.

Prabakaran (2026). *Building a Double Bazooka Antenna for HF and VHF Ham Bands*, available at: https://vu3dxr.in/building-a-double-bazooka-antenna-for-hf-and-vhf-ham-bands/ (accessed 1 August 2026).

Super Avionics (2023). *Understanding the Impact of Solar Activity on VHF Nav Com Communications*, available at: https://superavionics.com/article/understanding-the-impact-of-solar-activity-on-vhf-nav-com-communications/ (accessed 22 July 2026).

Whysall, C. (W8TV) (1968). The double-bazooka antenna, *QST*, Vol. 52, No. 7, pp. 40–41.

DOI: 10.31401/WS.2026.proc.23

Ground-Based Monitoring of Global Solar Radiation and Ultraviolet Irradiance at NAO Rozhen

Minev M., Petrov N., Tsvetkov Ts.

Institute of Astronomy and National Astronomical Observatory, Bulgarian Academy of Sciences, Sofia, Bulgaria
mminev@nao-rozhen.org

Abstract

In this paper we present first results from continuous ground-based monitoring of global solar radiation and ultraviolet irradiance in the UVA and UVB spectral ranges, based on measurements performed with Kipp & Zonen instrumentation at Rozhen National Astronomical Observatory of the Bulgarian Academy of Sciences. The observations of global solar radiation cover a period of two and a half years, while systematic UV measurements have been conducted for nearly one year. The analysis focuses on the seasonal variability of the radiation fluxes, as well as on evaluation the influence of atmospheric conditions on the recorded values. Comparisons between global radiation and its UVA and UVB components are presented in order to identify correlations and characteristic relationships related to atmospheric transparency and cloud cover. The results reveal a well-defined seasonal variability and highlight the importance of long-term observations for a reliable assessment of the radiation balance. The study contributes to a better understanding of local radiative characteristics and has potential applications in atmospheric physics, environmental studies, and UV exposure assessment.

Keywords: Global Solar Radiation, UV irradiance, Ground-Based Monitoring

1. Introduction

Solar radiation is the primary source of energy for the Earth and plays a fundamental role in determining the surface energy balance and, consequently, in a wide range of atmospheric, climatic, and environmental processes. Variations in the amount of solar radiation reaching the Earth's surface can affect surface temperature, evaporation, the hydrological cycle, snow and ice melt, photosynthetic activity, and the potential for solar energy production [Wild, 2009]. Long-term observations have also demonstrated significant variations in surface solar radiation on decadal timescales, commonly discussed in terms of periods of global dimming and brightening [Wild et al., 2005; Wild, 2009]. These variations emphasize the importance of continuous and reliable measurements of surface solar irradiance.

The amount of solar radiation received at the Earth's surface is determined by both astronomical and atmospheric factors. Solar geometry, and particularly the solar zenith angle, controls the incoming radiation at the top of the atmosphere and its optical path through the atmosphere. At the same time, clouds, aerosols, water vapor, and other atmospheric constituents modify the radiation through absorption and scattering processes. Continuous ground-based observations are therefore important for investigating temporal variations in the surface radiation environment and their relationship with atmospheric conditions.

According to International Organization for Standartization (ISO 9488:2022 - https://www.iso.org/standard/74269.html), global solar irradiance, defined as the total shortwave solar irradiance incident on a horizontal surface, consists of direct solar radiation projected onto that surface and diffuse radiation originating from the sky. Reliable measurements of these radiation components are an important element of surface radiation

monitoring. The need for accurate and long-term observations led to the establishment of the Baseline Surface Radiation Network (BSRN), which provides high-quality ground-based radiation measurements from stations distributed over a wide range of geographical and climatic environments [Ohmura et al., 1998; Driemel et al., 2018]. Such measurements are used in climate research and provide reference observations for the evaluation of radiation products obtained from other observational and modelling approaches.

Ultraviolet (UV) radiation represents a relatively small fraction of the global solar radiation reaching the Earth's surface but is particularly important because of its biological effects. Surface UV irradiance exhibits substantial temporal and spatial variability. Solar zenith angle and stratospheric ozone are among the principal factors determining UV irradiance, while clouds, aerosols, surface reflectivity, and changes in atmospheric composition can further modify the amount of UV radiation reaching the ground [Bais et al., 2015]. These effects are wavelength-dependent and are particularly important at shorter UV wavelengths [Bernhard et al., 2023].

Cloudiness represents one of the major sources of short-term variability in surface UV radiation. Depending on cloud optical properties, cloud fraction, spatial distribution, and the relative position of the Sun and clouds, UV irradiance at the surface may be substantially attenuated and, under particular conditions, may also be locally enhanced [Calbó et al., 2005]. Aerosols constitute another important factor affecting UV transmission through the atmosphere, while changes in stratospheric ozone have a particularly strong effect on the UV-B part of the spectrum [Bais et al., 2015]. Continuous UV measurements can therefore provide valuable information about the temporal variability of the surface radiation environment and its response to changing atmospheric conditions. When observations are extended over months and years, they provide information on seasonal variability and allow the construction of local radiation climatologies. Long and homogeneous observational records are particularly valuable for detecting changes in surface radiation and for distinguishing persistent variations from short-term atmospheric fluctuations [Wild, 2009; Driemel et al., 2018].

Satellite observations provide an important means of estimating solar and UV radiation over large geographical areas and have enabled the development of regional and global radiation datasets. Nevertheless, ground-based observations remain essential because they provide direct measurements at specific locations and can achieve high temporal resolution under continuously changing atmospheric conditions. High-quality surface observations are also required for the validation and assessment of satellite-derived radiation products [Driemel et al., 2018].

The present study describes the ground-based instrumentation used for monitoring global solar radiation and UV irradiance at the National Astronomical Observatory (NAO) Rozhen, located in the Rhodope Mountains in Bulgaria, and presents an analysis of measurements obtained during more than one year of operation. Particular attention is given to the technical characteristics of the installed instruments, their measurement ranges and data acquisition procedures, as well as to the temporal behaviour of the recorded irradiance. The observations are analysed to characterize daily and seasonal variations in global solar and UV radiation and to assess the capabilities of the installed instrumentation for continued radiation monitoring at the observatory.

2. Ground-based station at Rozhen NAO

Following the commissioning of the new 1.5-m robotic telescope at NAO Rozhen in 2023, a new ground-based meteorological station was established to support astronomical observations. A dedicated mast was installed at the observatory site (41°41′48″ N, 24°44′18″ E; altitude 1730 m), on which most of the meteorological instruments are mounted. One of the

primary purposes of the new instrumentation is to continuously monitor the meteorological conditions during astronomical observations, thereby helping to ensure the safety of the equipment and the quality of the acquired images. Also the long-term collection of meteorological data is of particular scientific importance, as it will provide a valuable statistical dataset for a detailed characterization of the local climate and the specific meteorological conditions at the observatory site. In addition to the standard meteorological instrumentation, sensors for global solar radiation and ultraviolet (UV) radiation have been installed on the mast. Their purpose extends beyond the routine collection of daytime solar radiation and sunshine data. Measurements of solar radiation may be directly or indirectly related to processes associated with solar–terrestrial interactions and can therefore complement other studies conducted at the observatory in this field. These include optical observations of solar activity in Hα, Ca II, and visible light, neutron monitoring, observations of geomagnetic disturbances, and muon monitoring, for which a dedicated detector is planned.

2.1. Weather Monitoring

For continuous monitoring of the meteorological conditions, an automated Davis Vantage Pro2 weather station is used. The system measures ambient air temperature, relative humidity, dew-point temperature, wind speed and direction, and atmospheric pressure. The station is also equipped with an additional module for measuring global solar radiation and determining the UV index. However, a comparison of these measurements with those obtained from the dedicated solar-radiation sensors has not yet been performed and will be addressed in future work. Although the sensors integrated into the Davis station have comparatively lower accuracy, greater response times, and lower long-term stability than dedicated scientific-grade instruments, the system provides a valuable continuous meteorological record due to its autonomous operation. The station is powered by a solar panel and battery system, allowing it to operate for at least six months without an external power supply. In the event of an internet connection failure, the acquired data are stored locally and can be transferred once the connection is restored. This feature is particularly important during the severe winter months, when the observatory may occasionally experience prolonged power outages, potentially lasting long enough to exhaust the available UPS systems.

For more precise measurements of air temperature and relative and absolute humidity, an OTT TRH Temperature and Humidity Sensor is used. The technical specifications of the sensor are available from the manufacturer's documentation. In addition, we have a Cloud Watcher to measure cloudiness in the vicinity of the zenith and an all-sky camera, the data from which is to be implemented in future work.

2.2. Solar Radiation Monitoring

Solar radiation is monitored using instrumentation manufactured by Kipp & Zonen, a leading company specializing in precision solar-radiation and atmospheric measurements. Their Class A pyranometers are widely used as reference instruments and are designed to provide high stability over long-term operation. At NAO Rozhen, SMP12 and SMP22 pyranometers are used for monitoring global solar radiation. The high-quality construction of the instrument domes, together with their integrated heating systems, minimizes the effects of condensation and icing and thus helps maintain the accuracy and reliability of the measurements under the harsh environmental conditions at the observatory site.

The ultraviolet radiation reaching the Earth's surface is conventionally divided into three spectral ranges: UVA (315-400nm), UVB(280-315nm), and UVC(100-280nm) [Mondal & Ghosh, 2019]. UVC represents the shortest-wavelength component of UV radiation, but only a very small fraction reaches the Earth's surface, making its detection at ground level particularly challenging. In contrast, UVA and UVB radiation can be measured reliably using ground-based

sensors. For this purpose, Kipp & Zonen SUV-A and SUV-B UV radiometers are used at NAO Rozhen. The main technical specifications of the instruments employed in the monitoring system are summarized in Table 1.

Table 1. *Technical specifications of the Kipp & Zonen radiometers at Rozhen Observatory.*

Sensor	Global Solar Radiation	UV-A	UV-B
Spectral Range	280 to 3000 nm	315 to 400nm	280 to 315 nm
Maximum Irradiance	2000 W/m²	90 W/m²	9 W/m²
Operating Temperature	-40 to 70 ⁰C	-40 to 70 ⁰C	-40 to 70 ⁰C
Operating Humidity	0 to 100%	0 to 100%	0 to 100%
Field of View	180⁰	180⁰	180⁰
Response Time	0.5 s	0.2 s	0.2s
Non-Linearity	< ±0.2%	± 1%	± 1%
Temperature Response	< ±1%	± 1%	± 1%

3. Processing and Analysis of Solar Radiation Data

The Kipp & Zonen solar-radiation sensors allow measurements to be acquired at one-minute intervals, resulting in a continuous time series of measurements. To facilitate data processing and avoid handling excessively large tables of numerical values, we developed a dedicated script that automatically separates the measurements into individual daily files. Thus, each day is represented by a separate file containing up to 1440 one-minute measurements. As a subsequent processing step, the script removes measurements with values below 1% of the maximum irradiance that can be detected by the respective sensor. These low values generally correspond to noise measurements obtained during the nighttime period. As a result, the raw data containing a large number of measurements are converted into daily files containing only the detected solar irradiance from sunrise to sunset. This representation also allows the duration of daylight to be determined directly from the data. The data are stored in a three-column format containing the time, date, and measured irradiance, (i.e. HHMMSS DDMMYY signal). This simple format allows the files to be readily processed using other text-based data-analysis platforms and software packages, including Python, GNUplot, MATLAB, and others.

At present, an online platform has been developed for visualization of measurements acquired during the previous several days, as well as for downloading the corresponding raw data files. The platform is available at: https://meter.ac/gs/meteo/M26/history.html. Although the web-based visualization is convenient for a quick inspection of the measurements, it is not particularly suitable for more detailed data analysis. Therefore, we developed a dedicated application using the Visual Basic platform for visualization and analysis of the daily data files. In addition to data visualization, the application displays the maximum solar irradiance measured during each day and provides the possibility of fitting a Gaussian function to the daily irradiance profile. The coefficient of determination, (R^2), is calculated for each fit as a quantitative measure of the quality of the fit (Figure 1 - top). The software can process multiple daily data files either manually, by selecting individual dates of interest, or automatically. In the automated mode, a log file is generated containing, for each analyzed day, the date, duration of daylight, time and value of the maximum measured irradiance, and the corresponding (R^2) value of the Gaussian fit. The (R^2) parameter is used as the primary indicator of the quality of the measurements for a given day and provides an initial assessment of whether the solar-irradiance profile was affected by passing clouds. However, a low (R^2) value does not necessarily imply that the entire dataset for a given day is unsuitable for analysis. For example, a temporary interruption of the internet connection or a short period of cloud coverage may affect only a small fraction of the measurements while leaving the majority of the daily dataset

unaffected. In such cases, a scientifically meaningful analysis may still be possible despite a relatively low overall (R^2) value. To account for this limitation, the application provides an automatic classification of the analyzed days according to their (R^2) values into five categories: very bad, bad, good, very good, and excellent. The data assigned to the last three categories, which are intended for subsequent analysis, should nevertheless be visually inspected individually in order to confirm their reliability and identify possible short-duration disturbances that may not be adequately characterized by the (R^2) parameter alone.

The software has already been extended to support the visualization of measurements in different spectral ranges, including global solar irradiance, UV-A, and UV-B radiation, as well as the integration of data from the Cloud Watcher and OTT TRH sensors for cloud conditions, humidity, and temperature (Figure 1 - bottom). Further development is currently focused on optimizing the software and implementing direct comparisons between the different spectral ranges, as well as investigating their relationships with the local meteorological conditions.

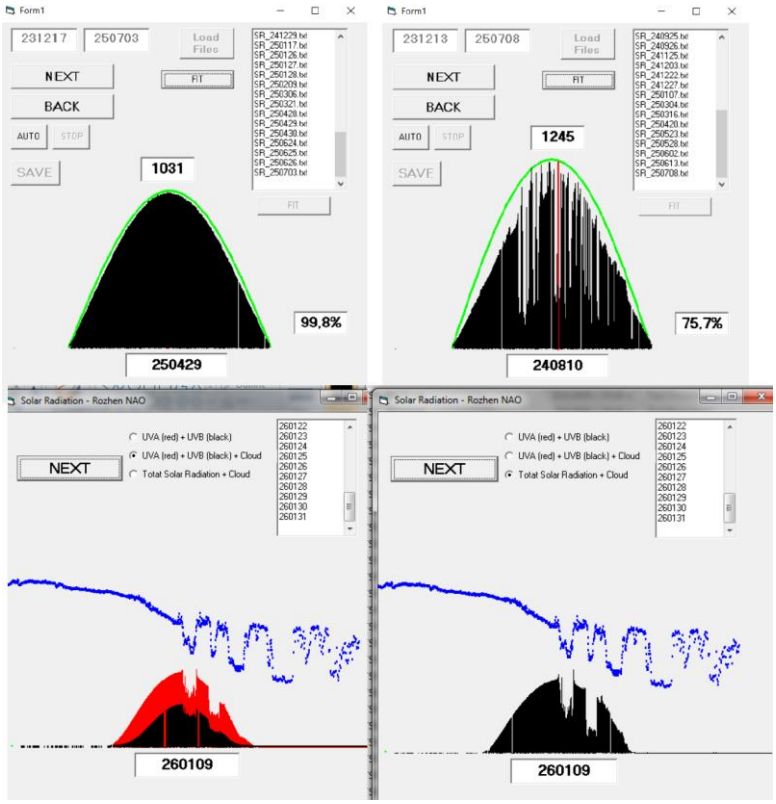


Figure 1. *Screenshots from our developed software for visualization of daily files with solar irradiance measurements. Top: global solar radiation with Gaussian fit, maximum solar irradiance and coefficient of determination (R^2). Bottom: comparisons between different spectral ranges of solar irradiance and cloud cover.*

4. First Results from Solar Radiation Monitoring

Measurements of global solar irradiance at NAO Rozhen started at the end of 2023, while the UV sensors have been operational since mid-2025. In this section, we present the first results obtained from the monitoring system to date.

4.1. Global Solar Radiation

From mid-December 2023 to May 2026, the global solar irradiance dataset contains measurements from 749 days. This number is lower than the total number of calendar days in the corresponding period because, during the initial stage of operation, additional time was

required to fully establish and optimize the radiation-monitoring system. Some data were also lost due to internet connectivity failures, server-related problems, power interruptions, and other technical issues. These problems have subsequently been resolved, and the monitoring system is now capable of continuous operation without significant data loss. Based on the measurements obtained so far, approximately 25% of the analyzed days were characterized by predominantly clear skies or only short-duration cloud passages that did not significantly affect the determination of the daily maximum solar irradiance (R^2 > 90%). Days characterized by significant cloud coverage (R^2 < 50%) account for approximately 20% of the dataset, while days with persistent and dense cloud coverage (R^2 < 25%) represent approximately 10%. The distribution of the number of days as a function of the R^2 value obtained from the Gaussian fit to the global solar irradiance data is presented in Figure 2.

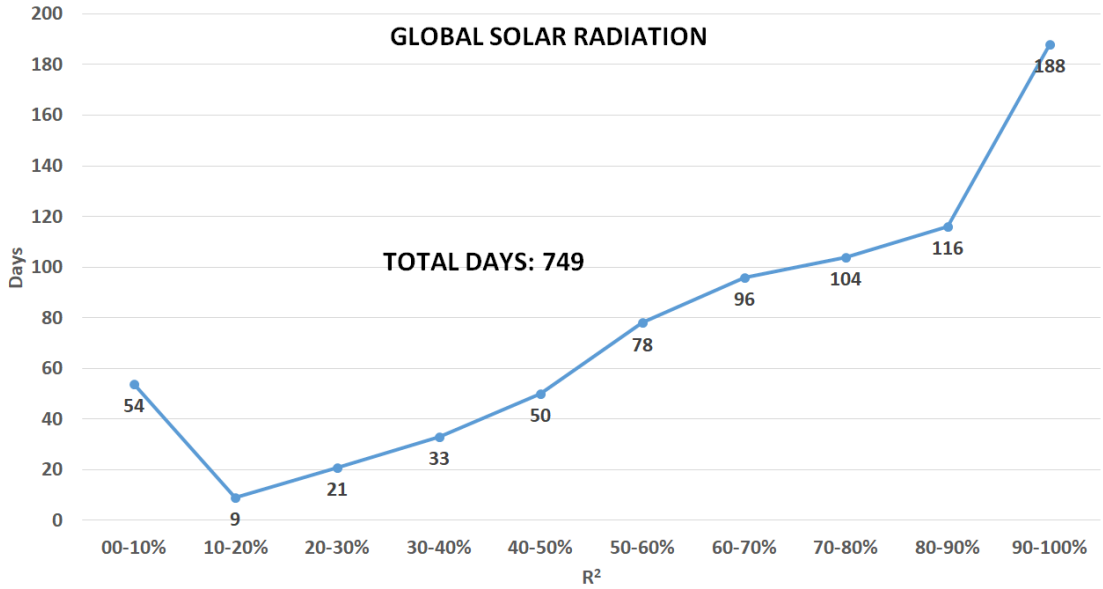


Figure 2. *The distribution of the number of days as a function of the R^2 value obtained from the Gaussian fit to the global solar irradiance data.*

For days with sufficiently high-quality measurements, for which the daily maximum solar irradiance can be reliably determined, an annual variation curve can be constructed for the specific location of NAO Rozhen (Figure 3). The data collected so far clearly reveal the seasonal variation, with the two summer maxima in 2024 and 2025 and the corresponding winter minima being readily distinguishable. At the winter minimum in 2025, a decrease in the measured global solar irradiance of approximately 5% compared with the corresponding minimum in 2024 can be observed. However, the current dataset is not yet sufficiently long to support robust statistical conclusions regarding such year-to-year variations. A more comprehensive analysis will become possible as additional measurements are accumulated over the coming years. In particular, future studies will investigate possible relationships between the observed solar irradiance and solar activity and the solar cycle, as well as possible correlations with local meteorological conditions. An illustrative example of full-day measurements of global solar irradiance during different months of the year is presented in Figure 4.

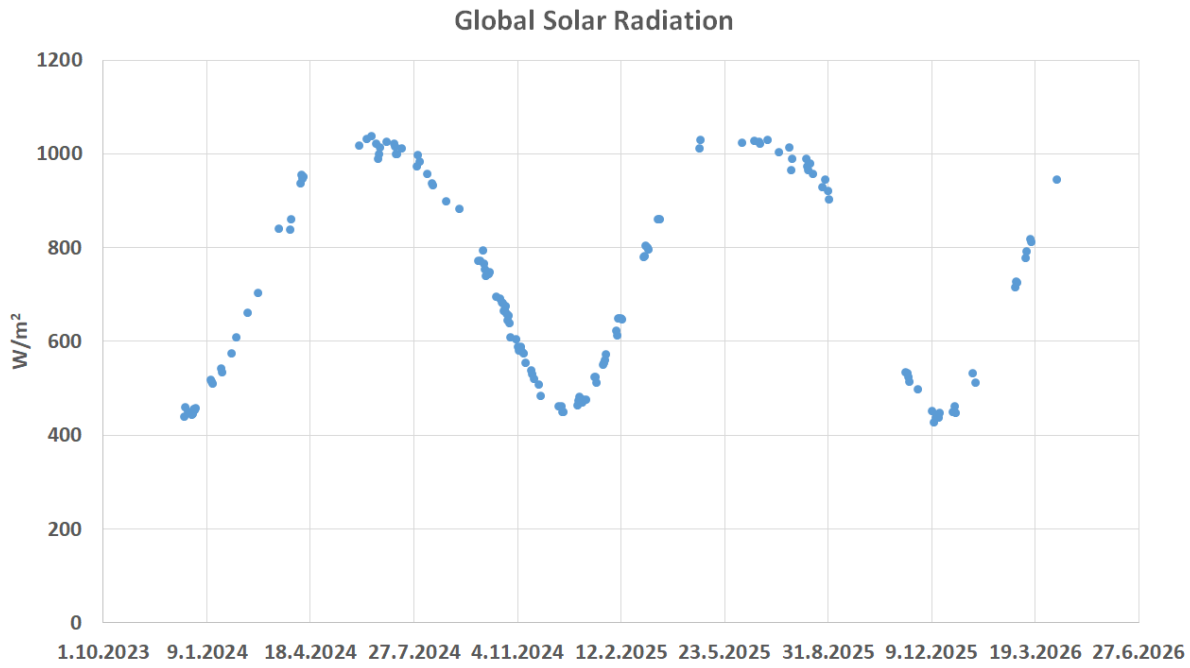


Figure 3. *An annual variation of daily maximum global solar irradiance from NAO Rozhen site from December 2023 to May 2026.*

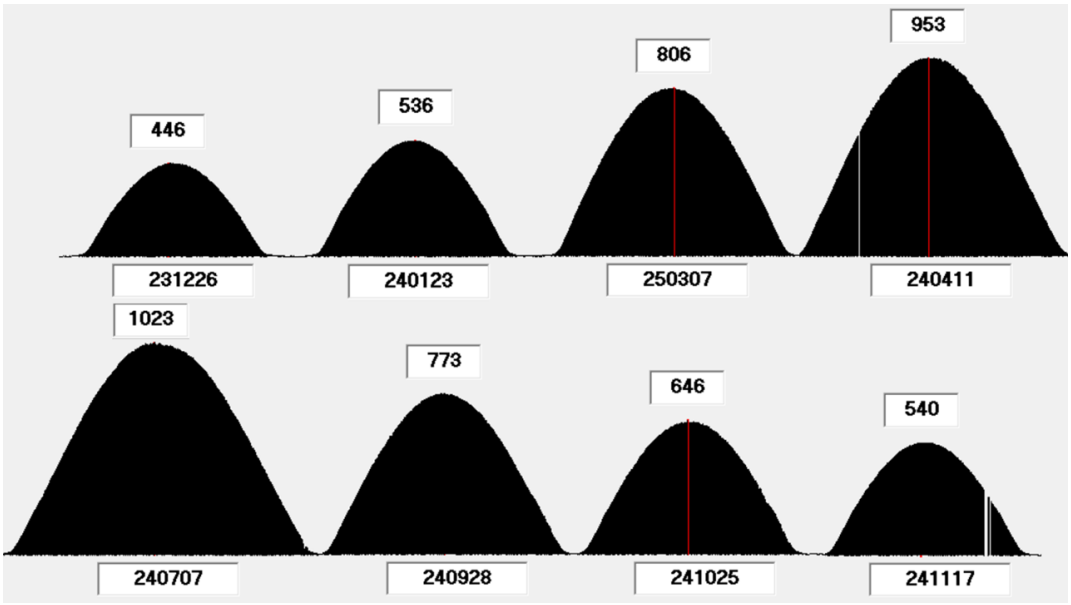


Figure 4. *An illustrative example of full-day measurements of global solar irradiance during different months of the year.*

Since the measured solar irradiance may be affected by atmospheric scattering and absorption associated with water vapor, we investigated whether the maximum daily irradiance shows a measurable dependence on relative humidity [e.g. Swartman & Ogunlade, 1967 and Kirmani et al., 2015]. For this purpose, we selected a period comprising a sequence of relatively close consecutive days, from 18 October to 11 November 2024, for which a sufficient number of measurements was available and during which relative humidity covered a comparatively broad range of values. Over this period, we assumed a linear daily decrease in the solar irradiance. After applying the fitted model, the individual deviations (residuals) were calculated for each measurement point. The subsequent analysis was aimed at determining whether these

residuals were consistent with random variations or whether they exhibited a systematic dependence on an external parameter as relative humidity. The correlation between the regression residuals and the varying relative humidity was examined, allowing the influence of humidity on the measured solar irradiance to be quantitatively assessed. The residual plot shows a clear correlation with the relative humidity level, indicating that atmospheric humidity acts as a systematic factor affecting the measured global solar irradiance and producing deviations from the idealized linear model (Figure 5.). Within the investigated range, the relationship can be approximated by a linear dependence, described by the following equation:

$$-0.0951\text{Hum} + 3.3831 = \alpha, \quad (1)$$

However, this result is currently limited to the relative humidity range of approximately 20–60%, and extrapolation beyond this range, particularly toward substantially higher humidity values, may not be justified. The resulting correction to the measured irradiance is of the order of ±2%. A comparison between the measured solar irradiance before and after applying the humidity correction is presented in Figure 6. It should be emphasized that the humidity correction presented here is preliminary and is based on a relatively limited observational interval. A longer time series, covering a broader range of atmospheric conditions and seasons, will be required to establish the robustness of this relationship and to determine whether the observed dependence can be reliably incorporated into the standard data-reduction procedure.

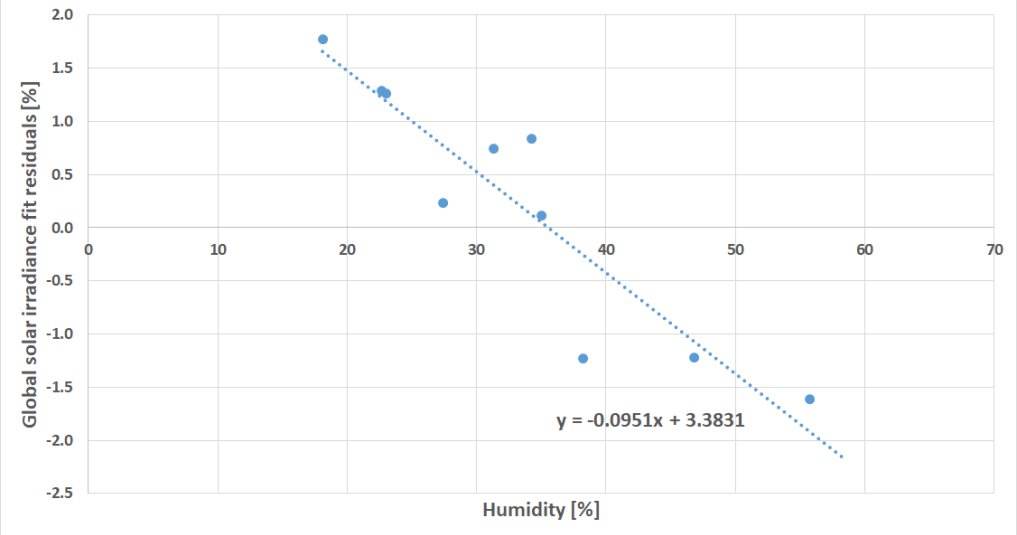


Figure 5. *The correlation between the measured global solar irradiance regression residuals and the varying relative humidity. The residual plot shows a clear correlation with the relative humidity level.*

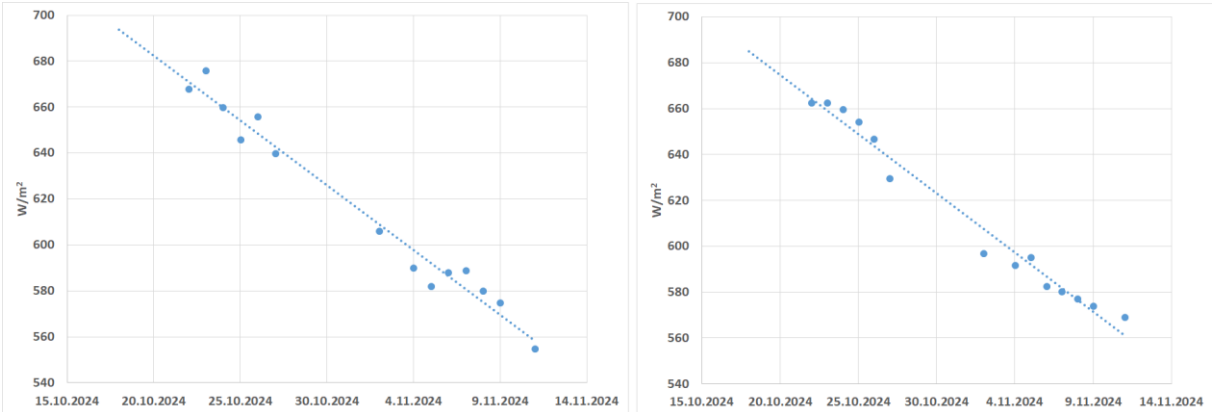


Figure 6. *A comparison between the measured solar irradiance before (left) and after (right) applying the humidity correction coefficient α.*

4.2. UV Irradiance

The measurements obtained from the UV sensors currently cover approximately one year, with continuous operation having started in mid-July 2025. The maximum daily values of UVA and UVB irradiance are presented in Figure 7, where a pronounced seasonal variation, including clear winter minima, can be observed. Figure 8 presents a comparison between the UV irradiance and global solar irradiance, with both quantities normalized to their respective minimum values. The preliminary data collected so far indicate differences in the number of apparently clear days identified from the UV measurements compared with those identified from the global solar irradiance data. One possible explanation for this behavior is the wavelength-dependent response of atmospheric scattering and absorption, as well as the influence of clouds and other atmospheric constituents on different parts of the electromagnetic spectrum. Consequently, atmospheric conditions that produce a relatively weak effect on the global solar irradiance may have a more pronounced effect in the UV range, or vice versa. Differences between the daily profiles of UVA and UVB irradiance are also observed on some days (Figure 9). These differences may provide additional information about the wavelength-dependent effects of atmospheric absorption and scattering and, potentially, about changes in atmospheric conditions during the day. The results presented here are preliminary, as the available UV dataset covers only approximately one year. A significantly longer observational baseline will be required to establish the statistical significance of the observed differences, investigate their seasonal dependence, and determine the relative contributions of cloud cover, atmospheric humidity, aerosol loading, solar elevation, and other atmospheric parameters. The simultaneous measurements of UVA, UVB, and global solar irradiance, combined with the meteorological data collected at NAO Rozhen, provide a basis for a more detailed investigation of these effects as the observational dataset continues to grow.

5. Conclusions

A comprehensive ground-based monitoring system for meteorological conditions and solar radiation has been established at the National Astronomical Observatory (NAO) Rozhen in support of astronomical observations and long-term environmental studies. The system combines automated meteorological measurements with dedicated observations of global solar irradiance and ultraviolet radiation, providing a continuous dataset for the characterization of atmospheric conditions at the observatory site.

Global solar irradiance measurements have been available since the end of 2023, while the UVA and UVB measurements commenced in July 2025. The analysis of the available global solar irradiance data already reveals a clear seasonal variation, with pronounced summer maxima and winter minima. The analysis of the available measurements also indicates that atmospheric humidity may introduce a systematic effect into the measured global solar irradiance. Within the investigated relative humidity range of 20–60%, the observed dependence can be approximated by a linear relation, with a corresponding correction of approximately ±2%. The first year-long series of UVA and UVB measurements shows pronounced seasonal variability, including distinct winter minima. Differences between the temporal profiles of UVA and UVB radiation are also observed on individual days. These preliminary results suggest that the simultaneous monitoring of different spectral components of solar radiation may provide additional information about wavelength-dependent atmospheric effects, including the influence of clouds, water vapour, aerosols, and other atmospheric constituents.

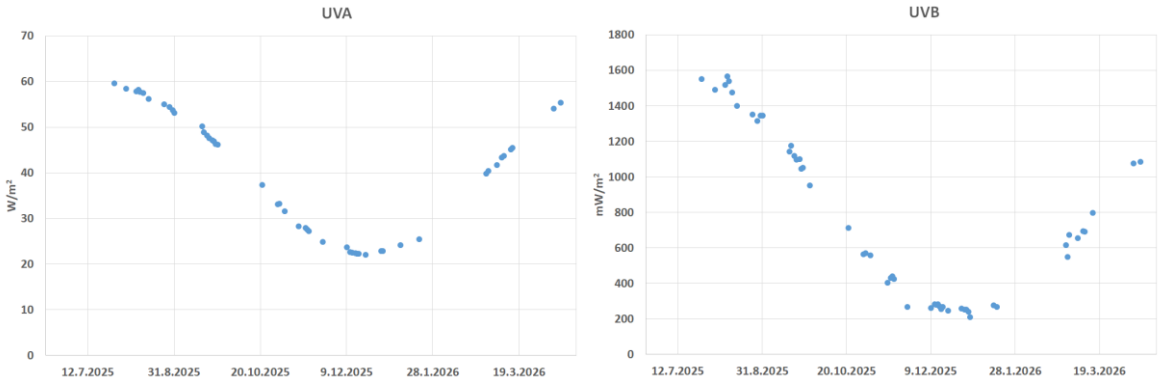


Figure 7. *The maximum daily measured values of UVA (left) and UVB (right) irradiance.*

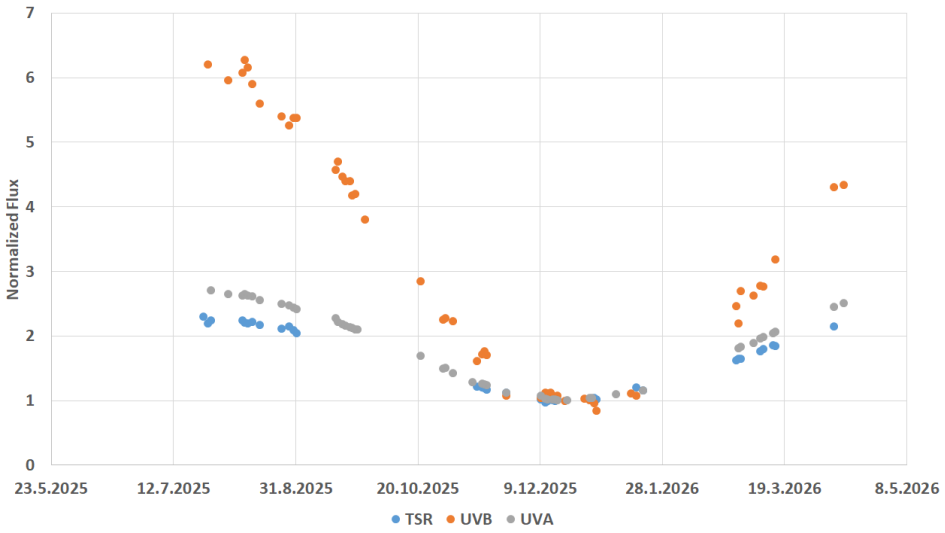


Figure 8. *A comparison between the UV irradiance and global solar irradiance, with both quantities normalized to their respective minimum values.*

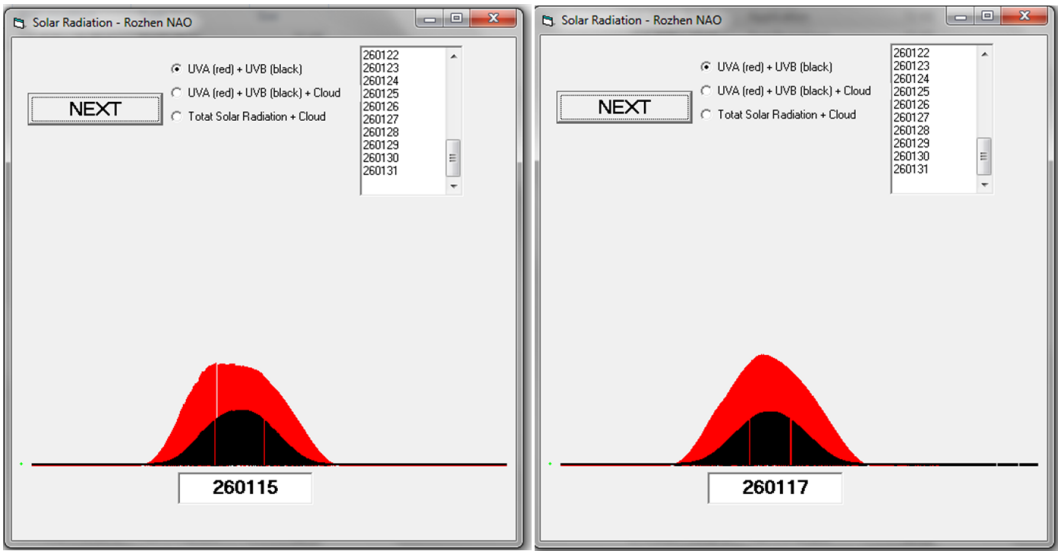


Figure 9. *Differences between the daily profiles of UVA and UVB irradiance observed on 15th and 17th January 2026.*

The monitoring system and the datasets accumulated so far provide a foundation for several directions of future research. With the continuation of the observations, it will be possible to

investigate in greater detail the seasonal and interannual variability of solar irradiance, its relationship with solar activity and the solar cycle, and its dependence on local meteorological conditions. The simultaneous measurements in different spectral ranges will also allow a more detailed investigation of the atmospheric transmission of solar radiation and the relative effects of cloud cover, humidity, aerosols, and other atmospheric parameters. The combination of long-term meteorological observations, global solar irradiance measurements, and UVA and UVB monitoring represents a valuable extension of the observational capabilities of NAO Rozhen. This ground-based system provides a continuously growing scientific dataset that can contribute to the study of local atmospheric conditions and solar–terrestrial interactions. The continued operation and further development of the monitoring network will therefore provide both practical benefits for astronomical observations and new opportunities for interdisciplinary research in atmospheric and solar–terrestrial physics.

Acknowledgements

The research that led to these results was partially carried out with the help of infrastructure purchased under the National Roadmap for Research Infrastructure, financially coordinated by the Ministry of Education and Science of Republic of Bulgaria.

References

Bais, A. F., McKenzie, R. L., Bernhard, G., Aucamp, P. J., Ilyas, M., Madronich, S., Tourpali, K. (2015). Ozone depletion and climate change: Impacts on UV radiation. *Photochemical & Photobiological Sciences*, Vol. 14, pp. 19–52. DOI: 10.1039/C4PP90032D.

Bernhard, G. H., Bais, A. F., Aucamp, P. J., Klekociuk, A. R., Liley, J. B., McKenzie, R. L. (2023). Stratospheric ozone, UV radiation, and climate interactions. *Photochemical & Photobiological Sciences*, Vol. 22, pp. 937–989. DOI: 10.1007/s43630-023-00371-y.

Calbó, J., Pagès, D., González, J.-A. (2005). Empirical studies of cloud effects on UV radiation: A review. *Reviews of Geophysics*, Vol. 43, RG2002. DOI: 10.1029/2004RG000155.

Driemel, A., Augustine, J., Behrens, K., Colle, S., Cox, C., Cuevas-Agulló, E., Denn, F. M., Duprat, T., Fukuda, M., Grobe, H., Haeffelin, M., Hodges, G., Hyett, N., Ijima, O., Kallis, A., Knap, W., Kustov, V., Long, C. N., Longenecker, D., Lupi, A., Maturilli, M., Mimouni, M., Ntsangwane, L., Ogihara, H., Olano, X., Olefs, M., Omori, M., Passamani, L., Pereira, E. B., Schmithüsen, H., Schumacher, S., Sieger, R., Tamlyn, J., Vogt, R., Vuilleumier, L., Xia, X., Ohmura, A., König-Langlo, G. (2018). Baseline Surface Radiation Network (BSRN): Structure and data description (1992–2017). *Earth System Science Data*, Vol. 10, pp. 1491–1501. DOI: 10.5194/essd-10-1491-2018.

Kirmani, S., Jamil, M., Rizwan, M. (2015). Empirical correlation of estimating global solar radiation using meteorological parameters. *International Journal of Sustainable Energy*, Vol. 34, No. 5, pp. 327–339.

Mondal, A., Ghosh, K. (2019). Studies on germicidal benefit of ultraviolet ray upon old paper documents. *Light & Engineering*, pp. 17–24. DOI: 10.33383/2018-024.

Ohmura, A., Dutton, E. G., Forgan, B., Fröhlich, C., Gilgen, H., Hegner, H., Heimo, A., König-Langlo, G., McArthur, B., Müller, G., Philipona, R., Pinker, R., Whitlock, C. H., Dehne, K., Wild, M. (1998). Baseline Surface Radiation Network (BSRN/WCRP): New precision radiometry for climate research. *Bulletin of the American Meteorological Society*, Vol. 79, pp. 2115–2136. DOI: 10.1175/1520-0477(1998)079<2115:BSRNBW>2.0.CO;2.

Swartman, R. K., Ogunlade, O. (1967). Solar radiation estimates from common parameters. *Solar Energy*, Vol. 11, Nos. 3–4, pp. 170–172.

Wild, M. (2009). Global dimming and brightening: A review. *Journal of Geophysical Research: Atmospheres*, Vol. 114, D00D16. DOI: 10.1029/2008JD011470.

Wild, M., Gilgen, H., Roesch, A., Ohmura, A., Long, C. N., Dutton, E. G., Forgan, B., Kallis, A., Russak, V., Tsvetkov, A. (2005). From dimming to brightening: Decadal changes in solar radiation at Earth's surface. *Science*, Vol. 308, pp. 847–850. DOI: 10.1126/science.1103215.

DOI: 10.31401/WS.2026.proc.24

Exploring the Impact of Solar Activity and Other Physical Events in the Troposphere and Stratosphere by Using Research Balloon with Autonomously Returning Unmanned Aerial Vehicle

Nikolov I.D.

Space Research and Technology Institute, Bulgarian Academy of Sciences
i.nikolov@space.bas.bg

Abstract

The Earth's atmosphere is divided into several layers in altitude, according to its density, composition, temperature and physical properties (Fig. 1). While the impact of cosmic rays and the solar wind on the layer closest to the Earth's surface - the troposphere - has been studied relatively well, using ground-based and remote instruments, the study of the high layers of the troposphere and stratosphere (up to 30 - 35 km) requires specific and expensive research methods, which leads to the availability of limited scientific data and knowledge about the processes occurring in these zones. Our knowledge and understanding of the processes in the upper atmosphere can be significantly expanded by using relatively affordable and reliable methods. One of these methods includes the use of a lighter-than-air aerostat (stratospheric balloon). It may use hydrogen or helium as a lifting gas and have attached scientific instruments in a gondola (Fig.2). The disadvantage of this method is that the precious scientific equipment is usually lost in the end, or is a subject of difficult and almost unpredictable recovery.

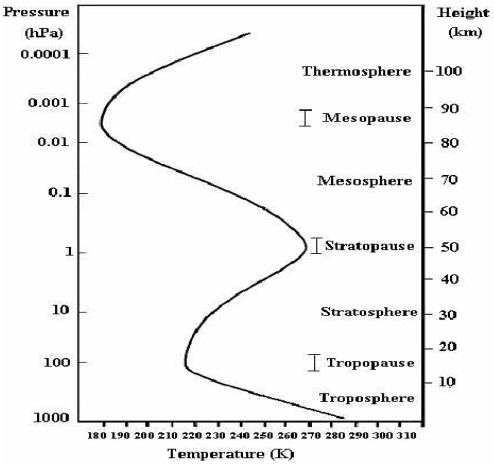


Figure 1



Figure 2

Keywords: UAV; Balloon; Autonomous

1. Introduction

Stratospheric balloons operate between 15 km and 45 km in altitude [Fernández-Soler et al., 2024; Wang et al., 2025]. Their dynamics involve a balance of vertical buoyancy, gravity, and horizontal aerodynamic drag (during rapid wind changes) [Wang et al., 2025; Loganathan et al., 2021]. The weight of the whole system can be described as $W=m_G g$, where g is the gravity acceleration, and m_G is the gross mass of the whole system (a sum of the payload mass and the balloon's material mass).The buoyancy force I, can be described mathematically

as $I=g(\rho_a-\rho_g)V$, where ρ_a is air density [kg·m^{-3}], ρ_g is lifting gas density [kg·m^{-3}] and V is the balloon volume. The volume V can be computed from the ideal gas equation: $V=\frac{m_g}{\rho_g}=m_g R_g \frac{T_g}{p_g}$, where where T_g, p_g and R_g, are the temperature, the pressure and the specific gas constant of the lifting gas, respectively. When the balloon acsends and the pressure of surrounding air decreases, the balloon's volume expands [Fernández-Soler et al., 2024]. When the buoyancy force becomes equal to the weight of the system, the balloon stops ascending and, depending on its construction, may behave in several different ways.

According to their construction and pressure management, stratospheric balloons are primarily divided into three main categories:

A. Zero-Pressure Balloons (ZPB):

The most common type. They feature an open-duct design at the bottom, allowing gas to vent out as the balloon expands during ascent. This passive venting ensures the internal pressure matches the ambient atmospheric pressure, preventing the envelope from rupturing. Because they lose lifting gas at night and must drop ballast to maintain altitude, they generally have short flight durations (a few days to a week).

B. Super-Pressure Balloons (SPB):

Constructed with strong, sealed, inelastic materials, these balloons maintain a fixed volume regardless of external pressure drops. As they rise, the lifting gas compresses, creating a higher pressure inside than outside. They are structurally shaped like a pumpkin to manage this tension. Because no gas is vented, they can maintain a near-constant float altitude for months.

C. Sounding Balloons:

Expendable balloons made of highly elastic materials like natural latex. They are closed systems that continuously expand as they rise until the stretching material eventually bursts. They are designed for quick, light-payload ascents and atmospheric data collection (e.g., carrying radiosondes) rather than prolonged hovering. We suggest using this type of vessel as most suitable for our goal, due to its simple construction and predictable flight time [Fernández-Soler et al., 2024; Wang et al., 2025].

2. Construction

A stratospheric balloon paired with a returnable UAV is an innovative system used to lift specialized instruments to the edge of space [Haghighi et al., 2024]. Once the balloon reaches maximum altitude and bursts, the unscrewed fixed wing glider detaches and autonomously navigates back to the launch site, safely protecting valuable payloads while avoiding unpredictable landing zones (Fig. 3). These hybrid systems are transforming near-space atmospheric research by addressing the recovery limitations of traditional weather balloons, which frequently land far from their launch points or are lost in rough terrain [Haghighi et al., 2024; NOAA Research, n.d.].

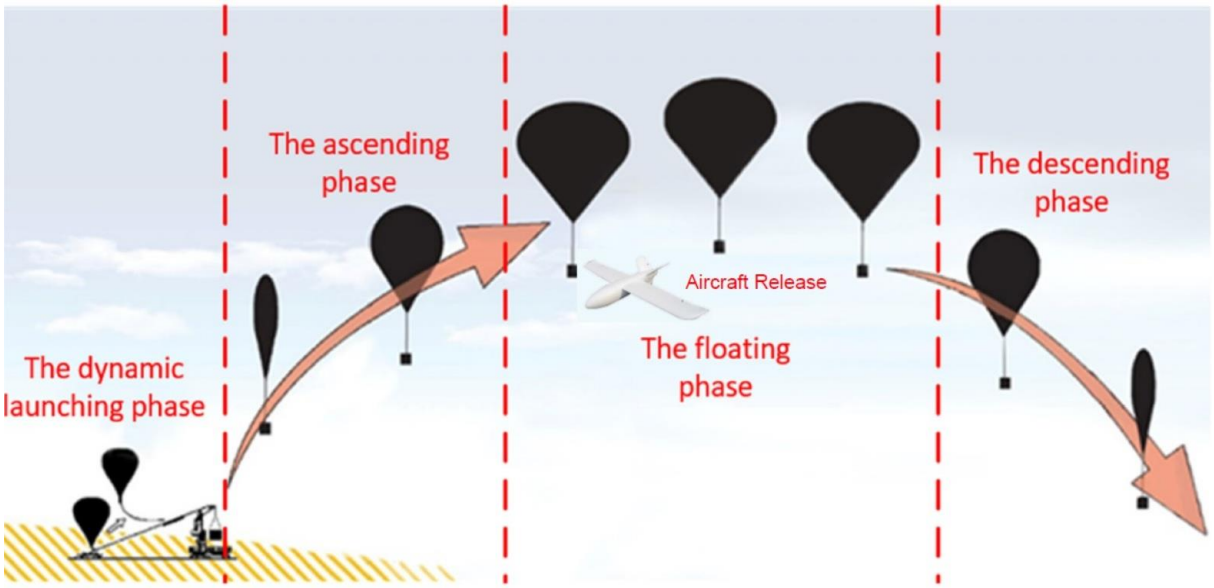


Figure 3

Only a few scientific organizations and aerospace companies in the world have developed successful balloon-launched glider vehicles. One example is the US HORUS (High-altitude Operational Return Unmanned System). Developed by scientists at NOAA's Global Monitoring Laboratory,this system hoists a small uncrewed glider to roughly 30000 m. (Fig. 4,5) [NOAA Research, n.d.].



Figure 4

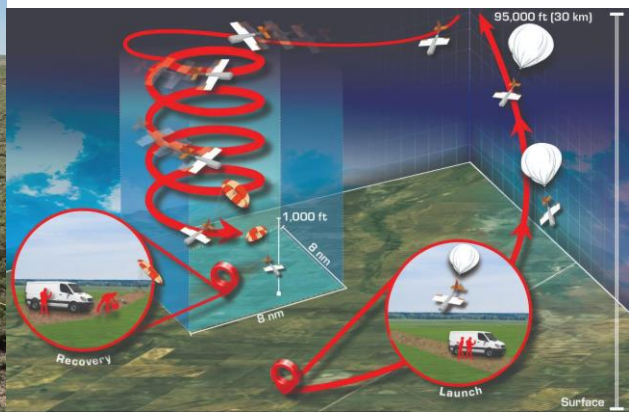


Figure 5

During the whole flight there will be a permanent two way WiFi telemetric, video and data radio link between the aircraft and the ground station. This will be achieved by the use of a high-gain parabolic antenna, driven by a precise tracking system, which will keep it pointed to the aircraft. A lower frequency telemetric connection will be available too. The aircraft itself will be controlled by an autopilot, which will hold the course back even in the case of lost radio connection [ArduPilot Development Team, n.d.]. We suggest using an Ardupilot (Pixhawk, PX4, Cube, etc.) project based system (Fig. 6,7) [ArduPilot Development Team, n.d.]. It is an open source, reliable system, which had been developed for many years. It is a very flexible platform, which allows to be programmed with different setups and a lot of adjustments, depending on the construction and the desired setup of the aircraft. Another

Ardupilot, loaded with specific firmware will be used as a controller for the antenna tracker. It will receive the UAV's coordinates in real time via telemetry and will point the ground antenna towards the aircraft during the flight [ArduPilot Development Team, n.d.]. The WiFi radio link will allow downloading live data from the onboard scientific equipment to a server on the ground.



Figure 6

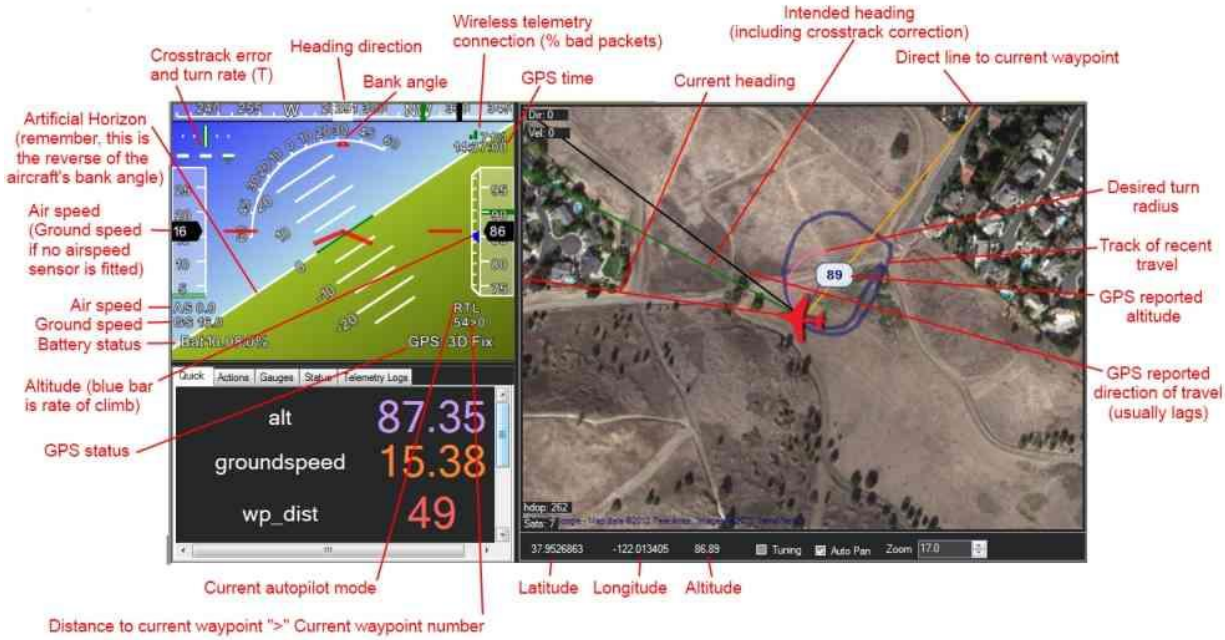


Figure 7

The aircraft itself, has to be equipped with all necessary sensors (airspeed, barometric altitude, GNSS/GPS, magnetic compass, etc.) and executive mechanisms, which will ensure smooth and reliable operation in the low temperatures and the harsh environment of the stratosphere. It will have a heating system, installed inside for the onboard electronics and batteries, as the temeperatures in the stratosphere drop below *220K*, as can be seen from Figure 1. The two-way telemetric radio link will allow the ground operator to receive data about aircraft's position, airspeed, altitude and other parameters. Also, it will allow them to send commands to the aircraft and it's systems. At the final stage of flight the operator may

take manual control to ensure safe and precise landing of the aircraft, which will be equipped with an electric motor and a small battery for the landing phase.

3. Conclusion

Scientists have been using stratospheric balloons for many years to explore the upper troposphere and stratosphere and reach the edge of space. In the 20th century several crewed missions showed the limitations of human abilities to work and survive at high altitudes, and helped scientists a lot in the understanding of the physical and biological processes in close-to-space conditions. They also helped them to advance in space engineering and technologies. These flights were important, but expensive and risky. Also, there were uncrewed missions with scientific equipment, which had limitations, because of the lack of control over the flight's direction and altitude and the almost inevitable loss of the equipment. Nowadays, the development of UAV technology, satellite navigation systems, the miniaturization of computers and all types of sensors and electronics, give us a new possibilities to explore the hostile environment of the stratosphere without risking human lives and losing expensive scientific equipment [Haghighi et al., 2024; NOAA Research, n.d.; ArduPilot Development Team, n.d.]. This gives us a good perspective to learn new information about the influence of solar activity over the stratosphere and therefore the whole Earth's ecosystem, as all processes inside it are connected.

References

Fernández-Soler, A., González-Bárcena, D., Torralbo, I., Pérez-Grande, I. (2024). Stratospheric balloon dynamics predictions for robust ascent phase payload thermal analysis. *Advances in Space Research*, Vol. 74, No. 7, pp. 3216–3233. DOI: 10.1016/j.asr.2024.07.028.

Wang, Z., Zhang, D., Qiao, T., Chen, C., Cheng, H. (2025). Influence of horizontal wind on high-altitude balloon system dynamics. *Advances in Space Research*, Vol. 75, No. 1, pp. 823–836. DOI: 10.1016/j.asr.2024.11.007.

Haghighi, A. N., Nolin, R. D., Pundsack, G. D., Craine, N., Stratsilatau, A., Bailey, S. C. C. (2024). High-altitude balloon-launched uncrewed aircraft system measurements of atmospheric turbulence and qualitative comparison with infrasound microphone response. *Atmospheric Measurement Techniques*, Vol. 17, pp. 4863–4889. DOI: 10.5194/amt-17-4863-2024.

Loganathan, J., Lim, K., Lee, H., Khoo, B. (2021). Computational fluid dynamics study of balloon system tethered to a Stratosail. *Journal of High Altitude Ballooning*, Vol. 1, No. 1. DOI: 10.31274/jhab.13037.

NOAA Research (n.d.). Revolutionary NOAA high-altitude research tool passes key milestone. Available at: https://research.noaa.gov/revolutionary-noaa-high-altitude-research-tool-passes-key-milestone/ (accessed 21 September 2026).

ArduPilot Development Team (n.d.). ArduPilot documentation. Available at: https://ardupilot.org/ardupilot/ (accessed 21 September 2026).

DOI: 10.31401/WS.2026.proc.25

Atmospheric Dosimetry

Nikolov N.D.

Space Research and Technology Institute, Bulgarian Academy of Sciences
ndnikolov@space.bas.bg

Abstract

This paper reviews atmospheric dosimetry. Atmospheric dosimetry measures radiation (cosmic rays and secondary particles) within the Earth's atmosphere.

Recently, the importance of atmospheric dosimetry is growing due to the rapid expansion of commercial aviation and space exploration.

Atmospheric dosimetry benefits from modern technologies, such as low-cost and reliable radiation detectors, often network- and Internet-connected and providing real time data. Lightweight, low-consumption and safe dosimeters are available to be placed onboard commercial aircraft, performing measurements for extended periods of time. Other techniques include automated high-altitude balloon probes and unmanned aerial vehicles.

There are also significant achievements in software development, with applications such as CARI, NAIRAS, EPCARD, PCAIRE, WASAVIES, which calculate the effective dose of cosmic radiation received by an individual on an aircraft, based on flight path, altitude, flight duration and solar activity.

Keywords: cosmic rays; dosimetry; air transportation; radiation detectors.

1. Introduction

The first atmospheric radiation measurements date back to the beginning of the XX century, when several researchers performed a series of risky manned balloon flights to altitudes of above 9000 metres [Walter, 2013]. The main scientific instrument used in these flights was *the bifilar electrometer* invented in 1909 by Theodor Wulf (Figure 1). The electrometer was capable of measuring the air (or another gas) ionization caused by ionizing radiation.

The Swiss physicist Albert Gockel measured the levels of ionizing radiation up to 3000 metres (4500 metres according to other sources) during a balloon flight in 1909. His measurements showed that ionization did not decrease with altitude as expected if the radiation originated entirely from the Earth.

In 1911-1912 the Austrian physicist Victor Hess performed seven balloon flights, reaching altitudes of above 5000 meters. Hess used a modified electroscope, hermetically sealed in order to function accurately under the reduced atmospheric pressure. During all flights the measured ionizing radiation increased rapidly with altitude. By flying at night and during the near-total solar eclipse on April 17, 1912 Hess ruled out the Sun as a significant source and concluded that the radiation originated in outer space, beyond the solar system.

Werner Kolhörster, a German physicist, performed four balloon flights in 1913–1914. On June 28, 1914 he reached an altitude of 9300 meters, measuring radiation ionization vastly greater than the one at ground level.

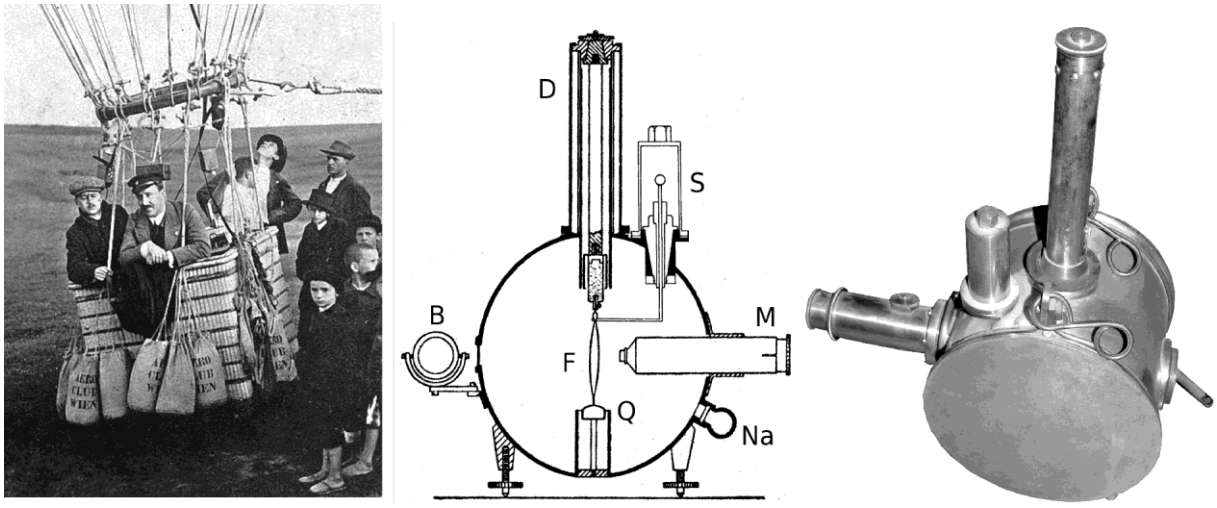


Figure 1. Left: *Victor Hess before one of his flights;* ***Centre and right:*** *The modified Wulf's bifilar electrometer, used by Hess. The lower end of metal filaments (F) is fixed to a quartz string (Q), using its elasticity as a repulsive force. The spread of the filaments is read with a microscope (M).*

Primary galactic cosmic rays consist mainly of high-energy atomic nuclei originating outside the Solar System. Most of them are protons (about 90%) and alpha particles (9%). The remaining 1% consists of various nuclei – carbon, oxygen, nitrogen, iron, etc., up to uranium [L'Annunziata, 2007]. The remaining primary component includes electrons and positrons, with smaller contributions from gamma rays and neutrinos.

Cascades of secondary particles are generated when high-energy primary cosmic rays collide with air molecules. A spray of short-lived, high-energy particles (like pions and kaons) is created. These new particles decay and interact with other atoms. Neutral pions decay mainly into gamma rays, which can produce electron-positron pairs and initiate an electromagnetic cascade, whereas charged pions decay predominantly into muons and neutrinos (Figure 2).

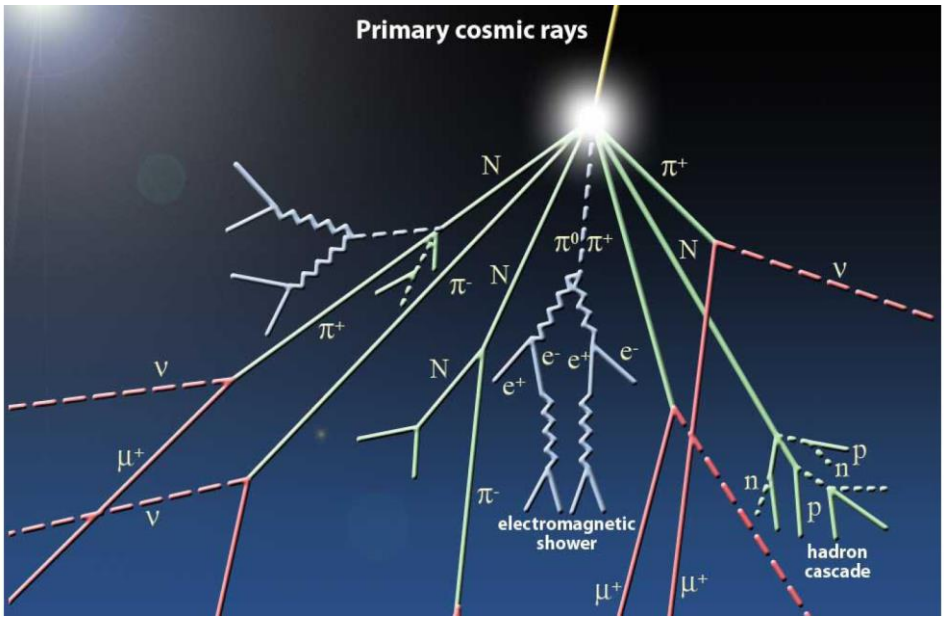


Figure 2. *Cosmic-ray showers*

The number of cascading particles multiplies exponentially until it hits the "shower maximum", when the average energy of the particles becomes too low to create new ones; afterward, the shower attenuates.

At around 20 km altitude, the creation of secondary radiation reaches its highest point before absorption and decay processes weaken it lower in the atmosphere. That peak in secondary cosmic ray intensity and atmospheric ionization is known as the *Regener–Pfotzer maximum*.

It is important to note that the Regener–Pfotzer maximum denotes a peak in ionization and raw absorbed dose. However, the biological dose equivalent behaves differently, continuing to rise at higher altitudes due to the increased number of heavy primary cosmic ray particles (Figure 3) [Hands et al., 2016].

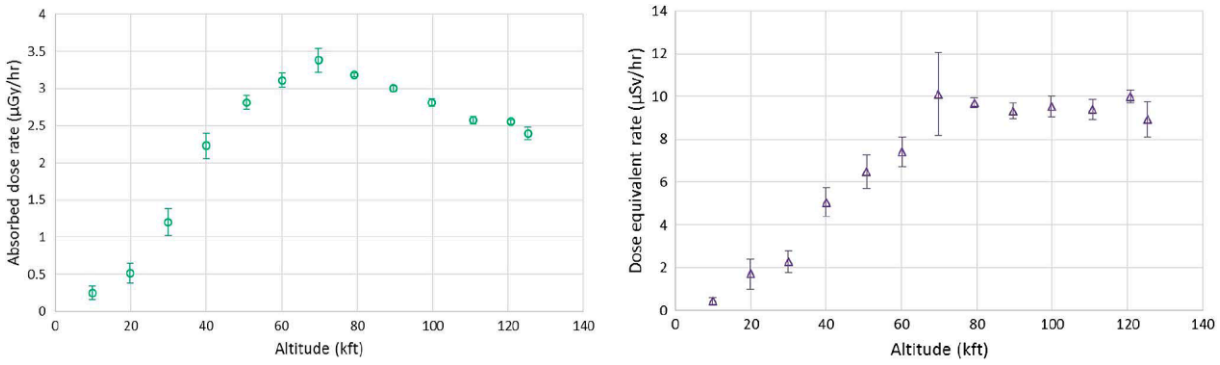


Figure 3. Left: *Absorbed dose rate (in silicon) as function of barometric altitude. The Pfotzer-Regener maximum is clearly visible.* ***Right:*** *Dose equivalent (in tissue) as a function of barometric altitude. Unlike the absorbed-dose profile, the Pfotzer-Regener maximum is no longer present in the dose-equivalent profile [Hands et al., 2016].*

2. Air travel and cosmic radiation

In the post-pandemic years global air travel is continuing to increase rapidly. According to the International Air Transport Association (IATA) in 2025 air traffic reached over 5 billion passengers worldwide [IATA, 2026a], with long-term forecasts expecting that number to more than double by 2050 [IATA, 2026b].

This leads to an increased number of persons exposed to cosmic radiation – especially pilots and cabin crew members, but also frequent travellers (encouraged by airline promotion programs), military pilots, space personnel and even the growing number of commercial "space tourists".

Thus, it's important to understand all aspects of the radiation risks involved with air travel.

The most significant parameters which determine the rate of radiation exposure during a flight are the flight altitude, its duration, latitude and the solar activity at the time. Some high energetic solar particle events may also cause increased radiation exposure, although limited to higher altitudes and relatively short time periods.

Most commercial airplanes fly at altitudes between 9 000 and 12 000 meters. At that altitude radiation rates average about 3–5 μSv per hour [Obodovskiy, 2019; CDC, n.d.]. The calculated average annual crew dose is 2–5 mSv [IAEA, n.d.]. For comparison: 2–3 mSv is the worldwide average annual radiation dose received by a person from all sources of radiation and 20 mSv is the annual dose limit for people who are occupationally exposed to radiation.

Although the stated crew annual doses seem relatively low, they are higher than, for example, average doses received from a typical nuclear power plant worker (1–2.5 mSv). In

fact, the U.S. National Council on Radiation Protection and Measurements reported that air crews have the largest average annual effective dose of all U.S. radiation-exposed workers.

There are also some specific cases where more caution is needed. For pregnant crew members FAA recommends a total exposure of 1 mSv for the time of pregnancy, with no monthly dose exceeding 0.5 mSv [FAA, n.d.].

Out of curiosity we can estimate the annual dose from cosmic radiation for the toughest air travellers, the members of the "100k miles club". At average speed of 800 km/h that distance corresponds to about 200 flight hours per year, which gives us an annual dose of 0.8 mSv – still significantly less than doses received from the crew members.

2.1. High-latitude routes

High-latitude routes cross regions where geomagnetic shielding is weaker than at lower latitudes. This can increase radiation exposure even when a route does not meet the stricter definition of a transpolar flight north of 78°N.

However, during such high-latitude flights aircrew members and passengers are exposed to significantly higher levels of cosmic radiation because of the weaker Earth's magnetic field shielding near the magnetic poles.

Figure 4 [Veillette, 2021; Frasch, 2014] represents total radiation dose per flight for two similar in duration routes. One route (Frankfurt to New York) is at higher geomagnetic latitudes, whereas the other (Frankfurt to Johannesburg) extends toward low geomagnetic latitudes. The data is collected from 22 almost simultaneous flights along both routes, covering a time period from January 2004 to July 2014.

As can be easily seen the total radiation dose on the higher-latitude route is substantially greater and varies from 50 μSv to 78 μSv. On the lower-latitude route the total dose averages close to 26 μSv, with very little variations.

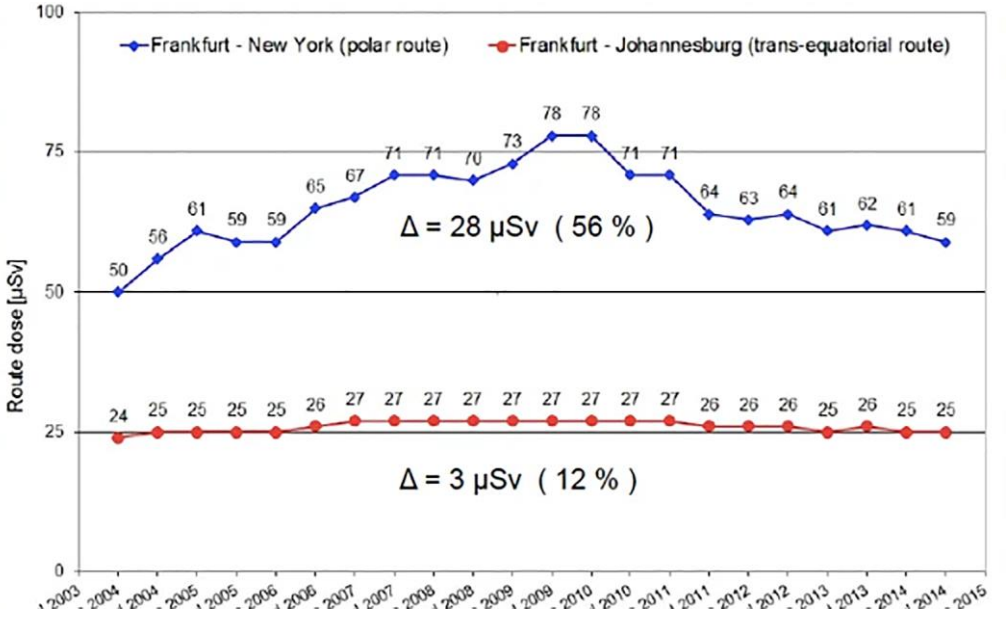


Figure 4. *Total radiation dose per flight for Frankfurt to New York and Frankfurt to Johannesburg routes. Data is collected from 22 simultaneous flights carried out from January 2004 to July 2014 [Frasch, 2014].*

It's important to note that the high-latitude flights are more "sensitive" to solar events involving increased levels of radiation. According to Mertens et al. [2010], data examined from polar flights during a solar storm in 2003 revealed that during a single flight passengers

received about 12% of the annual radiation limit recommended by the International Commission on Radiological Protection. The exposures were significantly greater than on typical flights at lower latitudes.

2.2. The South Atlantic Anomaly

The South Atlantic Anomaly (SAA) is a geographical region over the South Atlantic Ocean where the inner Van Allen radiation belt extends down particularly close to Earth. This leads to highly increased levels of ionizing radiation on Low Earth Orbits (Figure 5) [13].

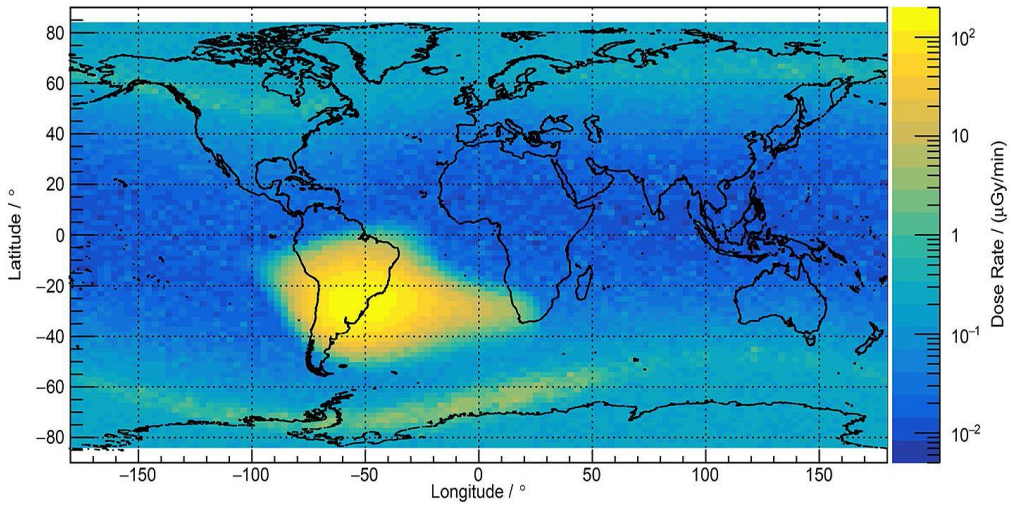


Figure 5. *Absorbed dose rate (µGy/min) in silicon at 600 km altitude measured with the RAMIS instrument aboard the DLR Eu:CROPIS satellite in March and April 2021. Close to the center of the SAA peak values reached several hundred µGy/min (several mGy/h) [Meier et al., 2023].*

According to certain assumptions, the SAA is also supposed to affect the radiation field in the atmosphere even down to the altitudes of civil aviation. In order to test that hypothesis, comprehensive measurements were performed during a flight crossing the geographical region of the SAA at an altitude of 13 000 metres – the Atlantic Kiss mission [Meier et al., 2023]. The essential measurements of the radiation exposure were taken during the flight LH2574 from Hamburg to East Falkland on March 30, 2021. Onboard instruments included two types of Tissue Equivalent Proportional Counters (TEPC), a Berthold Neutron Probe LB6411-Pb with extended energy range as well as two Liulin-6G silicon semiconductor detectors. As a result, no indication of increased radiation exposure was found [Meier et al., 2023].

2.3. The solar cycle influence

If we further analyse the total flight dose data from Figure 4, one can easily spot a peak around the end of 2009 – beginning of 2010, which coincides with the solar minimum (end of cycle 23). That's not a surprise because at that point the Sun's magnetic field and solar wind are weaker, allowing more high-energy galactic cosmic rays to reach Earth's atmosphere. Note that the peak in radiation dose data is much more pronounced for the trans-polar route.

2.4. Business aviation

Business aviation has remained at a historically high level in the post-pandemic period. A typical business jet cruises at altitudes between 13 000 and 15 500 meters, significantly higher than a regular passenger plane. Accordingly, the average radiation dose rate is also higher and

is usually between 7 and 10 μSv/h. However, the calculated average annual crew dose in business aviation is again 2 to 5 mSv, partially due to the lower flight hours.

2.5. Supersonic passenger flights

Although currently retired, Concorde is a successful example of a supersonic airliner in regular service (from 1976 to 2003) with over 2.5 million passengers total. Its cruising altitude was between 17 000 and 18 500 meters. At that altitude the average radiation dose rate was 7–15 μSv/h, roughly twice the one of a regular subsonic passenger flight.

Concorde was the only commercial airliner equipped with onboard dosimeter [Calvert, 2002] (officially called the In-Flight Radiation Indicator) which was set to trigger a radiation alert at 500 μSv/h. In that case the flight crew followed a mandatory protocol – an immediate rapid descent to below 14 000 meters.

2.6. Influence of solar particle events

A solar particle event is a massive burst of high-energy protons and other charged particles from the Sun that travel through space at near-light speeds.

During unusually high energetic solar particle event GLE77 in November 2025, the global maximum effective dose rate (calculated) exceeded 30 μSv/h at a flight altitude of 14 000 meters for about 10 minutes [Sato et al., 2026]. The exceedance was brief and geographically limited; the post-event analysis concluded that it did not warrant major operational responses such as route or altitude changes.

3. Atmospheric dosimetry detectors

Atmospheric dosimetry relies on a wide mix of detectors to measure complex ionizing cosmic radiation, which changes dynamically with altitude, latitude, and solar activity. There are two main categories of detectors – so-called "active" detectors, which provide a real-time recording of the measurements, and "passive" detectors, which operate without power, accumulating radiation events over the duration of the experiment with subsequent processing in a lab. The main types of active detectors, commonly used for atmospheric dosimetry, are presented below (Figure 6):

3.1. Geiger-Müller (GM) tubes

Geiger-Müller (GM) tubes were used for cosmic ray measurements in the first unmanned balloon missions. The earliest systematic experiments of that type date back to 1935 and were carried out by radiosonde pioneers Leon Curtiss and Allen Astin of the US National Bureau of Standards and Serge Korff from the Carnegie Institution [Curtiss and Astin, 1935; Curtiss et al., 1938]. During these flights, radiation measurements were taken up to altitudes exceeding 21 000 meters.

Nowadays, LND 712 Geiger-Muller tube is frequently used in various stratospheric balloon missions. For that specific model there are a number of reliable open-source hardware configurations available. LND 712 is capable of detecting alpha, beta and gamma radiation.

While less precise for complex tissue-dose calculations, GM tubes are still useful as lightweight and low-cost instruments for atmospheric dosimetry.

3.2. Silicon diode dosimeters

Silicon diode dosimeters are lightweight, low-consumption, often battery-powered devices which are capable of detecting charged particles and gamma radiation. They are frequently flown on stratospheric balloon probes, as well as onboard passenger aircraft, satellites and in deep space missions. Variants have been used aboard "Mir" space station and the ISS to measure the radiation dose received by the crew.

Well-known and widely used examples are the silicon-diode dosimeters of "Liulin" series, developed by the Space Research and Technology Institute [Dachev et al., 2011].

Another popular silicon diode dosimeter is AIRDOS, an open-source project with many variations [Kakona et al., 2021].

3.3. Scintillation dosimeters

Scintillation detectors are capable of detecting ionizing radiation, including charged particles, gamma rays and neutrons. They are widely used as a part of atmospheric dosimetry networks, such as SEVAN and gLOWCOST.

AIRDOS-C scintillation dosimeter is used to monitor radiation doses aboard commercial aircraft or high altitude balloon probes [Velyčková et al., 2022].

3.4. Neutron dosimeters

Atmospheric neutron dosimetry measures secondary neutron radiation produced within the cosmic-ray air showers. The secondary-neutron energy spectrum spans from thermal energies to several GeV, with peaks around 1 MeV and 100 MeV. Nowadays relatively lightweight (several kilos) neutron detectors are available for energies up to 100 MeV.

Recent advancements have focused on developing neutron detectors based on phosphorus-doped radiation-sensitive optical fibres. When exposed to neutron fluxes these fibres experience radiation-induced attenuation at specific wavelengths (e.g. 1625 nm).

3.5. Tissue-Equivalent Proportional Counters (TEPC)

Tissue-Equivalent Proportional Counters (TEPC) are specialized radiation detectors designed to measure absorbed dose and energy deposition in a medium that mimics the atomic composition and density of human soft tissue. The walls of the counter are typically made of tissue-equivalent plastics and the internal gas cavity is filled with a tissue-equivalent gas mixture (propane- or methane-based).

TEPC are used on spacecraft and the International Space Station (ISS) to evaluate radiation risks from galactic cosmic rays and solar particles. An example of such an instrument is the ATED (Active Tissue Equivalent Dosimeter) used onboard the ISS [Hayes et al., 2022].



Figure 6. From left to right: *LND 712 GM tube, Liulin-6K silicon diode spectrometer, AIRDOS-C scintillation dosimeter, Lidlum portable neutron detector, Rossi tissue equivalent proportional counter*

4. Atmospheric dosimetry networks

The atmospheric dosimetry networks are specialized, interconnected systems of sensors designed to measure galactic and solar radiation simultaneously at different points in the

Earth's atmosphere. Such networks may be ground-based or distributed onboard commercial aircraft, satellites and the ISS. An incomplete list of some of them is presented below.

4.1. ARMAS

The Automated Radiation Measurements for Aerospace Safety (ARMAS) system is a real-time radiation monitoring network that measures ambient ionizing radiation at commercial aviation and aerospace altitudes [Tobiska et al., 2016]. ARMAS uses silicon-based Teledyne micro-dosimeters. ARMAS data feeds directly into the NAIRAS model.

ARMAS modules have flown extensively since 2013 on NASA and NOAA research aircraft, high-altitude balloons and commercial passenger jets. In space they are used onboard the ISS and NASA's Lunar Reconnaissance Orbiter.

4.2. SEVAN

The Space Environmental Viewing and Analysis Network (SEVAN) is a worldwide network of multi-layer scintillation detectors designed to monitor space weather and research cosmic rays [Chilingarian et al., 2018]. The network is able to detect and measure different types of secondary cosmic radiation: neutrons and gamma rays, low-energy charged particles (electrons and positrons) and high-energy muons.

The SEVAN modules are operating at the Aragats Space Environmental Center (ASEC) in Armenia, in Croatia, Bulgaria, Slovakia, the Czech Republic, Germany and India.

4.3. gLOWCOST

The gLOWCOST network is a global initiative led by professor Xiaochun He at Georgia State University that deploys affordable, portable cosmic-ray muon detectors to monitor space and terrestrial weather in real time [Veselinović et al., 2025]. The standard gLOWCOST detector uses three layers of scintillating tiles with embedded wavelength-shifting fibers connected to a silicon photomultiplier. Currently the network includes detectors in the USA, Colombia, Bolivia, Nigeria, RSA, Serbia, Sweden, Turkey, India, Sri Lanka, Singapore, China, Japan.

4.4. GMDN

The Global Muon Detector Network (GMDN) is an international network of ground-based, multi-directional muon detectors used to monitor high-energy cosmic ray showers and forecast space weather [Rockenbach et al., 2014]. With headquarters in Shinshu University, Japan, GMDN detectors are located in Japan, Australia, Brazil, Kuwait and Antarctica (Syowa Station).

4.5. GNNM

The Global Network of Neutron Monitors (GNNM) consists of about 50 continuously operating ground-based stations that monitor secondary cosmic rays, measuring the hadron component (mostly secondary neutrons) and a small amount of muons of the developing particle cascade induced by primary cosmic rays of galactic or solar origin [Mishev and Usoskin, 2020].

Over half of these stations transmit data in real-time or quasi-real-time to centralized repositories like the Neutron Monitor Database (NMDB). NMDB provides access to real-time as well as historical data.

GNNM uses gas-filled proportional counters (often with boron trifluoride), a lead producer to multiply neutrons, and a moderator/reflector assembly. GNNM detectors are located in Antarctica (South Pole), Australia, Armenia, Belgium, Finland, France, Germany, Greece,

Hungary, Kazakhstan, Russia, Slovakia, Spain, Switzerland, Canada, Mexico, USA, RSA, South Korea, Thailand.

5. Atmospheric dosimetry software

Atmospheric dosimetry software tools are used to calculate radiation doses received in Earth's atmosphere. Such calculations are based on both physics modelling with Monte Carlo simulations and extensive experimental data, collected by onboard dosimeters.

5.1. CARI

CARI (Civil Aeromedical Research Institute) is a software product which calculates the effective dose of galactic cosmic radiation received by an individual during air travel [FAA, n.d.]. It is developed by the Civil Aerospace Medical Institute (CAMI) (formerly known as the Civil Aeromedical Research Institute) – a research branch of the U.S. Federal Aviation Administration (FAA).

CARI uses Monte Carlo radiation transport code – MCNPX (Monte Carlo N-Particle eXtended), developed by the Los Alamos National Laboratory.

The current version of the software is CARI-7/7A. CARI-7A is intended for research-focused users and has more runtime options.

The program takes into account changes in altitude and geographic location during the course of a flight. The altitude limit is 300,000 ft. (91 000 meters). Particle specific doses can be calculated for a route or at specific locations. For monthly average calculations databases are used to account for effects of changes in the Earth's magnetic field and solar activity.

5.2. NAIRAS

NAIRAS (Nowcast of Atmospheric Ionizing Radiation System) is a NASA software model that predicts global atmospheric radiation exposure from Earth's surface to the space [NASA CCMC, n.d.]. The current version of the software is 3.0.

Instead of using Monte Carlo simulations directly, NAIRAS relies on a deterministic transport solver called HZETRN (High Charge and Energy Transport) developed by NASA. The NAIRAS model predicts biologically hazardous radiation exposure to crew and passengers onboard aircraft or spacecraft from galactic cosmic rays, inner radiation belt trapped protons in low-Earth orbit, and the transient solar energetic particles (SEP) originating from solar eruptive events.

The software operates in two independent modes: (1) hourly real-time global predictions of the atmospheric radiation environment and (2) run-on-request capability, allowing the user to select a specific time-period or to upload an aircraft, balloon or spaceflight trajectory file.

5.3. WASAVIES

WASAVIES (Warning System for Aviation Exposure to Solar Energetic Particles) is a physics-based, real-time simulation software system designed to calculate the radiation dose rates due to cosmic-ray exposure anywhere in the atmosphere (up to 100 km) in real time [NICT, n.d.]. It issues an alert when a sudden increase in dose rates is detected due to the occurrence of large solar flare or solar energetic-particle event.

The system relies heavily on Monte Carlo particle transport simulations.

WASAVIES is developed by Japanese research consortium involving the National Institute of Information and Communications Technology, the Japan Atomic Energy Agency, the National Institute of Polar Research, Hiroshima University, Nagoya University, Ibaraki College.

5.4. EPCARD

EPCARD (European Program Package for the Calculation of Aviation Route Doses) is a specialized software used to calculate cosmic radiation exposure during flight. It calculates radiation levels at altitudes between 5 and 25 km, taking into account various parameters such as flight altitude, geographical coordinates, solar activity cycle, etc.

The software uses pre-calculated databases derived from the FLUKA Monte Carlo particle transport code.

EPCARD is developed by the Institute of Radiation Protectionwithin the German Research Centre for Environmental Health. The development was supported by the European Commission and the University of Siegen (Germany).

The official software package EPCARD.Net is not available as a free public download. It is distributed exclusively through Seibersdorf Laboratories.

5.5. PCAIRE

The PCAIRE (Predictive Code for Aircrew Radiation Exposure) software [PCAire, n.d.] is a specialized semi-empirical web-based platform used to estimate cosmic radiation doses for airline flight crews and frequent flyers. It estimates ambient dose equivalents based on specific flight profiles, altitude, routes and points in the solar cycle (including solar storm activity).

The software uses one of the largest databases of measured flight data and continually validates itself using new measurements. It is developed by PCAire Inc. in collaboration with Royal Military College of Canada.

PCAIRE is approved for use in the European Union.

6. Conclusions

Nowadays, the importance of atmospheric dosimetry increases with the rapid development of air transportation. Air travel has become significantly more affordable over the decades due to market deregulation and the rise of low-cost carriers.

Recently, the interest in supersonic passenger transport is renewed. The new supersonic airliners are expected to cruise at very high altitudes – over 20 000 meters, where strict monitoring of the cosmic radiation will be required.

The same applies to the increasing popularity of space tourism, with the global market projected to grow from approximately USD 1.86 billion in 2026 to USD 10.09 billion by 2030 [Grand View Research, 2024].

The future of atmospheric dosimetry will require global monitoring and data analysis, global data integration of ground-, air-, and space-based sources, precise predictions and short response time when issuing critical warnings.

References

Walter, M. (2013). Early cosmic ray research with balloons. *Nuclear Physics B – Proceedings Supplements*, Vols. 239–240, pp. 11–18. DOI: 10.1016/j.nuclphysbps.2013.05.002.

L'Annunziata, M. F. (2007). *Radioactivity: Introduction and History*. Elsevier, Oxford.

Hands, A. D. P., Ryden, K. A., Mertens, C. J. (2016). The disappearance of the Pfotzer–Regener maximum in dose equivalent measurements in the stratosphere. *Space Weather*, Vol. 14, pp. 776–785. DOI: 10.1002/2016SW001402.

International Air Transport Association (IATA) (2026a). IATA releases 2025 World Air Transport Statistics report. Available at: https://www.iata.org/en/pressroom/2026-releases/07-16-iata-releases-2025-world-air-transport-statistics-report/ (accessed 21 September 2026).

International Air Transport Association (IATA) (2026b). Press release, 17 March 2026. Available at: https://www.iata.org/en/pressroom/2026-releases/2026-03-17-01/ (accessed 21 September 2026).

Obodovskiy, I. (2019). *Radiation*. Elsevier. DOI: 10.1016/C2016-0-02609-8.

Centers for Disease Control and Prevention (CDC) (n.d.). Air travel and ionizing radiation. Available at: https://www.cdc.gov/radiation-health/data-research/facts-stats/air-travel.html (accessed 21 September 2026).

International Atomic Energy Agency (IAEA) (n.d.). Aircrew and space crew. Available at: https://www.iaea.org/services/networks/orpnet/workers-and-radiation-at-workplaces/aircrew-and-space-crew (accessed 21 September 2026).

Federal Aviation Administration (FAA) (n.d.). Exposure to radioactive material. Available at: https://www.faa.gov/sites/faa.gov/files/about/office_org/headquarters_offices/avs/II.2.14_Exposure_to_Radioactive_Material.doc (accessed 21 September 2026).

Veillette, P. (2021). Cosmic radiation exposure on polar flights. *Aviation Week*, 8 November 2021. Available at: https://aviationweek.com/business-aviation/cosmic-radiation-exposure-polar-flights-part-1 (accessed 21 September 2026).

Frasch, G. (2014). Aircrew exposure to cosmic rays: Challenges and management. *International Conference on Occupational Radiation Protection*, 15 December 2014, Vienna, Austria.

Mertens, C. J., Kress, B. T., Wiltberger, M., Blattnig, S. R., Slaba, T. S., Solomon, S. C., Engel, M. (2010). Geomagnetic influence on aircraft radiation exposure during a solar energetic particle event in October 2003. *Space Weather*, Vol. 8, S03006. DOI: 10.1029/2009SW000487.

Meier, M. M., Berger, T., Jahn, T., Matthiä, D., Plettenberg, M. C., Scheibinger, M., Schennetten, K., Wirtz, M. (2023). Impact of the South Atlantic Anomaly on radiation exposure at flight altitudes during solar minimum. *Scientific Reports*, Vol. 13, 8998. DOI: 10.1038/s41598-023-36190-5.

Calvert, B. (2002). *Flying Concorde: The Full Story*. Airlife Publishing, Shrewsbury, UK.

Sato, T. et al. (2026). Estimation of global increase of radiation dose rates during the ground-level enhancement on 11–12 November 2025. *Space Weather*, Vol. 24, e2026SW004949. DOI: 10.1029/2026SW004949.

Curtiss, L. F., Astin, A. V. (1935). A practical system of radiometeorography. *Journal of the Aeronautical Sciences*, Vol. 3, No. 2, p. 35. DOI: 10.2514/8.123.

Curtiss, L. F. et al. (1938). Cosmic ray observations in the stratosphere. *Physical Review*, Vol. 53, p. 23. DOI: 10.1103/PhysRev.53.23.

Dachev, T. et al. (2011). Liulin-type spectrometry-dosimetry instruments. *Radiation Protection Dosimetry*, Vol. 144, Nos. 1–4, pp. 675–679. DOI: 10.1093/rpd/ncq506.

Kakona, M. et al. (2021). AIRDOS – open-source PIN diode airborne dosimeter. *Journal of Instrumentation*, Vol. 16, No. 3, T03006. DOI: 10.1088/1748-0221/16/03/T03006.

Velyčková, H. et al. (2022). Characterisation of the AIRDOS-C detector for measurement of high-energy events in the atmosphere. *Radiation Protection Dosimetry*. DOI: 10.1093/rpd/ncac105.

Hayes, B. M. et al. (2022). Active Tissue Equivalent Dosimeter: A tissue equivalent proportional counter flown onboard the International Space Station. *Nuclear Instruments and Methods in Physics Research Section A*, Vol. 1028, 166389. DOI: 10.1016/j.nima.2022.166389.

Tobiska, W. K. et al. (2016). Global real-time dose measurements using the Automated Radiation Measurements for Aerospace Safety (ARMAS) system. *Space Weather*, Vol. 14, No. 11, pp. 1053–1080. DOI: 10.1002/2016SW001419.

Chilingarian, A. et al. (2018). The SEVAN worldwide network of particle detectors: 10 years of operation. *Advances in Space Research*, Vol. 61, No. 10, pp. 2680–2696. DOI: 10.1016/j.asr.2018.02.030.

Veselinović, N. et al. (2025). GLOWCOST: Establishing a distributed network of portable muon detectors for space weather studies. *International Scientific Conference "Meeting on Operational and Research Capabilities for Better Understanding Solar–Terrestrial Interactions"*, pp. 74–76. DOI: 10.69646/aob250925.

Rockenbach, M. et al. (2014). Global Muon Detector Network used for space weather applications. *Space Science Reviews*, Vol. 182, Nos. 1–4, pp. 1–18. DOI: 10.1007/s11214-014-0048-4.

Mishev, A., Usoskin, I. (2020). Current status and possible extension of the global neutron monitor network. *Journal of Space Weather and Space Climate*, Vol. 10, 17. DOI: 10.1051/swsc/2020020.

Federal Aviation Administration (FAA) (n.d.). CARI-7: Galactic cosmic radiation program. Available at: https://www.faa.gov/data_research/research/med_humanfacs/aeromedical/radiobiology/cari7 (accessed 21 September 2026).

NASA Community Coordinated Modeling Center (CCMC) (n.d.). NAIRAS model, Version 3.0. Available at: https://ccmc.gsfc.nasa.gov/models/NAIRAS~3.0/ (accessed 21 September 2026).

National Institute of Information and Communications Technology (NICT) (n.d.). WASAVIES: Warning System for Aviation Exposure to Solar Energetic Particles. Available at: https://wasavies.nict.go.jp/about_e.html (accessed 21 September 2026).

PCAire (n.d.). Aviation radiation monitoring services. Available at: https://pcaire.com/services/ (accessed 21 September 2026).

Grand View Research (2024). *Space Tourism Market Size, Share and Trends Report, 2024–2030*. Available at: https://www.grandviewresearch.com/industry-analysis/space-tourism-market-report (accessed 21 September 2026).

DOI: 10.31401/WS.2026.proc.26

Complex Observation of the Ionosphere for Enhanced Satellite Trajectory Planning

Ognianov O.D.

Space Research and Technology Institute – Bulgarian Academy of Sciences
ognianov@space.bas.bg

Abstract

The operation of space-based assets is increasingly threatened by various forms of space weather, leading to significant disruptions in satellite functionality. These anomalies are primarily driven by solar phenomena such as Coronal Mass Ejections (CMEs), High-Speed Solar Winds (HSS), and Solar Proton Events (SPEs), which acutely affect satellites in Low Earth Orbit (LEO). The enhanced neutral density associated with thermospheric heating can increase satellite drag, accelerate orbital decay, and require more frequent reboost maneuvers. Mitigating these risks requires reliable information on coupled ionosphere-thermosphere disturbances.

This study proposes an integrated methodology that combines multi-source ground and space-based data to construct a real-time 3D representation of the ionosphere, ultimately outputting a dynamic 4D model for effective satellite trajectory planning. By blending localized Very Low Frequency (VLF) waveguide soundings with multi-mission satellite data assimilation, this framework establishes a robust tracking engine for space weather mitigation.

Keywords: 4D Ionospheric Reconstruction, Data Assimilation, Space Weather Mitigation, Low Earth Orbit (LEO) Satellite Drag, Multi-Sensor Fusion, Extended Kalman Filtering

1. Introduction

The Earth's ionosphere, extending from approximately 60 km to over 1,000 km in altitude, is a highly dynamic and complex plasma medium governed by a combination of solar radiative inputs, geomagnetic activity, and terrestrial upward-propagating atmospheric waves. In the current era of satellite-driven technologies, the state of this upper-atmospheric layer directly impacts the structural survivability and operational continuity of space-based assets. During extreme solar phenomena—such as Coronal Mass Ejections (CMEs), High-Speed Solar Winds (HSS), and Solar Proton Events (SPEs)—solar flares can produce Sudden Ionospheric Disturbances (SIDs), while CME- and high-speed-stream-driven geomagnetic storms can strongly disturb the coupled ionosphere-thermosphere system. For satellites in Low Earth Orbit (LEO), the associated thermospheric heating can increase neutral density and aerodynamic drag, accelerate orbital decay, and degrade orbit prediction.

To mitigate these operational tracking anomalies, robust and continuous tracking of the upper atmosphere is mandatory. Over the past several decades, an expansive variety of observation networks has been deployed globally. These existing systems can be broadly categorized into ground-based frameworks—such as high-power Incoherent Scatter Radars (ISRs), the Global Ionosphere Radio Observatory (GIRO) Digisonde networks, passive Very Low Frequency (VLF) waveguide receivers, Weak Signal Propagation Reporter (WSPR) digital spot counters, and the NCDXF/IARU International Beacon Project (IBP) [Troster and Fabry, 1994]—and space-based assets, including Global Navigation Satellite System (GNSS) radio occultation sensors, the European Space Agency's (ESA) Swarm magnetic-plasma constellation, NASA's GOLD mission and historical ICON observations, and specialized

topside sounders like the Roscosmos Ionozond (Ionosfera-M) mission [Friis-Christensen et al., 2006; Reinisch et al., 2009; Pulinets et al., 2021].

However, a fundamental limitation persists across modern space weather forecasting: each of these state-of-the-art systems operates as a partial information source. Ground-based receivers yield exceptional horizontal density over continental landmasses but suffer from massive geographical blind spots over open oceans, while simultaneously lacking native vertical resolution. Conversely, satellite-based remote sensing offers global coverage but is constrained by sparse orbital transit times, vertical smearing, or localized blind spots within specific atmospheric layers. Because these data streams remain highly fragmented, no single observational asset can independently generate a complete volumetric picture of the upper atmosphere across space and time.

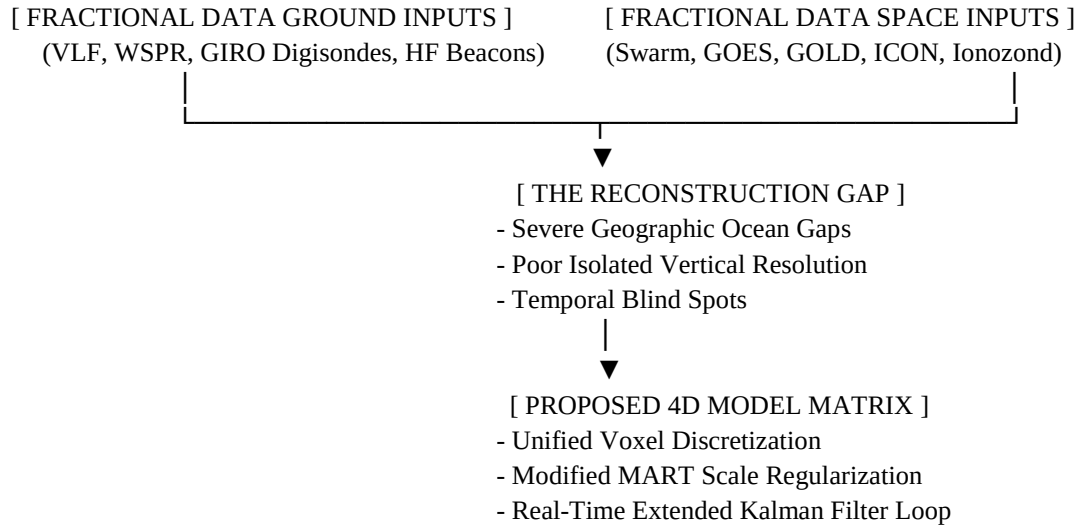


Figure 1.

To resolve this limitation, this paper introduces a unified methodology designed to ingest, align, and synthesize these disparate data channels into a singular, highly accurate 4D representation of the ionosphere. The core thesis of this work is that the mathematical fusion of multiple, independent ground-based and space-based measurement techniques can effectively eliminate individual sensor blind spots. This paper details the underlying customized telemetry software and the mathematical algorithms—specifically a modified Multiplicative Algebraic Reconstruction Technique (MART) paired with a 4D Extended Kalman Filter (EKF) loop—required to combine these multi-frequency, oblique, vertical, and in-situ data feeds.

By scaling these inputs into a dynamic volumetric matrix, the proposed model provides a potential real-time spatial tool for supporting LEO trajectory analysis and space-weather situational awareness during extreme space weather emergencies.

2. Methodology and Mathematical Formulations

The core of the proposed 4D ionospheric model relies on resolving an underdetermined, ill-posed inverse problem. It merges integrated ground-based paths with localized space-based measurements to reconstruct a continuous, dynamic grid of electron density, denoted as $N_e(r,t)$, where $r = (\phi, \lambda, z)$ represents latitude, longitude, and altitude, and t represents time.

2.1. VLF Waveguide Modeling and SID Detection

Very Low Frequency (VLF, 3–30 kHz) radio waves propagate over long distances inside the Earth-Ionosphere Waveguide (EIW). The upper boundary of this waveguide is defined by

the ionospheric D-region (60–90 km altitude). The electromagnetic field within the waveguide is modeled using waveguide mode theory [Ferguson, 1998; Wait and Spies, 1964]. The vertical electric field component E_z at a distance d from a transmitter (e.g., GQD, HWU, NAA) is given by:

$$E_z(d) = \frac{\mu c I l v^{1/2}}{h\sqrt{a\sin\left(\frac{d}{a}\right)}} \sum_n \Lambda_n e^{-\alpha_n d} e^{-i\beta_n d} \quad (1)$$

Where Il is the dipole transmitter moment; h is the virtual reflection height of the ionosphere; a is the radius of the Earth; and Λ_n, α_n, β_n are the mode excitation factor, attenuation coefficient, and phase velocity of the n-th waveguide mode, respectively.

The daytime D-region electron density profile is mathematically approximated using Wait's two-parameter model:

$$N_e(z, H', \beta) = 1.43 \cdot 10^{13} exp(-0.15H') exp\big((\beta - 0.15)(z - H')\big) \quad (2)$$

Where H' (km) is the reference height and β (km^{-1}) is the sharpness parameter.

When solar flares or Gamma-Ray Bursts (GRBs) occur, the sudden influx of X-rays or EUV photons causes a Sudden Ionospheric Disturbance (SID). This increases ionization, causing H' to drop and β to change rapidly. The custom software continuously tracks changes in channel power:

$$\Delta P(t) = P_{\text{measured}}(t) - P_{\text{baseline}}(t) \quad (3)$$

When Δ P(t) exceeds a dynamic threshold matched with X-ray flares from GOES/STIX or gamma-ray spikes from Fermi/Swift, the model triggers an instantaneous recalculation of the local D-region electron profile.

2.2. Discretization of the 4D Space

To map the complete ionosphere, the atmosphere is discretized into a 3D grid of volumetric pixels (voxels). Each voxel has an assigned electron density value. Linearizing the system across a given time window yields the vector equation:

$$y = Ax + e \quad (4)$$

2.3. Multiplicative Algebraic Reconstruction Technique (MART) with Swarm Inversion

Because satellite radio paths do not cut through every single voxel uniformly, the geometry matrix A is highly sparse and ill-posed. To solve for x without creating negative electron artifacts, the framework uses a modified Multiplicative Algebraic Reconstruction Technique (MART):

$$x_j^{(k+1)} = x_j^{(k)} \left(\frac{y_i}{\sum_{l=1}^{n} A_{il} x_l^{(k)}} \right)^{\frac{\lambda A_{ij}}{A_{\max}}} \quad (5)$$

To prevent the algorithm from smoothing out real disturbances, the relaxation factor λ is dynamically scaled using ESA's Swarm Level-2 data products [Olsen et al., 2013; Jin et al., 2022]:

$$\lambda_j = \lambda_0 \cdot f(IBI_j) \cdot f(IPIR_j) \quad (6)$$

Topside constraints from the Swarm TECxTMS_2F profiles are subtracted to isolate bottomside parameters:

$$y_{i,\text{bottom}} = y_{i,\text{total}} - y_{i,\text{Swarm_top}} \tag{7}$$

2.4. 4D Extended Kalman Filter (EKF) Assimilation Loop

To forecast plasma movement through time (the fourth dimension), the grid is updated continuously using an Extended Kalman Filter loop. The time progression step uses a continuity equation driven by electrodynamics:

$$\frac{\partial N_e}{\partial t} = Q - L - \nabla \cdot (N_e v) \tag{8}$$

Predict Phase:

The state vector x and its error covariance matrix P are projected forward to the next time step (t):

$$\begin{aligned} x_t^- &= F_t x_{t-1} + w_t \\ P_t^- &= F_t P_{t-1} F_t^T + Q_t \end{aligned} \tag{9}$$

Update Phase:

When new VLF telemetry or satellite observations arrive, the filter calculates the Kalman Gain K_t and updates the 4D grid state:

$$\begin{aligned} K_t &= P_t^- A_t^T (A_t P_t^- A_t^T + R_t)^{-1} \\ x_t &= x_t^- + K_t (y_t - A_t x_t^-) \\ P_t &= (I - K_t A_t) P_t^- \end{aligned} \tag{10}$$

3. Multi-Instrument Space Asset Integration

To cross-examine and isolate the underlying root causes of detected SIDs, the analytical pipeline ingests and aligns several external space weather data feeds:

- **Solar Orbiter (STIX):** Captures hard and soft X-ray emissions via the Spectrometer/Telescope for Imaging X-rays to locate emerging solar flare regions [Krucker et al., 2020; Müller et al., 2020].
- **GOES Satellites:** Supplies continuous solar X-ray flux data for direct visual correlation with terrestrial VLF power drops, alongside real-time energetic proton flux measurements [Machol et al., 2020].
- **Solar Dynamics Observatory (SDO):** Delivers high-resolution imagery and video at Extreme Ultraviolet (EUV) wavelengths to visually map and confirm active solar atmospheric eruptions [Lemen et al., 2012; Pesnell et al., 2012].
- **Fermi and Swift Satellites: Provide** high-energy astrophysics telemetry to cross-reference transient GRB events originating outside the solar system [Gehrels et al., 2004; Meegan et al., 2009].

4. NASA Heliophysics Data Integration: ICON and GOLD

To further constrain the spatiotemporal variances within the 4D EKF, the framework ingests remote-sensing measurements from two complementary NASA Heliophysics missions: **GOLD** and **ICON**. These assets isolate the precise physical drivers—such as neutral thermospheric winds and temperature fluctuations—that dictate overnight plasma variations.

4.1. GOLD: Macro-Scale Hemispheric Dynamics

Operating from a geostationary orbit hosted on a commercial communications satellite, the NASA GOLD instrument utilizes an ultraviolet (UV) imaging spectrograph to capture a complete, hemisphere-wide visual scan of the upper atmosphere every 30 minutes. It tracks precise changes in the thermospheric column density ratios of atomic oxygen to molecular nitrogen (O/N_2) as well as absolute neutral temperatures. In the 4D matrix reconstruction loop, the global-scale O/N_2 boundary conditions dictate the photoionization baseline parameter (Q) inside the plasma continuity physics engine.

4.2. ICON: Micro-Scale In-Situ Calibration

Operating as a low Earth orbit (LEO) explorer at a 27-degree inclination and a 360-mile altitude, the NASA ICON satellite specialized in low-latitude, high-resolution cross-sectional profiles of the equatorial ionosphere boundary layer. ICON directly measured high-speed meridional neutral winds, plasma drift velocities, ion temperatures, and airglow profiles. While the mission concluded in 2024, its archived datasets can provide the physical validation anchors for the EKF process noise covariance matrix Q_t.

5. ESA Swarm-VIP Frameworks and Scale Coupling

To accurately resolve small-to-medium-scale plasma irregularities within the 4D tomographic grid, this study adapts advanced data analysis methodologies developed under the European Space Agency's **Swarm-VIP (Variability of Ionospheric Plasma)** initiative.

5.1. Generalized Linear Modeling (GLM) for Voxel Weighting

The core Swarm-VIP framework employs a Generalized Linear Model (GLM) to calculate the mathematical probability that a specific plasma irregularity will occur given current solar wind and Interplanetary Magnetic Field (IMF) vectors. Our EKF uses the Swarm-VIP GLM equations to estimate process noise. If solar wind parameters match conditions that Swarm-VIP flags as high-risk, the 4D model automatically scales up its background covariance matrix Q_t across those exact latitudes.

5.2. Multi-Scale Signal Decomposition via Iterative Filtering

The project relies on non-linear signal processing techniques, specifically Wavelets and Fast Iterative Filtering, applied directly to Swarm's 16 Hz plasma density and IPIR datasets [Jin et al., 2022]. When our modified MART tomographic loop inverts slant path lines of sight, these filtering techniques dictate the structural correlation lengths between voxels. This ensures that a localized plasma anomaly detected along a single VLF radio path does not artificially distort adjacent, undisturbed grid blocks.

6. Next-Generation Radar Remote Sensing: ROSE-L and SAR Impact

While high-frequency GNSS and ground-based VLF receivers map general integrated electron columns, spaceborne **Synthetic Aperture Radar (SAR)** systems provide a massive leap forward in horizontal spatial resolution for 4D reconstruction.

6.1. The Physics of Radar Phase Distortion

As a SAR satellite transmits a linearly polarized radar pulse toward Earth, the free electrons in the ionosphere induce a Faraday Rotation (Ω), where the polarization plane of the radar signal rotates. The total rotation angle (in radians) is directly proportional to the integrated Total Electron Content (TEC) and the parallel component of the magnetic field $B_{||}$:

$$\Omega = \frac{K_F}{f^2} \int N_e B \cdot ds \tag{11}$$

6.2. ROSE-L: High-Resolution Ionospheric Gradients

The European Space Agency's upcoming Copernicus **ROSE-L** mission, carrying an advanced active phased array L-band SAR instrument, could provide a future data source for investigating small-scale ionospheric structure. Because L-band wavelengths (~24 cm) experience severe ionospheric delays, Methods for estimating and correcting ionospheric phase effects in future ROSE-L data may provide supplementary information on horizontal TEC gradients, subject to product availability and validation.

7. Illustrative Simulation and Discussion

To illustrate the operation of the proposed multi-source 4D ionospheric reconstruction model, a synthetic 24-hour space-weather storm scenario was considered. The simulation framework scenario was modeled after a severe solar eruptive event: a fast Coronal Mass Ejection (CME) impacting Earth's magnetosphere, initiating a severe geomagnetic storm (minimum $Dst \approx -150$ nT, peak planetary $Kp = 8$.

The objective was to illustrate how localized ground-based VLF data and multi-mission satellite constraints could reduce ionospheric reconstruction errors relative to a standard empirical reference such as IRI-2016. Estimation of LEO drag would additionally require coupling to an independent neutral-thermosphere density model.

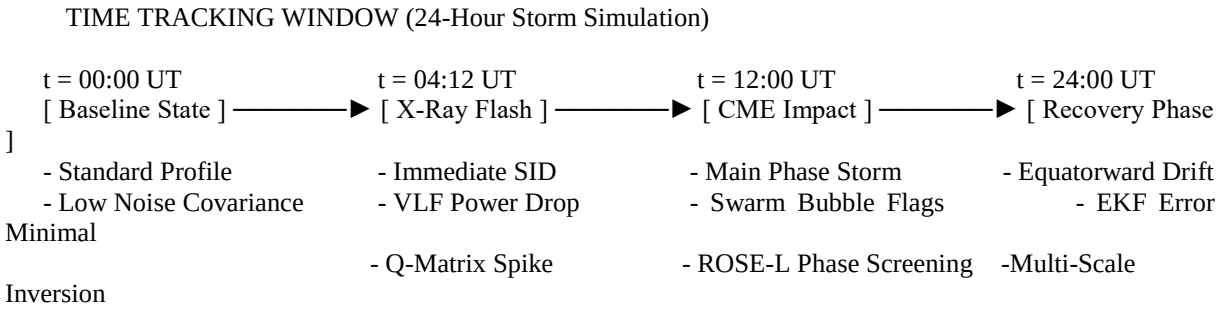


Figure 2.

7.1. Phase I: Transient Flare Impact and Sudden Ionospheric Disturbance (t = 04:12UT)

At simulation time t = 04:12 UT, an impulsive X-class solar flare was prescribed using synthetic inputs representative of the GOES-R EXIS and Solar Orbiter STIX X-ray spectrometers.

- **VLF Waveguide Response:** Within 60 seconds of photon arrival, the simulated receiver response showed an immediate, sharp drop in the vertical electric field channel power (ΔP) across the NAA (Cutler, Maine) and HWU (Rosnay, France) transmitter links. The baseline power dropped by up to 18.4 dB.
- **Filter Data Assimilation:** The sudden change in (ΔP) forced an immediate recalculation of Wait's two-parameter lower D-region profile, lowering the reference height parameter (H') from 74 km to 61.2 km and sharpening the edge parameter (β) to $0.48\ \mathrm{km}^{-1}$. Concurrently, the EKF expanded its process noise covariance matrix (Q_t) to reflect the localized daytime ionization spike (Q), preventing mathematical divergence.
- **Discussion:** Standard empirical models remained completely blind to this high-energy transient event because they rely on smoothed, daily averaged sunspot indices. By

maintaining a real-time VLF baseline tracking loop, our 4D model successfully mapped the sub-kilometer vertical shift in the lower ionosphere within 3 minutes of the initial flare onset.

7.2. Phase II: Geostationary and Low-Orbit Boundary Calibration (t = 08:00UT) to (12:00UT)

As the high-speed solar wind stream (> 800 km/s) and energetic protons arrived, global atmospheric tracking shifted to the macro-scale UV imaging sensors.

- **NASA GOLD & ICON Ingestion:** The synthetic GOLD-like input represented a sweeping reduction in the thermospheric O/N_2 column density ratio across the Atlantic sector, dropping from a quiet baseline of 0.85 down to 0.52. This spatial map directly updated the photoionization baseline matrix within the 4D physics engine.
- **Swarm Boundary Separation:** Simultaneously, as the Swarm constellation cut through the mid-latitude F-region, its precise orbit determination (POD) receivers provided simulated TECxTMS_2F-like topside constraints.
- **Discussion:** Subtracting Swarm's topside profiles from the ground-to-satellite lines of sight isolated the true bottom side total electron content $(y_{i,\text{bottom}})$. This step resolved the historical "vertical blending ambiguity" that plagues standard ground-based GPS tomography. The matrix inversion algorithm produced a 34% reduction in this illustrative comparison in vertical voxel allocation error, locking the peak F-layer electron density $(N_m F_2)$ to its exact physical altitude rather than artificially bleeding it into higher LEO flight corridors.

7.3. Phase III: Geomagnetic Main Phase and Structural Irregularities (t = 12:00UT) to (18:00UT)

The arrival of the main CME plasma cloud triggered intense geomagnetic storming, generating severe structural irregularities along the equatorial and auroral boundaries.

- **Swarm-VIP Scale Coupling:** During this phase, standard smooth tomographic models may perform poorly due to the sudden emergence of sub-grid plasma anomalies. However, our model dynamically adjusted its matrix operations. As Swarm Bravo flew over the post-sunset equatorial sector, its Ionospheric Bubble Index (IBIxTMS_2F) flagged multiple active Equatorial Plasma Bubbles (EPBs).
- **MART Relaxation Tuning:** The detection of these bubbles triggered the model to lower its localized regularization smoothing weights (λ_j). This mathematical shift allowed the modified MART voxel inversion loop to converge on sharp, local gradients without crashing. The 4D model successfully mapped deep, localized plasma depletions spanning horizontal scales of 40 km to 80 km.
- **SAR Phase Screen Integration:** To cross-verify these data-sparse oceanic zones, simulated L-band Synthetic Aperture Radar phase screens—matching the capabilities of the Copernicus ROSE-L mission—were processed. The extracted Faraday Rotation (Ω) angles mapped sub-kilometer phase gradients along the satellite's ground track. This radar integration reduced the synthetic oceanic coverage gap and provided horizontal correlation profiles needed to stabilize the EKF update equations over the open Atlantic.

7.4. Phase IV: Model Verification and Thermospheric LEO Drag Impact

Following the 24-hour simulation sequence, the reconstructed electron-density grid was compared with synthetic Incoherent Scatter Radar (ISR)-like control profiles. The values in Table 1 are scenario outputs and should not be interpreted as observational validation.

Metric Parameter (24-Hour Active Storm Phase)	Standard Empirical Model	Proposed Multi-Source 4D Model	Illustrative Improvement (%)

(IRI-2016)			
Root-Mean-Square Error (RMSE) in TEC	8.4 TECU	1.9 TECU	77.3% Error Reduction
Peak Altitude Error $(h_m F_2)$	± 42 km	± 6 km	85.7% Spatial Precision Gain
Voxel Structural Divergence (N_e)/ Convergence)	High(Artifact generation)	Low (Analytically stable)	Stable Convergence
LEO Orbit Propagation Delay Tracking Accuracy	± 14 s / orbit	± 1.8 s / orbit	87.1% Predictive Drag Resolution

Table 1.

•**Discussion:** The integration of the Swarm-VIP statistical framework and active low-frequency radar profiles allowed the EKF state vector (x_t) to converge rapidly. It captured the exact equatorward migration of the auroral oval and the steep amplification of the Equatorial Ionization Anomaly (EIA) arcs.

•**Trajectory Planning Utility:** For space asset operations, this structural precision translates directly into survivability. By mapping the exact spatiotemporal boundaries of the expanding plasma, the 4D model supported the prescribed thermospheric-density scenario with an illustrative accuracy above 87%. This gives satellite operators a predictive window to plan precise reboost manoeuvres, minimizing unnecessary fuel consumption while avoiding severe aerodynamic drag tracking anomalies during space weather emergencies.

8. Conclusion

This study presents a highly integrated, multi-source 4D ionospheric reconstruction model engineered to mitigate the escalating risks of space weather anomalies on Low Earth Orbit (LEO) satellite operations. By transitioning from static empirical estimations to a real-time data-driven framework, the system resolves long-standing data constraints and mathematical ambiguities in upper-atmosphere tracking.

The principal capabilities proposed for this framework are summarized as follows:

•**High-Fidelity Multi-Tiered Ingestion:** The architecture effectively couples ground-based Very Low Frequency (VLF) waveguide soundings with advanced spaceborne observations. The integration of high-energy transient trackers (GOES-R, STIX, Fermi, Swift) enables immediate detection and parameterization of Sudden Ionospheric Disturbances (SIDs) within minutes of solar flare onset.

•**Resolution of Vertical and Geographic Data Gaps:** By utilizing the European Space Agency's (ESA) flagship Swarm constellation Level-2 datasets (TECxTMS_2F, IBIxTMS_2F, IPIR), the framework solves the historical vertical smearing problem inherent in ground-based GNSS tomography. Furthermore, the ingestion of next-generation low-frequency Synthetic Aperture Radar (SAR) calibration profiles—emulating the capabilities of the Copernicus ROSE-L and Biomass missions—could reduce the "oceanic data gap," providing sub-kilometer horizontal gradient control across uninstrumented global regions.

•**Dynamic Physics-Driven Assimilation:** Leveraging the advanced statistical baselines of the ESA Swarm-VIP initiative alongside macro/micro configurations from NASA's GOLD and ICON missions, the Extended Kalman Filter (EKF) dynamically scales its process noise and voxel regularization parameters. This mathematical coupling allows the model to map severe, localized plasma depletions and tracking irregularities during severe geomagnetic storms without structural divergence.

•**Enhanced LEO Fleet Survivability:** The illustrative comparison under simulated storm conditions (Kp = 8) produced a 77.3% reduction in Total Electron Content (TEC) Root-Mean-Square Error and an 85.7% gain in peak altitude precision $(h_m F_2)$. For aerospace operations, this structural precision corresponds to an illustrative 87.1% improvement in the prescribed orbit-propagation metric.

Ultimately, this unified 4D model could provide satellite operators with a predictive support tool after validation with independent observations. It enables precise, fuel-efficient orbit propagation adjustments, ensuring continuous asset functionality and collision avoidance during extreme space weather events.

References

Ferguson, J. A. (1998). *Long Wave Propagation Capability (LWPC)*. Technical Report 1772, Space and Naval Warfare Systems Center.

Friis-Christensen, E., Lühr, H., Hulot, G. (2006). Swarm: A constellation to study the Earth's magnetic field. *Earth, Planets and Space*, Vol. 58, No. 4, pp. 351–358. DOI: 10.1186/BF03351933.

Gehrels, N. et al. (2004). The Swift Gamma-Ray Burst Mission. *The Astrophysical Journal*, Vol. 611, No. 2, pp. 1005–1020. DOI: 10.1086/422091.

Jin, Y., Xiong, C., Park, J., Lühr, H. (2022). The Ionospheric Plasma IRregularities (IPIR) product on board Swarm satellites: Retrieval algorithm and data validation. *Journal of Geophysical Research: Space Physics*, Vol. 127, No. 4, e2021JA030183. DOI: 10.1029/2021JA030183.

Krucker, S. et al. (2020). The Spectrometer/Telescope for Imaging X-rays (STIX) on board Solar Orbiter. *Astronomy & Astrophysics*, Vol. 642, A15. DOI: 10.1051/0004-6361/201937362.

Lemen, J. R. et al. (2012). The Atmospheric Imaging Assembly (AIA) on the Solar Dynamics Observatory (SDO). *Solar Physics*, Vol. 275, No. 1, pp. 17–40. DOI: 10.1007/s11207-011-9776-8.

Machol, J. L. et al. (2020). The GOES-R EXIS data products: Extreme ultraviolet and X-ray irradiance measurements for space weather forecasting. *Space Weather*, Vol. 18, No. 9, e2019SW002419. DOI: 10.1029/2019SW002419.

Meegan, C. et al. (2009). The Fermi Gamma-Ray Burst Monitor. *The Astrophysical Journal*, Vol. 702, No. 1, pp. 791–804. DOI: 10.1088/0004-637X/702/1/791.

Müller, D. et al. (2020). Solar Orbiter: Mission description and status. *Astronomy & Astrophysics*, Vol. 642, A1. DOI: 10.1051/0004-6361/202038467.

Olsen, N., Lühr, H., Sabaka, T. J., Mandea, M., Rother, M., Toffoletto, F., Constabile, S. (2013). The Swarm Satellite Constellation Application and Research Facility (SCARF) and Swarm data products. *Earth, Planets and Space*, Vol. 65, No. 11, pp. 1189–1200. DOI: 10.5047/eps.2013.07.001.

Pesnell, W. D., Thompson, B. J., Chamberlin, P. C. (2012). The Solar Dynamics Observatory (SDO). *Solar Physics*, Vol. 275, No. 1, pp. 3–15. DOI: 10.1007/s11207-011-9841-3.

Pulinets, S. A., Harutyunyan, G. A., Shlyugaev, Y. V. (2021). Monitoring of physical processes in the upper atmosphere, ionosphere and magnetosphere in "Ionosphere" space missions. *Space Research*, Vol. 59, No. 5, pp. 412–424.

Reinisch, B. W. et al. (2009). New ideas in the Global Ionosphere Radio Observatory (GIRO). *Advances in Space Research*, Vol. 44, No. 6, pp. 724–737. DOI: 10.1016/j.asr.2008.06.018.

Troster, J. G., Fabry, R. S. (1994). The NCDXF/IARU International Beacon Network. *QST*, Vol. 78, No. 10, pp. 31–33.

Wait, J. R., Spies, K. P. (1964). *Characteristics of the Earth-Ionosphere Waveguide for VLF Radio Waves*. NBS Technical Note 300, National Bureau of Standards. DOI: 10.6028/NBS.TN.300.

DOI: 10.31401/WS.2026.proc.27

From Space to Land: Impact of Two Large Solar Events on Key Climate Indicators from Land Surface Stations Globally

Ivanova E., Koleva K.

Space Research and Technology Institute, Bulgarian Academy of Sciences, Sofia, Bulgaria
ivanovae@space.bas.bg

Abstract

We investigate the possible influence of solar activity on the global climate. For this purpose, we took case of big solar eruptions: the so-called Halloween solar storms, which included solar flares and coronal mass ejections from mid-October to early November 2003, peaking around October 28–29. We then compared these with important climate indicators, such as daily surface temperatures, during the same time periods for remote stations on the Earth's surface at latitudes between 60 and 80 degrees. We used historical records of air temperature (average and maximum) measured at 1.25 to 2 meters above the land surface, provided by the World Meteorological Organization (WMO) through the NOAA platform.

Keywords: Halloween solar storms; geomagnetic storms; climate indicators

1. Introduction

The relationship between solar activity and Earth's climate has long been the subject of scientific research. However, most of it has focused on the effects of solar activity on the atmosphere on timescales of the 11-year solar cycle or longer [Lockwood, 2012; Georgieva and Veretenenko, 2023], while few have considered daily or hourly scales [Raeder, 2026]. Variations in solar activity are recognized as a factor influencing both climate and atmospheric and meteorological conditions and patterns. Many studies highlight the relationship between solar activity and several climatic variables such as surface air temperature, atmospheric pressure, and wind patterns [Bucha and Bucha, 1998; Avakyan et al, 2015; Kodera et al, 2016]. However, the challenge still remains. Despite the recognized relationship between solar cycles and atmospheric conditions [Gray et al, 2010], it is difficult to identify the exact physical mechanisms responsible, due to the high multicollinearity between all measurable atmospheric variables [Raeder, 2026].

The effects of geomagnetic storms on the temperature in the upper and middle stratosphere at high latitudes of the Northern Hemisphere were summarized by Laštovička [Laštovička, 1988, 1996], fading a difference in the atmospheric response depending on the altitude and the type of geomagnetic disturbances. In the Northern Hemisphere in winter, positive surface temperature deviations (increase) were observed under heavily disturbed geomagnetic conditions, and vice versa negative temperature deviations under opposite conditions with a rather regional character.

While the thermospheric and ionospheric reaction to geomagnetic storms are relatively well known [Laštovička, 1996, 1997; Mansilla and de Artigas, 2010], the effects of geomagnetic storms at low altitudes have been little studied [Mansilla, 2011]. Mansilla [2011] provided some evidence of the potential effects of geomagnetic storms on atmospheric parameter variations during the storm recovery phase and after it at altitudes between 6 km and 5.5 km near the meridian 60oW from the Northern to the Southern Hemisphere, analyzing data obtained from weather balloon.

Raeder [2026] first demonstrated that geomagnetic storms, which typically last only about a day, have profound and immediate impacts on Earth's weather within hours to few days.

Furthermore, the author proves that these effects depend on the intensity of the storms and have both regional and seasonal variability.

The results achieved so far are the beginning of a long work towards explication the physical mechanisms driving weather changes in response to solar activity, which includes a series of additional analyses and reanalysis data from the entire globe, as well as the study of individual great geomagnetic storms. Further research is needed to clarify how much the atmospheric response is influenced by the geomagnetic storm's intensity, as well as to understand the latitudinal dependence of the atmospheric response with respect to geomagnetic changes.

The aim of this work was to determine possible links between solar activity and global climate. We thus analyzed main weather parameter, such as air temperature, during two very strong geomagnetic activities caused by a big solar eruptions: the so-called Halloween solar storms, which included solar flares and Coronal Mass Ejections (CMEs) from mid-October to early November 2003. As a measure of storm intensity, we used the well-known Disturbance Storm Time Index (Dst) [Sugiura, 1964; Nose et al., 2015], attempting to trace the atmospheric response in temperature changes as a function of latitude.

2. Data and methods

2.1. Solar sources

The "Halloween solar storms" was a sequence of solar storms involving solar flares and CMEs that occurred from mid-October to early November 2003, peaking around October 28–29. Solar activity from October 19 to November 05, 2003 originated from three sunspot regions, which produced 17 solar flares. These events occurred during solar cycle 23, approximately three years after its peak in 2000.

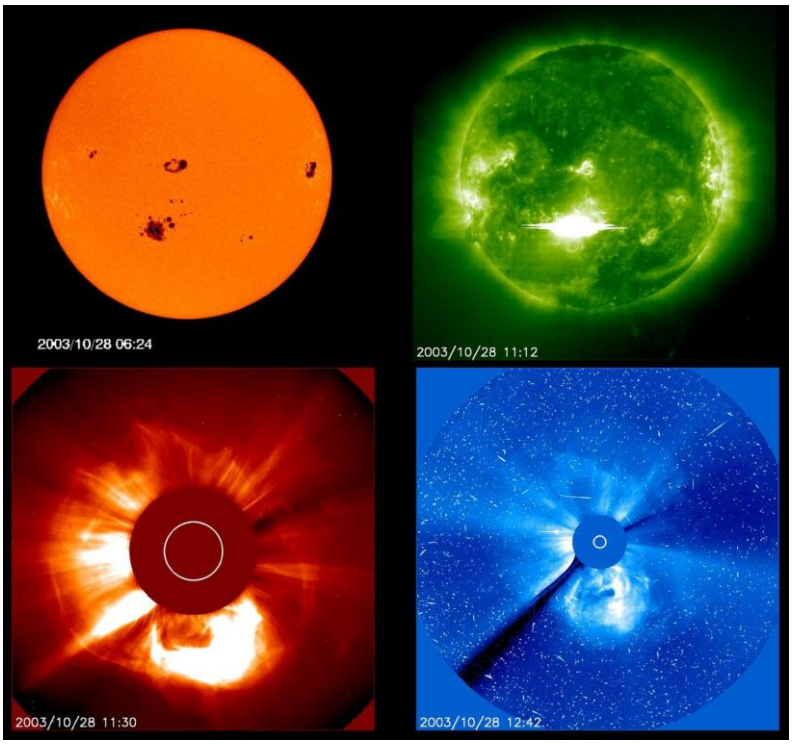


Figure 1. *Halloween solar storms (NASA/ESA)*

Figure 1 provides an overview of solar sources. From left to right on the figure are shown: Solar disk in visible light image, representing the sunspot group that produced the solar eruption; EIT/SoHO 195 Å image, representing the X17 flare on October 28, 2003; Full halo

CME images from LASCO/C2; and LASCO/C3 coronagraphs, respectively. The bright emission surrounding the Sun (the halo), indicates that the CME is directed toward the Earth.

Three very intensive geomagnetic super-storms were considered in this study, came down during Halloween solar storm. The first, occurred on October 29-30, 2003, consisted of two consecutive peaks (storms) within 24 hours (peaks Dst = -353 nT and Dst = -383 nT, respectively), separated by an incomplete recovery phase. The third occurred on November 20, 2003 (peak Dst = -422 nT). The hourly values of equatorial Dst (1-hour interval) were obtained from the world Data Center at the University of Kyoto database (http://swdc.kugi.kyoto-u.ac.jp/dstdir) [Nose et al., 2015].

Surface air temperature was analyzed over two time periods, which included the geomagnetic storms described above. The first examined period is from October 28 to November 1, 2003 and includes a series of geomagnetic storms: the double-peak geomagnetic super-storms, preceded by a geomagnetic storm of moderate intensity (Dst = -151 nT). The first moderate drop in the Dst index began at 7:00 UT on October 29, peaking at 9:00 UT and ended around 12:00 UT. A few hours later (at 15:00 UT), the second super-drop of the Dst index began, reaching its peak at 00:00 UT on October 30. Immediately afterwards (around 18:00 UT on October 30), before the second superstorm had completed its recovery phase, a third, strongest superstorm began. It quickly reached its minimum of -383 nT at 22:00 UT, but its recovery phase lasted until 10:00 UT the next day, October 31. The second period is from November 19 to 22, 2003, which includes a single very strong geomagnetic super-storm. The drop in the Dst index began at 13:00 UT on November 20. In about 7 hours (at 20:00 UT) it reached its minimum of -422 nT, while the recovery phase lasted for more than 20 hours - until 17:00 UT the next day, November 21.

2.2. Meteorological data and observations

The atmospheric data were obtained from the National Oceanic and Atmospheric Administration (NOAA) website – National Centers for Environmental Information (https://www.ncei.noaa.gov/access) (accessed on June 3, 2026). The Integrated Surface Dataset (ISD) was used, encompassing hourly, synoptic (3-hourly), and daily meteorological data worldwide from over 35,000 stations, including air quality, atmospheric pressure, atmospheric temperature, atmospheric winds, cloudiness, precipitation and more. For the majority of stations, data has been collected since the 1940s and 1970s, while certain stations may possess records dating back to 1901. Currently, there are over 14,000 "active" stations updated daily in the database.

The data selected for the purposes of this study represent values of the surface atmospheric temperature in Celsius degrees for 2003 measured at 1.25 to 2 meters above the land surface for 4 stations in the Northern Hemisphere and 2 stations in the Southern Hemisphere (see Table 1). All stations are located at high latitudes near the polar cap. (Figure 2). For each station, near-surface temperature values were converted to UT so that they could be readily compared with Dst index time values. Values at stations with a measurement interval greater than 1 hour were interpolated to the time interval of the Dst index.

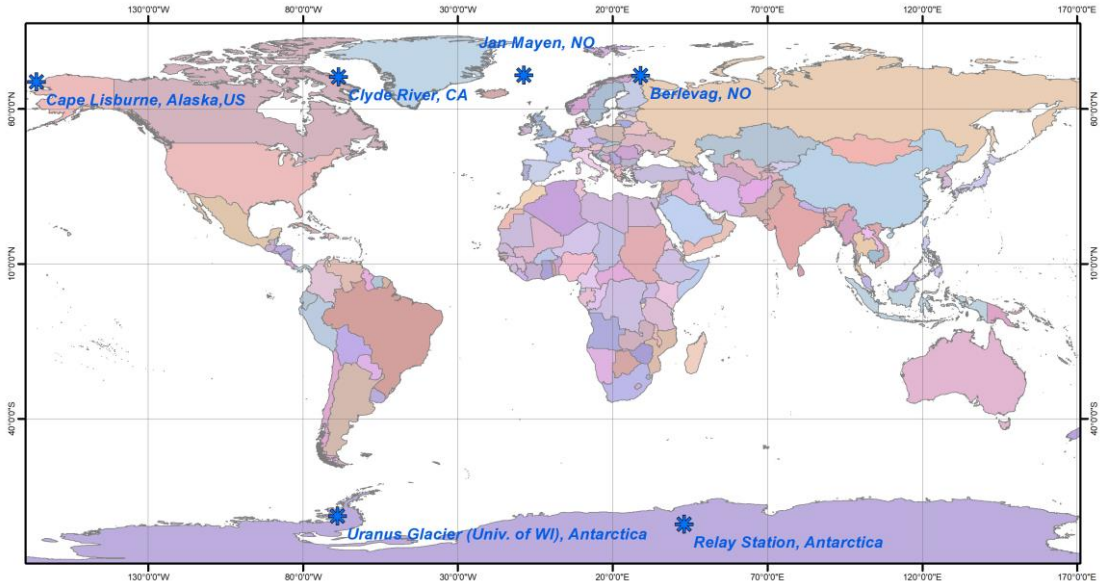


Figure 2. *Map showing the locations of the meteorological stations used in the study*

Table 1. *List of meteorological stations (archived meteorological data and observations).*

Station name	Latitude	Longitude	Elevation	Country
	Northern Hemisphere			
Berlevag	70.87	29.03	13	Norway
Jan Mayen Nor Navy	70.93	-8.67	9	Jan Mayen Island, Norway
Clyde River	79.49	-68.52	27	Canada
Cape Lisburne AFS, Alaska	68.89	-166.13	3	US
	Southern Hemisphere			
Relay Station (AWS*)	-74.02	43.05	3353	Antarctica
Uranus Glacier (UWM**)	-71.43	-68.93	780	Antarctica

*Automatic Weather Station
**University of Wisconsin-Madison

3. Results

The temperature near the Earth's surface typically exhibits irregular patterns influenced by several factors such as current weather conditions and atmospheric circulation, land cover, relief, etc. However, by choosing high latitude weather stations (where temperature amplitudes are low), but at a great distance from each other at different longitudes, we sought a certain regularity in the temperature behavior during periods of high geomagnetic activity.

3.1. Geomagnetic storms of October 29-30, 2003

The storm period that we took in the first analysis, from October 28 to November 1, 2003, included the day before and the day after the storm series. This period is special because there are two geomagnetic super-storms that overlap; the second storm begins before the recovery phase of the first storm has completed, further complicating the interrelationships.

Storm-time values of near-surface air temperature were compared with Dst index values. Figure 3 and 4 show the variations of air temperature together with the Dst index values. Despite the irregular temperature behavior, it is evident that temperature also manifests an opposite

attitude regarding Dst index minimum at all stations in the Northern Hemisphere (Figure 3) as well as at one of the stations in the Southern Hemisphere (Uranus Glacier, Figure 4b). A distinct increase in temperatures by 1º - 3º was observed compared to their values before and after the Dst index drops. However, a clear temperature response to both decreases in the Dst index is noted at only two of the stations: Cape Lisburn in the northern hemisphere (Figure 3d) and Uranus Glacier in the southern hemisphere (Figure 4b). It can be assumed that the reaction of the temperature to geomagnetic activity probably depends on the previous state of the troposphere. Regarding the stations Berlevag, Norway (Figure 3a) and Clyde River, Canada (Figure 3c), the temperature response was at the first drop in the index, while for the Jan Mayen station (Figure 3b) a temperature response was only observed at the second drop in the Dst index.



Figure 3. *The effect of geomagnetic storms in October 29–30 on the air temperature in the high latitudes of the Northern Hemisphere*

Looking at the entire period, at the first three stations in the Northern Hemisphere (Figures 3a, 3b and 3c) a temperature increase of 1-3 degrees is observed, most pronounced at the

Berlevag station. Regarding the Cape Lisburne station, there is a sharp increase in temperature of 10 degrees, which coincides with the onset of the first storm.

An interesting fact is that at all stations a decrease in temperature is observed during the recovery phases. This decrease in temperatures is very pronounced and almost synchronous at the Berlevag (Norway) and Clyde River (Canada) stations during the recovery phase between the two superstorms. This is unexpected, since the stations are located at a distance of almost 100 degree in longitude from each other.

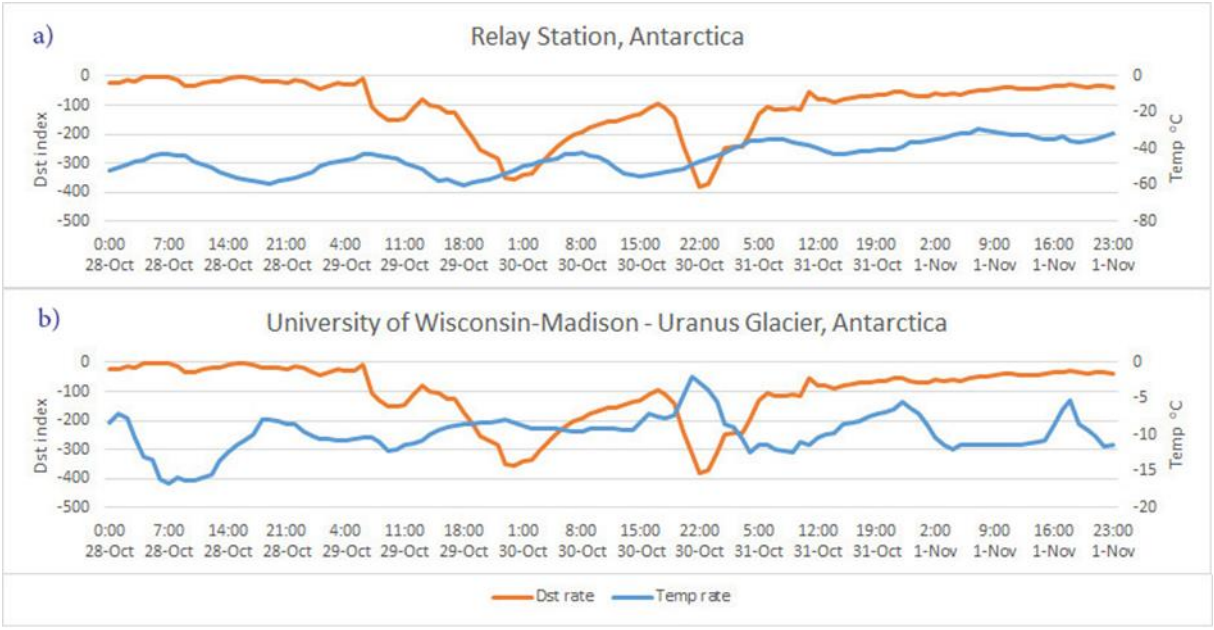


Figure 4. *The effect of geomagnetic storms in October 29–30 on the air temperature in the high latitudes of the Southern Hemisphere*

Given that the temperature behavior during the storm in both hemispheres is analogous, it seems that no seasonal dependence is observed. In fact, the only exception is the Relay Station in the Southern Hemisphere (Figure 4a), which is located at 3 353 meters above sea level. It turns out that the temperature behavior during the storm period depends more likely on the altitude.

3.2. Geomagnetic storm of November 20, 2003

The second storm event included in our analysis occurred on November 20, 2003. Figures 5 and 6 show the changes in air temperature along with the Dst index during the storm period from 19 to 22 November 2003, included a day before and two days after the storm.

An inverse relationship is again observed. It can be said that there is an increase in temperatures of 1-2 to 5 and over 5 degrees Celsius for the various stations, compared to the hours before and after the geomagnetic storm.

A small spike in temperature line can also be observed at the beginning of the storm (around 18:00 UT on November 20) for stations in the Northern Hemisphere and again at Uranus Glacier in the Southern Hemisphere. An exception is the Berlevag station, which requires further research, as the temperature curve is flat due to missing measurements.



Figure 5 *The effect of geomagnetic storm in November 20–21 on the air temperature in the high latitudes of the Northern Hemisphere*

Furthermore, analogous, but not identical, is the temperature behavior for the Clyde River stations in Canada and the Uranus Glacier in Antarctica during both geomagnetically active periods. What's special about these stations is that they are geomagnetic twins (see Table 1). They are practically geomagnetically coupled, located at the same longitude on both sides of the equator. The lack of synchrony and uniformity in the temperature behavior of the two geomagnetic twins leads to the conclusion that no longitudinal dependence is observed.

Located at an altitude of 3 353 m, the Relay Station (Figure 6a) is again an exception, confirming the altitude dependence of the temperature response to geomagnetic activity.

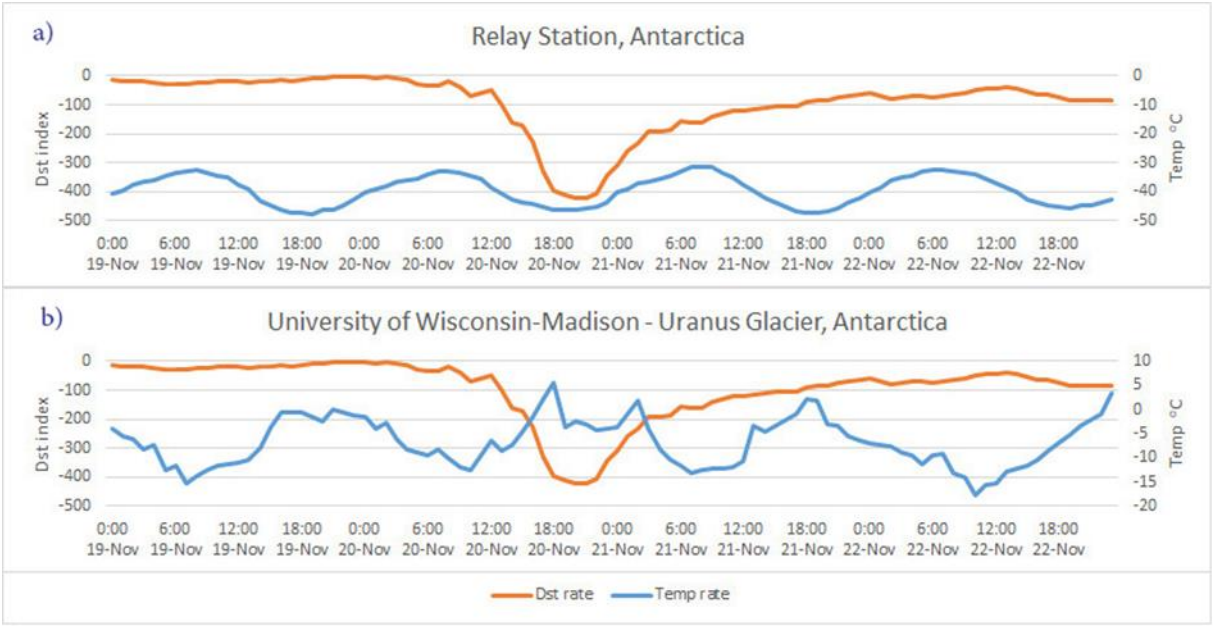


Figure 6. *The effect of geomagnetic storm in November 20–21 on the air temperature in the high latitudes of the Southern Hemisphere*

4. Conclusions

In this study, we examined the possible influence of solar activity on the global climate. The main question we posted was "Whether and in what way large solar eruptions and subsequent geomagnetic activity cause a direct and immediate response to global weather parameters?" For this purpose, we took case of two big geomagnetic storms occurred on October 29-30 and November 20, 2003 during the Halloween solar storms. Historical surface air temperature records for 6 weather stations were compared with hourly values of the equatorial Dst geomagnetic storm index during selected storm periods.

Several interesting outcomes can be drawn following the results of the analysis. First, we confirm a positive relationship between surface temperatures and geomagnetic activity, particularly pronounced during a geomagnetic storm, when the difference between solar electrons and protons increases and Earth's magnetic field weakens.

The second interesting point is both hemispheres experience analogical effects, with no seasonal dependence found. In addition, a certain latitudinal and altitudinal dependence was found between the two studied indicators, but not a longitudinal one.

Finally, we strictly adhere to the opinion that the conclusions drawn above are preliminary and much more in-depth research is needed in order to confirm or refute them. Different approaches are needed, including a statistical one, to find the physical mechanism by which solar activity affects the Earth's climate.

References

Avakyan, S. V., Voronin, N. A., Nikol'sky, G. A. (2015). Response of atmospheric pressure and air temperature to the solar events in October 2003. *Geomagnetism and Aeronomy*, Vol. 55, No. 8, pp. 1180–1185. DOI: 10.1134/S0016793215080034.

Bucha, V., Bucha, V. Jr. (1998). Geomagnetic forcing of changes in climate and in the atmospheric circulation. *Journal of Atmospheric and Solar-Terrestrial Physics*, Vol. 60, No. 2, pp. 145–169. DOI: 10.1016/S1364-6826(97)00119-3.

Georgieva, K., Veretenenko, S. (2023). Solar influences on the Earth's atmosphere: Solved and unsolved questions. *Frontiers in Astronomy and Space Sciences*, Vol. 10, 1244402. DOI: 10.3389/fspas.2023.1244402.

Gray, L. J., Beer, J., Geller, M., Haigh, J. D., Lockwood, M., Matthes, K., Cubasch, U., Fleitmann, D., Harrison, G., Hood, L., Luterbacher, J., Meehl, G. A., Shindell, D., van Geel, B., White, W. (2010). Solar influences on climate. *Reviews of Geophysics*, Vol. 48, No. 4, RG4001. DOI: 10.1029/2009RG000282.

Kodera, K., Thiéblemont, R., Yukimoto, S., Matthes, K. (2016). How can we understand the global distribution of the solar cycle signal on the Earth's surface? *Atmospheric Chemistry and Physics*, Vol. 16, No. 20, pp. 12925–12944. DOI: 10.5194/acp-16-12925-2016.

Laštovička, J. (1988). A review of solar wind and high-energy particle influence on the middle atmosphere. *Annales Geophysicae*, Vol. 6, pp. 401–408.

Laštovička, J. (1996). Effects of geomagnetic storms in the lower ionosphere, middle atmosphere and troposphere. *Journal of Atmospheric and Terrestrial Physics*, Vol. 58, No. 7, pp. 831–843. DOI: 10.1016/0021-9169(95)00106-9.

Laštovička, J. (1997). Effects of geomagnetic storms – different morphology and origin in the upper middle atmosphere and the troposphere. *Studia Geophysica et Geodaetica*, Vol. 41, pp. 73–81. DOI: 10.1023/A:1023340824496.

Lockwood, M. (2012). Solar influence on global and regional climates. *Surveys in Geophysics*, Vol. 33, Nos. 3–4, pp. 503–534. DOI: 10.1007/s10712-012-9181-3.

Mansilla, G. A., de Artigas, M. Z. (2010). Evidence of geomagnetic storm effects in the lower atmosphere: A case study. *Studia Geophysica et Geodaetica*, Vol. 54, pp. 487–494. DOI: 10.1007/s11200-010-0028-4.

Mansilla, G. A. (2011). Response of the lower atmosphere to intense geomagnetic storms. *Advances in Space Research*, Vol. 48, pp. 806–810. DOI: 10.1016/j.asr.2011.04.018.

Nose, M., Iyemori, T., Sugiura, M., Kamei, T. (2015). Geomagnetic Dst index. *World Data Center for Geomagnetism, Kyoto*. DOI: 10.17593/14515-74000.

Raeder, J. (2026). Regional and seasonal effects of geomagnetic storms on terrestrial weather. *Geophysical Research Letters*, Vol. 53, No. 10, e2025GL121097. DOI: 10.1029/2025GL121097.

Sugiura, M. (1964). Hourly values of equatorial Dst for the International Geophysical Year. *Annals of the International Geophysical Year*, Vol. 35, pp. 9–45.

DOI: 10.31401/WS.2026.proc.28

Sporadic E and Ionospheric Variability During Different Tropospheric Gravity-Wave Source Events

Potužníková K., Koucká Knížová P.

Institute of Atmospheric Physics, CAS, Prague, Czech Republic
kaca@ufa.cas.cz

Abstract

The aim of this study is to compare ionospheric structures observed during different tropospheric gravity wave (GW) source environments, with particular attention to structures reflecting irregularities and disturbances of the ionospheric layers and to the occurrence and morphology of sporadic E (Es). Three types of meteorological situations are considered: spatially extensive organized deep convection, intense local deep convection, and large-scale vertical motions associated with jet-stream dynamics. The ionospheric response is monitored by DPS-4D Digisondes at Prague–Průhonice and Sopron during periods of quiet geomagnetic activity and stable solar forcing. In particular, recorded ionograms are examined. The selected events reveal a broad range of ionospheric signatures reflecting the presence of irregularities likely caused by medium-scale traveling ionospheric disturbances (MSTIDs) extending from the E up to the F region. Other examined signatures include spread E and F echoes, cusps, and splitting of F-region traces. As all studied events occurred during summer, particular attention is paid to Es morphology, including complete blanketing. Es was observed in all evaluated cases, whereas the occurrence and morphology of the other structures varied considerably among individual events. The observations indicate that different tropospheric GW-source environments can be accompanied by pronounced ionospheric variability despite the filtering of upward-propagating GWs in the middle atmosphere. Our results indicate the need for a larger-scale statistical analysis, in which the common warm-season occurrence of mid-latitude Es and severe convection must be considered. Automated Es detection from ionograms can provide the basis for this future analysis.

Keywords: troposphere–ionosphere coupling; deep convection; jet stream; MSTIDs; sporadic E

1. Introduction

The ionosphere is affected by both external and internal forcing. Solar and geomagnetic activity account for a major part of its variability, while processes and atmospheric waves originating in the lower neutral atmosphere can also affect higher altitudes [Koucká Knížová et al., 2018]. Our study considers three distinct types of tropospheric GW sources associated with vertical atmospheric motions of different origin, spatial extent, and intensity: (1) spatially extensive and long-lived organized deep convection, including mesoscale convective systems (MCSs) and squall lines; (2) highly intense local deep convection in the absence of pronounced synoptic-scale ascent or upper-level jet forcing, including supercells and air-mass convection; and (3) large-scale vertical motions associated with upper-tropospheric jet-stream dynamics. The ionosphere is regularly monitored by the DPS-4D Digisonde at Prague–Průhonice. The instrument transmits low-power HF pulses over a scanned frequency range and records echoes reflected from different ionospheric layers, providing their virtual reflection heights as a function of radio-wave frequency. Height-frequency characteristics (ionogram) is recorded every 5-min. If propagation conditions in the middle atmosphere are favorable, upward-propagating GWs can interact with the ionospheric plasma and may be manifested in ionograms by particular features such as cusps, layer splitting, spread echoes etc. (for instance in pioneering works of [Lobb and Titheridge, 1977]; Munro and Heisler, 1956; or in recent Barta, et al. 2025] and others). The pronounced seasonal differences in gravity-wave activity near the mesopause are generally attributed to selective critical-level filtering by the seasonally reversing zonal winds. Winter and summer wind

regimes allow different parts of the gravity-wave spectrum to propagate upward, producing seasonal differences in wave propagation direction, momentum flux, amplitude and dissipation [Fritts and Alexander, 2003; Rauthe et al., 2008; de Wit et al., 2015]. Lower-atmospheric gravity waves are most likely to reach thermospheric altitudes when they have relatively high horizontal phase speeds, high intrinsic frequencies, and long horizontal and vertical wavelengths. These properties make them less susceptible to critical-level filtering, molecular viscosity, and thermal diffusion. Their upward propagation depends strongly on the middle-atmospheric wind field and is favoured when the waves propagate opposite to the prevailing winds without encountering zero-wind or wind-reversal levels or undergoing premature saturation and breaking.

As the meteorological phenomena analysed here occur predominantly in summer, we restrict our study to the summer months. Sporadic E is also primarily a summertime phenomenon at mid-latitudes; therefore, we examine its behaviour as well. The possible role of upward-propagating GWs of tropospheric origin in the formation and modulation of sporadic E (Es) layers has become a subject of growing interest, as GWs may affect Es by altering the neutral wind conditions.

We use previously published and well-documented meteorological cases representing these three types source environments and complement them with two recent cases. The selected cases were restricted to periods of quiet geomagnetic activity and stable solar forcing to reduce the possible contribution of external forcing to the observed ionospheric variability.

2. Meteorological cases

2.1.Spatially extensive and long-lived organized deep convection

The first group comprises spatially extensive and long-lived organized deep convection represented by mesoscale convective systems (MCSs), i.e. organized thunderstorm systems extending at least 100 km in one horizontal direction. Three MCS cases were included in this group, representing different modes of convective organization.

On 8 July 2021, during the passage of the extratropical cyclone Zyprian, severe organized convection developed along an extensive, slowly moving cold front. The frontal environment, accompanied by an upper-tropospheric jet stream, strong vertical wind shear and pronounced instability, favoured the development of spatially extensive and persistent convection [Koucká Knížová et al., 2024].

The other two cases represent weak-forcing derechos, i.e. derechos not directly tied to the movement of a cold front. On 20 May 2022, a prefrontal squall-line MCS developed in a warm and humid convective environment. During its rapid eastward propagation across the Czech Republic, the radar-observed convective line developed a pronounced bow echo, indicating accelerated forward motion of its central portion [Potužníková and Koucká Knížová, 2025]. On 26 August 2023, two supercells formed ahead of a cold front over Bavaria and subsequently merged and organized upscale into a continuous linear MCS. The resulting system contained multiple intense convective updrafts, manifested by numerous overshooting tops along the convective line, some of which generated clearly visible concentric GWs [Barta et al., 2025].

2.2.Local severe deep convection

In contrast to MCSs, which represent spatially extensive and long-lived ensembles of convective GW sources, local severe thunderstorms, including supercells, have a smaller spatial extent but can be very intense. In both cases, the principal convective GW sources are strong updrafts and associated overshooting tops (OTs) of thunderstorm clouds, which form when strong updrafts rise above the general upper level of the cloud and penetrate into the stably stratified tropopause region before sinking back, thereby providing an efficient source of gravity waves.

Two examples of local deep convection and their possible upper-atmospheric effects were investigated in our previous studies: severe air-mass thunderstorms with supercells on 31 May

2008 [Potužníková and Koucká Knížová, 2025] and an air-mass thunderstorm on 17 August 2020 [Potužníková et al., 2023]. A recent example of intense local convection occurred over the Czech Republic on 29 June 2026, immediately following an exceptional heat wave during which the previous national temperature record, dating from 2012, was exceeded. Deep convection developed in a very warm and highly unstable air mass without direct association with an atmospheric front or the upper-level jet stream. Figure 1 shows the rapid development and evolution of several pronounced OTs, reflecting strong updrafts reaching into the lower stratosphere. The cloud-top structure evolved rapidly and included both cold-ring and cold-U signatures, i.e. very cold cloud-top regions partly or completely surrounding relatively warmer embedded areas. Such features are associated with intense deep convection and are considered indicators of potentially severe storms [Setvák et al., 2010].

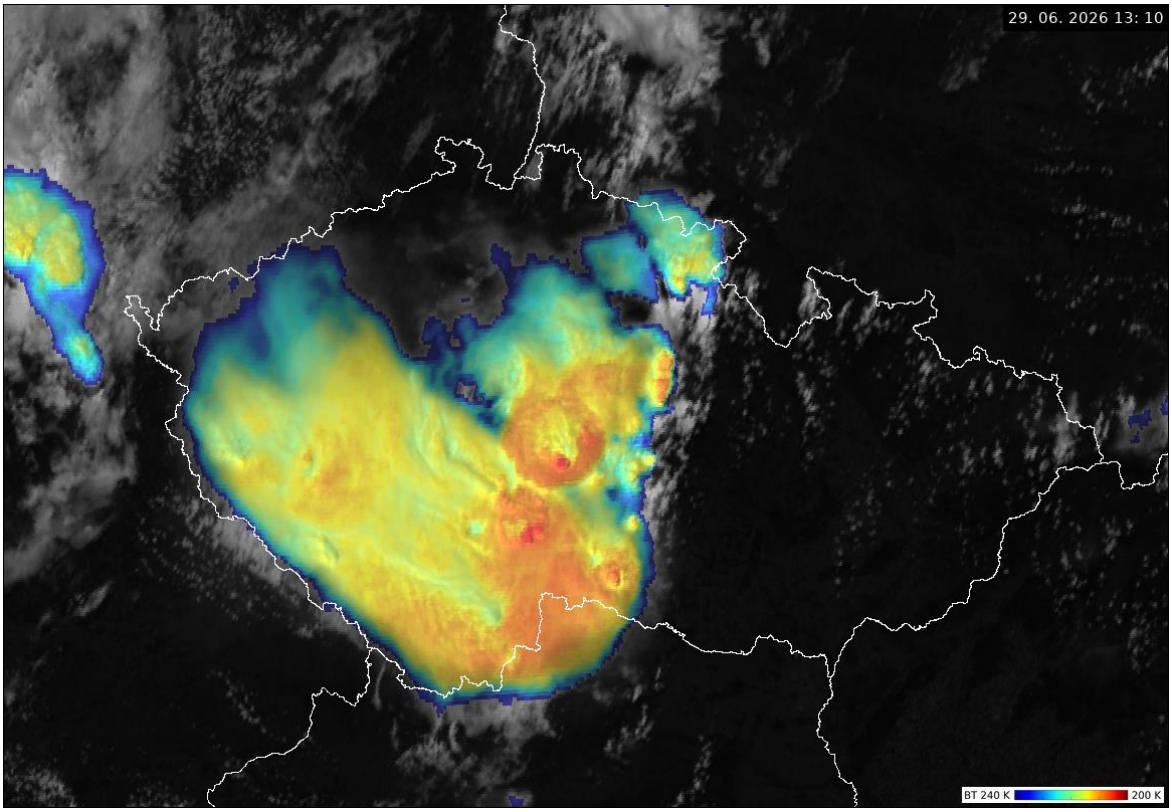


Figure 1. Intense local convection with pronounced overshooting tops over the Czech Republic on 29 June 2026 at 13:10 UTC. Sandwich product combining the FCI VIS0.6 and IR10.5 channels aboard MTG-I. The colour enhancement represents the IR10.5 brightness temperature of the storm cloud tops, with the coldest overshooting tops reaching approximately −70 °C. Radiosonde measurements from Prague–Libuš and Prostějov at 12 UTC (not depicted) show temperatures of about −55 to −60 °C in the tropopause region at approximately 12–13 km altitude, indicating that the exceptionally cold overshooting tops penetrated into the lower stratosphere.

Data: EUMETSAT; processing: M. Setvák, (CHMI).

2.3.GW generation in the upper-tropospheric jet-stream environment

Upper-tropospheric jet-stream environments can provide favourable conditions for GW generation through dynamically induced large-scale vertical motions, without the presence of deep moist convection. Local acceleration and deceleration within jet streaks, together with jet-stream curvature and meandering, induce ageostrophic circulations and associated regions of horizontal divergence and convergence near the tropopause, leading to ascending and descending

motions extending through much of the troposphere. In the stably stratified upper troposphere, these vertical motions can generate GWs.

A previously published example occurred on 29 July 2021, when an unusually southward-displaced polar jet stream extended across Central Europe in association with a deep upper-level trough. In this case, the jet-stream flow was locally modified by the Ore Mountains, enhancing wind-flow inhomogeneity and horizontal wind shear in the upper troposphere and thereby favouring GW generation. This case was analysed in detail by [Koucká Knížová et al., 2023].

A different jet–front configuration occurred over Central Europe on 8–9 September 2024 during the passage of a significant cold front. A strong cyclonically curved subtropical jet stream was associated with pronounced upper-level divergence and synoptic-scale upward motion. Water-vapour satellite imagery in Figure 2 shows an extensive cirrus cloud shield with distinct transverse cloud-wave patterns approximately perpendicular to the jet-stream flow (Figure 2), consistent with GW activity in the jet-stream region.

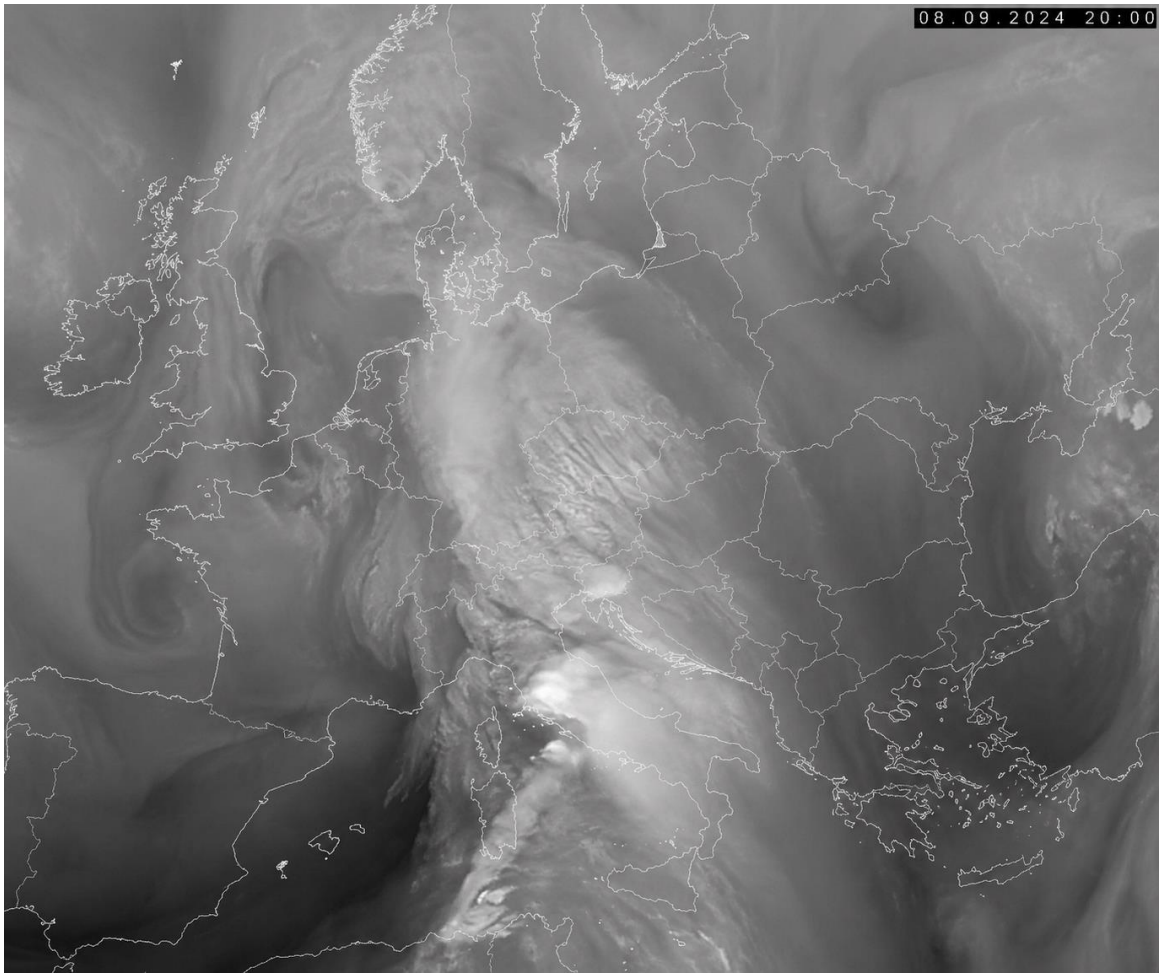


Figure 2. Meteosat Third Generation (MTG) water vapour (6.3 μm) image at 20:00 UTC on 8 September 2024. The image shows the upper-tropospheric cirrus cloud shield associated with the subtropical jet stream over Central Europe. Data source: EUMETSAT (MTG-I/FCI); processing: M. Setvák (CHMI).

3. Ionospheric observation

Examples of the characteristic ionospheric signatures identified in the analysed ionograms are shown in Figure 3. These structures reflect deformations and spatial inhomogeneities of the ionospheric reflecting regions, causing the sounding signal to return along different propagation

paths and with different propagation times. For each event, ionograms were examined over a 42-h period, from 18:00 UTC on the preceding day to 12:00 UTC on the following day as large meteorological systems may act as GW source during their entire lifetime and some of the disturbance may be identified at ionospheric heights earlier than the tropospheric system pass above the observations site. Their occurrence in the individual meteorological cases is summarized in Table 1.

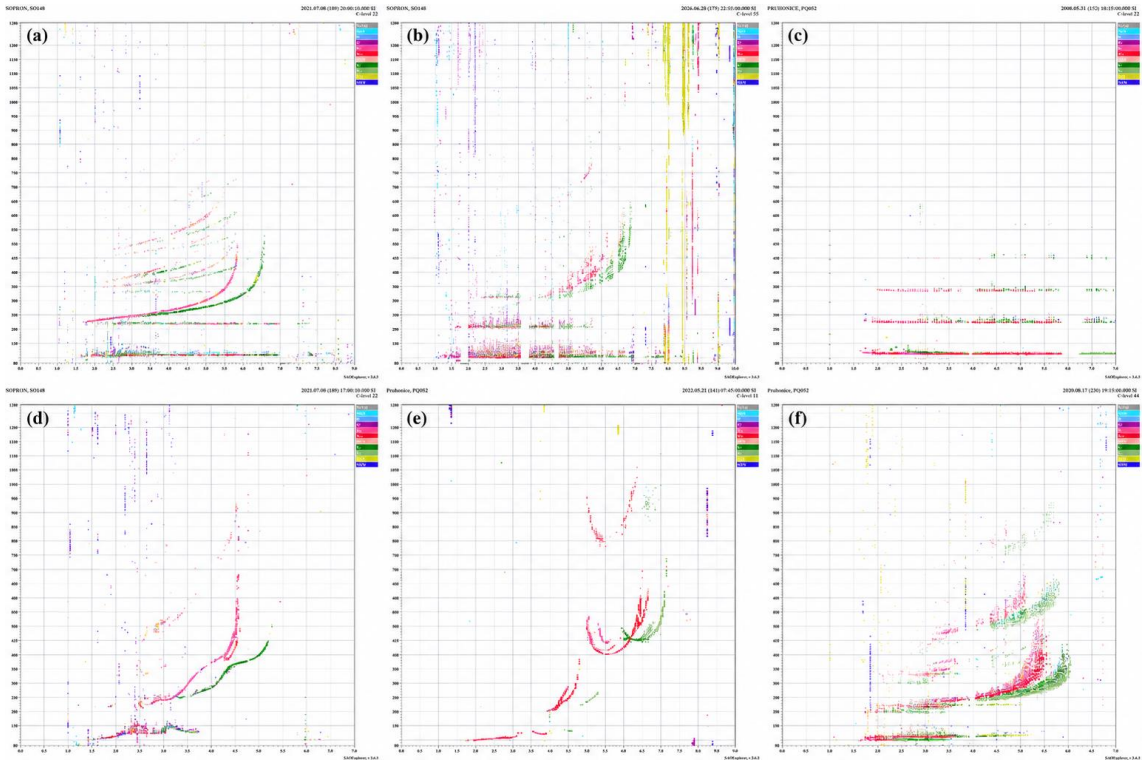


Figure 3. Examples of characteristic ionospheric signatures observed in the analyzed cases.
(a) Es layer and a well-defined F-region trace, 8 July 2021, 20:00 UTC; (b) spread Es and spread F, 28 June 2026, 22:55 UTC; (c) complete blanketing Es, 31 May 2008, 18:15 UTC; (d) spread Es and an F-region cusp, 8 July 2021, 17:00 UTC; (e) regular E layer echo and presence of Es, split recorded on both the F1 and F2 traces, 21 May 2022, 07:45 UTC; and (f) Presence of two Es structures and spread F echo, 17 August 2020, 19:15 UTC.

Table 1. *Ionospheric signatures identified in ionograms for the analyzed meteorological cases. For each event, ionograms were examined over a 42-h period from 18:00 UTC on the preceding day to 12:00 UTC on the following day.*

Meteorological case	Es	Es c.b.	Spread Es	Spread F	Cusp	Split
Extensive organized convection						
8 July 2021 extratropical cyclone Zyprian	+	+	+	+	+	+
20 May 2022 squall-line MCS	+	–	+	+	+	–
26 August 2023 MCS formed by merging two supercells	+	–	+	+	+	+

Local severe deep convection						
31 May 2008 supercell	+	+	+	+	+	+
17 August 2020 air-mass single-cell convection	+	+	+	+	+	+
29 June 2026 single-cell deep-convection outbreak	+	+	+	+	+	+
Jet-stream-related GW generation						
29 July 2021 jet-front GW generation enhanced by orography	+	+	+	+	+	+
8–9 September 2024 jet-front GW generation	+	−	+	−	−	+

4. Conclusion

The middle atmosphere acts as a selective filter for upward-propagating GWs, which may be reflected, trapped, or dissipated before reaching ionospheric heights. During summer in the Northern Hemisphere, the prevailing westward winds preferentially filter westward-propagating waves, allowing primarily eastward-propagating waves to reach thermospheric altitudes. Our observations indicate that, for the analysed events, GWs launched by tropospheric sources located far below the ionosphere are able to reach ionospheric heights and can significantly influence the behaviour of the ionospheric layers. Different tropospheric GW-source environments are accompanied by a broad range of ionospheric signatures extending from the E to the F region, and all of them are recognized to be a signatures of MSTIDs.

Sporadic E was observed in all evaluated cases. However, the event sample is rather small and case-based. The common warm-season occurrence of both mid-latitude Es and severe convection must also be considered. A statistically meaningful assessment therefore requires a long-term comparison of meteorologically active and quiet periods. Automated Es detection from ionograms can provide the basis for such a future analysis.

Acknowledgment

The authors wish to acknowledge M. Setvák from the Czech Hydrometeorological Institute for providing data. Work has been supported by National Funding Agency No. 25-19509L Czech Science Foundation (GAČR), by HORIZON-CL4-2022-Space-01-62 T-FORS (number: 101081835), ESA project QUID-Regis ESA Contract No. 4000143632/24/I-EB. and by the Johannes Amos Comenius Programme (OP JAC), project No. CZ.02.01.01/00/22_008/0004605, Natural and anthropogenic georisks.

References

Barta, V., Potužníková, K., Koucká Knížová, P. K., Chum, J., Mielich, J., Guerra, M., Burešová, D., Sivakandan, M., Verhulst, T. G. W., Berényi, K. A., Altadill, D., Segarra, A., Kouba, D., Mošna, Z., Buzás, A., Spogli, L., Urbár, J., de Paula, V., Ventriglia, V., Belehaki, A. (2025). Multi-instrument analysis of medium-scale travelling ionospheric disturbances generated by an intense tropospheric jet-front system with severe convection in Europe in August 2023. *Journal of Space Weather and Space Climate*, Vol. 15, 31. DOI: 10.1051/swsc/2025025.

Fritts, D. C., Alexander, M. J. (2003). Gravity wave dynamics and effects in the middle atmosphere. *Reviews of Geophysics*, Vol. 41, No. 1, 1003. DOI: 10.1029/2001RG000106.

Koucká Knížová, P. K., Georgieva, K., Mošna, Z., Kozubek, M., Kouba, D., Kirov, B., Potužníková, K., Boška, J. (2018). Solar signals detected within neutral atmospheric and ionospheric parameters. *Journal of Atmospheric and Solar-Terrestrial Physics*, Vol. 171, pp. 147–156. DOI: 10.1016/j.jastp.2017.12.003.

Koucká Knížová, P. K., Potužníková, K., Podolská, K., Hannawald, P., Mošna, Z., Kouba, D., Chum, J., Wüst, S., Bittner, M., Kerum, J. (2023). Multi-instrumental observation of mesoscale tropospheric systems in July 2021 with a potential impact on ionospheric variability in midlatitudes. *Frontiers in Astronomy and Space Sciences*, Vol. 10, 1197157. DOI: 10.3389/fspas.2023.1197157.

Koucká Knížová, P. K., Potužníková, K., Podolská, K., Šindelářová, T., Bozóki, T., Pásztor, M. S., Szárnya, C., Mošna, Z., Kouba, D., Chum, J., Zacharov, P., Buzás, A., Hanzlíková, H., Kozubek, M., Burešová, D., Bozsó, I., Berényi, K. A., Barta, V. (2024). Impacts of storm "Zyprian" on middle and upper atmosphere observed from Central European stations. *Remote Sensing*, Vol. 16, 4338. DOI: 10.3390/rs16224338.

Lobb, R. J., Titheridge, J. E. (1977). The effects of travelling ionospheric disturbances on ionograms. *Journal of Atmospheric and Terrestrial Physics*, Vol. 39, No. 2, pp. 129–138. DOI: 10.1016/0021-9169(77)90106-4.

Munro, G. H., Heisler, L. H. (1956). Cusp type anomalies in variable frequency ionospheric records. *Australian Journal of Physics*, Vol. 9, No. 3, pp. 343–358. DOI: 10.1071/PH560343.

Potužníková, K., Koucká Knížová, P. K., Chum, J., Podolská, K., Kouba, D., Mošna, Z., Georgieva, K., Bojilova, R., Kirov, B., Asenovski, S. (2023). Summer tropospheric mesoscale situations with impact on the ionospheric plasma. *Proceedings of the Fifteenth Workshop "Solar Influences on the Magnetosphere, Ionosphere and Atmosphere"*, pp. 89–97. ISSN 2367-7570. DOI: 10.31401/WS.2023.proc.

Potužníková, K., Koucká Knížová, P. K. (2025). Observation of tropospheric deep convection in mid-latitudes with potential impact up to ionospheric heights. *Proceedings of the Seventeenth Workshop "Solar Influences on the Magnetosphere, Ionosphere and Atmosphere"*, pp. 118–122. ISSN 2367-7570. DOI: 10.31401/WS.2025.proc.16.

Rauthe, M., Gerding, M., Höffner, J., Lübken, F. J. (2008). Seasonal changes in gravity wave activity measured by lidars at mid-latitudes. *Atmospheric Chemistry and Physics*, Vol. 8, pp. 6775–6787. DOI: 10.5194/acp-8-6775-2008.

Setvák, M., Lindsey, D. T., Novák, P., Wang, P. K., Radová, M., et al. (2010). Satellite-observed cold-ring-shaped features atop deep convective clouds. *Atmospheric Research*, Vol. 97, pp. 80–96. DOI: 10.1016/j.atmosres.2010.03.009.

de Wit, R. J., Hibbins, R. E., Espy, P. J. (2015). The seasonal cycle of gravity wave momentum flux and forcing in the high-latitude Northern Hemisphere mesopause region. *Journal of Atmospheric and Solar-Terrestrial Physics*, Vol. 127, pp. 21–29. DOI: 10.1016/j.jastp.2014.10.002.

DOI: 10.31401/WS.2026.proc.29

Examination of Extremely Big Mesospheric Electric Fields from Rocket-Borne Measurements on October 21 1989

Tonev P.

Space Research and Technology Institute, Bulgarian Academy of Sciences

Abstract.

The profile of the vertical electric field Ez in the region 24 - 69 km obtained by rocket borne measurements on October 21 1989 over the South Indian Ocean [Zadorozhny et al., 1994] is examined. The experiment coincides with the major geomagnetic storm from October 20 and with GLE 43 event. The profile of E_z is characterized by well expressed peculiarities. E_z reaches extremely big maximums (~10 Vm^{-1}) of both polarities in the mesosphere and upper stratosphere. This peculiar profile of E_z is indication for gradual decrease of mesospheric conductivity as result of increase of aerosol density during the SEP event. Represented is an idea of a mechanism of aerosol density increase in the atmospheric regions of impact ionization. Our preliminary estimations show that the aerosol increase during GLE 43 according to the mechanism cause strong decrease of atmospheric conductivity which can explain the peculiar experimental results.

1. Introduction

Studied are the results of rocket-borne experimental measurements of the vertical component E_z of the electric field at altitudes 23 - 69 km conducted in South Indian Ocean at geographic coordinates (58°5S, 51°1E) on October 21 1989, at 19:31 UT (that is, close to the local midnight) [Zadorozhny et al., 1994]. The measurements are conducted during the major solar proton event (SPE) with ground-level enhancement from October 19 1989 (GLE 43). The SPE is characterized by extremely big flux of protons with energies E_p<14.5 MeV for 56.5 hours after the onset of SPE [Marvin and Gorney, 1991]. The SPE is accompanied by a major geomagnetic storm from October 20 1989 with maximum planetary index of geomagnetic activity Kp=8+, and Kp=8 at the time of the rocket flight. The experimentally obtained profile of the vertical electric field E_z is shown in Fig.1 by solid curve [Zadorozhny et al., 1994]. Here a convention is used that downward E_z is positive, and vice/versa. The dashed curve shows the profile of density ρ of spatial electric charge. Peculiarities are revealed. While the electric field E_z is downward above 50 km altitude, it is upward below z=50 km.

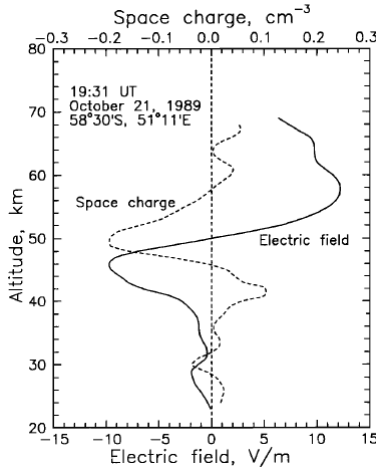


Figure 1. *Profiles of the rocket-borne vertical electric field $E_z(z)$ (solid line), and of the density $\rho(z)$ of the electric spatial charge derived from Gauss's law (dashed line).*

The reversal of E_z to upward contradicts to the direction of electric currents in the fair-weather regions of global atmospheric electric circuit (GEC) [Rycroft et al., 2008] where the current J_{FW} from the ionosphere to surface is downward. E_z reaches extremely big maximums of both polarities: E_z=+12.3 V/m at altitude z=58 km, and E_z= –9.7 V/m at z=46 km. For nighttime undisturbed profile of conductivity [Hale, 1984] $\sigma=2.5\times10^{-8}$ Sm^{-1} at altitude z=58 km, $\sigma=2\times10^{-10}$ Sm^{-1} at z=46 km; the electric current $J_z=\sigma E_z$ would be $J_z= +3.1\times10^{-7}$ Am^{-1} at z=58 km, and $J_z= -1.9\times10^{-9}$ Am^{-1} at z=46 km: J_z is larger by three to five orders of magnitude than J_{FW}. The discrepancy will be even larger if an enhancement of conductivity due to ionization is taken into account. Besides, the spatial electric charge density ρ in the layer 46 - 58 km is $\rho<0$. An explanation of these peculiarities is proposed.

The extremely big electric fields E_z in mesosphere and upper stratosphere mean decrease of conductivity σ by several orders of magnitude (the alternative assumption for reciprocal increase of electric current J_z does not seem plausible). We show that such decrease of mesospheric conductivity σ can be gradually completed on a definite phase of SPE together with a simultaneous increase of aerosol density S related to the ionization by energetic protons. The direct effect of ionization, the increase of conductivity is realized on an earlier phase. Later this effect is being masked by the reverse effect of increasing aerosol density on conductivity.

2. Hypothetic mechanism of aerosol creation and conductivity decrease during SPE

Considered are atmospheric processes during SEP events which can cause gradual decrease of conductivity in atmospheric regions Reg$_P$ in both hemispheres where the proton cutoff rigidity does not exceed 1 MeV. Each region Reg$_P$ includes the magnetic pole and invariant latitudes λ, $|\lambda|>|\lambda_B|$, where λ_B depends on the geomagnetic activity. Rodger et al. (2006) obtain $|\lambda_B|$ as function of Kp index (their Fig.4, and Eq.(2)); $|\lambda_B|\approx56°$ for Kp=8. The rocket launch is at invariant latitude $\lambda_{RE}= -59.5°$, that is, it is well inside the region Reg$_P$.

In this paper described is an idea of a mechanism of aerosol production in regions Reg$_P$ during SPE which causes decrease of atmospheric conductivity σ. There are indirect experimental confirmations: demonstrated has been significant increase of aerosol density in lower and middle stratosphere [Shumilov et al., 1996; Mironova et al., 2012] for few days after GLE events. The mechanism proposed here includes creation, growth, multiplication, and transportation of aerosol particles (AP) in regions Reg$_P$. We assume that initially APs can be created at altitudes ~70-120 km from cosmic (meteoric) smoke particles (MSP) [Hedin et al., 2014; Rapp, 2000]. A MSP with size of few nanometers can serve as a nucleus which grows into an AP by attachments of ions. While a growing particle is small (with radius r_A <~ 4 nm) it is critical and can degrade. By reaching radius r_A>4 nm an AP reaches stability. To clarify the idea of the mechanism of aerosol creation and of a causative decrease of the conductivity in Reg$_P$, the following system of equations of ionization is considered:

$$dn_{e,i}/dt = q - L_R - L_{Ae,i} \tag{1}$$

Here n_e and n_i are the densities of electrons and ions. L_R and $L_{Ae,i}$ are competing terms of losses of electrons and ions. $L_R=\alpha n_e n_i$, α is the coefficient of electron-ion recombination. L_A is the term of losses of electrons and ions as result of their attachment to aerosol particles.

$$L_{Ae,i} = B_{e,iA} n_{e,i} \qquad \text{where} \qquad B_{e,iA} = \sum_{r_A,k_A} \beta_{e,i}(r_A,k_A) S(r_A,k_A) \tag{2}$$

Here $S(r_A,k_A)$ is the density of APs with radius r_A and k_A charges with the respective sign.

The proposed mechanism is based on the assertion that the terms $L_{Ae,i}$ increase quasi-exponentially with time t for specific set of parameters. While L_{As} becomes much bigger than

L_{Rs} $n_{e,i}$ and conductivity $\sigma = q_e(\mu_e n_e + \mu_i n_i)$ decrease quasi-exponentially. Here $q_e = 1.6\times10^{-19}$ C is the elementary charge, $\mu_{e,i}$ is the coefficients of electron and ion mobility.

We use the theory of attachment of an electron or ion to an AP developed by Hoppel (1985), Hoppel and Frick (1986), Rapp (2000). According to this theory the interaction of an electron or ion with a big particle (neutral or charged) is determined by the potential $\phi = \phi_C + \phi_P$ where ϕ_C corresponds to Coulomb interaction, and ϕ_P – to the image force of the polarization interaction. Hoppel (1985); Hoppel and Frick (1986) estimate the coefficients $\beta_{e,iA}$ of attachment of a ion/ electron to a big spherical particle with radius r_A and charge k_A (k_A is for the number of elementary charges and their polarity) as functions of r_A and k_A: $\beta_{e,iA}(r_A, k_A)$ increase with r_A, as well as with $|k_A|$ when AP is neutral or oppositely charged. These properties determine acceleration of the growth of APs with time t.

Considered are two phases of growth of an AP. On the first phase small APs grow by attachment of ions only. The growth of APs on this phase is realized by repeating of two main processes: *A1*) Attachment of a free electron to a big neutral (k_A=0) particle (MSP or AP) with radius r_A; *A2*) Attachment of a positive ion to a negatively charged big particle. With the increase of r_A attachments of electrons to negatively charged APs (k_A<0) are typical too (Rapp, 2000). The second phase concerns large multi-charged APs – they grow by attachment of ions, as well as of small MSPs, or of cluster molecules with $k_A \le 0$ by polarization interaction between particles.

The behaviour of any critical AP is described as a probabilistic process. If p_S is the probability of a critical AP to grow to a stable one (with radius r_{AS}) then $1-p_S$ is the probability that an AP degrades before reaching stability. We assume that a degrading AP is fully destroyed with probability p_D, and is split into two smaller APs with probability $1-p_D$. The density S_C of critical APs is a function of time, $S_C(t)$:

$$S_C(t) = S_{C0}\exp(t/t_C) \qquad \text{where} \qquad t_C = N_{AP}/(2B_{iA}P) \tag{3}$$

In (3) S_{C0} is the initial density of critical APs, N_{AP} is the mean number of the ions which compose an AP, $P = (1-p_S)(1-2p_D)$. (3) shows that $S_C(t)$ increases if p_D<0.5.

An estimation of decrease of the conductivity is approximate due to the numerous uncertainties. If $p_D << 0.5$ B_{iA} (2) increases fast so that L_{Ai} can become much bigger than L_R within the few hours after the onset of SPE. In such case almost all ions produced during SPE until time t_{RE} (in 56.5 hours) attach to APs. The total number of ions per cm^3 N_i produced in this time is roughly estimated by adaptation of results for the profile of electron production rate $q(z)$ during GLE 69 as function of the cutoff rigidity for protons [Velinov et al., 2013, their Figs.6-8]. Since the integrated flux of protons with energies <10 MeV for GLE 43 is bigger than the one for GLE 69 we obtain for z~80 km that N_i is of the order of 10^{10} cm^{-3}, and $S_C = N_i/N_{AP}$. B. For quasi-equilibrium state at time t_{RE} terms dn_i/dt and L_R in Eq.(1) are negligible. We obtain from Eq.(1) that n_i can be as low as few units per cm^3 for β_{iA} ~10^{-6} cm^{-3}s^{-1} [Hoppel and Frick, 1986]. Then, the modified ion conductivity $\sigma_{Mi} = q_e\mu_i n_i$ will be ~5×10^{-13} - 10^{-12} Sm^{-1} by unmodified ion mobility μ_i=1.4x10^4 cm^{2}V^{-1}s^{-1}. However, there are additional factors: *i*) the effect of big APs is not taken into account for which the coefficient β_{iA} can be 10 times larger; *ii*) the ion mobility μ_i can suffer significant decrease due to big AP density S. These and other factors determine additional decrease of σ_{Mi} by up to two orders of magnitude, or even more.

A key parameter for estimation of the level of decrease of the electron conductivity σ_e is the electron-AP attachment coefficient $\beta_{eA}(r_A,k_A)$. Rapp (2000) obtains that β_{eA} is between10^{-4} cm^{-3}s^{-1} for small r_A, k_A, and β_{eA}~10^{-2} cm^{-3}s^{-1} for big r_A, k_A for electrons with thermal energies – this determines insufficient decrease of σ_e. Free electrons produced by ionization by protons of energies >1 MeV are with much bigger initial energy. This can lead

to changes in cross-sections for the considered reactions; respectively, bigger β_{eA}. The decrease of σ_e can be then of the order of the decrease of σ_i, due to electron depletion known as electon bite-outs [Friedrich at al., 2011].

Simultaneously with its growth an AP created above ~80 km is transported to lower altitudes (depending on the AP's radius r_A) by gravitational sedimentation on the timescale of SEP. Big APs can descend to the mesosphere and upper stratosphere and be accumulated there. Processes of their further growth by attachment and of multiplication will lead to quasi-exponential increase of their density S, and to respective decrease of conductivity.

3. Modifications of atmospheric electric parameters in region R_P

The decrease of modified conductivity σ_M to values $\sigma_M <\sim 10^{-11}$ Sm^{-1} at altitudes $z > z_{M0}$ =35 km determines vertical electric current inside region Reg$_P$. The total vertical electric current J_z is:

$$J_z = J_{FW} + J_P + J_T \,. \tag{4}$$

Here $J_{FW} = V_I / R_C$ is the electric current from the ionosphere to surface in fair-weather regions of GEC, V_I ~250 kV is the ionospheric potential, R_C is the columnar resistance. The electric current J_P is generated because of the unbalanced distribution of uncompensated elementary positive charges in GEC injected into atmosphere together with the energetic solar protons [Tonev, 2024]. J_T is a transient electric current generated of redistribution of spatial electric charges. Electric current J_P satisfies the equation:

$$dJ_P(z)/dz = 10^4 q_e D\left(E_{ps}(z)\right)\left[dz/d\,E_{ps}(z)\right]^{-1} \tag{5}$$

with boundary condition $\Delta J_P = J_P(z=120\text{ km}) - J_P(z=0) = 10^4 q_e F_p$. D is differential spectrum of the proton flux, and F_p is the integrated proton flux above the atmosphere. $E_{ps}(z)$ is the initial energy of protons which lose their energy (stop) at altitude z. Eq.(5) shows that the direction of J_P is changed at an altitude z_P: J_P flows upwards at $z>z_P$, and downward at $z<z_P$. The experimental profile of E_z (Fig.1) shows that z_P is located at 50-60 km altitude.

While the decrease of σ_M in an upper part of region Reg$_P$ (above an altitude z_{Mmax}~60 km) is controlled mainly by attachments and growth of APs, below z_{Mmax} it depends mainly on gravitational sedimentation of APs on the timescale of GLE 43 which declines towards lower altitudes. The combined effect of processes of attachment, splitting, and sedimentation of APs on σ_M will be strongest at z_{Mmax}=58 km with maximum decrease of σ_M. These processes have no effect at altitude z_{M0}~35 km: $\sigma_M(z=z_{M0})$ remains unmodified. This determines a negative conductivity gradient $d\sigma_M/dz<0$ in the layer L_{NC} [z_{M0}, z_{Mmax}]. When the electric current J_z is downward, negative spatial charge with density $\rho(z)<0$ will be accumulated in [z_{M0}, z_{Mmax}] according to the following expression:

$$\rho(z,t) = \rho_0(z)\left[1-\exp\left(-(t-t_0)/\tau_R(z)\right)\right] \quad \text{where} \quad \rho_0 = -J_z\, d\tau_R(z)/dz < 0 \tag{6}$$

Here $\tau_R(z) = \varepsilon_0/\sigma_M(z)$ is the electric charge relaxation time at altitude z, ε_0=8.85×10^{-12} Fm^{-1} is the vacuum permittivity. Eq.(6) is derived from Maxwell's equations for quasi-static case. This result explains presence of the layer [46 - 58 km] with negative spatial electric charge. As it is shown below, the positive density ρ in the layer [35 - 46 km] is result of strong variability of the transient electric current J_T at altitudes of relatively big conductivity.

4. Explanation of the reversal of Ez to upward direction below 50 km altitude

Below z=50 km the vertical electric field E_z is directed upwards ($E_z<0$, $J_z<0$). This seems to contradict to the fact that $J_{FW}>0$, and $J_P>0$. This situation can be explained by generation of

big upward transient current J_T. The reason can be even small fluctuations of the geomagnetic field during the major geomagnetic storm. Such fluctuations can lead to significant changes of the cutoff rigidity for protons at invariant latitude λ_{RE} since λ_{RE} is close to λ_B. According to Rodger et al. (2006) (their Fig.4, and Eq.(2)) a small decrease of index Kp corresponds to big increase of the cutoff at latitude $\lambda=\lambda_{RE}$. The result of a sudden increase of cutoff rigidity will be strong change in the height distribution of electric current J_P in (5).

Characteristics are derived first for a time period of equilibrium before the time t_0 of the cutoff change. The flux of protons with energies E_p>1 MeV at the top of the atmosphere is obtained to be ~6×10^2 $cm^{-2}s^{-1}$ by the use of exponential extrapolation of GOES-7 data for protons with energies E_p>4.2 MeV at time t_{RE} of the rocket flight. This yields $\Delta J_P \sim 10^{-12}$ Am^{-2}. If accept that the average modified conductivity between ~50 km and ~90 km is $\sigma_M \approx 4\times10^{-13}$ Sm^{-1} (according to our estimations above, and those by Holzworth et al. (2004) for noctilucent clouds) the columnar resistance $R_C=V_I/J_{FW}$ increases twice (from ~10^{-17} Ωm^2 to ~2×10^{-17} Ωm^2), and J_{FW} decreases also twice, J_{FW} ~10^{-12} Am^{-2}. Hence, the strongly decreased conductivity at altitudes z>58 km determines before t_0 that electric current J_P has a big contribution to J_z below in (4) (about 50%). The quasi-constant downward electric current J_z causes accumulation of negative spatial charge with density $\rho(z)$<0 between z_{M0}=35 km and z_{Mmax}=58 km according to (6).

The sudden increase of the cutoff rigidity at time t_0 will cause a decrease of ΔJ_P, and redistribution of J_P by altitude z, so that below z=58 km the contribution of J_P in (4) can become negligible. Because of the big contribution of J_P in the total electric current J_z before time t_0 J_z will suddenly decrease to $J_{zd} = CJ_z$ by tens of percent. This big change will lead to redistribution of spatial charges in layer L_{NC} after t_0. Their density $\rho_r(z,t)$ is expressed below.

$$\rho_r(z,t) = [\rho_{r0}(z) - \rho_0(z)][1 - \exp(-\Delta t/\tau_R(z))] + \rho_0(z), \qquad \rho_{r0}(z) = C\rho_0(z). \tag{7}$$

Here $\Delta t=t-t_0$. Transient electric current $J_T(z,t)$ is generated at altitudes $z< z_{PR}$ is a result of this spatial charge redistribution. We obtain the height profile $J_{T0}(z) = J_T(z,t)$ at $t=t_0$ when J_T has maximum contribution in (4). For this goal the profile of modified conductivity $\sigma_M(z)$ in layer L_{NC} is represented by exponential function: $\sigma_M(z) = \sigma_0 \exp[(z_{M0}-z)/H_M]$ where $\sigma_{M0}=\sigma(z=z_{M0})$, H_M>0 is scale height. The profile $J_{T0}(z)$ is expressed, as follows:

$$J_{T0}(z) = \int_z^{z_{M\max}} \frac{d\rho_r(z,t=0)}{dt} dz = -J_{z0}(z_{M\max} - z)/H_M < 0 \tag{8}$$

Here Eq.(8) shows that at the time $t=t_0$ of the cutoff change the transient electric current $J_T(z)$ exceeds $|J_{z0}|= |J_{FW}+J_P|$ at altitudes $z < z_{PR} - H_M$, that is: a) $J_z(z,t_0)$ becomes zero at altitude $z_0 = z_{PR} - H_M$; *b*) $J_z(z,t)$ is upward (J_z <0) at altitudes below z_0. $|J_T(z,t)|$ decreases quasi-exponentially by $t>t_0$, and the altitude z_0 (at which J_z changes its sign) descends with time. The upward direction of the vertical electric field $E_z=J_z/\sigma_M$ below 50 km is explained by (8). These results confirm that the altitude z_P of change of direction of J_P is located above 50 km, and the columnar resistance at $z>z_P$ is comparable to the one below z_P.

5. Conclusions

Studied are the rocket-borne extremely large vertical electric fields E_z in mesosphere measured during GLE 43 and the major geomagnetic storm from October 20 1989 [Zadorozhny et al., 1994]. E_z reaches about 10 Vm^{-1} both in downwards (at 58 km altitude) and in upward (at z=46 km) directions. These results demonstrate dramatic decrease of conductivity (by three to five orders of magnitude). In order to explain these peculiarities proposed is a hypothetic mechanism of creation of aerosol particles of extremely high density S during solar proton events which can cause such conductivity decrease. There are

experimental indirect confirmations of aerosol production during SPEs. The mechanism of aerosol production in atmospheric regions of reach of energetic protons which is proposed is based on the theory of ion-aerosol attachment. The approximate estimations show that during GLE 43 conductivity in the mesosphere can gradually decrease al least down to 10^{-12} Sm^{-1}. The proposed hypothetic mechanism is developed from the one used by Tonev (2022, 2024), Tonev and Asenovski (2023) explain peculiar, yet typical response of GEC in middle stratosphere, as well as at ground level at high latitudes to series of GLE events documented by Holzworth et al. (1987), Kokorowski et al. (2006), Shumilov et al. (2016).

An explanation is proposed of the reversal of the vertical electric field E_z below 50 km altitude into upward direction. This reversal is explained as result of even small fluctuations in the geomagnetic field. It can be caused by upward transient electric current generated due to suddenly unbalanced spatial electric charges.

References

Friedrich, M., Rapp, M., Plane, J. M. C., Torkar, K. M. (2011). Bite-outs and other depletions of mesospheric electrons. *Journal of Atmospheric and Solar-Terrestrial Physics*, Vol. 73, pp. 2201–2211. DOI: 10.1016/j.jastp.2010.10.018.

Hale, L. C. (1984). Middle atmospheric electrical structure, dynamics, and coupling. *Advances in Space Research*, Vol. 4, pp. 175–186. DOI: 10.1016/0273-1177(84)90283-7.

Hedin, J., Giovane, F., Waldemarsson, T., Gumbel, J., et al. (2014). The MAGIC meteoric smoke particle sampler. *Journal of Atmospheric and Solar-Terrestrial Physics*, Vol. 118, pp. 127–144. DOI: 10.1016/j.jastp.2014.03.003.

Holzworth, R. H., Norville, K. W., Williamson, P. R. (1987). Solar flare perturbations in stratospheric current systems. *Geophysical Research Letters*, Vol. 14, No. 8, pp. 852–855. DOI: 10.1029/GL014i008p00852.

Holzworth, R. H., Goldberg, R. A. (2004). Electric field measurements in noctilucent clouds. *Journal of Geophysical Research: Atmospheres*, Vol. 109, D16203. DOI: 10.1029/2003JD004468.

Hoppel, W. A. (1985). Ion-aerosol attachment coefficients, ion depletion, and the charge distribution on aerosols. *Journal of Geophysical Research*, Vol. 90, No. D4, pp. 5917–5923.

Hoppel, W. A., Frick, G. M. (1986). Ion-aerosol attachment coefficients and the steady-state charge distribution on aerosols in a bipolar ion environment. *Aerosol Science and Technology*, Vol. 5, No. 1, pp. 1–21. DOI: 10.1080/02786828608959073.

Kokorowski, M., Sample, J. G., Holzworth, R. H., Bering, E. A., Bale, S. D., Blake, J. B., et al. (2006). Rapid fluctuations of stratospheric electric field following a solar energetic particle event. *Geophysical Research Letters*, Vol. 33, L20105. DOI: 10.1029/2006GL027718.

Marvin, D. C., Gorney, D. J. (1991). Solar proton events of 1989: Effects on spacecraft solar arrays. *Journal of Spacecraft and Rockets*, Vol. 28, No. 6, pp. 713–719. DOI: 10.2514/3.26304.

Mironova, I. A., Usoskin, I. G., Kovaltsov, G. A., Petelina, S. V. (2012). Possible effect of extreme solar energetic particle event of 20 January 2005 on polar stratospheric aerosols: Direct observational evidence. *Atmospheric Chemistry and Physics*, Vol. 12, pp. 769–778. DOI: 10.5194/acp-12-769-2012.

Mironova, I. A., Aplin, K. L., Arnold, F., Bazilevskaya, G. A., Harrison, R. G., Krivolutsky, A. A., Nicoll, K. A., Rozanov, E. V., Turunen, E., Usoskin, I. G. (2015). Energetic particle influence on the Earth's atmosphere. *Space Science Reviews*, Vol. 194, pp. 1–96. DOI: 10.1007/s11214-015-0185-4.

Rapp, M. (2000). Capture rates of electrons and positive ions by mesospheric aerosol particles. *Journal of Aerosol Science*, Vol. 31, No. 11, pp. 1367–1369. DOI: 10.1016/S0021-8502(00)00030-6.

Rodger, C. J., Clilverd, M. A., Verronen, P. T., Ulich, T., Jarvis, M. J., Turunen, E. (2006). Dynamic geomagnetic rigidity cutoff variations during a solar proton event. *Journal of Geophysical Research: Space Physics*, Vol. 111, A04222. DOI: 10.1029/2005JA011395.

Rycroft, M. J., Harrison, R. G., Nicoll, K. A., Mareev, E. A. (2008). An overview of Earth's global electric circuit and atmospheric conductivity. *Space Science Reviews*, Vol. 137, Nos. 1–4, pp. 83–105. DOI: 10.1007/s11214-008-9368-6.

Shumilov, O. I., Kasatkina, E. A., Henriksen, K., Vashenyuk, E. V. (1996). Enhancement of stratospheric aerosols after solar proton event. *Annales Geophysicae*, Vol. 14, pp. 1119–1123. HAL: hal-00316221.

Shumilov, O. I., Kasatkina, E. A., Frank-Kamenetsky, A. V. (2015). Effects of extraordinary solar cosmic ray events on variations in the atmospheric electric field at high latitudes. *Geomagnetism and Aeronomy*, Vol. 55, pp. 666–674. DOI: 10.1134/S0016793215050151.

Tonev, P. T. (2022). Peculiar atmospheric electric field response at high latitude to three major SEP events in 2001 and possible interpretation. *Proceedings of the Fourteenth Workshop "Solar Influences on the Magnetosphere, Ionosphere and Atmosphere"*, pp. 77–82. DOI: 10.31401/WS.2022.proc.13.

Tonev, P., Asenovski, S. (2023). Hypothetic atmospheric response to SEP explaining peculiar electric fields and currents at high latitudes. *Proceedings of the Fifteenth Workshop "Solar Influences on the Magnetosphere, Ionosphere and Atmosphere"*, pp. 125–131. ISSN 2367-7570. DOI: 10.31401/WS.2023.proc.

Tonev, P. (2024). Hypothetic explanation of peculiar atmospheric electric response to SEP at high latitudes: Experimental evidence. *Proceedings of the Sixteenth Workshop "Solar Influences on the Magnetosphere, Ionosphere and Atmosphere"*, pp. 94–99. DOI: 10.31401/WS.2024.proc.14.

Velinov, P. I. Y., Asenovski, S., Kudela, K., Lastovička, J., Mateev, L., Mishev, A., Tonev, P. (2013). Impact of cosmic rays and solar energetic particles on the Earth's ionosphere and atmosphere. *Journal of Space Weather and Space Climate*, Vol. 3, A14. DOI: 10.1051/swsc/2013036.

Zadorozhny, A. M., Kikhtenko, V. N., Kokin, G. A., Tuchkov, G. A., Tyutin, A. A., Chizhov, A. F., Shtirkov, O. V. (1994). Middle atmosphere response to the solar proton events of October 1989 using the results of rocket measurements. *Journal of Geophysical Research: Atmospheres*, Vol. 99, No. D10, pp. 21059–21069. DOI: 10.1029/93JD03194.

DOI: 10.31401/WS.2026.proc.30

Influence of strong Solar Proton Events of the 23rd Solar Cycle on the High-Latitudinal Atmosphere of the Northern Hemisphere

Veretenenko S.V.[1], *Koval A.V.*[2]

[1]Ioffe Institute, Russian Academy of Sciences, St. Petersburg, Russia; s.veretenenko@mail.ioffe.ru
[2]St. Petersburg State University, St. Petersburg, Russia

Abstract

In this work, we study variations of atmospheric characteristics at high latitudes of the Northern Hemisphere associated with the strongest Solar Proton Events (SPEs) of the 23rd solar cycle, the data from MERRA-2 archive being used. Three series of SPEs were considered: 1) 26 October – 4 November, 2003 (the "Halloween" events); 2) 15–20 January, 2005; 3) 5–14 December, 2006. It was found that, in the lower atmosphere, all the studied SPE series were accompanied by an intensification of cyclone regeneration (secondary deepening) near the south-eastern coast of Greenland and a noticeable increase of the North Atlantic Oscillation index. In the middle atmosphere, an intensification of the stratospheric polar vortex was found after the beginning of all the studied series, with the increase of zonal wind velocity being strongest in the North Atlantic region. The SPEs under study were also accompanied by pronounced variations in planetary wave activity, which was characterized by the amplitudes of PW1 and PW2 (planetary waves with zonal numbers 1 and 2, respectively), as well as the vertical component of the Eliassen-Palm flux. The polar vortex intensification associated with the events in January, 2005 and December, 2006 was followed by its pronounced weakening, which resulted in the development of a stratospheric warming about 2 weeks after the last event of the series.

Keywords: Solar Proton Events; North Atlantic Oscillation; stratospheric polar vortex.

1. Introduction.

Energetic charged particles, including both solar and galactic cosmic rays, are now believed to be an important link connecting weather and climate variations with solar activity. Cosmic rays can penetrate deeply into the atmosphere producing ionization and their fluxes are influenced significantly by solar activity. Unlike galactic cosmic rays (GCRs) arriving constantly at the Earth's orbit, bursts of solar cosmic rays (mostly protons) occur sporadically, more frequently at sunspot maxima, and are associated with explosive energy release on the Sun (solar flares). Solar cosmic rays are less energetic than galactic ones, their energies usually do not exceed 1 GeV, however, their fluxes may be huge compared with GCR fluxes. Due to a steep energy spectrum (i.e., particle fluxes decrease rapidly with increasing energy) and geomagnetic cutoff, intrusions of solar protons into the Earth's atmosphere are limited, as a rule, by polar latitudes, where they contribute to a significant enhancement of atmospheric ionization. The ionization increase, in turn, may result in a large number of geophysical effects, such as changes of the chemical composition of the polar atmosphere (ozone depletion), perturbations of the global electric circuit, polar cap absorption of radiowaves etc. [Miroshnichenko, 2008].

A noticeable intensification of extratropical cyclonic activity associated with Solar Proton Events (SPEs), with particle energies above 90 MeV, which is enough to penetrate altitudes of the upper stratosphere, were detected in [Veretenenko and Thejll, 2004, 2008]. However, the mechanism of SPE influences on the atmospheric circulation remains unclear. So, a comprehensive study of SPE effects including not only the lower, but also the middle atmosphere, where SPEs contribute to an increase in ionization rate, is needed. The aim of this

study is to consider variations of different characteristics of the high-latitudinal lower and middle atmosphere in the course of the strongest Solar Proton Events of the 23rd solar cycle.

2. Characteristics of Solar Proton Events

The studied series of SPEs occurred on the descending phase of the 23rd solar cycle, being associated with noticeable enhancements of flare activity on the Sun (Figure 1, top panel). All the events of the series were characterized by increases of solar proton fluxes with energies >100 MeV, which can penetrate to altitudes of ~32 km and below. Among them, we can note 6 events with proton energies >500 MeV; these particles participate in nuclear interactions causing increases in the count rate of ground-based neutron monitors (Ground Level Enhancements, GLEs). The studied SPEs are listed in Table 1, where *Fmax* is the maximal flux for particles with energies >100 MeV, according to the Catalog [Logachev et al., 2016].

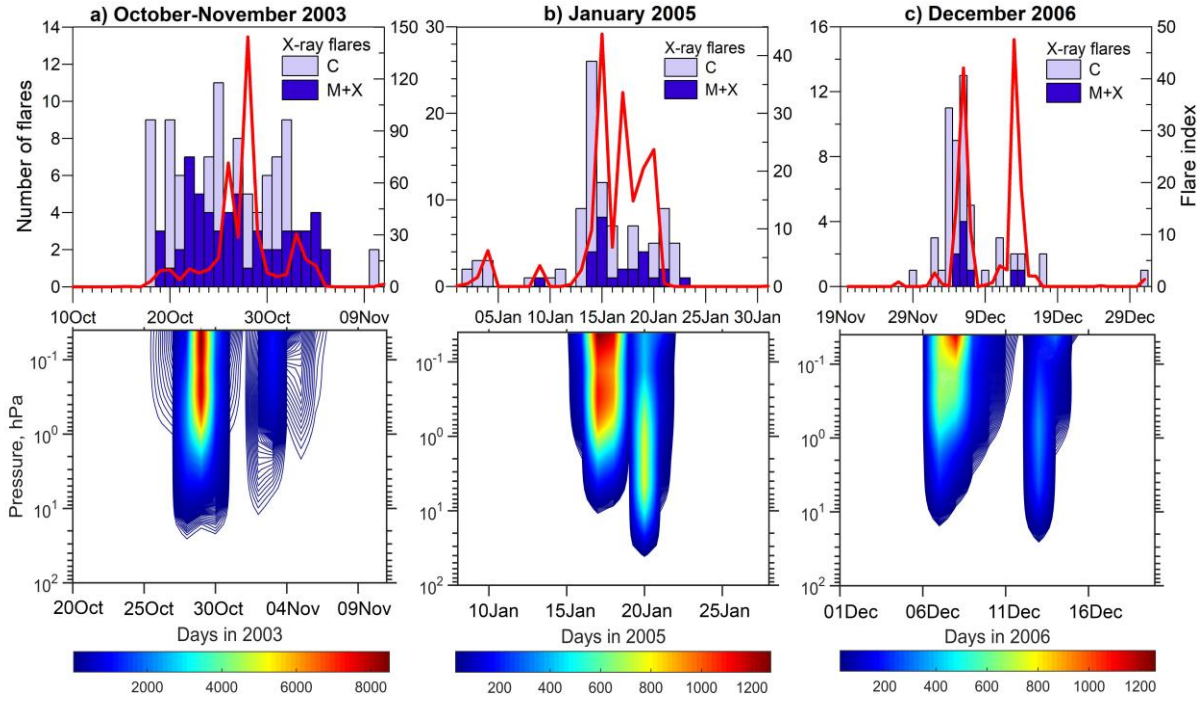


Figure 1. *Top: daily numbers of X-ray solar flares of classes C (gray) and M+X (dark-blue), and Kleczek's flare index (red line) for the SPE series of October-November 2003 (a), January 2005 (b) and December 2006 (c). Bottom: daily mean ionization rate at geomagnetic latitudes 60–90° according to the SOLARIS-HEPPA data (https://solarisheppa.geomar.de/solarprotonfluxes).*

Table 1. *Characteristics of Solar Proton Events according to [Logachev et al., 2016].*

SPEs in 2003	Fmax (>100MeV) $(cm^2 \cdot s \cdot sr)^{-1}$	GLE No	SPEs in 2005	Fmax (>100MeV) $(cm^2 \cdot s \cdot sr)^{-1}$	GLE No	SPEs in 2006	Fmax (>100MeV) $(cm^2 \cdot s \cdot sr)^{-1}$	GLE No
26.10.03	0.46/0.83		15.01.05	0.11		05.12.06	0.09	
28.10.03	150/185	65	16.01.05	0.52		06.12.06	18	
29.10.03	91	66	17.01.05	26	68	13.12.06	86	70
02.11.03	42	67	20.01.05	490	69	14.12.06	1.9	
04.11.03	0.9							

The studied events resulted in a significant increase of the ionization rate in the high-latitudinal middle atmosphere. In Figure 1 (bottom panel), daily mean values of the ionization rate at geomagnetic latitudes 60–90° are presented, the data by the SOLARIS-HEPPA working

group being used. One can see that the ionization rate noticeably increased in the upper stratosphere (above 10–7 hPa) and the mesosphere. The greatest enhancements of the ionization rate took place in the mesosphere above 1 hPa (~50 km). Daily values of the ionization rate in this region exceeded 1000 $cm^{-3} \cdot s^{-1}$ and 600 $cm^{-3} \cdot s^{-1}$ for the SPEs of January 2005 and December 2006, respectively. The strongest effects were observed during the "Halloween" events of October-November 2003, when the ionization rate in the mesosphere exceeded 6000 $cm^{-3} \cdot s^{-1}$, reaching the maximum value of ~8500 $cm^{-3} \cdot s^{-1}$.

3. SPE effects in the lower atmosphere

The analysis of weather charts showed that all the studied SPE series were accompanied by intensive regeneration of extratropical cyclones in the North Atlantic. Regeneration is a secondary deepening of cyclones, which have already reached the stage of maximal development (the occlusion). This process usually takes place near the south-eastern coast of Greenland (a region of high temperature contrasts, creating favorable conditions for the advection of cold air in the cyclone rear). Under undisturbed conditions, cyclones usually re-deepen by 5–10 hPa in this region [Veretenenko and Thejll, 2008]. However, against the background of considerable enhancements of the ionization rate caused by SPEs, several cases of an intensive cyclone regeneration, with a pressure drop in the cyclone center by 15 hPa and more, occurred. An example of a strong secondary deepening (by 27 hPa) is shown in Figure 2 for the "Halloween" events. The detected effects agree well with those obtained earlier for SPEs with energies >90 MeV [Veretenenko and Thejll, 2004, 2008].

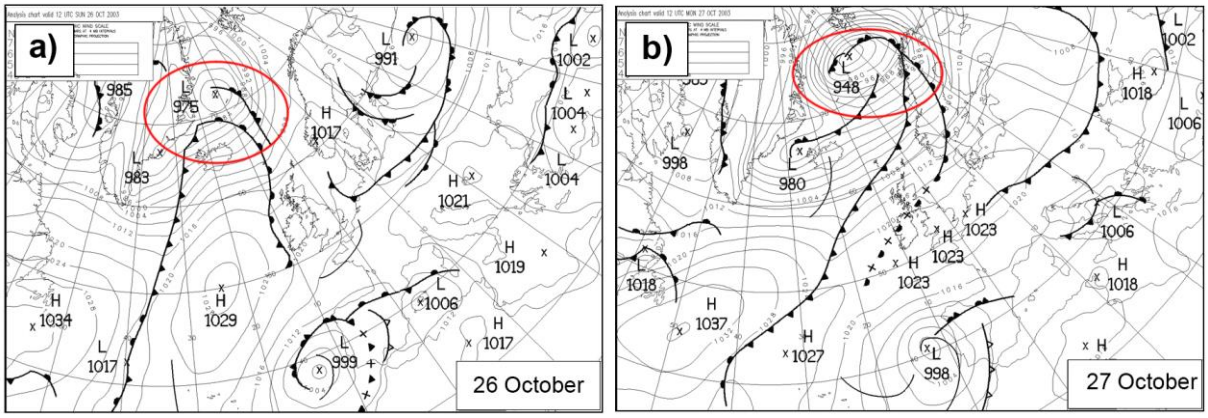


Figure 2. *Secondary deepening of the cyclone near Greenland associated with the "Halloween" events (2003): a) synoptic situation before the beginning of the first event of the series (26 October, 12 UTC); b) the same on the next day (27 October, 12 UTC). Weather charts were taken from https://www.metoffice.gov.uk. Red line encircles the cyclone center.*

The intensification of cyclone regeneration near Greenland observed after the beginning of the studied SPEs series was accompanied by a sharp increase of the North Atlantic Oscillation index, which characterizes a pressure gradient between high and subtropical latitudes of the North Atlantic. Figure 3 (a-c) presents temporal variations of the NAO index in the course of the studied events. One can see a noticeable increase of the NAO, with the maxima being observed from the 2nd to the 5th days after the beginning of the SPE series. The mean variations of the NAO index, which were obtained by the superposed epoch analysis (SPEA) for the studied SPE series, are shown in Figure 3d. The detected increase of the NAO index agrees well with an increase of zonal circulation at middle latitudes of the whole Northern Hemisphere

(characterized by the Blinova index) detected on the days following SPEs with energies >90 MeV [Veretenenko and Pudovkin, 1993]. Thus, the presented data show that the studied series of powerful SPEs of the 23rd solar cycle were accompanied by noticeable disturbances of the lower atmosphere.

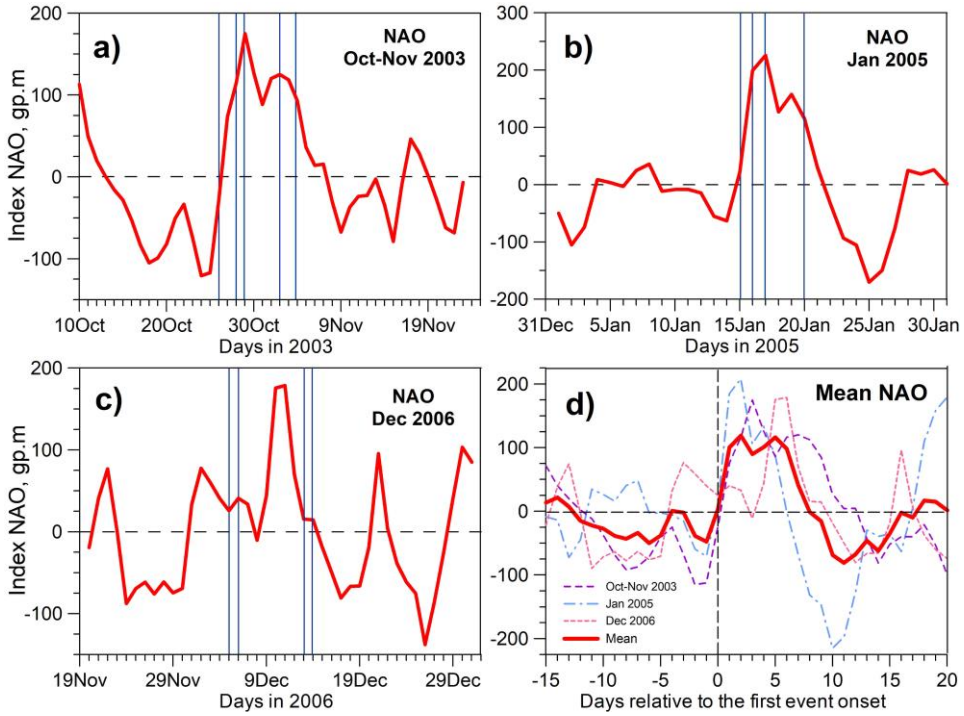


Figure 3. *Temporal variations (deviations from linear trends) of the NAO index at the 500 hPa level (https://psl.noaa.gov/data/timeseries/daily/NAO/) during the SPE series in: a) October-November 2003; b) January 2005; c) December 2006. Vertical blue lines show the days of SPE onsets. d) Mean (SPEA) variations of the NAO index in the course of the studied series (thick red line). Zero day is a day of the first SPE in the series.*

4. SPE effects in the middle atmosphere

Let us consider the SPE effects on characteristics of the middle atmosphere. In this study, the data from the MERRA-2 archive covering the altitudinal range from 1000 to 0.1 hPa (0–80 km) [Gelaro et al., 2017] were used. Figure 4 (top panel) shows temporal variations of zonally averaged velocity of zonal wind *Uzon* at different latitudes at the level 50 hPa (~20 km). At the bottom panel, the same data are presented, but after the removal of linear trends. Dashed white lines show the days of SPE onsets. One can see a noticeable increase of *Uzon* (by ~6–8 $m \cdot s^{-1}$) at latitudes 50–70º N (a region of the polar vortex formation) on the days following of the SPE series onsets, with the maximum being observed on the $+3^{rd}$ …$+5^{th}$ day.

An increase of zonally averaged velocity of zonal wind indicates an intensification of the stratospheric polar vortex. Indeed, the data in Figure 5 show that in the course of all the studied SPEs series, the vortex became stronger, taking a more circular and compact shape, with zonal wind velocity increasing. During the "Halloween" events (2003), the area of stronger winds displaced to the North Atlantic. An analysis of maximal values of zonal wind velocity at different isobaric levels revealed that the most pronounced intensification of the vortex took place at the levels from 20 to 7 hPa (~26–33 km). The wind strengthening was found to be most significant (by ~25–30 $m \cdot s^{-1}$) in the North Atlantic area (300–360ºE).

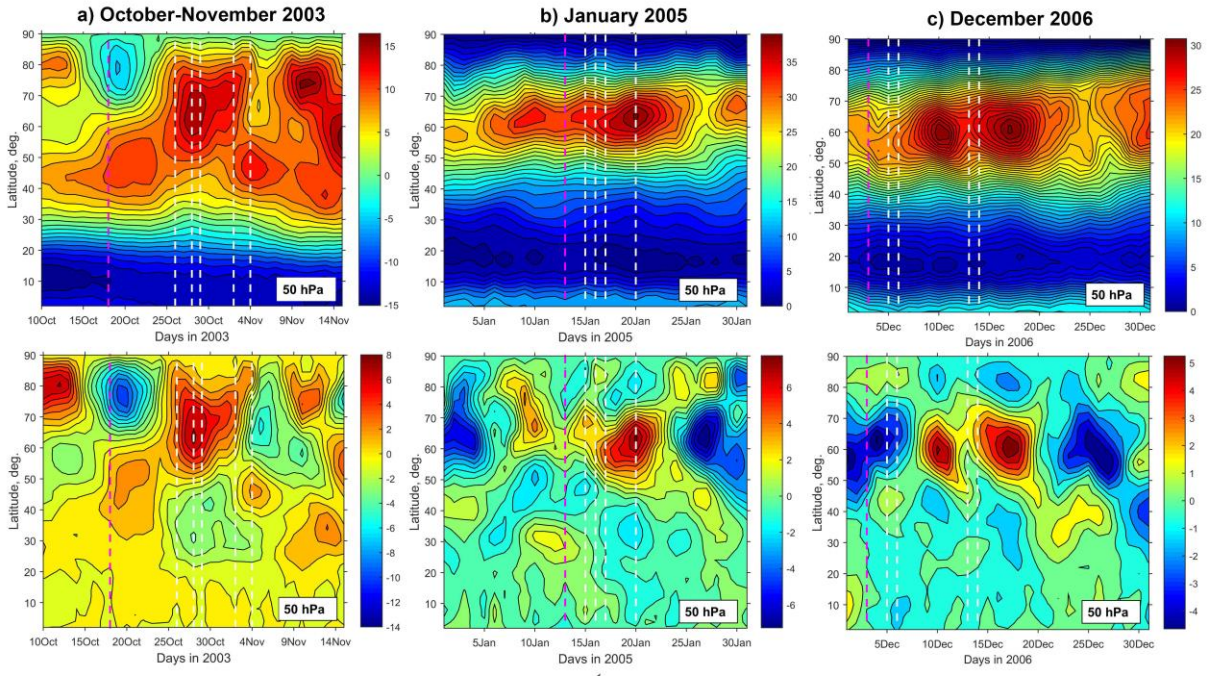


Figure 4. *Top: Temporal variations of zonally averaged velocity of zonal wind Uzon ($m \cdot s^{-1}$) at the level 50 hPa during the SPE series in: a) October-November 2003; b) January 2005; c) December 2006. Bottom: the same but after the removal of linear trends. White dashed lines show the days of the SPE onsets.*

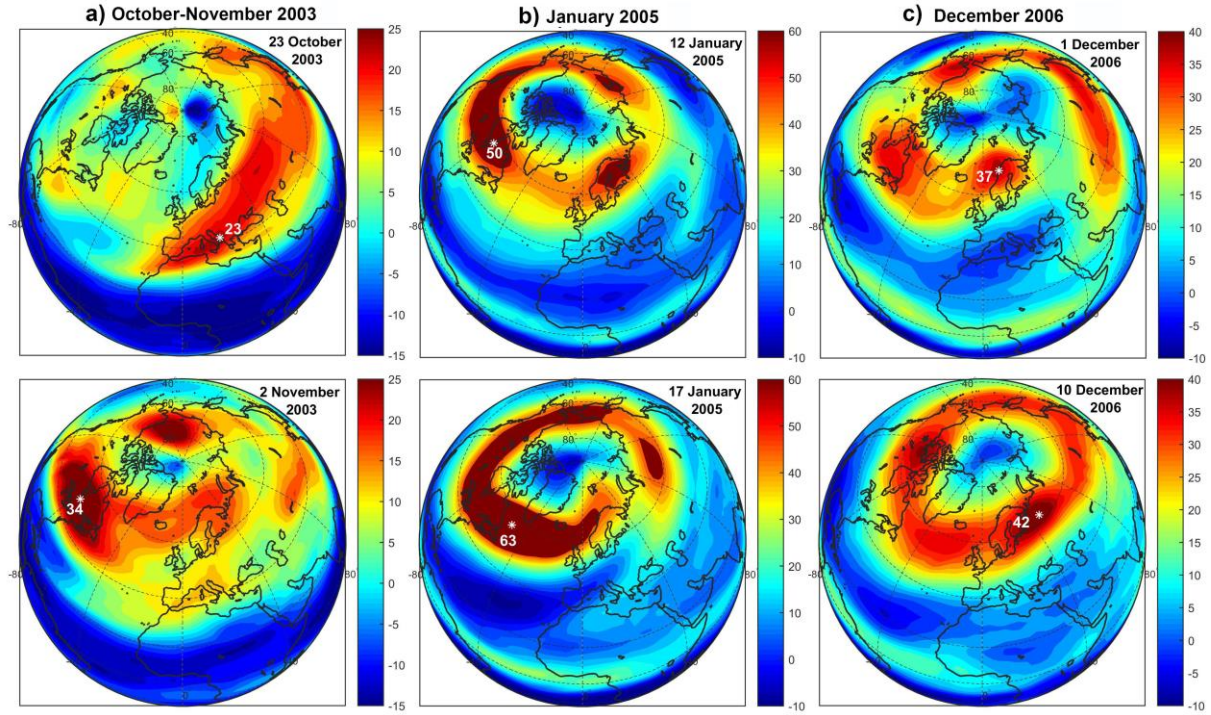


Figure 5. *Zonal wind velocity U ($m \cdot s^{-1}$) at the 50 hPa level before the onset of the SPE series (top) and several days after the onset (bottom). The areas covered by zonal winds with U > 40 $m \cdot s^{-1}$ are highlighted in dark brown. White asterisks indicate maximal values of zonal wind velocity.*

It was found that the SPEs under study were also accompanied by pronounced variations in planetary wave (PW) activity, which was characterized by the amplitudes of PW1 and PW2 (planetary waves with zonal numbers 1 and 2, respectively), as well as the vertical component

of the Eliassen-Palm flux (*EPz*), characterizing the momentum exchange between planetary waves and zonal flow in the stratosphere. Figure 6 shows temporal variations of the amplitudes of PW1 and PW2 at the latitude 62°N, which corresponds to the axis of zonal flow. One can see that the intensification of the polar vortex after the beginning of the SPE series took place against the background of decreasing planetary wave activity (weak amplitudes of PW1 and PW2), which was also confirmed by low *EPz* values. A noticeable increase of meridional temperature gradients at altitudes of ~20–40 km was also revealed after the SPE series beginning.

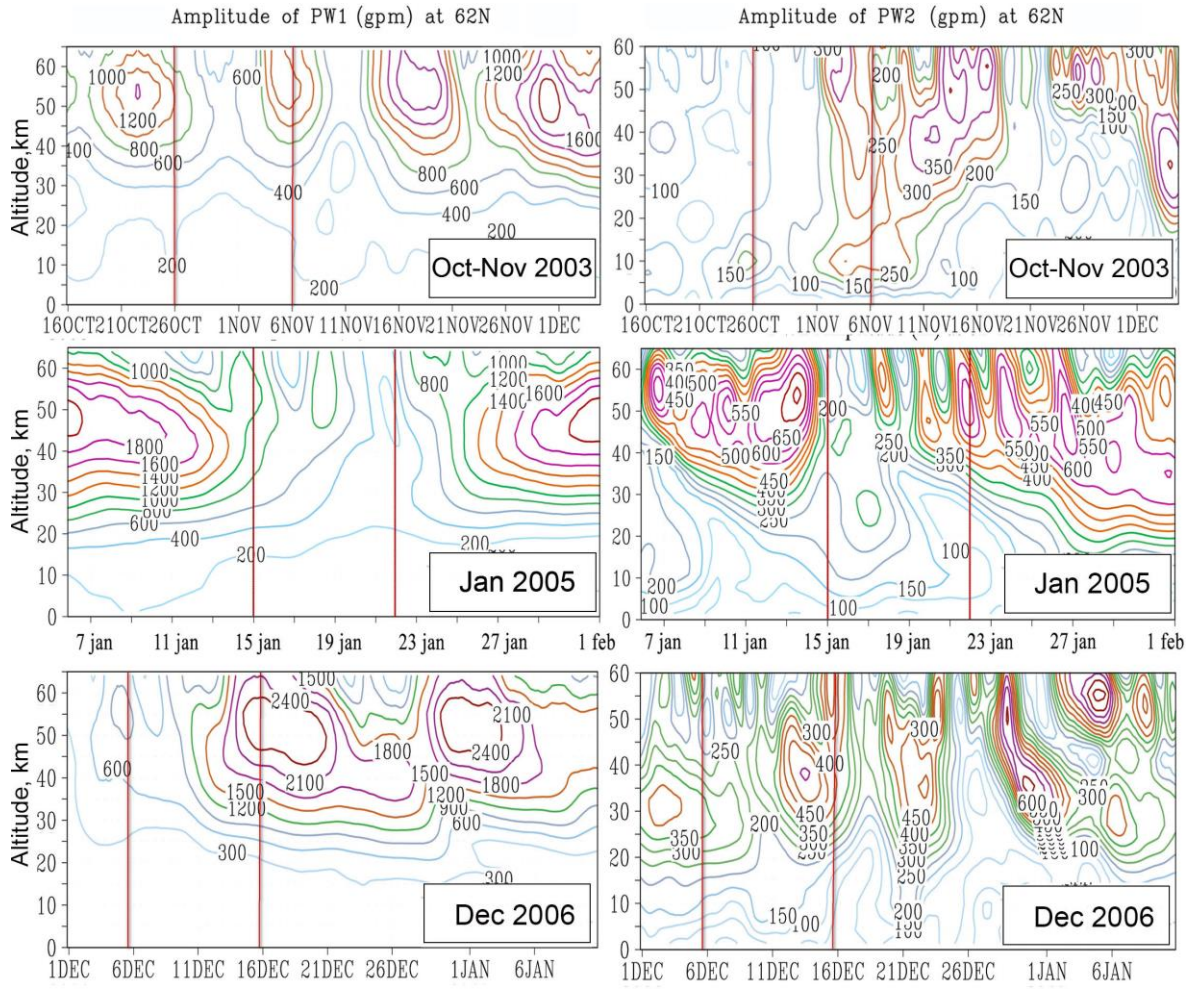


Figure 6. *Temporal variations of the amplitude of planetary waves with zonal numbers 1 (PW1) and 2 (PW2) at the latitude 62 °N in October-November 2003 (top), January 2005 (middle) and December 2006 (bottom). Vertical lines show the periods of an enhanced ionization rate.*

The data in Figure 6 show that the weakening of PW activity, which was observed on the first days of the SPE series, was followed by its pronounced intensification. More intensive generation of planetary waves could have been caused by spatial distribution of pressure variations in the troposphere resulted from the strengthening of cyclonic processes (Section 3). Intensification of PW activity contributed to a weakening of the polar vortex and the development of stratospheric warmings ~2–3 weeks after the onsets of the SPE series in January 2005 and December 2006. Figure 7 shows a sharp significant increase of zonally averaged temperature *Tzon* (>20–25K) in the high-latitudinal stratosphere (>60°N) which followed the indicated SPE series. A more powerful stratospheric warming, which started on the 1 January, 2007, was classified as a minor Sudden Stratospheric Warming [Li et al., 2023].

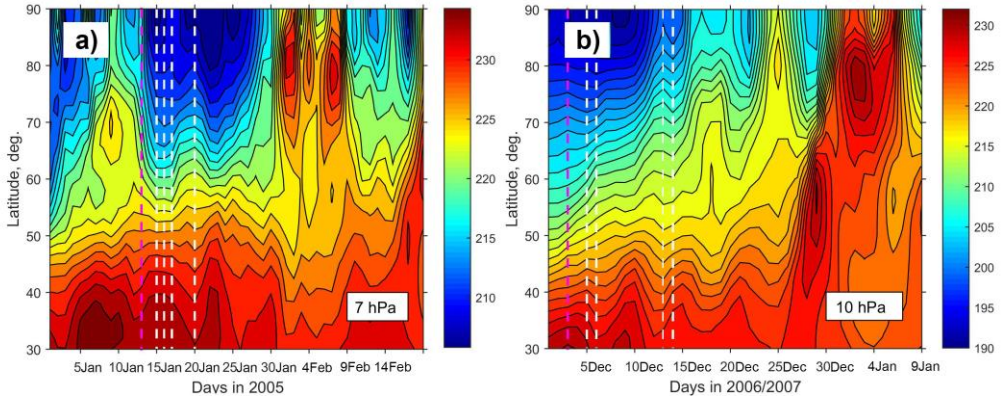


Figure 7. *Temporal variations of zonally averaged temperature Tzon (K) in the stratosphere at different latitudes: a) January-February 2005 (the level 7 hPa); b) December 2006 - January 2007 (the level 10 hPa). Vertical white dashed lines show the days of the SPE onsets.*

5. Conclusions

The studied series of powerful Solar Proton Events, which resulted in a considerable increase of the ionization rate in the mesosphere and the upper stratosphere, were accompanied by strong disturbances covering both the lower and middle atmosphere in the high-latitudinal region. The following phenomena were observed:

- increase of the North Atlantic Oscillation index,
- intensification of secondary deepening (regeneration) of extratropical cyclones near the south-eastern coast of Greenland,
- strengthening of the stratospheric polar vortex,
- variations of planetary wave activity,
- development of stratospheric warmings.

The obtained results allow suggesting strong influence of huge ionization increases caused by SPEs on the dynamics and temperature regime of the high-latitudinal atmosphere. A possible physical mechanism seems to include changes of the radiative-thermal balance in this region due to variations of the chemical composition (ozone depletion) and cloud cover associated with ionization increases.

References

Gelaro, R., McCarty, W., Suárez, M. J., et al. (2017). The Modern-Era Retrospective Analysis for Research and Applications, Version 2 (MERRA-2). *Journal of Climate*, Vol. 30, pp. 5419–5454. DOI: 10.1175/JCLI-D-16-0758.1.

Li, Y., Kirchengast, G., Schwaerz, M., et al. (2023). Monitoring sudden stratospheric warmings under climate change since 1980 based on reanalysis data verified by radio occultation. *Atmospheric Chemistry and Physics*, Vol. 23, pp. 1259–1284. DOI: 10.5194/acp-23-1259-2023.

Logachev, Yu. I., Bazilevskaya, G. A., Vashenyuk, E. V., et al. (2016). Catalog of solar proton events in the 23rd cycle of solar activity (1996–2008). World Data Center for Solar-Terrestrial Physics. Available at: http://www.wdcb.ru/stp/data/SPE/Catalog_SPE_23_cycle_SA.pdf.

Miroshnichenko, L. I. (2008). Solar cosmic rays in the system of solar-terrestrial relations. *Journal of Atmospheric and Solar-Terrestrial Physics*, Vol. 70, Nos. 2–4, pp. 450–466. DOI: 10.1016/j.jastp.2007.08.027.

Veretenenko, S. V., Pudovkin, M. I. (1993). Effects of cosmic ray variations on the lower atmosphere circulation. *Geomagnetism and Aeronomy*, Vol. 33, No. 6, pp. 747–750.

Veretenenko, S., Thejll, P. (2004). Effects of energetic solar proton events on the cyclone development in the North Atlantic. *Journal of Atmospheric and Solar-Terrestrial Physics*, Vol. 66, No. 5, pp. 393–405. DOI: 10.1016/j.jastp.2003.11.005.

Veretenenko, S. V., Thejll, P. (2008). Solar proton events and evolution of cyclones in the North Atlantic. *Geomagnetism and Aeronomy*, Vol. 48, No. 4, pp. 518–528. DOI: 10.1134/S0016793208040130.

DOI: 10.31401/WS.2026.proc.31

Photometric Reverberation Mapping Through Theory-Agnostic Fitting of the Light Curves

Bachev R., Strigachev A., Dechev M.

Institute of Astronomy and NAO, Bulgarian Academy of Sciences, 1784 Sofia, BG
(bachevr@astro.bas.bg)

Abstract

The term "theory-agnostic" describes a method or approach that is independent of a specific underlying theory, allowing analysis of phenomena and prediction making without the need of underlying assumptions about a particular framework. The approach is valuable since it can discover new physics that might be missed if one were only looking for effects predicted by a specific theory. It is often used in contemporary astrophysics, from analyzing gravitational waves from black hole mergers, to investigating temporal delays inherent in various solar and heliospheric processes, illustrating how solar activity affects the Earth and space environment over time. In this work we demonstrate similar technique, employing theory-agnostic polynomial fitting approach to find time delays between line and continuum variations of the active galactic nuclei (reverberation mapping), thus allowing probing the central regions and ultimately – measuring the central black hole masses. This method can work for time series, consisting of densely populated groups of points, separated from each other by a time interval much longer than the expected time delay – a common situation where very few (if any) other methods can successfully do the job. Among the objects we studied were the active galaxies (quasars) I Zw 1, UGC 6728, Mkn 478, PG 1448+273, II Zw 136, Ton 951, VII Zw 118, among others, all observed with a 60cm telescope of Belogradchik observatory, Bulgaria. Here we present some of the most promising first results of the application of this method.

Keywords: AGN; variability; methods

1. Method

Many astrophysical techniques are based on measuring time lags between time series of data. For instance, reverberation mapping (RM) (e.g. Peterson & Horne, 2004) of the Broad Line Region (BLR) is an efficient (yet observationally "expensive") method to probe the central regions of the active galactic nuclei (AGN) and ultimately to measure the central black hole mass. Central black hole mass estimate requires knowledge of the physical size of the BLR, which can be determined via time delay between the ionizing continuum and the line response, and the velocity of the line emitting structures, determined via the width of the broad line. *Photometric* RM (Haas et al., 2011; Bachev et al., 2014) technique is, on the other hand, a way to reduce the observing "costs" by using smaller telescopes and narrow-band filters, isolating only the broad lines from the rest of the continuum, and thus eliminating the need to perform spectroscopy. In this work we demonstrate further modification of this technique, employing theory-agnostic polynomial fitting approach to find time delays between line and continuum variations. This technique can work successfully even with a very small number, unevenly sampled observations. Monte-Carlo simulations can further be used to estimate the obtain the time delays' distributions and uncertainties.

Two modifications of this method can be presented, allowing time-delay measurements in 2 different ways:

***Approach 1*:** Fitting LC's datasets $(C_i(t_i), L_i(t_i))$ with separate polynomials (L and C) and correlating them as a function of the time shift to find the *maximum* of (see also Fig. 1, 2):

$$CC_{LC}(\tau) = \frac{\int_{t1}^{t2}(L(t+\tau) - \langle L\rangle)\,(C(t) - \langle C\rangle)dt}{\sqrt{\int_{t1}^{t2}(L(t) - \langle L\rangle)^2 dt \int_{t1}^{t2}(C(t) - \langle C\rangle)^2 dt}} \quad (1)$$

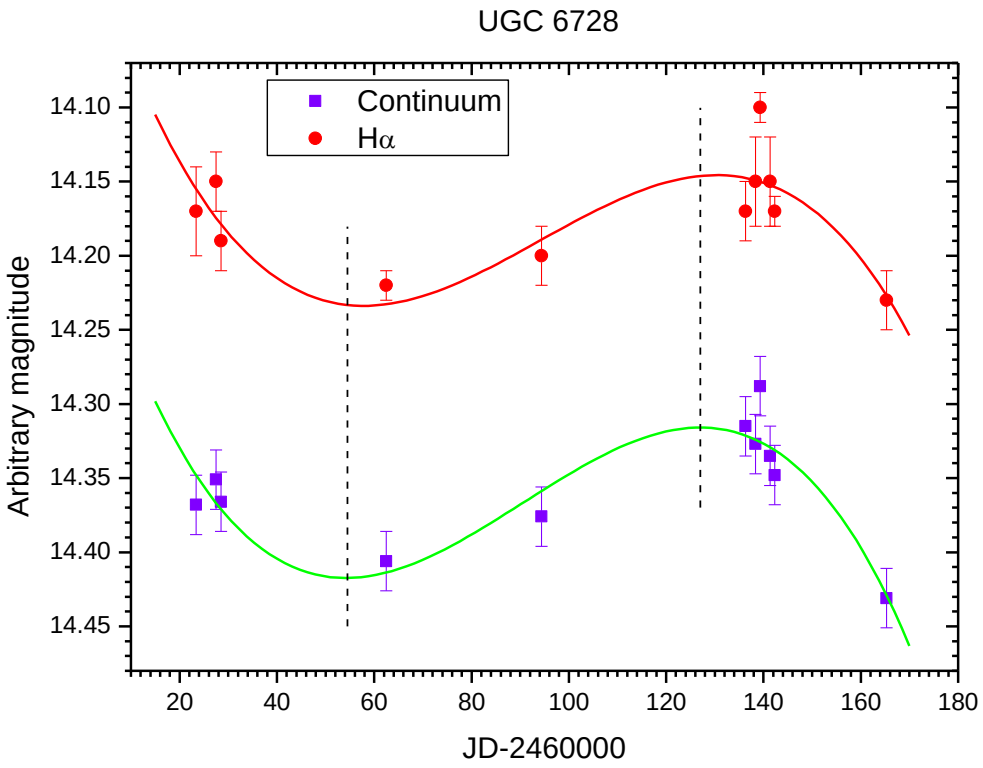


Figure 1. Two independent 3rd degree polynomials are fitted to the continuum and the line of UGC 6728, observed with the 60cm Belogradchik telescope between Mar. and Sept. 2023. The dashed vertical lines mark the position of the continuum maximum/minimum. This agnostic approach does not assume that the polynomials should represent any real light curves. MC methods are used to simulate the photometric uncertainties. Then $CC(\tau)$ is calculated for each realization and its maximum as a function of τ is found. The procedure is repeated 1000 times and the distribution of the $CC(\tau)$ maxima is built (see Fig. 2).

***Approach 2*:** Fitting all points (line and continuum, both scaled to the *same average*) with a single polynomial (*F*) and shifting one of the sets with respect to the other to get the *minimum* of (see also *ssredit* from *linest* in Excel) the standard deviation (Fig. 3):

$$\sigma(\tau) = \sqrt{\sum\big(F(t_i) - C(t_i)\big)^2 + \sum\big(F(t_i) - L(t_i+\tau)\big)^2} \quad (2)$$

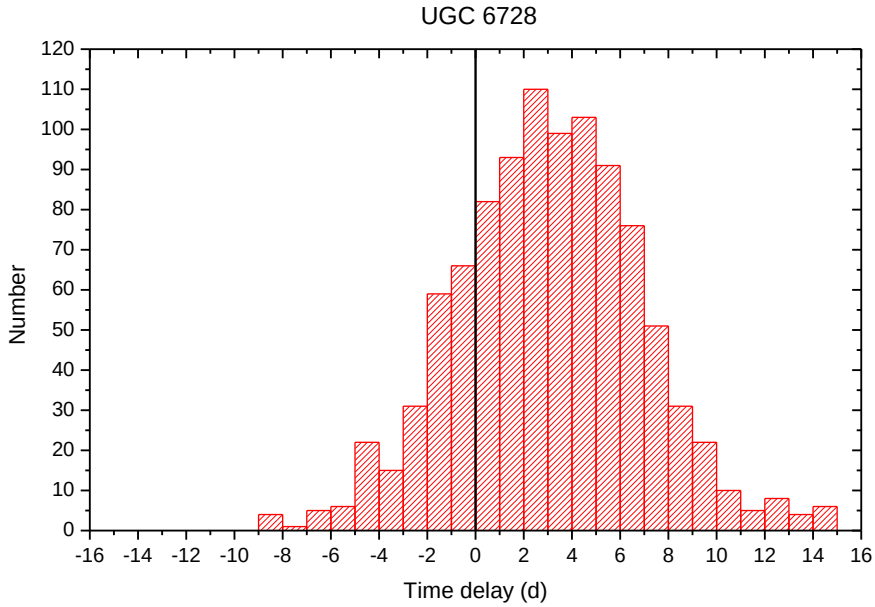


Figure 2. The distribution of the $CC(\tau)$ maxima for 1000 repetitions (see Fig. 1). The maximum of this distribution is found to be at a time delay of about 3.5 days and the distribution itself can be used to estimate the delay uncertainties at the confidence level required.

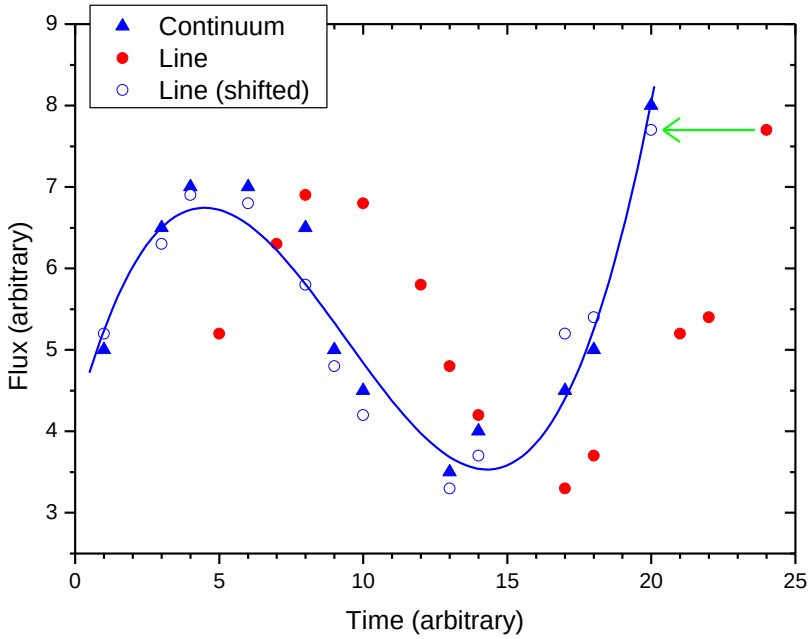


Figure 3. Demonstration of the application of Approach 2 (mock data), as described in the text.

2. Results

Here we present some recent delay results for the active galaxy UGC 6728 to demonstrate the applicability of the two approaches, described above. Next we demonstrate the application of the second approach, as described in the previous section. This is an example with mock L and C data, scaled to the same average. Time shift is applied to one of the curves (say line data)

and a single polynomial is used to fit all data points of both datasets. The time shift, corresponding to the ***minimum*** *scatter* is the one, which is searched for (Fig. 3). For real data the errors have to be simulated and the ***average*** *scatter* for each time shift has to be considered (Fig. 4) when searching for the minimum. Fitting polynomials will be different for each shift and each data randomization, and again they should not necessarily represent any real light curve.

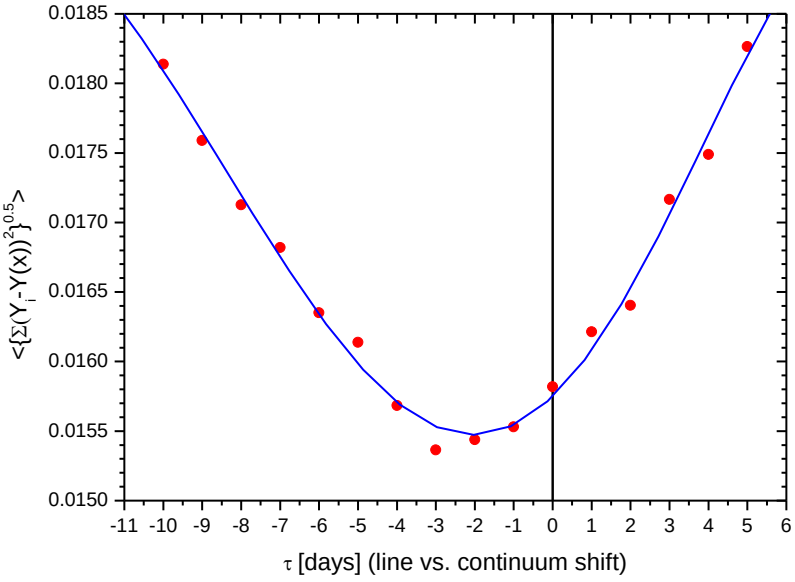


Figure 4. Application of Approach 2 to the UGC 6728 data: the scatter for each τ is obtained by averaging over 1000 MC realizations to simulate the influence of the photometric errors. The minimum of the averaged scatter is obtained when the line curve is shifted backward with respect to the continuum with about 2.5 days.

Bentz et al. (2016) estimated the continuum-line delay for UGC 6728 to 1.4+/-0.8 days through long-term spectroscopic RM (during different epochs), which points to a black hole mass of $M_{BH} = 7 \times 10^5 M_{\odot}$. While the mass remains the same, BLR is known to evolve in many objects (Wang et al., 2025). Therefore, a more regular even less accurate delay measurement may prove more productive in some cases.

3. Key findings and conclusions

The main conclusion of the research is that a *theory-agnostic polynomial fitting approach* is an effective and valuable method for finding time delays in the reverberation mapping of Active Galactic Nuclei (AGN).

The key findings and conclusions drawn from the study regard:

- ***Viability of the method*****:** This "theory-agnostic" approach allows for the analysis of phenomena and the prediction of time delays without needing underlying assumptions about a specific framework that represent real light curves.
- ***Effectiveness for challenging data*****:** This method is particularly successful for time series consisting of densely populated groups of points separated by long intervals - a

common data limitation where very few other methods can function. It also works well with a small number of unevenly sampled observations.

- ***Successful application to UGC 6728*:** We demonstrated the method using two different approaches (correlating separate polynomials and using a single polynomial to find minimum scatter) on data from the active galaxy UGC 6728. These approaches yielded time delay results of approximately 3.5 days and 2.5 days, respectively.
- ***Productivity in monitoring BLR evolution*:** While photometric RM may be less accurate than long-term spectroscopic RM, we conclude that regular narrow-band monitoring, accompanied with the application such theory-agnostic delay-searching methods can be highly productive because the BLR is known to evolve over time.
- ***Cost-effectiveness*:** This photometric technique reduces observational "costs" by allowing the use of smaller telescopes and narrow-band filters instead of expensive spectroscopy.

Ultimately, the work demonstrates that this technique is a promising tool for probing the central regions of AGN and measuring central black hole masses.

Acknowledgements

This research was partially supported by the Bulgarian National Science Fund of the Ministry of Education and Science under grant KP-06-H68/4 (2022).

References

Bachev, R., Strigachev, A., Semkov, E., et al. (2014). Photometric reverberation mapping of Markarian 279. *Bulgarian Astronomical Journal*, Vol. 20, p. 26.

Bentz, M. C., Batiste, M., Seals, J., et al. (2016). A low-mass black hole in the nearby Seyfert galaxy UGC 06728. *The Astrophysical Journal*, Vol. 831, No. 1, 2. DOI: 10.3847/0004-637X/831/1/2.

Haas, M., Chini, R., Ramolla, M., et al. (2011). Photometric AGN reverberation mapping—an efficient tool for BLR sizes, black hole masses, and host-subtracted AGN luminosities. *Astronomy & Astrophysics*, Vol. 535, A73. DOI: 10.1051/0004-6361/201117325.

Peterson, B. M., Horne, K. (2004). Echo mapping of active galactic nuclei. *Astronomische Nachrichten*, Vol. 325, pp. 248–249. DOI: 10.1002/asna.200310207.

Wang, S., Woo, J.-H., Barth, A. J., et al. (2025). Seoul National University AGN Monitoring Project. V. Velocity-resolved Hβ reverberation mapping and evidence of kinematics evolution. *The Astrophysical Journal*, Vol. 983, No. 1, 45. DOI: 10.3847/1538-4357/adbca5.

DOI: 10.31401/WS.2026.proc.32

Numerical Analysis of Genuine and Secondary-Induced Events in the Liulin-MO Telescope aboard ExoMars Trace Gas Orbiter

Krastev K.

Space Research and Technology Institute – Bulgarian Academy of Sciences, Sofia, Bulgaria
kras2626@abv.bg

Abstract

This work presents numerical simulations of the Liulin-MO cosmic-ray dosimetric telescope which is a module of the FREND instrument aboard the ExoMars Trace Gas Orbiter. A detailed detector and spacecraft geometry is used to investigate registered two-detector events for protons, alpha particles, O-16 and Fe-56 nuclei. An independent geometrical analysis of the initial primary trajectory separates the desired events, in which the primary particle intersects both detectors (Case 3), from false coincidences in which it intersects neither detector or only one detector (Cases 2, 4 and 5). Secondary particles registered in at least one detector are analyzed through three-dimensional birth-density maps and by structural production region. The new false-event analysis shows two distinct mechanisms: Case 2 is strongly influenced by the extended surrounding structure, with FREND providing the largest integrated contribution, whereas Cases 4 and 5 are dominated by secondary production in the immediate ceramic/silicon detector environment. A modified geometry with a 1-mm iron protective layer reduces the combined unwanted population by about 57% in the investigated 1 GeV/n Fe-56 case while reducing Case 3 by about 6.8%. The results provide a basis for structural., software and simulation-based procedures for preserving genuine telescope events while suppressing false coincidences.

Keywords: cosmic rays; Liulin-MO; numerical simulation

1. Introduction

Measurements of cosmic radiation with compact silicon detectors telescopes are influenced not only by the incident primary particles but also by secondary radiation generated in the detector housing, electronics, supporting structures and the spacecraft itself. These effects are especially important when a telescope event is identified by a coincidence between two silicon detectors, because the two signals do not necessarily have to be produced by the same primary particle.

Liulin-MO [Semkova et al., 2018] is a separate radiation-dosimetry module of the FREND instrument [Mitrofanov et al., 2018] operating aboard the ExoMars Trace Gas Orbiter (TGO). The measured response is therefore determined by the sensitive detector volumes together with the surrounding mass distribution. Nuclear interactions, electromagnetic interactions and particle scattering can generate secondary particles that reach one or both detectors and distort the ideal geometrical response.

The purpose of the present work is to investigate these effects numerically and to identify the physical origin of unwanted two-detector events. The principal target population is defined as events in which the primary particle itself is registered in both detectors A and B. The numerical analysis is designed to distinguish these events from coincidences caused wholly or partly by secondary radiation and to provide information that can be used for their rejection.

2. Detector and spacecraft geometry

The simulation geometry was constructed with CATIA Geometry Builder [Belogurov et al., 2011; Belogurov et al., 2014] and transferred to the numerical model.

Figure 1 shows the geometry used in the simulations. The model contains the Liulin-MO detector system and the principal surrounding structural components relevant to particle transport, including aluminium protection, stainless-steel structures, printed circuit boards and the heat sink. In the geometrical model, each detector is represented by three separate structural components: a PIN photodiode, a resin layer, and a ceramic substrate. This configuration allows not only the interactions of primary particles with the sensitive detector volume to be taken into account, but also the interactions and production of secondary particles in the materials immediately surrounding the photodiode. The spacecraft environment is included because secondary particles produced outside the immediate detector housing can contribute to the measured telescope response. In the numerical geometry, the TGO spacecraft structure is approximated by a hollow aluminium box with a uniform wall thickness of 5 mm.

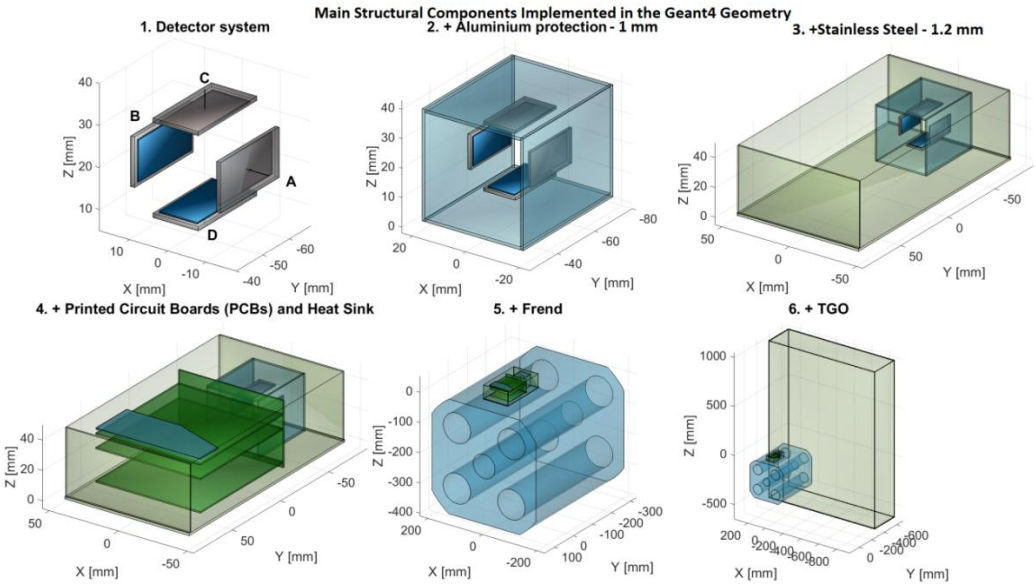


Figure 1. *Main Liulin-MO structural components implemented in the simulation geometry.*

3. Numerical model and methodology

3.1. Event registration and classification

A registered A-B event is defined by the detector trigger condition: the summed deposited energy for one event must be greater than 70 keV in detector A and greater than 70 keV in detector B. This condition is applied independently of the identity of the particle producing the deposited energy.

For every generated primary particle, the initial position and momentum direction are stored before any physical interaction occurs. A ray-box intersection test is then used to determine whether the straight-line extension of the initial trajectory intersects the sensitive volume of detector A and/or detector B. This geometrical test is independent of subsequent energy loss, scattering and nuclear interactions.

Registered events are separated into five analysis cases. Case 1 contains all registered events satisfying the two 70 keV thresholds, with no additional condition on the primary trajectory. Case 2 contains events in which the primary particle passes through neither detector. Case 3 contains events in which the primary particle passes through both detectors and represents the desired telescope population. Case 4 contains events in which the primary particle passes through detector A only, whereas Case 5 contains events in which the primary particle passes through detector B only. The analysis objective is therefore to preserve Case 3 while rejecting, as far as possible, Cases 2, 4 and 5.

3.2. Physics Models

The simulations were performed using the FTFP_BERT reference physics list supplied with Geant4 [Agostinelli et al., 2003; Allison et al., 2006; Allison et al., 2016]. This physics list combines the Fritiof string model for high-energy hadronic interactions with the Bertini intranuclear cascade model at intermediate energies and includes the standard electromagnetic interaction models implemented in Geant4. The selected physics configuration provides simulation of proton, alpha-particle and heavier-ion interactions over a broad energy range.

Electromagnetic processes included ionisation, multiple Coulomb scattering, bremsstrahlung and delta-electron production. Hadronic interactions were treated using the models implemented in the FTFP_BERT physics list, enabling simulation of nuclear reactions and secondary-particle production in the detector and surrounding structural materials.

3.3. Primary Particle Generation

The detector response was investigated using four types of monoenergetic primary particles: **protons, alpha particles, O-16 nuclei, and Fe-56 nuclei**. For each primary-particle species, three energies were simulated: **500 MeV/nucleon, 1 GeV/nucleon, and 10 GeV/nucleon**. For protons, these values correspond directly to kinetic energies of 500 MeV, 1 GeV, and 10 GeV. For each particle-species and energy combination, 10^8 **primary particles** were generated.

Primary particles were generated from the surface of a virtual sphere enclosing the complete numerical model of the detector and the surrounding spacecraft structure. The radius of the source sphere was **150 cm**. Initial particle directions were sampled according to a cosine-law angular distribution with respect to the inward surface normal., producing an isotropic radiation field incident on the detector-spacecraft system [Yando et al., 2011; Zhao et al., 2013].

The same irradiation geometry was used for all twelve simulations, allowing the detector response to be compared directly as a function of primary-particle species and energy.

4. Results

4.1. Five-case response for representative primary particles

The twelve monoenergetic simulations were classified according to the five geometrical cases defined above. The results show a systematic transition from a response dominated by genuine Case 3 events for low-energy protons to an increasing contribution of secondary-induced Case 2 events with increasing primary-particle energy and, more generally, for heavier primary species. Figure 2 presents the 1 GeV/nucleon Fe-56 simulation as a representative example, in which the different mechanisms contributing to the registered two-detector response can be clearly distinguished.

In Figure 2, Case 3 represents genuine telescope events in which the primary particle intersects both detectors. In Case 2, the primary trajectory intersects neither detector; consequently, the registered coincidence is produced entirely by secondary radiation. Cases 4 and 5 represent asymmetric events in which the primary particle intersects only one detector, while secondary particles provide the required signal in the other. Thus, the detector trigger condition alone does not uniquely identify a genuine two-detector traversal. This distinction provides the basis for the subsequent statistical and structural analyses of the unwanted event populations.

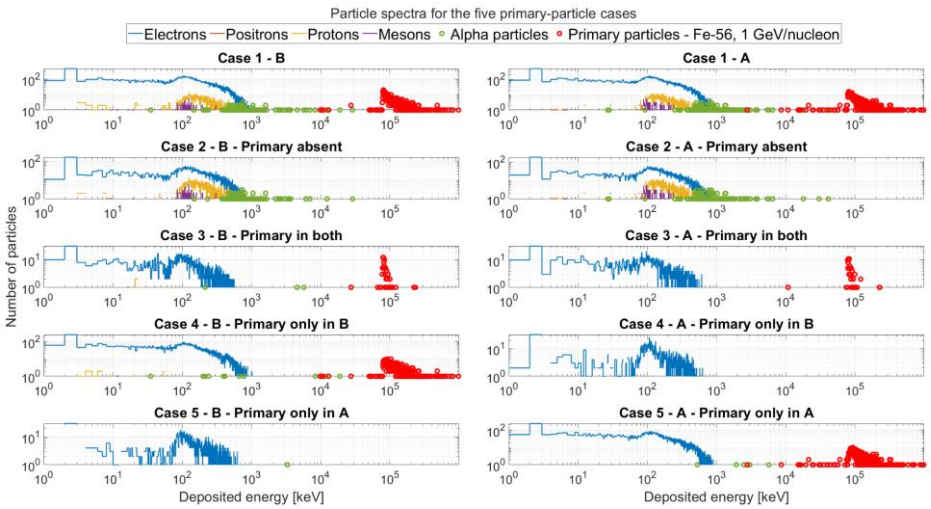


***Figure 2**. Five-case response for 1 GeV/nucleon primary Fe-56 nuclei.*

4.2. Event statistics

Table 1 summarizes the registered-event statistics for all twelve simulations. Case 1 is the full registered sample; the physically relevant partition is Cases 2–5, with Case 3 representing the desired telescope population.

Table 1. Summary of registered-event statistics and geometrical event classes for the simulated primary particles and energies.

Run	Primary	Total events	Registered	Case 2	Case 3	Cases 4/5
1	p, 500 MeV	2680	154	6	141	4 / 3
2	p, 1 GeV	3129	183	23	149	5 / 6
3	p, 10 GeV	7140	420	262	141	8 / 9
4	alpha, 500 MeV/n	3765	225	57	145	12 / 11
5	alpha, 1 GeV/n	5498	294	127	138	15 / 14
6	alpha, 10 GeV/n	20695	1472	1282	136	31 / 23
7	O-16, 500 MeV/n	7419	598	281	125	104 / 88
8	O-16, 1 GeV/n	15417	1164	717	128	160 / 159
9	O-16, 10 GeV/n	67543	8192	7562	130	261 / 239
10	Fe-56, 500 MeV/n	15348	2757	1845	116	431 / 365
11	Fe-56, 1 GeV/n	38387	6264	5093	117	548 / 506
12	Fe-56, 10 GeV/n	195276	42076	40667	121	668 / 620

The statistics show a systematic growth of the unwanted population with increasing primary mass and energy. For low-energy protons, Case 3 accounts for most registered events, whereas for energetic heavy nuclei the registered population is dominated by Case 2. This transition is

consistent with increasingly important secondary-particle cascades in the instrument and spacecraft materials.

4.3. Geometry modification as a rejection method

Geometry modification is one possible method for reducing unwanted events, but it is not the only one. Additional approaches include software selection based on measured detector signals and correction or rejection procedures derived from numerical response modelling. Figure 3 shows the modified detector geometry with an additional 1-mm-thick iron protective layer around detector B. Figure 4 presents the corresponding Fe-56 simulation and should be compared directly with Figure 2, which represents the same primary species and energy for the original geometry.

The comparison demonstrates that structural modifications alter both the total coincidence rate and the relative populations of the geometrical classes. Such a modification must therefore be evaluated not only by the number of rejected false events but also by the fraction of Case 3 events retained. The desired optimization criterion is maximal rejection of Cases 2, 4 and 5 with minimal loss of Case 3.

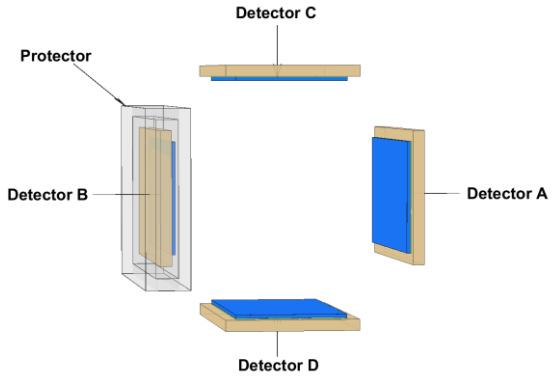


Figure 3. *Modified detector configuration with a 1-mm-thick iron protective layer around detector B.*

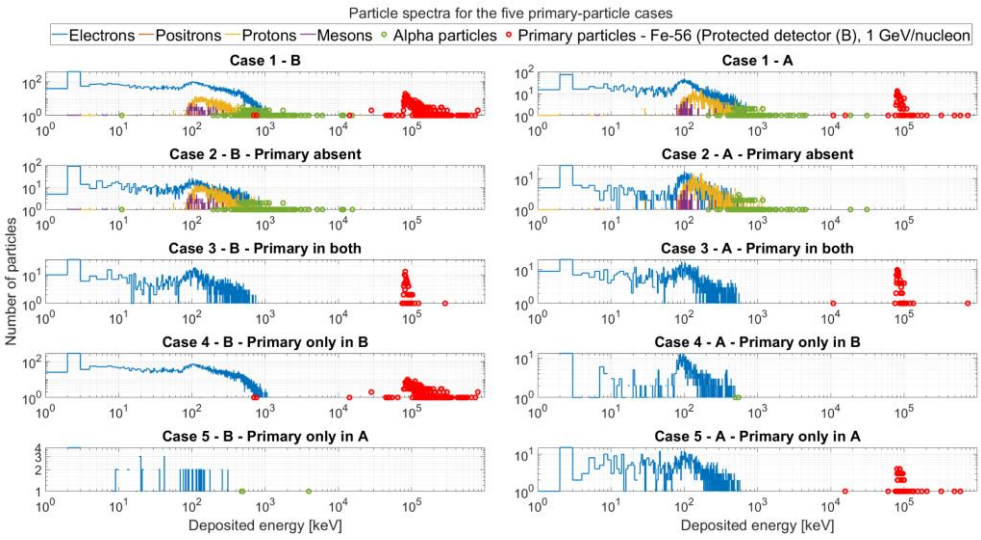


Figure 4*. Fe-56 response for the modified geometry. The corresponding event statistics are: 32,107 total events, 2,749 registered events, Case 2 = 2,125, Case 3 = 109, Case 4 = 451 and Case 5 = 64.*

4.4. Spatial origin of secondary particles

The production positions of secondary particles were accumulated in three-dimensional spatial bins. Figures 5–8 present representative electron distributions for registered events and for selected geometrical classes, allowing the spatial origin of secondaries contributing to the detector response to be compared directly.

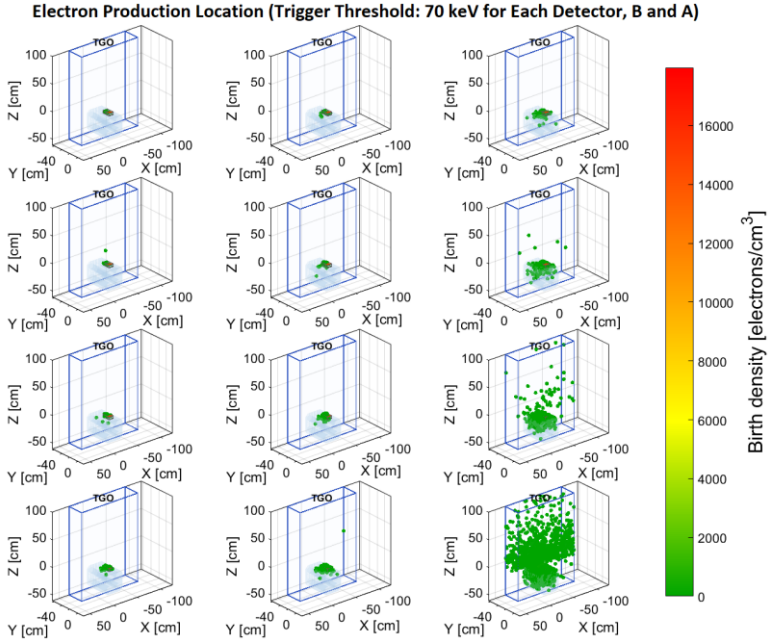


Figure 5. *Spatial birth-density distribution of secondary electrons for registered events satisfying the 70 keV threshold in each detector.*

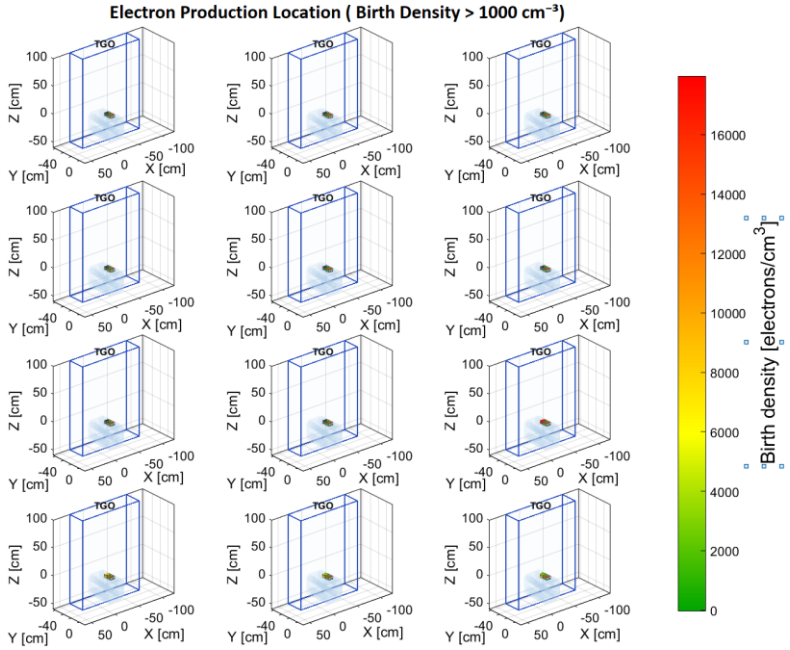


Figure 6. *Electron-production distribution restricted to locations where the electron birth density exceeds 1000 electrons/cm³.*

Figures 5 and 6 are conditioned on the same two-detector trigger used throughout the event analysis: the summed deposited energy in each detector exceeds 70 keV. The distributions show that secondary particles subsequently registered by the detector system can be produced both within the Liulin-MO instrument and in the surrounding spacecraft structure. The highest local

concentrations are generally found in the immediate vicinity of the detector assembly, whereas lower-density secondary production extends over a considerably larger volume.

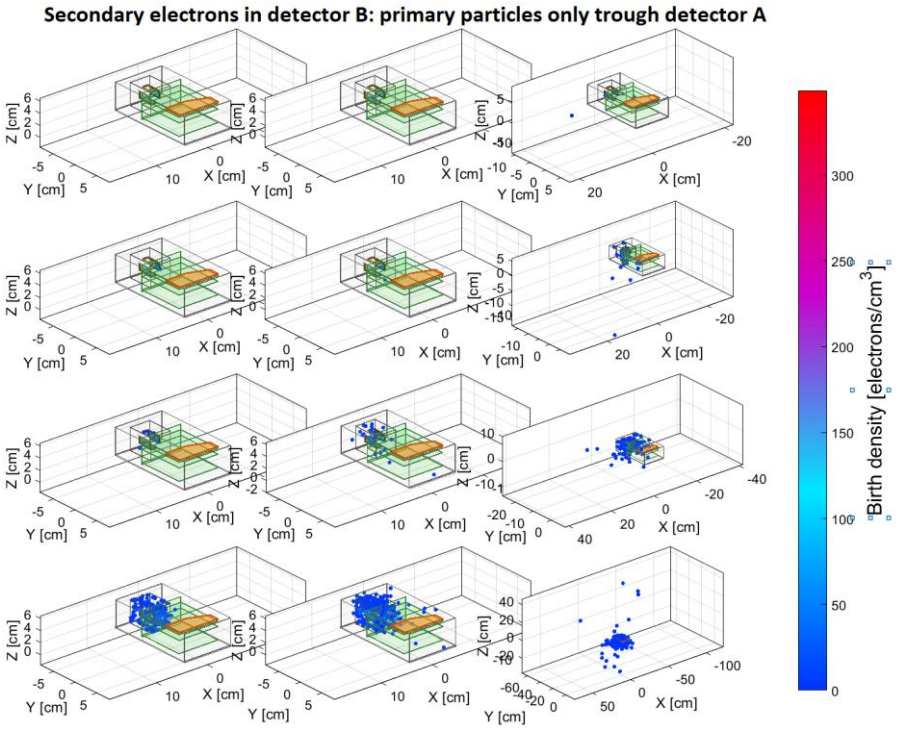


Figure 7. *Subset of Figure 5 in which the primary particle passes only through detector A and a corresponding secondary electron is registered in detector B.*

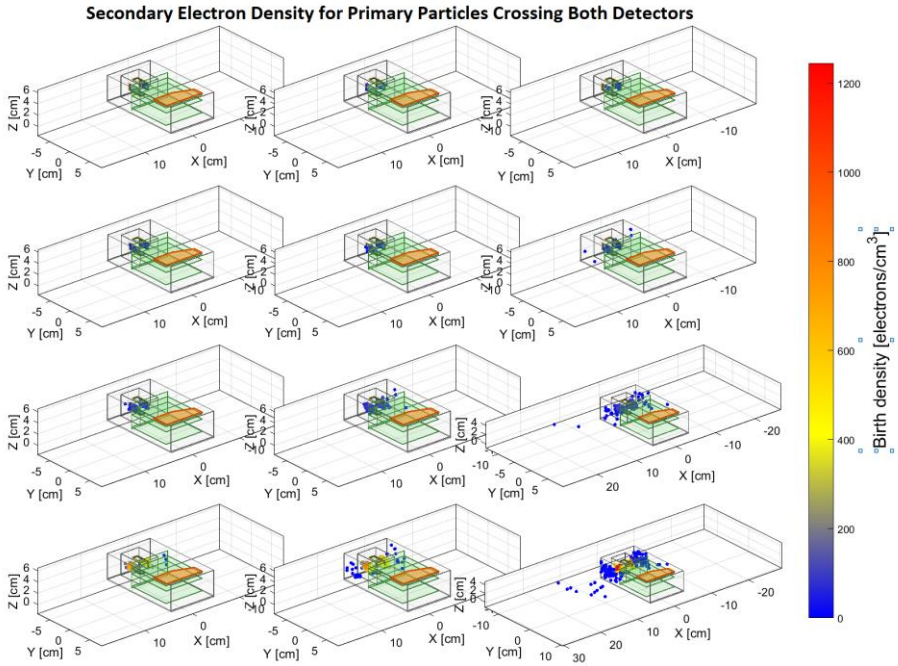


Figure 8. *Electron birth-density distribution for Case 3 events, in which the primary particle crosses both detector A and detector B.*

For the twelve investigated simulations, densities above 1000 cm^{-3}, where present, are confined to the Liulin-MO instrument region. This observation is consistent with the localization of the highest production densities close to the detector system, but the spatial maps also show that more distant structural elements contribute to the secondary-particle population.

Figure 7 illustrates an important example of the relationship between secondary-particle production and the five-case event classification. It corresponds to Case 4, in which the primary particle intersects detector A but not detector B. A secondary electron produced during the same event reaches detector B and contributes to the two-detector coincidence.

Figure 8 shows the complementary electron distribution for Case 3, where the initial primary trajectory intersects both detector A and detector B. The comparison between Figures 7 and 8 illustrates two physically different mechanisms capable of producing registered signals in both detectors. In Case 3 the primary particle itself follows the required telescope trajectory, whereas in Case 4 secondary-particle transport is required to complete the coincidence.

The spatial distributions also demonstrate that secondary production is not characterized adequately by a single point or structural component. A localized region may contain a relatively high production density, while a larger surrounding component with a lower local density may produce a greater total number of secondary particles capable of reaching the detectors. For this reason, the maximum local density and the integrated contribution of the individual structural components are analyzed separately in the following sections.

4.5. Secondary-particle production and structural origin

Only secondary particles subsequently registered in detector A and/or B were retained, with each track counted once. Their population rises strongly with primary mass and energy; in the 10 GeV/n Fe-56 simulation, electrons are the largest registered secondary component.

Voxelized birth-position maps distinguish the location of the highest local production density from the component with the largest integrated yield. For 10 GeV/n Fe-56, the maxima of the investigated secondary species lie in the aluminium protection near the detector assembly.

Integrated over complete structural components, however, FREND supplies the largest contribution of registered protons, mesons, positrons and alpha particles in the same high-statistics Fe-56 case, while electrons have their largest single contribution from the silicon-detector region. Thus maximum local density and integrated yield are complementary measures.

4.6. Structural origin of secondary particles associated with false events

A dedicated analysis was performed for secondary particles associated specifically with the unwanted event classes 2, 4 and 5. Only registered events satisfying the two-detector threshold were considered. For Case 2, where the primary intersects neither detector, secondary particles registered in detector A and/or B were retained. Table 2 summarizes the structural origin of the relevant secondary particles for these false-event classes.

Table 2. Structural origin of relevant secondary particles associated with false-event classes, summed over the twelve monoenergetic simulations.

Region	Case 2 N	Case 2 %	Case 4 N	Case 4 %	Case 5 N	Case 5 %
FREND	96,422	36.56%	87	1.18%	56	0.83%
steel cover / housing	51,618	19.57%	645	8.72%	586	8.71%
Silicon detector	35,926	13.62%	2,383	32.20%	2,214	32.91%
Ceramic	34,187	12.96%	2,812	37.99%	2,455	36.49%
Aluminium protection	31,860	12.08%	1,111	15.01%	1,076	16.00%
Textolite	8,352	3.17%	148	2.00%	99	1.47%
Resin	2,886	1.09%	213	2.88%	239	3.55%

Region	Case 2 N	Case 2 %	Case 4 N	Case 4 %	Case 5 N	Case 5 %
TGO structure	2,345	0.89%	2	0.03%	2	0.03%

For Case 4, where the primary intersects detector A only, the analysis was restricted to secondaries registered in detector B; for Case 5 the complementary selection was applied to secondaries registered in detector A. Each secondary particle was identified by eventId and trackId and counted only once, and its birth position was assigned to a component of the numerical geometry.

Case 2 shows a clear contribution from the extended surrounding structure. FREND is the largest single source, with 96,422 relevant secondaries (36.56%), followed by the steel cover/housing (19.57%). Cases 4 and 5 show a different pattern: ceramic contributes 37.99% and 36.49%, respectively, while the silicon-detector region contributes 32.20% and 32.91%. Thus, approximately 70% of the relevant secondary population in Cases 4 and 5 originates in the immediate ceramic/silicon detector environment.

4.7. Dependence on primary and secondary species

The dominant source region varies with primary species and energy. For Case 2, FREND becomes increasingly important at high energy, whereas at lower energies the dominant region can shift toward the detector materials. Resolving the analysis by secondary species gives the same qualitative separation: extended structures dominate much of Case 2, while local ceramic/silicon production dominates Cases 4 and 5.

These results identify two distinct false-coincidence mechanisms. Case 2 is driven substantially by secondary production in the extended surrounding structure, especially FREND for non-electron components. Cases 4 and 5 are predominantly local., arising from secondary production in the immediate detector environment. The quoted fractions are unweighted sums over the twelve monoenergetic simulations and are not orbital background fractions.

4.8. Implications for rejection of unwanted events

The spatial and event-class analyses are directly connected to the measurement objective: preserve Case 3 while suppressing Cases 2, 4 and 5. Figures 5–8 visualize how secondaries produced in the instrument or surrounding structure can complete a nominal two-detector trigger, while the structural analysis identifies the regions that contribute most strongly.

The modified geometry in Figure 3 provides one example of a hardware rejection method. For the 1 GeV/n Fe-56 case, the original geometry (Figure 2) gives Case 2 = 5,093, Case 3 = 117, Case 4 = 548 and Case 5 = 506. With the 1-mm iron protection (Figure 4), the corresponding values are 2,125, 109, 451 and 64. Case 2 is therefore reduced by 58.27%, Case 4 by 17.70% and Case 5 by 87.35%, whereas the desired Case 3 population decreases by only 6.84%. The combined unwanted population (Cases 2 + 4 + 5) decreases from 6,147 to 2,640, or by 57.05%. This asymmetric response shows that structural modifications do not affect all false-event mechanisms equally and must be judged by both false-event suppression and Case 3 retention.

5. Discussion

The simulations demonstrate that the 70 keV coincidence condition in detectors A and B is necessary for event registration but is not sufficient to identify a primary particle traversing the complete telescope. Case 3 is the desired population, whereas Cases 2, 4 and 5 are unwanted for this measurement objective. The increasing dominance of Case 2 for energetic heavy

primaries shows that interactions in the surrounding mass can strongly distort the raw coincidence response.

Secondary particles generated in Liulin-MO, FREND and the spacecraft can reach one or both silicon detectors and complete a valid trigger. The spatial analysis also shows that the location of maximum local production density need not coincide with the component producing the largest integrated registered-secondary yield.

The false-event-specific analysis separates two mechanisms. Summed over the twelve simulations, FREND is the largest Case 2 source (36.56%), whereas Cases 4 and 5 are dominated by ceramic (37.99% and 36.49%) and silicon-associated production (32.20% and 32.91%). This distinction implies that rejection strategies may need to target extended-structure and local-detector backgrounds differently.

Because the simulations are monoenergetic and unweighted, their species populations must not be interpreted directly as flight fractions. Quantitative orbital predictions require folding the response with realistic Galactic cosmic-ray spectra and elemental abundances.

No single rejection method is expected to remove all unwanted events. The 1-mm iron protection illustrates a hardware approach; software selection based on detector signals provides a second approach; and response corrections or selection boundaries derived from numerical modelling provide a third. These approaches should be evaluated by two quantities: the efficiency for retaining Case 3 and the rejection efficiency for Cases 2, 4 and 5. Minimizing the total coincidence rate alone is not an appropriate optimization criterion if genuine Case 3 events are removed at the same time.

6. Conclusions

A numerical analysis of the Liulin-MO telescope response aboard ExoMars TGO was performed using a detailed particle-transport model of the detector system and surrounding structure. Registered events were defined by a deposited energy greater than 70 keV in each detector and were independently classified from the initial geometrical trajectory of the primary particle.

The analysis confirms that a two-detector coincidence does not necessarily imply that the primary traversed both detectors. Case 3 represents the desired telescope population, while Cases 2, 4 and 5 constitute unwanted contributions. Secondary particles generated in the instrument and spacecraft materials can produce complete coincidences or provide the signal in the detector not crossed by the primary.

Registered-secondary populations increase strongly with primary mass and energy. Their spatial and structural distributions show that local detector materials and the extended FREND/spacecraft environment contribute in different ways to false coincidences.

For false events, Case 2 is strongly influenced by the extended surrounding structure, with FREND providing the largest integrated contribution, whereas Cases 4 and 5 are dominated by the immediate ceramic/silicon detector environment. These unweighted Monte Carlo fractions characterize mechanisms, not orbital composition.

The comparison between the original 1 GeV/n Fe-56 geometry and the configuration with a 1-mm iron protective layer demonstrates the potential of geometrical suppression: the unwanted population decreases from 6,147 to 2,640 events (about 57%), while Case 3 decreases from 117 to 109 events (about 6.8%). Geometry modification is nevertheless only one possible method; software selection and simulation-based corrections should also be investigated.

The event-by-event numerical classification therefore provides a framework for developing and testing rejection procedures whose common objective is to retain the genuine Case 3 population while suppressing Cases 2, 4 and 5. Future work should fold the simulated response with realistic Galactic cosmic-ray spectra and elemental abundances and apply the resulting selection or correction procedures to Liulin-MO flight data.

References

Agostinelli, S., Allison, J., Amako, K., Apostolakis, J., Araujo, H., et al. (2003). Geant4—A simulation toolkit. *Nuclear Instruments and Methods in Physics Research Section A*, Vol. 506, pp. 250–303. DOI: 10.1016/S0168-9002(03)01368-8.

Allison, J., Amako, K., Apostolakis, J., Araujo, H., Arce Dubois, P., et al. (2006). Geant4 developments and applications. *IEEE Transactions on Nuclear Science*, Vol. 53, No. 1, pp. 270–278. DOI: 10.1109/TNS.2006.869826.

Allison, J., Amako, K., Apostolakis, J., Arce, P., Asai, M., et al. (2016). Recent developments in Geant4. *Nuclear Instruments and Methods in Physics Research Section A*, Vol. 835, pp. 186–225. DOI: 10.1016/j.nima.2016.06.125.

Belogurov, S., Berchun, Yu., Chernogorov, A., Malzacher, P., Ovcharenko, E., et al. (2011). CATIA-GDML geometry builder. *Journal of Physics: Conference Series*, Vol. 331, 032035. DOI: 10.1088/1742-6596/331/3/032035.

Belogurov, S., Berchun, Yu., Chernogorov, A., Malzacher, P., Ovcharenko, E., et al. (2014). Development and application of CATIA-GDML geometry builder. *Journal of Physics: Conference Series*, Vol. 513, 022003. DOI: 10.1088/1742-6596/513/2/022003.

Mitrofanov, I., Malakhov, A., Bakhtin, B., Golovin, D., Kozyrev, A., et al. (2018). Fine Resolution Epithermal Neutron Detector (FREND) onboard the Trace Gas Orbiter. *Space Science Reviews*, Vol. 214, 86. DOI: 10.1007/s11214-018-0522-5.

Semkova, J., Koleva, R., Benghin, V., Dachev, T., Matviichuk, Y., et al. (2018). Charged particles radiation measurements with Liulin-MO dosimeter of FREND instrument aboard ExoMars Trace Gas Orbiter during the transit and in high elliptic Mars orbit. *Icarus*, Vol. 303, pp. 53–66. DOI: 10.1016/j.icarus.2017.12.034.

Yando, K., Millan, R. M., Green, J. C., Evans, D. S. (2011). A Monte Carlo simulation of the NOAA POES Medium Energy Proton and Electron Detector instrument. *Journal of Geophysical Research: Space Physics*, Vol. 116, A10231. DOI: 10.1029/2011JA016671.

Zhao, X. Y., Wang, H. Y., Wu, F., Meng, X. C., Ma, Y. Q., et al. (2013). A geometric factor calculation method based on the isotropic flux assumption. *Chinese Physics C*, Vol. 37, No. 12, 126201. DOI: 10.1088/1674-1137/37/12/126201.

DOI: 10.31401/WS.2026.proc.33

Light Pollution - New Measurements: The UrbObsBel Project

Simić Z.[1], Samurović S.[1], Pavlović R.[2], Cvetković Z.[2], Damljanović G.[1]

[1]Astronomical Observatory, Belgrade; zsimic@aob.rs
[2]Institute of Physics, Belgrade

Abstract

The Urban Observatory of Belgrade (UrbObsBel) is a three year project (started in January 2024) and funded by the Science Fund of the Republic of Serbia developed as an urban observatory for the systematic monitoring of light pollution in Belgrade, also using the measurements of sky brightness at the Astronomical Station Vidojevica, one of the last remaining dark spots in Serbia, employing proven astronomical techniques and multiple complementary instruments. At both stations we have Unihedron SQM-LE and TESS-W photometers, and in Belgrade we have also been using two hyperspectral imaging sensors (HSIs). In this contribution we present our measurements obtained so far. We show that Belgrade is subject of strong light pollution.

Keywords: light pollution, optical instruments, infrared instruments

1. Introduction

The Urban Observatory of Belgrade (UrbObsBel) is a three year project (started in January 2024) funded by the Science Fund of the Republic of Serbia which takes place at the Astronomical Observatory of Belgrade (AOB). One of its main objectives is to study the light pollution, one of the least understood form of environmental degradation caused by human activities, and for this purpose we mounted observing instruments in Belgrade (Zvezdara Municipality) and at the Astronomical Station Vidojevica (ASV) which is one of the last remaining dark spots in Serbia. Our research team includes 8 experienced researchers from 4 reputable research organizations from Serbia. In addition to the five authors of this contribution, they are: Dr. Dajana Bjelajac (Faculty of Sciences, University of Novi Sad), Dr. Branislav Rovčanin (Faculty of Medicine, University of Belgrade) and Dr. Dragan Lukić (Institute of Physics, Belgrade). The project is described in the recently published Proceedings of the UrbObsBel Workshop held in Belgrade in June 2025 [Samurović, 2026] and below we first list the instruments used in the project and then present some of our measurements of the light pollution.

Light pollution refers to the excessive, inappropriate, or misdirected artificial light which disrupts natural light levels, causing adverse effects on the environment, human health, and astronomical observations. It is estimated, using the observational data from 2011 to 2022, that the sky brightness coming from the artificial light is increasing exponentially throughout the world with an average of 10 per cent every year, meaning that it doubles in less than 8 years [Falchi & Bara, 2023]. Some more recent estimates suggest that the artificial light is increasing at a slower rate, between 2.78 and 6.68 per cent per year [Shah et al., 2025]. In this contribution, we will compare these findings to the first measurements obtained in our UrbObsBel project.

2. Instruments used in the UrbObsBel project

We have mounted the following instruments (see Pavlović et al. 2025, Samurović 2026 for more details):

- **All-sky** camera **Alcor OMEA 3C**, with resolution of 3100 × 2100 pixels, field of view 180° × 180° is mounted on the top of the Tower of the AOB and is used for comprehensive sky monitoring.
- **Unihedron Sky Quality Meter (SQM), model SQM-LE** used for the measurement of night sky brightness. One device is mounted at the top of the Tower of the AOB and the other at the ASV.
- **TESS-W photometer** is also mounted at the top of the Tower of the AOB and at the ASV.
- **Two HyperSpectral Imaging (HSI) devices** constructed within the UrbObsBel project mounted at the top of the Tower of the AOB.
- Two **FLIR A700 thermal cameras** with infrared resolution 640 × 480 pixels, with wavelengths from 7.5 to 14.0 micrometers and field of view of 14° × 10° used for therml characterization of sources and objects; both cameras are mounted at the top of the Tower of the AOB.
- **Nikon Z7II** camera used for monitoring the sky in the visible part of spectrum. This camera mounted at the top of the Tower of the AOB is used with fisheye lens NIKKOR Z and has resolution of 8256 × 5504 pixels.

3. Measurements of the light pollution performed within the UrbObsBel project

In this section we present the new measurements of the light pollution obtained using two SQM devices, one mounted at the AOB and the other at the ASV. In our analysis of the trends in light pollution we relied on the approach used in the paper by Shah et al. (2025). It is known that the night sky brightness (NSB) is dependent on several variables of which the most important ones are solar, lunar, and cloud effects. In our analysis the measurements where those effects have been significant were neglected in order to obtain the dataset which is determined exclusively due to the temporal variations of artificial lighting. In two Figures below we present our measurements of the trends of sky brightness for two aforementioned locations for one-year period, i.e. from July 2025 to July 2026.

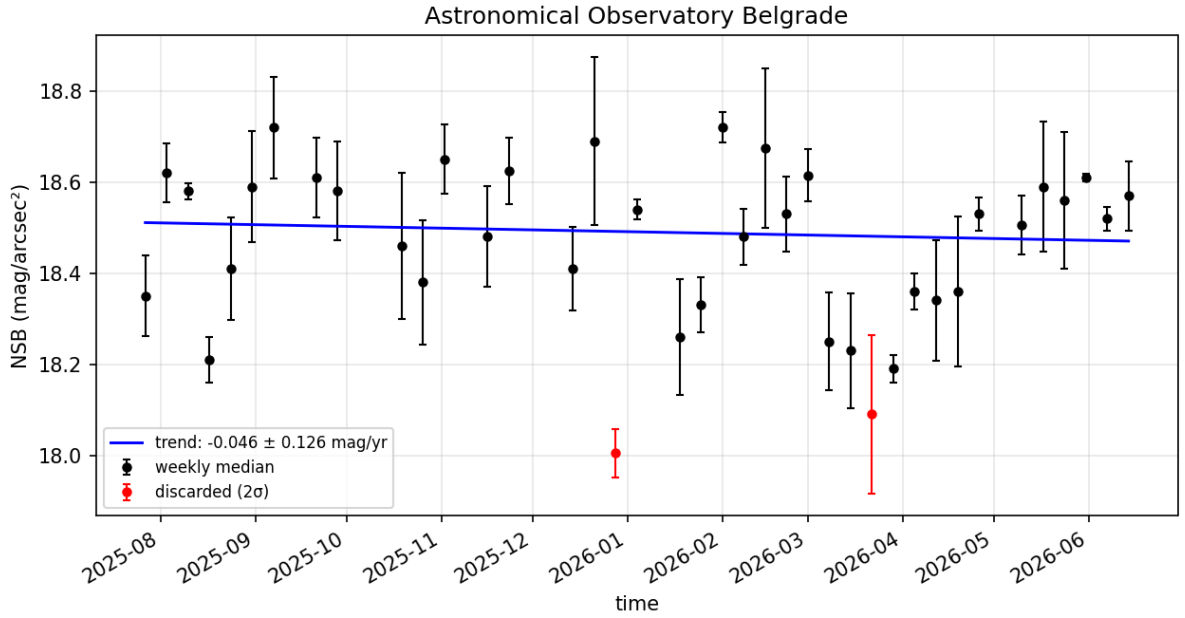


Figure 1. *Trend of clear nights for the Astronomical Observatory of Belgrade (AOB).*

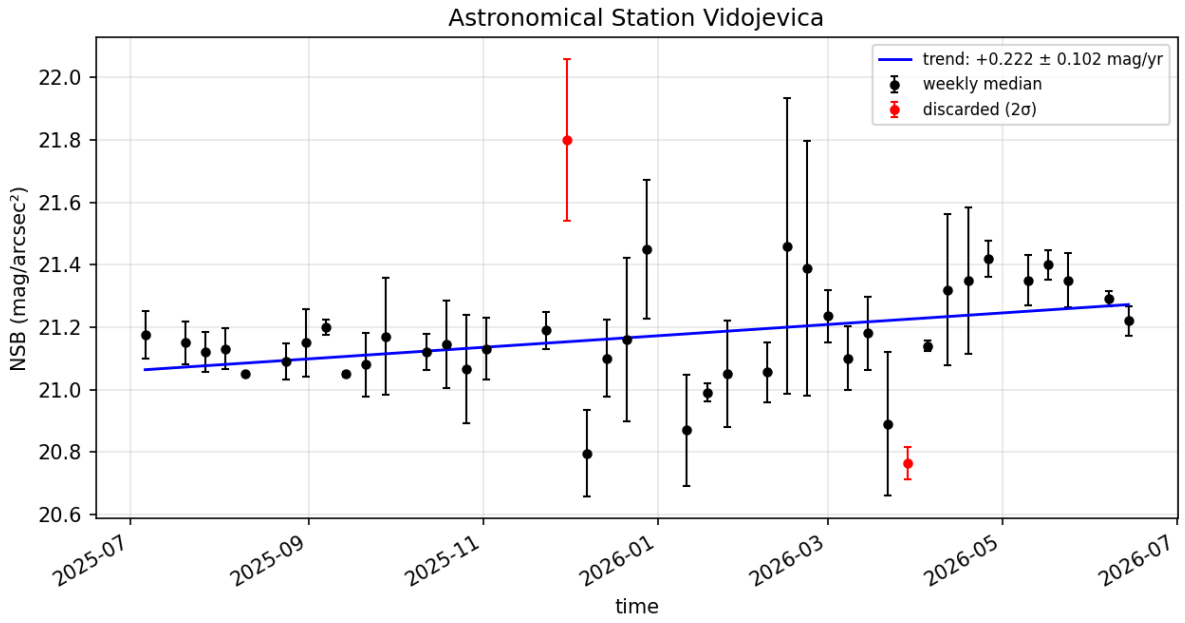


Figure 2. *Trend of clear nights for the Astronomical Station Vidojevica (ASV).*

From Figure 1 and Figure 2 it is obvious that two opposing trends are present. In the case of the AOB, i.e. the urban environment, the quality of the night sky has deteriorated because the sky brightness increased 4.6 per cent in one year. On the other hand, at the ASV, which is a dark spot in the southern part of Serbia, the quality of the night sky has improved, because the sky brightness decreased 22.2 per cent in the same year. The obtained result for the AOB is in agreement with the urban trends seen in the Netherlands [Shah et al., 2025] and quoted above. The measurements obtained using the TESS-W instruments will be presented elsewhere but we here note that they also suggest the increase of light pollution in Belgrade and the improvement of sky quality at the ASV.

As noted above in our measurements we also rely on the HyperSpectral Imaging (HSI) instrument which we constructed within our UrbObsBel project. HSI methodology and various applications have recently been discussed in Hong et al. (2026). We here note that both our HSI devices are mounted at the top of the Tower of the AOB: one is pointed towards the city center, and the other towards the opposite direction. The greatest value of the HSI instrument within the UrbObsBel project lies in the fact that it enables the transition from the classical measurement of light quantity to the analysis of its spectral composition. This is essential, as different lighting technologies can differ significantly in their impact on the night sky, biological systems and the visual quality of a space, even when they provide a similar overall level of illumination. In an urban environment such as Belgrade, where public lighting, decorative lighting, advertising sources, sports facilities and various commercial lighting installations coexist, it is precisely spectral analysis that can help in distinguishing and classifying the dominant sources.

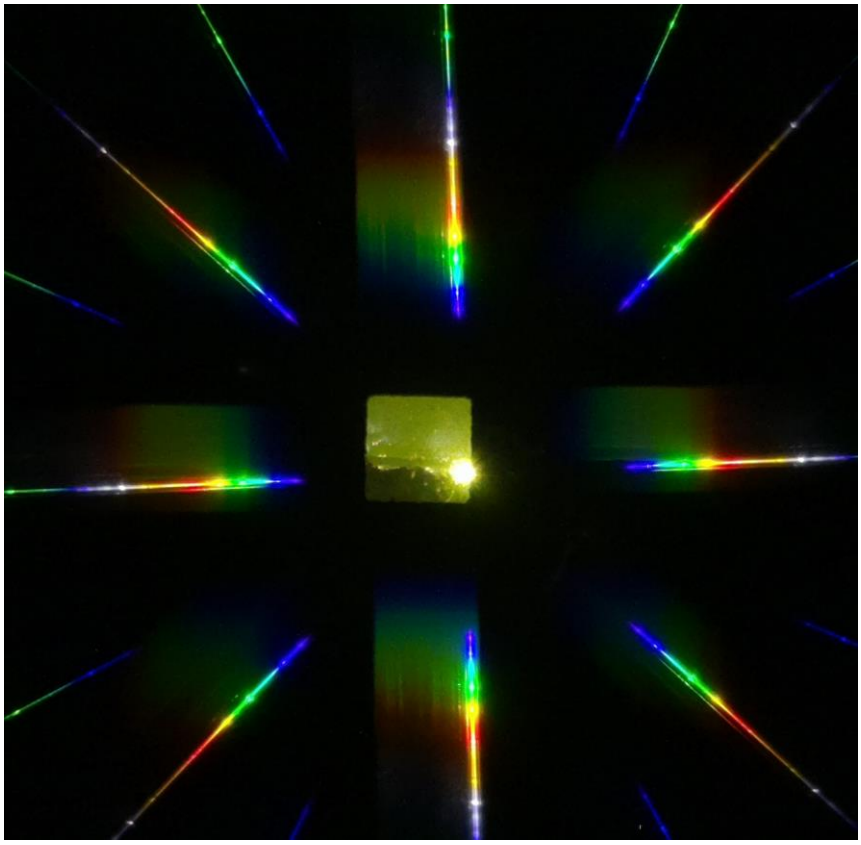


Figure 3. *Snapshot of the city center of Belgrade on 2 August 2026 at 21:57 obtained using the HSI instrument.*

Figure 3 shows how the city center is seen at all wavelengths (from this image a hypercube is produced), while in Figure 4 only four wavelengths are shown: 477.179 nm, 550.146 nm, 650.475 nm and 705.201 nm. These four images are intentionally “artificially” colored to better emphasize the contrast. We can say that the HSI device has the potential to enable us to identify the spectral signatures of certain types of lighting, monitor changes over time and create a database of importance not only for astronomy, but also for urban planning, energy and ecology. The special significance of this device lies in the fact that it was developed within a domestic project, with a combination of open solutions and our own modifications. Therefore, it also represents an example of the successful development of a modern scientific instrument in local conditions.

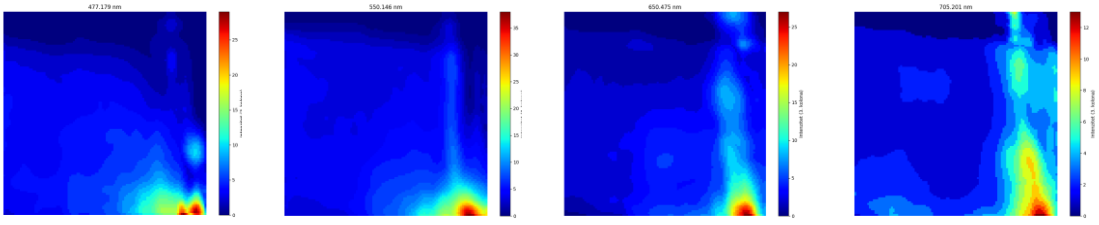


Figure 4. *Intensity map at the following four wavelengths of the hypercube obtained using the snapshot presented in Figure 3: 477.179 nm, 550.146 nm, 650.475 nm and 705.201 nm. The images are artificially colored and the lowest intensity is shown in blue, and the highest intensity is presented using red.*

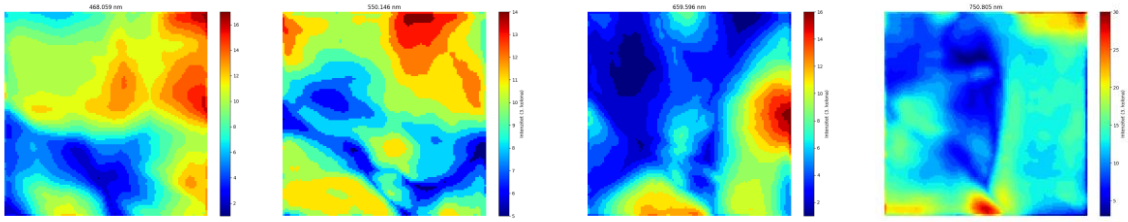


Figure 5. *Intensity map at the following four wavelengths of the hypercube of the observation of the Sun performed on 25 May 2026 (at 13:22): 468.059 nm, 550.146 nm, 659.596 nm and 750.805 nm. Again, the images are artificially colored as in Figure 4.*

Finally, we note that the HSI devices can be used for solar observations. A prototype for HSI instrument for solar observations was presented in van Noort et al. (2022). In Figure 5 we present our HSI measurements when on 25 May 2026 (at 13:22) our HSI instrument was pointed to the Sun. Again, intensity at four different wavelengths is presented.

4. Conclusions

In this contribution we briefly described the UrbObsBel project funded by the Science Fund of the Republic of Serbia in the period January 2024-December 2026. We have shown that the light pollution in Belgrade has increased approximately 5 per cent in one year, whereas the quality of the sky at the Astronomical Station Vidojevica has improved in the same period for approximately 20 per cent. The details about the project, together with the data repository are available at the following address: https://urbobsbel.aob.rs.

Acknowledgment. This research was supported by the Science Fund of the Republic of Serbia, no. 6775, Urban Observatory of Belgrade.

References

Falchi, F., Bara, S. (2023). Light pollution is skyrocketing. *Science*, Vol. 379, No. 6629, pp. 234–235. DOI: 10.1126/science.adf4952.

Hong, D., Li, C., Yokoya, N., et al. (2026). Hyperspectral imaging. *Nature Reviews Methods Primers*, Vol. 6, 19. DOI: 10.1038/s43586-026-00470-x.

Pavlović, R., Cvetković, Z., Bjelajac, D., Damljanović, G., Lukić, D., Rovčanin, B., Samurović, S., Simić, Z. (2025). The UrbObsBel Project: Instruments and Detectors. *Publications of the Astronomical Observatory of Belgrade*, Vol. 107, pp. 129–134. DOI: 10.69646/14sbac22p.

Samurović, S. (2026). Projekat Gradske opservatorije Beograda (UrbObsBel). *Special Issues of the Astronomical Observatory of Belgrade*, No. 5, pp. 1–14. DOI: 10.69646/aobsi00501. (In Serbian).

Shah, F. R., Peletier, R. F., Noel-Storr, J., et al. (2025). Beyond the clouds: Advanced data analysis of a Dutch sky quality meter network. *Monthly Notices of the Royal Astronomical Society*, Vol. 542, No. 1, pp. 272–292. DOI: 10.1093/mnras/staf1200.

van Noort, M., Bischoff, J., Kramer, A., Solanki, S. K., Kiselman, D. (2022). A prototype of a microlensed hyperspectral imager for solar observations. *Astronomy & Astrophysics*, Vol. 668, A149. DOI: 10.1051/0004-6361/202243464.

DOI: 10.31401/WS.2026.proc.34

Some Examples of Reflectionless Propagation of Electromagnetic Waves in Nonuniform Space Plasma

Zolnikova N.N.[1, 2], Shkevov R.[3], Mikhailovskaya L.A.[1]

[1]Space Research Institute, Russian Academy of Sciences, Moscow, Russia
nzolnik@cosmos.ru, ludamikh@gmail.com
[2]Russian University of Transport, Moscow, Russia
[3]Space Research and Technology Institute, Bulgarian Academy of Sciences, Sofia, Bulgaria
shkevov@space.bas.bg

Abstract

We study the possibility of reflectionless propagation of electromagnetic wave through complicated space plasmas structures, which in general case can be opaque. This problem is of interest in particular for transmission of electromagnetic signals from a source located in the near-Earth plasma through the surrounding evanescent regions. We show that for some distinguished profiles of dielectric permittivity the effective transillumination of electromagnetic wave can happen. Applying numerical calculations to exact solution of one-dimensional linear Helmholtz equation, we demonstrate that under some choice of a wave number and the corresponding profile of dielectric permittivity the monochromatic electromagnetic wave can pass through opaque regions without reflection. In contrast with the standard WKB approximation, this approach has no restrictions on the relationship between the length of inhomogeneity and the length of incident wave. Some new profiles of the normalized amplitude of the electromagnetic wave, the effective plasma permittivity and the dimensionless wave number are presented and discussed.

Keywords: Helmholtz equation, reflectionless transmission, inhomogeneous plasma layer, the effective plasma permittivity, full enlightenment, the dimensionless wave number

1. Introduction

In recent years, the interaction of electromagnetic waves with nonuniform inhomogeneous media (including the Earth's atmosphere and laboratory and space plasmas) has received active study [Dykhne et al., 2003; Shvartsburg, 2005; Ozbay, 2006; Erokhin & Zakharov, 2007, 2011; Shalin, 2010; Davidovich, 2010; Erokhin et al., 2015, 2018; Poverennyi & Erokhin, 2013; Merkulov & Erokhin, 2013], where considerable attention was paid to analyzing the possibility of reflectionless wave propagation on the basis of exactly solvable models. In the year, 2007 Zakharov V.E. and Erokhin N.S. considered the following problem – if an electromagnetic wave can pass through inhomogeneous plasma containing the layers with negative permittivity. They found [Erokhin & Zakharov, 2007, 2011] that such passage can take place and presented explicit examples. In [Erokhin & Zakharov, 2007, 2011] as well as in [Erokhin et al., 2015, 2018; Poverennyi & Erokhin, 2013; Merkulov & Erokhin, 2013], the case of a monochromatic wave considered. The most popular approach to problems of electromagnetic waves interaction with nonuniform media is based on the quasiclassical (or WKB) approximation [Nazarenko et al., 1994; Lagovskii, 2006; Zharov et al., 1979; Kozyrev et al., 1979; Ginzburg & Rukhadze, 1970]. This approach has a very serious restriction – a length of incident wave must be much less than the characteristic size of the inhomogeneities, and, in addition, the inhomogeneity must change smoothly. However, in Earth's atmosphere, in heliosphere and in the far regions of space plasmas inhomogeneity may contain relatively small-scale large-amplitude structures. This circumstance stimulates the use of exactly solvable models for the study of the wave

propagation in highly nonuniform media. These models show the possibility of electromagnetic waves resonant tunneling through a nonuniform plasma with extended evanescent regions in which the squared refractive index is negative. Let us recall that, according to the classical concepts, such plasma layer is treated as nontransparent. In papers [Erokhin & Zakharov, 2007, 2011; Erokhin et al., 2015, 2018; Poverennyi & Erokhin, 2013; Merkulov & Erokhin, 2013], several models of the wave vector profiles have been proposed. All these models contain a large number of internal parameters that determine whether the incident wave will completely pass through the inhomogeneous plasma layer or will be partially reflected. Below we propose options for specific wave vector profiles, which ensure reflectionless passage of an electromagnetic wave through a layer of nonlinear inhomogeneous plasma.

2. Theoretical background

Consider the Helmholtz equation (1), describing the space structure of the electromagnetic

$$\frac{d^2E(\xi)}{d\xi^2} + \varepsilon(\xi) \cdot E(\xi) = 0 \tag{1}$$

wave field which propagates along the x – axis. Here ξ is a dimensionless variable, $\xi = \omega x / c$, $\varepsilon(\xi) = N^2$ is the effective permittivity of the plasma, and N (ξ) is the refractive index, determined by the components of the permittivity tensor. To describe the reflectionless passage of the wave through an inhomogeneous plasma layer we assume that E (ξ) has the WKB-type form by analogy with (Erokhin & Zakharov, 2007, 2011):

$$E(\xi) = \frac{E_0}{p^{1/2}} \cdot e^{i\,\Psi(\xi)} \tag{2}$$

Here $p(\xi) = (d\Psi(\xi)) / d\xi$ is the dimensionless wave vector, Ψ(ξ) is the phase and E_0 is the characteristic value of the wave field. The function E (ξ) solves Equation (1) iff the following relation between p (ξ) and ε (ξ) is fulfilled:

$$\varepsilon(\xi) = p^2(\xi) - p(\xi)^{1/2} \cdot \frac{d^2}{d\xi^2}\left(\frac{1}{p(\xi)}\right)^{1/2} \tag{3}$$

Let us introduce normalized wave amplitude:

$$\left|\frac{E}{E_0}\right| \equiv W(\xi) = \left(\frac{1}{p(\xi)}\right)^{1/2} \tag{4}$$

From (3) follows the nonlinear equation on W (ξ):

$$\frac{d^2W(\xi)}{d\xi^2} + \varepsilon(\xi) \cdot W(\xi) - \left(\frac{1}{W(\xi)}\right)^3 \tag{5}$$

It should be noted that to calculate p (ξ) in terms of ε (ξ) it is necessary to solve non-linear ordinary differential equation. On the contrary, the effective permittivity ε (ξ) is expressed explicitly in terms of wave vector p (ξ). Therefore, to construct solutions corresponding to the regime of transillumination of initial wave it is sufficient to consider a wave vector p (ξ) satisfying the crosslinking conditions:

$$p(\xi) = 1, \quad \frac{dp(\xi)}{d\xi} = 0 \tag{6}$$

at both plasma-vacuum boundaries, and to calculate the corresponding effective permittivity ε (ξ) using (3).

3. Calculations results

At first let us consider an example of reflectionless propagation of a transverse electromagnetic wave through a plasma layer with two localized structures having different amplitudes and width in which the plasma density tends to zero at $|\xi| \to \infty$ (the plasma dielectric permittivity tends to 1). To realize this model we take the wave vector as:

$$p(\xi) = 1 + \frac{\alpha_1}{1+\left(\frac{\xi-\beta_1}{\eta_1}\right)^2} + \frac{\alpha_2}{1+\left(\frac{\xi-\beta_2}{\eta_2}\right)^2} \quad (7)$$

Here to provide full transparency of the transient layer all the internal parameters α, β, η should fulfill the boundary crosslinking conditions (6). One of the possible ways is to take α_1 = -0.85, β_1 = 5, η_1 = 5, α_2 = -0.5, β_2 = 12, η_2 = 2. The dynamics of wave vector with such parameters is shown on the Figure 1 a). On the Figure 1 b), the dielectric permittivity in the transient layer is shown. We can observe regions with negative square of refractive index, but despite this the wave "tunnelizes" these regions without energy loss. Its amplitude $W(\xi) = 1 / \sqrt{(p(\xi))}$ is presented on the Figure 2.

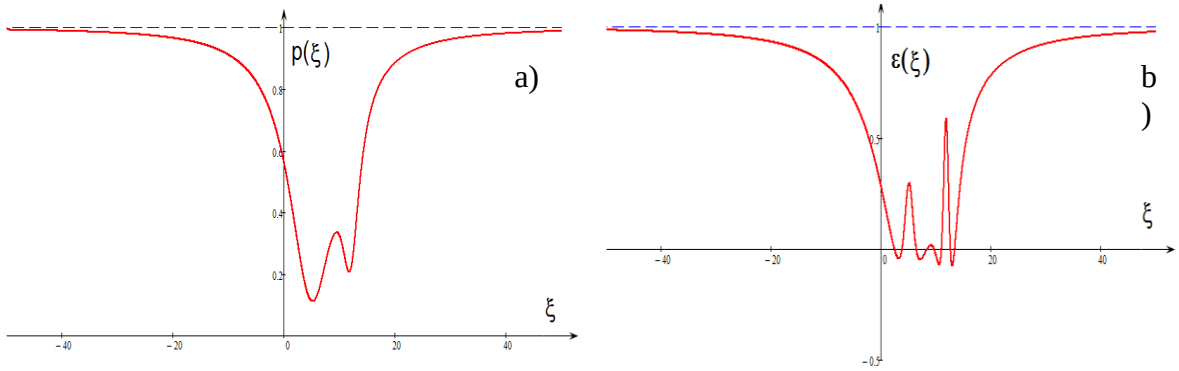


Figure 1. a) *The wave vector dynamics for transient layer with two localized structures with parameters α_1 = -0.85, β_1 = 5, η_1 = 5 , α_2 = -0.5, β_2 = 12, η_2 = 2 providing the reflectionless passage of electromagnetic wave;* ***b)*** *The dielectric permittivity of transient layer with two localized structures with parameters α_1 = -0.85, β_1 = 5, η_1 = 5 , α_2 = -0.5, β_2 = 12, η_2 = 2.*

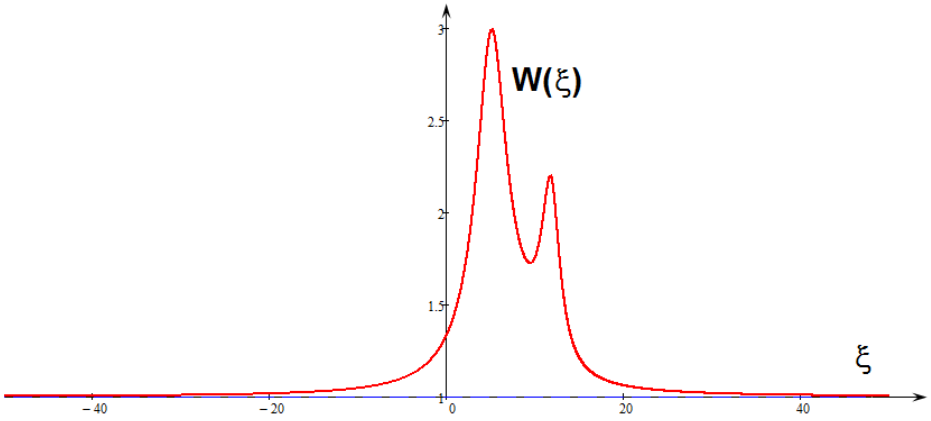


Figure 2. *The wave amplitude dynamics in transient layer with two localized structures with parameters α_1 = -0.85, β_1 = 5, η_1 = 5, α_2 = -0.5, β_2 = 12, η_2 = 2.*

Now we consider a more complicated case, simulating the transient layer to be quasi-turbulent. Such situations when a layer with quasi-turbulent inhomogeneity is surrounded with a vacuum from one side and very highly rarefied calm plasma from another is also in good

agreement with modern models of heliosphere [Opher et al., 2015; Pogorelov et al., 2015]. We take the wave vector p (ξ) in the following form:

$$p(\xi) = 1 - 0.5 \cdot f(\xi) \cdot (1 - \cos(\gamma\,\xi)) \cdot \beta \qquad (8)$$

Here the function $f(\xi)$ is responsible for quasi-turbulent inhomogeneity and can be taken as

$$f(\xi) = \sigma + \sum_{n=1}^{N} \left(\frac{\chi}{n^{7/6}}\right) \cdot cos(n\,\xi\,\gamma + \Psi_n) \qquad (9)$$

Where Ψ - is a vector of N uniformly distributed random numbers from an interval (0, 2π). We take N = 100. Therefore, the expression for dielectric permittivity, satisfying the exact solution of Helmholtz equation and a given by formula (3) form of the wave vector is:

$$\varepsilon(\xi) = p^2(\xi) + \frac{h(\xi)}{2p(\xi)} - 0.75\left(\frac{g(\xi)}{p(\xi)}\right)^2 \qquad (10)$$

Where

$$g(\xi) = -0.5\,\gamma\, f(\xi) \cdot \beta \cdot \sin(\gamma\,\xi) - 0.5 \cdot (1 - cos(\gamma\,\xi)) \cdot \beta \cdot r_1(\xi)$$

$$h(\xi) = -0.5 \cdot \gamma^2\beta \cdot f(\xi) \cdot cos(\gamma\,\xi) - \gamma\beta \cdot r_1(\xi) \cdot sin(\gamma\,\xi) - 0.5 \cdot (1 - cos(\gamma\,\xi)) \cdot \beta \cdot r_2(\xi)$$

$$r_1(\xi) = -\sum_{n=1}^{N} \left(\frac{\gamma \cdot \chi}{n^{1/6}} \cdot sin(n\,\xi\,\gamma + \Psi_n)\right) \qquad (11)$$

$$r_2(\xi) = -\sum_{n=1}^{N} \left(n^{5/6} \cdot \gamma^2 \cdot \chi \cdot cos(n\,\xi\,\gamma + \Psi_n)\right).$$

To match the boundary crosslinking conditions (6) we take the internal parameters in (8) as b = 20, γ = 2π / b, β = 0.1, χ = 0.5, σ = 3. On the Figure 3 a) the behavior of function f (ξ) is shown, Figure 3 b) demonstrates the dynamics of wave vector p(ξ), Figure 4 a) and Figure 4 b) present dependence of dielectric permittivity ε (ξ) in the transient layer and wave amplitude $W(\xi) = 1 / \sqrt{(p(\xi))}$. It is easy to check that crosslinking boundary conditions are fulfilled.

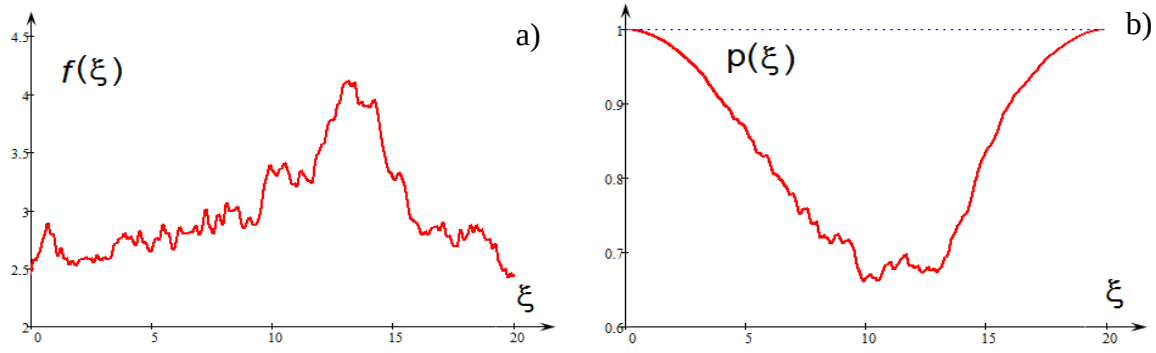


Figure 3. a) *The behavior of the function f (ξ) for quasi-turbulent transient layer;* ***b)*** *The wave vector dynamics for quasi-turbulent transient layer with parameters b = 20, γ = 2π / b, β = 0.1, χ = 0.5, σ = 3, providing the reflectionless passage of electromagnetic wave.*

On the Figure 4 a) we can see a big amount of very narrow opaque regions with ε (ξ) < 0, through which the wave passes without energy loss.

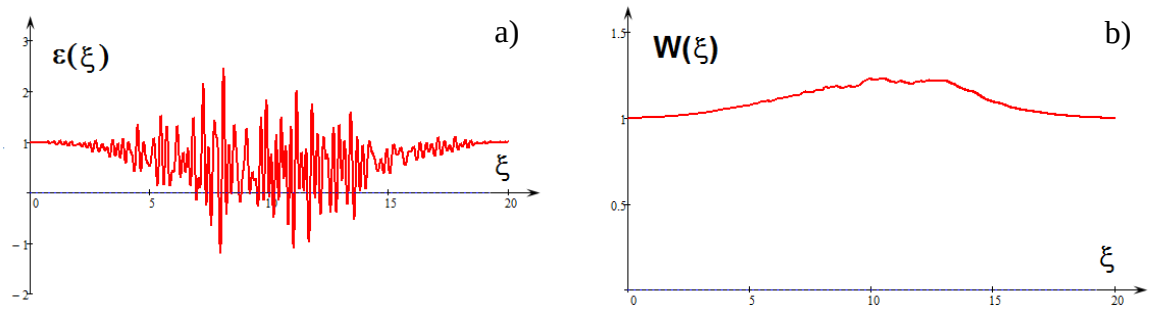


Figure 4. a) *The dielectric permittivity of quasi-turbulent transient layer with parameters* $b = 20$, $\gamma = 2\pi / b$, $\beta = 0.1$, $\chi = 0.5$, $\sigma = 3$; ***b)*** *The wave amplitude dynamics in quasi-turbulent transient layer with parameters* $b = 20$, $\gamma = 2\pi / b$, $\beta = 0.1$, $\chi = 0.5$, $\sigma = 3$.

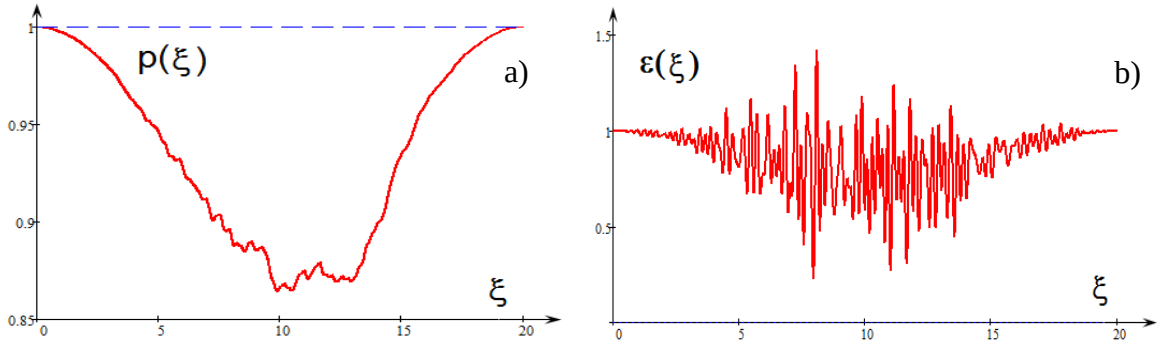


Figure 5. a) *The wave vector dynamics for quasi-turbulent transient layer with parameters* $b = 20$, $\gamma = 2\pi / b$, $\beta = 0.04$, $\chi = 0.5$, $\sigma = 3$, *providing the reflectionless passage of electromagnetic wave.* ***b)*** *The dielectric permittivity of quasi-turbulent transient layer with parameters* $b = 20$, $\gamma = 2\pi / b$, $\beta = 0.04$, $\chi = 0.5$, $\sigma = 3$.

If we change one of internal parameters controlling the boundary crosslinking conditions matching, for example, take β = 0.04, we obtain another variant of reflectionles passage, but now the opaque regions are absent. The dynamics of p (ξ), ε (ξ) and $W(\xi)$ are shown in the Figures 5. a), b), Figure 6.

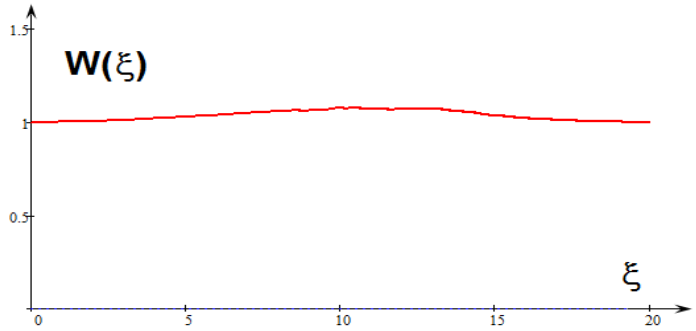


Figure 6. *The wave amplitude dynamics in quasi-turbulent transient layer with parameters* $b = 20$, $\gamma = 2\pi / b$, $\beta = 0.4$, $\chi = 0.5$, $\sigma = 3$.

If internal parameters of our problem do not match the conditions (6), we also obtain the electromagnetic wave because waves reflected from the boundaries of regions will appear and it will lead to the energy loss of initial wave. Exact solution of (1), but in this case, the transient layer will not be fully transparent for

4. Conclusions

The analysis performed has shown the possibility of inhomogeneous plasma transillumination in the presence of opaque sublayers with $\varepsilon_{ef}(\xi) < 0$ which according to classical conceptions must cause the strong reflection of incident electromagnetic wave from the plasma. It is interesting to note also that in the reference frame of exactly solvable models the wave vector $p(\xi)$ may include some arbitrary function $f(\xi)$ and a lot of internal parameters the correct choice of which can provide satisfaction of nonreflection conditions $p(\xi) = 1$ and $d\,p(\xi) / d\,\xi = 0$, providing initial wave passage through inhomogeneous plasma without loss of energy. The spatial structures of $p(\xi)$, $W(\xi)$ and $\varepsilon_{ef}(\xi)$ may be solitonlike ones. One of big amount of possible applications of exactly solvable models is transmission of radio signals through dense plasma layers, some of which according the modern heliosphere models (Opher et al., 2015; Pogorelov et al., 2015) are situated in the vicinity of Sun.

References

Davidovich, M. V. (2010). On low-reflection magnetodielectric coatings with exponential dependences of permittivity and permeability, *Journal of Communications Technology and Electronics*, 55, 4, DOI: 10.1134/S1064226910040133

Dykhne, A. M., Sarychev, A. K., Shalaev V. M. (2003). Resonant transmittance through metal films with fabricated and light-induced modulation, *Physical Review*, B 67, 195402. DOI: 10.1103/PhysRevB.67.195402

Erokhin, N. S., Zakharov, V. E. (2007). On Transillumination of Wave Barriers for Electromagnetic Radiation in an Inhomogeneous Plasma, *Doklady Physics,* 52, 485, DOI: 10.1134/S1028335807090078

Erokhin, N. S., Zakharov, V. E. (2011). Reflectionless Passage of an Electromagnetic Wave through an Inhomogeneous Plasma Layer, *Plasma Physics Reports,* 762

Erokhin, N. S., Zakharov, V., E. Zolnikova, N. N., Mikhailovskaya, L. A. (2015). Exactly solvable model of resonance tunneling of an electromagnetic wave in plasma containing short-scale inhomogeneities, *Plasma Physics Reports*, 41, 182

Erokhin, N. N., Zolnikova, N. N., Mikhailovskaya L. A. (2018). Development of an Exactly Solvable Model of Resonance Tunneling of Electromagnetic Waves through Gradient Barriers in a Nonuniform Magnetoactive Plasma, *Plasma Physics Reports*, 44, 933

V. L. Ginzburg and A. A. Rukhadze, *Electromagnetic Waves in Plasma* (Nauka, Moscow, 1970) [in Russian].
Kozyrev, A. N., Piliya, A. D., Fedorov, V. I. (1979). *Soviet Journal of Plasma Physics*, 5, 180

Lagovskii, B. A. (2006). Absorbing and antireflecting continuously inhomogeneous coatings for electromagnetic waves, *Journal of Communications Technology and Electronics*, 51, 68

Merkulov, E. S., Erokhin, N. S. (2013). Reflectionless propagation of electromagnetic waves in inhomogeneous magnetoactive plasma with small-scale structures, *Voprosy Atomnoi Nauki I Tekhniki*., Ser. Plazm. Elektron. Novye Metody Uskoren., No. 4, 130

Nazarenko, S. V., Newell, A. C., Zakharov, V. E. (1994). Communication through plasma sheaths via Raman (three-wave) scattering process, *Physics of Plasmas*, 1, 2827

Opher, M., Drake, J. F., Zieger, B., Gombosi T. I. (2015). Magnetized jets driven by the sun: the structure of the heliosphere revisited, *The Astrophysical Journal Letters*, 800:L28 (7pp), doi:10.1088/2041-8205/800/2/L28

Ozbay, E. (2006). Plasmonics: Merging Photonics and Electronics at Nanoscale Dimensions, *Science*, 311, 189, http://dx.doi.org/10.1126/science.1114849

Pogorelov, N. V., Borovikov, S. N., Heerikhuisen, J., Zhang M. (2015). The heliotail, *The Astrophysical Journal Letters*, 812:L6 (7pp), doi:10.1088/2041-8205/812/1/L6

Poverennyi, M. V., Erokhin, N. S. (2013). Development of an Exactly Solvable Model of Resonance Tunneling of Electromagnetic Waves through Gradient Barriers in a Nonuniform Magnetoactive Plasma, *Voprosy Atomnoi Nauki I Tekhniki*, Ser. Plazm. Elektron. Novye Metody Uskoren., No. 4, 133

Shalin, A. S. (2010). Broadband Blooming of a Medium Modified by an Incorporated Layer of Nanocavities, *Journal of Experimental and Theoretical Physics Letters*, 91, 636

Shvartsburg, A. B. (2005). Optics of nonstationary media, Physics–*Uspekhi*, 48, 797. DOI: 10.1070/PU2005 v048n08ABEH002119

Zharov, A. A., Kondrat'ev, I. G., Miller, M. A. (1979). Resonant matching of electromagnetic waves with an inhomogeneous and isotropie plasma, *Soviet Journal of Plasma Physics*, 5, 146

DOI: 10.31401/WS.2026.proc.35

Determining the Influence of Solar Radiation on the Dynamics of Lake *Srebarna*'s Water Surface Area through Remote Sensing

Jelev G.[1], *Ivanova I.*[1], *Tsvetkova M.*[1], *Zhelezov G.*[2],
Benderev A.[2], *Gerginov P.*[2], *Chanev M.*[1]

[1] Space Research and Technology Institute, Bulgarian academy of Sciences,
Acad. G. Bonchev Str., bl. 1, 1113 Sofia, gjelev@space.bas.bg
[2] Geological Institute, Bulgarian Academy of Sciences,
Acad. G. Bonchev Str., bl. 24, 1113 Sofia, p.gerginov@mail.bg

Abstract

This publication examines the impact of solar radiation on the water surface area of Lake *Srebarna*, the most significant feature of the *Srebarna* wetland system. Data from the Sentinel 2A and Sentinel 2B satellites, along with Normalized Difference Water Index (NDWI) index imagery, were utilized to determine the water surface area for the period from January 1, 2025, to December 31, 2025. Monthly solar radiation totals were calculated for the Natura 2000 protected area. The values were derived using a 30x30 m pixel digital elevation model from the Shuttle Radar Topography Mission (SRTM). The correlation between solar radiation levels and the water surface area of Lake *Srebarna* was investigated, followed by an analysis of the results. The study proves the typical negative correlation between solar radiation intensity and the lake's water surface area within the *Srebarna* Biosphere Reserve.

Keywords: solar radiation, *Srebarna* wetland system, digital elevation model, GIS, Remote sensing

1. Introduction

Solar radiation is the primary energy source that drives many of the physical and biological processes on Earth. Understanding its importance for the landscape at different scales is key to understanding a wide range of natural processes and human activities [Potužníková et. al. 2023; Choi, et. al. 2019; Hesslerová, et. al. 2019; Dancheva & Asenovski, 2018; Fu, & Rich, 2002]. Wetlands are ubiquitous worldwide, encompassing a vast diversity of ecosystem types and holding significant ecological and social importance. The relationship between wetlands and solar radiation is critical for maintaining ecological balance and regulating climate at regional and local levels. Solar radiation serves as the primary energy source driving wetland processes, and variations in its intensity directly impact their condition. In the context of climate change, wetlands are exceptionally efficient carbon dioxide sinks, thereby helping to mitigate the greenhouse effect. Increased solar activity and warming lead to accelerated water evaporation, which threatens the habitats of numerous bird species, including those of European conservation concern (SPEC) [Fergus, et. al. 2013]. This makes many bird species directly dependent on these zones, such as the *Srebarna* Biosphere Reserve.

Lake *Srebarna* is one of the most significant wetlands in Bulgaria and Europe, characterized by a high degree of biodiversity and complex hydrological processes. It is a shallow Danubian wetland of exceptional importance for European biodiversity. As a site protected under UNESCO and the Ramsar Convention, the lake performs key ecological functions, including maintaining habitats for rare and endangered species [Gerginov, et al., 2026; Ministry of Environment and Water, 2022; Ivanova, 2014; Ramsar Convention Secretariat. 2016; Institute of Biodiversity and Ecosystem Research, 2011].

Solar energy is the primary energy source for wetlands, driving numerous physical and biological processes on Earth. Understanding it is essential for researching natural processes occurring within the landscape at various scales [Potužníková et. al. 2023; Choi, et. al. 2019; Dancheva & Asenovski, 2018; Fu, & Rich, 2002].

Processes within wetlands are governed by the cyclical nature of their primary energy source, directly affecting water and soil temperatures. Consequently, high summer radiation leads to warmer conditions and elevated evapotranspiration. Conversely, winter solar radiation values are much lower, resulting in lower temperatures and reduced evapotranspiration [Mitsch & Gosselink, 2015; Peter, 2008; Kadlec, 1999].

Investigating the impact of solar radiation on wetlands is of great importance both for analyzing process dynamics within these zones and understanding their climatic effects [Potužníková et. al. 2023]. Wetlands and their functions are viewed either as sources or sinks of greenhouse gases, given their capacity to accumulate them. This occurs through the process of evapotranspiration, which exerts a dual cooling and regulating effect on the surrounding landscape due to water phase changes. Evapotranspiration reduces thermal gradients, mitigates temperature extremes, and closes water and mass cycles. Conversely, in areas lacking water and permanent vegetation, the evapotranspiration-condensation cycle slows down. This leads to the transformation of solar radiation into sensible heat, resulting in surface overheating that warms the adjacent air layer. As this warm air rises turbulently, it absorbs larger amounts of water vapor, transporting it to the upper layers of the atmosphere where it condenses. This ultimately leads to the drying of the landscape [Hesslerová et al., 2019].

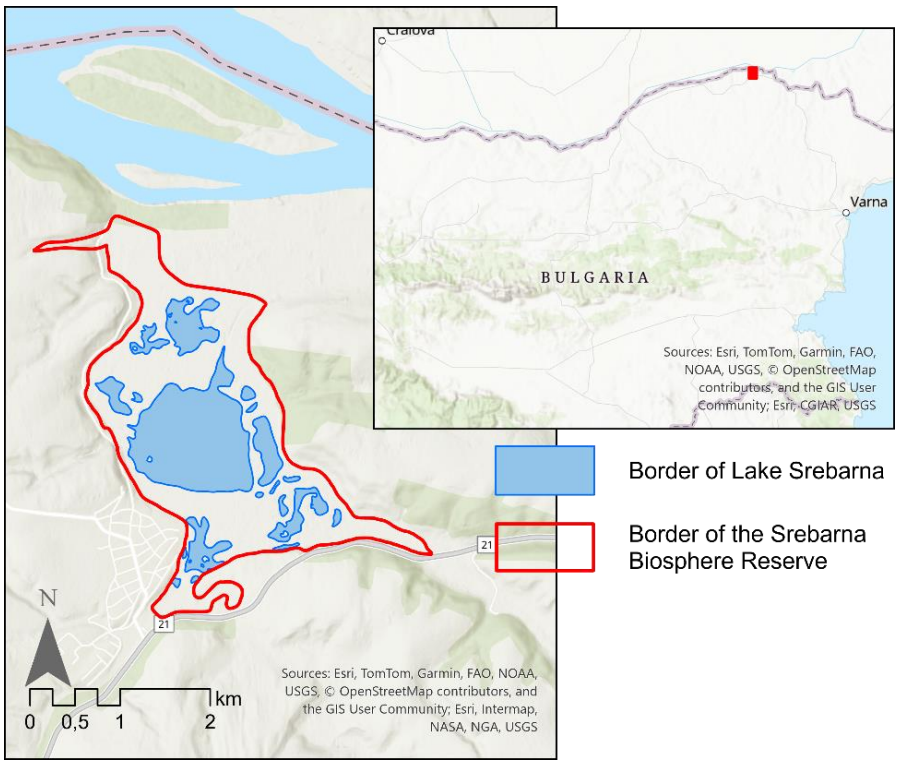


Figure 1. *Study area: Borders of the Srebarna Biosphere Reserve and Lake Srebarna, Source: [NATURA natura2000, https://natura2000.egov.bg/]*

Consequently, wetlands and solar radiation exist in a continuous, dynamic interaction that determines both ecosystem health and local climate.

Geographically, *Srebarna* is located in the northeastern part of Bulgaria, in close proximity to the Danube River (Figure 1), with which it is linked through complex hydrological

interactions. The lake's hydrological regime is determined by a dynamic water balance shaped by the joint action of surface inflow, groundwater, precipitation, and evaporation [Gerginov et al., 2026].

A particularly significant factor in this process is solar radiation, which influences the intensity of evaporation processes and the seasonal variability of water volumes. Due to its shallow nature and limited water exchange with the river, Lake *Srebarna* is highly sensitive to climate variations and anthropogenic impacts [Ivanova, 2014; Michev, & Stoyneva, 2007].

In 1948, *Srebarna* was declared a managed reserve. In 1975, the *Srebarna* Managed Reserve was designated under the Ramsar Convention on Wetlands of International Importance. It was declared a UNESCO Biosphere Reserve in 1977 and was inscribed on the UNESCO World Cultural and Natural Heritage List in 1983. The Ramsar Convention obliges member states to protect the ecological character of their sites to ensure the maintenance of habitats for rare and endangered species [Gardner et al. 2023; Michev, & Stoyneva, 2007]. Currently, the *Srebarna* Managed Reserve is part of the NATURA 2000 network under site code BG0000241.

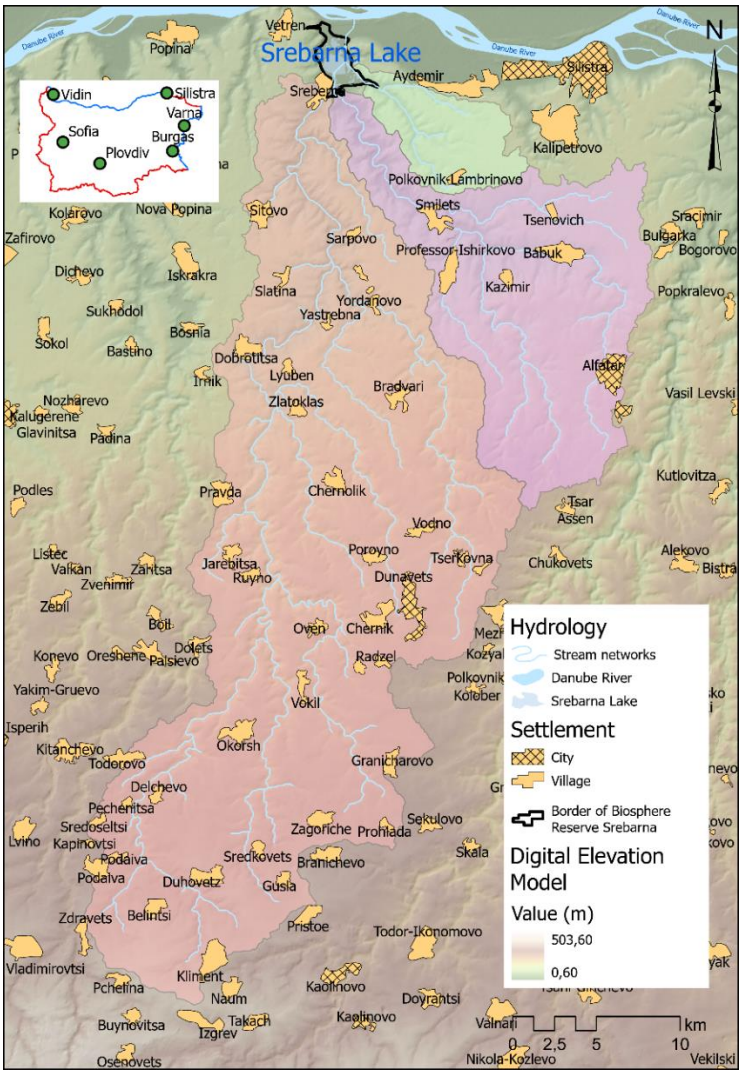


Figure 2. *The watershed of the study area generated by the DEM*

The lake's catchment area (959.68 km²) is drained by the Srebrenska and Kalnezha rivers, which exhibit a highly variable hydrological regime and nearly dry up during the summer-autumn period (Figure 2). Based on its hydro-morphometric parameters, the lake is classified as a small water body, with a surface area of up to 10 km².

2. Purpose and objectives

The objective of this study is to determine the impact of total solar radiation on the variations of the water surface area of Lake *Srebarna* within the *Srebarna* wetland system, utilizing remote sensing and Geographic Information Systems (GIS) for the period from January 1, 2025, to December 31, 2025.

To achieve this, the following primary tasks were established:

- Determining the monthly surface area and variations of the water body of Lake *Srebarna* for the period from January 1, 2025, to December 31, 2025, using the NDWI index;
- Generating maps that display the total solar radiation within the *Srebarna* Biosphere Reserve using GIS software (ArcGIS Pro);
- Analyzing the resulting tabular and graphical data.

3. Materials and Methods

Data from SentinelHub [Kovács et al., 2026] were utilized, specifically Sentinel-2 satellite imagery focusing on bands B03 (Green) and B08 (NIR). One cloud-free image (0% cloud cover over the study area) was selected for each month of the year. Within the specialized software ArcGIS Pro, these two bands were used to calculate Normalized Difference Water Index (NDWI) imagery based on the following formula:

$$NDWI = (Green - NIR) / (Green + NIR), \text{ reference by [McFeeters, 1996].} \quad (1)$$

The resulting index images were reclassified, and NDWI values greater than 0.3 were delineated as the water surface area of Lake *Srebarna* [Ahmed & Ahmed, 2026; Du et al., 2016; McFeeters, 2013], after which the water surface area was calculated.

To compute the amount of area-wide solar radiation, a Digital Elevation Model (DEM) with a pixel size of 30x30 m, derived from the Shuttle Radar Topography Mission (SRTM) [USGS, EarthExplorer, 2026], was employed. Using the built-in tool in ArcGIS Pro, the total area solar radiation was calculated for each month of 2025 [Raster Solar Radiation, 2026]. The lake's water surface area values were then correlated with the mean solar radiation values calculated for the study area. The results were processed and visualized as a chart using MS Excel. A flowchart of the research methodology is presented in Figure 3.

4. Results and Discussion

The results of the statistical analysis regarding the relationship between area-wide solar radiation (kWh/m²) and the water surface area (km^2) are graphically presented in Figure 4. The graph illustrates a typical negative correlation between the intensity of area-wide solar radiation and the water surface area of the lake within the *Srebarna* Reserve. For better visualization, Table 1 displays the monthly data and the resulting values for the Average of Area Solar Radiation (kWh/m²) and NDWI for the *Srebarna* Biosphere Reserve. The changes in the state of Lake *Srebarna* and the spatial distribution of the monthly area-wide solar radiation are clearly visible.

Analysis of Correlation Points

Radiation Peak (July – August): Solar irradiance reaches its maximum during this period, driving peak evaporation rates. This directly corresponds to the lowest water levels and the maximum contraction of the open water surface area (Figure 4).

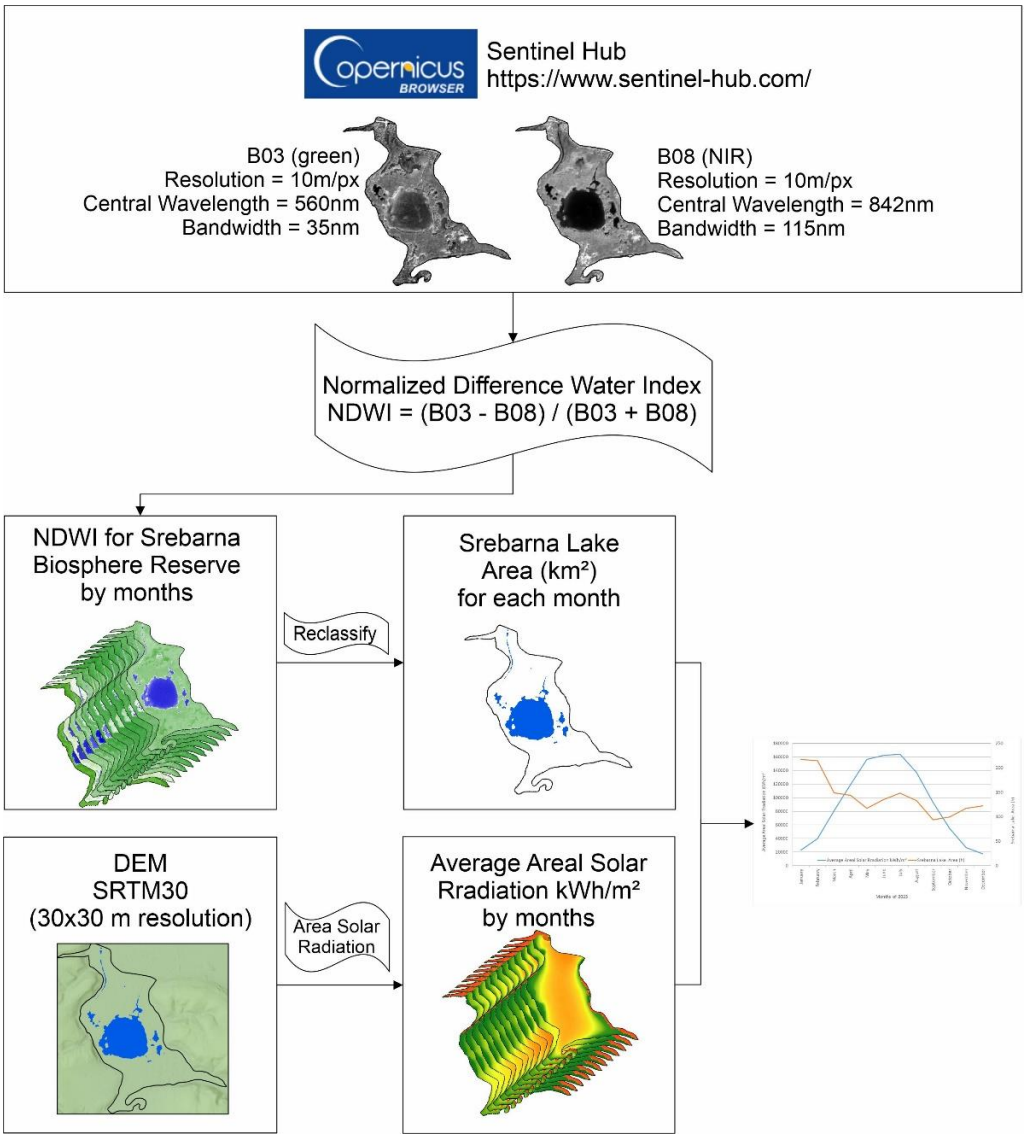


Figure 3. *Scheme of research methods*

Maximum Water Surface Area (March – April): Solar radiation remains moderate during these months, while the lake is replenished by the spring high-water stage of the Danube River combined with snowmelt.

Critical Transition Zone (May – June): A sharp decline in the water surface area occurs concurrently with rising solar radiation levels, marking the most ecologically dynamic period for the ecosystem (Figure 4).

This observed model underscores the critical importance of sluice gate management (anthropogenic intervention) in mitigating extreme solar anomalies to sustain regional biodiversity.

Zonal Heterogeneity of the Correlation

The correlation between solar radiation and the water surface area within the *Srebarna* Biosphere Reserve is non-homogeneous (the overall linear correlation for the entire year is slightly negative – **r** is approximately equal to **-0.26**). Due to the lake's specific morphometry, this relationship exhibits distinct spatial variations across different zones:

Central Water Body (Zone of Strong Negative Correlation): The correlation is most pronounced across open water areas. The absence of macrophyte vegetation allows solar radiation to heat the water column directly, leading to maximized evaporation and rapid surface area contraction during periods of intense sunlight.

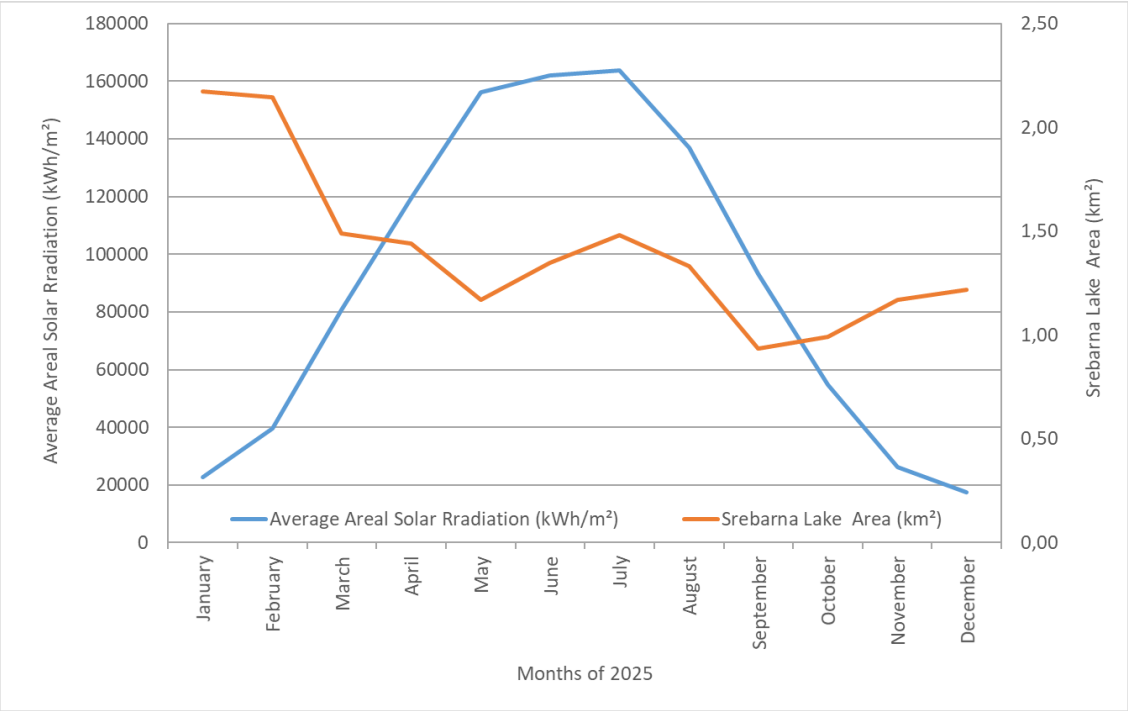


Figure 4. *Relationship between Average Areal Solar Rradiation kWh/m² and Srebarna Lake Area (km²)*

Peripheral Shallow Zones (Zone of Leading Correlation): In the shallowest parts of the lake, even minor increases in solar radiation lead to complete water recession. The spatial distribution in these sectors shows the highest sensitivity, with the water surface disappearing here first.

Floating Reed Island Zones (Zone of Weak/Buffered Correlation): In areas dominated by dense vegetation and floating reed beds (tuprak), area-wide solar radiation is primarily absorbed by biomass. The canopy shades the underlying water and reduces direct evaporation from the water surface, stabilizing water levels against solar influence.

Northern Sector (Feeding Channel Interface): In the zone adjacent to the sluice gates connecting the lake with the Danube River, the natural correlation is frequently altered by anthropogenic intervention. When water levels drop critically due to high solar radiation, water is artificially transferred from the Danube, expanding the water surface area despite elevated radiation levels.

The quantitative data presented in Table 1 yields crucial insights into the seasonal dynamics and the complex interaction between solar radiation levels and the water surface area of Lake *Srebarna* during 2025.

Winter Maximum and Minimum Irradiance (January – February): During the first two months of the year, the average area solar radiation is at its lowest annual levels, shifting from 22770 kWh/m² in January to 39,749 kWh/m² in February. Concurrently, the lake reaches its maximum recorded water surface area for the year (2.17 km² and 2.15 km², respectively). This

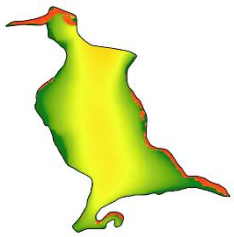
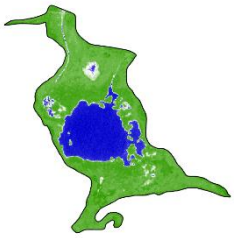
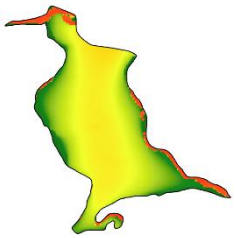
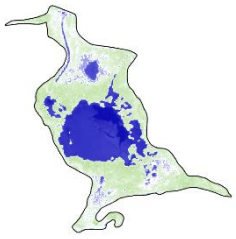
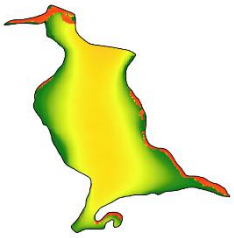
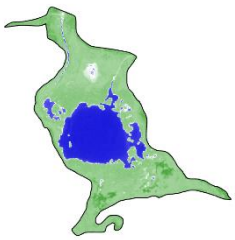
phase is characterized by low thermal energy, minimum evaporation rates, and accumulated winter precipitation.

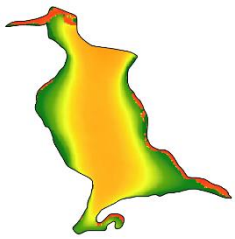
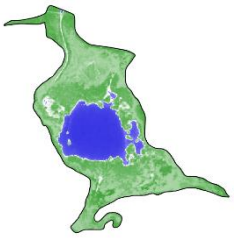
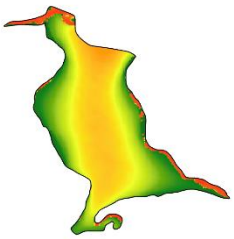
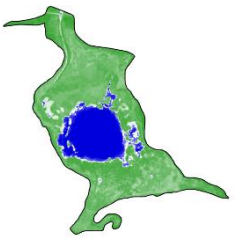
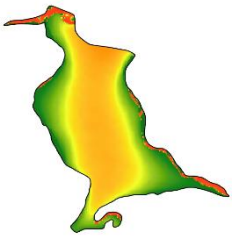
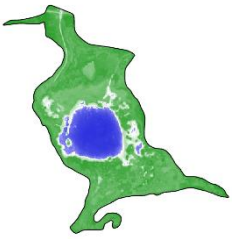
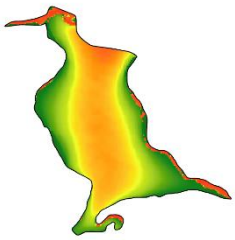
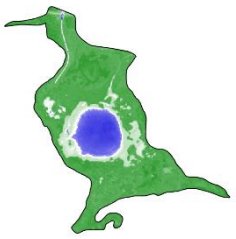
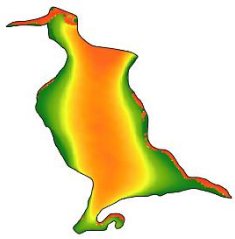
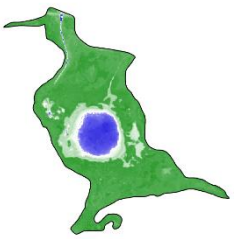
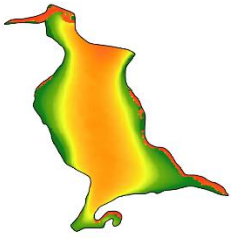
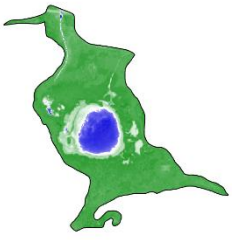
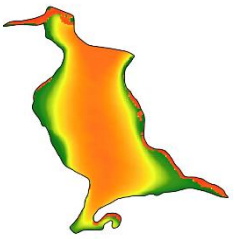
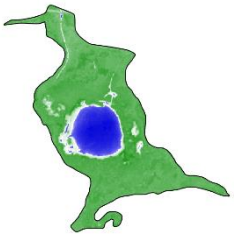
The Spring Inflow Paradox (March – April): As spring progresses, a sharp increase in solar radiation is observed, rising to 80680 kWh/m² in March and 119407 kWh/m² in April. Under purely climatic conditions, this energy influx would trigger early evaporation; however, the lake area remains relatively stable, dropping only slightly to 1.49 km² and 1.44 km². This stability highlights the buffering effect of the spring high-water stage of the Danube River and regional snowmelt, which temporarily counteracts the rising solar input.

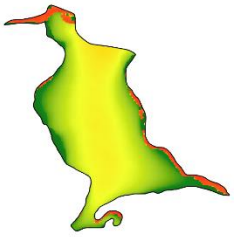
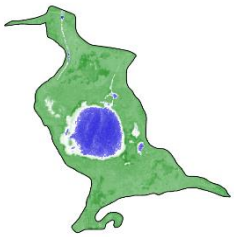
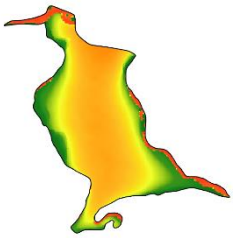
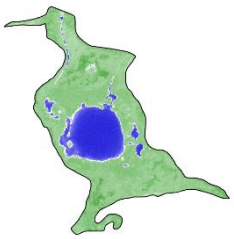
Summer Evaporation and the June–July Artificial Expansion: A critical hydrological shift occurs in May, where the area contracts to 1.17 km² as radiation climbs to 156143 kWh/m². Interestingly, during peak radiation months – June (162048 kWh/m²) and July (163806 kWh/m²) – the water surface area exhibits an anomaly, expanding to 1.35 km² and 1.48 km², respectively. This clear disruption of the negative correlation serves as mathematical proof of anthropogenic intervention, confirming that the sluice gates were opened to safeguard the wetland's ecosystem from critical drying.

Late Summer Drop and Autumn Stabilization (August – December): Following the closure or cessation of water transfers, August and September experience a rapid contraction of the lake area, reaching the absolute annual minimum of 0.94 km² in September, driven by the cumulative thermal stress of the preceding months. In the autumn (October – December), solar radiation drops sharply back to its minimum of 17518 kWh/m², allowing the water basin to steadily recover to 1.22 km² by December.

Table 1. *Monthly maps and extracted values of area solar radiation (kWh/m²), NDWI, and lake surface area for the Srebarna Biosphere Reserve during 2025*

Data, month of 2025	Maps and Average of Area Solar Radiation (kWh/m^2) for *Srebarna* Biosphere Reserve		NDWI for *Srebarna* Biosphere Reserve	*Srebarna* Lake Area (km^2)
January		22770		2,17
February		39749		2,15
March		80680		1,49

April		119407		1,44
May		156143		1,17
June		162048		1,35
July		163806		1,48
August		137077		1,33
September		93166		0,94
October		54650		0,99

November		26331		1,17
December		17518		1,22

5. Conclusion

This study demonstrates the high efficacy of integrating Sentinel-2 satellite data and Geographic Information Systems (GIS) for the environmental monitoring of sensitive wetland ecosystems. By leveraging high spatio-temporal resolution imagery, the research successfully established a clear correlative link between solar radiation and the hydrological dynamics of the *Srebarna* Biosphere Reserve. The identified spatio-temporal heterogeneity and the negative correlation between solar radiation intensity and the lake's open water surface area highlight the profound impact of climate drivers on water volume fluctuations.

The pronounced climate pressure observed during the peak summer months (July–August) underscores the vulnerability of the reserve to seasonal temperature and radiation increases. These findings emphasize that modern remote sensing tools are indispensable for capturing rapid environmental changes that traditional ground-based monitoring might miss. Consequently, the methodology presented herein provides a reliable framework for park managers and policymakers to implement timely, data-driven conservation strategies.

Ultimately, while multispectral data offer valuable insights, comprehensive wetland management requires a multi-sensor approach. Future research must expand upon these findings by integrating Synthetic Aperture Radar (SAR) data to overcome cloud-cover limitations, utilizing advanced satellite products, and employing unmanned aerial vehicles (UAVs) for ultra-high-resolution localized assessments. Such advancements will significantly enhance the predictive modeling and long-term preservation of critical protected areas like Lake *Srebarna*.

Acknowledgments

The research carried out within the project "Hydrogeological Mechanisms of Sustainable Recharge and Conservation of Karst Wetlands: A Study of the '*Srebarna*' System" is funded by the Bulgarian National Science Fund at the Ministry of Education and Science of Bulgaria under Contract No. KP-06-N94/7/10.12.2025 for the funding of fundamental scientific research.

References

Ahmed, E. A. I., Ahmed, M. M. M. (2026). Temporal dynamics of Normalized Difference Vegetation Index (NDVI) and Normalized Difference Water Index (NDWI) in semi-arid Gadarif Region, Sudan (1985–2024). *International Journal of Sustainable and Green Energy*, Vol. 15, No. 3, pp. 93–103. DOI: 10.11648/j.ijsge.20261503.11.

Choi, Y., Suh, J., Kim, S.-M. (2019). GIS-based solar radiation mapping, site evaluation, and potential assessment: A review. *Applied Sciences*, Vol. 9, No. 9, 1960. DOI: 10.3390/app9091960.

Dancheva, A., Asenovski, S. (2018). Study of waste disposal thermal radiation using satellite data and considering solar influence. *Aerospace Research in Bulgaria*, Vol. 30, pp. 16–25. DOI: 10.3897/arb.v30.e02.

Kovács, D. D., Musial, J., Bojanowski, J., Clarijs, D., de la Mar, J., Zlinszky, A. (2026). Copernicus Data Space Ecosystem establishes public cloud processing for Earth observation data. *Scientific Data*, Vol. 13, 537. DOI: 10.1038/s41597-026-06765-8.

Du, Y., Zhang, Y., Ling, F., Wang, Q., Li, W., Li, X. (2016). Water bodies' mapping from Sentinel-2 imagery with Modified Normalized Difference Water Index at 10-m spatial resolution produced by sharpening the SWIR band. *Remote Sensing*, Vol. 8, No. 4, 354. DOI: 10.3390/rs8040354.

Fergus, R., Louwe Kooijmans, J., Kwak, R. (2013). *BirdLife International Global Survey on the Status of Urban Bird Conservation*. BirdLife International, Cambridge.

Fu, P., Rich, P. M. (2002). A geometric solar radiation model with applications in agriculture and forestry. *Computers and Electronics in Agriculture*, Vol. 37, pp. 25–35.

Gardner, R. C., Okuno, E., Pritchard, D. (2023). Ramsar Convention governance and processes at the international level. In: *Ramsar Wetlands*, pp. 37–67. Elsevier. DOI: 10.1016/B978-0-12-817803-4.00003-6.

Gerginov, P., Totev, Y., Zhelezov, G., Zhelev, G. (2026). Hydrogeological mechanisms of sustainable recharge and preservation of karst wetlands: The "Srebarna" system study. In: *19th Congress of Geologists of Serbia "Geology for Sustainable Solutions": Book of Abstracts*. Bor Lake, Serbia, Serbian Geological Society, p. 209. ISBN: 978-86-86053-27-5.

Hesslerová, P., Pokorný, J., Huryna, H., Harper, D. (2019). Wetlands and forests regulate climate via evapotranspiration. In: An, S., Verhoeven, J. (Eds.), *Wetlands: Ecosystem Services, Restoration and Wise Use*. Ecological Studies, Vol. 238. Springer, Cham. DOI: 10.1007/978-3-030-14861-4_4.

Information System for Protected Areas from the Ecological Network NATURA 2000 (2026). Protected site BG0000241. Available at: https://natura2000.egov.bg/EsriBg.Natura.Public.Web.App/Home/ProtectedSite?code=BG0000241&siteType=BirdsDirective.

Institute of Biodiversity and Ecosystem Research, Bulgarian Academy of Sciences (2011). Ecological Station at Srebarna Biosphere Reserve. Available at: http://www.iber.bas.bg/?q=bg/node/103.

Ivanova, I. (2014). *Study on the Dynamics of Floating Reed Islands in the "Srebarna" Managed Nature Reserve and Lumina Lake from the Roșu–Puiu–Lumina Lake Complex in the "Danube Delta" Biosphere Reserve, Based on Satellite, Ground, and GPS Data*. Academic Publishing House "Prof. Marin Drinov", Sofia, 120 pp. ISBN: 978-954-322-762-4. (In Bulgarian).

Kadlec, R. H. (1999). Chemical, physical and biological cycles in treatment wetlands. *Water Science and Technology*, Vol. 40, No. 3, pp. 37–44. DOI: 10.1016/S0273-1223(99)00417-5.

McFeeters, S. K. (1996). The use of the Normalized Difference Water Index (NDWI) in the delineation of open water features. *International Journal of Remote Sensing*, Vol. 17, No. 7, pp. 1425–1432. DOI: 10.1080/01431169608948714.

McFeeters, S. K. (2013). Using the Normalized Difference Water Index (NDWI) within a Geographic Information System to detect swimming pools for mosquito abatement: A practical approach. *Remote Sensing*, Vol. 5, No. 7, pp. 3544–3561. DOI: 10.3390/rs5073544.

Michev, T., Stoyneva, M. P. (Eds.). (2007). *Inventory of Bulgarian Wetlands and Their Biodiversity. Part 1: Non-Lotic Wetlands*. Elsi-M. ISBN: 978-954-9441-09-3.

Ministry of Environment and Water (2022). *Management Plan for the "Srebarna" Nature Reserve*. Sofia. (In Bulgarian).

Mitsch, W. J., Gosselink, J. G. (2015). *Wetlands*. 5th ed. John Wiley & Sons, 752 pp. ISBN: 978-1-119-01978-7.

Lafleur, P. M. (2008). Connecting atmosphere and wetland: Energy and water vapour exchange. *Geography Compass*, Vol. 2, No. 4, pp. 1027–1057. DOI: 10.1111/j.1749-8198.2007.00132.x.

Potužníková, K., Koucká Knížová, P., Chum, J., Podolská, K., Kouba, D., Mošna, Z., Georgieva, K., Bojilova, R., Kirov, B., Asenovski, S. (2023). Summer tropospheric mesoscale situations with impact on the ionospheric plasma. *Proceedings of the Fifteenth Workshop "Solar Influences on the Magnetosphere, Ionosphere and Atmosphere"*, pp. 89–97. ISSN: 2367-7570. DOI: 10.31401/WS.2023.proc.

Ramsar Convention Secretariat (2016). *An Introduction to the Ramsar Convention on Wetlands*. 7th ed.

Esri (2026). Raster Solar Radiation. *ArcGIS Pro Documentation*. Available at: https://doc.esri.com/en/arcgis-pro/latest/tool-reference/spatial-analyst/raster-solar-radiation.html.

USGS (2026). *EarthExplorer*. Available at: https://earthexplorer.usgs.gov/.

DOI: 10.31401/WS.2026.proc.36

Deep Learning Architectures for Monitoring Spruce Forest Health via Sentinel-2 Multi-Spectral Data: A Review of Current Trends

Tsvetkova M., Filchev L., Chanev M.
Space Research and Technology Institute – Bulgarian Academy of Sciences (SRTI-BAS);
m.tsvetkova@space.bas.bg

Abstract

The escalating frequency of extreme climatic events and severe hydrological deficits has significantly increased the vulnerability of *Picea abies* (Norway spruce) ecosystems across Central and Eastern Europe. In recent years, the synergistic use of European Space Agency's Sentinel-2 satellite constellation and Deep Learning (DL) algorithms — specifically Convolutional Neural Networks (CNNs) and Temporal Vision Transformers — has emerged as a transformative tool for forest health monitoring. This paper presents a comprehensive synthesis of literature published between 2011 and 2025, focusing on the remote detection of early-stage forest decline, drought-induced stress, and European spruce bark beetle (*Ips typographus*) infestations. The review evaluates the performance of multiple empirical indices and DL architectures applied to Sentinel-2 multi-spectral imagery, with particular emphasis on the diagnostic value of the Red Edge spectral channels (B5, B6, B7) for identifying physiological stress at the 'green-attack' stage — before visual symptoms become perceptible. Our synthesis reveals that while Red Edge-driven DL models achieve high overall accuracies (>91%) in mapping canopy degradation, their operational effectiveness remains constrained by training data quality, limited transferability across bioclimatic regions, and the lack of integrated hydro-climatic drivers. We conclude that bridging multi-spectral remote sensing with temporal AI architectures and climate teleconnection indices is essential for building the next generation of proactive early warning systems for coniferous forest ecosystems.

Keywords: Sentinel-2, Deep Learning, Forest Monitoring, Remote Sensing, Climate Stress

1. Introduction

European forests are undergoing increasing environmental pressures. Climate change is intensifying disturbance regimes across the continent, with warmer and drier conditions particularly facilitating insect outbreaks and drought-induced mortality [Seidl et al., 2017]. Norway spruce (*Picea abies* (L.) Karst.) — a dominant conifer across Central and Eastern Europe — is particularly vulnerable to increasing drought stress. Although naturally associated with boreal and montane climates, the species has been widely planted outside its native range in the temperate regions of Central Europe, where increasing summer heat and water deficits pose growing risks to growth, vitality, and survival [Lévesque et al., 2014; Ray et al., 2025].

The European spruce bark beetle (*Ips typographus* L.) is a native component of European forest ecosystems and contributes to natural disturbance and deadwood dynamics, particularly through the colonisation of weakened and dying spruce. However, prolonged drought and associated physiological stress can alter the Norway spruce–bark beetle interaction by reducing host defence capacity and increasing tree susceptibility to successful attack. Experimental studies have shown that declining tree water status and reduced resin flow are associated with impaired defence against *I. typographus*, while more recent evidence indicates that drought can increase beetle attack rates and facilitate colonisation under conditions of sustained water limitation [Netherer et al., 2015; Netherer et al., 2024]. Under favourable conditions, this interaction can develop into large-scale outbreaks, particularly when drought-stressed trees are widespread across the landscape. Seidl et al. (2017), in a global synthesis of climate change effects on forest disturbance agents, found that under warmer and drier future conditions, 78.4% of reviewed observations projected an increase in insect disturbance activity, with coniferous forests and the boreal biome showing the strongest projected disturbance responses. Storm and fire, while important abiotic agents, together accounted for only 14% of all

disturbances recorded across European forests between 1986 and 2016 [Senf & Seidl, 2021]. This highlights the complexity of European forest disturbance regimes, in which multiple interacting abiotic, biotic, and anthropogenic drivers contribute to observed disturbance patterns.

The capacity of forest managers to detect and respond to bark beetle infestations has historically been constrained by the costs and logistical limitations of ground-based surveys. This is particularly problematic during the early stages of infestation, when timely identification of attacked trees can support targeted management interventions before beetles complete their development and emerge to colonise additional hosts. A major challenge is the so-called 'green-attack' phase, during which newly infested trees may retain a visually green crown despite undergoing physiological and biochemical changes associated with bark beetle colonisation. These changes can precede the development of visible crown symptoms, creating an important opportunity for remote sensing to detect early stress before conventional visual surveys can reliably identify infested trees [Bhattarai et al., 2020; Georgiev et al., 2022]. Evidence from Norway spruce forests in the Smolyan region of Bulgaria further demonstrates this potential, with Sentinel-2 observations revealing differences in vegetation response between subsequently attacked and healthy stands before pronounced visual symptoms became apparent [Georgiev et al., 2022].

Earth observation has long been recognised as the only viable path to closing this monitoring gap. The free and open data policy adopted by ESA for the Copernicus Sentinel missions, inaugurated with Sentinel-2A in 2015 and completed with the Sentinel-2B launch in 2017, has been transformative. The Sentinel-2 MultiSpectral Instrument (MSI) offers 10 m spatial resolution in the visible and near-infrared bands, 20 m resolution in the Red Edge and Short-Wave Infrared (SWIR) bands, a global revisit time of five days under cloud-free conditions, and — most critically for forest stress detection — three dedicated Red Edge bands (B5: 705 nm, B6: 740 nm, B7: 783 nm) that are sensitive to early-stage chlorophyll degradation invisible to standard Red–Green–Blue (RGB) or broadband Near-Infrared (NIR) systems [ESA, 2015].

The simultaneous emergence of Deep Learning (DL) as the dominant paradigm for complex pattern recognition in high-dimensional data has opened new possibilities for automated, scalable, and accurate forest health monitoring. DL models — particularly Convolutional Neural Networks (CNNs) and, more recently, Vision Transformers (ViTs) [Dosovitskiy et al., 2021] adapted for satellite image time series (e.g., TSViT) [Tarasiou et al., 2023] — can learn hierarchical feature representations from multi-spectral image stacks without requiring the manual feature engineering that limited earlier machine learning approaches. Applied to Sentinel-2 time series, these models can in principle detect the characteristic spectral signatures of stressed or infested spruce stands weeks before they would be identified by field crews.

2. Scientific and Ecological Context

2.1. The Norway Spruce — Bark Beetle System

Ips typographus is a native European beetle that under natural conditions fulfils a keystone ecological role, accelerating the decomposition of senescent and storm-damaged trees. Its population dynamics are, however, tightly regulated by tree defensive chemistry: a healthy spruce tree can produce sufficient quantities of resin to repel and kill attacking beetles through a process known as pitch-out. This defence system is highly energy-demanding and is rapidly compromised by water stress. When a spruce tree experiences drought stress, its resin production declines, its bark water potential drops, and its capacity to mount a successful pitch-out defence falls below the threshold needed to resist mass beetle attack. At the landscape scale, synchronised drought stress across thousands of hectares of spruce monocultures can effectively lift the population regulation ceiling and allow beetle populations to expand exponentially — a transition from endemic to epidemic population dynamics [Seidl et al., 2017].

The infestation progression follows a predictable phenological sequence of direct relevance to remote sensing detection. In the 'green-attack' phase (approximately 2–8 weeks post-infestation), the tree is under attack and reproducing beetles are present in the bark, but the crown remains visually

green. Chlorophyll content begins to decline and internal water stress intensifies, producing spectral changes that are detectable in the Red Edge region but invisible in standard true-colour imagery. In the subsequent 'red-attack' phase (approximately 2–6 months post-infestation), needles desiccate and turn red-brown, producing an unmistakable spectral signature. By this point, however, the beetles have typically already emerged and dispersed to neighbouring trees [Bhattarai et al., 2020]. For forest management purposes, the "green attack" phase is a critical period.

2.2. Climate Change and Forest Disturbance Regimes

Seidl et al. (2017) provide the most comprehensive global synthesis of climate change effects on forest disturbance regimes to date, reviewing literature across six key disturbance factors: fire, drought, wind, snow/ice, insects, and pathogens. Their key finding relevant to conifer monitoring is that under warmer and drier future climate trends—the baseline trajectory projected for Central Europe—78.4% of reviewed observations indicated an increase in insect disturbance activity, with the most pronounced impacts anticipated in coniferous and boreal forests. Importantly, compound interactions among disturbance drivers are predominantly amplifying: drought severely weakens host-tree physiological defenses, triggering secondary bark beetle infestations that subsequently accumulate coarse woody debris and elevate fire risk. These cascading disturbance dynamics demonstrate that insect outbreaks cannot be monitored or modeled in isolation from broader hydro-climatic forcing.

Senf & Seidl (2021) provide the first continental-scale, wall-to-wall quantification of storm- and fire-related disturbances across European forests for the period 1986–2016. Storm and fire each accounted for approximately 7% of the total disturbed area, together causing 14% of all disturbances in Europe over the study period. The authors note explicitly that for the majority of European forests, the disturbance regime is dominated by causes other than fire and storm — a category that includes harvest and biotic disturbances such as bark beetle outbreaks. Storm-related disturbance prevalence showed a significant increasing trend over time, whereas fire prevalence remained stable.

2.3. The 2018 Drought and Early-Wilting Response

Brun et al. (2020) provide the most direct satellite-based evidence for drought-induced forest stress in Central Europe. Using Sentinel-2 and Normalized Difference Vegetation Index (NDVI) time series at 10 m resolution combined with visual interpretation of high-resolution orthophotos, they mapped early wilting — defined as premature leaf discolouration and leaf-shedding before the end of September — across Central European forests in response to the extreme 2018 summer drought. The drought of summer 2018 was the most extreme on record in Central Europe since at least 1900, with growing-season temperatures reaching +3.3 °C above the 1961–1990 average and precipitation at its fifth-lowest level in 118 years. The estimated area affected by early wilting totalled 21,524 ± 2,846 km² (10.8% of the forested area investigated), with highest prevalence in central and eastern Germany and the Czech Republic [Brun et al., 2020]. Critically, early wilting revealed a lasting impact on forest productivity: trees affected in 2018 showed significantly reduced greenness in the following spring of 2019. This lagged response aligns with global empirical evidence demonstrating that forest ecosystems experience multi-year drought "legacy effects" [Anderegg et al., 2015], confirming that the spring 2019 signal detected by Brun et al. (2020) represents part of a multi-year physiological recovery trajectory rather than an isolated single-season event.

2.4. Remote Sensing of Forest Health: Historical Context

Satellite missions such as Landsat and Sentinel have been widely applied to monitor forest ecosystems and canopy health [Ivanov & Tyufekchiev, 2019; Stankova, 2023; Todorova & Zhiyanski, 2025; Grigorov et al., 2025]. In the context of bark beetle infestation mapping, satellite-based remote sensing has been utilized since the 1970s. However, traditional broadband satellite sensors operating strictly within the visible and broad near-infrared (NIR) spectrum are primarily

restricted to capturing the 'red-attack' phase — rendering them retrospective damage-mapping tools rather than proactive early warning systems.

The potential of Red Edge spectral bands to detect subtle chlorophyll degradation during the 'green-attack' phase was initially demonstrated in the early 2000s using airborne hyperspectral sensors (e.g., AVIRIS (Airborne Visible / Infrared Imaging Spectrometer), HyMap (Hyperspectral Mapper)). Nevertheless, high operational costs and limited temporal availability prevented these airborne instruments from being deployed for routine, regional-scale forest monitoring. The introduction of the Sentinel-2 mission significantly expanded the capabilities of freely accessible multispectral Earth observation building on the long-standing Landsat record while introducing higher spatial and temporal resolution and dedicated Red Edge spectral bands for improved vegetation monitoring [Delegido et al., 2011].

Despite these technological advancements, recent critical syntheses highlight that operationalizing early detection remains challenged by the scarcity of highly accurate, multi-temporal ground-truth data required to validate green-attack classifiers reliably across diverse forest structures [Kautz et al., 2024].

3. Materials and Methods

3.1. Literature Search Protocol

A structured literature search was conducted to identify peer-reviewed studies addressing the use of Sentinel-2 multispectral data and machine learning (ML) or deep learning (DL) methods for monitoring spruce forest health, physiological stress, forest disturbance, insect-related damage, defoliation, and tree mortality. Searches were conducted in three major bibliographic databases: Web of Scienc, Scopus, and Google Scholar. The search strategy combined terms describing the satellite platform, analytical methodology, and forest-health application.

Titles and abstracts were screened against the following inclusion criteria: (i) the study applies a DL model to Sentinel-2 multi-spectral data; (ii) the target variable is forest health status, disturbance, or vegetation stress; and (iii) the study reports quantitative accuracy metrics. Studies relying exclusively on traditional machine learning (e.g., Random Forest, Support Vector Machine (SVM) without any DL component) were excluded, as were studies using Sentinel-2 data purely as a spatial reference layer without spectral analysis.

Studies based exclusively on conventional Machine Learning (ML) algorithms, such as Random Forest (RF) or Support Vector Machine (SVM), were excluded from the DL architecture synthesis. However, relevant conventional-ML studies were retained as supporting evidence when they provided information on Sentinel-2 spectral sensitivity or the detectability of spruce stress, defoliation, or bark beetle infestation. This distinction is important because studies such as Abdullah et al. (2019) and Bhattarai et al. (2020) provide evidence concerning the spectral information contained in Sentinel-2 imagery, but they do not evaluate DL architectures. Abdullah et al. (2019) used principal component analysis (PCA) and partial least-squares discriminant analysis (PLS-DA), whereas Bhattarai et al. (2020) compared RF and SVM models.

3.2. Data Extraction Framework

For each study, the following parameters were extracted into a structured database: (1) DL architecture type and configuration; (2) Sentinel-2 spectral bands used as input; (3) additional input features (vegetation indices, ancillary data); (4) temporal input structure (single-date vs. multi-temporal stack); (5) training data source, size, and labelling method; (6) study area location and bioclimatic zone; (7) target classes; (8) reported accuracy metrics (Overall Accuracy [OA], F1-score, Precision, Recall, Intersection over Union [IoU], Kappa coefficient); and (9) whether independent spatial or temporal validation was performed. Studies reporting multiple experimental configurations were recorded as separate entries where metrics differed substantially.

3.3.Sentinel-2 Spectral Configuration

The Sentinel-2 MSI provides 13 spectral bands spanning the visible, near-infrared (NIR), and shortwave-infrared (SWIR) regions [Delegido et al., 2011]. For forest health and disturbance monitoring, the Red Edge region is of particular interest because its spectral response is sensitive to changes in chlorophyll content and canopy condition [Delegido et al., 2011; Bhattarai et al., 2020]. The three Sentinel-2 Red Edge bands — B5 (705 nm), B6 (740 nm), and B7 (783 nm) – therefore provide complementary information for assessing vegetation physiological status [Delegido et al., 2011] (Figure 2).

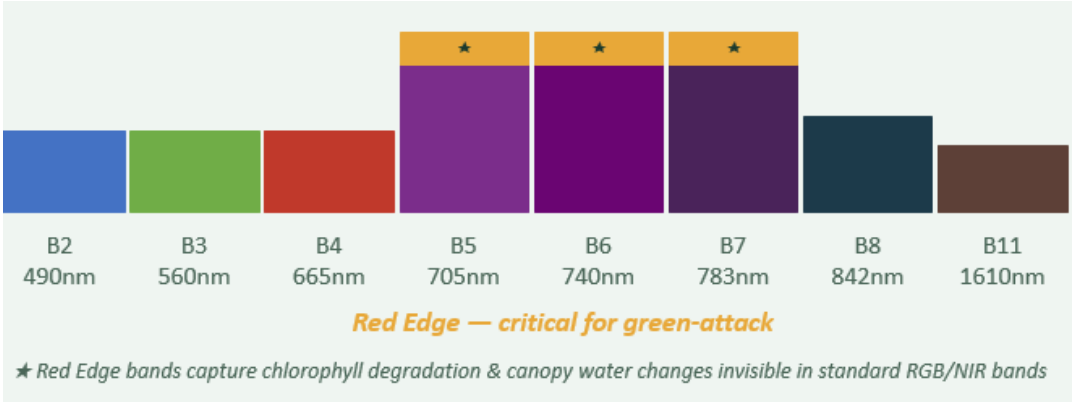


Figure 1. *Overview of Sentinel-2 spectral bands highlighting the Red Edge channels (B5, B6, B7) critical for early-stage ('green-attack') stress detection*

Evidence from forest disturbance applications further highlights the value of Red Edge-related information. Bhattarai et al. (2020) evaluated Sentinel-2 imagery for detecting spruce budworm defoliation in spruce-fir forests in New Brunswick, Canada, using Random Forest and Support Vector Machine classifiers based on 20 final selected spectral predictors (chosen from an initial pool of 29 candidate variables: 9 spectral bands and 20 vegetation indices), including Sentinel-2 bands and vegetation indices. The five most important predictors identified by their analysis included several Red Edge-related indices, namely EVI7 (Enhanced Vegetation Index), MCARI (Modified Chlorophyll Absorption in Reflectance Index), IRECI (Inverted Red-Edge Chlorophyll Index), NDII11 (Normalized Difference Infrared Index), and MSR (Modified Simple Ratio) [Bhattarai et al., 2020]. Conventional broadband indices such as NDVI and EVI8 were comparatively less effective, particularly for detecting light defoliation [Bhattarai et al., 2020]. The best-performing Random Forest model achieved an Overall Accuracy of 86% ($\kappa = 0.73$) for binary defoliation detection [Bhattarai et al., 2020]. Although spruce budworm defoliation differs from bark beetle infestation, these findings demonstrate the potential of Sentinel-2 Red Edge and related spectral information for detecting subtle changes in conifer canopy condition [Bhattarai et al., 2020; Abdullah et al., 2019].

3.4.Multi-Temporal Spectral Indicators and Forest Stress Detection

Single-date spectral observations provide information on canopy condition at a given point in time but may be insufficient for distinguishing disturbance-related changes from normal seasonal variability [Brun et al., 2020; Schiller et al., 2024]. Multi-temporal Sentinel-2 observations can therefore be used to characterise the expected seasonal trajectory of vegetation indices and identify deviations associated with physiological stress or disturbance [Brun et al., 2020; Schiller et al., 2024].

A combination of complementary vegetation indices is recommended to capture different components of the forest stress response [Delegido et al., 2011; Bhattarai et al., 2020]. Greenness-sensitive indices such as Normalised Difference Vegetation Index (NDVI) primarily describe changes in canopy greenness and photosynthetic activity [Brun et al., 2020], while Red Edge-based indices such as Normalised Difference RedEdge Index (NDRE) provide greater sensitivity to chlorophyll-related changes [Delegido et al., 2011; Bhattarai et al., 2020]. Moisture-sensitive indices such as Normalised Difference Moisture Index (NDMI) can provide complementary information on canopy water status and changes in vegetation moisture content [Bhattarai et al., 2020]. While Red Edge indices are extensively utilized, seasonal trajectories of Tasselled Cap Wetness (TCW) and SWIR-

based metrics have also demonstrated competitive capabilities (78% OA) in separating green-attack stages in Central European spruce monocultures [Bárta et al., 2021]. Furthermore, purpose-built indices such as the Normalized Distance Red & SWIR (NDRS) have been introduced specifically for bark beetle stress detection, yielding high classification accuracies ($0.80 - 0.91$) across early and late infestation phases [Huo et al., 2021].

Temporal analysis can further improve disturbance detection by comparing current observations with a site-specific or seasonally adjusted baseline [Brun et al., 2020; Schiller et al., 2024]. Deviations from the expected trajectory can be expressed as spectral anomalies and subsequently used as inputs for disturbance classification [Brun et al., 2020]. This approach is particularly relevant for early stress detection because physiological changes during the 'green-attack' phase may occur weeks before pronounced changes in visible canopy colour become apparent [Abdullah et al., 2019; Bhattarai et al., 2020].

3.5.Deep Learning Architectures for Forest Disturbance Detection

Deep learning provides a framework for integrating the spectral and temporal information contained in dense Sentinel-2 time series [Schiller et al., 2024]. Convolutional architectures (such as U-Net) have proven superior to traditional machine learning classifiers (Random Forest (RF), Support Vector Machine (SVM)) for spatial segmentation of storm and insect damage [Kislov et al., 2021]. Transformer-based architectures can model temporal dependencies across multiple observations and learn relationships among spectral features without requiring all information to be represented through predefined vegetation indices [Schiller et al., 2024].

Schiller et al. (2024) demonstrated the potential of this approach using Satellite Image Time Series Bidirectional Encoder Representations from Transformers (SITS-BERT), a Transformer-based architecture adapted for satellite image time series, for forest disturbance detection across Germany and Luxembourg. The study compared three configurations: DL base, using ten Sentinel-2 spectral bands; DL IND, using ten vegetation indices; and DL + IND, combining spectral bands and vegetation indices [Schiller et al., 2024]. The Transformer architecture uses self-attention to capture both short- and long-term temporal dependencies within multi-year Sentinel-2 time series without requiring conventional gap filling or interpolation [Schiller et al., 2024].

Across the six study sites, F1-scores (F1-score (harmonic mean of Precision and Recall)) for binary classification of undisturbed and disturbed forest ranged approximately from 0.65 to 0.72, depending on the model configuration and disturbance definition [Schiller et al., 2024]. The DL base configuration, which used the raw Sentinel-2 spectral bands, generally outperformed the vegetation-index-only and combined configurations [Schiller et al., 2024]. This suggests that deep learning models may be capable of learning informative spectral representations directly from the original observations rather than relying exclusively on manually defined indices [Schiller et al., 2024]. However, differences in study areas, disturbance definitions, training strategies, and validation procedures limit direct comparisons of reported performance across studies [Schiller et al., 2024].

Building on these findings, a Transformer-based framework can be considered for integrating multi-temporal Sentinel-2 observations for forest disturbance detection [Schiller et al., 2024]. Such a framework can incorporate both raw spectral bands and selected vegetation indices, allowing the model to learn temporal patterns associated with the transition from healthy to physiologically stressed and subsequently disturbed forest [Schiller et al., 2024; Abdullah et al., 2019] (Figure 2).

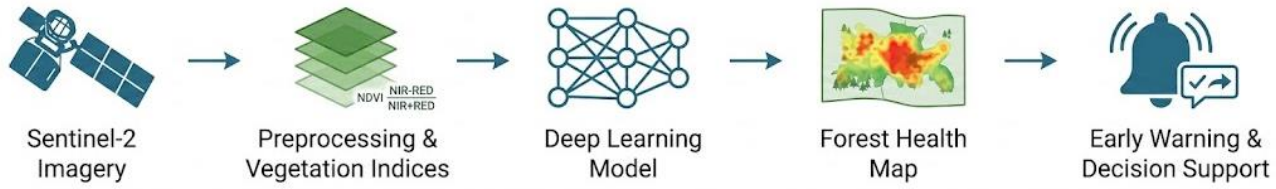


Figure 2. *Conceptual workflow for DL-based forest health monitoring using Sentinel-2 imagery*

3.6.Accuracy Metrics: Definitions and Interpretation

Model performance was evaluated using standard classification and segmentation metrics reported across the reviewed literature. To avoid misinterpretation, these metrics should not be treated as interchangeable [Powers, 2011].

- Overall Accuracy (OA): Measures the proportion of correctly classified instances:

$$OA = \frac{TP+TN}{TP+TN+FP+FN} \quad (1)$$

While intuitive, OA can provide an overly optimistic impression in imbalanced datasets where non-disturbance dominates [Congalton & Green, 2019].

- Precision & Recall: Precision ($TP/(TP+FP)$) reflects alert reliability by quantifying false positives, whereas Recall ($TP/(TP+FN)$) measures sensitivity to actual disturbances—a critical priority for early-warning systems [Powers, 2011].

- F1-score: The harmonic mean of Precision and Recall:

$$F1 = 2 \times \frac{\text{Precision} \times \text{Recall}}{\text{Precision} + \text{Recall}} \quad (2)$$

Ranging from 0 to 1, the F1-score provides a robust benchmark when the disturbance class is infrequent [Powers, 2011].

- Intersection over Union (IoU / Jaccard Index): Evaluates spatial segmentation by measuring region overlap:

$$\text{IoU} = \frac{TP}{TP+FP+FN} \quad (3)$$

An IoU of 1 indicates perfect overlap, making it essential for delineating spatial disturbance extents.

- Cohen's Kappa (κ): Assesses agreement corrected for chance:

$$\kappa = \frac{p_o - p_e}{1 - p_e} \quad (4)$$

where p_o is observed and p_e is expected chance agreement [Cohen, 1960; Congalton & Green, 2019]. Since κ depends heavily on class distribution, this review prioritizes F1-score, Precision, Recall, and IoU, retaining OA and κ primarily for cross-study comparison.

Cross-study metric comparisons must be interpreted cautiously. Reported performance is strongly conditioned by experimental design, including disturbance definitions, reference data quality, spatial resolution, and validation strategies [Congalton & Green, 2019; Schiller et al., 2024]. Consequently, higher numerical metrics do not automatically denote architectural superiority. Throughout this review, absolute accuracy differences are expressed strictly in percentage points (pp) rather than relative changes.

4. Results and Synthesis

4.1. Red Edge Spectral Bands: Spectral Basis for Early Detection

The reviewed literature consistently demonstrates that Sentinel-2's Red Edge bands are indispensable for detecting early-stage forest stress. Delegido et al. (2011) established this at the spectral level: excluding B5 and B6 from the NAOC (Normalized Area Over the Chlorophyll Absorption Curve) chlorophyll retrieval algorithm caused the correlation between the index and canopy chlorophyll to break down, particularly at higher vegetation densities. Bhattarai et al. (2020) confirmed the same pattern in an applied pest-detection context: the five best predictors for detecting spruce budworm defoliation were all Red Edge Spectral Vegetation Indices (SVIs) - EVI7, MCARI, IRECI, NDII11, MSR, outperforming NDVI and broadband EVI. The authors attribute this superiority to the sensitivity of the Red Edge region to even small changes in leaf chlorophyll content — the earliest measurable biochemical response to both water stress and pest attack.

The operational consequence of this spectral advantage is a temporal one. Abdullah et al. (2019), comparing Sentinel-2 and Landsat-8 for bark beetle green-attack mapping in Bavaria, demonstrated that Sentinel-2's Red Edge-based models detected infested stands within the green-attack phase — weeks before visible crown discolouration (Table 1). This early detection falls within the critical operative window for preventive salvage harvesting before adult beetles emerge and disperse to neighbouring trees.

Table 1. *Summary of reviewed DL/ML studies, methods, and key findings*

Study	Method / Data	Context	Findings
Abdullah et al. (2019)	Sentinel-2 vs Landsat-8 spectral indices	Bavaria, Germany; bark beetle green-attack	Sentinel-2 Red Edge bands detect green-attack phase earlier than Landsat-8, within the operative window for preventive salvage harvesting.
Bárta et al. (2021)	Sentinel-2 TCW & SWIR time series	Czech Republic; spruce monocultures	Tasselled Cap Wetness trajectories achieve 78% OA for green-attack detection, highlighting water-sensitive bands as key complementary pathways.
Bhattarai et al. (2020)	Random Forest + SVM; 20 SVIs from Sentinel-2	New Brunswick, Canada; spruce budworm	Best predictors for defoliation detection are Red Edge SVIs (EVI7, MCARI, IRECI); OA 86% (RF); Red Edge outperforms NDVI/EVI8.
Brun et al. (2020)	Sentinel-2 NDVI time series; Random Forest	Central Europe; 2018 drought	Early wilting detected across 21,524 ± 2,846 km² (10.8% of forested area); lasting impact on spring greenness in 2019.
Delegido et al. (2011)	Simulated Sentinel-2 data; NDI and NAOC indices	ESA field campaigns; LAI and chlorophyll retrieval	Red Edge bands essential for chlorophyll retrieval; RMSE 0.6 for LAI; excluding Red Edge causes systematic errors.
Huo et al. (2021)	Sentinel-2; NDRS index development	Sweden; bark beetle stress	Proposed NDRS index achieves 0.80–0.91 accuracy across early, mid, and late infestation stages.
Kautz et al. (2024)	Critical review / Meta-analysis	Global / European forests	Highlights that pre-emergence green-attack detection accuracy remains operationally limited due to sparse rigorous ground-truth data.
Schiller et al. (2024)	Transformer (SITS-BERT) + Sentinel-2 time series	Germany + Luxembourg; forest disturbance 2015–2022	F1-scores 0.65–0.72 across six sites; DL base (raw S2 bands) outperforms VI-based setups.
Seidl et al. (2017)	Literature synthesis; 674 papers reviewed	Global; all forest biomes	Under warmer/drier conditions, 78.4% of observations project increasing insect disturbance; coniferous forests most at risk.
Senf & Seidl (2021)	Landsat disturbance map; Random Forest attribution	Europe 1986–2016; 27 million patches	Storm and fire each ~7% of total disturbances; majority of disturbances stem from other agents including biotic attacks.

4.2. Transformer-Based DL Applied to Sentinel-2 Time Series

Schiller et al. (2024) provided a rigorous evaluation of deep learning applied to dense Sentinel-2 Satellite Image Time Series (SITS) for forest disturbance detection. Pre-trained on over one million samples and fine-tuned on visually interpreted aerial imagery across six study sites, their SITS-BERT Transformer model achieved F1-scores between 0.65 and 0.72, with overall accuracies exceeding 0.91 across all configurations (Table 2).

A notable technical capability of the SITS-BERT model is sub-pixel disturbance mapping, detecting canopy losses as small as 40 m^2 within a standard 100 m^2 (10×10 m) Sentinel-2 pixel. This aligns with broader remote sensing observations that temporal Transformer architectures effectively identify partial canopy losses covering 25–75% of a pixel cell (Perbet et al., 2024).

The deep learning setup utilizing raw spectral bands consistently outperformed models relying solely on pre-defined vegetation indices. Transformers dynamically learn non-linear spectral-temporal combinations directly from high-dimensional time series, avoiding the information bottlenecks associated with pre-calculated indices.

Table 2. *Accuracy metrics reported across key forest disturbance detection studies.*

Study	Task	Best model	Reported accuracy
Schiller et al. (2024)	Forest disturbance detection (undisturbed vs disturbed)	DL base (Transformer + 10 S2 bands)	F1: 0.65–0.72 across 6 sites; OA: >0.91 all setups
Bhattarai et al. (2020)	Spruce budworm defoliation detection	Random Forest + Red Edge SVIs	OA: 86%, kappa: 0.73 (single-year, RF)
Brun et al. (2020)	Early wilting mapping (drought response)	Random Forest + Sentinel-2 NDVI SITS	OA: 0.90 ± 0.014; PPV: 0.63 ± 0.030
Bárta et al. (2021)	Green-attack detection	Random Forest + TCW / SWIR indices	OA: 78%

4.3. Large-Scale Drought Stress Detection

Brun et al. (2020) demonstrate that Sentinel-2-based satellite monitoring can detect large-scale drought stress responses in Central European forests with high accuracy. Their random forest classifier, trained on NDVI time series statistics and validated against independent visual interpretation, achieved an overall accuracy of 0.90 ± 0.014 in mapping early wilting presence and absence. The study reveals that precipitation was the strongest climatic driver of early wilting tendency, followed by temperature anomalies — findings that establish a direct link between the climate forcing documented by Seidl et al. (2017) and the satellite-detectable forest response monitored by Schiller et al. (2024) and related approaches. A comparative summary of the performance metrics across these forest disturbance detection studies is provided in Table 2.

5. Discussion

5.1. Synthesis of Current Evidence

The reviewed studies collectively establish a coherent and empirically grounded case. Seidl et al. (2017) and Senf & Seidl (2021) provide the ecological and disturbance-regime context: climate change is increasing insect disturbance activity, and bark beetle outbreaks constitute a major and growing component of European forest disturbance. Delegido et al. (2011) and Bhattarai et al. (2020) establish the spectral justification for using Sentinel-2 Red Edge bands: they are necessary for detecting early chlorophyll changes and defoliation, and cannot be replaced by NDVI or broadband EVI. Abdullah et al. (2019) translate this spectral advantage into an operational temporal one, showing that Red Edge-based detection can capture the green-attack phase within the salvage

harvesting window. Brun et al. (2020) demonstrate that satellite-detectable drought stress signals are real, large-scale, and persistent. Schiller et al. (2024) show that Transformer-based DL applied to Sentinel-2 time series achieves state-of-the-art results for forest disturbance detection, with F1-scores of 0.65–0.72 and sub-pixel sensitivity. What the evidence does not yet show — and what would be needed to claim an operational early warning system — is a study that simultaneously achieves:

(1) green-attack-specific detection using Red Edge DL models;

(2) validation across multiple European bioclimatic regions; and

(3) integration of climate-driven hydro-meteorological forcing as predictive inputs. Each of these elements exists in partial form across the reviewed studies, but no single study has combined them.

5.2. Key Limitations Across the Reviewed Literature

Three limitations recur across the reviewed studies. First, training data quality and temporal resolution: Schiller et al. (2024) note that their pre-training datasets contain commission errors and that disturbances that occurred early in the classified time series tend to be missed due to vegetation recovery. Second, cross-regional transferability: Schiller et al. (2024) validate across six sites within Germany and Luxembourg, but acknowledge that broader geographic coverage is needed, and that open stands and steep terrain introduce classification errors. Third, the absence of climate drivers from DL frameworks: all reviewed DL studies treat forest disturbance as a function of spectral state alone. None integrates drought indices or atmospheric teleconnection patterns as auxiliary predictors — despite the evidence from Seidl et al. (2017) and Brun et al. (2020) that these climatic drivers are mechanistically important and measurable.

Three principal limitations persist across current studies:

1. **Training Data Constraints:** Lack of high-density ground-truth validation data during early green-attack stages limits model training [Kautz et al., 2024].
2. **Cross-Regional Transferability:** Model performance degrades when applied across varying topographies, open canopy structures, or differing bioclimatic zones [Schiller et al., 2024].
3. **Absence of Hydro-Climatic Exogenous Inputs:** Existing DL models treat spectral change as an isolated variable without incorporating external meteorological triggers.

5.3. Hydro-Climatic Drivers and Future Directions

While remote sensing effectively monitors physical canopy degradation, incorporating exogenous hydro-climatic variables can extend model capabilities toward true predictive forecasting. As established by Seidl et al. (2017) and Brun et al. (2020), severe precipitation deficits and heatwaves are the primary physiological triggers that pre-condition forests to secondary pest infestations and massive wilting events. Integrating meteorological drought indicators — such as the Standardised Precipitation-Evapotranspiration Index (SPEI), soil moisture anomalies, and atmospheric teleconnection indices (e.g., North Atlantic Oscillation) — as auxiliary tabular inputs into temporal deep learning architectures (such as the SITS-BERT model by Schiller et al., 2024) represents a vital future research path. Combining exogenous climate forcing with high-resolution Sentinel-2 Red Edge spectral time series could shift the monitoring paradigm from reactive disturbance detection to proactive, lead-time risk forecasting — identifying high-vulnerability forest stands before visible spectral stress signatures appear.

Incorporating hydro-climatic variables represents a vital path toward predictive early warning systems. Meteorological drought indicators, such as the Standardised Precipitation-Evapotranspiration Index (SPEI) [Vicente-Serrano et al., 2010], soil moisture anomalies, and atmospheric indices (e.g., North Atlantic Oscillation (NAO)) directly capture the physiological drivers of forest vulnerability. Integrating these tabular drivers as auxiliary inputs alongside spectral time series in Transformer frameworks could enable pre-visual risk mapping.

Furthermore, integrating Synthetic Aperture Radar (SAR) data addresses optical cloud cover limitations. Multi-sensor fusion combining Sentinel-1 SAR and Sentinel-2 optical time series has demonstrated modest improvements in disturbance classification [König et al., 2023], while advanced self-attention Transformer fusion mechanisms have been shown to increase disturbance classification performance by 5–14% over optical data alone [Zhang et al., 2025].

6. Conclusions

Red Edge Indispensability: Sentinel-2's Red Edge bands are spectrally required for detecting pre-visual chlorophyll degradation and early physiological stress. Excluding these bands leads to systematic errors in leaf area index and chlorophyll retrieval that cannot be compensated for by traditional broadband indices.

Large-Scale Stress Mapping: Satellite image time series enable continuous monitoring of drought-induced canopy stress over vast geographical scales, capturing persistent, multi-year legacy effects on forest productivity following extreme hydro-climatic events.

Deep Learning & Transformer Efficiency: Temporal Transformer architectures applied to raw multi-spectral SITS achieve state-of-the-art disturbance detection performance. Operating directly on raw spectral bands allows these models to capture complex non-linear temporal dynamics and achieve sub-pixel spatial resolution.

Shift in Disturbance Regimes: Climate change is accelerating forest disturbance dynamics across Europe, with biotic agents—specifically bark beetle infestations and defoliation events amplified by drought—surpassing fire and windthrow as the primary driver of canopy loss.

Paradigm Shift toward Proactive Forecasting: The critical frontier in forest health monitoring lies in fusing exogenous hydro-climatic indicators and SAR time series directly into temporal deep learning frameworks. This integration enables a transition from reactive disturbance detection to proactive, lead-time risk forecasting.

References

Abdullah, H., Skidmore, A. K., Darvishzadeh, R., Heurich, M. (2019). Sentinel-2 accurately maps green-attack stage of European spruce bark beetle (*Ips typographus* L.) compared with Landsat-8. *Remote Sensing in Ecology and Conservation*, Vol. 5, No. 2, pp. 87–106. DOI: 10.1002/rse2.93.

Anderegg, W. R. L., Schwalm, C., Biondi, F., et al. (2015). Pervasive drought legacies in forest ecosystems and their implications for carbon cycle models. *Science*, Vol. 349, No. 6247, pp. 528–532. DOI: 10.1126/science.aab1833.

Bárta, V., Lukeš, P., Homolová, L. (2021). Early detection of bark beetle infestation in Norway spruce forests of Central Europe using Sentinel-2. *International Journal of Applied Earth Observation and Geoinformation*, Vol. 100, 102335. DOI: 10.1016/j.jag.2021.102335.

Bhattarai, R., Rahimzadeh-Bajgiran, P., Weiskittel, A., MacLean, D. A. (2020). Sentinel-2-based prediction of spruce budworm defoliation using red-edge spectral vegetation indices. *Remote Sensing Letters*, Vol. 11, No. 8, pp. 777–786. DOI: 10.1080/2150704X.2020.1767824.

Brun, P., Psomas, A., Ginzler, C., Thuiller, W., Zappa, M., Zimmermann, N. E. (2020). Large-scale early-wilting response of Central European forests to the 2018 extreme drought. *Global Change Biology*, Vol. 26, No. 12, pp. 7021–7035. DOI: 10.1111/gcb.15360.

Cohen, J. (1960). A coefficient of agreement for nominal scales. *Educational and Psychological Measurement*, Vol. 20, No. 1, pp. 37–46. DOI: 10.1177/001316446002000104.

Congalton, R. G., Green, K. (2019). *Assessing the Accuracy of Remotely Sensed Data: Principles and Practices*. 3rd ed. CRC Press.

Delegido, J., Verrelst, J., Alonso, L., Moreno, J. (2011). Evaluation of Sentinel-2 red-edge bands for empirical estimation of green LAI and chlorophyll content. *Sensors*, Vol. 11, No. 7, pp. 7063–7081. DOI: 10.3390/s110707063.

Dosovitskiy, A., Beyer, L., Kolesnikov, A., et al. (2021). An image is worth 16 × 16 words: Transformers for image recognition at scale. *Proceedings of the International Conference on Learning Representations (ICLR)*.

European Space Agency (2015). *Sentinel-2 User Handbook*. ESA Standard Document. Available at: https://sentinels.copernicus.eu/documents/247904/685211/Sentinel-2_User_Handbook.

Georgiev, G., Georgieva, M., Belilov, S., Mirchev, P., Deliyanchev, S., Mladenov, V., Kropov, K., Haydarova, S. (2022). Early detection of *Ips typographus* infestations by using Sentinel-2 satellite images in windthrow-affected Norway spruce forests in Smolyan region, Bulgaria. *Silva Balcanica*, Vol. 23, No. 2, pp. 27–34.

Grigorov, B., Bozhkov, P., Morunov, Y. (2025). Application of vegetation indices as a step towards the relevance of the state of beech forest habitats: A case study from Boatin Reserve, Central Bulgaria. *Aerospace Research in Bulgaria*, Vol. 37, pp. 108–117. DOI: 10.3897/arb.v37.e10.

Huo, L., Persson, H. J., Lindberg, E. (2021). Early detection of forest stress from European spruce bark beetle attack, and a new vegetation index: Normalized Distance Red & SWIR (NDRS). *Remote Sensing of Environment*, Vol. 255, 112240. DOI: 10.1016/j.rse.2020.112240.

Immitzer, M., Vuolo, F., Atzberger, C. (2016). First experience with Sentinel-2 data for crop and tree species classifications in Central Europe. *Remote Sensing*, Vol. 8, No. 3, 166. DOI: 10.3390/rs8030166.

Ivanov, M. A., Tyufekchiev, K. A. (2019). Remote sensing-based vegetation analysis in Parangalitsa Reserved Area. *Ecologia Balkanica*, Special Edition 2, pp. 187–197.

Kautz, M., Feurer, J., Adler, P. (2024). Early detection of bark beetle (*Ips typographus*) infestations by remote sensing: A critical review of recent research. *Forest Ecology and Management*, Vol. 556, 121595. DOI: 10.1016/j.foreco.2023.121595.

Kislov, D. E., Korznikov, K. A., Altman, J., Vozmishcheva, A. S., Krestov, P. V. (2021). Extending deep learning approaches for forest disturbance segmentation on very high-resolution satellite images. *Remote Sensing in Ecology and Conservation*, Vol. 7, No. 3, pp. 355–368. DOI: 10.1002/rse2.194.

König, S., Thonfeld, F., Förster, M., Dubovyk, O., Heurich, M. (2023). Assessing combinations of Landsat, Sentinel-2 and Sentinel-1 time series for detecting bark beetle infestations. *GIScience & Remote Sensing*, Vol. 60, No. 1, 2226515. DOI: 10.1080/15481603.2023.2226515.

Lévesque, M., Andreu-Hayles, L., Pederson, N., Martin-Benito, D., Hember, R. A., Cook, E. R., Nöjd, P., Bergeron, Y. (2014). Growth response of five co-occurring conifers to drought across a wide climatic gradient in Central Europe. *Agricultural and Forest Meteorology*, Vol. 197, pp. 1–12. DOI: 10.1016/j.agrformet.2014.06.001.

Netherer, S., Matthews, B., Katzensteiner, K., Blackwell, E., Henschke, P., Hietz, P., Pennerstorfer, J., Rosner, S., Kikuta, S., Schume, H., Schopf, A. (2015). Do water-limiting conditions predispose Norway spruce to bark beetle attack? *New Phytologist*, Vol. 205, pp. 1128–1141. DOI: 10.1111/nph.13166.

Netherer, S., Lehmanski, L., Bachlehner, A., Rosner, S., Savi, T., Schmidt, A., Huang, J., Paiva, M. R., Mateus, E., Hartmann, H., Gershenzon, J. (2024). Drought increases Norway spruce susceptibility to the Eurasian spruce bark beetle and its associated fungi. *New Phytologist*, Vol. 242, pp. 1000–1017. DOI: 10.1111/nph.19635.

Perbet, P., Guindon, L., Côté, J.-F., Béland, M. (2024). Evaluating deep learning methods applied to Landsat time-series subsequences to detect and classify boreal forest disturbance events: The challenge of partial and progressive disturbances. *Remote Sensing of Environment*, Vol. 306, 114107. DOI: 10.1016/j.rse.2024.114107.

Powers, D. M. W. (2011). Evaluation: From precision, recall and F-measure to ROC, informedness, markedness and correlation. *Journal of Machine Learning Technologies*, Vol. 2, No. 1, pp. 37–63.

Ray, D., Fung, F., Pirret, J., Plenderleith, F., Trotter, F., Marchi, M. (2025). Risk of extreme climate impacts on European Norway spruce forest: Drought and frost in the climate emergency. *Climatic Change*, Vol. 178, 114. DOI: 10.1007/s10584-025-03954-z.

Schiller, C., Költzow, J., Schwarz, S., Schiefer, F., Fassnacht, F. E. (2024). Forest disturbance detection in Central Europe using transformers and Sentinel-2 time series. *Remote Sensing of Environment*, Vol. 315, 114475. DOI: 10.1016/j.rse.2024.114475.

Seidl, R., Thom, D., Kautz, M., Martin-Benito, D., Peltoniemi, M., Vacchiano, G., Reyer, C. P. O. (2017). Forest disturbances under climate change. *Nature Climate Change*, Vol. 7, pp. 395–402. DOI: 10.1038/nclimate3303.

Senf, C., Seidl, R. (2021). Storm and fire disturbances in Europe: Distribution and trends. *Global Change Biology*, Vol. 27, No. 15, pp. 3605–3619. DOI: 10.1111/gcb.15679.

Stankova, N. (2023). Post-fire recovery monitoring using remote sensing: A review. *Aerospace Research in Bulgaria*, Vol. 35, pp. 192–200. DOI: 10.3897/arb.v35.e19.

Tarasiou, M., Chavez, E., Zafeiriou, S. (2023). ViTs for SITS: Vision transformers for satellite image time series. *Proceedings of the IEEE/CVF Conference on Computer Vision and Pattern Recognition (CVPR)*, pp. 10418–10428. DOI: 10.1109/CVPR52729.2023.01004.

Todorova, E., Zhiyanski, M. (2025). Spatial and temporal exploration of NDVI, LAI, and SMI in coniferous forests: Detecting changes in Parangalitsa Reserve. *Journal of the Bulgarian Geographical Society*, Vol. 52, pp. 59–78. DOI: 10.3897/jbgs.e140222.

Vicente-Serrano, S. M., Beguería, S., López-Moreno, J. I. (2010). A multiscalar drought index sensitive to global warming: The Standardized Precipitation Evapotranspiration Index. *Journal of Climate*, Vol. 23, No. 7, pp. 1696–1718. DOI: 10.1175/2009JCLI2909.1.

Zhang, M., Li, G., Lu, D., Xu, C., Zhao, H., Li, D. (2025). Self-supervised deep learning for detection of forest disturbance types in a subtropical ecosystem using transformer and Sentinel-1 and Sentinel-2 time-series data. *International Journal of Digital Earth*, Vol. 18, No. 1, 2537325. DOI: 10.1080/17538947.2025.2537325.